The Journal on Advanced Studies in Theoretical and Experimental Physics, including Related Themes from Mathematics

PROGRESS IN PHYSICS

"All scientists shall have the right to present their scientific research results, in whole or in part, at relevant scientific conferences, and to publish the same in printed scientific journals, electronic archives, and any other media."
— Declaration of Academic Freedom, Article 8

JULY 2013   VOLUME 3

CONTENTS

CONTENTS

On the Propagation of Light in an Expanding Universe

Yuri Heymann

3 rue Chandieu, 1202 Geneva, Switzerland. E-mail: y.heymann@yahoo.com

The equation of the propagation of light in an expanding Universe is derived based on the definition of comoving distances. A numerical method is proposed to solve this equation jointly with the Friedmann equation. As the equation of the propagation of light in an expanding Universe defines a horizon of the visible Universe, this puts a constraint on cosmological models in order to be consistent with an upper limit for redshifts observed from galaxies. This puzzle is challenging current expansionist cosmological models.

1 Introduction

Euclidean Distances were introduced in [1] in order to derive the galactic density profile which is the evolution of galactic density over time. We define the Euclidean Distance as the equivalent distance that would be traversed by a photon between the time it is emitted and the time it reaches the observer if there were no expansion of the Universe. The comoving distance is the distance between two points measured along a path defined at the present cosmological time. The comoving distance between objects moving with the Hubble flow is deemed to remain constant in time. The Euclidean Distance is also the proper distance at the time of emission for a source of light, which is the comoving distance multiplied by the scale factor at the time of emission. From this relationship, the equation of the propagation of light in an expanding Universe is derived.

2 Equation of the propagation of light in an expanding Universe

As the Euclidean Distance is the proper distance at the time light was emitted from a source of light, it is equal to the comoving distance times the scale factor at the time of emission. By convention the scale factor is equal to one at the present time. Therefore, we have

$$y = a(t)\chi, \tag{1}$$

and

$$\chi = c \int_{t=T_b-T}^{T_b} \frac{dt}{a(t)}, \tag{2}$$

where χ is the comoving distance, y the Euclidean Distance, a the scale factor, T_b the time from the hypothetical big bang (which is the present time), and T the light travel time between observer and the source of light.

By differentiating (1) with respect to time we get:

$$\frac{dy}{dt} = \dot{a}\chi + a\dot{\chi}. \tag{3}$$

As $I = \int_{t_1}^{t_2} f(t)\,dt$ leads to $\frac{dI}{dt} = \frac{dt_2}{dt} f(t_2) - \frac{dt_1}{dt} f(t_1)$, from (2) we get:

$$\dot{\chi} = -\frac{c}{a(t)}. \tag{4}$$

As $H(t) = \dot{a}/a$, (1) leads to:

$$\dot{a}\chi = y\,H(t), \tag{5}$$

Combining (3), (4) and (5) we get:

$$\frac{dy}{dt} = -c + H(t)\,y, \tag{6}$$

where y is the Euclidean Distance between the observer and a photon moving towards the observer.

We have just derived the equation of the propagation of light in an expanding Universe from the definition of comoving distances. This equation defines a horizon of the visible Universe at $\frac{dy}{dt} = 0$.

3 Numerical method to compute Euclidean Distances from the Friedmann equation

Equation (6) can be solved numerically using a discretization method. Let us set $t = T_b - T$ with T_b the hypothetical time since the big bang, and T the light travel time between observer and the photon. Therefore, $dt = -dT$, and (6) can be rewritten as follows:

$$\frac{dy}{dT} = c - H(T)\,y. \tag{7}$$

By discretization over small intervals ΔT, (7) leads to:

$$\frac{y_{n+1} - y_n}{\Delta T} = c - H(T_n)\,y_n. \tag{8}$$

Therefore, we obtain:

$$y_{n+1} = c\,\Delta T + y_n\,(1 - H(T_n)\,\Delta T), \tag{9}$$

with initial conditions: $y_0 = 0$ and $T_0 = 0$, and $T_{n+1} = T_n + \Delta T$.

The Friedmann equation expresses H as a function of redshift z. We still need a description of H as a function of T in order to solve (9). For this purpose we compute a curve for the light travel time T versus redshift z using the Friedmann equation, with (11). Then we fit an empirical equation for $H(T)$ over the curve $H(z)$ versus T.

The light travel time versus redshift is computed as follows (derived from $dt = da/\dot{a}$):

$$T = c \int_{1/(1+z)}^{1} \frac{da}{\dot{a}} . \qquad (10)$$

Because $H = \dot{a}/a$, (10) can be rewritten as follows:

$$T = c \int_{1/(1+z)}^{1} \frac{da}{H a} . \qquad (11)$$

This integral is solved numerically using a solver such as Matlab.

The Friedmann equation that is used in this problem is as follows:

$$H = H_0 \sqrt{\Omega_R a^{-4} + \Omega_M a^{-3} + \Omega_k a^{-2} + \Omega_\Lambda} , \qquad (12)$$

with Ω_R the radiation energy density today, Ω_M the matter density today, Ω_k the spatial curvature density today, and Ω_Λ a cosmological constant for the vacuum energy density today. We may alternatively express H as a function of redshift from cosmological redshift relationship by setting $a = \frac{1}{1+z}$, where the scale factor is equal to unity as the present time.

4 Results and discussion

First let us solve the above problem with the assumptions used in the lambda-cdm model [2]. The radiation energy density is generally considered neglegible, hence $\Omega_R = 0$. The common assumption in the lambda-cdm is that Ω_k is equal to zero, and $\Omega_\Lambda = 1 - \Omega_M$. To obtain a description of H as a function of T, we fit a polynomial function of order six to the $H(z)$ curve, which gives the following empirical formula for $\Omega_M = 0.3$ and $H_0 = 71 \, km \, s^{-1} \, Mpc^{-1}$: $H(T) = 0.074663 - 0.049672 \, T + 0.056296 \, T^2 - 0.021203 \, T^3 + 0.0036443 \, T^4 - 0.00029054 \, T^5 + 0.0000088134 \, T^6$, with T in $Glyr$ and $H(T)$ in $Glyr^{-1}$. From the discretization method (9) we obtain an horizon of the visible Universe at redshift $z = 1.6$. A variant of the lambda-cdm model would be to remove the cosmological constant for the vacuum energy density ($\Omega_\Lambda = 0$), and replace this term by the spatial curvature density $\Omega_k = 1 - \Omega_M$. This variant gives almost the same result with a horizon of the visible Universe at redshift $z = 1.5$. On the other hand if H is constant over time, the horizon of the visible Universe would have a redshift that tends to infinity.

The results obtained with the equation we derived for the propagation of light solved jointly with the Friedmann equation are inconsistent with observations as it is common to observe galaxies with redshifts up to 6, and more recently beyond 8.5 [3]. This problem has been raised in the past – the recession velocity of all galaxies with $z \geq 1.5$ has been found to exceed the speed of light in all viable cosmological models [4]. A calculation based on null geodesics using gravitational radius is proposed in [5]. Their hypothesis is that the

comoving distance and proper distance do not track the propagation of light through the Hubble flow. The puzzle of the propagation of light in an expanding Universe and the horizon of the visible Universe appears to be an interesting challenge for current expansionist cosmological models.

References

1. Heymann Y. Building galactic density profiles. *Progress in Physics*, 2011, v. 4, 63–67.

2. Wright E. L. A Cosmology Calculator for the World Wide Web. *The Publications of the Astronomical Society of the Pacific*, 2006, v. 118, 1711–1715.

3. Ellis R. S., McLure R. J., Dunlop J. S., Robertson B. E., Ono Y., Schenker M. A., Koekemoer A., Bowler R. A. A., Ouchi M., Rogers A. B., Curtis-Lake E., Schneider E., Charlot S., Stark D. P., Furlanetto S. R., and Cirasuolo M. The abundance of star-forming galaxies in the redshift range 8.5-12: new results from the 2012 Hubble Ultra deep field campaign. *The Astrophysical Journal Letters*, 2013, v. 763, 1–6.

4. Davis T. and Lineweaver C. H. Expanding Confusion: Common Misconceptions of Cosmological Horizons and the Superluminal Expansion of the Universe. *Publications of the Astronomical Society of Australia*, 2004, v. 21, 97–109.

5. Bikwa O., Melia F., and Shevchuk A. Photon Geodesics in FRW Cosmologies. *Monthly Notices of the Royal Astronomical Society*, 2012, v. 421, 3356–3361.

On the Luminosity Distance and the Hubble Constant

Yuri Heymann

3 rue Chandieu, 1202 Geneva, Switzerland. E-mail: y.heymann@yahoo.com

By differentiating luminosity distance with respect to time using its standard formula we find that the peculiar velocity is a time varying velocity of light. Therefore, a new definition of the luminosity distance is provided such that the peculiar velocity is equal to c. Using this definition a Hubble constant $H_0 = 67.3 \, \text{km s}^{-1} \, \text{Mpc}^{-1}$ is obtained from supernovae data.

1 Introduction

The luminosity distance is an important concept in cosmology as this is the distance measure obtained from supernovae data using the distance modulus. The standard formula of the luminosity distance is $d_L = (1 + z) \, d_M = d_M/a$, where d_L is the luminosity distance and d_M the comoving transverse distance [1, p. 421]. As shown below this definition implies that the peculiar velocity is a time varying velocity of light, and therefore a new definition is proposed where the speed of light is constant.

2 Definition of the luminosity distance and the peculiar velocity from light propagation

From there we will use the notation r_L for the luminosity distance as it represents the radius of a sphere for light propagating from the center which is the point of emission of the light source. The standard formula of the luminosity distance for a flat Universe is as follows:

$$r_L = \frac{\chi}{a}, \tag{1}$$

and

$$\chi = c \int_0^{t_0} \frac{dt}{a}, \tag{2}$$

where r_L is the luminosity distance, χ the comoving distance, a the scale factor at the time of emission, t the time which is equal to zero at the origin set at the center of the sphere from which light is emitted, and t_0 the time when light reaches the earth.

Let us apply the change of coordinates $T = t_0 - t$, where T is the light travel time between the observer and the photon. Hence, $dt = -dT$, and (2) can be rewritten as follows:

$$\chi = -c \int_T^0 \frac{dT}{a} = c \int_0^T \frac{dT}{a}. \tag{3}$$

By differentiating (1) with respect to T we get:

$$\frac{dr_L}{dT} = \frac{\dot{\chi}}{a} - \frac{\dot{a}}{a^2} \chi. \tag{4}$$

As $I = \int_{t_1}^{t_2} f(t) \, dt$ leads to $\frac{dI}{dt} = \frac{dt_2}{dt} f(t_2) - \frac{dt_1}{dt} f(t_1)$, from (3) we get:

$$\dot{\chi} = \frac{c}{a}. \tag{5}$$

Using (1) we get:

$$\frac{\dot{a}}{a^2} \chi = \frac{\dot{a}}{a} r_L. \tag{6}$$

Because $H = \frac{1}{a} \frac{da}{dt} = -\frac{1}{a} \frac{da}{dT}$, equation (6) can be rewritten as follows:

$$\frac{\dot{a}}{a^2} \chi = -H \, r_L. \tag{7}$$

Combining (4), (5) and (7) we get:

$$\frac{dr_L}{dT} = \frac{c}{a^2} + H \, r_L. \tag{8}$$

The term $H \, r_L$ represents the expansion for the radius of our sphere, and $\frac{c}{a^2}$ is the peculiar velocity. From light propagation we see that the standard formula of luminosity distance implies a time varying velocity of light.

A new equation is proposed for the luminosity distance where the peculiar velocity is always equal to c. Considering a sphere of radius r'_L for the propagation of light emitted from a point at the center, and that the sphere inflates over time due to the expansion of the Universe and the velocity of light, we obtain:

$$\frac{dr'_L}{dT} = c + H \, r'_L, \tag{9}$$

with boundary condition $r'_L = 0$ at $T = 0$. Where r'_L is the luminosity distance, T the light travel time between emission and reception of the light source, and H the Hubble constant at time T.

3 Solving the equation of the luminosity distance

In this section we assume that the Hubble constant does not vary over time and is always equal to H_o.

By integrating (9) we get:

$$r'_L = \frac{c}{H_0} \left(\exp(H_0 \, T) - 1 \right). \tag{10}$$

This equation can be rewritten as follows:

$$T = \frac{1}{H_0} \ln \left(1 + \frac{H_0}{c} r'_L \right). \tag{11}$$

The expression of the light travel time versus redshift is as follows:

$$T = \int_{1/(1+z)}^{1} \frac{da}{H \, a} = \frac{1}{H_0} \ln(1 + z). \tag{12}$$

By combining (11) and (12) we get:

$$r'_L = \frac{c}{H_0} z.$$ (13)

4 Calculation of the Hubble constant from supernovae data

Let us compute the Hubble constant from supernovae using the relationship in (13) . In order to compute the luminosity distance we use the redshift adjusted distance modulus provided in [2] which is as follows:

$$m - M = -5 + 5 \log r'_L + 2.5 \log(1 + z).$$ (14)

The distance modulus $\mu = m - M$ is the difference between the apparent magnitude m and the absolute magnitude M.
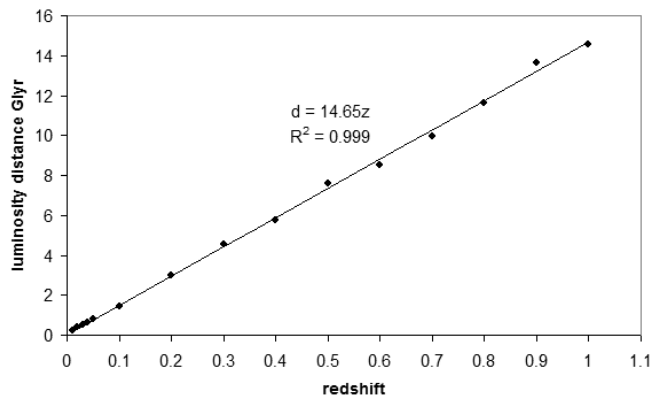
Fig. 1: Luminosity distance in Glyr versus redshift plot for supernovae. Data source: http://supernova.lbl.gov/Union/

In Fig. 1 we have a plot of the luminosity distance versus redshift that was obtained with (14) using supernovae data. This plot is rectilinear with a slope of 14.65 where the luminosity distance is expressed in *Glyr* (billion light years). The Hubble constant which is the inverse of the slope from (13) is equal to $H_0 = 67.3 \, \mathrm{km \, s^{-1} \, Mpc^{-1}}$.

5 Conclusion

In this study it has been shown that the standard formula of the luminosity distance implies that the peculiar velocity is a time varying velocity of light. Given our choice for the luminosity distance equation which is based on a peculiar velocity always equal to c, we find that the solution to this equation requires a Hubble constant that does not change over time in order to fit the supernovae data.

References

1. Weinberg S. Gravitation and Cosmology: Principles and applications of the general theory of relativity. John Wiley and Sons, 1972.

2. Heymann Y. Redshift Adjustment to the Distance Modulus. *Progress in Physics*, 2012, v. 1, 6–7.

Electric Dipole Antenna: A Source of Gravitational Radiation

Chifu E. Ndikilar* and Lawan S. Taura†

*Physics Department, Federal University Dutse, Nigeria
†Physics Department, Bayero University Kano, Nigeria
E-mail: ebenechifu@yahoo.com

In this article, the gravitational scalar potential due to an oscillating electric dipole antenna placed in empty space is derived. The gravitational potential obtained propagates as a wave. The gravitational waves have phase velocity equal to the speed of light in vacuum (c) at the equatorial plane of the electric dipole antenna, unlike electromagnetic waves from the dipole antenna that cancel out at the equatorial plane due to charge symmetry.

1 Introduction

Gravitational waves were predicted to exist by Albert Einstein in 1916 on the basis of the General Theory of Relativity. They are usually produced in an interaction between two or more compact masses. Such interactions include the binary orbit of two black holes, a merge of two galaxies, or two neutron stars orbiting each other. As the black holes, stars, or galaxies orbit each other, they send out waves of "gravitational radiation" that reach the Earth. A lot of efforts have been made over the years to detect these very weak waves. In this article, we show theoretically, how the gravitational potential of an electric dipole antenna placed in empty space propagates as gravitational waves.

2 Gravitational radiation from an electric dipole antenna

Recall that an electric dipole antenna is a pair of conducting bodies (usually spheres or rectangular plates) of finite capacitance connected by a thin wire of negligible capacitance through an oscillator. The charges reside on the conducting bodies (electrodes) but may travel from one to the other through the wire. The oscillator causes the charges to be built up on the electrodes such that at any time they are equal and opposite and the variation is sinusoidal with angular frequency ω [1].

Let the electric dipole antenna be represented by a pair of spheres seperated by a distance s with a sinusoidal charge Q as shown in figure 1.

If the total mass of each sphere at any time is M_0 and its radius R_s and assuming an instantaneous mass distribution which varies with the motion of electrons, then at each time t, the mass density ρ_0 is given by

$$\rho_0 = \Lambda_0 + \rho_e \sin \omega t \qquad (1)$$

where

$$\Lambda_0 = \frac{M_0}{4\pi R_s^3}$$

and

$$\rho_e = \frac{Nm_e}{4\pi R_s^3}$$
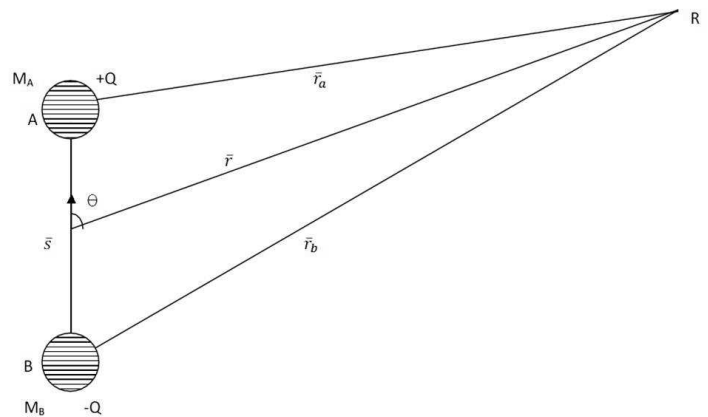
Fig. 1: Amplified diagram of an electric dipole antenna.

where N is the number of electrons moving in the dipole antenna and m_e is the electronic mass. For this mass distribution, the gravitational field equation can be written as [2]

$$\nabla^2 \Phi = \begin{cases} 0 & \text{if } r > R \\ 4\pi G\rho_0 & \text{if } r < R \end{cases} \qquad (2)$$

Now, consider a unit mass placed at a point R in empty space, far off from the electric dipole as in figure 1, then by Newton's dynamical theory, the gravitational scalar potential Φ at R at any time t can be defined as

$$\Phi(\bar{r}, t) = \frac{GM_a(\bar{r}_a, t)}{|\bar{r} - \bar{r}_a|} + \frac{GM_b(\bar{r}_b, t)}{|\bar{r} - \bar{r}_b|}. \qquad (3)$$

To maintain equal and opposite charges at the electrodes, the sinusoidal movement of electrons must be in such a way that the masses of the two spheres are the same and determined at point R to be given by

$$M_a(\bar{r}_a, t) = M_b(\bar{r}_b, t) = M_0 e^{i\omega(t')}. \qquad (4)$$

Thus, the gravitational potential at R becomes

$$\Phi(\bar{r}, t) = \frac{GM_0 e^{i\omega(t')}}{r_a} + \frac{GM_0 e^{i\omega(t'')}}{r_b}. \qquad (5)$$

Using the fact that gravitational effects propagate at the speed of light c from General Relativity [3], equation (5) can be written as

$$\Phi(\bar{r}, t) = \frac{GM_0 e^{i\omega(t-\frac{r_a}{c})}}{r_a} + \frac{GM_0 e^{i\omega(t-\frac{r_b}{c})}}{r_b}. \qquad (6)$$

From figure 1 and the cosine rule it can be shown that

$$r_a \approx r - \frac{s}{2}\cos\theta = r\left(1 - \frac{s}{2r}\cos\theta\right)$$

and

$$r_b \approx r + \frac{s}{2}\cos\theta = r\left(1 + \frac{s}{2r}\cos\theta\right)$$

and assuming that $r \gg s$ then

$$t - \frac{r_a}{c} = t - \frac{r}{c} + \frac{s}{2c}\cos\theta \qquad (7)$$

$$t - \frac{r_b}{c} = t - \frac{r}{c} - \frac{s}{2c}\cos\theta. \qquad (8)$$

Substituting equations (7) and (8) into equation (6) yields

$$\Phi(\bar{r}, t) = \frac{GM_0}{r} e^{i\omega(t-\frac{r}{c})} \left(\frac{e^{\frac{is}{2\lambda}\cos\theta}}{1 - \frac{s}{2r}\cos\theta} + \frac{e^{-\frac{is}{2\lambda}\cos\theta}}{1 - \frac{s}{2r}\cos\theta} \right) \qquad (9)$$

where $\lambdabar = \frac{\lambda}{2\pi} = \frac{c}{\omega}$. λ is the wavelength of the gravitational wave.

Series expansion of the exponential term and denominator of the fractions in the brackets of equation (9) to the first power of $\frac{s}{\lambda}$ and $\frac{s}{r}$ yields

$$\Phi(\bar{r}, t) = \frac{2GM_0}{r\lambdabar} e^{i\omega(t-\frac{r}{c})} \left(\lambdabar + \frac{is^2}{4r}\cos^2\theta \right). \qquad (10)$$

Equation (10) is valid provided $s << r$ and $s << \lambda$ for arbitrary s and λ.

But from complex analysis it can be shown that,

$$\lambdabar + \frac{is^2}{4r}\cos^2\theta = \left(\lambdabar^2 + \frac{s^4\cos^4\theta}{16r^2} \right)^{1/2} e^{i\sigma} \qquad (11)$$

where

$$\sigma = \arctan\left(\frac{s^4\cos^4\theta}{16r^2\lambdabar^2} \right).$$

Thus equation (10) becomes,

$$\Phi(\bar{r}, t) = \frac{2GM_0}{r\lambdabar} e^{i\omega(t-\frac{r}{c})} \left(\lambdabar^2 + \frac{s^4\cos^4\theta}{16r^2} \right)^{1/2} e^{i\sigma} \qquad (12)$$

or

$$\Phi(\bar{r}, t) = \frac{2GM_0}{r\lambdabar} \left(\lambdabar^2 + \frac{s^4\cos^4\theta}{16r^2} \right)^{1/2} e^{i\omega(t-\frac{r}{c}+\frac{1}{\omega}\sigma)}. \qquad (13)$$

From equation (13), it is deduced that the gravitational potential propagates as a wave with phase $t - \frac{r}{c} + \frac{1}{\omega}\sigma$.

The following remarks can be deduced from the expression of gravitational potential in this field:

- For
$$s^4\cos^4\theta \gg 16r^2\lambdabar^2$$
it is clear that
$$\arctan\left(\frac{s^4\cos^4\theta}{16r^2\lambdabar^2} \right) \approx \frac{\pi}{2}.$$
Thus in this case, the phase velocity of the gravitational potential is c.

- If $s^4\cos^4\theta$ is not much greater than $16r^2\lambdabar^2$ then the phase velocity of propagation is larger than c. This provides a crucial condition for the propagation of gravitational waves from an electric dipole antenna at velocities greater than the speed of light.

- At the equatorial plane of the electric dipole antenna, $\theta = \frac{\pi}{2}$ and
$$\Phi(\bar{r}, t) = \frac{2GM_0}{r} e^{i\omega(t-\frac{r}{c})}.$$
This indicates that at the equatorial plane; the gravitational wave propagates at a phase velocity of c, unlike in the case of electromagnetic waves, where fields of the two electrodes cancel out each other due to charge symmetry.

- Also, the gravitational field varies as $\frac{1}{r}$ and thus the wave dies out as one moves away from the dipole antenna. This is in agreement with the prediction by Astrophysicists that as gravitational waves travel from galaxies towards the Earth, their intensities die off and they become too weak when they get to planet Earth.

3 Conclusion

The major significance of this article is that, although the electric dipole antenna is not made up of massive compact bodies, the generation of gravitational radiation has been shown theoretically. Hence, this article highlights the fact that gravitational radiation can be produced by an interaction of two masses irrespective of their sizes. The use of gravitational potential which is a dynamical parameter also signifies that the existence of gravitational waves can also be predicted using Newton's theory of gravitation.

References

1. Jones D.S. The Theory of Electromagnetism. Macmillan, New York, 1964.

2. Howusu S.X.K. Complete Dynamical Theories of Physics. Jos University Press, 2010.

3. Weinberg S. Gravitation and Cosmology: Principles and Applications of the General Theory of Relativity. J. Wiley, New York, 1972.

The Heisenberg Uncertainty Principle and the Nyquist-Shannon Sampling Theorem

Pierre A. Millette

E-mail: PierreAMillette@alumni.uottawa.ca, Ottawa, Canada

The derivation of the Heisenberg Uncertainty Principle (HUP) from the Uncertainty Theorem of Fourier Transform theory demonstrates that the HUP arises from the dependency of momentum on wave number that exists at the quantum level. It also establishes that the HUP is purely a relationship between the effective widths of Fourier transform pairs of variables (i.e. conjugate variables). We note that the HUP is not a quantum mechanical measurement principle *per se*. We introduce the Quantum Mechanical equivalent of the Nyquist-Shannon Sampling Theorem of Fourier Transform theory, and show that it is a better principle to describe the measurement limitations of Quantum Mechanics. We show that Brillouin zones in Solid State Physics are a manifestation of the Nyquist-Shannon Sampling Theorem at the quantum level. By comparison with other fields where Fourier Transform theory is used, we propose that we need to discern between measurement limitations and inherent limitations when interpreting the impact of the HUP on the nature of the quantum level. We further propose that while measurement limitations result in our perception of indeterminism at the quantum level, there is no evidence that there are any inherent limitations at the quantum level, based on the Nyquist-Shannon Sampling Theorem.

1 Introduction

The Heisenberg Uncertainty Principle is a cornerstone of quantum mechanics. As noted by Hughes [1, see pp. 265–266], the interpretation of the Principle varies

- from expressing a limitation on measurement as originally derived by Heisenberg [2] (Heisenberg's microscope),
- to being the variance of a measurement carried out on an ensemble of particles [3] [4],
- to being inherent to a microsystem [5], meaning essentially that there is an indeterminism to the natural world which is a basic characteristic of the quantum level.

Greenstein retains only the first and last alternatives [6, see p. 51].

However, the Heisenberg Uncertainty Principle can be derived from considerations which clearly demonstate that these interpretations of the principle are not required by its mathematical formulation. This derivation, based on the application of Fourier methods, is given in various mathematical and engineering textbooks, for example [7, see p. 141].

2 Consistent derivation of the Heisenberg Uncertainty Principle

In the Fourier transform literature, the Heisenberg Uncertainty Principle is derived from a general theorem of Fourier theory called the Uncertainty Theorem [7]. This theorem states that the effective width of a function times the effective width of its transform cannot be less than a minimum value given by

$$W(f)\, W(\tilde{f}) \geqslant 1/2 \qquad (1)$$

where f is the function of interest and $\tilde{f}$ is its Fourier transform. $W(f)$ is the effective width of function f, defined by

$$|W(f)|^2 = \frac{\int_{-\infty}^{\infty} |f(u)|^2 [u - M(f)]^2 du}{\int_{-\infty}^{\infty} |f(u)|^2 du} \qquad (2)$$

and $M(f)$ is the mean ordinate defined by

$$M(f) = \frac{\int_{-\infty}^{\infty} |f(u)|^2 u\, du}{\int_{-\infty}^{\infty} |f(u)|^2 du}. \qquad (3)$$

There are several points that must be noted with respect to this derivation:

Eq.(1) applies to a Fourier transform pair of variables. Taking the simple case of time t and frequency ν to illustrate the point: If we consider the function f to be the function that describes a time function t, then the width of the function, $W(f)$, can be denoted as $W(f) = \Delta t$. The Fourier transform of function t is the frequency function ν and the width of this function can be denoted as $W(\tilde{t}) = W(\nu) = \Delta \nu$. Substituting in (1), the Uncertainty Theorem then yields

$$\Delta t\, \Delta \nu \geqslant 1/2. \qquad (4)$$

However, if one wishes to use the circular frequency $\omega = 2\pi\nu$ instead, (4) becomes

$$\Delta t\, \Delta \omega \geqslant \pi. \qquad (5)$$

It is thus necessary to take special care to clearly identify the Fourier transform variable used as it impacts the R.H.S. of the resulting Uncertainty relation (see for example [8] and [9, pp. 21–22]).

Equations (4) and (5) above correspond to the following definitions of the Fourier transform respectively [8]:

Equation (4):

$$f(t) = \int_{-\infty}^{\infty} \tilde{f}(v) \exp(2\pi i v t) dv \qquad (6)$$

$$\tilde{f}(v) = \int_{-\infty}^{\infty} f(t) \exp(-2\pi i v t) dt \qquad (7)$$

Equation (5):

$$f(t) = \frac{1}{2\pi} \int_{-\infty}^{\infty} \tilde{f}(\omega) \exp(i\omega t) d\omega \qquad (8)$$

$$\tilde{f}(\omega) = \int_{-\infty}^{\infty} f(t) \exp(-i\omega t) dt \qquad (9)$$

Sometimes the factor $1/2\pi$ is distributed between the two integrals (the Fourier and the Inverse Fourier Transform Integrals) as $1/\sqrt{2\pi}$. In Physics, (8) and (9) are preferred, as this eliminates the cumbersome factor of 2π in the exponential (see for example [10, p. 12]), but care must then be taken to ensure the resulting factor of $1/2\pi$ in (8) is propagated forward in derivations using that definition.

Using the relation $E = hv$, where h is Planck's constant, in (4) above, or the relation $E = \hbar\omega$, where $\hbar = h/2\pi$, in (5) above, one obtains the same statement of the Heisenberg Uncertainty Principle namely

$$\Delta E \, \Delta t \geqslant h/2 \qquad (10)$$

in both cases.

Similarly for the position x, if we consider the function f to be the function that describes the position x of a particle, then the width of the function, $W(f)$, can be denoted as $W(f) = \Delta x$. The Fourier transform of function x is the function $\tilde{x} = \lambda^{-1}$ and the width of this function can be denoted as $W(\tilde{x}) = W(\lambda^{-1}) = \Delta(\lambda^{-1})$ which we write as $\Delta\lambda^{-1}$ for brevity. You will note that we have not used the wavenumber function k, as this is usually defined as $k = 2\pi/\lambda$ (see for example [11] and references). Substituting in (1), we obtain the relation

$$\Delta x \, \Delta\lambda^{-1} \geqslant 1/2. \qquad (11)$$

In terms of the wavenumber k, (11) becomes

$$\Delta x \, \Delta k \geqslant \pi. \qquad (12)$$

Given that the momentum of a quantum particle is given by $p = h/\lambda$ or by $p = \hbar k$, both (11) and (12) can be expressed as

$$\Delta x \, \Delta p \geqslant h/2. \qquad (13)$$

Equations (10) and (13) are both different statements of the Heisenberg Uncertainty Principle.

The R.H.S. of these equations is different from the usual statement of the Heisenberg Uncertainty Principle where the

value $\hbar/2$ is used instead of the value $h/2$ obtained in this analysis. The application of (4) to circular variables (i.e. using ω in (4) instead of (5)) would result in the (incorrect) expression

$$\Delta t \, \Delta\omega \geqslant 1/2 \qquad (14)$$

and the more commonly encountered (incorrect) expression

$$\Delta E \, \Delta t \geqslant \hbar/2. \qquad (15)$$

However, Heisenberg's original derivation [2] had the R. H.S. of (13) approximately equal to h, and Greenstein's re-derivation [6, see p. 47] of Heisenberg's principle results in the value $h/2$. Kennard's formal derivation [12] using standard deviations established the value of $\hbar/2$ used today. This would thus seem to be the reason for the use of the value $\hbar/2$ in the formulation of the Heisenberg Uncertainty Principle.

Recently, Schürmann et al [13] have shown that in the case of a single slit diffraction experiment, the standard deviation of the momentum typically does not exist. They derive the conditions under which the standard deviation of the momentum is finite, and show that the R.H.S. of the resulting inequality satisfies (13). It thus seems that (13) is the more general formulation of the Heisenberg Uncertainty Principle, while the expression with the value $\hbar/2$ derived using standard deviations is a more specific case.

Whether one uses $\hbar/2$ or $h/2$ has little impact on the Heisenberg Uncertainty Principle as the R.H.S. is used to provide an order of magnitude estimate of the effect considered. However, the difference becomes evident when we apply our results to the Brillouin zone formulation of Solid State Physics (as will be seen in Section 5) since this now impacts calculations resulting from models that can be compared with experimental values.

3 Interpretation of the Heisenberg Uncertainty Principle

This derivation demonstrates that the Heisenberg Uncertainty Principle arises because x and p form a Fourier transform pair of variables. It is a characteristic of Quantum Mechanics that conjugate variables are Fourier transform pairs of variables. Thus the Heisenberg Uncertainty Principle arises because the momentum p of a quantum particle is proportional to the de Broglie wave number k of the particle. If momentum was not proportional to wave number, the Heisenberg Uncertainty Principle would not exist for those variables.

This argument elucidates why the Heisenberg Uncertainty Principle exists. Can it shed light on the meaning of the Heisenberg Uncertainty Principle in relation to the basic nature of the quantum level? First, we note that the Uncertainty Principle, according to Fourier transform theory, relates the effective width of Fourier transform pairs of functions or variables. It is not a measurement theorem *per se*. It does not describe what happens when Fourier transform variables are

measured, only that their effective widths must satisfy the Uncertainty Principle.

Indeed, as pointed out by Omnès [14, see p. 57], "it is quite legitimate to write down an eigenstate of energy at a well-defined time". Omnès ascribes this seeming violation of the Heisenberg Uncertainty Principle to the fact that time is not an observable obtained from an operator like momentum, but rather a parameter. Greenstein [6, see p. 65] makes the same argument. However, time t multiplied by the speed of light c is a component of the 4-vector x^μ and energy E divided by c is a component of the energy-momentum 4-vector P^μ. The time component of these 4-vectors should not be treated differently than the space component. The operator versus parameter argument is weak.

What Omnès' example shows is that the impact of the effective widths Δt and ΔE of the Heisenberg Uncertainty Principle depends on the observation of the time function t and of the energy function E that is performed. A time interval Δt can be associated with the time function t during which is measured the energy eigenstate function E which itself has a certain width ΔE, with both widths (Δ) satisfying (10). This example demonstrates that the Heisenberg Uncertainty Principle is not a measurement theorem as often used. Rather, it is a relationship between the effective widths of Fourier transform pairs of variables that can have an impact on the observation of those variables.

A more stringent scenario for the impact of the energy-time Heisenberg Uncertainty Principle is one where the time and energy functions are small quantities. For example, we consider the impact of Δt on the observation of τ_n, the lifetime of an atom in energy eigenstate n, and the impact of ΔE on the transition energy E_{mn}, for a transition between states n and m during spectral line emission. The conditions to be able to observe τ_n and E_{mn} are:

$$\tau_n \gtrsim \Delta t \tag{16}$$

$$E_{mn} \gtrsim \Delta E. \tag{17}$$

Using (10) in (16),

$$\tau_n \gtrsim \Delta t \gtrsim h/(2\Delta E). \tag{18}$$

Hence

$$\Delta E \gtrsim \frac{h}{2}\frac{1}{\tau_n}. \tag{19}$$

As state n increases, the lifetime τ_n decreases. Eq.(19) is thus more constrained in the limit of large n. Using the following hydrogenic asymptotic expression for τ_n from Millette et al [15]

$$\tau_n \sim \frac{n^5}{\ln(n)} \tag{20}$$

into (19), (17) becomes

$$E_{mn} \gtrsim \Delta E \gtrsim \frac{h}{2}k\frac{\ln(n)}{n^5} \tag{21}$$

where $1/k$ is the constant of proportionality of (20) given by

$$k = \frac{2^6}{3}\sqrt{\frac{\pi}{3}}Z^2\alpha^3 cR_H \tag{22}$$

where Z is the nuclear charge of the hydrogenic ion, α is the fine-structure constant, and R_H is the hydrogen Rydberg constant. Eliminating the middle term, (21) becomes

$$E_{mn} \gtrsim \frac{h}{2}k\frac{\ln(n)}{n^5}. \tag{23}$$

Applying L'Hôpital's rule, the R.H.S. of the above equation is of order

$$\text{R.H.S.} \sim O\left(\frac{1}{n^5}\right) \text{ as } n \to \infty \tag{24}$$

while the L.H.S. is of order [16, see p. 9]

$$\text{L.H.S.} \sim O\left(\frac{1}{n^2}\right) \text{ as } n \to \infty. \tag{25}$$

Given that (24) tends to zero faster than (25), (23) is satisfied. Both τ_n, the lifetime of the atom in energy eigenstate n, and the transition energy E_{mn} for the transition between states n and m satisfy the conditions for observation of the spectral line emission. Thus for the time interval Δt, given by (16), associated with the time function τ_n for the transition energy function E_{mn} which itself has a certain width ΔE, given by (17), both Δ's satisfy (10) as expected, given the observation of spectral line emission.

4 Quantum measurements and the Nyquist-Shannon Sampling Theorem

At the quantum level, one must interact to some degree with a quantum system to perform a measurement. When describing the action of measurements of Fourier transform variables, one can consider two limiting measurement cases: 1) truncation of the variable time series as a result of a fully interacting measurement or 2) sampling of the variable time series at intervals which we consider to be regular in this analysis, in the case of minimally interacting measurements. As we will see, the action of sampling allows for measurements that otherwise would not be possible in the case of a single minimal interaction.

It should be noted that the intermediate case of a partial measurement interaction resulting for example in a transfer of energy or momentum to a particle can be considered as the truncation of the original time series and the initiation of a new time series after the interaction. The advantage of decomposing measurement actions in this fashion is that their impact on Fourier transform variables can be described by the Nyquist-Shannon Sampling Theorem of Fourier transform theory. This theorem is a measurement theorem for Fourier transform variables based on sampling and truncation operations.

The Nyquist-Shannon Sampling Theorem is fundamental to the field of information theory, and is well known in digital signal processing and remote sensing [17]. In its most basic form, the theorem states that the rate of sampling of a signal (or variable) f_s must be greater than or equal to the Nyquist sampling rate f_S to avoid loss of information in the sampled signal, where the Nyquist sampling rate is equal to twice that of the highest frequency component, f_{max}, present in the signal:

$$f_s \geqslant f_S = 2f_{max}. \qquad (26)$$

If the sampling rate is less than that of (26), aliasing occurs, which results in a loss of information.

In general, natural signals are not infinite in duration and, during measurement, sampling is also accompanied by truncation of the signal. There is thus loss of information during a typical measurement process. The Nyquist-Shannon Sampling theorem elucidates the relationship between the process of sampling and truncating a variable and the effect this action has on its Fourier transform [18, see p. 83]. In effect, it explains what happens to the information content of a variable when its conjugate is measured.

Sampling a variable x at a rate δx will result in the measurement of its conjugate variable $\tilde{x}$ being limited to its maximum Nyquist range value $\tilde{x}_N$ as given by the Nyquist-Shannon Sampling theorem:

$$\tilde{x} \leqslant \tilde{x}_N \qquad (27)$$

where

$$\tilde{x}_N = 1/(2\delta x). \qquad (28)$$

Combining these two equations, we get the relation

$$\tilde{x}\,\delta x \leqslant 1/2, \quad \text{for } \tilde{x} \leqslant \tilde{x}_N. \qquad (29)$$

Conversely, truncating a variable x at a maximum value x_N ($x \leqslant x_N$) will result in its conjugate variable $\tilde{x}$ being sampled at a rate $\delta\tilde{x}$ given by the Nyquist-Shannon Sampling theorem $\delta\tilde{x} = 1/(2x_N)$ resulting in the relation

$$\delta\tilde{x}\,x \leqslant 1/2, \quad \text{for } x \leqslant x_N. \qquad (30)$$

The impact of the Nyquist-Shannon Sampling theorem is now considered for a particle's position x and momentum p. Applying the theorem to the case where a particle's trajectory is truncated to x_N, we can write from (30), for $x \leqslant x_N$,

$$x\,\delta\lambda^{-1} \leqslant 1/2, \quad \text{for } x \leqslant x_N \qquad (31)$$

or

$$x\,\delta k \leqslant \pi, \quad \text{for } x \leqslant x_N \qquad (32)$$

which becomes

$$x\,\delta p \leqslant h/2, \quad \text{for } x \leqslant x_N \qquad (33)$$

where δp is the p-domain sampling rate and the x values can be measured up to x_N (corresponding to the equality in the equations above).

Conversely, applying the theorem to the case where a particle's trajectory is sampled at a rate δx, one can also write from (29), for $\tilde{x} \leqslant \tilde{x}_N$, where $\tilde{x}$ stands for either of λ^{-1}, k, or p,

$$\delta x\,\lambda^{-1} \leqslant 1/2, \quad \text{for } \lambda^{-1} \leqslant \lambda_N^{-1} \qquad (34)$$

or

$$\delta x\,k \leqslant \pi, \quad \text{for } k \leqslant k_N \qquad (35)$$

which becomes

$$\delta x\,p \leqslant h/2, \quad \text{for } p \leqslant p_N \qquad (36)$$

where δx is the x-domain sampling rate and k_N is the wave number range that can be measured. For the case where the equality holds, we have $k_N = \pi/\delta x$ where k_N is the Nyquist wave number, the maximum wave number that can be measured with a δx sampling interval.

Sampling in one domain leads to truncation in the other. Sampling (δx) and truncation (x_N) in one domain leads to truncation (k_N) and sampling (δk) respectively in the other. As x and k form a Fourier transform pair in quantum mechanics, the Nyquist-Shannon Sampling theorem must also apply to this pair of conjugate variables. Similar relations can be derived for the E and ν pair of conjugate variables.

5   Implications of the Nyquist-Shannon Sampling Theorem at the quantum level

Equations (32) and (35) lead to the following measurement behaviors at the quantum level:

Lower-bound limit: If the position of a particle is measured over an interval x_N, its wave number cannot be resolved with a resolution better than sampling rate δk as given by (32) with $x = x_N$. If the momentum of a particle is measured over an interval k_N, its position cannot be resolved with a resolution better than sampling rate δx as given by (35) with $k = k_N$.

Upper-bound limit: If the position of a particle is sampled at a rate δx, wave numbers up to k_N can be resolved, while wave numbers larger than k_N cannot be resolved as given by (35). If the momentum of a particle is sampled at a rate δk, lengths up to x_N can be resolved, while lengths longer than x_N cannot be resolved as given by (32).

The lower-bound limit is similar to how the Heisenberg Uncertainty Principle is usually expressed when it is used as a measurement principle, although it is not strictly equivalent. The Nyquist-Shannon Sampling Theorem provides the proper formulation and limitations of this type of measurement.

The upper-bound limit suggests a different type of quantum measurement: regular sampling of a particle's position or momentum. In this case, one can obtain as accurate a measurement of the Fourier transform variable as desired, up to

the Nyquist-Shannon Sampling limit of $h/2$ (i.e. in the interval $[0, h/2]$).

An example of this phenomenon occurs in Solid State Physics where the translational symmetry of atoms in a solid resulting from the regular lattice spacing, is equivalent to an effective sampling of the atoms of the solid and gives rise to the Brillouin zone for which the valid values of k are governed by (35). Setting $\delta x = a$, the lattice spacing, and extending by symmetry the k values to include the symmetric negative values, one obtains [19, see p. 34], [20, see p. 100], [10, see p. 21]:

$$-\pi/a \leqslant k \leqslant \pi/a \qquad (37)$$

or alternatively

$$k \leqslant |\pi/a|. \qquad (38)$$

This is called the reduced zone scheme and π/a is called the Brillouin zone boundary [21, see p. 307]. The Brillouin zones of Solid State Physics are thus a manifestation of the Nyquist-Shannon Sampling theorem at the quantum level.

In essence, this is a theory of measurement for variables that are Fourier transform pairs. The resolution of our measurements is governed by limitations that arise from the Nyquist-Shannon Sampling theorem. Equations (32) and (35) are recognized as measurement relationships for quantum-mechanical conjugate variables. Currently, Quantum Mechanics only considers the Uncertainty Theorem but not the Sampling Theorem. The two theorems are applicable to Quantum Mechanics and have different interpretations: the Uncertainty Theorem defines a relationship between the widths of conjugate variables, while the Sampling Theorem establishes sampling and truncation measurement relationships for conjugate variables.

The value δx is a sampled measurement and as a result can resolve values of p up to its Nyquist value p_N given by the Nyquist-Shannon Sampling theorem, (36). This is a surprising result as the momentum can be resolved up to its Nyquist value, in apparent contradiction to the Heisenberg Uncertainty Principle. Yet this result is known to be correct as demonstrated by the Brillouin zones formulation of Solid State Physics. Physically this result can be understood from the sampling measurement operation which builds up the momentum information during the sampling process, up to the Nyquist limit p_N. It must be remembered that the Nyquist limit depends on the sampling rate δx as per the Nyquist-Shannon Sampling theorem, (36). The Nyquist value must also satisfy (26) to avoid loss of information in the sampling process, due to aliasing.

This improved understanding of the Heisenberg Uncertainty Principle and its sampling counterpart allows us to clarify its interpretation. This is based on our understanding of the behavior of the Uncertainty Theorem and the Nyquist-Shannon Sampling Theorem in other applications such as, for example, Digital Signal Processing.

6 Measurement limitations and inherent limitations

It is important to differentiate between the measurement limitations that arise from the properties of Fourier transform pairs previously considered, and any inherent limitations that may or may not exist for those same variables independently of the measurement process. Quantum theory currently assumes that the inherent limitations are the same as the measurement limitations. This assumption needs to be re-examined based on the improved understanding obtained from the effect of the Uncertainty and Sampling Theorems in other applications.

The properties of Fourier transform pairs considered in the previous sections do not mean that the underlying quantities we are measuring are inherently limited by our measurement limitations. On the contrary, we know from experience in other applications that our measurement limitations do not represent an inherent limitation on the measured quantities in Fourier Transform theory: for example, in Digital Signal Processing, a signal is continuous even though our measurement of the signal results in discrete and aliased values of limited resolution subject to the Nyquist-Shannon Sampling Theorem (analog and digital representation of the signal). The effective width of the signal and its transform are related by the Uncertainty theorem. Even though the time and frequency evolution of a signal that we measure is limited by our measurement limitations, the time domain and frequency domain signals are both continuous, independently of how we measure them.

The measurement limitations apply equally to the macroscopic level and to the quantum level as they are derived from the properties of Fourier transform pairs of variables which are the same at all scales. However, at the quantum level, contrary to our macroscopic environment, we cannot perceive the underlying quantities other than by instrumented measurements. Hence during a measurement process, the quantum level is limited by our measurement limitations. However, assuming that these measurement limitations represent inherent limitations and form a basic characteristic of the quantum level is an assumption that is not justified based on the preceding considerations. Indeed, the Nyquist-Shannon Sampling Theorem of Fourier Transform theory shows that the range of values of variables below the Heisenberg Uncertainty Principle value of $h/2$ is accessible under sampling measurement conditions, as demonstrated by the Brillouin zones formulation of Solid State Physics.

7 Overlap of the Heisenberg Uncertainty Principle and the Nyquist-Shannon Sampling Theorem

Brillouin zone analysis in Solid State Physics demonstrates that one can arbitrarily measure k from 0 up to its Nyquist limit, as long as the variable x is sampled at a constant rate (rather than performing a single x measurement). The Nyquist-Shannon Sampling Theorem can thus be considered to

cover the range that the Heisenberg Uncertainty Principle excludes.

However, one should recognize that the coverage results from two disparate theorems, and one should be careful not to try to tie the two Theorems at their value of overlap π. The reason is that one expression involves the widths of conjugate variables as determined by (1) to (3), while the other involves sampling a variable and truncating its conjugate, or vice versa as determined by (32) and (35). The equations are not continuous at the point of overlap π. Indeed, any relation obtained would apply only at the overlap π and would have no applicability or physical validity on either side of the overlap.

8 Discussion and conclusion

In this paper, we have shown that a consistent application of Fourier Transform theory to the derivation of the Heisenberg Uncertainty Principle requires that the R.H.S. of the Heisenberg inequality be $h/2$, not $\hbar/2$. This is confirmed when extending the analysis to the Brillouin zones formulation of Solid State Physics.

We have noted that the Heisenberg Uncertainty Principle, obtained from the Uncertainty Theorem of Fourier Transform theory, arises because of the dependency of momentum on wave number that exists at the quantum level. Quantum mechanical conjugate variables are Fourier Transform pairs of variables.

We have shown from Fourier Transform theory that the Nyquist-Shannon Sampling Theorem affects the nature of-measurements of quantum mechanical conjugate variables. We have shown that Brillouin zones in Solid State Physics are a manifestation of the Nyquist-Shannon Sampling Theorem at the quantum level.

We have noted that both the Sampling Theorem and the Uncertainty Theorem are required to fully describe quantum mechanical conjugate variables. The Nyquist-Shannon Sampling Theorem complements the Heisenberg Uncertainty Principle. The overlap of these Theorems at the $h/2$ equality value is a mathematical artifact and has no physical significance.

We have noted that the Uncertainty Theorem and the Nyquist-Shannon Sampling Theorem apply to Fourier Transform pairs of variables independently of the level at which the theorems are applied (macroscopic or microscopic). Conjugate variable measurement limitations due to these Theorems affect how we perceive quantum level events as these can only be perceived by instrumented measurements at that level. However, based on our analysis, quantum measurement limitations affect our perception of the quantum environment only, and are not inherent limitations of the quantum level, as demonstrated by the Brillouin zones formulation of Solid State Physics.

The application of the Nyquist-Shannon Sampling Theorem to the quantum level offers the possibility of investigat-ing new experimental conditions beyond the Brillouin zone example from Solid State Physics considered in this paper, allowing a unique vista into a range of variable values previously considered unreachable due to the Heisenberg Uncertainty Principle. Regular sampling of position allows us to determine momentum below its Nyquist limit, and similarly the regular sampling of momentum will allow us to determine position below its Nyquist limit.

References

1. Hughes R. I. G. The Structure and Interpretation of Quantum Mechanics. Harvard University Press, Cambridge, 1989.

2. Heisenberg W. Über den anschaulichen Inhalt der quantentheoretischen Kinematik und Mechanik. *Zeit. für Phys.*, 1927, v. 43, 172–98; quoted in Hughes R. I. G. The Structure and Interpretation of Quantum Mechanics. Harvard University Press, Cambridge, 1989.

3. Popper K. R. Quantum Theory and the Schism in Physics. Rowan and Littlefield, Totowa, NJ, 1982; quoted in Hughes R. I. G. The Structure and Interpretation of Quantum Mechanics. Harvard University Press, Cambridge, 1989.

4. Margenau H. The Nature of Physical Reality. McGraw Hill, New York, 1950; quoted in Hughes R. I. G. The Structure and Interpretation of Quantum Mechanics. Harvard University Press, Cambridge, 1989.

5. Davies P. C. W. Quantum Mechanics. Routledge, London, 1984; quoted in Hughes R. I. G. The Structure and Interpretation of Quantum Mechanics. Harvard University Press, Cambridge, 1989.

6. Greenstein G. and Zajonc A. G. The Quantum Challenge, Modern Research on the Foundations of Quantum Mechanics. Jones and Bartlett Publishers, Sudbury, Mass., 1997.

7. Cartwright M. Fourier Methods for Mathematicians, Scientists and Engineers. Ellis Norwood Ltd, London, 1990.

8. Weisstein E. MathWorld. http://mathworld.wolfram.com/FourierTransform.html.

9. Griffiths R. B. Consistent Quantum Theory. Cambridge University Press, Cambridge, 2002.

10. Ziman J. M. Principles of the Theory of Solids, 2nd ed. Cambridge University Press, Cambridge, 1979.

11. Weisstein E. World of Physics. http://scienceworld.wolfram.com/physics/Wavenumber.html.

12. Kennard E. H. Zur Quantenmechanik einfacher Bewegungstypen. *Zeit. für Phys.*, 1927, v. 44, 326.

13. Schürmann T. and Hoffman I. A closer look at the uncertainty relation of position and momentum. *Found. of Phys.*, 2009, v. 39, 958–63.

14. Omnès R. The Interpretation of Quantum Mechanics. Princeton University Press, Princeton, New Jersey, 1994.

15. Millette P. A. and Varshni Y. P. New asymptotic expression for the average lifetime of hydrogenic levels. *Can. J. Phys.*, 1979, v. 57, 334–5.

16. Bethe H. A. and Salpeter E. E. Quantum Mechanics of One- and Two-Electron Atoms. Plenum Publishing Corp., New York, NY, 1977.

17. Oppenheim A. V. and Willsky A. S., Signals and Systems. Prentice-Hall Inc., Englewood Cliffs, New Jersey, 1983.

18. Brigham E. O. The Fast Fourier Transform. Prentice-Hall Inc., Englewood Cliffs, New Jersey, 1974.

19. Harrison W. A. Electronic Structure and the Properties of Solids. Dover Publications, New York, 1989.

20. Chaikin P. M. and Lubensky T. C. Principles of Condensed Matter Physics. Cambridge University Press, Camvridge, 1995.

21. Kittel C. Introduction to Solid State Physics. John Wiley and Sons, New York, 1971.

The Cause of the Increased Luminosity Distances of Supernovae Recorded in the Cosmological Data

Emmanuil Manousos

Astrophysics Laboratory , Faculty of Physics, National and Kapodistrian University of Athens,
Panepistimiopolis, GR 15783 Zographos, Athens, Greece. E-mail: emanoussos@phys.uoa.gr

The law of selfvariations quantitatively determines a slight increase of the masses and charges as the common cause of quantum and cosmological phenomena. It predicts and explains the totality of the cosmological data. In this article we present the prediction of the law concerning the increased luminosity distances of distant astronomical objects. The prediction we make is in agreement with the cosmological data for the luminosity distances of type Ia supernovae.

1 Introduction

The science of Physics possesses today a plethora of knowledge that allows us to seek the first principles governing physical reality. We can search for a small number of propositions-axioms that could reproduce the totality of our knowledge in Physics. The theory of selfvariations has emerged along this line of reasoning.

We make two hypotheses: The rest masses and electric charges of the material particles increase slightly with the passage of time (selfvariations), and the consequences of this increase propagate in four-dimensional spacetime with a vanishing arc length. Starting from these two hypotheses we conclude that the selfvariations occur in a strictly defined manner. We call the quantitative mathematical determination of the way in which the selfvariations occur, the law of selfvariations.

The law of selfvariations contains an exceptionally large amount of data and information. It is related to the quantum phenomena, the potential fields, and the cosmological data. With the evidence we have in our disposal, and the mathematical calculations we have performed, we can propose the law of selfvariations as the common cause of quantum phenomena and cosmological data. The consequences of the law of selfvariations extend from the microcosm up to the observations we conduct billions of light years away. Equation

$$\left(m_0 c^2 + ih\frac{\dot{m}_0}{m_0}\right)^{\cdot} = 0,$$

with unique unkown the rest mass m_0 of particles, both contains as physical information, and justifies, the whole corpus of the current cosmological observational data.

Specifically for the cosmological data, the law of selfvariations predicts and justifies: the redshift of distant astronomical objects and Hubble's law, the cosmic microwave background radiation, the large-scale structures of matter in the Universe, the fact that the Universe is flat, the fact that the total energy-content of the Universe is zero, the fact that the very early Universe went through a phase of ionization, the arrow of time in the macrocosm and its breakdown in the

microcosm, the fact that the luminosity distances of distant astronomical objects will always be measured larger than the actual distances. It is this last prediction that we present in the current article.

Since the observations of distant astronomical objects correspond to past time, the rest masses of the material particles in these objects are smaller than the corresponding masses we measure in the laboratory, due to the selfvariations. Therefore, the energy resulting from fusion and fission in distant astronomical objects is less than expected. These distant astronomical objects are fuelled with a smaller than expected amount of energy in order to emit the electromagnetic radiation we observe today from Earth. This fact reduces the luminosity of distant astronomical objects.

In the last decade of the previous century two independent research groups under A.G. Riess and S. Perlmutter, measured the decrease of the luminosity for a large number of type Ia supernovae at great distances. In order to explain the observational data within the framework of the standard cosmological model, the hypothesis of dark energy was introduced.

We have today a large amount of observational data confirming the decrease of luminosity at large distances. All these measurements result in a specific diagram correlating the luminosity-distance with the redshift of distant astronomical objects. This diagram, as it results from the cosmological data, is exactly the same with the one predicted theoretically by the law of selfvariations. In the next paragraph we present the diagram that we theoretically predict.

2 The luminosity distances of distant astronomical objects will always be measured greater than their real distances

The law of selfvariations [1, 2] predicts the relation

$$r = \frac{c}{k} \ln\left(\frac{A}{1 - (1 + z)(1 - A)}\right),$$

between the distance r and the redshift z of distant astronomical objects. For the dimensionless parameter A, it holds that

$A \to 1^-$, since it obeys the inequality

$$\frac{z}{1+z} < A < 1,$$

for every value of the redshift z. The parameter k is constant, and is related to the Hubble parameter H through equation

$$\frac{kA}{1-A} = H.$$

The law of selfvariations predicts that the energy $E(z)$ resulting from fusion, and which powers the distant astronomical objects, is decreased compared with the corresponding energy E measured in the laboratory, according to relation

$$E(z) = \frac{E}{1+z}.$$

Because of this, the luminosity of distant astronomical objects is decreased, relative to the expected one. This has as a consequence that the luminosity distances R of distant astronomical objects are measured larger than the actual distances r, $R > r$. From the mathematical calculations [1, 2] we obtain

$$R = r\sqrt{1+z},$$

between the distances R and r.

Combining the previous equations we get the luminosity distance R as a function of the redshift z of distant astronomical objects:

$$R = \frac{cA\sqrt{1+z}}{(1-A)H} \ln\left(\frac{A}{1-(1+z)(1-A)}\right).$$

In the diagram in figure 1 we present the diagram of $R = R(z)$ for $A = 0.975$, $A = 0.990$, $A = 0.995$, $A = 0.999$, $H = 60\,\text{km/s\,Mpc}$, $c = 3 \times 10^5\,\text{km/s}$ up to $z = 1.5$. In order to explain the inconsistency of the Standard Cosmological Model with the diagram in figure 1, the existence of dark energy was invented and introduced.

Type Ia supernovae are astronomical objects for which we can measure their luminosity distance for great distances. The measurements already conducted [3, 4] agree with the diagram in figure 1.

In the measurements conducted for the determination of the Hubble parameter H, the consequences of equation $R = r\sqrt{1+z}$ have not been taken into account. For small values of the redshift z, the value $H = 60\,\text{km/s\,Mpc}$ results. The measurements made up to date, have included astronomical objects with a high redshift z, thus raising the value of parameter H to between 72 and 74 km/s Mpc. Today we perform measurements of very high accuracy. Taking into consideration the consequences of equation $R = r\sqrt{1+z}$, we predict that the value of parameter H will be measured independently of the redshift z of the astronomical object. We, of course, refer to measurements of the parameter H that are based on the luminosity distance of the astronomical objects.

<div align="center">Submitted on: March 03, 2013 / Accepted on March 08, 2013</div>
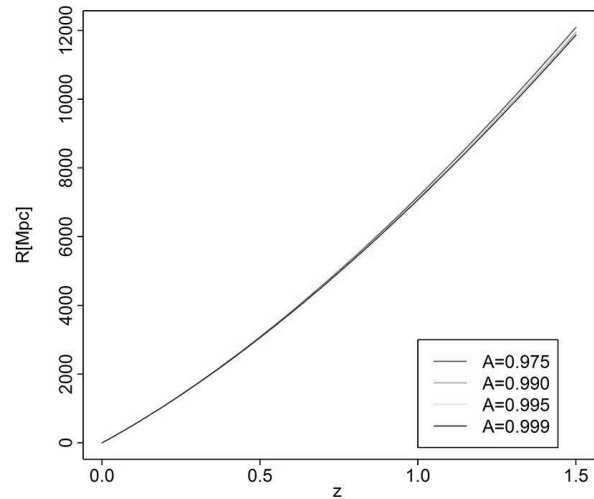
Fig. 1: The diagram of $R = R(z)$ for $A = 0.975$, $A = 0.990$, $A = 0.995$, $A = 0.999$, $H = 60$ km/s Mpc, $c = 3 \times 10^5$ km/s up to $z = 1.5$. The measurement of the luminosity distances of type Ia supernova confirms the theoretical prediction of the law of selfvariations.

References

1. Manousos E. A common underlying cause for quantum phenomena and cosmological data. viXra:1302.0115 v2.

2. Manousos E. The theory of self-variations. A continuous slight increase of the charges and the rest masses of the particles can explain the cosmological data. *Nuovo Cimento B*, 2007, 359–388.

3. Adam G. Riess et al. Observational Evidence from Supernovae for an Accelerating Universe and a Cosmological Constant. *The Astronomical Journal*, 1998, v. 29 (3), 423–428.

4. Perlmutter, S. et al. Measurements of Omega and Lambda from 42 High-Redshift Supernovae. *The Astrophysical Journal*, 1999, v. 517 (2), 565–586.

Intrinsic Charges and the Strong Force

Bo Lehnert

Alfvén Laboratory, Royal Institute of Technology, 10044 Stockholm, Sweden. E-mail: Bo.Lehnert@ee.kth.se

According to a revised quantum electrodynamic theory, there are models of leptons such as the electron which possess both a net integrated electric charge and a much larger intrinsic charge of both polarities. From estimates based on such models, the corresponding Coulomb force due to the intrinsic charges then becomes two orders of magnitude larger than that due to the conventional net charge. This intrinsic charge force can also have the features of a short-range interaction. If these results would generally hold true, the intrinsic charge force could either interact with a strong force of different origin and character, or could possibly become identical with the strong force.

1 Introduction

According to quantum mechanics there exists a nonzero lowest energy level, the Zero Point Energy. The vacuum is therefore not merely an empty space, but includes a "photon gas" of related electromagnetic vacuum fluctuations. The pressure of this gas is a physical reality, as demonstrated by the force between two metal plates proposed by Casimir [1] and first confirmed experimentally by Lamoreaux [2].

These circumstances have formed the starting point of a revised quantum electrodynamical approach by the author [3]. In the latter a *nonzero* electric field divergence div **E** is introduced in the *vacuum* state. In its turn, the nonzero electric field divergence admits an additional degree of freedom into the electromagnetic field equations. The latter then possess new solutions both in the steady and the time-dependent states, having applications to modified models of leptons and photons.

In this paper an example is given in Section 2 on the consequences of a nonzero electric field divergence in a steady state. It demonstrates that the local variations of the charge density $\bar{\rho} = \varepsilon_0 \mathrm{div}\,\mathbf{E}$ can result in considerable *intrinsic* charges of both signs, being much larger than the total *net* integrated charge. The possible effects of the intrinsic charges on the Coulomb interaction will then be outlined in Section 3, first in respect to the magnitude of the resulting forces, and then to the range of the same forces in a simple "Gedanken experiment". In Section 4 a comparison is finally made to the strong nuclear force.

2 An Example given by the Revised Electron Model

In the revised quantum electrodynamic theory there are steady states which do not exist in conventional theory [3]. These states include net as well as intrinsic electric charges, electric currents, static electromagnetic fields and related forces. To illustrate the resulting charge distributions, an example is here taken from a corresponding electron model. The features of the model will shortly be summarized here, with reference to details in the original descriptions [3].

In the revised theory the field configuration is shown to become derivable from a generating function

$$F = G_0\, G\,(\rho, \theta) \qquad G = R\,(\rho) \cdot T\,(\theta) \qquad (1)$$

in spherical coordinates (r, θ, φ) of an axisymmetric case being independent of the angle φ. Here G_0 stands for a characteristic amplitude, $\rho = r/r_0$ with r_0 as a characteristic radial length, and

$$R = \rho^{-\gamma} e^{-\rho} \qquad \gamma > 0 \qquad (2)$$

$$T = 1 + a_1 \sin\theta + a_2 \cos 2\theta + a_3 \sin 3\theta + a_4 \cos 4\theta + \dots \quad (3)$$

with $a_1, a_2, a_3, \dots$ as constant amplitude factors. The radial function R has to be divergent at the origin $r = 0$ to result in a net integrated charge. Thereby a revised renormalisation procedure is applied to make this divergence result in a finite net integrated charge. This leads to forms of the net charge q_0, magnetic moment M_0, rest mass m_0, and angular momentum (spin) s_0 as given by

$$q_0 = 2\pi\varepsilon_0 c_{rG} A_q, \qquad (4)$$

$$s_0 = \frac{1}{2}\pi\left(\frac{\varepsilon_0}{c^2}\right) C c_{rG}^2 A_s, \qquad (5)$$

$$M_0 m_0 = \left(\frac{\pi\varepsilon_0}{c}\right)^2 C c_{rG}^3 A_M A_m. \qquad (6)$$

Here $C = \pm c$, c_{rG} is a finite counter factor in the renormalisation process, and

$$A_k = \int_0^\pi I_{k\theta}\, d\theta \qquad k = q, M, m, s \qquad (7)$$

with $I_{k\theta}$ being functions of the amplitude factors of equation (3) and the variable $s \equiv \sin\theta$. The factor c_{rG} includes the amplitude G_0 which can have either sign and becomes negative in the case of the electron.

Two quantum conditions are considered here. The first is $s_0 = \pm h/4\pi$ on the spin which results in a normalized net charge

$$q^* = \left|\frac{q_0}{e}\right| = \left(\frac{f_0 A_q^2}{A_s}\right)^{1/2} \qquad f_0 = \frac{2\varepsilon_0 ch}{e^2} \qquad (8)$$

where e is the experimentally determined elementary charge and $f_0 \cong 137.036$ is the inverted value of the fine-structure constant. The second condition concerns the magnetic moment and becomes

$$\frac{M_0 m_0}{q_0 s_0} = \frac{A_M A_m}{A_q A_s} = 1 + \delta_M \tag{9}$$

with $\delta_M = 1/2\pi f_0 \cong 0.0011614$. Here it has to be observed that the fourteenth term in equation (7.56) of Reference [3] should read $-699.7897637 a_2 a_3$.

In the four-amplitude case (a_1, a_2, a_3, a_4) the normalized charge q^* will here be studied with conditions (8) and (9) imposed, and as functions of a_3 and a_4 in $a_3 a_4$-space. Then q^* is found to have a minimum for large positive values of a_3 and a_4, within a narrow channel positioned around a plateau defined by the experimental value $q^* = 1$. The width of the channel is only a few percent of q^*. At the plateau the amplitude values are therefore replaced by

$$\bar{a}_i = a_i/a_\infty \qquad a_\infty \gg 1 \qquad i = 1, 2, 3 \ldots \tag{10}$$

As an illustration of the resulting intrinsic and net electric charges, we now use an example where $\bar{a}_1 = -1.91$, $\bar{a}_2 = -2.51$, $\bar{a}_3 = \bar{a}_4 = 1$. The corresponding integrand $\bar{I}_{q\theta}$ of equation (7) in the plateau region then becomes

$$\begin{aligned} \bar{I}_{q\theta} &= 2sT - 4s^3 T - sD_\theta T + \\ &\quad + 2s^3 D_\theta T + 2s D_\theta \left(s^2 T \right) - s D_\theta \left(s^2 D_\theta T \right) = \\ &= 44.9s + 288s^2 - 2159s^3 - 1320s^4 + \\ &\quad + 7559s^5 + 1120s^6 - 5760s^7 \end{aligned} \tag{11}$$

with the operator

$$D_\theta = -\frac{\partial^2}{\partial\theta^2} - \frac{\cos\theta}{\sin\theta}\frac{\partial}{\partial\theta}. \tag{12}$$

From the corresponding equation (7) this yields $\bar{A}_q \cong 4.600$, $\bar{A}_M \cong 4.37$, $\bar{A}_m \cong 2832$, $\bar{A}_s \cong 2648$ and results in

$$\frac{\bar{A}_M \bar{A}_m}{\bar{A}_q \bar{A}_s} \cong 1.017$$

and $q^* \cong 1.046$.

The obtained value of $\bar{A}_q$ corresponds to the net charge q_0 of equation (4). The detailed charge distribution as a function of s is given by equation (11) and has been plotted in Fig. 1. According to the figure the negative part of the intrinsic charge in the range $0 < \theta < \pi$ is estimated to have the corresponding value $\bar{A}_{q-} \cong 117.3$. The positive part of the intrinsic charge further corresponds to $\bar{A}_{q+} = \bar{A}_{q-} + \bar{A}_q \cong 121.9$.

In the example given here there is thus an outbalanced intrinsic charge proportional to $\bar{A}_{q-} = \bar{A}_{q+} - \bar{A}_q$, plus a net integrated charge proportional to $\bar{A}_q$. The ratio between these charges becomes

$$c_{in} = \frac{\bar{A}_{q-}}{\bar{A}_q}. \tag{13}$$
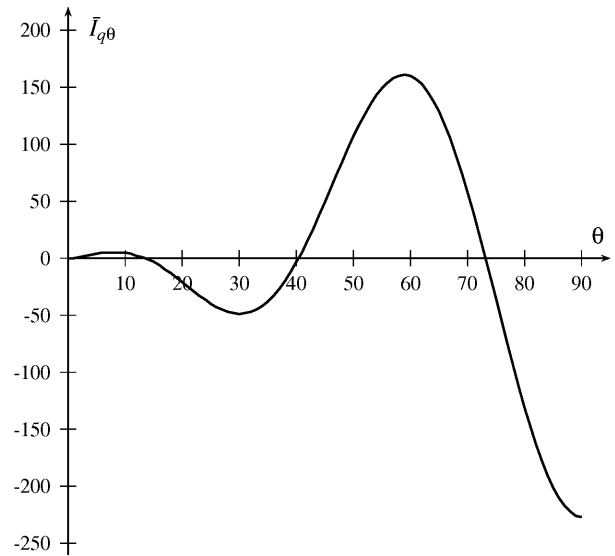
Fig. 1: The local contribution $\bar{I}_{q\theta}$ of equation (10) to the electric charge integral $\bar{A}_q$ as a function of the polar coordinate θ, in the range $0 < \theta < \pi/2$ and with θ given in degrees.

In the example of Fig. 1 it has the value $c_{in} \cong 26.5$, thus indicating that the intrinsic charge considerably exceeds the net charge.

Also the electromagnetic force

$$\mathbf{f} = \bar{\rho} \left(\mathbf{E} + \mathbf{C} \times \mathbf{B} \right) \tag{14}$$

per unit volume has to be taken into account. It consists of the electrostatic and magnetostatic contributions $\bar{\rho}\mathbf{E}$ and $\bar{\rho}\mathbf{C} \times \mathbf{B}$ where $\mathbf{E}$ and $\mathbf{B}$ are the electric and magnetic field strengths, the velocity vector $\mathbf{C}$ has the modulus $|\mathbf{C}| = \pm c$ and c is the velocity of light. In a cylindrically symmetric case the local electric and magnetic contributions can outbalance each other, but only partly in a spherical axisymmetric case [3]. In the latter case the average radial force can on the other hand be balanced at least for specific solutions of the field equations, but this requires further detailed analysis in every case.

3 Intrinsic Coulomb Forces

The intrinsic charge ratio c_{in} is likely to have consequences when considering the mutual Coulomb forces.

3.1 General Aspects

For any distribution of electric charges the local contribution Δf_{12} to the mutual Coulomb force becomes

$$\Delta f_{12} = \frac{(\Delta q_1)(\Delta q_2)}{4\pi\varepsilon_0 r_{12}^2} \tag{15}$$

where and Δq_1 and Δq_2 are two interacting charge elements separated by the distance r_{12}. The charge ratio of equation

(13) thus predicts that the intrinsic Coulomb forces in some cases even may be represented by a factor c_{in}^2 as compared to those in a conventional analysis. For the values of $c_{in}^2 \cong 702$ in the example of Section 2 these forces could then roughly be estimated to be more than two orders of magnitude larger than the conventional ones. However, the effective magnitude of the intrinsic charge force will also depend on the specific geometry of the charge distribution, as being demonstrated by a simple discussion in the following subsection.

3.2 A Gedanken Experiment

To crudely outline the forces which can arise from the intrinsic charges, a simple "Gedanken experiment" is now performed according to Fig. 2. It concerns the interaction between two rigid mutually penetrable spherical configurations, $(_1)$ and $(_2)$, of charge $+Q$ at their centra and charge $-Q$ at their peripheries. The resulting electrostatic field strengths are $\mathbf{E}_1$ and $\mathbf{E}_2$, and the external space is field-free. When these configurations, being simulated as "particles", are apart as in Fig. 2(a), their mutual interaction force F_{12} remains zero. As soon as particle $(_2)$ starts to penetrate particle $(_1)$, part of the negative charge cloud at the periphery of particle $(_2)$ will interact with the electric field $\mathbf{E}_1$ of particle $(_1)$. This generates an attractive force $F_{12} > 0$, as shown by Fig. 2(b). When particle $(_2)$ further penetrates into the field region of particle $(_1)$, however, the mutual interaction force $F_{12} < 0$ changes sign and becomes repulsive as shown in Fig. 2(c). Between cases (a) and (b) there is an equilibrium with $F_{12} = 0$.

The relative magnitude of the maximum force F_{12} in the case of Fig. 2(b) can be estimated by noticing that it is generated by the fraction g_2 of the charge $-Q$ at the periphery of particle $(_2)$, in the field $\mathbf{E}_1$ of particle $(_1)$. With the charge ratio

$$c_{in} = \frac{Q}{e} \tag{16}$$

of the particles $(_1)$ and $(_2)$ this yields an estimated ratio

$$f_{in} = g_2 \, c_{in}^2 \tag{17}$$

between the intrinsic forces and those which would have been present in a conventional case. With an estimated factor $g_2 \cong 1/4$ for the fraction of negative charge of particle $(_2)$ being present in the field $\mathbf{E}_1$ of Fig. 2(b), and with $c_{in} \cong 702$ due to the example of Section 2, this results in the force ratio $f_{in} \cong 176$.

In reality, however, the mutual interaction in Fig. 2(b) and Fig. 2(c) becomes more complex and includes a rearrangement of the charge geometry. Thus, even if these simple considerations are somewhat artificial, they appear to indicate that the intrinsic Coulomb forces can become about two orders of magnitude larger than the conventional ones. The intrinsic forces can also in some cases have the character of a short-range interaction.

Provided that the present model of charged leptons also can be applied in a first crude approximation to a bound
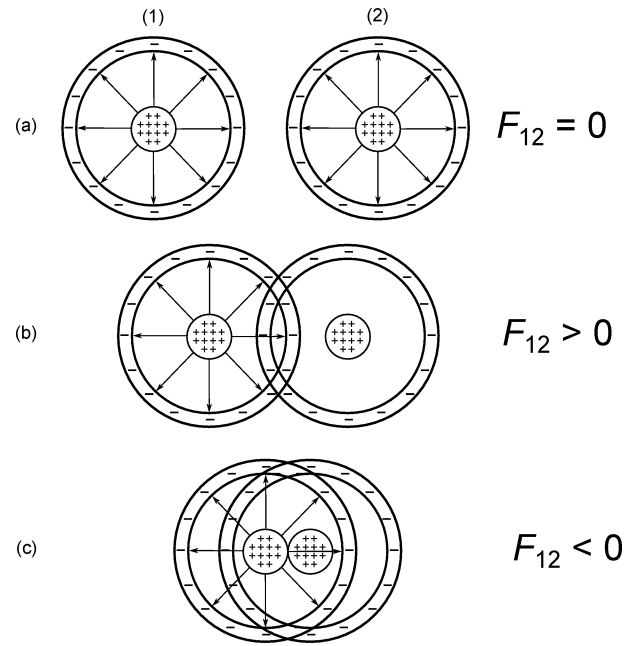
Fig. 2: "Gedanken experiment" where two rigid mutually penetrable spherical configurations ("particles"), $(_1)$ and $(_2)$, are approaching each other. The "particles" have charges $+Q$ at their centra, and $-Q$ at their peripheries, resulting in the internal electric field strengths $\mathbf{E}_1$ and $\mathbf{E}_2$. The mutual interaction force F_{12} is zero when the particles are apart in (a), $F_{12} > 0$ is attractive when they first start to interact in (b), and $F_{12} < 0$ is finally repulsive when they are close together in (c).

quark, its characteristic radius r_ε can be estimated. It would become $r_\varepsilon = c_{rG}/c_G$ where c_{rG} and c_G are counter factors of a revised renormalisation procedure [3]. This results in radii in the range $10^{-16} < r_\varepsilon < 10^{-14}$ m for the u, d and s quarks.

4 A Comparison to the Strong Force

The strong force keeps the atomic nucleus together, and it acts on its smallest constituents, the quarks. As concluded from experiments on deep inelastic scattering of energetic electrons by hadrons, the latter include the quarks. According to reviews by French [4], Walker [5] and others, these strong forces have the following features:

- They are primarily attractive.
- They seem to be essentially the same for neutrons and protons.
- Their range is short and not greater than 2×10^{-15} m.
- Within this range they are very strong, i.e. two orders of magnitude larger than those due to conventional electromagnetics.

The strong force can be compared to the intrinsic Coulomb force discussed in this context, also in respect to a possible quark model being somewhat similar to that of the electron as

described in Section 2. The following points should then be noticed:

- The present considerations suggest that the intrinsic charge force can become two orders of magnitude larger than that due to the conventional net charge. The intrinsic charge force thus appears to be of the same order as the strong force, and may also appear in terms of a short-range interaction, on scales of the order of 10^{-15} m.

- It then follows that the intrinsic charge force either will interact with a strong force of different origin and character, or will possibly become identical with the strong force.

References

1. Casimir H. B. G. On the Attraction between two Perfectly Conducting Plates. *Proc. Kon. Nederland Akad. Wetensch.*, 1948, v. B51, 793–795.

2. Lamoreaux S. K. Demonstration of the Casimir Force in the 0.6 to 6 μm Range. *Physical Review Letters*, 1997, v. 78, 5–8.

3. Lehnert B. Revised Quantum Electrodynamics, Nova Science Publishers, New York, 2013, Ch. 6 and Ch. 7.

4. French A. P. Principles of Modern Physics, New York, John Wiley and Sons, 1958, Ch. 9.10.

5. Walker J. S. Physics, Fourth Edition, Pearson International Edition, Addison-Wesley, 2010, page 1144.

————————————

Relations between Distorted and Original Angles in STR

Florentin Smarandache

Arts and Science Division, University of New Mexico, 705 Gurley Ave., Gallup, NM 87301, USA. E-mail: smarand@unm.edu

Using the Oblique-Length Contraction Factor, which is a generalization of Lorentz Contraction Factor, one shows several trigonometric relations between distorted and original angles of a moving object lengths in the Special Theory of Relativity.

1 Introduction

The lengths at oblique angle to the motion are contracted with the Oblique-Length Contraction Factor $OC(v, \theta)$, defined as [1-2]:

$$OC(v, \theta) = \sqrt{C(v)^2 \cos^2 \theta + \sin^2 \theta} \qquad (1)$$

where $C(v)$ is just Lorentz Factor:

$$C(v) = \sqrt{1 - \frac{v^2}{c^2}} \in [0, 1] \text{ for } v \in [0, c]. \qquad (2)$$

Of course

$$0 \le OC(v, \theta) \le 1. \qquad (3)$$

The Oblique-Length Contraction Factor is a generalization of Lorentz Contractor $C(v)$, because: when $\theta = 0$, or the length is moving along the motion direction, then $OC(v, 0) = C(v)$. Similarly

$$OC(v, \pi) = OC(v, 2\pi) = C(v). \qquad (4)$$

Also, if $\theta = \pi/2$, or the length is perpendicular on the motion direction, then $OC(v, \pi/2) = 1$, i.e. no contraction occurs. Similarly $OC(v, \frac{3\pi}{2}) = 1$.

2 Tangential relations between distorted acute angles vs. original acute angles of a right triangle

Let's consider a right triangle with one of its legs along the motion direction (Fig. 1).
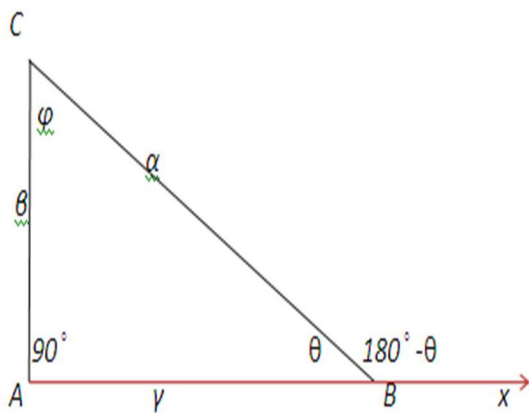
Fig. 1:

$$\tan \theta = \frac{\beta}{\gamma} \qquad (5)$$

$$\tan(180° - \theta) = -\tan \theta = -\frac{\beta}{\gamma} \qquad (6)$$

After contraction of the side AB (and consequently contraction of the oblique side BC) one gets (Fig. 2):
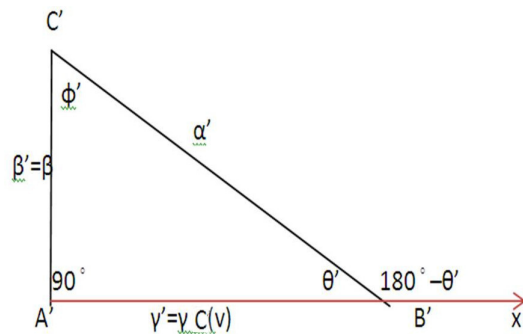
Fig. 2:

$$\tan(180° - \theta') = -\tan \theta' = -\frac{\beta'}{\gamma'} = -\frac{\beta}{\gamma C(v)}. \qquad (7)$$

Then:

$$\frac{\tan(180° - \theta')}{\tan(180° - \theta)} = \frac{-\dfrac{\beta}{\gamma C(v)}}{-\dfrac{\beta}{\gamma}} = \frac{1}{C(v)}. \qquad (8)$$

Therefore

$$\tan(\pi - \theta') = -\frac{\tan(\pi - \theta)}{C(v)} \qquad (9)$$

and consequently

$$\tan(\theta') = \frac{\tan(\theta)}{C(v)} \qquad (10)$$

or

$$\tan(B') = \frac{\tan(B)}{C(v)} \qquad (11)$$

which is the Angle Distortion Equation, where θ is the angle formed by a side travelling along the motion direction and another side which is oblique on the motion direction.

The angle θ is increased (i.e. $\theta' > \theta$).

$$\tan \varphi = \frac{\gamma}{\beta} \quad \text{and} \quad \tan \varphi' = \frac{\gamma'}{\beta'} = \frac{\gamma C(v)}{\beta} \qquad (12)$$

whence:

$$\frac{\tan \varphi'}{\tan \varphi} = \frac{\dfrac{\gamma C(v)}{\beta}}{\dfrac{\gamma}{\beta}} = C(v). \qquad (13)$$

So we get the following Angle Distortion Equation:

$$\tan \varphi' = \tan \varphi \cdot C(v) \qquad (14)$$

or

$$\tan C' = \tan C \cdot C(v) \qquad (15)$$

where φ is the angle formed by one side which is perpendicular on the motion direction and the other one is oblique to the motion direction.

The angle φ is decreased (i.e. $\varphi' < \varphi$). If the traveling right triangle is oriented the opposite way (Fig. 3)
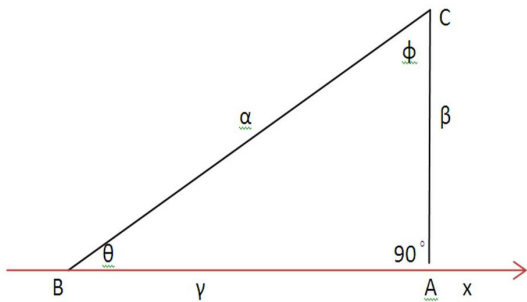
Fig. 3:

$$\tan \theta = \frac{\beta}{\gamma} \quad \text{and} \quad \tan \varphi = \frac{\gamma}{\beta}. \qquad (16)$$

Similarly, after contraction of side AB (and consequently contraction of the oblique side BC) one gets (Fig. 4)

$$\tan \theta' = \frac{\beta'}{\gamma'} = \frac{\beta}{\gamma C(v)} \qquad (17)$$

and

$$\tan \varphi' = \frac{\gamma'}{\beta'} = \frac{\gamma C(v)}{\beta} \qquad (18)$$

$$\frac{\tan \theta'}{\tan \theta} = \frac{\dfrac{\beta}{\gamma C(v)}}{\dfrac{\beta}{\gamma}} = \frac{1}{C(v)} \qquad (19)$$

or

$$\tan \theta' = \frac{\tan \theta}{C(v)} \qquad (20)$$
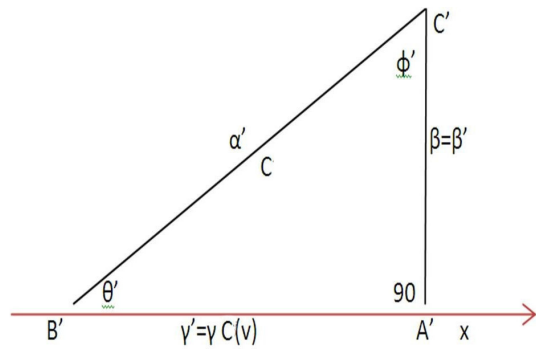
Fig. 4:

and similarly

$$\frac{\tan \varphi'}{\tan \varphi} = \frac{\dfrac{\gamma C(v)}{\beta}}{\dfrac{\gamma}{\beta}} = C(v) \qquad (21)$$

or

$$\tan \varphi' = \tan \varphi \cdot C(v). \qquad (22)$$

Therefore one got the same Angle Distortion Equations for a right triangle traveling with one of its legs along the motion direction.

3 Tangential relations between distorted angles vs. original angles of a general triangle

Let's suppose a general triangle ΔABC is travelling at speed v along the side BC as in Fig. 5.
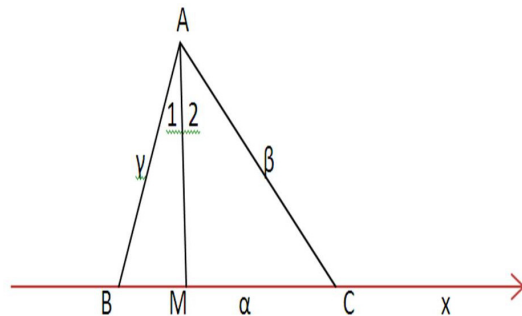
Fig. 5:

The height remains not contracted: $AM \equiv A'M'$. We can split this figure into two traveling right sub-triangles as in Fig. 6.

In the right triangles $\Delta A'M'B'$ and respectively $\Delta A'M'C'$ one has

$$\tan B' = \frac{\tan B}{C(v)} \quad \text{and} \quad \tan C' = \frac{\tan C}{C(v)}. \qquad (23)$$

Also

$$\tan A_1' = \tan A_1 C(v) \quad \text{and} \quad \tan A_2' = \tan A_2 C(v). \qquad (24)$$
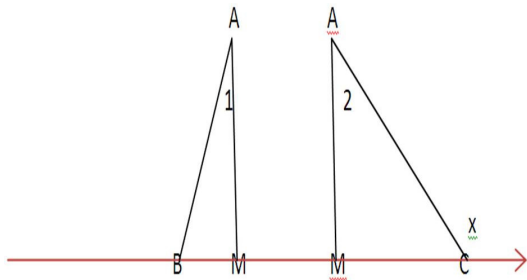
Fig. 6:
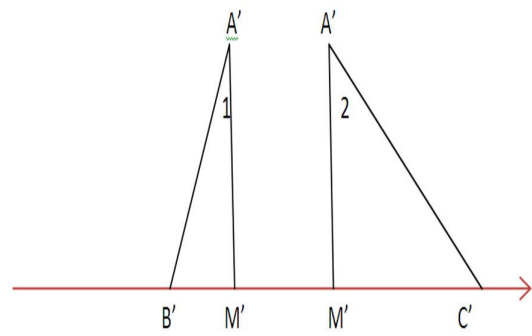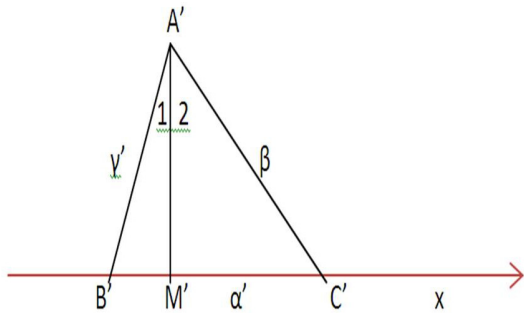
Fig. 7:

But

$$
\begin{aligned}
\tan A' &= \tan(A'_1 + A'_2) = \frac{\tan A'_1 + \tan A'_2}{1 - \tan A'_1 \tan A'_2} \\
&= \frac{\tan A_1 C(v) + \tan A_2 C(v)}{1 - \tan A_1 C(v) \tan A_2 C(v)} \\
&= C(v) \cdot \frac{\tan A_1 + \tan A_2}{1 - \tan A_1 \tan A_2 C(v)^2} \\
&= C(v) \cdot \frac{\dfrac{\tan A_1 + \tan A_2}{1 - \tan A_1 \tan A_2} \cdot (1 - \tan A_1 \tan A_2)}{1 - \tan A_1 \tan A_2 C(v)^2} \\
&= C(v) \cdot \frac{\tan(A_1 + A_2)}{1} \cdot \frac{1 - \tan A_1 \tan A_2}{1 - \tan A_1 \tan A_2 C(v)^2}.
\end{aligned}
$$

$$
\tan A' = C(v) \cdot \tan(A) \cdot \frac{1 - \tan A_1 \tan A_2}{1 - \tan A_1 \tan A_2 C(v)^2}. \tag{25}
$$

We got

$$
\tan A' = \tan(A) \cdot C(v) \cdot \frac{1 - \tan A_1 \tan A_2}{1 - \tan A_1 \tan A_2 C(v)^2} \tag{26}
$$

Similarly we can split this Fig. 7 into two traveling right sub-triangles as in Fig. 8.

Fig. 8:

4 Other relations between the distorted angles and the original angles

1. Another relation uses the Law of Sine in the triangles ΔABC and respectively $\Delta A'B'C'$:

$$
\frac{\alpha}{\sin A} = \frac{\beta}{\sin B} = \frac{\gamma}{\sin C} \tag{27}
$$

$$
\frac{\alpha'}{\sin A'} = \frac{\beta'}{\sin B'} = \frac{\gamma'}{\sin C'}. \tag{28}
$$

After substituting

$$
\alpha' = \alpha C(v) \tag{29}
$$

$$
\beta' = \beta \mathscr{O}C(v, C) \tag{30}
$$

$$
\gamma' = \gamma \mathscr{O}C(v, B) \tag{31}
$$

into the second relation one gets:

$$
\frac{\alpha C(v)}{\sin A'} = \frac{\beta \mathscr{O}C(v, C)}{\sin B'} = \frac{\gamma \mathscr{O}C(v, B)}{\sin C'}. \tag{32}
$$

Then we divide term by term the previous equalities:

$$
\frac{\dfrac{\alpha}{\sin A}}{\dfrac{\alpha C(v)}{\sin A'}} = \frac{\dfrac{\beta}{\sin B}}{\dfrac{\beta \mathscr{O}C(v, C)}{\sin B'}} = \frac{\dfrac{\gamma}{\sin C}}{\dfrac{\gamma \mathscr{O}C(v, B)}{\sin C'}} \tag{33}
$$

whence one has:

$$
\begin{aligned}
\frac{\sin A'}{\sin A \cdot C(v)} &= \frac{\sin B'}{\sin B \cdot \mathscr{O}C(v, C)} \\
&= \frac{\sin C'}{\sin C \cdot \mathscr{O}C(v, B)}.
\end{aligned} \tag{34}
$$

2. Another way:

$$
A' = 180° - (B' + C') \quad \text{and} \quad A = 180° - (B + C) \tag{35}
$$

$$
\begin{aligned}
\tan A' &= \tan[180° - (B' + C')] = -\tan(B' + C') \\
&= -\frac{\tan B' + \tan C'}{1 - \tan B' \cdot \tan C'}
\end{aligned}
$$

$$
= \quad -\frac{\dfrac{\tan B}{C(v)} + \dfrac{\tan C}{C(v)}}{1 - \tan B \cdot \tan C / C(v)^2}
$$

$$
= \quad -\frac{1}{C(v)} \cdot \frac{\tan B + \tan C}{1 - \tan B \cdot \tan C / C(v)^2}
$$

$$
= \quad -\frac{\tan(B + C)}{C(v)} \cdot \frac{1 - \tan B \tan C}{1 - \tan B \cdot \tan C / C(v)^2}
$$

$$
= \quad -\frac{-\tan[180° - (B + C)]}{C(v)} \cdot \frac{1 - \tan B \cdot \tan C}{1 - \tan B \cdot \tan C / C(v)^2}
$$

$$
= \quad \frac{\tan A}{C(v)} \cdot \frac{1 - \tan B \cdot \tan C}{1 - \tan B \cdot \tan C / C(v)^2}.
$$

We got

$$
\tan A' = \frac{\tan A}{C(v)} \cdot \frac{1 - \tan B \cdot \tan C}{1 - \tan B \cdot \tan C / C(v)^2}. \qquad (36)
$$

References

1. Smarandache F. New Relativistic Paradoxes and Open Questions. Somipress, Fes, 1983.

2. Smarandache F. Oblique-Length Contraction Factor in the Special Theory of Relativity, *Progress in Physics*, 2013, v. 1, 60–62.

3. Einstein A. On the Electrodynamics of Moving Bodies. *Annalen der Physik*, 1905, v. 17, 891–921.

4. Smarandache F. Absolute Theory of Relativity and Parameterized Special Theory of Relativity and Noninertial Multirelativity. Somipress, Fes, 1982.

The Electron-Vacuum Coupling Force in the Dirac Electron Theory and its Relation to the Zitterbewegung

William C. Daywitt

National Institute for Standards and Technology (retired), Boulder, Colorado. E-mail: wcdaywitt@me.com

From the perspective of the Planck vacuum theory, this paper argues that the standard estimate of the onset radius for electron-positron pair production as the Dirac electron is approached (in its rest frame) is significantly overestimated. The standard value is taken to be the electron Compton radius, while the estimate derived here from the coupling force is over four times smaller. The resulting separation of the Compton radius from the onset radius leads to a clear explanation of the zitterbewegung in terms of vacuum dynamics, making the zitterbewegung a relevant part of the electron theory.

1 Dirac Electron

The size of the electron has been a long debated question. In classical physics the idea that the electron radius r_0 is purely electromagnetic leads to the calculation

$$r_0 = \frac{e^2}{mc^2} = 2.82 \times 10^{-13} \tag{1}$$

centimeters, while the electron's Compton radius

$$r_c = \frac{e^2}{\alpha mc^2} = \frac{e_*^2}{mc^2} = 3.86 \times 10^{-11} \tag{2}$$

is larger by the factor $1/\alpha \, (\approx 137)$, where $\alpha \, (= e^2/e_*^2)$ is the fine structure constant. The standard caveat at this point in the calculations is that, for any radius smaller than r_c (like r_0), classical considerations are irrelevant due to the possible appearance of electron-positron pairs. So the onset radius for electron-position pair production is an important parameter in the Dirac theory of the electron. What follows takes a detailed look at the structure of the second ratio in (2) and suggests that an onset radius derived from the coupling force the Dirac electron (De) exerts on the vacuum state produces a better estimate of that radius.

In the Planck vacuum (PV) theory [1] the product $e_*^2 = (-e_*)(-e_*)$ in (2) consists of two distinctively different charges. One of the bare charges belongs to the De (a massive point charge $(-e_*, m)$ that obeys the Dirac equation and that is coupled to the Dirac vacuum [2]), and the other to the separate Planck particles constituting the PV negative-energy state. In addition, it can be argued [3] that the force

$$\frac{e_*^2}{r^2} \tag{3}$$

is a polarization-distortion force that the free-space De exerts on the omnipresent PV state. Since this force exists between the electron charge and the individual Planck-particle charges within the PV, a potential

$$V(r) = -\int_{r_1}^{r} \frac{e_*^2}{r^2} dr = \left(\frac{1}{r} - \frac{1}{r_1}\right)e_*^2 \tag{4}$$

can be defined for the De-PV system, except for the difficulty in determining the integration constant r_1.

The massive point charge $(-e_*, m)$ has two parts, its charge $(-e_*)$ and its mass m. Thus, in addition to the polarization force (3), the De distorts the PV due to a gravitational-like attraction between its mass and the individual masses of the Planck particles in the PV. This curvature force is given by [3]

$$-\frac{mc^2}{r} = -\frac{mc^2 G}{r G} = -\frac{mm_* G}{r_* r} \tag{5}$$

where m_* and r_* are the mass and Compton radius of the individual Planck particles and G is Newton's gravitational constant. $(G = e_*^2/m_*^2$ and $e_*^2 = r_* m_* c^2$ are used in deriving the final ratio in (5).) This force is the force of attraction the massive point charge at $\langle r \rangle \approx 0$ exerts on the negative-energy Planck particle at a radius r from that charge. Now the total De distortion force becomes

$$\frac{e_*^2}{r^2} - \frac{mc^2}{r} \tag{6}$$

and, as seen in the next section, the r_1-problem of the previous paragraph disappears. Part of the response to the De force (6) acting on the PV is hidden in the Dirac equation as the zitterbewegung.

[The average $\langle r \rangle \approx 0$ signifies a small, but unknown, radius encircling the massive point charge $(-e_*, m)$ and in which the electron mass is created (see the Appendix). This average is more properly expressed as $\sqrt{\langle r^2 \rangle} \ll r_c$.]

2 Dirac Equation

The force difference in (6) vanishes at the De's Compton radius

$$r_c = \frac{e_*^2}{mc^2} \tag{7}$$

which is that radius where the polarization and curvature forces have the same magnitude. This is a central parameter in the theory of the electron-positron system, for the free-

particle Dirac equation can be expressed as (using $c\hbar = e_*^2$) [4, p. 74]

$$ie_*^2 \left(\frac{\partial}{c\partial t} + \boldsymbol{\alpha} \cdot \nabla \right) \psi = mc^2 \beta \psi \qquad \text{or}$$

$$ir_c \left(\frac{\partial}{c\partial t} + \boldsymbol{\alpha} \cdot \nabla \right) \psi = \beta \psi \qquad (8)$$

where, in the rest frame of the De, the parameter r_c represents the radius of an imaginary sphere surrounding the massive point charge and on which the PV is undistorted (where (9) and (10) vanish).

Now the De-PV coupling force

$$F(r) = \frac{e_*^2}{r^2} - \frac{mc^2}{r} \qquad (9)$$

leads, in place of (4), to the potential

$$V(r) = -\int_{r_c}^{r} F(r)dr = \left(\frac{1}{r} - \frac{1}{r_c} \right) e_*^2$$

$$-mc^2 \ln \frac{r_c}{r} \qquad (r \leqslant r_c) \qquad (10)$$

with no undetermined constants.

Recalling that any sufficiently strong positive potential acting on the vacuum state enables electron-positron pair production to take place in free space (see any relativistic discussion of the Klein Paradox, e.g. [4, p. 131]), it is reasonable to conclude that the point at which pairs may begin to show up as the De is approached is where $V(r) = 2mc^2$ since the positive energy in free space and negative energy of the PV begin to overlap at this potential. Then solving (10) for r yields the quadrature formulas

$$\frac{r_c}{r} - \ln \frac{r_c}{r} = 3 \qquad \text{or} \qquad \frac{\exp(r_c/r)}{r_c/r} = e^3 \qquad (11)$$

either one of which produces $r \approx r_c/4.5$. This pair-production onset radius is significantly smaller than the standard estimate ($r \sim r_c$) because the curvature-force term in (9) compresses the PV state, countering the polarization force that expands that state and exposes its energies to free space. This important result implies that, for any $r > r_c/4.5$, there can be no exchange of free electrons with electrons from electron-positron pairs associated with the PV state.

3   QED Comparison

The standard estimate of the onset radius is based on virtual electron-positron transitions and the time-energy uncertainty relation [5, p. 323]

$$\Delta t\, \Delta E \sim \hbar \quad \longrightarrow \quad c\Delta t \sim \frac{c\hbar}{\Delta E} = \frac{e_*^2}{2mc^2} = \frac{r_c}{2} \qquad (12)$$

where the original free electron jumps into the positron hole and the electron from the pair becomes the new free electron. As this process takes place at a high rate, the resulting cloud of "hide-and-seek" electrons is perceived as a spread-out point electron with a radius $r \sim r_c/2$. This radius is usually rounded off to $r \sim r_c$. It is interesting that arbitrarily replacing r_1 in (4) by r_c leads to the estimate $r = r_c/3$.

Whatever the true magnitude of the onset radius, it is worth noting the following quantum electrodynamic conclusions [5, pp. 402–403]: the interaction of the De with the quantum vacuum spreads out the point-like nature of the De and leads to a natural scale r_c for the model; the De in some respects behaves as though it increases in size from a point particle to a particle with a radius of about one r_c; it is improbable that the electron has "structure"; and the apparent spread of the De does not alter the fact that the electron in QED is still regarded as a pure point particle. In addition to these conclusions, high-energy scattering experiments probing small distances indicate that the electron, if not a point particle, is certainly not larger than about 10^{-15} cm ($r_c/39,000$).

Except for the magnitude of the onset and spread radii, the calculations in Sections 1 and 2 are mostly in agreement with the spirit of the QED conclusions of the previous paragraph. Also the earlier assumption at the end of Section 1, that $\langle r \rangle \approx 0$, is in line with the experimental result ($r_c/39,000$) at the end of the previous paragraph.

Since the onset radius is an important concept in the electron model, a definitive calculation of this radius is crucial to understanding the electron — indeed, contrary to the standard view, it is shown in the present paper that the Compton radius r_c and the pair-creation onset radius $r_c/4.5$ are two *distinctly different* parameters, the first referring to the vanishing-coupling-force sphere centered on the point electron (in its rest frame), and the second to the possible onset of electron-positron pairs. This separation of the Compton and onset radii leads to a believable zitterbewegung model.

4   Zitterbewegung

The zitterbewegung (a highly oscillatory, microscopic motion with velocity c) has been a long-time mathematical conundrum. Barut and Bracken [6, p. 2458] reexamine the Schrödinger calculations leading to the zitterbewegung and replace his "microscopic momentum" vector with a "relative momentum" vector in the rest frame of the particle. Of interest here are the two resulting commutator brackets ($\hbar = r_c mc$ and $c\hbar = e_*^2$ are used)

$$[Q_j, H_r] = ir_c c P_j \qquad \text{and}$$

$$[P_j, H_r] = -4i\frac{mce_*^2}{r_c^2} Q_j \qquad (13)$$

from the theory, where ($j = 1, 2, 3$) and $H_r = mc^2 \beta$ is the Dirac Hamiltonian in the rest frame.

Applying the Heisenberg-picture time derivative

$$\dot{A} = \frac{i}{\hbar}[H_r, A] \qquad (14)$$

to the commutators in (13) leads to the "relative momentum"

$$P_j = m\dot{Q}_j \qquad \text{and} \qquad \dot{P}_j = -4\left(\frac{e_*^2}{r_c^3}\right)Q_j \qquad (15)$$

which describes the dynamics of a harmonic oscillator with angular frequency

$$\omega = \left(\frac{4 \cdot e_*^2}{mr_c^3}\right)^{1/2} = \left(\frac{4 \cdot r_c mc^2}{mr_c^3}\right)^{1/2} = \frac{2c}{r_c} \, . \qquad (16)$$

Since the Compton relation derives from the equality of the polarization- and curvature-force magnitudes on the r_c-sphere surrounding the massive point charge, the oscillator dynamics must be due to a reaction of the PV to the De perturbing force $e_*^2/r^2 - mc^2/r$, *not* to a direct dynamical involvement of the massive point charge itself. This latter conclusion is supported by the fact that the eigenvalues of the $\dot{Q}_j$ operator are $\pm c$, outlawing the involvement of a massive particle whose velocity must be less that c.

The "spring constant", $4(e_*^2/r_c^3)$, in (15) is easily shown to be related to the r_c-sphere, for $r = r_c + \Delta r$ in (9) leads to

$$F(r_c + \Delta r) = \frac{e_*^2}{(r_c + \Delta r)^2} - \frac{mc^2}{r_c + \Delta r}$$

$$= -\frac{(e_*^2/r_c^3)\Delta r}{(1 + \Delta r/r_c)^2} \approx -\left(\frac{e_*^2}{r_c^3}\right)\Delta r \qquad (17)$$

where $F(r_c) = 0$, and $\Delta r \ll r_c$ in the final ratio.

The Schrödinger "microscopic coordinate"

$$\boldsymbol{\xi} = \left[\boldsymbol{\alpha}(0) - \frac{mc^2}{H}\frac{\widehat{\mathbf{p}}}{mc}\right] \cdot \frac{ir_c}{2}\frac{mc^2}{H}\exp\left[-i\frac{2c}{r_c}\frac{H}{mc^2}t\right] \qquad (18)$$

is retained in the Barut-Bracken analysis [6, eqn. 19]. The first part of this operator equation corresponds to the macroscopic motion of the massive point charge and the second part to the high-frequency zitterbewegung superimposed on the macroscopic motion. In the rest frame of the massive charge (18) reduces to [6, eqn. 34]

$$Q_j(t) = [\boldsymbol{\xi}_r(t)]_j = \alpha_j(0) \cdot \frac{ir_c}{2}\beta\exp\left[-i\frac{2c}{r_c}\beta t\right] \neq 0 \qquad (19)$$

the nonvanishing of which emphasizes again that the zitterbewegung is not fundamentally associated with the motion of the particle, as the particle leading to (19) is at rest. (The rest frame operators $H_r = mc^2\beta$ and $H_r^{-1} = \beta/mc^2$ are used in (19)).

5 Comments and Summary

The preceding calculations have separated the Compton radius (r_c) from the onset radius ($r_c/4.5$), with the result that the Compton radius is no longer associated with electron-positron pair production, being outside the onset radius. Thus the zitterbewegung is not related to the pair-production characteristic of an over-stressed ($V(r) \geqslant 2mc^2$) PV state. Instead, the zitterbewegung is seen to be the consequence of a PV-resonance phenomenon (with the resonant frequency $2c/r_c$) associated with the r_c-sphere. Also, most of the confusion surrounding the zitterbewegung is the result of attempting to attribute the phenomenon directly to the dynamics of the electron particle rather than the dynamics of the vacuum state. Finally, the zitterbewegung can now be seen, not as a mathematical curiosity, but as an integral part of the Dirac electron theory.

The following picture of the Dirac electron emerges: centered at the origin of the rest frame is the massive point charge with an effective volumetric radius $\langle r \rangle \approx 0$; surrounding this charge is a hypothetical sphere of radius $r_c/4.5$ within which the positive energy of the free electron and the negative energy of the PV overlap, allowing electron-positron pairs to be excited; surrounding this combination is a spherical annulus of radius $r_c/4.5 < r \leqslant r_c$, where pair production does not occur; and beyond the r_c-sphere ($r \geqslant r_c$) is a region of diminishing PV stress, a compression that decreases with increasing r according to the force difference (9).

Appendix: Electron Mass

The massless point charge is denoted by $(-e_*)$ and the massive point charge by $(-e_*, m)$, where m is the electron mass. In the PV theory this mass is an acquired property of the electron, resulting from the point charge being driven by the random electromagnetic zero-point background field [7,8]. Furthermore, the energy absorbed by the charge from the field is re-radiated back into free space in a detailed-balance manner, leaving the isotropy and spectral density of the zero-point background unchanged [9].

The derived mass is

$$m = \frac{4r_c e_*^2}{9r_*^2 c^2}\frac{\left\langle (dr'/dt)^2 \right\rangle}{c^2} \qquad (A1)$$

where $e_* r'$ is the dipole moment of the point charge $(-e_*)$ about $r' = 0$ as it is being driven by the zero point field. The relative root-mean-square velocity of the charge within $\langle r \rangle \approx 0$ is [7]

$$\left(\frac{\left\langle (dr'/dt)^2 \right\rangle}{c^2}\right)^{1/2} = \frac{3}{2}\frac{r_*}{r_c} \sim 10^{-22} \qquad (A2)$$

which is vanishingly small because of the large density ($\sim 1/r_*^3$) of Planck particles in the PV contributing simultaneously to the zero-point background field; endowing the corresponding field spectrum with frequencies as high as $\sim c/r_*$,

where r_* is the Planck length. It is predominately the high frequencies in the spectrum that define the mass and prevent the r-m-s velocity from significantly increasing in magnitude [10].

The squared charge e_*^2 in (A1) comes from squaring the time derivative of the dipole moment $e_* r'$. Thus (A1) implies that *the center-of-mass and the center-of-charge are the same.* The question of centers often comes up in the discussion of the zitterbewegung [11, pp. 62–64] and is a reflection of the fact that the zitterbewegung is being explained in terms of the massive-charge motion rather than the $2c/r_c$ resonance associated with the r_c-sphere and the vacuum state.

References

1. Daywitt W.C. The Planck vacuum. *Progress in Physics*, 2009, v. 1, 20–26.

2. Dirac P.A.M. A Theory of Electrons and Protons. *Proceedings of the Royal Society of London A*, 1930, v. 126, 360–365.

3. Daywitt W.C. The Dirac Electron in the Planck Vacuum Theory. *Progress in Physics*, 2010, v. 4, 69–71.

4. Gingrich D.M. Practical Quantum Electrodynamics. CRC, The Taylor & Francis Group, Boca Raton, London, New York, 2006.

5. Milonni P.W. The Quantum Vacuum – an introduction to quantum electrodynamics. Academic Press, New York, 1994.

6. Barut A.O. and Bracken A.J. *Zitterbewegung* and the internal geometry of the electron. *Physical Review D*, 1981, v. 23, no. 10, 2454–2463.

7. Daywitt W.C. The Source of the Quantum Vacuum. *Progress in Physics*, 2009, v. 1, 27–32.

8. Puthoff H.E. Gravity as a zero-point-fluctuation force. *Physical Review A*, 1989, v. 39, no. 5, 2333–2342.

9. Boyer T.H. Random electrodynamics: the theory of classical electrodynamics with classical electrodynamic zero-point radiation. *Physical Review D*, 1975, v. 11, no. 4, 790–808.

10. Daywitt W.C. Neutron Decay and its Relation to Nuclear Stability. To be published in *Galilean Electrodynamics* (pre-published in www.planckvacuum.com). See the appendix of this reference.

11. Grandy Jr. W.T. Relativistic Quantum Mechanics of Leptons and Fields. Kluwer Academic Publishers, Dordrecht—London, 1991.

Geometrical Derivation of the Lepton PMNS Matrix Values

Franklin Potter

Sciencegems.com, 8642 Marvale Drive, Huntington Beach, CA, USA. E-mail: frank11hb@yahoo.com

The linear superposition of generators of the 3 discrete binary rotational subgroups [332], [432], [532] of the Standard Model determine the PMNS matrix elements. The 6 leptons are 3-D entities representing these 3 groups, one group for each lepton family.

1 Introduction

Numerous attempts to derive the neutrino PMNS matrix from various discrete group horizontal symmetries have led to partial success. Herein I determine the true source of the PMNS matrix elements by using the linear superposition of the generators for 3 discrete binary rotational subgroups of the Standard Model (SM) electroweak gauge group $SU(2)_L \times U(1)_Y$.

In a series of articles [1–4] I have proposed 3 discrete binary rotational subgroups of the SM gauge group for 3 lepton families in R^3 and the related 4 discrete binary rotational subgroups in R^4 for 4 quark families, one binary group for each family. The generators for these 7 binary groups are quaternions operating in R^3, in R^4, and in C^2. I use these binary group quaternion generators to calculate the matrix elements for the PMNS mixing matrix for the leptons.

In another article under preparation I use the same approach, with an important modification, to calculate the standard CKM mixing matrix for the quarks as well as a proposed CKM4 mixing matrix for four quark families.

The SM local gauge group $SU(2)_L \times U(1)_Y \times SU(3)_C$ defines an electroweak(EW) interaction part and a color interaction part. The EW isospin states define the flavor of the fundamental lepton and quark states. However, experiments have determined that these left-handed flavor states are linear superpositions of mass eigenstates.

For the 3 lepton families, one has the neutrino flavor states ν_e, ν_μ, ν_τ and the mass states ν_1, ν_2, ν_3 related by the PMNS matrix U_{ij}

$$\begin{bmatrix} \nu_e \\ \nu_\mu \\ \nu_\tau \end{bmatrix} = \begin{bmatrix} U_{e1} & U_{e2} & U_{e3} \\ U_{\mu1} & U_{\mu2} & U_{\mu3} \\ U_{\tau1} & U_{\tau2} & U_{\tau3} \end{bmatrix} \begin{bmatrix} \nu_1 \\ \nu_2 \\ \nu_3 \end{bmatrix}$$

From experiments [5], the PMNS angles have been estimated to be

$$\theta_{12} = 32.6° - 34.8°, \quad \theta_{13} = 8.5° - 9.4°,$$

$$\theta_{23} = 37.2° - 39.8°, \quad \delta = (0.77 - 1.36)\pi.$$

Consequently, for the normal hierarchy of neutrino masses, one has the empirically determined PMNS matrix

$$\begin{bmatrix} 0.822 & 0.547 & -0.150 + 0.038i \\ -0.356 + 0.0198i & 0.704 + 0.0131i & 0.614 \\ 0.442 + 0.0248i & -0.452 + 0.0166i & 0.774 \end{bmatrix}$$

which can be compared to my resultant derived PMNS matrix in the standard parametrization

$$\begin{bmatrix} 0.817 & 0.557 & -0.149e^{-i\delta} \\ -0.413 - 0.084e^{i\delta} & 0.605 - 0.057e^{i\delta} & -0.673 \\ -0.383 + 0.090e^{i\delta} & 0.562 + 0.061e^{i\delta} & 0.725 \end{bmatrix}$$

In the SM the EW isospin symmetry group that defines the lepton and quark flavor states is assumed to be the Lie group SU(2) with its two flavor eigenstates per family. In this context there is no fundamental reason for Nature to have more than one fermion family, and certainly no reason for having 3 lepton families and at least 3 quark families. As far as I know, this normal interpretation of the SM provides no answer that dictates the actual number of families, although the upper limit of 3 lepton families with low mass neutrinos is well established via Z^0 decays and via analysis of the CMB background. There are claims also that one cannot have more than 15 fundamental fermions (plus 15 antifermions) without violating certain cosmological constraints.

My geometrical approach makes a different choice, for I utilize discrete binary rotational subgroups of SU(2) instead, a different subgroup for each family. Each discrete binary group has two eigenstates and three group generators, just like SU(2). Whereas the three generators for the SU(2) Lie group are essentially the 2 x 2 Pauli matrices, the three generators for each of the 3 lepton discrete binary groups [332], [432], [532], (also labeled 2T, 2O, 2I) in R^3 and the 4 quark discrete groups [333], [433], [343], [533], (also labeled 5-cell, 16-cell, 24-cell, 600-cell) in R^4 are not exactly the Pauli matrices.

I propose that this difference between the discrete subgroup generators and the Pauli matrices is the fundamental source of the lepton and the quark mixing matrices, and the calculated results verify this conjecture. In other words, one requires the mixing of the different family discrete groups in order to have a complete set of three generators equivalent to the three SU(2) generators, separately for the leptons and for the quarks. The mixing matrices, PMNS and CKM4, express this linear superposition of the discrete group generators.

2 The PMNS calculation

In order to calculate the PMNS values one can use either unit quaternions or unitary 2x2 complex matrices. The unit quaternion generators are equivalent to the SU(2) generators.

The unit quaternion q = a + b$\mathbf{i}$ + c$\mathbf{j}$ + d$\mathbf{k}$, where the coefficients a, b, c, d are real numbers for the one real and three imaginary axes. The unit quaternion spans the space R^4 while the imaginary prime part spans the subspace R^3. With $i^2 = j^2 = k^2 = -1$, the quaternion can be expressed as an SU(2) matrix

$$\begin{bmatrix} a + bi & c + di \\ -c + di & a - bi \end{bmatrix}$$

Both the quaternions and the SU(2) matrices operate in the unitary plane C^2 with its two orthogonal complex axes, so the quaternion can be written also as q = u + v$\mathbf{j}$, with u = a + b$\mathbf{i}$ and v = c + d$\mathbf{i}$. The three Pauli matrices σ_x, σ_y, σ_z, are the simple quaternions k, j, and i, respectively.

For the three lepton families, each family representing its own binary rotational group, [332], [432], and [532], two of the three generators R_i, i = 1, 2, 3, in each group are equivalent to two of the three Pauli matrices. Therefore, only the remaining generator for each lepton family contributes to the mixing that produces the PMNS matrix. That is, in the notation of H.M.S. Coxeter [6], R_1 = j, R_3 = i, and

$$R_2 = -i\cos\frac{\pi}{q} - j\cos\frac{\pi}{p} + k\sin\frac{\pi}{h} \qquad (1)$$

for the three binary groups [p q r] and the h values 4, 6, and 10, respectively.

Defining the golden ratio $\phi = (\sqrt{5}+1)/2$, the appropriate generators R_2 are listed in the table. The sum of all three R_2 generators should be k, so one has three equations for three unknowns, thereby determining the listed multiplicative factor for each R_2 generator's contribution to k after overall normalization.

Table 1: Lepton Family Discrete Group Assignments

Family	Group	R_2	Factor	Angle°
ν_e, e	[332]	$-\frac{1}{2}i - \frac{1}{2}j + \frac{1}{\sqrt{2}}k$	-0.2645	105.337
ν_μ, μ	[432]	$-\frac{1}{2}i - \frac{1}{\sqrt{2}}j + \frac{1}{2}k$	0.8012	36.755
ν_τ, τ	[532]	$-\frac{1}{2}i - \frac{\phi}{2}j + \frac{\phi^{-1}}{2}k$	-0.5367	122.459

The resulting angles in the table are determined by the arccosines of the factors, but they are twice the rotation angles required in R^3, a property of quaternion rotations. Using one-half these angles produces

$$\theta_1 = 52.67°, \quad \theta_2 = 18.38°, \quad \theta_3 = 61.23°, \qquad (2)$$

resulting in

$$\theta_{12} = 34.29°, \quad \theta_{13} = -8.56°, \quad \theta_{23} = -42.85°. \qquad (3)$$

Note that $|\theta_{12} - \theta_{13}| = |\theta_{23}|$ because of normalization.

Products of the sines and cosines of these angles in the standard parameterization are the PMNS entries, producing matrix values which compare favorably with the empirical estimates, as shown earlier. One has $\sin^2 \theta_{12} = 0.3176$ and $\sin^2 \theta_{13} = 0.0221$, both within 1σ of the empirically determined values from the neutrino experiments, according to the Particle Data Group in 2012. However, $\sin^2 \theta_{23} = 0.4625$ is outside the PDG 1σ range but agrees with the recent T2K [7] estimate $\sin^2 2\theta_{23} = 1.0$, making $|\theta_{23}| = 45°$ with $\delta \simeq 0$.

3 Conclusions

This fit of the PMNS mixing matrix derived from the three separate R_2 generators indicates that the lepton families faithfully represent the discrete binary rotational groups [332], [432], and [532] in R^3 that were introduced first in my geometrical approach back in 1986 and expanded in detail over the past two decades. In particular, the 6 lepton states are linear superpositions of the two degenerate basis states in each of the 3 groups. My approach within the realm of the Standard Model local gauge group makes the ultimate *unique* connection to the discrete group Weyl E_8 x Weyl E_8 in 10-D spacetime and to the Golay-24 code in information theory [1].

One can conclude that leptons are 3-dimensional objects, geometrically different from the quarks which require a 4-dimensional space for their existence. Their mass ratios derive from a mathematical syzygy relation to the j-invariant of elliptic modular functions associated with these specific binary groups. In addition, one can predict that no more lepton families exist because the appropriate binary rotational symmetry groups in 3-D space have been exhausted. However, sterile neutrinos remain viable [1, 4].

Acknowledgements

References

1. Potter F. Our Mathematical Universe: I. How the Monster Group Dictates All of Physics. *Progress in Physics*, 2011, v. 4, 47–54.

2. Potter F. Discrete Rotational Subgroups of the Standard Model dictate Family Symmetries and Masses. DISCRETE'08 Conference, 2008. Online: www.sciencegems.com/DISCRETE08.PDF

3. Potter F. Unification of Interactions in Discrete Spacetime. *Progress in Physics*, 2006, v. 1, 3–9.

4. Potter F. Geometrical Basis for the Standard Model. *International Journal of Theoretical Physics*, 1994, v. 33, 279–305. Online: www.sciencegems.com/gbsm.html

5. Fogli G.L. et al. Global analysis of neutrino masses, mixings and phases. arXiv: 1205.5254v3.

6. Coxeter H.S.M. Regular Complex Polytopes. Cambridge University Press, Cambridge, 1974.

7. Abe K. et al. Evidence of Electron Neutrino Appearance in a Muon Neutrino Beam. arXiv: 1304.0841v1.

Higgs-Like Particle due to Revised Quantum Electrodynamics

Bo Lehnert

Alfvén Laboratory, Royal Institute of Technology, SE-10044 Stockholm, Sweden. E-mail: Bo.Lehnert@ee.kth.se

A Higgs-like particle having zero net electric charge, zero spin, and a nonzero rest mass can be deduced from an earlier elaborated revised quantum electrodynamical theory which is based on linear symmetry breaking through a nonzero electric field divergence in the vacuum state. This special particle is obtained from a composite longitudinal solution based on a zero magnetic field strength and on a nonzero divergence but a vanishing curl of the electric field strength. The present theory further differs from that of the nonlinear spontaneously broken symmetry by Higgs, in which elementary particles obtain their masses through an interaction with the Higgs field. An experimental proof of the basic features of a Higgs-like particle thus supports the present theory, but does not for certain confirm the process which would generate massive particles through a Higgs field.

1 Introduction

As stated in a review by Quigg [1] among others, the Higgs boson is a particle of zero electric charge and nonzero rest mass. The magnitude of the mass is, however, so far not predicted by theory. Several authors and recently Garisto and Argawal [2] have further pointed out that this particle is a spin-zero boson.

In this investigation will be shown that a particle with such basic properties can be deduced from an earlier elaborated revised quantum electrodynamical theory [3], and the consequences of this will be further discussed here.

2 Steady Axisymmetric States of Revised Quantum Electrodynamics

For the field equations of the revised theory to be used in this context, reference is made to earlier detailed deductions [3]. The latter are based on a broken symmetry between the field strengths $\mathbf{E}$ and $\mathbf{B}$, through the introduction of a nonzero divergence $\text{div}\,\mathbf{E} = \bar{\rho}/\varepsilon_0$ as being based on the quantum mechanical Zero Point Energy of the vacuum state. In a spherical frame (r, θ, φ) of reference in an axially symmetric steady state with $\partial/\partial\varphi = 0$ and $\partial/\partial t = 0$, this leads to a magnetic vector potential $\mathbf{A} = (0, 0, A)$ and a space charge current density $\mathbf{j} = (0, 0, C\bar{\rho})$ due to the source $\bar{\rho}$. Here $C = \pm c$ represents the two spin directions, with c standing for the velocity constant of light. Introducing the normalized radius $\rho = r/r_0$ with r_0 as a characteristic length, and the separable generating function

$$F(r, \theta) = CA - \phi = G_0 G(\rho, \theta) = G_0 R(\rho) \cdot T(\theta) \quad (1)$$

where ϕ is the electrostatic potential, this yields

$$CA = -(\sin\theta)^2 DF \quad (2)$$

$$\phi = -\left[1 + (\sin\theta)^2 D\right] F \quad (3)$$

$$\bar{\rho} = -\frac{\varepsilon_0}{r_0^2 \rho^2} D\left[1 + (\sin\theta)^2 D\right] F \quad (4)$$

with the operator

$$
\begin{aligned}
D &= D_\rho + D_\theta \\
D_\rho &= -\frac{\partial}{\partial\rho}\left(\rho^2 \frac{\partial}{\partial\rho}\right) \\
D_\theta &= -\frac{\partial^2}{\partial\theta^2} - \frac{\cos\theta}{\sin\theta}\frac{\partial}{\partial\theta}.
\end{aligned}
\quad (5)
$$

The field strengths then become

$$\mathbf{B} = \text{curl}\,\mathbf{A} = \text{curl}\left[0, 0, -\frac{1}{C}(\sin\theta)^2 DF\right] \quad (6)$$

$$\mathbf{E} = -\nabla\phi = \nabla\left\{\left[1 + (\sin\theta)^2 D\right] F\right\} \quad (7)$$

for an elementary mode generated by a given function F determined by the radial and polar parts $R(\rho)$ and $T(\theta)$. Here $\text{curl}\,\mathbf{E} = 0$.

As a first step we consider the convergence properties of R and the symmetry properties of T with respect to the equatorial plane $\theta = \pi/2$. There are four alternatives of which there is one with a divergent R at the origin $\rho = 0$ and with a T of top-bottom symmetry, thereby leading to a net integrated electric charge q_0 and magnetic moment M_0. The other three alternatives all lead to vanishing q_0 and M_0 [3], and we can here choose any of these. Then the local electric field and its divergence are still nonzero, whereas the net integrated electric charge vanishes.

As a second step two elementary modes $(^+)$ and $(^-)$ are now considered for which $C = \pm c$ and there is the same function F. For these modes the corresponding field strengths are related by

$$\mathbf{B}^+ = -\mathbf{B}^- \qquad \mathbf{E}^+ = \mathbf{E}^- \quad (8)$$

according to Equations (6) and (7). Since the field equations are linear, the sum of the two solutions $(^+)$ and $(^-)$ also becomes a solution of the field equations, thereby resulting in the field strengths

$$\mathbf{B}_H = \mathbf{B}^+ + \mathbf{B}^- = 0 \quad (9)$$

$$\mathbf{E}_H = \mathbf{E}^+ + \mathbf{E}^- = \nabla\left\{\left[1 + (\sin\theta)^2 D\right] 2F\right\}. \quad (10)$$

These strengths then stand for a "composite" mode having zero integrated charge q_o, zero magnetic moment M_0, and zero spin s_0, but a nonzero rest mass

$$m_0 = \frac{4\pi\varepsilon_0}{c^2} r_0 G_0^2 J_m = \left(\frac{1}{2}\varepsilon_0 E_{eq}^2\right)\left(\frac{4}{3}\pi r_0^3\right). \quad (11)$$

Here $E_{eq}^2 = 6(G_0/r_0)^2 J_m$, the dimensionless integral is

$$J_m = \int_0^\infty \int_0^\pi I_m \, d\rho \, d\theta \qquad I_m = fg \quad (12)$$

and

$$f(\rho,\theta) = -(\sin\theta) D\left[1 + (\sin\theta)^2 D\right] G \quad (13)$$

$$g(\rho,\theta) = -\left[1 + 2(\sin\theta)^2 D\right] G \quad (14)$$

when a convergent radial part R is now being chosen [3].

It has first to be observed that this composite mode can be related to an option of the Higgs boson which is not truly a fundamental particle but is built out of as yet unobserved constituents, as also stated by Quigg [1]. Moreover, the vanishing magnetic field $\mathbf{B}_H$ of Equation (9) is in a way related to the longitudinal "S-wave" of the earlier theory [3], as well as to the longitudinal state of a massive boson mentioned by Higgs [4]. Finally, the magnitude of the nonzero mass is so far not predicted by theory [1]. From Equation (11) it should be due to the energy density of an equivalent electric field E_{eq}. The absence of a magnetic field may also make the particle highly unstable.

3 Discussion

An experimental proof of an existing Higgs-like particle with zero net electric charge, zero spin, and nonzero rest mass could thus be taken as support of the present revised quantum electrodynamical theory [3]. The latter is characterized by intrinsic linear symmetry breaking, leading in general to nonzero rest masses of elementary particles.

Such a proof does on the other hand not for certain become a full experimental confirmation also for the same particle to provide all other elementary particles with mass through the completely different spontaneous nonlinear symmetry breaking interaction between the Higgs field and massless particle concepts of the Standard Model [1, 4].

Possible the present approach [3] and that of Higgs [1, 4] could have a point in common. This is trough the Zero Point Energy field being present all over space on one hand [3], and a generally existing Higgs field in space on the other [1, 4].

References

1. Quigg C. The coming revolution in particle physics. *Scientific American*, February 2008, 38–45.

2. Garisto R. and Agarwal A. The import of the Higgs boson. *Scientific American*, September 2012, page 16.

3. Lehnert B. Revised quantum electrodynamics. Nova Science Publishers, New York 2013, Chapter 6.

4. Higgs P.W. Spontaneous symmetry breakdown without massless bosons. *Physical Review*, 1966, v. 145, 1156–1163.

Key to the Mystery of Dark Energy: Corrected Relationship between Luminosity Distance and Redshift

T. X. Zhang

Department of Physics, Alabama A & M University, Normal, Alabama 35762. E-mail: tianxi.zhang@aamu.edu

A new possible explanation to the luminosity distance (D_L) and redshift (Z) measurements of type Ia supernovae (SNeIa) is developed. Instead of modifying the theory of general relativity or the Friedmann equation of cosmology with an extra scalar field or unknown energy component (e.g., dark energy), we re-examine the relationship between the luminosity distance and the cosmological redshift ($D_L - Z$). It is found that the $D_L - Z$ relation previously applied to connect the cosmological model with the measured SNeIa data is only valid for nearby objects with $Z \ll 1$. The luminosity distances of all distant SNeIa with $Z \gtrsim 1$ had been underestimated. The newly derived $D_L - Z$ relation has an extra factor $\sqrt{1 + Z}$, with which the cosmological model exactly explains all the SNeIa measurements without dark energy. This result indicates that our universe has not accelerated and does not need dark energy at all.

1 Introduction

There are five possible ways to explain the luminosity distance (D_L) and redshift (Z) measurements of type Ia supernovae (SNeIa) according to the general relativity (GR), which derives the Friedmann equation (FE) with the Friedmann-Lemaitre-Robertson-Walker (FLRW) metric of the 4D spacetime (Figure 1).

The most simple and direct way is the famous Lambda Cold Dark Matter (ΛCDM) model, currently accepted as the standard one, which introduces a cosmological constant Λ to the field equation of GR (Eq. 1), referred as a candidate of dark energy [1-2],

$$G_{\mu\nu} + \Lambda g_{\mu\nu} = \frac{8\pi G}{c^4} T_{\mu\nu}, \tag{1}$$

where $G_{\mu\nu}$ is the Einsteinian curvature tensor of spacetime, $T_{\mu\nu}$ is the energy-momentum tensor of matter, c is the light speed in free space, and G is the gravitational constant. The cosmological constant Λ was first introduced actually by Albert Einstein himself into his field equation, Eq. (1), in order to have a static universe about a century ago, and then discarded after the universe was found to be expanding [3].

The second way that has also been comprehensively studied is the scalar-tensor (S-T) theory, which introduces a scalar field Φ, usually time-dependent, to the action of spacetime (S_G) [4-5]. This category includes also the four-dimensional $f(R)$, galileon, and five-dimensional Kaluza-Klein theories with scalar fields [6-12]. The third way is the scalar perturbation (SP) theory, which inputs perturbation scalars Ψ and Φ, usually time-independent, into the FLRW metric rather than into the action S_G [13-15]. The S-T and SP theories may be equivalent because both attempt to modify the curvature of spacetime. The cosmological constant Λ can also be added to S_G for a less curvature of spactime or to the action of matter S_M for an extra energy component. The fourth possible way

is according the black hole universe (BHU) model, recently developed by the author [16-18], in which the expansion and acceleration of the universe are driven by the external energy.

The procedures that the above four models commonly follow in the explanation of the SNeIa measurements include the following four steps: (1) Modifying the FE with an appropriate input of Λ, scalar field, perturbation, or external energy; (2) Determining the expansion rates (Hubble parameter) of the universe according to their modified FEs; (3) Submitting their expansion rates into the $D_L - Z$ relation; (4) Comparing the obtained redshift dependence of their luminosity distances with the SNeIa measurements. Fitting the models to the data determines the amount of the input such as $\Omega_\Lambda \sim 0.73$ for the ΛCDM model [1-2] and $\ddot{M}(t) \sim 10^{17}$ kg/s^2 for the BHU model [18].

In this paper, a new and most probable explanation for the SNeIa measurements is developed without attempting to modify the theory of gravitation or the model of cosmology by inserting one or more fields or constants into GR or FE. Instead, we will re-examine the $D_L - Z$ relationship that connects the cosmological model with the SNeIa data. We will derive a new $D_L - Z$ relation and further compare this new relation with the SNeIa measurements to examine whether or not our universe needs the dark energy or has recently accelerated.

2 Mystery of Dark Energy

The greatest unsolved problem in the modern cosmology is the mystery of dark energy [19]. This currently most accepted hypothesis for the standard cosmological model to quantitatively explain the measurements of distant type Ia supernovae strongly relies on the $D_L - Z$ relation that is used to bridge the measured SNeIa data and the theoretical model of cosmology.

However, the $D_L - Z$ relation that was usually applied to analyze the measurements of distant type-Ia supernovae,
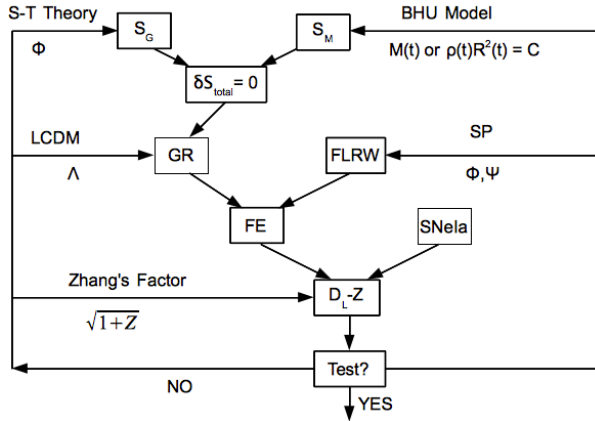
Fig. 1: Flow chat for five possible ways to explain the luminosity distance and redshift measurements of type Ia supernovae. They are: (1) GR with the cosmological constant Λ; (2) Gravitational theory with a scalar field Φ; (3) FLRW metric with perturbations Φ and Ψ; (4) Black hole universe model with increasing input of external energy $\dot{M} > 0$; and (5) Luminosity distance-redshift relation with a factor of $\sqrt{1+Z}$. This Study focuses on the fifth possible explanation.

$$D_{\mathrm{L}} \simeq c(1+Z)R(t_o) \int_{t_e}^{t_o} \frac{dt}{R(t)}, \qquad (2)$$

is an approximate expression that is only valid for nearby objects with $Z \ll 1$ in a flat universe [20]. Here t_e is the time when the light is emitted, t_o is the time when the light is observed, $R(t)$ is the scale factor, which is defined from the FLRW metric [21-24],

$$ds^2 = -c^2 dt^2 + R^2(t) \left[\frac{dr^2}{1 - kr^2} + r^2 \left(d\theta^2 + \sin^2\theta d\phi^2 \right) \right], \quad (3)$$

and governed by the Friedmann equation [25],

$$H^2(t) \equiv \frac{\dot{R}^2(t)}{R^2(t)} = \frac{8\pi G \rho_M(t)}{3} - \frac{kc^2}{R^2(t)} + \frac{\Lambda}{3}, \qquad (4)$$

according to the standard cosmological model, where $\rho_M(t)$ is the matter density, k is the curvature ($k = 0$ for a flat universe), Λ is the cosmological constant (or a candidate of dark energy), the coordinates $\{t, r, \theta, \phi\}$ are co-moving coordinates, and $H(t)$ is the Hubble parameter, which, at the present time, is called the Hubble constant and measured at $H_0 \sim 70$ km/s/Mpc [3, 26-27].

In the FLRW universe due to the time dependent scalar factor, light gets redshifted. According to the theory of GR, light travels on null geodesics (i.e., $ds^2 = 0$). Then along a radial light path, we have

$$\frac{cdt}{R(t)} = \frac{dr}{\sqrt{1 - kr^2}}. \qquad (5)$$

It follows from Eq. (5) that

$$\int_{t_e}^{t_o} \frac{cdt}{R(t)} = \int_{t_e+\delta t_e}^{t_o+\delta t_o} \frac{cdt}{R(t)} = \int_{r_1}^{0} \frac{dr}{\sqrt{1 - kr^2}}. \qquad (6)$$

Subtracting the first integral from the second and assuming $\delta t_e, \delta t_o \ll R(t)/\dot{R}(t)$, we get

$$\frac{\delta t_e}{R(t_e)} = \frac{\delta t_o}{R(t_o)}. \qquad (7)$$

Since $\delta t_e = 1/\nu_e = \lambda_e/c$ and $\delta t_o = 1/\nu_o = \lambda_o/c$, the cosmological redshift Z can be determined according to the scale factor $R(t)$ as

$$1 + Z \equiv \frac{\lambda_o}{\lambda_e} = \frac{\nu_e}{\nu_o} = \frac{\delta t_o}{\delta t_e} = \frac{R(t_o)}{R(t_e)}. \qquad (8)$$

Here λ and ν are the light wavelength and frequency, respectively. Light from a source object is redshifted because the time interval or scale factor is increased. The reason for an individual photon to be observed with smaller frequency (or energy) is due to that the time interval of observation is greater.

The scale factor is related to the energy and curvature via Eq. (4) and to the redshift via Eq. (8). In terms of Eqs. (4) and (8), the luminosity distance-redshift relation Eq. (2) can be reformed as

$$
\begin{aligned}
D_{\mathrm{L}} &\simeq c(1+Z) \int_0^Z \frac{dz'}{H(z')} \\
&= \frac{c}{H_0}(1+Z) \int_0^Z \frac{dz'}{\sqrt{\Omega_M(1+z')^3 + \Omega_\Lambda}},
\end{aligned} \qquad (9)
$$

with $1 = \Omega_M + \Omega_\Lambda$. For an arbitrary k, Eq. (9) is generally represented as

$$
D_{\mathrm{L}} \simeq \frac{c}{H_0\sqrt{|\Omega_k|}}(1+Z)S\left(\sqrt{|\Omega_k|} \times \int_0^Z \frac{dz'}{\sqrt{\Omega_M(1+z')^3 + \Omega_k(1+z')^2 + \Omega_\Lambda}} \right), \qquad (10)
$$

where

$$
S(x) = \begin{cases} \sin(x), & \text{if } k < 0 \\ x, & \text{if } k = 0 \\ \sinh(x), & \text{if } k > 0 \end{cases} \qquad (11)
$$

and $1 = \Omega_M + \Omega_\Lambda + \Omega_k$.

Comparing the luminosity distance and redshift measurements of distant SNeIa with the luminosity distance-redshift relation determined in terms of Eqs. (2), (4), and (8) or Eq. (9) or Eq. (10) with $k = 0$, two supernova research groups [1-2], respectively, claimed that the universe has recently accelerated, so that the universe is dominated ($\Omega_\Lambda \sim 0.73$) by the dark energy.

However, re-examining the derivation of the luminosity distance-redshift relation, Eq. (2) so that Eqs. (9) and (10),
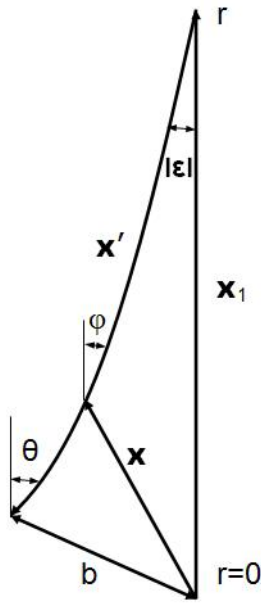
Fig. 2: Quantities used in the calculation of parallaxes and apparent luminosities [20]. The angles and the curvature of the light ray are greatly exaggerated.

we find that this relation is just an approximate relation only valid for nearby objects with $Z \ll 1$. Certainly, we cannot use it to correctly figure out the measurements of distant type Ia supernovae with $Z \gtrsim 1$. In the following, we will derive a new, more accurate and applicable also to distant objects, luminosity distance-redshift relation, which is perfectly consistent with all the measurements of type Ia supernovae without the input dark energy.

3 New $D_L - Z$ Relation

Now, the luminosity distance-redshift relation is derived by following the standard method as shown by [20] that calculates the parallaxes and apparent luminosities according to the path of light rays that leave from a source at $t = t_e$ and $r = r_e = R(t_e)r_1$ and pass to the observer at $t = t_o$ near $r = 0$ (see Figure 2). At the observation time $t = t_o$, the light source locates at $r = r_o = R(t_o)r_1$. Here, r_1 is the commoving distance defined by

$$r_1 = c \int_{t_e}^{t_o} \frac{dt}{R(t)}, \tag{12}$$

from the FLRW metric.

In the coordinate system x'^μ in which the light source is at the origin, the ray path is given by a position vector

$$\vec{x'} = \vec{n}\rho, \tag{13}$$

where $\vec{n}$ is a fixed unit vector and ρ is a variable positive parameter describing positions along the path. The coordinate

system x'^μ can be transformed to another coordinate system x^μ in which the observer is at the origin (e.g., the center of the telescope) and the light source is at $\vec{x}_1$. In the observer coordinate system, the ray path can be represented by (Eq. 14.4.2 of [20])

$$\vec{x} = \vec{x'} + \vec{x}_1 \left(\left(1 - kx'^2\right)^{1/2} - \left\{ 1 - \left(1 - kx_1^2\right)^{1/2} \right\} \frac{(\vec{x'} \cdot \vec{x}_1)}{x_1^2} \right). \tag{14}$$

For a flat universe ($k = 0$), the ray path in the coordinate system (Eq. 14) can be simplified as

$$\vec{x} = \vec{x'} + \vec{x}_1. \tag{15}$$

The parametric equation of the ray path, given by substituting Eq. (13) in Eq. (15), is then

$$\vec{x}(\rho) = \vec{n}\rho + \vec{x}_1. \tag{16}$$

The distance of light ray to the origin in the observer coordinate system will be

$$
\begin{aligned}
|\vec{x}| &= \sqrt{\left(\vec{x'} + \vec{x}_1\right) \cdot \left(\vec{x'} + \vec{x}_1\right)} \\
&= \sqrt{x_1^2 + \rho^2 - 2x_1\rho \cos\phi} \\
&\sim \sqrt{(x_1 - \rho)^2 + x_1\rho\phi^2},
\end{aligned}
\tag{17}
$$

where we have considered the angle ϕ between $\vec{n}$ and $-\vec{x}_1$ is small and thus $\cos\phi \sim 1 - \phi^2/2$.

At the emission time t_e, we have

$$\rho|_{t=t_e} = 0, \tag{18}$$

$$|\vec{x}|_{t=t_e} = |\vec{x}_1|_{t=t_e} = r_e = r_1R(t_e), \tag{19}$$

$$\phi|_{t=t_e} = |\vec{\epsilon}|, \tag{20}$$

while at the observation time t_o, we have

$$\rho|_{t=t_0} = r_o = r_1R(t_o), \tag{21}$$

$$|\vec{x}|_{t=t_o} = b, \tag{22}$$

$$|\vec{x}_1|_{t=t_o} = r_o = r_1R(t_o), \tag{23}$$

$$\phi|_{t=t_o} = \theta = |\vec{\epsilon}|R(t_o)/R(t_e). \tag{24}$$

Substituting the quantity properties Eqs. (21)-(24) at $t = t_o$ into Eq. (17), we obtain the impact parameter as

$$b = R(t_o)r_1\theta = \frac{R^2(t_o)}{R(t_e)}r_1|\vec{\epsilon}|. \tag{25}$$

To calculate apparent luminosities, we consider a circular telescope mirror of radius b, placed with its center at the origin and its normal along the line of sight to the light source.

The fraction of all emitted photons that reach the mirror is the ratio of the solid angle to 4π,

$$\frac{\pi|\vec{\epsilon}|^2}{4\pi} = \frac{\pi b^2}{4\pi r_1^2} \frac{R^2(t_e)}{R^4(t_o)}. \tag{26}$$

Since light is red-shifted, the energy or frequency of each photon observed is reduced in comparison with the photon emitted by a factor of $R(t_e)/R(t_o)$. This energy or frequency reduction is equivalent to the increase of the time interval for observation relative to that for emission. If the effect of the redshift on the apparent luminosity is considered, then we should not consider the effect of the time interval increase on the apparent luminosity. This is also consistent with the electromagnetic wave theory of light, from which the energy emitted per unit time of emission is only one redshift factor greater than the energy observed per unit time of observation. Therefore, the total power P received by the mirror is the total power emitted by the source, its absolute luminosity L, times a factor $R(t_e)/R(t_o)$, and times the fraction (Eq. 26):

$$P = L \frac{\pi b^2}{4\pi r_1^2} \frac{R^3(t_e)}{R^5(t_o)}. \tag{27}$$

The apparent luminosity l is the power per unit mirror area

$$l = \frac{P}{\pi b^2} = \frac{L}{4\pi r_1^2} \frac{R^3(t_e)}{R^5(t_o)}. \tag{28}$$

Then the luminosity distance can be obtained

$$D_{\text{L}} = \left(\frac{L}{4\pi l}\right)^{1/2} = r_1 R(t_o) \left[\frac{R(t_o)}{R(t_e)}\right]^{3/2}$$

$$= c(1 + Z)^{3/2} R(t_o) \int_{t_e}^{t_o} \frac{dt}{R(t)}. \tag{29}$$

The luminosity distance Eq. (29) derived here is $\sqrt{1 + Z}$ times that we conventionally used, Eq. (2). This factor leads to an explanation of type Ia supernova measurements without dark energy. Using Eqs. (4) and (8) for a flat universe ($k = 0$) without dark energy ($\Lambda = 0$), we can integrate Eq. (29) and obtain the luminosity distance-redshift relation as

$$D_{\text{L}} = \frac{2c}{H_0}(1 + Z)\left(\sqrt{1 + Z} - 1\right). \tag{30}$$

Eq. (30) dees not include any free parameter and reduces to the Hubble law at $Z \ll 1$.

The two significant corrections, which have been made in the above derivation of the luminosity distance in comparison with the derivation done in [20] are: 1) θ is not about equal to $|\vec{\epsilon}|$ for a distant light source but increased by a factor $R(t_o)/R(t_e)$, and 2) the light is red-shifted and the time interval increases are equivalent in physics $\nu_o/\nu_e = \delta t_e/\delta t_o = R(t_e)/R(t_o)$ and thus they reduce the apparent luminosity only

by $R(t_e)/R(t_o)$ rather than its square. This is also supported by the electromagnetic wave theory of light.

The early derivation, including the simplified version as given in [28] and other cosmological books, the fraction of the light received in a telescope of aperture πb^2 on earth is $\pi b^2/[4\pi r_1^2 R^2(t_o)]$ and so the factor $1/d^2$ in the formula for the apparent luminosity l was replaced by $1/[r_1^2 R^2(t_o)]$. This replacement or modification for the apparent luminosity l was made according to the view of the emitter rather than from the view of the observer. From the view of the emitter (or a person standing on the source object), all light rays radially diverge from the source object isotropically and in straight lines. All the photons emitted at t_e reach the surface of the sphere drawn around the source object by radius $r_1 R(t_o)$. The angle of emission of a photon from the source object is equal to the angle of incidence of the photon to the mirror of telescope.

From the view of the observer, however, the source object is moving away in an increasing speed. The light rays travel in curved lines and anisotropically as shown in Figure 2. The angle of emission of a photon from the source object $|\vec{\epsilon}|$ is smaller than the angle of incidence of the photon to the mirror of telescope θ by a factor of $R(t_e)/R(t_o)$. That is, from the view of the observer, the factor $1/d^2$ in the formula for l must be replaced with $1/[r_1^2 R^4(t_o)/R^2(t_e)]$ as shown in Eq. (26). On the other hand, according the electromagnetic wave theory, the energy of radiation does not depend on the frequency. Only the increase of time interval would reduce the apparent luminosity. This may be examinable in experiments using a sound wave.

Figure 3 plots the luminosity distance-redshift relation (red line) along with the type Ia supernova measurements (blue dots. Credit: Union 2.1 compilation of 580 SNIA data from Supernova Cosmology Project). In this plot the Hubble constant is chosen to be $H_0 \sim 70$ km/s/Mpc. In the upper panel of Figure 3, the distance modulus, which is defined by $\mu = 5 \log_{10} D_{\text{L}} - 5$ with D_{L} in parsecs, is plotted as a function of redshift; while in the lower panel of Figure 3, the distance modulus difference between the measured SNeIa data and analytical results derived from Eq. (30). The chi-square statistic is obtained as

$$\chi^2 = \sum_{j=1}^{580} \frac{\left(\mu_j^{\text{obs}} - \mu_j^{\text{the}}\right)^2}{\sigma_j^2} \sim 589. \tag{31}$$

Then the reduced chi-square is given by $\chi^2_{\text{red}} = 589/580 \sim 1.015$. It is seen that the derived luminosity distance-redshift relation is perfectly consistent with the measurements of type Ia supernovae. Therefore, with the new luminosity distance-redshift relation, the SNeIa measurements do not show the existence of dark energy.

The analysis and measurements for the structure and weak lensing of the CMB might not be accurate enough as were thought to provide an independent check or evidence on the
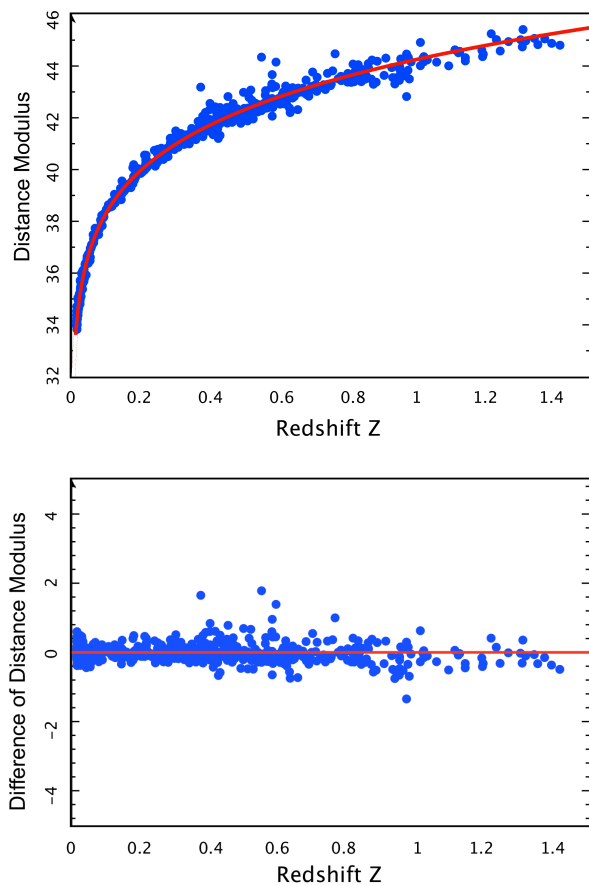
Fig. 3: Luminosity distance-redshift relation of type Ia supernovae. Blue dots are measurements credited by the Union2 compilation of 580 SNeIa data from Supernova Cosmology Project. Red lines are analytical results from this study. The upper panel plots the distance modulus as a function of redshift, while the lower panel plots the distance modulus difference between the measurement data and theoretical results.

existence of dark energy [29-30]. Recently, Sawangwit and Shank [31-32] looked at the CMB observations and find the errors in the data to be much larger than previously thought. The CMB power spectrum is very sensitive to the beam profiles. If their results are further confirmed to be correct, then it will also become less likely that dark energy dominates the universe.

4 Summary

The luminosity distance-redshift relation that we previously applied to connect the models with the SNeIa measurements is an approximate expression only valid for nearby objects. This is because that the traditional derivation of the $D_L - Z$ relation has the following two defects: (1) the light emitting angle is about equal to the light incident angle, which is not true for light from a distant source object according to the view

of the observer on the earth, and (2) the redshift of light and the increase of time interval doubly reduce the energy flux of the received light, which is physically incorrect because the redshift of light is caused by the increase of time interval. The electromagnetic wave theory of light also supports that the apparent luminosity is reduced only by one redshift factor due to the time interval increase. We have corrected these defects and derived a new relationship between luminosity distance and redshift with a factor of $\sqrt{1 + Z}$. With this new $D_L - Z$ relation, we have perfectly explained the SNeIa measurements according to the standard cosmological model without dark energy ($\Lambda = 0$). Therefore, we can conclude that the universe has not accelerated and does not need the dark energy at all. The luminosity distance-redshift relation often used previously is only valid for nearby objects and thus the luminosity distances of all distant type Ia supernovae had been underestimated. This study provides us a possible solution to the mystery of dark energy.

References

1. Riess A.G. et al. Observational evidence from supernovae for an accelerating universe and a cosmological constant. *Astronomical Journal*, 1998, v. 116, 1009–1038.

2. Perlmutter S. et al. Measurements of Omega and Lambda from 42 High-Redshift Supernovae. *Astrophysical Journal*, 1999, v. 517, 565–586.

3. Hubble E. A relation between distance and radial velocity among extra-galactic nebulae. *Proceedings of the National Academy of Sciences of the United States of America*, 1929, v. 15, 168–173.

4. Brans C.H., Dicke R.H. Mach's principle and a relativistic theory of gravitation. *Physical Review* 1961, v. 124, 925–935.

5. Riazuelo A., Uzan J.P. Cosmological observations in scalar-tensor quintessence. *Physical Review D*, 2002, v. 66, 023525.

6. Buchdahl H.A. Non-linear Lagrangians and cosmological theory. *Monthly Notices of the Royal Astronomical Society*, 1970, v. 150, 1–8.

7. Sotiriou T.P., Faraoni V. f(R) theories of gravity. *Reviews of Modern Physics*, 2010, v. 82, 451–497.

8. Chow N., Khoury J. Galileon cosmology. *Physical Review D*, 2009, v. 80, 024037.

9. Freund P.G.O. Kaluza-Klein cosmologies. *Nuclear Physics B*, 1982, v. 209, 146–156.

10. Wesson P.S., Liu H. and Ahluwalia D.V. The cosmological constant problem and Kaluza-Klein theory. *International Journal of Modern Physics D*, 2001, v. 10, 905–912.

11. Zhang T.X. Electric redshift and quasars. *Astrophysical Journal Letters*, 2006, v. 636, L61–L64.

12. Zhang T.X. Gravitational field shielding and supernova explosions. *Astrophysical Journal Letters*, 2010a, v. 725, L117–L121.

13. Mukhanov V.F., Feldman H.A., Brandenberger R.H. Theory of cosmological perturbations. *Physics Reports*, 1992, v. 215, 203–333.

14. Bernardeau F., Colombi S., Gaztanaga E., Scoccimarro R. Large-scale structure of the Universe and cosmological perturbation theory. *Physics Reports*, 2002, v. 367, 1–248.

15. Wands D., Malik K.A., Lyth D.H., Liddle A.R. New approach to the evolution of cosmological perturbations on large scales. *Physical Review D*, 2000, v. 62, 043527.

16. Zhang T.X. A new cosmological model: black hole universe. *Bulletin of the American Astronomical Society*. 2007, v. 39, 1004–1004.

17. Zhang T.X. A new cosmological model: black hole universe. *Progress in Physics*, 2009, v. 2, 3-11.

18. Zhang T.X. Cosmic microwave background radiation and black hole universe. *Astrophysics and Space Science*, 2010b, v. 330, 157–165.

19. Peebles P.J. and Ratra B. The cosmological constant and dark energy. *Reviews of Modern Physics*, 2003, v. 75, 559–606.

20. Weinberg S. Gravitation and Cosmology, John Wiley & Sons, Inc., 1972.

21. Friedmann A. Über die Krümmung des Raumes. *Zeitschrift für Physik*, 1922, v. 10, 377–386.

22. Lemaitre G. Expansion of the universe, A homogeneous universe of constant mass and increasing radius accounting for the radial velocity of extra-galactic nebulae. *Monthly Notices of the Royal Astronomical Society*, 1931, v. 91, 483–490.

23. Robertson H.P. Kinematics and World-Structure. *Astrophysical Journal*, 1935, v. 82, 284–301.

24. Walker A.G. On Milne's theory of world-structure. *Proceedings of the London Mathematical Society*, 1937 v. 42, 90–127.

25. Friedmann A. Über die Möglichkeit einer Welt mit konstanter negativer Krümmung des Raumes. *Zeitschrift für Physik*, 1924, v. 21, 326–332.

26. Suyu S.H. et al. Dissecting the Gravitational lens B1608+656. II. Precision Measurements of the Hubble Constant, Spatial Curvature, and the Dark Energy Equation of State. *Astrophysical Journal*, 2010, v. 711, 201–221.

27. Tytler D. et al. Cosmological Parameters σ_8, the baryon density Ω_b, the vacuum energy density Ω_Λ, the Hubble constant and the UV background Intensity from a calibrated measurement of H I Ly? absorption at $z = 1.9$. *Astrophysical Journal*, 2004, v. 617, 1–28.

28. Weinberg S. Cosmology, Oxford Univ. Press, 2008

29. Corasaniti P.S., Giannantonio T., Melchiorri A. Constraining dark energy with cross-correlated CMB and large scale structure data. *Physical Review D*, 2005, v. 71, 123521.

30. Sherwin B.D. et al. Evidence for Dark Energy from the Cosmic Microwave Background Alone Using the Atacama Cosmology Telescope Lensing Measurements. *Physical Review Letters*, 2011, v. 107, 021302.

31. Sawangwit U. Shanks T. Beam profile sensitivity of the WMAP CMB power spectrum. *Monthly Notices of the Royal Astronomical Society*, 2010a, v. 407, L16–L20.

32. Sawangwit U., Shanks T. Lambda-CDM and the WMAP power spectrum beam profile sensitivity. 2010, eprint arXiv:1006.1270.

ΔI=1 Signature Splitting in Signature Partners of Odd Mass Superdeformed Nuclei

A.M. Khalaf*, M.D. Okash†, M.H. Ghomiem* and W.A. Muhammad*

*Physics Department, Faculty of Science, Al-Azhar University, Cairo, Egypt. E-mail: ali_khalaf43@hotmail.com
†Physics Department, Faculty of Science (Girls College), Al-Azhar University, Cairo, Egypt

The spins, transition energies, rotational frequencies, kinematic and dynamic moment of inertia of rotational bands of signature partners pairs of odd–A superdeformed bands in A∼190 region were calculated by proposing a simple model based on collective rotational model. Simulated search program was written to determine the model parameters. The calculated results agree with experimental data for fourteen signature partner pairs in Hg/Tl/Pb/Bi/nuclei. We investigated the ΔI=1 signature splitting by extracted the difference between the average transitions I+2 ⟶ I and I ⟶ I-2 energies in one band and the transition I+1 ⟶ I-1 energies in its signature partner. Most of the signature partners in this region show large amplitude staggering. The signature splitting has the effect of increasing dynamical moment of inertia J^2 for favored band and decreasing J^2 for the unfavored band.

1 Introduction

Since the first observation of superdeformation in ^{152}Dy [1] and in ^{191}Hg [2] more than 350 settled SD bands in more than 100 nuclei have been will established in several mass regions of nuclear chart A∼190, 150, 130 [3–6]. With the aid of large γ-ray detectors arrays, new regions of SD nuclei have been discovered encircle mass A∼80, 60, 70, 90 regions. The A∼190 mass region is of special interest, more than 85 SD bands have now been observed in this mass region alone in Au, Hg, Tl, Pb, Bi and Po nuclei. The SD states in A∼190 mass region have been observed down to quite low spin also many SD bands in the A∼190 show the same smooth rise in the dynamical moment of inertia as rotational frequency increase, which is associated [7–9] with the successive gradual alignments of a pair of nucleons occupying specific high-N intruder orbitals in the presence of pairing correlations.

Spin assignment is one of the most difficult and still unsolved problems in the study of nuclear superdeformation, because spins have not been determined experimentally in SD nuclei. This is due to the difficulty of establishing the excitation of a SD band into known yrast states. Several related approaches to assign the spins of SD bands in terms of there observed γ-ray energies were proposed [10–28]. For all approaches an extrapolation fitting procedure was used.

The development of large γ-ray arrays has allowed experimentalists to find new phenomena at high angular momenta. For example some SD nuclear bands in mass regions A∼150 and A∼190 show an unexpected regular staggering effects in the transition energies $E_γ$ (a zigzag behavior as a function of rotational frequency or spin). At high rotational frequencies a ΔI=2 staggering was observed [29–39]. It has attracted much attention and interest, and has thus become one of the most frequently debated subjects.

The ΔI=2 rotational bands are perturbed and two ΔI=4 rotational sequences emerge with an energy splitting of about some hundred eV. This is commonly called ΔI=4 bifurcation or as C_4 oscillation, because the SD-energy levels are consequently separated into two spin sequences with spin values I_0, I_0+4, I_0+8,... and I_0+2, I_0+6, I_0+10,... respectively.

Many ΔI=1 signature splitting have been observed in ND nuclei for different bands, like odd-even staggering (OES) in the gamma vibrational band at low spin [40], the beat odd-even ΔI=1 staggering patterns observed in the octuple bands [41] and the ΔI=1 odd-even staggering structure of alternating parity bands in even-even nuclei [42, 43].

There is another kind of staggering happens in SD odd-A nuclei, the ΔI=1 signature splitting in signature partner pairs. It was seen that most of SD rotational bands in odd-A nuclei in the A∼190 region are signature partners [44–53]. Most of these signature partners show large amplitude signature splitting and the bandhead moments of inertia of each pair are almost identical.

2 Sketch of the Model

In the model used, the excitation energy of a SD State E(I) and spin I is expressed as:

$$\hat{I}^2 = I(I+1) = \sum_n b_n E^n(I). \tag{1}$$

With $\hat{I}$ $[I(I+1)]^{1/2}$. If we restrict to three terms only, then

$$I(I+1) = b_0 + b_1 E(I) + b_2 E^2(I). \tag{2}$$

Solving for E(I) we get the two-parameters formula for E(I)

$$E(I) = E_0 + a\left([1 + bI(I+1)]^{1/2}\right) \tag{3}$$

with a,b and E_0 simply expressed by b_0, b_1 and b_2

$$a = \frac{1}{2b_2}[b_1^2 - 4b_0b_2]^{1/2} \tag{4}$$

$$b = \frac{4b_2}{b_1^2 - 4b_0 b_2} \tag{5}$$

$$E_0 = a - \frac{b_1}{2b_2} \tag{6}$$

where b characterizes the nuclear softness.

The rigid rotor limit corresponds to b$\longrightarrow$0 and a, E_0 keeping finite. The value of the parameter a increases slowly with I. It is expected that a better expression may be obtained if a weak I dependence of the parameter a is taken into account. So equation (3) is tentatively modified as follows:

$$E(I) = a\left([1 + b(I)(I + 1)]^{1/2} - 1\right) + cI(I + 1) \tag{7}$$

with an additional parameter c. Leading to a form for the gamma transition energies

$$E_\gamma(I) = a\left([1+bI(I+1)]^{1/2} - [1+b(I-2)(I-1)]^{1/2}\right) + 2c(2I+1). \tag{8}$$

The kinematic J^1 and dynamic J^2 moment of inertia associated with the a, b, c, formula are:

$$J^1 = ab[1 + bI(I + 1)]^{1/2} + \frac{1}{2c} \tag{9}$$

$$J^2 = ab[1 + bI(I + 1)]^{3/2} + \frac{1}{2c}. \tag{10}$$

The bandhead moment of inertia is

$$J_0 = \frac{\hbar^2}{ab + 2c}.$$

Each SD nucleus is described by three adjustable parameters a, b and c which are determined by fitting procedure of all known levels.

For the SD bands, one can extract the rotational frequency, dynamic and kinematic moment of inertia by using the experimental intra band E_2 transition energies as follows:

$$\hbar\omega = \frac{1}{4}[E_\gamma(I + 2) + E_\gamma(I)] \tag{11}$$

$$J^2(I) = \frac{4\,\hbar^2}{\triangle E_\gamma} \tag{12}$$

$$J^1(I - 1) = \frac{\hbar^2(2I - 1)}{E_\gamma} \tag{13}$$

where

$$E_\gamma = E(I) - E(I - 2),$$

$$\triangle E_\gamma = E_\gamma(I + 2) - E_\gamma(I).$$

It is seen that whereas the extracted J^1 depends on I proposition, J^2 does not.

3 Analysis of ΔI=1 signature splitting in SD signature partner

To investigate the ΔI=1 staggering in signature partner pairs of odd SD band, one must extract the differences between the average transition I+2⟶I and I⟶I-2 energies in one band the transition I+1⟶I and I⟶I-1 energies in the signature partner

$$\triangle^2 E_\gamma(I) = \frac{1}{2}\Big[E_\gamma(I{+}2 \longrightarrow I) + E_\gamma(I \longrightarrow I{-}2) \\ -2E_\gamma(I{+}1 \longrightarrow I{-}1)\Big]$$

where E_γ(I) is proposed in equation (8).

4 Numerical Calculation and Discussions

Our selected data set includes fourteen signature partner pairs in ten odd SD nuclei in the A∼ 190 mass region, namely:

[191]Hg (SD2, SD3)	[193]Hg (SD1, SD2)	[193]Hg(SD3, SD4)
[193]Hg (SD3, SD4)	[195]Hg (SD3, SD4)	[191]Tl(SD1, SD2)
[193]Tl (SD1, SD2)	[195]Tl (SD1, SD2)	[193]Pb(SD3, SD4)
[193]Pb (SD5, SD6)	[195]Pb (SD1, SD2)	[195]Pb(SD3, SD4)
[197]Pb (SD1, SD2)	[197]Bi (SD2, SD3)	

The experimental transition energies are taken from reference [3]. To parameterize the spins of the SD bands, we assumed various values for the bandhead spin I_0 for each SD band and the model parameters a, b and c are adjusted by using a computer simulated search program in order to obtain a minimum root mean square deviation

$$\chi = \left[\frac{1}{N}\sum_{i=1}^{N}\frac{E_\gamma^{exp}(I) - E_\gamma^{Theor}(I)}{\triangle E_\gamma^{exp}(I)}\right]^{1/2}.$$

Of the calculated energies E_γ^{cal} from the observed energies E_γ^{exp}, where N is the number of data points considered and $\triangle E_\gamma^{exp}$ is the uncertainty of the γ-transition energies. The fitting procedure was repeated with spin I_0 fixed at the nearest half integer.

Table (1) gives the optimized model parameters a, b, c, the bandhead spin proposition I_0 and the lowest transition energies E_γ ($I_0+2 \longrightarrow I_0$) for each SD band.

The systematic behavior of kinematic J^1 and dynamic J^2 moments of inertia are guideline for the spin prediction and to understand the properties of the SD bands. We studied the variation of J^1 and J^2 as a function of rotational frequency $\hbar\omega$. The value of J^1 and J^2 approaches each other at the bandhead spin I_0 . The J^1 moment of inertia is found to be smaller than that of J^2 for all values of $\hbar\omega$. Both J^1 and J^2 plots are concave upwards. In general the bandhead moments of inertia in our selected signature partners odd-A SD nuclei $J_0 \cong (94 \pm 4)\hbar$ MeV^{-1} are longer than that of the yrast SD bands in neighboring even-even nuclei. The best fitted parameters were used to calculate the theoretical transition energies extracted from our proposed model.

Table 1: The calculated best model parameters a, b, c and suggested bandhead spins I_0 for our selected signature partners in the odd SD nuclei in A $\simeq$ 190 region.

SD Bands	a MeV	b 10^{-4} MeV	c MeV	I_0 $\hbar$	E_γ keV
^{191}Hg(SD2)	19074.6639	3.0809	2.3765	10.5	252.4
^{191}Hg(SD3)	15810.8517	3.6987	2.4037	11.5	272
^{193}Hg(SD1)	1569.7883	23.4445	3.7662	9.5	233.2
^{193}Hg(SD2)	12654.6097	4.3858	2.6051	10.5	254
^{193}Hg(SD3)	12243.4329	4.4984	2.6289	9.5	233.5
^{193}Hg(SD4)	12654.6098	4.3858	2.6051	10.5	254
^{195}Hg(SD3)	72779.9405	1.8708	-0.9723	10.5	284.5
^{195}Hg(SD4)	22034.6647	2.4110	2.4673	15.5	341.9
^{191}Tl(SD1)	307519.2819	0.7272	-5.7903	11.5	276.77
^{191}Tl(SD2)	249002.6385	0.8532	-5.2350	12.5	296.75
^{193}Tl(SD1)	13573.6592	3.7666	2.6759	9.5	227.3
^{193}Tl(SD2)	6380.8736	5.3776	3.5196	8.5	206.6
^{195}Tl(SD1)	6380.8738	5.3776	3.5196	5.5	146.2
^{195}Tl(SD2)	33124.3911	2.4266	1.2551	6.5	167.5
^{193}Pb(SD3)	4702.3802	6.2778	3.8243	10.5	251.5
^{193}Pb(SD4)	16892.1756	3.5957	2.2986	11.5	273
^{193}Pb(SD5)	4337.5276	8.2523	3.6196	8.5	213.2
^{193}Pb(SD6)	3574.7877	9.4219	3.7378	9.5	234.6
^{195}Pb(SD1)	600.9413	13.4593	4.6737	7.5	162.58
^{195}Pb(SD2)	15864555.765	0.0139	-5.9659	6.5	182.13
^{195}Pb(SD3)	2362.3559	13.4225	3.9167	7.5	198.2
^{195}Pb(SD4)	18884.3711	3.5500	2.0732	8.5	213.6
^{197}Pb(SD1)	9713.0371	2.5870	3.8497	7.5	183.7
^{197}Pb(SD2)	724986.6813	0.1798	-1.3692	6.5	204.6
^{197}Bi (SD2)	6.09E+08	8.24E-07	-245.7806	8.5	166.2
^{197}Bi (SD3)	6.09E+08	8.24E-07	-245.7806	9.5	186.7

To investigate the ΔI=1 signature splitting, the difference between the averaged transitions I+2⟶I and I⟶I-2 energies in one band and the transition I+1⟶I-1 energies in its signature partner $\triangle^2 E_\gamma(I)$ are determined and its value as a function of spin I for each signature partner pairs are plotted in figure (1). Most of there signature partners show large amplitude staggering with the exception of ^{193}Hg (SD1, SD2), ^{193}Pb (SD5, SD6) and ^{195}Pb (SD3, SD4).

A clear out amplification of $\triangle^2 E(I)$ is seen in ^{193}Pb (SD3, SD4). For most cases one finds that $\triangle^2 E(I)$ is very small at lower spins, increasing faster and faster as the spin I increase. The of $\triangle^2 E(I)$ in ^{193}Tl (SD1, SD2) and ^{195}Tl (SD1, SD2) are remarkable similar.

5 Conclusion

The nuclear superdeformed rotational bands of signature partners of odd-mass number in the A~190 region have been studied in the framework of a simple formula based on collective rotational model containing three parameters. The formula connected directly the unknown spin and the energy of

the level the spins of the observed levels were extracted by assuming various values to the lowest spin of the bandhead at the nearest half integer. The optimized three parameters have been deduced by using a computer simulated search program in order to obtain a minimum root mean square deviation of the calculated transition energies from the measured energies.

The calculated transition energies, level, spins, rotational frequencies, kinematic and dynamic moments of inertia are examined for fourteen signature partner pairs. To investigate the ΔI=1 signature splitting for each signature partner pair, we calculated the difference between the average transitions I+2 ⟶I and I⟶I-2 energies in one band and the transition I+1⟶I-1 energies in its signature partner. Most of the signature partners in this region show large amplitude ΔI=1 staggering.

References

1. Twin P.J., Nyak B.M. Observation of a Discrete-Line Superdeformed Band up to 60ℏ in ^{152}Dy. *Physical Review Letters*, 1986, v. 57, 811–814.
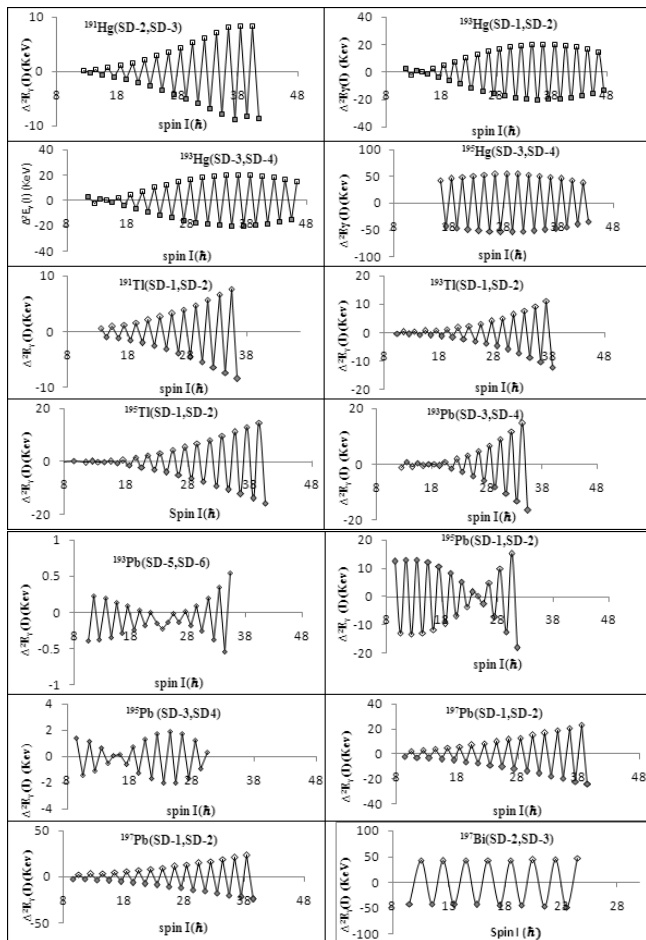
Fig. 1: The $\Delta I=1$ signature splitting in some signature partners of odd-A superdeformed nuclei.

2. Moore E. F., Janssens R.V.F et al. Observation of superdeformation in 191Hg. *Physical Review Letters*, 1989, v. 63, 360–363.

3. Singh Balraj. Table of Superdeformed Nuclear Bands and Fission Isomers. *Nuclear Data Sheets*, 2006, v. 107 1–224.

4. Singh Balraj, Zywine Roy, Richard B. Firestone. Table of Superdeformed Nuclear Bands and Fission Isomers. *Nuclear Data Sheets*, 2002, v. 97 (1), 241–592.

5. Han X.L. and Wu C.L. At. Data NUCLEAR SUPERDEFORMATION DATA TABLES. *Nuclear Data Tables*, 1996, v. 117, 117.

6. Singh B., Firestone R.B., Chu S.Y.E. Table of superdeformed nuclear bands and fission isomers. *Egypt Journal of Physics*, 1996, v. 78, 1–177.

7. Ye D., Janssens R.V.F. et al. Superdeformed band in ^{192}Hg. *Physics Review*, 1990, v. C41, R13–R17.

8. Riley M.A., Cullen D.M. et al. Multiple superdeformed bands in ^{194}Hg and their dynamical moments of inertia. *Nuclear Physics*, 1990, v. A512, 178–188.

9. Drigert M.W., Carpenter M.P. et al. Superdeformed bands in ^{189,190}Hg. *Nuclear Physics*, 1991, v. A530, 452–474.

10. Stephens F.S. Spin alignment in superdeformed rotational bands. *Nuclear Physics*, 1990, v. A520 c91–c104.

11. Becker J.A., N. Roy, Henry E.A. et al. Level spin and moments of inertia in superdeformed nuclei near A=194. *Nuclear Physics*, 1990, v. A520, c187–c194.

12. Draper J.E., Stephens F.S. et al. Spins in superdeformed bands in the mass 190 region 190 region. *Physics Review*, 1990, v. C42, R1791–R1795 .

13. J. E. Draper J.E., Stephens F.S. et al. J Superdeformation in ^{196,198}Pb. *ibid*, 1991, v. 42, R179.

14. Zeng J.Y., Meng J. et al. Spin determination and quantized alignment in the superdeformed bands in ^{152}Dy, ^{151}Tb, and ^{150}Gd. *Physical Review*, 1991, v. C44, R1745–R1748.

15. Becker J.A., Henry E.A. et al. Level spin for superdeformed nuclei near A=194. *Physical Review*, 1992, v. C46, 889–903.

16. Piepenbring R., Protasov K.V. Superfluid liquid model with triplet pairing for superdeformed in A 130-150 region. *Z.Physics*, 1993, v. A347 (7), 27–35.

17. Xu Furong, Hu Jimin et al. Cranking Bohr-Mottelson Hamiltonian applied to superdeformed bands in A 190 region. *Physical Review*, 1994, v. C49, 1449–1453.

18. Fan H-Y., Jing S.-C. Even and Odd Binomial States. *Communications in Theoretical Physics*, 1995, v. 24, 125–128.

19. Hegazi A.M., Ghoniem M.H., Khalaf A.M. Superdeformation in ^{154}Er. *Egypt Journal of Physics*, 1999, v. 30 (3), 293–R1174.

20. Khalaf A.M. et al. Band Head of the Superdeformed Bands in the A ~ 150 Mass region Nuclei. *Egypt Journal of Physics*, 2002, v. 33 (1), 67–87.

21. Khalaf A.M. et al. Spin Prediction and Systematics of Moments of inertia of superdeformed Nuclear Rotational Band in the Mass Region A∼190. *Egypt Journal of Physics*, 2002, v. 33 (3), 585–602.

22. Khalaf A.M. et al. Deascription of Rotational Bands in Superdeformed Nuclei by Using Two-parameter Empirical Formula. *Egypt Journal of Physics*, 2003, v. 34 (2), 159–177.

23. Khalaf A.M. et al. Properties of Superdeformed Rotational Bands of Odd Nuclei in the Mass-190 Region Using Harris Expansion. *Egypt Journal of Physics*, 2003, v. 34 (2), 195–215.

24. Khalaf A.M. et al. Analysis of Rotational Bands in Superdeformed Nuclei Using sdg Interacting Boson Model. *Egypt Journal of Physics*, 2004, v. 34 (1), 79–104.

25. Khalaf A.M. and Sirag M.M. Prediction of Nuclear Superdeformed Rotational Bands Using Incremental Alignments. *Egypt Journal of Physics*, 2006, v. 37 (3), 277–293.

26. Khalaf A.M., Allam M.A., Saber E. Rotational Bands of Superdeformed Nuclei in Framework of Variable Moment of Inertia Model. *Egypt Jurnal of Physics*, 2006, v. 73 (3), 195.

27. Khalaf A.M., Allam M.A., Saber E. Signature Partners in Odd Superdeformed Nuclei in Mass Region A∼190. *Egypt Journal of Physics*, 2008, v. 39 (1), 41–65.

28. Khalaf A.M., Allam M.A. and Sirag M.M. Bandhead Spin Determination and Moments of inertia of Superdeformed Nuclei in Mass Region 60-90 Using Variable Moment of inertia Model. *Egypt Journal of Physics*, 2010, v. 41 (2), 13–27.

29. Flibotte S. et al. $\Delta I= 4$ bifurcation in a superdeformed band: Evidence for a C_4 symmetry band. *Physical Review Letters*, 1993, v. 71, 4299–4302.

30. Cederwall B. et al. New features of superdeformed bands in ^{194}Hg. *Physica Scripta*, 1994, v. 72 3150–3153.

31. Flibotte S. Hackman G. et al. Multi-particle excitations in the superdeformed ^{149}Gd nucleus. *Nuclear Physics*, 1995, v. A584, 373–396.

32. Carpenter M.P., Janssens R.V.F. Identification of the unfavored N=7 superdeformed band in ^{191}Hg. *Physical Review*, 1995, v. 51, 2400–2405.

33. Bernstein L.A. and Hughes J.R. Superdeformation in ^{154}Er. *Physical Review*, 1995, v. C52, R1171–R1174.

34. de Angelis G. and Wyss R. Spectroscopy in the second well of the ^{148}Gd nucleus Two quasiparticle and collective excitations. *Physical Review*, 1996, v. C35, 679–688.

35. Fischer S.M., Carpenter M.P. et al. Alignment additivity in the two-quasiparticle superdeformed bands of ^{192}Tl. *Physical Review*, 1996, v. C35, 2126—2133.

36. Semple A.T., Nolan P.J. Energy Staggering in Superdeformed bands in ^{131}Ce, ^{132}Ce and ^{133}Ce. *Physical Review Letter*, 1996, v. 76, 3671–3674.

37. Krücken R., Hackman G. et al. Test of ΔI=2 staggering in the superdeformed bands of ^{194}Hg. *Physical Review*, 1996, v. C45, R2109–R2113.

38. Cederwall B. et al. PROPERTIES OF SUPERDEFORMED BANDS IN DY-153. *Physical Review*, 1995, v. B346, 244–250.

39. Haslip D.S., Flibotte S., and de France G. Δ*I*=4 Bifurcation in Identical Superdeformed Bands. *Physical Review Letters*, 1997, v. 78, 3447–3450.

40. Singh M., Bihari C. et al. Evidence of rigid triaxiality in some xenon nuclei. *Canadian Journal of Physics*, 1995, v. 85 (8), 899–910.

41. Bonatsos D., Daskaloyannis C. Δ*I*=1 staggering in octupole bands of light actinides: "Beat" patterns. *Physics Letters*, 2000, v. C62, 24301–24313.

42. Wiedenhöver I, Janssens R.V.F. et al. Octupole Correlations in the Pu Isotopes: From Vibration to Static Deformation. *Physical Review Letters*, 1999, v. 83, 2143–2146.

43. Minkov N., Yotov P., Drenska S. Parity shift and beat staggering structure of octupole bands in a collective model for quadrupole-octupole deformed nuclei. *Journal of Physics G – Nuclear Physics*, 2006, v. 32, 497–503.

44. Duprat J. Azaiez F. et al. M1 transitions between superdeformed states in ^{195}Tl: the fingerprint of the i132 proton intruder orbital. *Physical Letter*, 1994, v. B341, 6–11.

45. Joyce M.J. et al. First measurement of magnetic properties in a superdeformed nucleus:^{193}Hg. *Physical Review Letters*, 1993, v. 71, 2176–2179.

46. Hughes J.R., Becker J.R. et al. Superdeformation in ^{193}Pb and the effects of the N=7 intruder orbital. *Physical Review*, 1990, v. C51, R447–R451.

47. Farris L.P., Henry E.A. et al. Neutron blocking and delayed proton pair alignment in superdeformed ^{195}Pb. *Physical Review*, 1996, v. C 51, R2288–R2292.

48. Baunem S. et al. The $i_{13/2}$ proton intruder orbital in the superdeformed ^{193}Tl nucleus: Effective magnetic moment and blocking of proton pairing. *Physical Review*, 1996, v. C53, R9–R13.

49. Carpenter M.P., Janssens R.V.F. and Flocard H. Identification of the unfavored N=7 superdeformed band in ^{191}Hg. *Physical Review*, 1995, v. C51, 2400–2405.

50. Joyce M.J., Sharpey-Schafer J.V. and Flocard H. The N = 7 unfavoured superdeformed band in ^{193}Hg; coriolis splitting and neutron shell structure at extreme deformation *Physical Letter*, 1999, v. B340, 150–154.

51. Joyce M.J., Sharpey-Schafer and Riley M.A. Microscopic study of the properties of identical bands in the A=150 mass region *Physical Review*, 1999, v. C59, 3120–3127.

52. Hackman G. and Krücken R. Structure of superdeformed bands in ^{195}Hg *Physical Review*, 1997, v. C55, 148–154.

53. Clark R.M., Bouneau S. et al. Superdeformation in the bismuth nuclei. *Physical Review*, 1995, v. C51, R1052–R1056.

54. Hibbert I.M., Wadsworth R. et al. Superdeformed structures in ^{197,198}Pb. *Physical Review*, 1996, v. C54, 2253–2258.

Nuclear Shape Transition Using Interacting Boson Model with the Intrinsic Coherent State

A.M. Khalaf*, H.S. Hamdy† and M.M. El Sawy‡

*Physics Department, Faculty of Science, Al-Azhar University, Cairo, Egypt. E-mail: ali_khalaf43@hotmail.com
†Department of Physics, Faculty of Science, Beni-Suef University, Beni-Suef, Egypt.
‡Demonstrator at Basic Science department, Engineering Faculty, The British University, Cairo, Egypt. E-mail: maiamy4@gmail.com

The values of the potential energy surface (PES) for the even-even isotopic chains of Nd/Sm/Gd/Dy are studied systematically using the simplified form of interacting boson model (IBM) with intrinsic coherent state. The critical points have been determined for each isotope chain. The phase diagrams exhibits first-order shape phase transition from spherical U(5) to deformed axial symmetric prolate SU(3) when moving from light isotopes to heavy ones.

1 Introduction

We note that in the interacting boson model-1 (IBM-1) [1, 2] one describes an even-even nucleus as a system of N bosons able to occupy two levels, one with angular momentum restricted to zero (s boson) and one with angular momentum 2 (d boson).

The bosons are assumed to interact via a two-body residual interaction. Denoting by b_i (i=1,...,6) the creation (annihilation) operators for bosons ($b_1 = s, b_{2,...,6} = d$) it is easy to see that the 36 operators $G_{ii^-} = b_i^\dagger b_{i^-}$ close under the Lie algebra of U(6). This simple model allows the utilization of algebraic symmetric for approaching different type of nuclear spectra, known as dynamical symmetries and corresponding to un-harmonic vibrator (U(5) Symmetry) [3], rigid deformations (SU(3) Symmetry) [4] and γ-instability (O(6) Symmetry) [5]. In these special cases it is possible to find analytical solutions of the boson Hamiltonian and deal with small deviations from these symmetries using different perturbation methods.

However, real nuclei may deviate considerably from the simple dynamical limits. This is represented in the Casten triangle [1–6] with vertices corresponding to the standard dynamical symmetries and the sides of the triangle represent direct transition between the limiting cases, whereas all complex transition regions are contained in the area. Phase transitions between these shapes were studied, and it is known that the phase transition from U(5) to O(6) is second order, while any other transitions within the Casten triangle from a spherical to deformed shape is first order [7–23].

Now, there is a class of symmetries that are formulated in terms of the Bohr Hamiltonian and that can be applied to critical point situation [24–26]. In particular, at the critical point from spherical to γ-unstable shapes, called E(5) [24], at the critical point from spherical to axially deformed shapes, called X(5) [25] and the critical point from axially deformed shapes to triaxial shapes, called Y(5) [26]. Since the introduction of these limits many theoretical [27–32] and experimental [33–39] studies have been presented in order to look

for nuclei that exhibit the properties of critically and to classify the corresponding phase transitions. Many studies have extended these original models to more complex situations [40–44].

The relation between the Bohr-Mottelson collective model [45] and the IBM was established [46, 47] on the basis of an intrinsic (or coherent) state for the IBM. Via this coherent state formalism, a potential energy surface (PES) E(β, γ) in the quadruple deformation variables β and γ can be derived for any IBM Hamiltonian and the equilibrium deformation parameters β_0 and γ_0 are then found by minimizing E(β, γ). The deformation parameter β measures the axial deviation from sphericity, while the angle variable γ controls the departure from axial symmetry.

In the present work, we investigate shape phase transition within the IBM-1 using coherent state formalism for various rare earth isotopic chains. The paper is organized as follows. First the IBM and the symmetry triangle used in the present work is briefly described in section 2. In this variation of the IBM, the coherent state approach is treated to produce PES's in section 3. The location of the critical point in the shape transition is identified in section 4. We review the concept of dynamical symmetry in section 5. In section 6 a systematic study of isotopic chains on Nd/Sm/Gd/Dy related to the U(5)-SU(3) shape transition is given and main conclusions arising from the present results are discussed.

2 The IBM-1 Hamiltonian and Coherent State

Denoting by $C_n[G]$ the nth-order Casmir operator of the Lie group G, the general sd-IBM Hamiltonian with up to two-body interactions can be written in the following form:

$$
\begin{aligned}
H &= \epsilon C_1[U(5)] + k_1 C_2[U(5)] \\
&+ k_2 C_2[O(5)] + k_3 C_2[O(3)] \\
&+ k_4 C_2[SU(3)] + k_5[O(6)]
\end{aligned}
\tag{1}
$$

The Casmir operators are defined by the following equations

$$
C_1[U(5)] = \hat{n}_d
\tag{2}
$$

$$C_2[U(5)] = \hat{n}_d(\hat{n}_d + 4) \qquad (3)$$

$$C_2[O(5)] = 4\left[\frac{1}{10}(\hat{L}.\hat{L} + \hat{T}_3.\hat{T}_3)\right] \qquad (4)$$

$$C_2[O(3)] = 2(\hat{L}.\hat{L}) \qquad (5)$$

$$C_2[SU(3)] = \frac{2}{3}\left[2(\hat{Q}.\hat{Q}) + \frac{3}{4}(\hat{L}.\hat{L})\right] \qquad (6)$$

$$C_2[O(6)] = 2\left[N(N+4) - 4(\hat{P}.\hat{P})\right] \qquad (7)$$

where $\hat{n}_d$, $\hat{P}$, $\hat{L}$, $\hat{Q}$ and $\hat{T}_3$ are the boson number, pairing, angular momentum, quadruple and octuple operators defined as

$$\hat{n}_d = (d^{\dagger}\tilde{d})^{(0)} \qquad (8)$$

$$\hat{P} = \frac{1}{2}(\tilde{d}\tilde{d}) - \frac{1}{2}(\tilde{s}\tilde{s}) \qquad (9)$$

$$\hat{Q}[\chi] = [d^{\dagger}\tilde{s} + s^{\dagger}\tilde{d}]^2 + \chi[d^{\dagger}x\tilde{d}]^{(2)} \qquad (10)$$

$$\hat{L} = \sqrt{10}[d^{\dagger}x\tilde{d}]^{(1)} \qquad (11)$$

$$\hat{T}_3 = [d^{\dagger}x\tilde{d}]^{(3)} \qquad (12)$$

where $s^{\dagger}(s)$ and $d^{\dagger}(d)$ are monopole and quadruple boson creation (annihilation) operators respectively. The study of shape phase transition in even-even nuclei can be well done from the simple two parameter IBM Hamiltonian, the well known consistent-Q Hamiltonian

$$H = \varepsilon\hat{n}_d - k\hat{Q}(\chi) \cdot \hat{Q}(\chi). \qquad (13)$$

The symbol $(\cdot)$ represents the scalar product and the scaler product of two operators with angular momentum L is defined as $\hat{T}_L.\hat{T}_L = \Sigma_M(-1)^M\hat{T}_{LM}\hat{T}_{L-M}$ where $\hat{T}_{LM}$ corresponds to the M component of the operator $\hat{T}_L$.

The Hamiltonian of equation (13) describes the main features of collective nuclei, it contains the dynamical symmetries of the IBM for spherical choices of the coefficients ε, k and χ, and allows to describe the transitional regions between any of symmetry limits as well. In discussing phase transitions, it is convenient to introduce the control parameter η, such as:

$$\frac{\eta}{1-\eta} = \frac{1}{N}\frac{\varepsilon}{k} \qquad (14)$$

where N is the total number of boson. Hamiltonian(1) can be written in the second form

$$H = C\left[\eta\hat{n}_d - \frac{1-\eta}{N}\hat{Q}(\chi).\hat{Q}(\chi)\right]. \qquad (15)$$

With

$$C = \varepsilon + Nk, \qquad \eta = \frac{\varepsilon/k}{N + \varepsilon/k}. \qquad (16)$$

The second form equation (15) avoids the infinities inherent in the use of the ratio of ε/k as η varies from 0 to 1. The factor C in equation (15) is only a scale factor and η and χ are therefore the two parameters that determine the structure. The values of the control parameter η ranges from 0 to 1 and χ is located in the interval of $-\sqrt{7}/2$ (-1.32) to $\sqrt{7}/2$ (+1.32).

Let us consider the Hamiltonian of equation (5) and the effects of its two parameters η and χ. Clearly, one of the most important features of the IBM is the existence of three distinct dynamical symmetries (DS), each representing a well defined phase of nuclear collective motion. The three DS are: the U(5) symmetry for spherical vibrational nuclei (η=1), the SU(3) symmetry for prolate deformed nuclei (η=0, χ= $-\sqrt{7}/2$) and the O(6) symmetry for γ-unstable deformed nuclei (η=0, χ=0), the SU(3) symmetry for oblate deformed nuclei corresponding to (η=0, χ=+$\sqrt{7}/2$). For intermediate values of the control parameters η and χ, the potential energy surface (PES) function will describe a certain point on the IBM symmetry triangle located between the three limits.

Comparing the simplified Hamiltonian equation (15) with equation (1) we see that only two terms of the general form are considered. Rewriting equation (15) in the form of equation (1), we get:

$$\begin{aligned}
H &= \left[\eta + \frac{2}{7N}(1-\eta)\chi\left(\chi + \frac{\sqrt{7}}{2}\right)\right]C_1[U(5)] \\
&+ \frac{2}{7N}(1-\eta)\chi\left(\chi + \frac{\sqrt{7}}{2}\right)C_2[U(5)] \\
&+ \frac{1}{N}(\eta - 1)\left(1 + \frac{3}{\sqrt{7}}\chi + \frac{2}{7}\chi^2\right)C_2[O(5)] \\
&+ \frac{1}{14N}(1-\eta)\chi\left(\chi + 2\sqrt{7}\right)C_2[0(3)] \\
&+ \frac{1}{\sqrt{7}N}(\eta - 1)\chi C_2[SU(3)] \\
&+ \frac{1}{N}(1-\eta)\left(1 + \frac{2}{\sqrt{7}\chi}\right)C_2[O(6)].
\end{aligned} \qquad (17)$$

In IBM-1, the intrinsic coherent normalized state of a nucleus with N valence bosons outside the doubly-closed shell state is given by:

$$|N\beta\gamma\rangle = \frac{1}{\sqrt{N!}}(\Gamma_C^{\dagger})^N|0\rangle \qquad (18)$$

where $|0\rangle$ denotes the boson vacuum, and

$$\Gamma_C^{\dagger} = \frac{1}{\sqrt{1+\beta^2}}\left[s^{\dagger} + \beta\cos\gamma d_0^{\dagger} + \frac{1}{\sqrt{2}}\beta sin\gamma(d_2^{\dagger} + d_{-2}^{\dagger})\right]. \qquad (19)$$

Here $\beta \geq 0$ and $0 \leq \gamma \leq \pi/3$ are intrinsic shape parameters. We get the PES by calculating the expectation value of Hamiltonian (17) on the boson condensate equation (18). The

corresponding PES as a function of the deformations β and γ is given by:

$$
\begin{aligned}
E(N,\eta,\chi,\beta,\gamma) = \\
= \;\; & -5(1-\eta) + \frac{1}{(1+\beta^2)^2} \\
& \left\{ \left[N\eta - (1-\eta)\left(4N+\chi^2-8\right) \right]\beta^2 \right. \\
& + \left[N\eta - (1-\eta)\left(\frac{(2N+5)}{7}\chi^2-4\right) \right]\beta^4 \\
& \left. + 4N(1-\eta)\sqrt{\tfrac{2}{7}}\chi\beta^3\cos 3\gamma \right\}
\end{aligned}
\tag{20}
$$

3 Location of the Critical Symmetries

Minimization of the PES equation (20) with respect to β for given values of the control parameters η and χ, gives the equilibrium value β_e. The phase transition is signaled by the condition at $\beta = 0$

$$
\frac{d^2E}{d\beta^2} = 0,
\tag{21}
$$

which fixes the critical value of the control parameter η. The critical point in the above equation (20) is given by the value of η where the coefficient at β^2 vanishes, i.e.

$$
\eta_{critical} = \frac{4N+\chi^2-8}{5N+\chi^2-8}.
\tag{22}
$$

At this value, the second β derivative for $\beta = 0$ changes its sign, which means that $\beta = 0$ maximum becomes a local minimum. Note that the critical point (22) depends on χ, it changes between: $\eta(-\sqrt{7}/2) = (16N-25)/(20N-25)$ at U(S)-SU(3) side if the symmetry triangle, and $\eta(0) = (16N-32)/(20N-32)$ at the U(5)-O(6) side, condition (12) gives in the case of large-N limit the value 4/5.

If we ignore the contribution of one-body term of the quadruple-quadruple interaction and in large N limit (N-1≃N) and $\gamma = 0$, equation (20) takes the form

$$
\begin{aligned}
E(N,\eta,\chi,\beta) = \;\; & \frac{N\beta^2}{(1+\beta^2)^2}\left[5\eta-4+4\sqrt{\tfrac{2}{7}}\beta\chi(1-\eta) \right. \\
& \left. +\beta^2\left(\eta-\tfrac{2}{7}\chi^2(1-\eta)\right) \right].
\end{aligned}
\tag{23}
$$

The deformation parameter $\beta = 0$ is always a stationary point. For $\eta < 4/5$, $\beta = 0$ is a maximum, while for $\eta > 4/5$, it becomes a minimum. In the case of $\eta = 4/5$, $\beta = 0$ is an inflection point. The $\eta = 4/5$ is the point at which a minimum at $\beta = 0$ starts to develop and defines the antispinodal line. For $\chi \neq 0$, there exists a region, where two minima, one spherical and one deformed, coexist. This region is defined by the point at which the $\beta = 0$ minimum appears (antispinodal point) and the point at which the $\beta \neq 0$ minimum appears (spinodal point). For $\eta = 1$, the system is in the symmetry
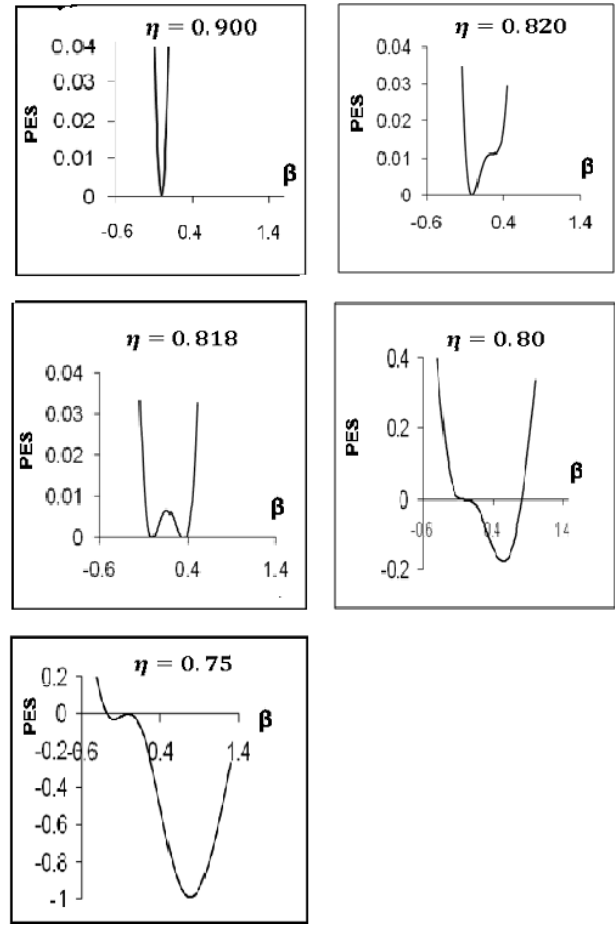
Fig. 1: Potential energy surface (PES) equation (3) for N=10 calculated with IBM without normalization along the axial trajectory $\gamma = 0°, 60°$ as a function of the shape parameter β. The curves describe the first order shape phase transition between spherical to prolate deformed U(5)-SU(3) for control parameter η: $\eta = 0.900$, $\eta = 0.820$ (spinodal), $\eta = 0.818$ (critical point), $\eta = 0.800$ (antispinodal) and $\eta = 0.750$.
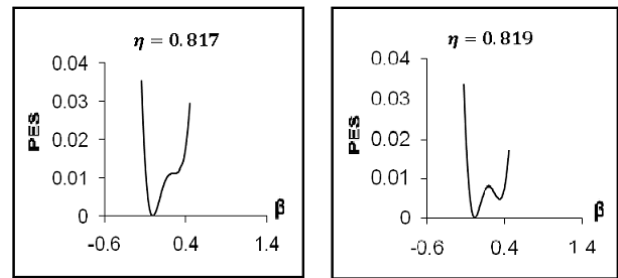
Fig. 2: For two cases in the coexistence region $\eta = 0.817$ and $\eta = 0.819$.

phase since the PES has a unique minimum at $\beta = 0$. When η decreases, one reaches the spinodal point $\eta = 0.820361$ for $\chi = -\sqrt{7}/2$ as illustrated in Fig. (1) for boson number N=10.
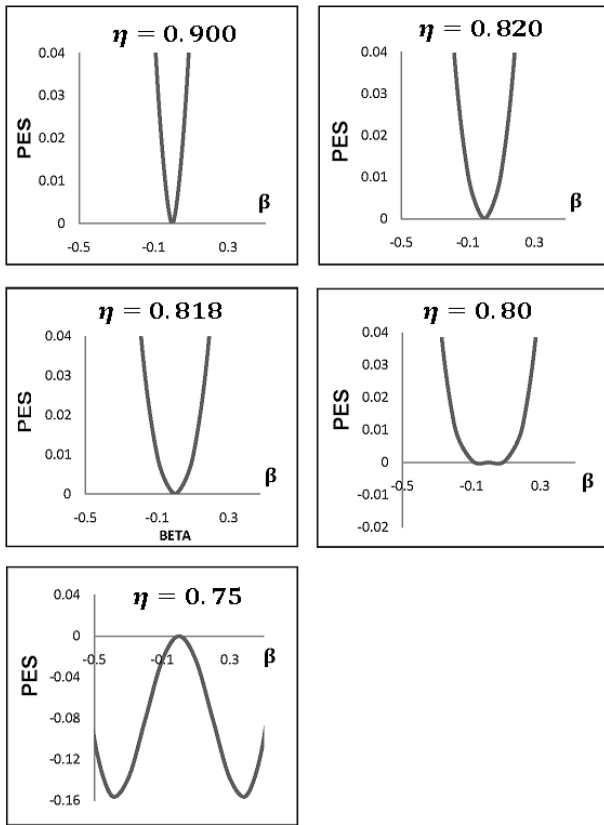
Fig. 3: For $\chi = 0$.

In the coexistence region, the critical point is at the situation in which both minima of spherical point is at the situation in which both minima of spherical and deformed are degenerate. At the critical point, the two degenerated minima are at $\beta_0 = 0$ and $\beta_0 = -\sqrt{7}/4$ and their energy is equal to zero. The critical point line is at $\eta_c = (4 + 2/7\chi^2)/(5 + 2/7\chi^2)$.

The $\chi = -\sqrt{7}/2$ provides $\eta_c = 9/11$ (0.818181). According to the previous analysis, a first order phase transition appears for $\eta \neq 0$, $\chi \neq 0$, while for $\chi = 0$ there is an isolated point of second order phase transition as a function of η. Spinodal, antispinodal and critical point coincide at the critical value $\eta = 4/5$.

We show in Figures (1,2,3) a sketch at this evolution for the special case $\chi = -\sqrt{7}/2$, the two cases in the coexistence region and for $\chi = 0$. From Figure (3), we observe the evolution from the spherical potential $\eta = 0.9$, whose minima is found at $\beta = 0$ to potentials with well-deformed minima $\eta = 0.75$. For intermediate η values one finds a set of potential energy curves which are practically degenerated along the prolate axis in the interval $[0, 0.4]$. These curves show two minima, on spherical and a prolate deformed one. In particular, for $\eta = 0.81818$, the spherical and the prolate deformed minima are degenerate and this condition defines precisely the critical point of the first order phase transition where the

order parameter is the deformation β.

For $\eta = 1$, the Hamiltonian H of equation (15) reduces to the U(5) limit of the IBM corresponds to a spherical shape with vibration

$$H(U(S)) = \hat{n}_d. \tag{24}$$

The PES of H is given by:

$$E(U(5)) = \frac{N\beta^2}{1 + \beta^2}. \tag{25}$$

The equilibrium value of the deformation parameter β is easily obtained by solving $\partial E/\partial \beta = 0$ to give $\beta_e = 0$ which corresponds to a spherical shape.

For $\eta = 0$ and $\chi = \mp\sqrt{7}/2$, the schematic Hamiltonian of equation (15) reproduces the SU(3) Limit corresponds to a shape of ellipsoid with rotation (or axial rotation)

$$H((SU(3)) = -\frac{1}{N}\hat{Q}(\chi).\hat{Q}(\chi). \tag{26}$$

If we eliminate the contributions of the one-body terms of quadruple-quadruple interaction, for this case the PES of H is given by:

$$E((SU(3)) = -\frac{(N-1)}{(1+\beta^2)^2}(4\beta^2 + \frac{1}{2}\beta^4 \pm 2\sqrt{2}\beta^3 cos3\gamma). \tag{27}$$

The equilibrium values are given by solving $\frac{dE}{d\beta} = \frac{\partial E}{\partial \gamma} = 0$ to give $\beta_e = \sqrt{2}$ and $\gamma_e = 0$ for $\chi = -\sqrt{7}/2$ and by $\beta_e = \sqrt{2}$ and $\gamma_e = \pi/3$ for $\chi = \sqrt{7}/2$ corresponding to prolate and oblate deformed shape respectively.

For $\eta = 0$ and $\chi = 0$, one recovers the O(6) limit corresponds to γ-unstable

$$H(O(6)) = -\frac{1}{N}\hat{Q}(\chi = 0).\hat{Q}(\chi = 0). \tag{28}$$

Eliminating the one-body terms, the PES depends only on β

$$E(O(6)) = -\frac{(N-1)}{(1+\beta^2)^2}4\beta^2. \tag{29}$$

The equilibrium value is given by $\beta_e = 1$, corresponding to a γ-unstable deformed shape. For intermediate values of the control parameters η and χ, the PES function will describe a certain point on the IBM symmetry triangle, located between the three limits.

4 First-Order U(5)-SU(3) Phase Transition in Nd/Sm/Gd/Dy Rare Earth Nuclei

In a first order phase transition, the state of the rearrangement happens, which means that there involves an irregularity at the critical point.

The study is carried out considering specific isotopic chains of even-even rare earth nuclei $_{60}$Nd, $_{62}$Sm, $_{64}$Gd and $_{66}$Dy displaying first order phase transition from sphericity to
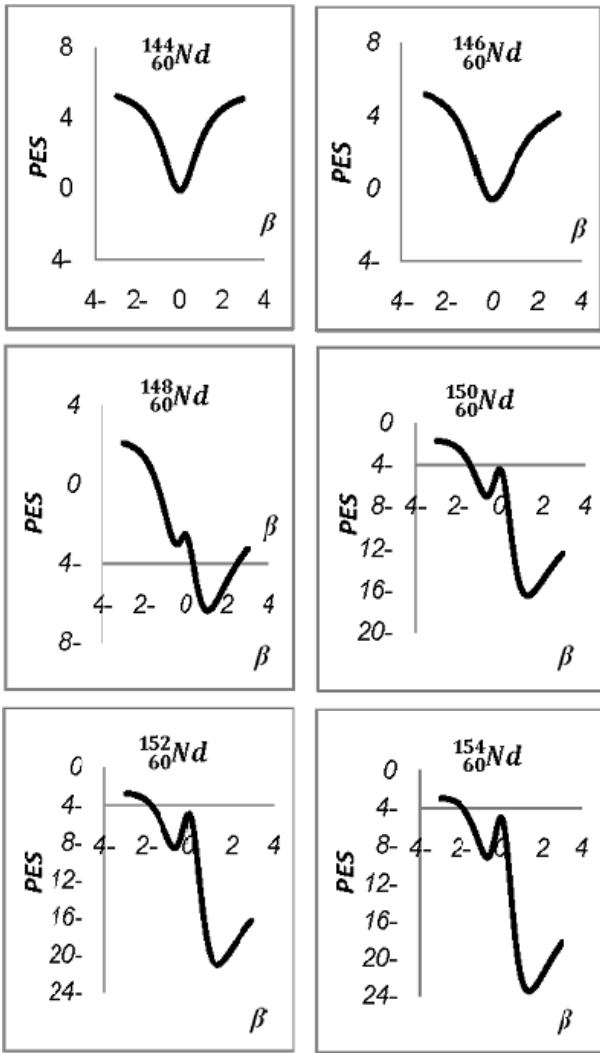
Fig. 4: PES for first order shape phase transition between spherical to prolate deformed U(5)-SU(3) for Neodymium isotope chain $^{144-154}_{60}$Nd (with $N_\pi = 5$ proton bosons and $N_\nu = 1 - 6$ neutron bosons).

Fig. 5: The same as Fig. (4) but for Samarium isotope chain $^{146-160}_{62}$Sm (with $N_\pi = 6$ proton bosons and $N_\nu = 1$–8 neutron bosons).

axial symmetric deformed U(S)-SU(3). That is for the nuclei included in this study; all chains begin as vibrational with energy ratio $R_{(4/2)} = E(4^+_1)/E(2^+_1)$ near 2.0 and move towards rotational $R_{(4/2)} = 3.33$ as neutron number is increased. For control parameter $\eta = 1$, we get the U(5) limit and for $\eta = 0$ and $\chi = -\sqrt{7}/2$ the SU(3) limit. For intermediate values of the control parameters η and χ, the PES function will describe a certain point on the IBM symmetry triangle, located between the U(5) and SU(3) limits. To describe a phase transition, one has to establish the values of the control parameter for each nucleus.

For our rare-earth nuclei, we keep χ at the fixed value $\chi = -\sqrt{7}/2$, because some Gd isotopes clearly exhibit the character of the SU(3) dynamical symmetry. This assumption

is very successful in describing the Sm nuclei which form neighboring nuclei.

The system passes from the U(5) to the SU(3) limit when the number of bosons is increasing from N=6 towards N=17. The values of the control parameter η is adjusted for each nucleus by using a computer simulated search program in order
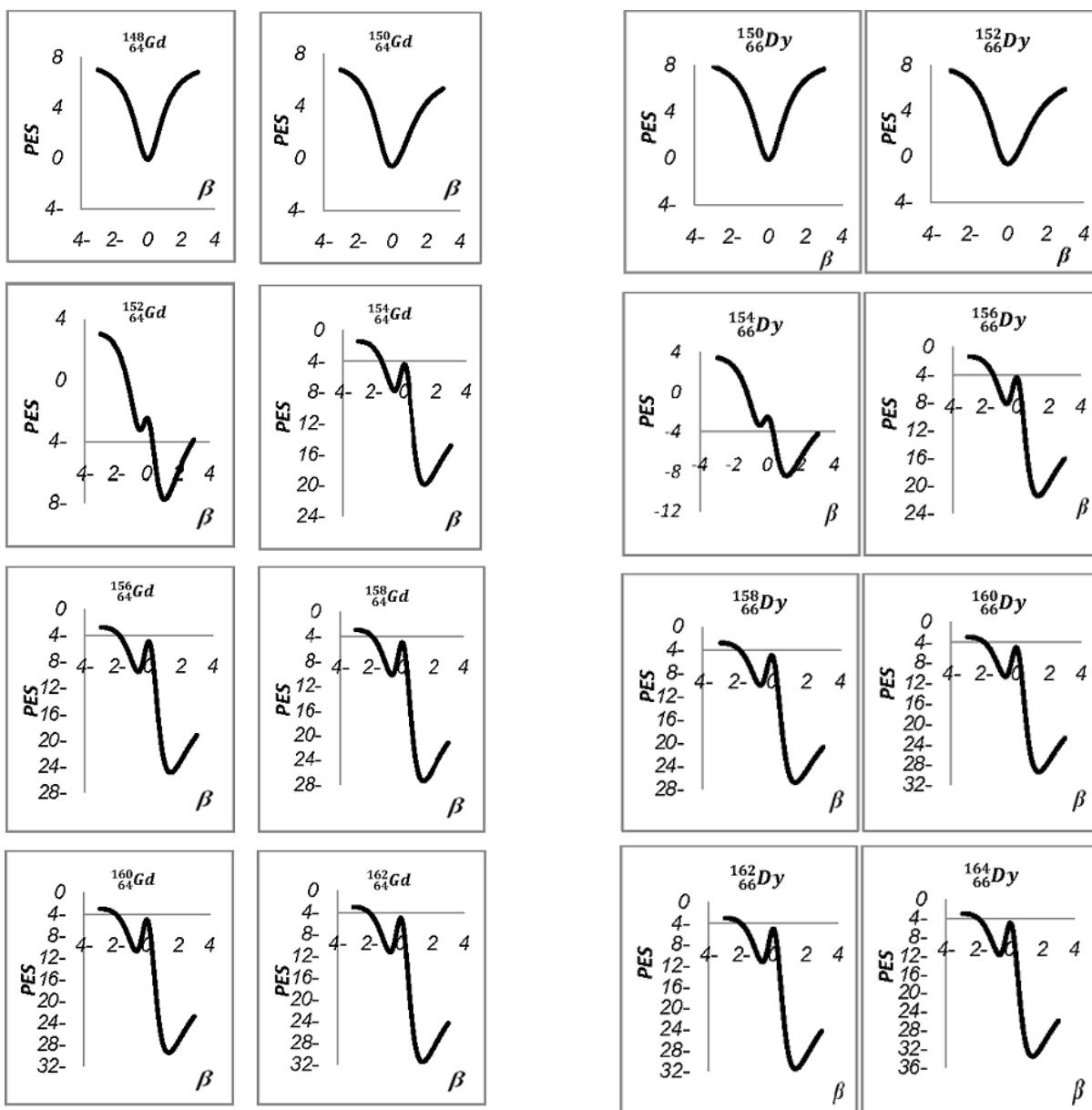
Fig. 6: The same as Fig. (4) but for Gadolinium isotope chain $^{148-162}_{64}$Gd (with $N_\pi = 7$ proton bosons and $N_\gamma = 1-9$ neutron bosons).

Fig. 7: The same as Fig. (4) but for Dysprosium isotope chain $^{150-166}_{66}$Dy (with $N_\pi = 8$ proton bosons and $N_\gamma = 1-9$ neutron bosons).

to describe the gradual change in the structure as boson number is varied and to reproduce the properties of the selected states of positive parity excitation ($2^+_1, 4^+_1, 6^+_1, 8^+_1, 0^+_2, 2^+_3, 4^+_3, 2^+_2, 3^+_1$ and 4^+_2) and the two neutron separation energies of all isotopes in each isotopic chain. Typically, η decreasing from 1 to 0 as boson number increases and the nuclei evolve from vibrational to rotational as expected. This trend is observed for the studied isotopic chains and illustrated in figures (4-7) by plotting the PES from Hamiltonian (12) as a function of quadruple deformation parameter β for different values of the

Fig. 8: Position of the absolute minima β_{min} versus the total number of bosons N from N = 6 to N = 17.

Table 1: Neutron Number.

Nucleus	η/N_{crit}			
$_{66}$Dy	0.08183	0.07339	0.04166	0.00993
$_{64}$Gd	0.08183	0.07339	0.04166	0.00993
$_{62}$Sm	0.0982	0.08807	0.5	0.01192
$_{60}$Nd	0.10911	0.09786	0.55555	0.01324
N	84	86	88	90

Nucleus	η/N_{crit}			
$_{66}$Dy	0.00149	0.0002	0.0000	0.0000
$_{64}$Gd	0.00149	0.0002	0.0000	0.0000
$_{62}$Sm	0.00179	0.00024	0.00003	0.0000
$_{60}$Nd	0.00199	0.00027		
N	92	94	96	98

the control parameter η and varying boson number N.

Here, we observe that the transition from spherical to prolate deformed occurs between N=9 and N=12. In the $^{144-154}$Nd, the nuclei $^{146-150}$Nd are transitional isotopes between the spherical nucleus ^{144}Nd and the well prolate deformed nuclei $^{152-154}$Nd. The ^{150}Gd nucleus still shows a vibrational structure while $^{156-162}$Gd are considered as rather good SU(3) example.

The $^{158-162}$Gd are corresponds to $\eta = 0$. One can observe a sudden transition in the Gd isotopes from a vibrational region into the rotational SU(3) limit. The control parameter η for each nucleus is shown in Table (1). The position of the absolute minimum $\beta_{min}(N)$ of the different PES's is illustrated in Figure (8).

Table (1) lists values of the control parameter η/N_{crit} for each Nd/Sm/Gd/Dy isotopic chain as a function of the neutron number.

5 Conclusion

In the present paper we have analyzed systematically the $PES's$ for the even-even Nd/Sm/Gd/Dy isotopes using the simplified form of IBM in its sd-boson interaction. We have analyzed the critical points of the shape phase transitional region U(5)-SU(3) in the space of two control parameters η and χ.

In all isotopic chains one observes a change from spherical U(5) shape to axially symmetric deformed shape SU(3) when moving from the lighter to the heavier isotopes.

References

1. Iachello F. and Arima A. The Interacting Boson Model. Cambridge University Press, Cambridge, England, 1987.

2. Frank A. and VanIsacker P. Algebraic Methods in Molecular and Nuclear Structure Physics. Wiley, New York, 1994.

3. Arima A. and Iachello F. Interacting Boson Model of Collective States I: The Vibrational Limit. *Annals of Physics*, 1976, v. 99, 253–317.

4. Arima A. and Iachello F. Interacting Boson Model of Collective States II: The Rotational Limit. *Annals of Physics*, 1978, v. 101, 201–238.

5. Arima A. and Iachello F. Interacting Boson Model of Collective States IV: The O(6) limit. *Annals of Physics*, 1979, v. 102, 123–468.

6. Casten R.E. Nuclear structure from a simple persective. Oxford University, Oxford, 1990.

7. Jolie J. et al. Quantum Phase Transition for γ-Soft Nuclei. *Physical Review Letters*, 2001, v. 87, 162501–162504.

8. Jolie J. et al. Triple Point of Nuclear Deformation. *Physical Review Letters*, 2002, v. 89, 182502–182504.

9. Jolie J. et al. Shape phase transitions in odd-mass nuclei using a supersymmetric approach. *Physical Review*, 2002, v. C70, 011305R–011308R.

10. Jolie J. et al. Two-Level Interacting Boson Models Beyond The Mean Field. *Physical Reveiw*, 2007, v. C75, 014301R - 014310R.

11. Iachello F. and Zamfir N.V. Quantum Phase Transitions in Mesoscopic Systems. *Physical Review Letters*, 2004, v. 92(3), 212501–212504.

12. Cejnar P. Shape phase transitions in rotating nuclei via cranking the interacting boson model. *Physical Review*, 2002 v. C65, 044312–044320.

13. Cejnar P., Heinze S., and Jolie J. Ground-State Shape Phase Transitions in Nuclei: Thermodynamic analogy and fitie N-effects. *Physical Review*, 2003 v. C68, 034326-034326.

14. Cejnar P. Landau Theory of Shape Phase Transitions in the Cranked Interacting Boson Model. *Physical Review Letters*, 2003, v. 90, 112501–112504.

15. Cejnar P., Heinze S. and Dobes J. Thermodynamic Analogy for Quantum Phase Transitions at Zero Temperature. *Physical Review*, 2005, v. C71, 011304R–011309R.

16. Rowe D.J., Turner P.S. and Rosensteel G. Scaling Properties and Asymptotic Spectra of Finite Models of Phase Transitions as They Approach Macroscopic Limits. *Physical Review Letters*, 2004, v. 93, 232502–232505.

17. Rowe D.J. Quasi Dynamical Symmetry in an Interacting Boson Model Phase Transition. *Physical Review Letters*, 2004, v. 93, 122502–122505.

18. Liu Y.X., Mu L.Z. and Wei H. Approach to The Rotation Driven Vibrational to Axially Rotational Shape Phase Transition Along The Yrast Line of a Nucleus. *Physics Letters*, 2006, v. B633, 49–53.

19. Zhang Y., Hau Z. and Liu Y.X. Distinguishing a First Order From a Second Order Nuclear Shape Phase Transition in The Interacting Boson Model. *Physical Review*, 2007, v. C76, 011305R–011308R.

20. Arios J.M., Dukelsky J. and Garcia-Ramos J.E. Quantum Phase Transitions in the Interacting Boson Model: Integrability, Level Repulsion and Level Crossing. *Physical Review Letters*, 2003, v. 91, 162502–162504.

21. Garcia-Ramos J.E. et al. Two-Neutron Separation Energies, Binding Energies and Phase Transitions in The Interacting Boson Model. *Nuclear Physics*, 2001, v. A688, 735–754.

22. Liu M.L. Nuclear Shape-Phase Diagrams. *Physical Review*, 2007, v. C76, 054304–054307.

23. Heyde K. et al. Phase Transitions Versus Shape Coexistence. *Physical Review*, 2004, v. C69, 054304–054309.

24. Iachello F. Dynamic Symmetrcies at The Critical Point. *Physical Review Letters*, 2000, v. 85, 3580–3583.

25. Iachello F. Analytic Prescription of Critical Point Nuclei in a Spherical Axially Deformed Shape Phase Transtion. *Physical Review Letters*, 2001, v. 87, 052502–052506.

26. Iachello F. Phase Transition an Angle Variables. *Physical Review Letters*, 2003, v. 91, 132502-132507.

27. Caprio M.A. and Iachello F. Analytic descriptions for transitional nuclei near the critical point. *Nuclear Physical*, 2007, v. A781, 26–66.

28. Arios J.M. E2 transitions and quadrupole moments in the E(5) symmetry. *Physical Review* , 2001, v. 63, 034308–034312.

29. Caprio M.A. Finite well solution for the E(5) Hamiltonian. *Physical Review*, 2002, v. C65, 031304R–031307R.

30. Caprio M.A. Consequences of wall stiffness for a β-soft potential. *Physical Review*, 2004, v. C69, 044307 - 044314.

31. Fortunato L. and Vitturi A. New analytic solutions of the collective Bohr Hamiltonian for a β-soft, γ-soft axial rotor. *Journal of Physics G: Nuclear and Particle Physics*, 2004, v. 30, 627–632.

32. Fortunato L. Soft triaxial rotovibrational motion in the vicinity of $\gamma = \pi/6$. *Physical Review*, 2004, v. 70, 011302R–011305R.

33. Zamfir N.V. et al. ^{102}Pd: An E(5) nucleus? *Physical Review*, 2002, v. C51, 044325–044332.

34. Clark R.M. et al. Searching for E(5) behavior in nuclei. *Physical Review*, 2004, v. C69, 064322–064328.

35. Krücken R. et al. B(E2) Values in ^{150}Nd and the Critical Point Symmetry X(5). *Physical Reviw Letters*, 2003, v. 88, 232501 - 232504.

36. Clark R.M. et al. Searching For X(5) Behavior in Nuclei. *Physical Review*, 2003, v. C68, 037301–037304.

37. Tonev D. et al. Transition Probabilities in ^{154}Gd: Evidence for X(5) Critical Point Symmetry. *Physical Review*, 2004, v. C69, 034334–034340.

38. McCutchan E.A. et al. Low Spin States in ^{162}Yb and The X(5) Critical Point Symmetry. *Physical Review*, 2004, v. C69, 024308–024317.

39. Dewald A. et al. Test of the critical point symmetry X(5) in the mass A=180 region. *Journal of Physics G: Nuclear and Particle Physics*, 2005, v. 31, S1427.

40. Pietralla N. and Gorbachentso O.M. Evolution of the "β excitation" in axially symmetric transitional nuclei. *Physical Review*, 2004, v. C70 011304R–011308R.

41. Bonatsos D. et al. X(3): an exactly separable γ-rigid version of the X(5) critical point symmetry. *Physical Letters*, 2006, v. B632, 238–242.

42. Bonatsos D. et al. γ-rigid solution of the Bohr Hamiltonian for $\gamma = 30°$ compared to the E(5) critical point symmetry. *Physical Letters*, 2005, v. B621, 102–108.

43. Bonatsos D. et al. Z(5): critical point symmetry for the prolate to oblate nuclear shape phase transition. *Physical Letters*, 2004, v. B588, 172–179.

44. Levoi G. and Arias J. M. The sextic oscillator as a γ-independent potential. *Physical Review*, 2004, v. C69, 014304-014309.

45. Bohr A. and Mottelson. Nuclear Structure v. II. Benjamin, New York, 1975.

46. Ginocchio J. N. and Kirson M.W. Relationship between the Bohr Collective Hamiltonian and the Interacting-Boson Model. *Physical Reviw Letters*, 1980, v. 44, 1744–1747.

47. Dieperink A.E.L., Scholten O. and Iachello F. Classical Limit of the Interacting Boson Model. *Physical Reviw Letters*, 1980, v. 44, 1747–1750.

The Self-Gravity Model of the Longitudinal Span
of the Neptune Arc Fraternité

K.H. Tsui, J.A. Souza, and C.E. Navia

Instituto de Fisica - Universidade Federal Fluminense, Campus da Praia Vermelha,
Av. General Milton Tavares de Souza s/n, Gragoata, 24.210-346, Niteroi, Rio de Janeiro, Brasil.
E-mail: tsui@if.uff.br

According to recent work [13, 14], the Neptune Adams ring main arc Fraternité is re-
garded as captured by the corotation elliptic resonance (CER) potential of Galatea. The
minor arcs Egalité (2,1), Liberté, and Courage are located at positions where the time
averaged forces, due to the 42-43 corotation-Lindblad resonances under the central field
of Neptune, vanish. With adequately chosen Fraternité mass and Galatea eccentricity,
this model gives minor arc locations compatible to observed positions, and allows a
dynamic transport of materials among arcs. To complement this model, the effect of
self-gravity of Fraternité, with a distributed mass, is evaluated together with the CER
potential to account for its 10° longitudinal span. Although self-gravity is the collective
action of all the particles in the arc, each individual particle will see the self-potential
with a central maximum as an external potential generated by other particles.

1 Introduction

From the very first observations of the Neptune Adams ring
arcs [6, 12], plus the subsequent observations [2, 11], the A-
dams arcs seemed to change in arc locations and in bright-
ness. More recently, these dynamic natures of the arcs, Fra-
ternité, Egalité (2,1), Liberté, and Courage, have been con-
firmed beyond any doubt in another ground observation [1].
Measuring from the center of the main arc Fraternité, they
extend a total of about 40° ahead of Fraternité. Occasion-
ally, some arcs flare up and others fade away. Furthermore,
the arc configuration appears to be changing in time as well.
The leading arc Courage appears to have leaped over to an-
other CER site recently [1]. Although the twin arc Egalité
(2,1) is small, it is a very bright arc. According to de Pater et
al [1], its relative intensity to Fraternité varied from 17 per-
cent higher in 2002 to seven percent lower in 2003 totaling
a 24 percent relative change over a short period of time. The
angular span of the twin arc Egalité appeared to be 30 percent
larger in 2005 and 1999 publications than in 1989 Voyager 2
results. This widening of Egalité was accompanied by a cor-
responding narrowing of Fraternité, which indicated a likely
exchange of material between the two. As for Liberté, 1999
data showed it was about 3° ahead of its position in Voyager 2
pictures. For the 2005 results, the 2002 data appeared to show
Liberté as a twin arc separated by about 4.5° with the leading
twin at the original Voyager 1989 location, while in 2003 it
returned again as one single arc at the Voyager location. With
respect to the normally low intensity arc Courage, it flared in
intensity to become as bright as Liberté in 1998 indicating a
possible exchange of material between the two arcs. Most in-
terestingly, it was observed in the 2005 data that Courage has
moved 8° ahead from 31.2° to 39.7° [1].

According to the prevailing theories, based on the restrict-
ed three-body framework (Neptune-Galatea-arcs) with a con-
servative disturbing potential, these arcs are radially and lon-

gitudinally confined by the corotation resonance potential of
the inner moon Galatea. In order to account for these arcs, the
84/86 corotation resonance due to the inclination of Galatea
(CIR) had been invoked to give a potential site of 4.18° [4].
Later on, because of its eccentricity (CER), the 42/43 reso-
nance was considered giving a resonant site of 8.37° on the
Adams ring arcs [3, 5, 10]. The arc particles librate about the
potential maximum imposed by the corotational resonance
satellite Galatea. Dissipated energy of the particle is replen-
ished by the Lindblad resonance. Nevertheless, well estab-
lished as it is, there are several difficulties. Firstly, with Fra-
ternité centered at the potential maximum spanning approxi-
mately 5° on each side, it crosses two unstable potential poi-
nts which ought to reduce the angular spread. Secondly, the
minor arcs leading ahead of Fraternité are mislocated with
the CIR or CER potential maxima. Furthermore, should the
arcs were confined by the corotation potential, there ought to
be arcs in other locations along the Adams ring distributed
randomly instead of clustered near Fraternité.

2 Time-dependent arcs

Recently, there is a model that considers Fraternité as being
captured by the CER potential of Galatea. With Fraternité
having a finite mass, the minor arcs are clustered at locations
along the Adams ring where the time averaged force vanishes
under the corotation-Lindblad resonances [13, 14]. The finite
mass of Fraternité has been suggested by Namouni [9] and
Porco [10] to pull on the pericenter precession of Galatea to
account for the mismatch between the CER pattern speed and
the mean motion of the arcs. The arc locations are determined
by the Lindblad resonance reaction of the arc itself. Because
the force vanishes only on a time averaged base, as compar-
ing to the stationary CER potential in the rotating frame, the
arc material could migrate on a long time scale from one site
to another leading to flaring of some arcs and fading of oth-

ers. This could also generate twin arcs (Egalité, Liberté) and displace Courage from 31.2º to 39.7º (resonant jump) [1], as required by observations. Although there are only arcs in the leading positions ahead, arcs in the trailing positions behind could be allowed in this model. According to this Lindblad reaction model, only Fraternité f is confined by the externally imposed CER potential of Galatea x which reads

$$\Phi_c = \frac{Gm_x}{a_x} \frac{1}{2} \left(2n + a_x \frac{\partial}{\partial a_x} \right) \frac{1}{a_x} b_{1/2}^{(n)}(\alpha) \, e_x \cos \phi_{fx}, \quad (1)$$

where $\vec{r}_x = (r_x, \theta_x)$ and $\vec{r} = (r, \theta)$ are the position vectors of Galatea x and Fraternité mass distribution, a_x and a are the respective semi-major axes, ϕ_x and e_x are the arguments of perihelion and eccentricity of x, $\phi_{fx} = (n\theta - (n-1)\theta_x - \phi_x)$ is the corotation resonance variable, $b_{1/2}^{(n)}(\alpha)$ is the Laplace coefficient, $\alpha = a_x/a < 1$, and $n = 43$. With $a_x = 61952.60$ km, $a = 62932.85$ km, and $\alpha = 0.98444$ [2, 11], the CER potential is

$$\Phi_c = \frac{Gm_x}{a_x} 34 \, e_x \cos \phi_{fx}. \quad (2)$$

To complement this model, we consider the self-gravity of Fraternité, which has a distributed mass, on the CER potential to account for its longitudinal 10º arc span. We first consider a qualitative spherical self-gravity physical model to grasp the 10º arc span. We begin with the Gauss law of the gravitational field

$$\nabla \cdot \vec{g}(\vec{r}) = -4\pi G \rho(\vec{r}), \quad (3)$$

$$\vec{g} = +\nabla \Phi. \quad (4)$$

Under a qualitative physical model of arc span, we take a spherical uniform mass distribution of radius r_0. Solving for the potential $\Phi(r_*)$ inside the sphere with $\rho(\vec{r}) = \rho_0$ and outside the sphere with $\rho(\vec{r}) = 0$ respectively, where r_* is measured from the center of Fraternité, and matching the potential and the gravitational field across the boundary, we get

$$\Phi_f = -\frac{1}{2} \frac{Gm_f}{r_0} \left(\frac{r_*}{r_0} \right)^2 + \frac{3}{2} \frac{Gm_f}{r_0}, \quad 0 < r_* < r_0, \quad (5)$$

$$\Phi_f = +\frac{Gm_f}{r_*}, \quad r_0 < r_* < \infty. \quad (6)$$

This potential shows a normal $1/r_*$ decaying form for $r_0 < r_*$, but a r_*^2 form for $r_* < r_0$. Writing in terms of a_x and m_x, we have for $0 < r_* < r_0$, $\delta\theta < \delta\theta_0$,

$$\Phi_f = -\frac{1}{2} \frac{Gm_f}{a_x} \frac{a_x}{r_0} \left(\frac{r_*}{r_0} \right)^2 + \frac{3}{2} \frac{Gm_f}{r_0}$$
$$= -\frac{1}{2} \frac{Gm_x}{a_x} \frac{m_f}{m_x} \frac{a_x}{r_0} \left(\frac{a}{r_0} \right)^2 (\delta\theta)^2 + \frac{3}{2} \frac{Gm_x}{a_x} \frac{m_f}{m_x} \frac{a_x}{r_0}, \quad (7)$$

and for $r_0 < r_* < \infty$, $\delta\theta_0 < \delta\theta$,

$$\Phi_f = +\frac{Gm_f}{a_x} \frac{a_x}{r_*} = +\frac{Gm_x}{a_x} \frac{m_f}{m_x} \frac{1}{\delta\theta}. \quad (8)$$
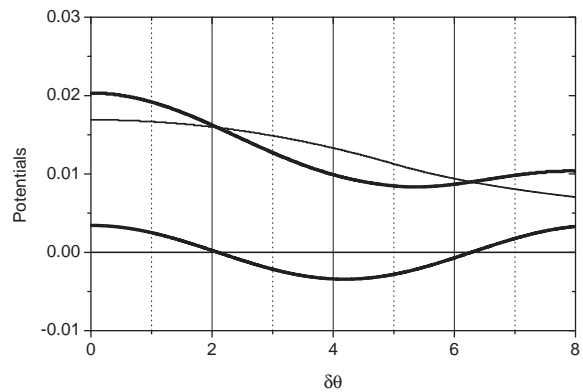
Fig. 1: The CER sinusoidal potential of Galatea in thick line, the self-potential of Fraternité with spherical model in thin line, and the sum of the two in thick line are plotted in units of Gm_x/a_x.

where r_* is now taken on the longitudinal direction along the arc, so that we can write $r_* = a\delta\theta$ and $r_0 = a\delta\theta_0$ with $\delta\theta$ as the angular span in radian. Taking $m_f/m_x = 10^{-3}$, $e_x = 10^{-4}$, and $\delta\theta_0 = 5º = 0.087$ rad, which are within the estimates of the arc parameters [9], we have plotted in Fig. 1 the sinusoidal CER potential in thick line with a minimum around $\delta\theta = 4º$ and the self-potential in thin line in units of Gm_x/a_x. The superposition of the two in thick line is also shown in the same figure. The superimposed potential has a maximum at the center and a minimum around $\delta\theta = 5º$. Although self-gravity is resulted from all the particles of the arc, each individual particle will see the self-potential as an external potential. The particles will girate in stable orbit about the central maximum of the superpositioned CER potential and self-potential.

3 Self-gravity

We now present an elongated ellipsoid model of self-gravity. For an ellipsoidal mass distribution with uniform density ρ_0 over a volume

$$\left(\frac{x}{a_1} \right)^2 + \left(\frac{y}{a_2} \right)^2 + \left(\frac{z}{a_3} \right)^2 = 1, \quad (9)$$

where $a_1 > a_2 > a_3$, the potential in space for the gravitational field $\vec{g}(\vec{r})$ have been addressed in honorable treatises such as Kellogg [7] and Landau and Lifshitz [8]. Here, we follow the celebrated original work of Kellogg [7] especially in Section 6 of Chapter 7. The potential in space of this homogeneous ellipsoid is given by

$$\Phi_f(x, y, z) = G \rho_0 \pi a_1 a_2 a_3 \times$$
$$\int_0^\infty \frac{d\lambda}{\sigma^{1/2}(\lambda)} \left[1 - \frac{x^2}{a_1^2 + \lambda} - \frac{y^2}{a_2^2 + \lambda} - \frac{z^2}{a_3^2 + \lambda} \right], \quad (10)$$

where

$$\sigma(\lambda) = \left(a_1^2 + \lambda \right) \left(a_2^2 + \lambda \right) \left(a_3^2 + \lambda \right), \quad (11)$$

and where λ parameterizes a family of ellipsoids. Consider a prolate ellipsoid with $a_1 > a_2 = a_3$. This ellipsoid has a circular cross section on the y-z plane and an axis of symmetry in x. The y-z plane of $x = 0$ is the equatorial plane. In this prolate case, the self-potential inside and outside the ellipsoid is given respectively by [7, Exercise 6, p.196]

$$\Phi_f(x, r) = G\rho_0 \frac{4\pi}{3} a_1 a_2 a_3 \frac{1}{f^2} \times$$
$$\left[\left(4x^2 - 2r^2 - f^2\right) \frac{1}{2f} \ln\left(\frac{2a_1 - f}{2a_1 + f}\right)^{1/2} + \right. \tag{12}$$
$$\left. + \frac{4a_1^2\left(2x^2 - r^2\right) - 2f^2x^2}{2a_1\left(4a_1^2 - f^2\right)} \right],$$

$$\Phi_f(x, r) = G\rho_0 \frac{4\pi}{3} a_1 a_2 a_3 \frac{1}{f^2} \times$$
$$\left[\left(4x^2 - 2r^2 - f^2\right) \frac{1}{2f} \ln\left(\frac{s - f}{s + f}\right)^{1/2} + \right. \tag{13}$$
$$\left. + \frac{s^2\left(2x^2 - r^2\right) - 2f^2x^2}{s\left(s^2 - f^2\right)} \right],$$

where

$$\left(\frac{f}{2}\right)^2 = a_1^2 - a_2^2,$$
$$r^2 = y^2 + z^2,$$

f is the distance between the two foci, r is the perpendicular distance to the axis of symmetry, s is the sum of distances from the two foci to the point of interest $\vec{r}$. The inside potential can be obtained from the outside potential by using $s = 2a_1$. To evaluate the potential on the axis of symmetry, we take $r = 0$. Denoting $m_f = \rho_0(4\pi/3)a_1 a_2 a_3$ and considering $a_1 \gg a_2$, we get

$$\Phi_f(x) = -\frac{Gm_f}{a_x} \frac{a_x}{4a_1} \left[\ln\left(\frac{2a_1}{a_2}\right) - 1\right] \left(\frac{\delta\theta}{\delta\theta_0}\right)^2 +$$
$$+ \frac{Gm_f}{a_x} \frac{a_x}{4a_1} \ln\left(\frac{2a_1}{a_2}\right), \quad \delta\theta < \delta\theta_0, \tag{14}$$

$$\Phi_f(x) = -\frac{Gm_f}{a_x} \frac{a_x}{4a_1} \left[\frac{1}{2}\ln\left(\frac{x + f/2}{x - f/2}\right)\left(\frac{\delta\theta}{\delta\theta_0}\right)^2 -\right.$$
$$\left. - \left(\frac{\delta\theta}{\delta\theta_0}\right)\right] + \frac{Gm_f}{a_x} \frac{a_x}{4a_1} \frac{1}{2}\ln\left(\frac{x + f/2}{x - f/2}\right), \quad \delta\theta_0 < \delta\theta, \tag{15}$$

for the self-potential inside and outside the ellipsoid respectively. Taking again $m_f/m_x = 10^{-3}$, with $a_x = 61952.60$ km for Galatea, and semi-major axes $a_1 = 5500$ km and $a_2 = 55$ km, the CER potenial, the self-potential, and the superposition of the two with a minimum around $\delta\theta = 5^\circ$ are shown in Fig. 2.
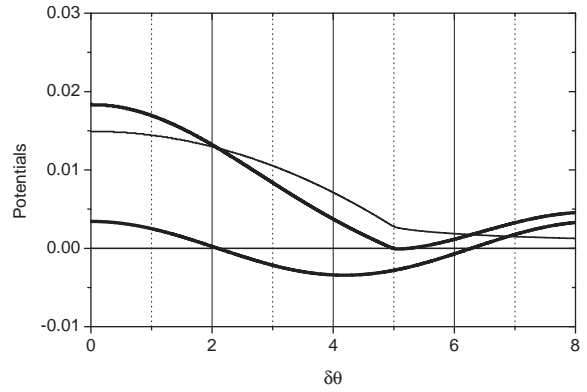

Fig. 2: The CER sinusoidal potential of Galatea in thick line, the self-potential of Fraternité with ellipsoidal model in thin line, and the sum of the two in thick line are plotted in units of Gm_x/a_x.

With Fraternité 1×10^{-3} of the mass of Galatea, the self-potential actually exceeds the CER potential in magnitude, as shown in Fig. 2. Each test mass would be librating around the potential maximum, dominated by the self-gravity of the collective mass distribution. Should Fraternité be elongated further while maintaining the total mass, it would increase the semi-major axis a_1 of the ellipsoid. This would reduce the amplitude of the self-potential of (14) through the $(a_x/4a_1)$ factor in the constant term, and weaken the self-potential. The elongation would feed the minor arcs. With this self-gravity model, not just the minor arcs are dynamically changing [1], the main arc Fraternité could be under a dynamical process as well.

4 Conclusions

In order to explain the 10° arc span of Fraternité, we draw attention to the fact that Fraternité, as an arc, has a significant mass. This mass is a distributed mass, instead of a point-like mass, such that its self-gravity should be taken into considerations to account for its angular span. We have used two models to evaluate the self-potential in the longitudinal direction. First is the tutorial spherical model, as a proof of principle study, with a uniform mass distribution over a sphere of radius r_0. Second is the elongated ellipsoidal model for a more realistic evaluation. Using the accepted range of Fraternité parameters, the ellipsoid model shows that the self-potential of the arc could be the cause of its angular span. For a longer arc, the ellipsoid gets longer and the ratio a_1/a_2 becomes larger. Eventually, for a complete ring, the ellipsoid is infinitely long and the self-potential in the longitudinal direction becomes constant. The effects of self-gravity are felt only in the transverse direction for a planetary ring.

References

1. de Pater I., et al. The dynamic neptunian ring arcs: evidence for a gradual disappearance of Liberte and resonant jump of Courage. *Icarus*, 2005, v. 174, 263–272.

2. Dumas C., et al. Stability of Neptune's ring arcs in question. *Nature*, 1999, v. 400, 733–735.

3. Foryta D. W. and Sicardy B. The dynamics of the Neptunian Adams ring's arcs. *Icarus*, 1996, v. 123, 129–167.

4. Goldreich P., Tremaine S., and Borderies N. Towards a theory for Neptune's arc rings. *Astronomical Journal*, 1986, v. 92, 490–494.

5. Horanyi M. and Porco C. C. Where exactly are the arcs of Neptune? *Icarus*, 1993, v. 106, 525–535.

6. Hubbard W. B., et al. Occultation detection of a neptunian ring like arc. *Nature*, 1986, v. 319, 636–640.

7. Kellogg O. D. Foundations of Potential Theory. Dover Publications, New York, 1953.

8. Landau L. D. and Lifshitz E. M. The Classical Theory of Fields. Pergamon Press, Oxford, 1975.

9. Namouni F. and Porco C. C. The confinement of Neptune's ring arcs by the moon Galatea. *Nature*, 2002, v. 417, 45–47.

10. Porco C. C. An explanation for Neptune's ring arcs. *Science*, 1991, v. 253, 995–1001.

11. Sicardy B., et al. Images of Neptune's ring arcs obtained by a ground based telescope. *Nature*, 1999, v. 400, 731–732.

12. Smith B. A., et al. Voyager 2 at Neptune: imaging science results. *Science*, 1989, v. 246, 1422–1449.

13. Tsui K. H. The configuration of Fraternite-Egalite2-Egalite1 in the Neptune ring arcs system. *Planetary Space Science*, 2007, v. 55, 237–242.

14. Tsui K. H. The dynamic nature of the Adams ring arcs - Fraternite, Egalite (2,1), Liberte, Courage. *Planetary Space Science*, 2007, v. 55, 2042–2044.

Probabilistic Factors as a Possible Reason of the Stability of Planetary and Electronic Orbits

Anatoly V. Belyakov

E-mail: belyakov.lih@gmail.com

An explanation is proposed that probabilistic factors cause the existence of the stable planetary orbits and electronic ones. It is confirmed when constructing frequency distributions of relevant virials.

Why there are stable planetary orbits and electronic ones, and how are they formed at all? This is all the more incomprehensible because the centrifugal forces and gravitational forces (or electrostatic ones for the atom) have a different dependence on the distance that leads only to *an unstable equilibrium.* Sure, there are some hidden factors, they may be probabilistic ones.

Thus, K. I. Dombrowski has revealed a possible connection of the sizes of planetary orbits to density of rational numbers on the number axis [1]. On the other hand, S. E. Shnoll has experimentally observed dependence of the fine structure of the normal distributions of various physical processes upon the algorithms that determine these processes [2]. It can be assumed that discrete nature of the normal distributions (and, apparently, any others) has a fundamental character.

An array of numbers that are the result of some computation algorithm can be analyzed by means of the frequency distribution*. As an example, one considers the distribution of orbits in the Bohr's atom planetary model and in the solar system.

It is known the orbital radii of the electron in the Bohr's atom to be proportional to the squares of integers. Though the existence of the orbits, i.e. the certain electronic levels, is due to quantum laws, however, this fact can also be explained by probabilistic factors.

According to the Bohr's model and proceeding from the balance of the Coulomb's and centrifugal forces, the orbital radii of the electron are in the simplest case proportional to expression $(z/v)^2$, where z can be regarded as a geometric mean value between the number of the elementary charges of a nucleus and electrons interacting with each other, and v is the orbital velocity of the electron in some dimensionless units.

Let z and v take arbitrary values, for example, from 1 to 100. Then the frequency distribution of the array of values of the function $(z/v)^2$ has the form shown in Fig. 1.

One can see that the peaks of the first order along the Y-axis (i.e. the most probable value) have next in values of the

---

*Frequency distributions provide a possibility for bonding the probability of the appearance of numerical values of a function in the area where it exists. That is, the frequency distributions show the reproducibility of numerical values of the function due to allowed varying its arguments. There is a ready-to-use function "frequency" in Excel©; any other software can be applied as well.
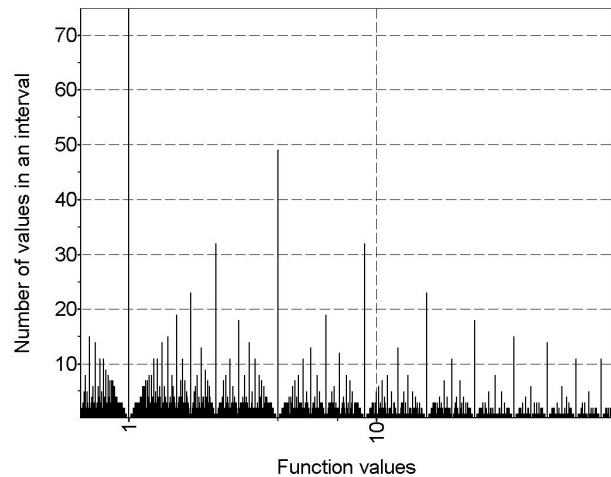
Fig. 1: Frequency distribution obtained with number of the numerical values in the scale 9,800 (of those, nonzero intervals are 3,300).

function $(z/v)^2$ along the X-axis: 1, 4, 9, 16, etc., that is, orbital radii in the Bohr's atom are proportional to the squares of integers, i.e. to the squares of electronic orbit numbers. Such distributions (or quadratic parts thereof) were also found in other, more complicated cases.

Let one consider the distribution of the planetary orbits in the solar system. Their stability can to some extent be explained by the phenomenon of orbital resonance, but this explanation is certainly not enough. As for the well-known Titius-Bode formula, then it should not be found in any of the known laws.

The equation relating the orbital radius of a planet R_0, its orbital velocity v_0 and the mass M of a central body is:

$$R_0 = \frac{\gamma M}{v_0^2}, \tag{1}$$

where γ is the gravitational constant.

In this case it would seem the frequency distribution for the orbit positions cannot be built because the function has only one variable argument v_0, while others are permanent. However, one can assume that during formation of the solar system the mass of the central body has not been equivalent to a point with a mass equal to the mass of the Sun, and other disturbing factors could have been.
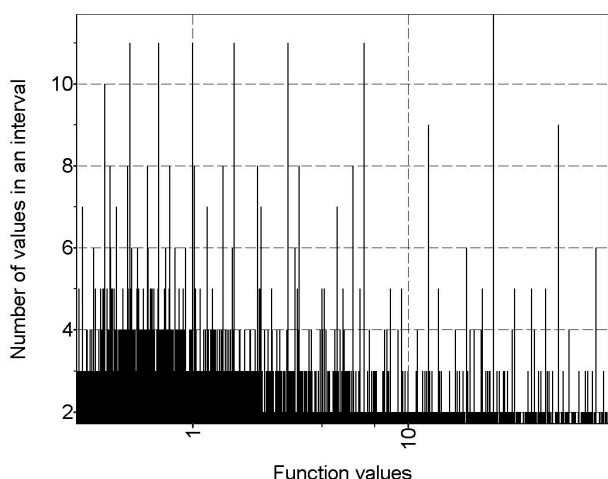
Fig. 2: Frequency distribution obtained with number of the numerical values in the scale 110,000 (of those, nonzero intervals are 48,800), $j = 0.5 \ldots 1.8$, $v = 0.02 \ldots 2$.

Therefore one can introduce a varied factor j in the formula and write (1) as follows:

$$R = \frac{j}{v^2}, \qquad (2)$$

where R is the radius of the planetary orbit in astronomical units (a.u.), v is the orbital velocity in the units of the orbital velocity of the Earth.

Fig. 2 shows an example of the frequency distribution of the array of values of the function (2) at $j = 0.5 \ldots 1.8$ with a step 0.025 and at $v = 0.05 \ldots 2$ with a step 0.01. Although the form of the distribution depends on the range of variation j and v, the number of intervals they are divided, split range mode (step-by-step or random), and the number of processed values, but in all cases the amplitude peaks or the frequency concentrations are revealed on graphs.

In Fig. 2 from left to right the peaks of the first order (the highest) are located at the radii (in a.u.): 0.39, 0.50 (a possible orbit), 0.70, 1.0, 1.55, 2.75, 6.2, 12.3, 18.7 (a second-order peak), 25, 31 (a second-order peak), 50, and 74. Moreover, most of the values are in good agreement with the actual orbital radii of the planets. In comparison, their actual values are: 0.39, 0.72, 1, 1.52, 2.5-3.0, 5.2, 9.54, 19.2, 30.6, 30–50, 38–98, including the asteroids orbit (2.5–3.0) and the tenth planet orbit (38–98).

Of course, such simple simulation can not give a complete numerical coincidence. The more important thing is a possibility for the frequency distributions to determine the most probable values of the functions describing various processes or objects; therefore, the most stable (preferred) states of these processes or objects can also be determined [3, 4].

References

1. Dombrowski K. I. Rational numbers distribution and resonance. *Progress in Physics*, 2005, v. 1, 65–67.

2. Shnoll S. E. Cosmic physical factors in random processes. Svenska fysikarkivet, Stockholm, 2009.

3. Belyakov A. V. Is the field of numbers a real physical field? On the frequent distribution and masses of the elementary particles. *Progress in Physics*, 2010, v. 3, 53–60.

4. Belyakov A. V. Finding the fine structure of the solutions of complicate logical probabilistic problems. *Progress in Physics*, 2010, v. 4, 36–39.

Double Surface and Atom Orbit

Janez Špringer

Cankarjeva cesta 2, 9250 Gornja Radgona, Slovenia, EU. E-mail: info@lekarna-springer.si

Previously (*Progr. Phys.*, 2013, v. 2, 105–106), one introduced the double surface model to explain the heterogeneous curvature of the present world. In this paper one investigates the strength of the mentioned concept in the light of forming the stable electron orbits around the atom nucleus. The conclusion is that the nature of the elliptic side of the proposed double surface offers the possibility of providing the uniform motion of the electron on the atom orbit as well as prevents the electron falling into the nucleus.

1 Theoretical background

The double surface [1] has the elliptic and hyperbolic side where the path with its translation and rotation component [2] is provided. According to this concept we have to deal with two different paths whose average is a mirror of the inverse fine structure constant. The fact that the elliptic path s can equal its translation component n [1] seems to be crucial for forming the stable electron orbits around the atom nucleus.

1.1 The elliptic side

The path on the elliptic side of the double surface can be described with the sphere law of cosines:

$$\cos\frac{s}{R} = \cos\frac{n}{R}\cos\frac{\pi}{R}. \qquad (1)$$

On the left, s denotes the elliptic path. On the right, n and π denote the translation and rotation component of that path, respectively [2].

At $s = n$ the elliptic radius R has the potency to occupy the infinite values, since

$$\cos\frac{\pi}{R} = 1, \quad \text{when} \quad \frac{\pi}{R} = 2m\pi. \qquad (2)$$

The elliptic radius expressed in Compton wavelengths of the electron is then related to the arbitrary natural number m by

$$R_{elliptic} = \frac{1}{2m}, \quad \text{where} \quad m \in \mathbb{N}_0. \qquad (3)$$

For the electron only the first 431 radii are physically plausible unless one cannot imagine that the sphere could be smaller than the physical body itself. In the units of Compton wavelengths of the electron the selected elliptic radii are the next:

$$
\begin{aligned}
R_{elliptic} \quad &= R_0, R_1, R_2 \cdots, R_{430}\\
&= \infty, \frac{1}{2}, \frac{1}{4}, \cdots \frac{1}{860} > r_{electron}.
\end{aligned}
\qquad (4)
$$

The greatest elliptic radius is infinite:

$$R_0 = \infty. \qquad (5)$$

The greatest finite elliptic radius is a half of the Compton wavelength of the electron:

$$R_1 = \frac{1}{2}. \qquad (6)$$

The smallest elliptic radius is a little bit greater than the classical electron radius itself:

$$R_{430} = \frac{1}{860} > r_{electron} = \frac{1}{2\pi\alpha^{-1}} \approx \frac{1}{861,02}. \qquad (7)$$

1.2 The hyperbolic side

The path on the hyperbolic side of the double surface can be described with the hyperbolic law of cosines:

$$\cosh\frac{s}{R} = \cosh\frac{n}{R}\cosh\frac{\pi}{R}. \qquad (8)$$

On the left, s denotes the hyperbolic path. On the right, n and π denote the translation and rotation component of that path, respectively [2].

According to the double surface model [1] where the characteristic values for the path and its translation component on Bohr orbit are $s = 137.072031\cdots$ and $n = 137$, the hyperbolic radius R is calculated by the equation (8) as the only one and finite:

$$R_{hyperbolic} \approx 71,520117 \text{ Compton wavelengths of the electron}. \qquad (9)$$

2 Physical consequences on the atom level

In the double surface model Bohr radius expressed in the units of Compton wavelengths of the electron is deduced from the average path on the elliptic and hyperbolic side of the orbit:

$$R_{Bohr} = \frac{\alpha_{elliptic}^{-1} + \alpha_{hyperbolic}^{-1}}{4\pi} = \frac{\alpha^{-1}}{2\pi}. \qquad (10)$$

The difference between $\alpha_{observed}^{-1}$ and $\alpha_{measured}^{-1}$ on the fifth decimal which was important for predicting the exact inverse fine structure previously [1], is not significant enough to be taken into account in the calculations made in this paper. From the relation (3) and (4) is seen that the radius of the elliptic side of the double surface is greater than Bohr radius only once, i.e. when $R_{elliptic} = \infty$. The infinite elliptic radius allows the

electron to move uniformly on Bohr orbit. On the other hand the 430 finite elliptic radii do not permit the electron to fall into the nucleus, because they are always much smaller than Bohr radius:

$$R_{1,2,\cdots 430} \ll R_{Bohr},$$

$$\text{since } \frac{1}{2}, \frac{1}{4}, \cdots, \frac{1}{860} < R_{Bohr} \approx 22,81. \tag{11}$$

The conclusion would be the same, if the number of the finite elliptic radii is infinite.

Thus according to the present concept the electron is closed on the elliptic sphere of the multi-sizable radius. Its destiny is to be in some way glued on Bohr orbit in the Hydrogen atom. In other atoms the similar phenomenon is expected, because their atomic radii are greater than the Bohr one and therefore still greater than the finite elliptic ones:

$$R_{atom} \geqslant R_{Bohr} \gg R_{1,2,\cdots 430}. \tag{12}$$

3 Conclusion

The infinite elliptic radius of the double surface enables the uniform motion of the electron on the atom orbit. The finite radii prevent the electron falling into the nucleus. From this point of view the concept of the double surface with its elliptic side as a sphere of the multi-sizable radius satisfies the demand for forming the stable electron orbits around the atom nucleus.

Respecting Plato the correct theory is only one amongst many ones revealed in the realm of the reasonable ideas.
(The Author)

Acknowledgment

Gratitude to the editors for any kind of support in lifting the veil of the physical truth.

Dedication

This fragment is dedicated to my sister Darinka.

References

1. Špringer J. Double Surface and Fine Structure. *Progress in Physics*, 2013, v. 2, 105–106.

2. Špringer J. Fine Structure Constant as a Mirror of Sphere Geometry. *Progress in Physics*, 2013, v. 1, 12–14.

Multi-planet Exosystems All Obey Orbital Angular Momentum Quantization per Unit Mass predicted by Quantum Celestial Mechanics (QCM)

Franklin Potter

Sciencegems.com, 8642 Marvale Drive, Huntington Beach, CA 92646 USA. E-mail: frank11hb@yahoo.com

Quantum celestial mechanics (QCM) predicts that all orbiting bodies in gravitationally bound systems exhibit the quantization of orbital angular momentum *per unit mass*. I show that the 15 known multi-planet systems with four or more planets obey this QCM prediction. This angular momentum constraint could be the explanation for their orbital stability for billions of years, suggesting that viable models of the formation and evolution of gravitational systems must include QCM.

1 Introduction

According to recent calculations, our Solar System is unstable [1] and should have existed for only a few 100 million years! However, the Solar System has existed for more than 4.5 billion years. Obviously, some fundamental physics concept is missing. H. G. Preston and I have proposed [2] that the missing constraint is the quantization of orbital angular momentum *per unit mass* for all orbiting bodies in gravitationally bound systems. Herein I establish that all 15 known multi-planetary systems with four or more planets exhibit this constraint.

In several previous papers [2–4] we derived Quantum Celestial Mechanics (QCM) from the general theory of relativity and successfully applied QCM to numerous gravitationally bound systems, including the planets of the Solar System, the moons of the Jovian Planets, the five moons of Pluto, the Galaxy rotation velocity, gravitational lensing, clusters of galaxies, the cosmological redshift of the Universe, the circumbinary planet Kepler-16, and the S-stars at our Galaxy center.

QCM predicts that a body of mass μ orbiting a central massive object in a gravitationally bound system obeys the angular momentum L per unit mass quantization condition

$$\frac{L}{\mu} = mcH \tag{1}$$

with m an integer and c the speed of light. The Preston gravitational distance H requires only two physical parameters to determine all the possible QCM states in the system, the system's total angular momentum L_T and its total mass M_T:

$$H = \frac{L_T}{M_T c}. \tag{2}$$

In order to use this restriction, one assumes that the orbiting body is at or near its QCM equilibrium orbital radius r and that the orbital eccentricity ϵ is low so that our nearly circular orbit approximation leading to these particular equations holds true. Therefore, the L of the orbiting body will agree with its Newtonian value $L = \mu \sqrt{GM_T r(1 - \epsilon^2)}$.
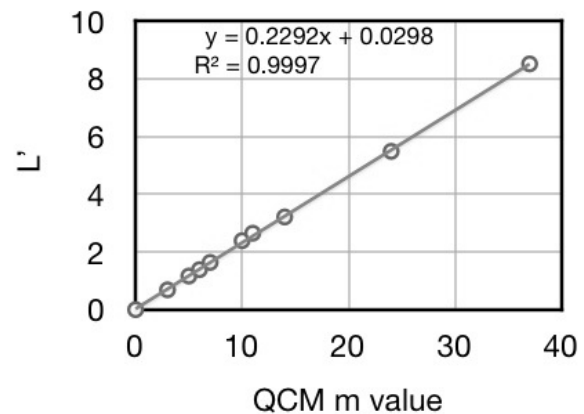
Fig. 1: The HD10180 System fit to QCM.

Every Newtonian orbit is an equilibrium orbit, but not so for QCM orbits. For a body not at the QCM equilibrium orbital radius for the QCM state or for particles near the QCM equilibrium orbital radius that could collect into a massive body, there exists a small QCM acceleration. Usually a time frame of tens or hundreds of millions of years are needed to achieve dynamic QCM equilibrium with its extremely small remnant radial oscillations. Therefore, QCM is expected to play an important role in the formation and eventual stability of multi-planetary systems over billions of years.

For circular orbits or nearly circular orbits there is a principal number $n = m + 1$ associated with the energy *per unit mass* quantization for a QCM state

$$\frac{E_n}{\mu} = -\frac{r_g^2 c^2}{8n^2 H^2} = -\frac{G^2 M_T^2}{2n^2 L_T^2} \tag{3}$$

with r_g the Schwarzschild radius of the system. The derived Schrodinger-like gravitational wave equation dictates all the physics via solutions that are hydrogen-like wave functions.

The QCM fit to the orbital parameters of all known planets of a multi-planet system determines the total angular momentum of that system, a value which can be used to predict whether more planets can be expected and/or whether

the equivalent of an Oort cloud is required. Recall that for our own Solar System the Oort Cloud dominates the total angular momentum, being a factor of at least 50 greater than the total planetary orbital momentum. Without the Oort Cloud angular momentum, QCM predicts that all the planetary orbital radii would be within the radius of the Sun! By including the angular momentum of the Oort Cloud, QCM suggests that the planets formed near to their present orbital radii.

Many exoplanetary systems have their Jupiter size planets at extremely small orbital radii, within about 1.5 AU from the star, with many more smaller planets even closer. There is the question of why such massive planets are so close to their star. One possible answer is that the system total angular momentum value is low compared to the QCM value needed to "push" the system further out. That is, QCM predicts that a larger total angular momentum for the system means larger QCM orbital spacings.

2   Multi-planetary results

Multi-planet systems are in the database called the Exoplanets Data Explorer [5], but complete data sets for HD 10180 [6], HD 40307 [7], Tau Ceti [8], GJ 676A [9], and Upsilon Andromedae [10] are only in research articles. There are hundreds of two and three planet systems which I choose to exclude herein even though they also exhibit the QCM constraint. As more planets orbiting these systems are identified, their fits to the QCM prediction can be determined.

In Table 1 are listed the host star, the star mass in solar units, the number of planets N, their QCM m values, and the slope b for $L/\mu = bx + a$ in the plot of $L' = L/\mu$ versus m for all the planets of the particular system. The plot for HD10180 is shown as an example, with the uncertainty bars for L' within the circle data points. By using both the semimajor axis and the orbital period as constraints, one obtains a linear regression fit with $R^2 > 0.999$. The system's predicted total angular momentum $L_T = b M_T$ multiplied by 10^{15} kg m^2/s.

From the QCM predicted L_T values, one learns that these 15 multi-planet systems have more angular momentum which is to be contributed by additional orbiting bodies such as planets and/or the equivalent of the Oort Cloud.

3   Conclusions

All the 15 analyzed multi-planet systems obey the QCM orbital angular momentum per unit mass quantization condition. The integers for the m values are not sequential, implying that the history of each system plays an important role in which orbital states are occupied. For example, mass depletion in a region caused by the faster formation of a large planet might not leave enough mass for another planet to form at a nearby QCM equilibrium orbital radius.

The resulting fits are evidence that the quantization of orbital angular momentum per unit mass is an important phys-

Table 1: QCM Multi-Planet m Values

System	Mass	N	m Values	b
HD 10180	1.055	9	3,5,6,7,10,11,14,24,37	0.23
Sun	1	8	3,4,5,6,12,17,25,31	0.77
HD 40307	0.752	6	8,11,14,17,20,29	0.10
Kepler-11	0.954	6	10,11,13,15,17,23	0.13
Kepler-20	0.912	5	14,17,21,25,40	0.06
Kepler-33	1.291	5	8,11,13,15,16	0.16
Kepler-62	0.690	5	6,8,9,17,22	0.14
Tau Ceti	0.783	5	8,11,16,19,30	0.15
55 Cancri	1.026	5	4,10,16,27,76	0.13
GJ 581	0.311	4	7,9,12,21	0.05
GJ 676A	0.71	4	3,6,20,34	0.25
GJ 876	0.334	4	5,13,17,22	0.07
HR 8799	1.472	4	12,16,20,27	1.65
Mu Arae	1.077	4	4,12,15,29	0.38
Ups Andr	1.01	4	2,10,18,27	0.42

ical factor in planetary systems and should not be ignored in studies of their formation, stability, and evolution.

References

1. Hayes W. B. Is the Outer Solar System Chaotic? arXiv: astro-ph/0702179v1.

2. Potter F. Pluto Moons exhibit Orbital Angular Momentum Quantization per Mass. *Progress in Physics*, 2012, v. 4, 3–4.

3. Preston H. G., Potter F. Exploring Large-scale Gravitational Quantization without h-bar in Planetary Systems, Galaxies, and the Universe. arXiv: gr-qc/030311v1.

4. Potter F., Preston H. G. Cosmological Redshift Interpreted as Gravitational Redshift. *Progress in Physics*, 2007, v. 2, 31–33.

5. Wright J. T. et al. The Exoplanet Orbit Database. http://adsabs.harvard.edu/abs/2011PASP..123..412W

6. Tuomi M. Evidence for 9 planets in the HD 10180 system. arXiv: 1204.1254.

7. Tuomi M., et al. Habitable-zone super-Earth candidate in a six-planet system around the K2.5V star HD 40307. arXiv: 1211.1617.

8. Tuomi M., et al. Signals embedded in the radial velocity noise. Periodic variations in the τ Ceti velocities. arXiv: 1212.4277.

9. Anglada-Escudé G., Tuomi M. A planetary system with gas giants and super-Earths around the nearby M dwarf GJ 676A. Optimizing data analysis techniques for the detection of multi-planetary systems. arXiv: 1206.7118v2.

10. Curiel S., et al. A fourth planet orbiting υ Andromedae. *Astronomy and Astrophysics*, 2011, v. 525, A78.

The Gravitational Field: A New Approach

Patrick Marquet

patrick.marquet6@wanadoo.fr

In this paper, we consider the Einstein field equations with the cosmological term. If we assume that this term is slightly varying, it induces a vacuum background field filling the space. In this case, inspection shows that the gravitational field is no longer represented by a pseudo-tensor, but appears on the right hand side of the field equations as a true tensor together with the bare mass tensor thus restoring the same conservation condition as obeyed by the Einstein tensor.

Introduction

Soon after his theory of General Relativity was published in 1916, Einstein rapidly turned to the unifying of the gravitational field with electromagnetism (which at that time was considered as the second fundamental field).

The quest for such an universal scheme ended in 1955 with the Einstein-Schrödinger theory (see for example [1]) definitely abandoned since as the quantum field theories gained the increasing successes and have been long substantiated by numerous experimental confirmations.

Basically, the unified principle adopted by the successive authors (Kaluza-Klein, Weyl, Eddington, et al.) relied either on extra dimensions, or on an extension of the Riemannian theory with additional space-time curvatures introduced to yield the electromagnetic field characteristics, and where the stress-energy tensor regarded as provisional, will be eventually absent [2, 3, 4].

Total geometrization of matter and electromagnetism was anyhow the original focus.

To understand this long period of research, one should remember that Einstein always claimed that the energy-momentum tensor (s) which can appear in the right hand side of his field equations, was "clumsy"; in short, he considered this form as an unsatisfactory solution which had to fit differently in his equations.

Einstein's argument is actually strongly supported by the following fact: while his tensor exhibits a *conceptually* conserved property, any corresponding stress energy-tensor *does not*, which leaves the theory with a major inconsistency.

When pure matter is the source, the problem has been "cured" by introducing the so-called "pseudo-tensor" that "conveniently" describes the gravitational field of this mass so that the four-momentum of both matter and its gravity field is conserved.

Unfortunately by essence this pseudo-tensor cannot appear in the field equations, and so the obvious physical defect emphasized by Einstein, still remains to-day as a stumbling block.

In this paper, we tackle this problems by proceeding as follows: in contrast to the previous theories, the energy-momentum tensor of the source is here strengthened, although we restrict our study to neutral massive flow.

In this respect, it is shown that the gravitational field of a massive body is no longer described by a *pseudo-tensor*, but appears as a *true tensor* in the field equations as it should be, in order to balance the conceptually conserved property of the Einstein tensor.

To achieve this goal we do:

- We first formulate the field equations with a massive source in density notation;

- We write the conservation law for the Einstein tensor density derived from the Bianchi identities, which cannot apply to the energy-momentum tensor density as a source;

- We then include a variable term that supersedes the so-called cosmological term Λg_{ab} in the field equations, still complying with the conservation property of the Einstein tensor density in GR;

- Under this latter assumption, we will then formally show that the gravity field of a massive source is no longer described by a vanishing *pseudo tensor* but it reduces to a true tensor describing a *persistent* vacuum background field resulting from the existence of the variable term.

1 The field equations in General Relativity

1.1 The tensor representation

In the General Theory of Relativity (GR), it is well known that by varying the action

$$S = L_E \, d^4 x \,,$$

where the *Lagrangian density* is given by

$$L_E = \sqrt{-g}\, G^{ab} \left(\begin{Bmatrix} e \\ ab \end{Bmatrix} \begin{Bmatrix} d \\ de \end{Bmatrix} + \begin{Bmatrix} d \\ ae \end{Bmatrix} \begin{Bmatrix} e \\ bd \end{Bmatrix} \right), \qquad (1.1)$$

$$g = \det \| g_{ab} \| \qquad (1.2)$$

one infers the *symmetric Einstein tensor*

$$G_{ab} = R_{ab} - \frac{1}{2}\, g_{ab} R, \qquad (1.3)$$

where

$$R_{bc} = \partial_a \begin{Bmatrix} a \\ bc \end{Bmatrix} - \partial_c \begin{Bmatrix} a \\ ba \end{Bmatrix} + \begin{Bmatrix} d \\ bc \end{Bmatrix} \begin{Bmatrix} a \\ da \end{Bmatrix} - \begin{Bmatrix} d \\ ba \end{Bmatrix} \begin{Bmatrix} a \\ dc \end{Bmatrix} \qquad (1.4)$$

is the *Ricci tensor* with its contraction R, the *curvature scalar*, while $\begin{Bmatrix} e \\ ab \end{Bmatrix}$ denote the Christoffel Symbols of the second kind.

The 10 *source free field equations* are

$$G_{ab} = 0. \qquad (1.5)$$

The second rank Einstein tensor G_{ab} is symmetric and is only function of the metric tensor components g_{ab} and their first and second order derivatives.

The relation

$$\nabla_a G_b^a = 0 \qquad (1.6)$$

is the conservation identities provided that the tensor G_{ab} has the form [5]

$$G_{ab} = k \left[R_{ab} - \frac{1}{2} g_{ab}(R - 2\Lambda) \right], \qquad (1.7)$$

k is a constant, which is here taken 1, is usually named cosmological constant Λ.

When a source is present, the field equations become

$$G_{ab} = R_{ab} - \frac{1}{2} g_{ab}R - g_{ab}\Lambda = \varkappa T_{ab}, \qquad (1.8)$$

where T_{ab} is the energy-momentum tensor of the source.

1.2   The tensor density representation

We first set

$$\boldsymbol{g}^{ab} = \sqrt{-g} \, g^{ab} \qquad (1.9)$$

and the Einstein tensor density is

$$\boldsymbol{G}^{ab} = \sqrt{-g} \, G^{ab}, \quad \boldsymbol{G}_a^c = \sqrt{-g} \, G_a^c, \qquad (1.10)$$

$$\boldsymbol{R}^{ab} = \sqrt{-g} \, R^{ab}. \qquad (1.11)$$

In density notations, the field equations with the source (1.8) will read

$$\boldsymbol{G}^{ab} = \boldsymbol{R}^{ab} - \frac{1}{2} \boldsymbol{g}^{ab} \boldsymbol{R} - g^{ab}\zeta = \varkappa \boldsymbol{T}^{ab}. \qquad (1.12)$$

Here in place of the constant cosmological term Λ which should be here represented by $\Lambda \sqrt{-g}$, we have introduced a *scalar density* denoted as

$$\zeta = \Xi \sqrt{-g}. \qquad (1.13)$$

Unlike Λ, the scalar Ξ is slightly variable and represents the *Lagrangian* characterizing a specific *vacuum background field* as will be shown below.

2   The conservation identities

2.1   Tensor version for the Einstein tensor

From the Bianchi identities applied to the Riemann tensor

$$R_{\cdot\cdot bc\,;\,i}^{ci\cdot\cdot} + R_{\cdot\cdot ib\,;\,c}^{ci\cdot\cdot} + R_{\cdot\cdot ci\,;\,b}^{ci\cdot\cdot} = 0 \qquad (2.1)$$

we infer the conservation conditions which apply to the Einstein tensor without Ξ, and hereinafter denoted by

$$^{\circ}G_b^a = R_b^a - \frac{1}{2} \, g_b^a R. \qquad (2.2)$$

The Einstein tensor thus satisfies intrinsically the conservation law:

$$\nabla_a \, ^{\circ}G_b^a = 0. \qquad (2.3)$$

2.2   Tensor density version for the Einstein tensor

In the same way, we start with the Einstein tensor density without the cosmological term

$$^{\circ}\boldsymbol{G}^{ab} = \boldsymbol{R}^{ab} - \frac{1}{2} \, \boldsymbol{g}^{ab} \boldsymbol{R}. \qquad (2.4)$$

With (2.3), let us write down

$$\nabla_a \, ^{\circ}\boldsymbol{G}_b^a = \partial_a \, ^{\circ}\boldsymbol{G}_b^a + \begin{Bmatrix} a \\ ca \end{Bmatrix} ^{\circ}\boldsymbol{G}_b^c - \begin{Bmatrix} c \\ ba \end{Bmatrix} ^{\circ}\boldsymbol{G}^a = \frac{\partial_a \, ^{\circ}\boldsymbol{G}_b^a}{\sqrt{-g}} - \begin{Bmatrix} c \\ ba \end{Bmatrix} ^{\circ}\boldsymbol{G}_c^a = 0,$$

which is easily found to be

$$\frac{\partial_a \, ^{\circ}\boldsymbol{G}_b^a}{\sqrt{-g}} - \frac{1}{2} \, ^{\circ}\boldsymbol{G}^{ea} \, \partial_b \, g_{ea} = 0 \qquad (2.5)$$

using $dg_{ai} = -g_{ab}g_{ic}dg^{bc}$ and $dg^{ai} = -g^{ab}g^{ic}dg_{bc}$ the formula (2.5) can be also written as

$$\partial_a \, ^{\circ}\boldsymbol{G}_b^a - \frac{1}{2} \, \boldsymbol{G}^{ea} \, \partial_b \, g_{ea} = 0. \qquad (2.6)$$

The latter equation is the conservation condition for $^{\circ}\boldsymbol{G}^{ab}$ which is equivalent to (2.3).

2.3   Conservation of the energy-momentum tensor

2.3.1   Problem statement

Let us consider the energy-momentum tensor for neutral matter density ρ:

$$T_{ab} = \rho \, u_a \, u_b \qquad (2.7)$$

as the right hand side of the field equations

$$^{\circ}G_{ab} = R_{ab} - \frac{1}{2} \, g_{ab}R = \varkappa T_{ab}. \qquad (2.8)$$

The conservation condition for this tensor are written

$$\nabla_a T_b^a = \frac{1}{\sqrt{-g}} \, \partial_a \boldsymbol{T}_b^a - \frac{1}{2} \, T^{ac} \, \partial_b \, g_{ac} = 0 \qquad (2.9)$$

with the tensor density

$$\boldsymbol{T}_b^a = \sqrt{-g}\, T_b^a. \qquad (2.10)$$

However, across a given hypersurface dS_b, the integral

$$P^a = \int T^{ab} \sqrt{-g}\, dS_b \qquad (2.11)$$

is conserved only when

$$\partial_a \boldsymbol{T}_b^a = 0. \qquad (2.12)$$

From (2.6) inspection still shows that

$$\partial_a \boldsymbol{T}_b^a = \frac{1}{2}\, \boldsymbol{T}^{cd}\, \partial_b\, g_{cd} \qquad (2.13)$$

but here, unlike the Einstein tensor $°G_{ab}$ which is *conceptually conserved* $(\nabla_a °G_b^a = 0)$, the conditions

$$\nabla_a T_b^a = 0$$

or

$$\partial_a \boldsymbol{T}_b^a = 0$$

are thus never satisfied in a general coordinates system.

Therefore, the Einstein tensor $°G_{ab}$ which *intrinsically* obeys a conservation condition, is related with a massive tensor $T_{ab}(\rho)$ which obviously *fails to satisfy the same requirement*:

$$°G_{ab} = \varkappa T_{ab}. \qquad (2.14)$$

As a matter of fact, a correct formulation would consist of explicitly writing down the mass density with its gravity field, i.e. with a pseudo-tensor $(t_{ab})_{field}$.

As is known, the name *pseudo-tensor* is chosen since this quantity can be transformed away by a suitable choice of coordinates.

Hence, we should write

$$G_{ab} = \varkappa \left[(T_{ab})_{matter} + (t_{ab})_{field} \right]. \qquad (2.15)$$

This is classically interpreted by requiring that the **total** 4-momentum vector P^a of *matter* with its *gravitational field*

$$P^a = \left[(T^{ab})_{matter} + t^{ab})_{field} \right] \sqrt{-g}\, dS_b \qquad (2.16)$$

must be together conserved*

---

*Some authors [8] state that integrating $\nabla_k T_i^k = 0$ yields a conservation law for a vector $P^a = T^{ab} K_b$ when the metric admits a Killing vector $\boldsymbol{K}$: $P_{;a}^a = T_{;a}^{ab} K_b + T^{ab} K_{b;a}$ and since T^{ab} is symmetric, we have for the Lie derivative $K_{b;a} = \frac{1}{2} \boldsymbol{L}_K g_{ab} = 0$, then $P_{;a}^a = 0$.

2.3.2 The gravity pseudo-tensor

In order to follow this way, Landau and Lifshitz [6] started from the unsuitable tensor equation (2.9)

$$\nabla_k T_i^k = \frac{1}{\sqrt{-g}}\, \partial_k \boldsymbol{T}_i^k - \frac{1}{2}\, T^{kl}\, \partial_i\, g_{kl} = 0.$$

They thus consider a special choice of a set of the coordinates which cancels out all first derivatives of the g_{ik} at a given 4-space-time point.

In this system, the energy-momentum tensor expression is given by

$$T^{ik} = \frac{1}{2\varkappa}\, \partial_e(-g)^{-1} \left[\partial_d\, (-g) \left(g^{ik} g^{ed} - g^{ie} g^{kd} \right) \right]. \qquad (2.17)$$

As $\left\{ {i \atop ke} \right\}$ are postulated to be zero at the considered point, we may extract the factor $(-g)^{-1}$ from the derivative in the latter equation, so

$$(-g)\, T^{ik} = \partial_e \boldsymbol{H}^{ike} = \frac{1}{2\varkappa}\, \partial_e \left(\partial_d \boldsymbol{H}^{iked} \right).$$

The quantity

$$\boldsymbol{H}^{iked} = (-g) \left(g^{ik} g^{ed} - g^{ie} g^{kd} \right) \qquad (2.18)$$

can be regarded as a "double tensor density" and is often referred to, as the "superpotential of Landau-Lifshitz" [7]. Now, in any other arbitrary system, generally

$$\partial_e \boldsymbol{H}^{ike} - (-g)\, T^{ik} \neq 0,$$

and so, we will have to bring a small tensor correction t_{LL}^{ik} (Landau-Lifshitz pseudo-tensor) which is accepted as representing the gravitational field of matter:

$$\partial_e \boldsymbol{H}^{ike} = (-g) \left(T^{ik} + t_{LL}^{ik} \right).$$

This equation implies the condition

$$\partial_k \left[(-g) \left(T^{ik} + t_{LL}^{ik} \right) \right] = 0, \qquad (2.19)$$

which is the conservation law for the classical total four-momentum vector density of both matter and gravitational field written as

$$\boldsymbol{P}^i = \int \left[(-g) \left(T^{ik} + t_{LL}^{ik} \right) \right] dS_k, \qquad (2.20)$$

(compare with (2.11)).

After a tedious calculation, the final form of the symmetric tensor t_{LL}^{ik} as a function of the g_{ik}, is found to be

$$(-g)\, t_{LL}^{ik} = \frac{1}{2\varkappa} \left[\boldsymbol{g}_{,l}^{ik} \boldsymbol{g}_{,m}^{lm} - \boldsymbol{g}_{,l}^{il} \boldsymbol{g}_{,m}^{km} + \frac{1}{2}\, g^{ik} g_{lm} \boldsymbol{g}_{,p}^{ln} \boldsymbol{g}_{,n}^{pm} - \right.$$
$$- \left(g^{il} g_{mn} \boldsymbol{g}_{,p}^{kn} \boldsymbol{g}_{,l}^{mp} + g^{kl} g_{mn} \boldsymbol{g}_{,p}^{in} \boldsymbol{g}_{,l}^{mp} \right) + g_{lm} g^{np} \boldsymbol{g}_{,n}^{il} \boldsymbol{g}_{,p}^{km} +$$
$$\left. + \frac{1}{8} \left(2g^{il} g^{km} - g^{ik} g^{lm} \right) \left(2g_{np} g_{qr} - g_{pq} g_{nr} \right) \boldsymbol{g}_{,l}^{nr} \boldsymbol{g}_{,m}^{pq} \right]. \qquad (2.21)$$

Therefore, the Einstein field equations can be eventually written in the form:

$$H_{\cdots,kd}^{iked} = 2\varkappa\,(-g)\left(T^{ie} + t_{LL}^{ie}\right). \qquad (2.22)$$

Unfortunately, the quantity t_{LL}^{ie} which now appears on the right hand side of the field equations as it should be, is not a *true tensor*.

Hence, we are once more faced with a contradiction: the left hand side of the field equations for a massive source is a true tensor, while the right hand side is not, which reveals a major inconsistency within the theory.

2.4 Introduction of a background field tensor

Let us now try to remove this ambiguity.

We start by writing the global energy-momentum tensor density of the massive source splitting up bare matter and pure field:

$$T_b^a = (T_b^a)_{matter} + (t_b^a)_{field}. \qquad (2.23)$$

The field tensor density $(t_b^a)_{field}$ is in turn composed of two parts: *gravity field + vacuum background field*

$$(t_b^a)_{field} = (t_b^a)_{gravity} + (t_b^a)_{background\,field} \qquad (2.24)$$

with

$$(t_{ab})_{background\,field} = \frac{\varsigma}{2\varkappa}\,g_{ab} = \frac{\Xi\,\sqrt{-g}}{2\varkappa}\,g_{ab}. \qquad (2.25)$$

According to the standard theory, we next re-formulate the field equations with a *bare* massive source

$$G^{ab} = R^{ab} - \frac{1}{2}\,g^{ab}R - g^{ab}\varsigma = \varkappa(T^{ab})_{matter} \qquad (2.26)$$

under the form

$$G^{ab} = R^{ab} - \frac{1}{2}\,g^{ab}R = \varkappa(T^{ab})_{matter} + g^{ab}\varsigma. \qquad (2.27)$$

3 Expliciting the field equations in density notation

3.1 Taking account of the Lagrangian Ξ

Reverting to (2.13), we now write for the *bare* matter tensor density

$$\partial_a(T_b^a)_{matter} = \frac{1}{2}\,(T^{cd})_{matter}\,\partial_b\,g_{cd}. \qquad (3.1)$$

Inspection then shows that

$$R_{il}\,dg^{il} = \sqrt{-g}\left[-R^{ie} + \frac{1}{2}\,g^{ie}R\right]dg_{ie} =$$
$$= -\varkappa(T^{ie})_{matter}\,dg_{ie}. \qquad (3.2)$$

Taking now into account the Lagrangian formulation for R_{il}, which is

$$R_{il} = \frac{\delta L_E}{\delta g^{il}} = \partial_k\frac{\partial L_E}{\partial(\partial_k g^{il})} - \frac{\partial L_E}{\partial g^{il}}, \qquad (3.3)$$

we obtain

$$-\varkappa(T^{il})_{matter}\,dg_{il} = \partial_k\frac{\partial L_E}{\partial(\partial_k g^{il})} - \frac{\partial L_E}{\partial g^{il}}\,dg^{il} =$$
$$= \partial_k\frac{\partial L_E\,dg^{il}}{\partial(\partial_k g^{il})} - \partial L_E,$$

that is

$$-\varkappa(T^{il})_{matter}\,\partial_m g_{il} = \partial_k\left[\frac{\partial L_E\,\partial_m(\partial g^{il})}{\partial(\partial_k g^{il})} - \delta_m^k\,L_E\right] =$$
$$= 2\varkappa\,\partial_k(t_m^k)_{field}, \qquad (3.4)$$

where $(t_m^k)_{field}$ denotes the field tensor density extracted from

$$2\varkappa(t_m^k)_{field} = \frac{\partial L_E\,\partial_m(\partial g^{il})}{\partial(\partial_k g^{il})} - \delta_m^k\,L_E \qquad (3.5)$$

so, that we have the explicit canonical form

$$(t_m^k)_{field} = \frac{1}{2\varkappa}\left[\frac{\partial L_E\,\partial_m(\partial g^{il})}{\partial(\partial_k g^{il})} - \delta_m^k\,L_E\right] \qquad (3.6)$$

and where

$$\partial_k(T_i^k)_{matter} = \frac{1}{2}\,(T^{ek})_{matter}\,\partial_k g_{ei} = -\partial_k(t_i^k)_{field}.$$

that is, the required conservation relation

$$\partial_k\left[(T_i^k)_{matter} + (t_i^k)_{field}\right] = 0. \qquad (3.7)$$

Then, re-instating the term ζ according to (2.24) and (2.25), the gravitational field tensor density now reads:

$$(t_m^k)_{gravity} = \frac{1}{2\varkappa}\left[\frac{\partial L_E\,\partial_m(\partial g^{il})}{\partial(\partial_k g^{il})}\right] - \delta_m^k(L_E - \zeta). \qquad (3.8)$$

The presence of the scalar density ζ characterizing the background field is here of central importance, as it means that $(t_m^k)_{gravity}$ can never be zero in contrast to the classical theory, and as a result, it constitutes a *true tensor*. Such a gravity field never completely cancels out, but far from its matter source, it sharply decreases down to the level of the background field described by the tensor density $(t^{ab})_{background\,field}$.

In addition, we clearly see that ζ represents the *lagrangian density* characterizing the background field, thus lending support to our initial hypothesis regarding the lagrangian Ξ.

In this picture, the vacuum is permanently filled with this homogeneous background energy field ensuring a smooth continuity with the gravitational field of a neighbouring mass.

3.2 Classical formulation

When the term Ξ is kept constant like the cosmological term Λ, the tensor density (3.8) reduces to

$$(t_m^k)_{pseudogravity} = \frac{1}{2\varkappa}\left[\frac{\partial L_E\,\partial_m(\partial g^{il})}{\partial(\partial_k g^{il})} - \delta_m^k\,L_E\right], \qquad (3.9)$$

which is just the classical *gravity pseudo-tensor density* that may now vanish in a given space-time point.

In this case, expressed with the explicit form of the Lagrangian density $\boldsymbol{L}_E$ written in (1.1), the expression (3.9) becomes:

$$(t_m^k)_{pseudogravity} = \frac{1}{2\varkappa} \left[\left\{ {k \atop i\,l} \right\} \partial_m \boldsymbol{g}^{il} - \left\{ {i \atop i\,l} \right\} \partial_m \boldsymbol{g}^{lk} - \delta_m^k \boldsymbol{L}_E \right]. \quad (3.10)$$

This is the *mixed Einstein-Dirac pseudo-tensor density* [9] which is not symmetric on k and m, and is therefore not suitable for basing a definition of angular momentum on.

3.3 Field equations

The field equations with a massive source, which are

$$\boldsymbol{G}^{ab} = \boldsymbol{R}^{ab} - \frac{1}{2} g^{ab} \boldsymbol{R} - g^{ab}\zeta = \varkappa (\boldsymbol{T}^{ab})_{matter}, \quad (3.11)$$

may be now eventually re-written

$$^\circ\boldsymbol{G}^{ab} = \boldsymbol{R}^{ab} - \frac{1}{2} g^{ab} \boldsymbol{R} = \varkappa \left[(\boldsymbol{T}^{ab})_{matter} + (\boldsymbol{t}^{ab})_{gravity} \right] \quad (3.12)$$

with the explicit appearance of the gravity field as defined in (3.8) and which is now represented by a *true* tensor density.

Like we emphasized above, far from the mass, the "source free" field equations should always retain a non zero right hand side

$$^\circ\boldsymbol{G}^{ab} = \boldsymbol{R}^{ab} - \frac{1}{2} g^{ab} \boldsymbol{R} = \varkappa (\boldsymbol{t}^{ab})_{background\,field}, \quad (3.13)$$

which are the analogue of (1.7):

$$\boldsymbol{G}^{ab} = \boldsymbol{R}^{ab} - \frac{1}{2} g^{ab} \boldsymbol{R} - g^{ab}\zeta = 0. \quad (3.14)$$

In this case, the conservation law applied to the right hand side of the tensor field equations is straightforward:

$$\nabla_a (t_b^a)_{background\,field} = \nabla_a \left(\frac{\Xi}{2\varkappa} \delta_b^a \right) = 0, \quad (3.15)$$

from which readily follows

$$\partial_a (t_b^a)_{background\,field} = \partial_a \left(\frac{\zeta}{2\varkappa} \delta_b^a \right) = 0. \quad (3.16)$$

3.4 Physical description

We would like now to give a simple but instructive picture of the situation where a static mass is placed in the vacuum background energy field. Let us write the energy-momentum tensor for matter and its gravitational field as in (3.12):

$$T_{ab} = (\rho u_a u_b)_{matter} + (t_{ab})_{gravity}. \quad (3.17)$$

In virtue of the principle of equivalence, any *bare mass of volume V together with its gravitational field*, can be expressed through the time component of a 4-momentum P^a according to

$$P^0 = \int \left(T_1^1 + T_2^2 + T_3^3 - T_0^0 \right) \sqrt{-g} \, dV, \quad (3.18)$$

where T_a^a are the skew components of the energy-momentum tensor (3.17), which implicitly contains the gravity field [10].

Now, we formulate (3.18) under the equivalent form:

$$P^0 = P_0 = \int \left(\boldsymbol{T}_1^1 + \boldsymbol{T}_2^2 + \boldsymbol{T}_3^3 - \boldsymbol{T}_0^0 \right) dV. \quad (3.19)$$

In the immediate vicinity of the mass, it is easy, to show that generalizing (3.19) leads to the 4-momentum vector that includes the right hand side of (3.12):

$$P_a = \int \left[(\boldsymbol{T}_a^b)_{matter} + (\boldsymbol{t}_a^b)_{gravity} \right] dS_b. \quad (3.20)$$

Far from the source, we have obviously

$$(P_a)_{background\,field} = \int \left[(\boldsymbol{t}_a^b)_{background\,field} \right] dS_b, \quad (3.21)$$

where $(\boldsymbol{t}_a^b)_{background\,field}$ is a true tensor density, and the conservation law applied to P^a holds for all configurations, in accordance with (3.7) and (3.16).

4 Conclusions and outlook

In this short paper, we have sketched here a possible way out of the gravitational field pseudo-tensor.

From the beginning of General Relativity, the cosmological constant Λ has played an unsavory role. Einstein included this constant in his theory, because he wanted to have a cosmological model of the Universe which he wrongly thought static.

But to-day, a cosmological term seems to be badly needed to explain some astronomical observed clues, within the basic dynamical expanding model of Robertson-Walker [11], even though its occurrence was never clearly explained.

However, there is no reason *à priori* to consider this cosmological term as constant everywhere.

In this respect, the background field hypothesis is rewarding in terms of several physical advantages:

- The ill-defined gravitational pseudo-tensor is now a true tensor, and it appears explicitly in the field equations with a massive source;

- The background persistent homogeneous energy field is then formally shown to be a consequence of the above derivation and it is actually regarded as the (sharply decreasing) continuation of any mass gravity field tensor;

- The inferred global energy-momentum tensor intrinsically satisfies the conservation law as well as the background field alone in the source free field equations, without introducing any other arbitrary ingredients or modification of the General Theory of Relativity.

References

1. Einstein A. The meaning of Relativity. Appendix II. Translated in French by M. Solovine and M. A. Tonnelat, Gauthier-Villars, Paris, 1954.

2. Tonnelat M. A. Les Théories Unitaires de l'Electromagnétisme et de la Gravitation. Gauthier-Villars, Paris, 1959, p.18.

3. Eddington A. S. The mathematical Theory of Relativity. Cambridge University Press, Cambridge, 1924.

4. Lichnérowicz A. Les Théories Relativistes de la Gravitation et de l'Electromagnétisme. Masson et Cie, Paris, 1955.

5. Cartan E. La Géométrie des Espaces de Riemann. 1925. Re-print, Gauthier-Villars, Paris, 1946.

6. Landau L., Lifshitz E. The Classical Theory of Fields. Addison-Wesley, Reading, Massachusetts, 1962.

7. Straumann N. General Relativity and Relativistic Astrophysics. Springer-Verlag, Berlin, 1984, p.159.

8. Hawking S.W., Ellis G.F.R. The Large Scale Structure of Space-Time. Cambridge University Press, Cambridge, 1987, p.62.

9. Dirac P.A.M. General Theory of Relativity. Princeton University Press, 2nd edition, 1975, p.61.

10. Tolman R.C. Static Solutions of Einstein's Field Equations for Sphere of Fluid. *Physical Review*, 1939, v. 55, no. 4, 364–373.

11. Kramer D., Stephani H., Hertl E., Mac Callum M. Exact Solutions of Einstein's Field Equations. Cambridge University Press, Cambridge, 1979.

The Role of Evection in Optical Measurements of Light Beam Deflection from the Sun's Disk (the Einstein Effect)

Sergey N. Shapovalov

SCC RF Arctic and Antarctic Research Institute. 38 Bering St., St. Petersburg 199397, Russia
E-mail: shapovalov@aari.ru, tel. +7 (812) 3373157

The relationship between the optical results of light beam deflection from the disk of the Sun ($\delta\varphi$) obtained during observations of the total solar eclipses, from 1919 till 1973, and the evection, the major perturbation from the Sun, based on the theory of the Moon's motion, is analysed. The dependence of $\delta\varphi$ upon the temporal changes of the evection was found. The expected $\delta\varphi$ optical results for the total solar eclipses, for the period from 22.09.2003 till 29.12.2103, were calculated. Based on the comparison of calculated evection values with fluctuations of intensity of solar radiation within 603–607 nm range obtained through the spectral observations on solar radiation in Antarctica, the modulatory role of the evection in deflecting the light beam at the near-Earth space was concluded.

Optical measurements of the star beam deflection from the Sun disk were performed by a number of researchers during the total solar eclipses, from 29.05.1919 till 30.06.1973, with the purpose of checking the $\delta\varphi$ angle value (1.75″) obtained by Einstein, following his development of the General Theory of Relativity (GTR) [1]. In case the radio measurements only are considered in the practical estimates of the Einstein effect, $\delta\varphi$ values match with the theory within 1% range [2]. For example, an average value of 1.73″(±0.07″) was obtained in radar measurements of Mercury, Venus and Mars, whereas measurements of quasars and pulsars using radio interferometry produced an estimate of 1.76″(±0.08). Deflection of the beam from the Sun disk is described by the equation:

$$\delta\varphi = -\frac{4GM_\odot}{R_\odot c^2},\qquad(1)$$

where the "minus" sign corresponds to the deflection of the beam to the center of the Sun; $G = 6.67\times10^{-11}$ H×m^2/kg^2 is the gravitational constant; $M_\odot = 1.99\times10^{30}$ kg is the mass of the Sun; $c = 3\times10^8$ m/s is the speed of light; $R_\odot = 6.96\times10^8$ m is the radius of the Sun.

Based on the optical observations of the eight total solar eclipses, the author's average result together with a confidence interval of measurements makes $\delta\varphi = 1.83 \pm 0.40$, and the recalculated measurement result is $\delta\varphi = 2.0\pm0.13$, which, in view of the low accuracy and the considerable spread of measurements, is consistent with the GTR. According to the published data [3–10], the results of $\delta\varphi$ optical measurements for the total solar eclipses observed from 1919 till 1973 were as follows:

    29.05.1919: (1.98, 0.93, 1.61),

    21.09.1922: (1.42, 1.75, 2.16, 1.72, 1.83, 1.77),

    09.05.1929: (2.24),

    19.06.1936: (2.73, 2.13, 1.28),

    20.05.1947: (2.01),

    25.02.1952: (1.70, 1.82),

    02.10.1959: (2.17),

    30.06.1973: (1.66).

Observations referring to the date 19.06.1936 should be considered as ineffectual, since the absolute value error exceeds 200%. To date, the list of known errors includes:

— Deviation of the Sun's shape from the sphericity, 9.2″×10^{-2};

— The Earth's motion along the ecliptic (2.88″×10^{-2});

— Beam refraction in the atmosphere of the Sun (0.004″);

— Refraction and dispersion in the Earth atmosphere (0.01″–0.1″);

— Offset of the observer from the Sun-Moon-Earth line;

— The influence of the gravitational field of the Moon and the Earth during the total eclipse event, by an addition to the relativistic beam deflection (5.8″×10^{-4});

— Wavelength dependence of the light beam (2.5″×10^{-4});

— Dependence on solar activity;

— Astroclimatic characteristics of a particular observation station;

— Additive error caused by inaccurate scale matching between the day and night astroimages (0.25″).

It should be noted that through the history of $\delta\varphi$ measurements the list of errors has expanded considerably; however, the accuracy of estimates is not yet improved. Summing the values of all the errors, the magnitude of the total correction is apparently insignificant. Therefore, dispersion of $\delta\varphi$ results is probably due to the influence of some unknown factors.

The major solar-induced disturbances are described by terms in the formula of the geocentric ecliptic longitude of the Moon [11, 12]. Full description of this formula includes 1,500 terms [13], where evection, variation and annual inequality are the most important. When limited to the largest
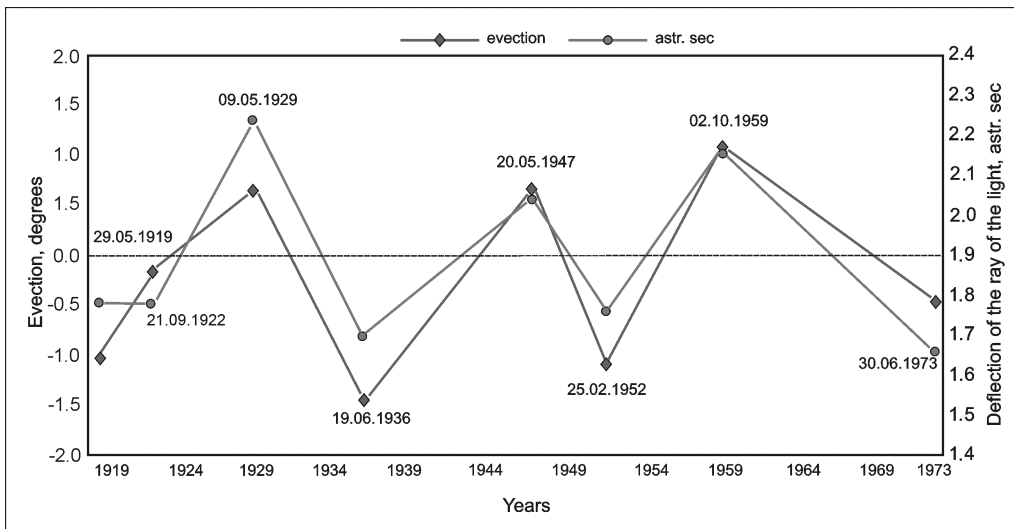
Fig. 1: Comparison of the evection angle values with the results of optical measurements taken as average values and excluding errors for the dates of the total solar eclipses, 1919–1973.

in amplitude terms, the formula is as follows:

$$\lambda = L + 6.289° \sin l - 1.274° \sin(l - 2D) +$$
$$+ 0.658° \sin 2t + 0.214° \sin 2l -$$
$$- 0.186° \sin l' - 0.114° \sin 2F, \qquad (2)$$

where L is the mean longitude (void of the periodic disturbances) of the Moon in the orbit, l, D, l', F are the main arguments in the lunar theory.

In the first five inequalities of the formula (2), the terms bearing coefficients 6.289 and 0.214 are determined by ellipticity of unperturbed (Keplerian) orbit, whereas the terms with coefficients 1.274 (evection, 31.8 days), 0.658 (variation, 14.8 days) and 0.186 (annual inequality, 186.2 days) are caused by gravitational perturbations from the Sun. The periods of these inequalities, according to the theory of motion of the Moon, exist in the short-period nutation of the Earth's axis, as well [14]. In this paper we consider the contribution of the evection, the main and the largest in amplitude perturbation from the Sun, as the most significant deviation of the true motion of the Moon from its motion defined by Kepler's laws. Evection was discovered by Ptolemy (2AD) when observing the Moon in the 1st and 3rd quarters (in quadrature points). The physical explanation of the evection was developed by Newton. Evection can be represented as a difference in the equation of the center [13] generated by the term $1.274° \sin(l - 2D)$:

$$e_\odot = 5.02 \sin l + 0.214 \sin 2l, \qquad (3)$$

$$e_\odot = 7.56 \sin l + 0.214 \sin 2l. \qquad (4)$$

This effect is determined by the gravitational influence of the Sun to the Moon. In syzygial points of the lunar orbit (new moon and full moon), this term is subtracted from the senior term of the equation (3), and it is added in quadrature. During the new moon and full moon, $2D = 0°$, or $360°$ (3), which is the same in the context of trigonometric functions. In the first and last quarters, $D = 90°$, or $270°$ (4). So, the known manifestations of the evection in the near-Earth space motivated the studies of its contribution to the results of $\delta\varphi$ assessments obtained during observations of the total solar eclipses, from 1919 till 1973.

The *evection* values were calculated upon the Julian dates of the total solar eclipses. Fig. 1 shows a comparison of the evection angle values with the results of optical measurements taken as average values and excluding errors for the dates of the total solar eclipses. Anomalous results $0.93''$ (1919) and $2.73''$ (1936) were omitted from the calculations of average values, as they fell outside the range of average result and the confidence interval of all measurements.

Fig. 2 shows the distribution of dependency of optical results from the evection. Continuous curve, which includes $0.93''$ (1919) and $2.73''$ (1936) values, represents averaging of results depending on the evection and is described as:

$$\delta\varphi(M) = 1.7227 + 0.2058\,x + 0.3163\,x^2. \qquad (5)$$

The dotted curve, which excludes $0.93''$ (1919) and $2.73''$ (1936) values, represents averaging of results depending on the evection and is described as follows:

$$\delta\varphi(E) = 1.723 + 0.316\,x^2. \qquad (6)$$

As demonstrated in the Figure, $\delta\varphi(M)$ has a lower left-hand shift against $\delta\varphi(E)$ characterized by the term $0.2058\,x$ (5), due to the low values obtained during the observations of 1919 ($\delta\varphi = 0.93''$) and 1936 ($\delta\varphi = 1.28''$). According to $\delta\varphi(E)$ distribution in Fig. 2, deflection of beams in
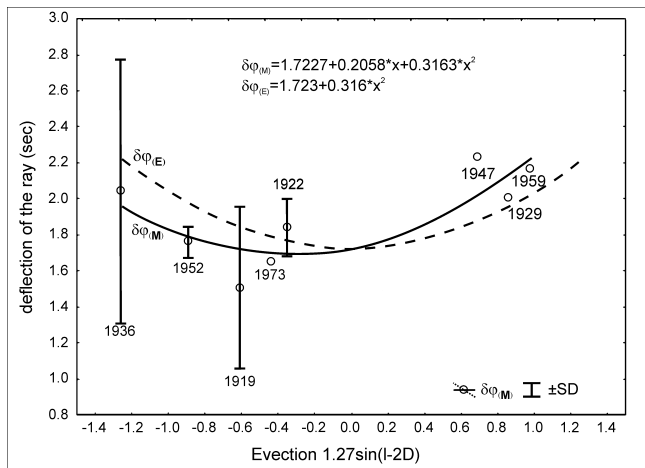
Fig. 2: Distribution of $\delta\varphi$ values according to the *evection* values, 1919–1973: $\delta\varphi(M)$ averaged optical results dependent on the evection, 0.93″ (1919) and 2.73″ (1936) values included; $\delta\varphi(E)$ averaged optical results dependent on the evection, 0.93″ (1919) and 2.73″ (1936) values excluded.

the evection extremes ($\pm 1.274°$) should correspond to $\delta\varphi \approx 2.25 \pm 10\%$, and to $\delta\varphi \approx 1.72$ in case of 0, i.e., conform to the Einstein result. Using the expression (6), the expected $\delta\varphi$ values calculated for optical observations at the dates of the total solar eclipse, from 23.11.2003 till 29.12.2103, are presented in Table 1.

Along with the deviations in the motion of the Moon from the Keplerian orbit and the short-period nutation of the Earth axis, the evection mechanism is detected in spectral zenith observations of the atmosphere at Novolazarevskaya station (Antarctica). These observations are aimed to investigate the fluctuations of energy and intensity of scattered solar UV radiation under the 11-year SA cycle. Measurements of fluctuations are recorded in the following ranges: 303–305 nm, 331–332.5 nm, 329.5–334 nm, 336–345 nm, 297–307 nm, 321–331 nm, 297–330 nm, and 603–607 nm, during the polar summer (September – February). Detailed description of the methodology of observations is cited in [15].

To test the influence of the evection factor on variations of the light flux, fluctuations measurements in the range of 603–607 nm (as the most proximate band to the central part of the solar spectrum) were selected from the available set of registered channels. Based on the observations during the polar summer 2007–2008 and 2008–2009, data analysis of the intensity channel was performed, in average daily standard deviation (SD) units, to build the time series and provide temporal comparison with the calculated values of the evection. Figs. 3 and 4 show the distribution pattern of SD values (603–607 nm), to be compared with the evection changes.

The figures show a reasonably good phase and periodic matching between the SD (603–607 nm) dynamics and the evection changes during the polar summer of 2007–2008. However, Fig. 4 shows the broken phase matching at certain

Eclipses	$\delta\varphi(E)$	Eclipses	$\delta\varphi(E)$	Eclipses	$\delta\varphi(E)$
23.11.2003	1.75	26.12.2038	2.02	03.08.2073	2.11
08.04.2005	2.24	21.06.2039	1.82	27.01.2074	2.23
03.10.2005	2.09	15.12.2039	1.72	24.07.2074	2.13
29.03.2006	1.89	30.04.2041	2.23	16.01.2075	2.03
22.09.2006	1.74	25.10.2041	2.01	13.07.2075	1.76
07.02.2008	2.22	20.04.2042	1.81	06.01.2076	1.73
01.08.2008	2.16	14.10.2042	1.72	22.05.2077	2.19
26.01.2009	1.88	28.02.2044	2.22	15.11.2077	2.02
22.07.2009	1.74	23.08.2044	2.09	11.05.2078	1.83
15.01.2010	1.75	16.02.2045	1.89	04.11.2078	1.72
11.07.2010	1.9	12.08.2045	1.74	01.05.2079	1.86
20.05.2012	1.78	05.02.2046	1.74	24.10.2079	1.96
13.11.2012	1.72	02.08.2046	1.98	10.03.2081	1.82
10.05.2013	1.91	11.06.2048	1.74	03.09.2081	1.72
03.11.2013	2.11	05.12.2048	1.75	27.02.2082	1.79
09.03.2016	1.92	31.05.2049	1.89	24.08.2082	2.07
01.09.2016	2.02	25.11.2049	2.17	03.07.2084	1.72
26.02.2017	2.23	20.05.2050	2.22	27.12.2084	1.79
21.08.2017	2.23	30.03.2052	1.91	22.06.2085	1.98
02.07.2019	2.03	22.09.2052	2.01	16.12.2085	2.16
26.12.2019	2.2	20.03.2053	2.23	11.06.2086	2.24
21.06.2020	2.18	12.09.2053	2.2	21.04.2088	1.99
14.12.2020	2.11	24.07.2055	2.11	14.10.2088	2.09
10.06.2021	1.82	16.01.2056	2.19	10.04.2089	2.24
04.12.2021	1.72	12.07.2056	2.19	04.10.2089	2.14
20.04.2023	2.22	05.01.2057	2.02	23.09.2090	1.77
14.10.2023	2.1	01.07.2057	1.83	15.08.2091	2.18
08.04.2024	1.89	26.12.2057	1.73	07.02.2092	2.23
02.10.2024	1.75	11.05.2059	2.23	03.08.2092	2.13
17.02.2026	2.22	05.11.2059	2.01	27.01.2093	1.94
12.08.2026	2.17	30.04.2060	1.82	23.07.2093	1.77
06.02.2027	1.88	24.10.2060	1.72	16.01.2094	1.73
02.08.2027	1.74	20.04.2061	1.86	02.06.2095	2.19
26.01.2028	1.74	13.10.2061	1.96	27.11.2095	1.93
22.07.2028	1.99	28.02.2063	1.81	22.05.2096	1.76
01.06.2030	1.74	24.08.2063	1.72	15.11.2096	1.73
25.11.2030	1.75	17.02.2064	1.79	11.05.2097	1.85
21.05.2031	1.9	12.08.2064	1.98	04.11.2097	2.05
14.11.2031	2.1	22.06.2066	1.74	21.03.2099	1.82
09.05.2032	2.23	17.12.2066	1.8	14.09.2099	1.72
30.03.2033	1.78	11.06.2067	1.89	10.03.2100	1.78
20.03.2034	1.91	06.12.2067	2.17	04.09.2100	2.06
12.09.2034	2.02	31.05.2068	2.24	28.02.2101	2.21
09.03.2035	2.23	11.04.2070	2	15.07.2102	1.72
02.09.2035	2.19	04.10.2070	2.1	08.01.2103	1.79
13.07.2037	2.12	31.03.2071	2.23	04.07.2103	1.97
05.01.2038	2.19	23.09.2071	2.2	29.12.2103	2.22
02.07.2038	2.19	12.09.2072	1.77		

Table 1: Expected $\delta\varphi$ results for the total solar eclipses, from 23.11.2003 till 12.29.2103.
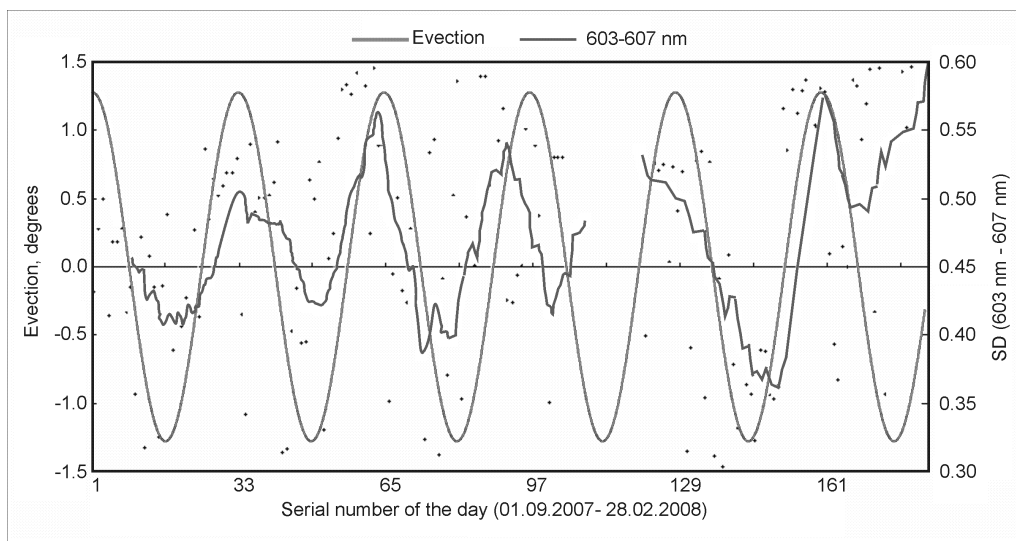
Fig. 3: Comparison of temporal changes in the evection and the average daily standard deviation (SD) of radiation intensity in the 603–607 nm (9 pt. mov. aver.) range, for the period from 01.09.2007 till 28.02.2008.
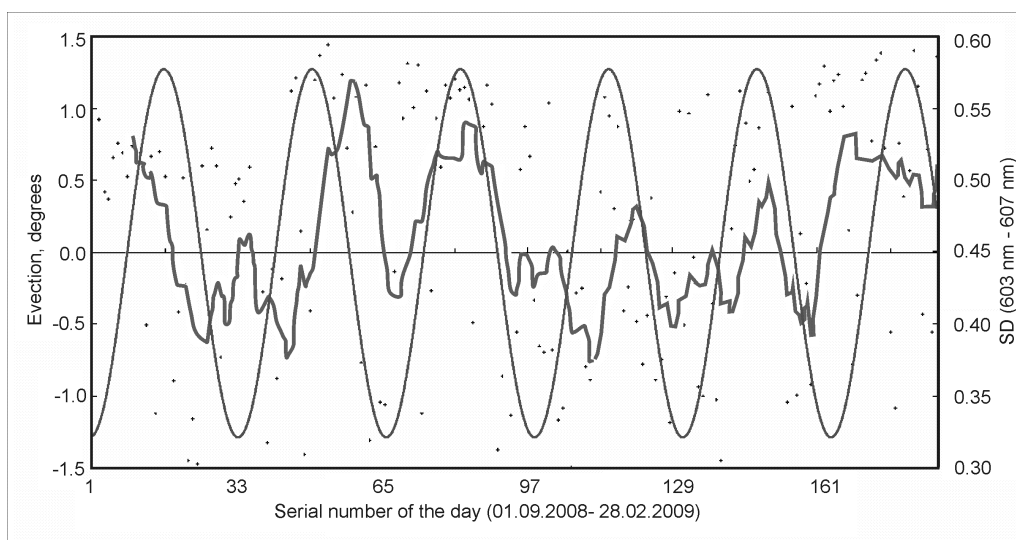

Fig. 4: Comparison of temporal changes in the evection and the average daily standard deviation (SD) of radiation intensity in the 603–607 nm (9 pt. mov. aver.) range, for the period from 01.09.2008 till 28.02.2009.

extended sections. In our view, such failures may be related to the SA stages. Among the above errors, $\delta\varphi$ dependence from SA and astroclimatic characteristics of observation stations remain understudied. Astroclimatic characteristics are determined by the weather conditions and optical properties of the atmosphere and both are connected with the SA manifestations. Although the mechanism of SA effects on the surface layer of the atmosphere remains unclear to date, this connection is revealed by the long-term observations of weather services.

In a brief discussion of relationship between $\delta\varphi$ and the evection, previously disregarded in research practice, a 3-body Einstein model should be mentioned, which considers the Earth and the Moon as point-like objects. This model is undeniable in the evaluation of mass gravitation of the Earth–Moon and the Sun. The major solar disturbances cause deviation from the Keplerian orbit of the Moon motion and, at the same time, deviations in the Earth axis in the short-period nutation (31.8 and 14.8 days), provide periodic gravitational influence on the Earth–Moon system. Obviously, this influence

is manifested in the Einstein effect through the modulation property of optical beams.

Conclusions

— The values of $\delta\varphi$ optical results reveal statistical correlation with the temporal change of the evection;

— In the evection extreme points ($\pm 1.274°$), deflection of optical beams from the solar disk is expected to approach $\delta\varphi \approx 2.25 \pm 10\%$;

— When the evection values $\approx 0°$, it is expected to approach $\delta\varphi = 1.72 \pm 10\%$;

— In conformity with $\delta\varphi(E)$, introduction of correction for the evection into the formula (1) is justified.

References

1. Einstein A. *Ann. Phys.*, 1916, Bd.49, 769.

2. Ginzburg V.L. Theoretical physics and astrophysics. Nauka, Moscow, 1980.

3. Crommelin A. Results of the total solar eclipse of May 29 end the relativity theories. *Nature*, 1920, v.104, 280–281.

4. Hopmann J. Die Deutung der Ergebnisse der amerikanischen Einstein expedition. *Phys. Z.*, 1923, Bd.24, No.21/22, 476–485.

5. Eddington A.S. The deflection of light during a solar eclipse. *Nature*, 1919, v.104, no.271, 454.

6. Mikhailov A.A. Einstein's effect observations. *Astronomicheskiy Zhurnal*, 1956, no.33, 912–927.

7. Freundlich E.F., von Kluber H.V., Brunn A. Ergebniss der Potsdamer Expedition zur Beib chtung der Sonnenfinsternis von 1929, Mai 9 die Ablenkung des Lichtes in Schwerefeld der Sonne. *Phys. Ber.*, 1931, No.1, 2838–2839.

8. Schmeidler F. Neuer Versuch einer Messung der relativitischen Lichtablenkung. *Astron. Nachrichten*, 1963, Bd.287, No.1-2, 7–16.

9. Jones B.F. Texas Mauritanian Eclipse Team. Gravitational deflection of light: Solar eclipse of 30 June 1973. I. Description of procedures and final results. *Astron. J.*, 1974, v.81, 452–454.

10. Jones B.F. Gravitational deflection of light: solar eclipse of 30 June 1973. II. Plate reduction. *Astron. J.*, 1974, v.81, 455–463.

11. Astronomicheskiy Ezhegodnik. Part 1. Inst. Appl. Astron., Russian Acad. Sci., St. Petersburg, 1998.

12. Meeus J. Astronomical formulae for calculators. Mir, Moscow, 1988.

13. Brown F.H. Tables of the motion of the Moon. New Hawen, 1919.

14. Kulikov K.A. Rotation of the Earth. Nedra, Moscow, 1985.

15. http://www.aari.nw.ru/clgmi/geophys/data_nvl_ru.html

Mass and Charge Selfvariation: A Common Underlying Cause for Quantum Phenomena and Cosmological Data

Emmanuil Manousos

Astrophysics Laboratory, Faculty of Physics, National and Kapodistrian University of Athens,
Panepistimiopolis, GR 15783 Zographos, Athens, Greece. E-mail: emanoussos@phys.uoa.gr

The physical theories of the last century do not possess the completeness necessary in order to justify the quantum phenomena and the cosmological data. In this article, we present the law of selfvariations and suggest it as the common cause of quantum and cosmological phenomena. There is an intermediate state between matter and the photon, which is the cause of quantum phenomena. The cosmological data are condensed in a single equation with one unknown. The consequences of the law of selfvariations extend from the microcosm to the observations we make billions of light-years away.

Contents:

1 Introduction

The study we present in the current edition is based on two assumptions that are taken as axioms. The first assumption is that the rest masses m_0 and electric charges q of material particles increase with the passage of time (selfvariations). The second assumption is that the consequences of the selfvariations propagate through four-dimensional spacetime with a zero arc length: $dS^2 = 0$. The set of consequences arising from these two assumptions constitutes the "theory of self-variations".

An immediate consequence of the statements-axioms we have introduced, is the concept of the generalized photon: a particle carrying energy E, linear momentum **P**, and moving with velocity v, of magnitude $\|v\| = c$, in every inertial frame of reference. The generalized photon correlates the material particle with its surrounding spacetime. In its simplest version, the generalized photon is emitted by the material particle into its surrounding spacetime. When the material particle is electrically charged, the generalized photon, apart from energy and momentum, also carries electric charge.

In figure 1, the arbitrary motion of a material point particle moving with velocity **u** in an inertial frame of reference $O(x, y, z, t)$ is represented.

A generalized photon is emitted by the material particle at time $w = t - \frac{r}{c}$, from point $E(x_p(w), y_p(w), z_p(w), w)$, and arrives at time t at point $A(x, y, z, t)$. The velocity of the generalized photon in Figure 1, is

$$v = \frac{c}{r}\mathbf{r}$$

where $r = \|\mathbf{r}\|$. We express the vector $\frac{v}{c}$ in the trigonometric form

$$\frac{v}{c} = \begin{bmatrix} \frac{v_x}{c} \\ \frac{v_y}{c} \\ \frac{v_z}{c} \end{bmatrix} = \begin{bmatrix} \cos\delta \\ \sin\delta\cos\omega \\ \sin\delta\sin\omega \end{bmatrix}.$$

Furthermore, we define the following two vectors

$$\beta = \begin{bmatrix} -\sin\delta \\ \cos\delta\cos\omega \\ \cos\delta\sin\omega \end{bmatrix}$$

and

$$\gamma = \begin{bmatrix} 0 \\ -\sin\omega \\ \cos\omega \end{bmatrix}.$$

The vectors $\frac{v}{c}, \beta, \gamma$ constitute a right-handed, orthonormal vector basis that accompanies the generalized photon in
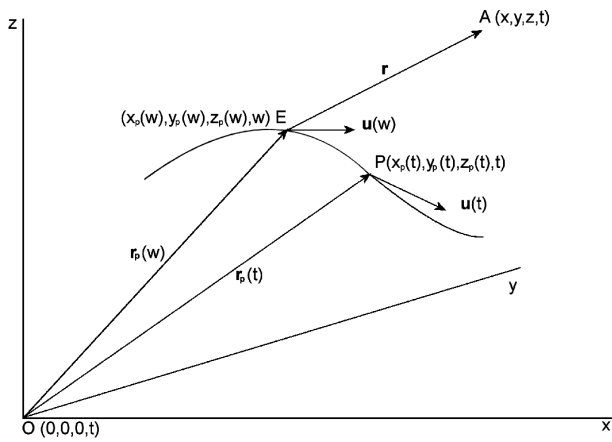
Fig. 1: A material point particle moving arbitrarily. As the material particle moves from point $E(x_p(w), y_p(w), z_p(w), w)$ to point $P(x_p(t), y_p(t), z_p(t), t)$, the generalized photon moves from point $E(x_p(w), y_p(w), z_p(w), w)$ to point $A(x, y, z, t)$.

its motion. The consequences of the selfvariations are expressed as functions of the parameters $w = t - \frac{r}{c}, r, \delta, \omega$. The basic study of the selfvariations leads to two fundamental theorems: the "Fundamental Mathematical Theorem", and the "Trajectory Representation Theorem". The first theorem allows us to correlate any change in energy manifested on the material particle at point $E(x_p(w), y_p(w), z_p(w), w)$ with a corresponding change in energy at point $A(x, y, z, t)$ of Figure 1. The second theorem represents the tangent vector, the curvature and the torsion of the trajectory of the material particle onto the geometric characteristics of the generalized photon in the surrounding spacetime. The two theorems allow us to express quantitatively the consequences of the selfvariations on the surrounding spacetime of the material particle. As a consequence of the selfvariations, in the surrounding spacetime of the material particle there is energy of density D

$$D = -c \frac{\partial m_0}{\partial w} \frac{1}{4\pi\gamma^3 r^2 \left(1 - \frac{\boldsymbol{v} \cdot \mathbf{u}}{c^2}\right)^4}$$

and momentum of density $\mathbf{J}$

$$\mathbf{J} = D \frac{\boldsymbol{v}}{c^2}$$

where

$$\gamma = \frac{1}{\sqrt{1 - \frac{u^2}{c^2}}},$$

and $\mathbf{u} = \mathbf{u}(w)$.

If the material particle is electrically charged, then in the surrounding spacetime there is also electric charge of density ρ

$$\rho = -\frac{\partial q}{c\partial w} \frac{1}{4\pi\gamma^2 r^2 \left(1 - \frac{\boldsymbol{v} \cdot \mathbf{u}}{c^2}\right)^3}$$

and electric current of density $\mathbf{j}$

$$\mathbf{j} = \rho \boldsymbol{v}.$$

The Lienard-Wiechert potentials

$$V = \frac{q}{4\pi\varepsilon_0 r \left(1 - \frac{\boldsymbol{v} \cdot \mathbf{u}}{c^2}\right)}$$

and

$$\mathbf{A} = \frac{q}{4\pi\varepsilon_0 c^2 r \left(1 - \frac{\boldsymbol{v} \cdot \mathbf{u}}{c^2}\right)} \mathbf{u}$$

are not compatible with the theory of selfvariations. Therefore, they are replaced by the potentials of the selfvariations

$$V = \frac{q\left(1 - \frac{u^2}{c^2}\right)}{4\pi\varepsilon_0 r \left(1 - \frac{\boldsymbol{v} \cdot \mathbf{u}}{c^2}\right)^2} + \frac{q(\boldsymbol{v} \cdot \boldsymbol{\alpha})}{4\pi\varepsilon_0 c^3 \left(1 - \frac{\boldsymbol{v} \cdot \mathbf{u}}{c^2}\right)^2}$$

$$A = V \frac{\boldsymbol{v}}{c^2}$$

where $\boldsymbol{\alpha} = \boldsymbol{\alpha}(w)$ is the acceleration of the material particle.

The potentials of the selfvariations are separated into two individual pairs

$$V_u = \frac{q\left(1 - \frac{u^2}{c^2}\right)}{4\pi\varepsilon_0 r \left(1 - \frac{\boldsymbol{v} \cdot \mathbf{u}}{c^2}\right)^2}$$

$$A_u = V_u \frac{\boldsymbol{v}}{c^2}$$

and

$$V_\alpha = \frac{q(\boldsymbol{v} \cdot \boldsymbol{\alpha})}{4\pi\varepsilon_0 c^3 \left(1 - \frac{\boldsymbol{v} \cdot \mathbf{u}}{c^2}\right)^2}$$

$$A_\alpha = V_\alpha \frac{\boldsymbol{v}}{c^2}.$$

The (V_u, A_u) pair gives the electromagnetic field $(\boldsymbol{\varepsilon}_u, \boldsymbol{B}_u)$ that accompanies the electrically charged material particle

$$\boldsymbol{\varepsilon}_u = \frac{q\left(1 - \frac{u^2}{c^2}\right)}{4\pi\varepsilon_0 r^2 \left(1 - \frac{\boldsymbol{v} \cdot \mathbf{u}}{c^2}\right)^3} \left(\frac{\boldsymbol{v}}{c} - \frac{\mathbf{u}}{c}\right)$$

$$\boldsymbol{B}_u = \frac{q\left(1 - \frac{u^2}{c^2}\right)}{4\pi\varepsilon_0 r^2 \left(1 - \frac{\boldsymbol{v} \cdot \mathbf{u}}{c^2}\right)^3} \frac{\mathbf{u}}{c} \times \frac{\boldsymbol{v}}{c}.$$

The (V_α, A_α) pair gives the electromagnetic radiation

$$\boldsymbol{\varepsilon}_\alpha = \frac{q}{4\pi\varepsilon_0 c^2 r \left(1 - \frac{\boldsymbol{v} \cdot \mathbf{u}}{c^2}\right)^2} \left[\frac{\frac{\boldsymbol{v}}{c} - \boldsymbol{\alpha}}{1 - \frac{\boldsymbol{v} \cdot \mathbf{u}}{c^2}} \left(\frac{\boldsymbol{v}}{c} - \frac{\mathbf{u}}{c}\right) - \boldsymbol{\alpha} \right]$$

$$B_\alpha = \frac{q}{4\pi\varepsilon_0 r \left(1 - \dfrac{\boldsymbol{v}\cdot\mathbf{u}}{c^2}\right)} \left[\frac{\frac{v}{c}\alpha}{1 - \dfrac{\boldsymbol{v}\cdot\mathbf{u}}{c^2}} \left(\frac{\mathbf{u}}{c} \times \frac{\boldsymbol{v}}{c}\right) - \frac{\boldsymbol{v}}{c} \times \alpha \right].$$

The pair $(V_\alpha, \boldsymbol{A}_\alpha)$ of the electromagnetic radiation potentials does not depend on the distance r. For each couple $(\boldsymbol{\varepsilon}, \boldsymbol{B})$ the following relation holds

$$\boldsymbol{B} = \frac{\boldsymbol{v}}{c^2} \times \boldsymbol{\varepsilon}.$$

The energy-momentum tensor for the generalized photon that results from the selfvariation of the rest mass m_0 of the material particle is given by the matrix Φ^{ij}

$$\Phi^{ij} = \frac{D}{c^2} \begin{bmatrix} c^2 & cv_x & cv_y & cv_z \\ v_x c & v_x^2 & v_x v_y & v_x v_z \\ v_y c & v_y v_x & v_y^2 & v_y v_z \\ v_z c & v_z v_x & v_z v_y & v_z^2 \end{bmatrix}$$

where

$$\begin{bmatrix} c \\ v_x \\ v_y \\ v_z \end{bmatrix} = \begin{bmatrix} v^0 \\ v^1 \\ v^2 \\ v^3 \end{bmatrix}, \qquad i, j = 0, 1, 2, 3.$$

The energy-momentum tensor for the generalized photon that results from the selfvariation of the electric charge q of the material particle is given by the matrix Φ^{ij}

$$\Phi^{ij} = \begin{bmatrix} W & cS_x & cS_y & cS_z \\ cS_x & \sigma_{11} & \sigma_{12} & \sigma_{13} \\ cS_y & \sigma_{21} & \sigma_{22} & \sigma_{23} \\ cS_z & \sigma_{31} & \sigma_{32} & \sigma_{33} \end{bmatrix} - \frac{\rho V}{c^2} \begin{bmatrix} c^2 & cv_x & cv_y & cv_z \\ v_x c & v_x^2 & v_x v_y & v_x v_z \\ v_y c & v_y v_x & v_y^2 & v_y v_z \\ v_z c & v_z v_x & v_z v_y & v_z^2 \end{bmatrix}$$

where $(S_x, S_y, S_z) = \mathbf{S} = \varepsilon_0 \boldsymbol{\varepsilon} \times \boldsymbol{B}$ is the Poynting vector,

$$W = \frac{1}{2}\varepsilon_0 \left(\boldsymbol{\varepsilon}^2 + c^2 \boldsymbol{B}^2\right)$$

and

$$\sigma_{\alpha\beta} = \varepsilon_0 \left(-\varepsilon_\alpha \varepsilon_\beta - c^2 B_\alpha B_\beta + W\delta_{\alpha\beta}\right)$$

$$\delta_{\alpha\beta} = \begin{cases} 1, & \text{if } \alpha = \beta \\ 0, & \text{if } \alpha \neq \beta \end{cases}$$

where $\alpha, \beta = 1, 2, 3$ and

$$(\varepsilon_1, \varepsilon_2, \varepsilon_3) = (\varepsilon_x, \varepsilon_y, \varepsilon_z) = \boldsymbol{\varepsilon}$$

$$(B_1, B_2, B_3) = (B_x, B_y, B_z) = \boldsymbol{B}.$$

The energy-momentum tensors Φ^{ij} give us important information about the energy content of the surrounding spacetime of the material particle. Furthermore, they are related with the gravitational and the electromagnetic interaction. As we progress in our study however, it becomes evident that there is information about the energy content and the properties of spacetime, that is not contained within the Φ^{ij} tensors.

The study we presented up to this point has been conducted without a quantitative determination of the selfvariations. We made the assumption of the selfvariations in order to undertake the relevant calculations, but we have not determined quantitatively the rate at which they evolve, i.e. the $\frac{\partial m_0}{\partial w}$ and $\frac{\partial q}{\partial w}$. In order to study the consequences of the selfvariations, we have to quantitatively determine these rates.

The quantitative determination of the selfvariations is made on the basis of the total energy E_s and the total momentum $\mathbf{P_s}$ emitted simultaneously in all directions, by the material particle. The rest mass m_0 and the electric charge q of the material particle vary according to the operators

$$\frac{\partial}{\partial t} \rightarrow -\frac{i}{\hbar} E_s$$

$$\nabla \rightarrow \frac{i}{\hbar} \mathbf{P_s}$$

where h is Planck's constant, and $\hbar = \frac{h}{2\pi}$. The law of selfvariations expresses a continuous interaction between the material particle and the generalized photons.

The partial contribution of an individual generalized photon to the law of selfvariations is determined by the percentage-function Φ. Due to this, function Φ has a fundamental role in the energy content of the generalized photon.

The energy E and momentum $\mathbf{P}$ of the generalized photon that is related to the selfvariation of the rest mass m_0 of the material particle, are given by the equations

$$E = \Phi \frac{i\hbar}{1 - \dfrac{\boldsymbol{v}\cdot\mathbf{u}}{c^2}} \frac{\partial m_0}{m_0 \partial w} + i\hbar \frac{\partial \Phi}{\partial t}$$

$$\mathbf{P} = \Phi \frac{i\hbar}{1 - \dfrac{\boldsymbol{v}\cdot\mathbf{u}}{c^2}} \frac{\partial m_0}{m_0 c \partial w} \frac{\boldsymbol{v}}{c} - i\hbar \nabla\Phi.$$

The equations that give the energy and momentum of the generalized photon that is related to the selfvariation of the electric charge of the material particle, are of similar form.

The energy E and the momentum $\mathbf{P}$ of the generalized photon do not obey the simple relation

$$\mathbf{P} = E \frac{\boldsymbol{v}}{c^2}.$$

That relation is a special case of the general relation

$$\mathbf{P} = E \frac{\boldsymbol{v}}{c^2} - \frac{i\hbar}{r} \frac{\partial \Phi}{\partial \delta} \boldsymbol{\beta} - \frac{i\hbar}{r\sin\delta} \frac{\partial \Phi}{\partial \omega} \boldsymbol{\gamma}.$$

The generalized photon determines the relation of the material particle with the surrounding spacetime. Furthermore, it is related with the energy content of spacetime and, hence, with the very properties of spacetime. Because of this, a large part of the study we present in the present edition concerns the generalized photon and its properties. The resulting equations contain an exceptionally large body of data and information.

Thus, we shall confine ourselves to a brief report for the structure and the properties of the generalized photon.

The generalized photon carries four energy-momentum pairs, each of which transforms autonomously, independently of the rest, according to Lorentz-Einstein. Two of these pairs do not possess rest energy, do not depend on the distance r from the material particle, are defined both on the material particle and on the surrounding spacetime, while they do not possess intrinsic angular momentum (spin). The other two energy-momentum pairs have, respectively, rest energy

$$\pm \frac{c\hbar}{r} \frac{\partial \Phi}{\partial \delta}$$

$$\pm \frac{c\hbar}{r \sin \delta} \frac{\partial \Phi}{\partial \omega}.$$

Their energy and momentum are inversely proportional to the distance r from the material particle, they are not defined on the material particle but only on the surrounding spacetime, while they possess intrinsic angular momentum (spin), given respectively by

$$-i\hbar \frac{\partial \Phi}{\partial \delta} \gamma$$

$$\frac{i\hbar}{\sin \delta} \frac{\partial \Phi}{\partial \omega} \beta.$$

The total intrinsic angular momentum $\mathbf{S}$ of the generalized photon is given by relation

$$\mathbf{S} = \frac{i\hbar}{\sin \delta} \frac{\partial \Phi}{\partial \omega} \beta - i\hbar \frac{\partial \Phi}{\partial \delta} \gamma.$$

The intrinsic angular momentum of the generalized photon exhibits some remarkable properties. The first is that it does not depend on the distance r from the material particle, while it is also defined on the material particle itself. Furthermore, the component

$$S_u = i\hbar \frac{\partial \Phi}{\partial \omega}$$

in the direction of the velocity of the material particle, remains invariant under the action of the Lorentz-Einstein transformations and is, therefore, constant in all inertial reference frames. Another property of the intrinsic angular momentum of the generalized photon is that it does not vanish even if we consider that the material particle is motionless. In other words, the generalized photon carries intrinsic angular momentum even in the inertial reference frame in which the material particle is at rest. In that sense, we can characterize the intrinsic angular momentum of the generalized photon as "rest angular momentum". One final property, which is not included in the present edition is the following: during the interaction of the generalized photon with a material particle, the variation ΔS of the angular momentum of the generalized photon manifests a component along the direction of the vector $\frac{v}{c}$.

Of particular interest is the fact that the generalized photon, in its general version, implies the existence of rest energy in the surrounding spacetime of the material particle. The existence of this energy results as a general consequence of the equations of the theory of selfvariations.

We remind that the law of the selfvariations has been stated on the basis of the total energy E_s and the total momentum $\mathbf{P_s}$ of the generalized photons emitted simultaneously and in all directions by the material particle. We can easily prove that between the energy E_s and the momentum $\mathbf{P_s}$ the following relation holds

$$\mathbf{P_s} = E_s \frac{\mathbf{u}}{c^2}$$

where $\mathbf{u} = \mathbf{u}(w)$ is the velocity of the material particle at the moment of emission of the generalized photons. The energy E_s is always correlated with a rest energy E_0 ($E_0 \neq 0$) through equation $E_s = \gamma E_0$, where $\gamma = \frac{1}{\sqrt{1 - \frac{u^2}{c^2}}}$. Therefore, in the energy E_s, which results from the aggregation of the generalized photons, a rest mass of $\frac{E_0}{c^2} \neq 0$ is implicit. The law of selfvariations expresses exactly the interaction between the rest mass m_0 of the material particle, and the rest mass $\frac{E_0}{c^2}$ that results from the aggregation of the generalized photons.

The physical object that results from the aggregation of the generalized photons, always accompanies the material particle. Because of this, we named it "accompanying particle". The accompanying particle has rest mass $\frac{E_0}{c^2}$, while in the part of spacetime it occupies it holds that $dS^2 = 0$. The combination $\frac{E_0}{c^2} \neq 0$ and $dS^2 = 0$, leads to the conclusion that the accompanying particle corresponds to an intermediate state between "matter" ($\frac{E_0}{c^2} \neq 0$) and the "photon" ($dS^2 = 0$). This intermediate state of matter is the cause of quantum phenomena, and its prediction constitutes one of the most important results of the theory of selfvariations.

In Nature, the system material particle-accompanying particle exists and behaves as a "generalized particle" which extends in a part of spacetime. The part of space occupied by the generalized particle can be the point where the material particle is located, or it can extend up to an infinite distance away from the material particle. In the part of spacetime where the generalized particle extends, the trajectories and velocities of the generalized photons are altered with respect to the strictly defined trajectories and velocities presented in Figure 1. There is an extreme case where the concepts of trajectory and velocity of the generalized photon become meaningless; they are not defined. The same is true for the trajectory and velocity of the material particle in case it is located in the part of spacetime occupied by the generalized particle. This prediction provides us with the basic idea about the method we have to develop in order to study the generalized particle.

One way in which to study the internal structure and physical properties of the generalized particle, is to eliminate the velocity, which also represents the trajectory, from the equa-

tions of the theory of selfvariations. This elimination of the velocity can be accomplished in several ways. One is to introduce into the equations of the theory of selfvariations the potential energy U of the material particle. The resulting equation is the time-independent wave equation of Schrödinger

$$\nabla^2 \Psi = -\frac{2m_0(\varepsilon - U)}{\hbar^2}\Psi.$$

The differential equations of the theory of selfvariations are of first order. When we convert them to second order equations, we can eliminate the velocity without having to introduce potential energy, or any other physical quantity, into the equations. The elimination of velocity leads to the Klein-Gordon equation. As a special case of the Klein-Gordon for $m_0 = 0$, we get the wave equation

$$\nabla^2 \Psi - \frac{\partial^2 \Psi}{c^2 \partial t^2} = 0$$

which appears in Maxwell's theory of electromagnetism.

Observing the way in which we use Schrödinger's operators in quantum mechanics, we realize that, what we are primarily doing, is to eliminate the kinematic characteristics of the material particle from the resulting differential equations. Dirac does the same thing in the method he develops, in combination, of course, with his additional assumptions, in order to derive his eponymous equation.

In order to study the internal structure of the generalized particle we have to answer specific questions. These questions, and more generally all the issues concerning the generalized particle, are completely different from the ones we usually have to answer when we study physical reality.

The material particle can be located at any position in the part of spacetime it occupies. Judging by the success of quantum mechanics and by the high accuracy calculations it permits, we conclude that statistical interpretation is one way of studying the internal structure of the generalized particle. However, the theory of selfvariations poses a question, the answer to which, leads us to an unknown territory of physical reality.

In order to study the internal structure of the generalized particle we have to answer the question, how is the total rest mass of the generalized particle distributed between the material particle (m_0) and the accompanying particle $\left(\frac{E_0}{c^2}\right)$. During the quantitative determination of this particular distribution, the Schrödinger and Klein-Gordon equations show up, together with the wave equation of Maxwell's electromagnetic theory. In the part of spacetime occupied by the generalized particle, an external cause suffices to shift the rest mass towards either the material particle or the accompanying particle. In the first case, the generalized particle behaves as a material particle, which moves on a defined trajectory, with defined velocity, energy, etc. In the second case, the generalized particle spreads in spacetime, while the consequences

of the aggregation of the generalized photons are intensified. This is the phenomenon we observe in the double-slit experiment.

The law of selfvariations results in the differential equation

$$\left(m_0 c^2 + i\hbar \frac{\dot{m}_0}{m_0}\right)^{\bullet} = 0$$

the only unknown being the rest mass m_0 of the material particles. This simple equation contains as information and rationalizes, the totality of the cosmological data within a Universe that is flat and static, with the exception of a very slight variation of the fine structure constant predicted by the equations of the theory of selfvariations for observations at distances greater than 6×10^9 ly. The redshift z of a distant astronomical object located at distance r is given by equation

$$z = \frac{1 - A\exp\left(-\dfrac{kr}{c}\right)}{1 - A} - 1$$

where k is a constant and A is a scalar parameter that obeys the inequality

$$\frac{z}{1 + z} < A < 1$$

for every value of the redshift z. Therefore, the value of parameter A is close to 1, with $A < 1$. The distance $r = r(z)$ of a distant astronomical object as a function of the redshift z, is given by equation

$$r = \frac{c}{k}\ln\left(\frac{A}{A - z(1 - A)}\right).$$

In figure 2 we present the plot of the function $r = r(z)$ for $A = 0.900, A = 0.950, A = 0.990, A = 0.999$ up to $z = 5$. We observe that, as we increase the value of parameter A, the curve tends to become a straight line. This result is not accidental. It is proven that, for $A \to 1^-$, function $r = r(z)$ gives Hubble's law.

The energy $E(z)$ which fuels the radiance of astronomical objects, and which originates from the process of fusion, and generally from the conversion of mass into energy, is smaller than the corresponding energy E in our galaxy, according to equation

$$E(z) = \frac{E}{1 + z}.$$

Therefore, the intrinsic luminosity of the astronomical object is lower than the standard luminosity we use. As a consequence, the luminosity distance R we measure is in fact greater than the real distance r of distant astronomical objects. The relevant calculations lead to equation

$$R = r\sqrt{1 + z}.$$

Consideration the arithmetic values of the parameters that factor into function $R = R(z)$, we obtain equation

$$R = 5000 \, z\sqrt{1 + z}$$
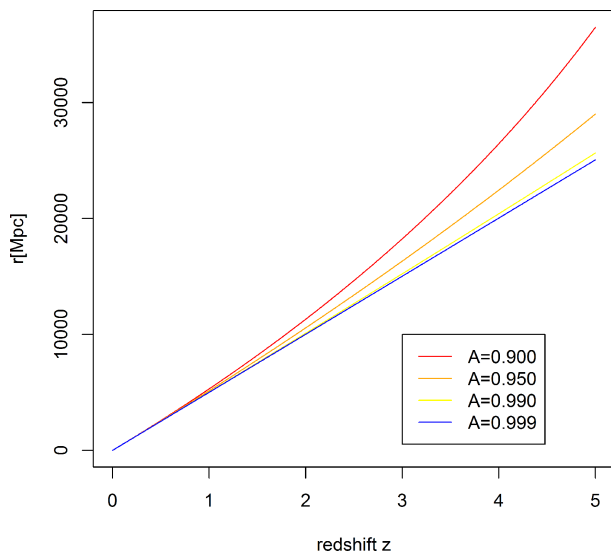
Fig. 2: The plot $r = r(z)$ of the distance of an astronomical object as a function of redshift z, for $A = 0.900, A = 0.950, A = 0.990, A = 0.999$. As the value of the parameter A is increased, the curve $r = r(z)$ tends to a straight line.
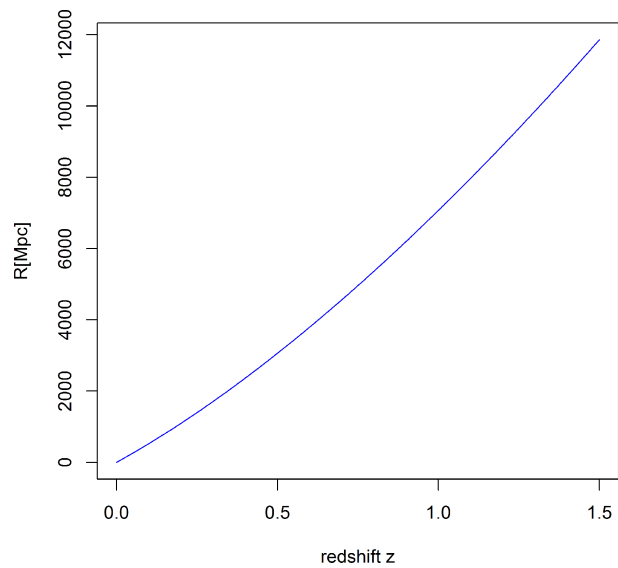
Fig. 3: The plot of the luminosity distance R of astronomical objects as a function of the redshift z. The measurement of the luminosity distances of type I_α supernova, confirms the theoretical prediction of the law of selfvariations.

where the luminosity distance R is given in Mpc. In figure 3 we present the plot of function $R = R(z)$ up to $z = 1.5$.

Type I_α supernovae are cosmological objects for which we can measure the luminosity distance at great distances. At the end of the last century, these measurements were performed by the independent scientific groups of Adam J. Riess and Saul Perlmutter. The graph that results from those measurements, exactly matches diagram in figure 3, which is theoretically predicted by the law of selfvariations. The concept of dark energy was invented in order to justify the inconsistency between the Standard Cosmological Model and diagram in figure 3.

At cosmological scales, the rest mass $m_0(r)$ with which an astronomical object exerts gravitational action at distance r from itself, is given by equation

$$m_0(r) = m_0 \frac{0.001}{1 - 0.999 e^{-2 \times 10^{-7} r}}$$

where m_0 is the laboratory value of the rest mass. The distance r is measured in Mpc.

For values of r of the order of kpc, it turns out that $m_0 = m_0(r)$. For $r = 100$ kpc we get $m_0(r) = 0.99999\, m_0$. Consequently, the strength of the gravitational interaction is not affected on the scale of galactic distances. The selfvariations do not affect the stability of the solar system and of galaxies.

On the contrary, at distances of the order of magnitude of Mpc, a clearly smaller value of mass $m_0(r)$ compared to m_0, is predicted. For $r = 100$ Mpc we get $m_0(r) = 0.98\, m_0$. For even larger distances, the ratio $\frac{m_0(r)}{m_0}$ becomes even smaller. For an astronomical object located at a distance corresponding to redshift $z = 9$, it is $\frac{m_0(r)}{m_0} = 0.1$. The strength of the

gravitational interaction exerted by an astronomical object with $z = 9$ on our galaxy is just 10% of the expected. For still greater distances, the gravitational interaction practically vanishes. This is why gravity cannot play the role attributed to it by the Standard Cosmological Model.

The Thomson scattering coefficient

$$\sigma_\tau = \frac{8\pi}{3} \frac{q^4}{m_0^2 c^2}$$

as well as the Klein-Nishina scattering coefficient

$$\sigma = \frac{3}{8} \sigma_\tau \frac{m_0 c^2}{E} \left[\ln\left(\frac{2E}{m_0 c^2} \right) + \frac{1}{2} \right]$$

obtain different values, namely

$$\sigma_\tau(r) = \frac{8\pi}{3} \frac{q^4(r)}{m_0^2(r) c^2}$$

and

$$\sigma(r) = \frac{3}{8} \sigma_\tau(r) \frac{m_0(r) c^2}{E(r)} \left[\ln\left(\frac{2E(r)}{m_0(r) c^2} \right) + \frac{1}{2} \right]$$

respectively, at distant astronomical objects. The mathematical calculations give

$$\frac{\sigma_\tau(r)}{\sigma_\tau} = \frac{\sigma_\tau}{\sigma} = \left(\frac{1 - A \exp\left(-\frac{kr}{c} \right)}{1 - A} \right)^2.$$

At very large distances ($r \to \infty$), and equivalently for the very early Universe, we get

$$\frac{\sigma_\tau(r \to \infty)}{\sigma_\tau} = \frac{\sigma(r \to \infty)}{\sigma} = \left(\frac{1}{1-A}\right)^2.$$

Because of the inequality $\frac{z}{1+z} < A < 1$ we see that $A \to 1^-$ and, therefore, the Thomson and Klein-Nishina scattering coefficients obtain enormous values in the very early Universe. Consequently, in its very early stages, the Universe went through a phase during which it was opaque to electromagnetic radiation. The cosmic microwave background radiation originates from that period. The theory of selfvariations predicts that, in that phase, the temperature of the Universe was slightly above 0 K. Furthermore, it predicts that the cosmic microwave background radiation originates from the whole extent of the space occupied by the Universe.

The ionization and excitation energy $X_n(r) = X_n(z)$ of the atoms of distant astronomical objects differs from the laboratory value X_n according to equation

$$X_n(z) = \frac{X_n}{1+z}.$$

This equation has consequences regarding the degree of ionization of distant astronomical objects. In other words, the redshift z affects the degree of ionization of atoms in distant astronomical objects. Boltzmann's formula

$$\frac{N_n}{N_1} = \frac{g_n}{g_1} \exp\left(-\frac{X_n}{KT}\right)$$

gives the number of excited atoms N_n, that occupy the energy level n on a stellar surface which is in thermodynamic equilibrium. With X_n we denote the excitation energy from the ground energy level 1 to the energy level n, T denotes the temperature of the stellar surface in Kelvins $K = 1.38 \times 10^{-23} \frac{J}{K}$ is Boltzmann's constant, and g_n is the degree of degeneracy of energy level n (that is, the number of energy levels in which the energy level n splits in a magnetic field). At distant astronomical objects Boltzmann's formula becomes

$$\frac{N_n}{N_1} = \frac{g_n}{g_1} \exp\left(-\frac{X_n}{KT(1+z)}\right).$$

From this equation it follows that the degree of ionization at distant astronomical objects is greater than expected. The mathematical calculations lead to the conclusion that the Universe went through a phase of ionization. The dependence of the degree of ionization, as well as of the Thomson and Klein-Nishina scattering coefficients, on the redshift z, demands an overall re-evaluation of the electromagnetic spectra we receive from distant astronomical objects.

The law of selfvariations correctly predicts the structures in the Universe. It predicts the monstrous webs of matter in between vast expanses of empty space which we observe with current observational instruments. At smaller scales, it predicts galaxies and galactic clusters.

The theory of selfvariations also solves a fundamental problem concerning physical reality, which the physical theories of the last century were unable to solve: the arrow of time is included within the equations of the theory of selfvariations. The Universe comes from the vacuum and evolves towards a particular direction defined by the selfvariations. As mentioned earlier, at cosmological scales, all the equations resulting from the law of selfvariations give at the limit, for $r \to \infty$, that the initial form of the Universe only slightly differs from the vacuum at a temperature of 0 K. The origin of matter from the vacuum, in combination with the principles of conservation, with which the law of selfvariations agrees, necessitate that the energy content of the Universe remains zero. The selfvariations continually "remove" the Universe from the state of the vacuum, while at the same time the Universe remains consistent with its origin.

In contrast to what happens at the macrocosm, the equations predict that in the laboratory the arrow of time does not exist. This prediction definitively solves the problem with the arrow of time.

A measure of the future evolution of the Universe is the rate of increase of the redshift z predicted by the law of self-variations. Substituting the arithmetic values of the parameters into the corresponding equation, we get

$$\dot{z} = z \cdot 6.3 \times 10^{-11} \text{year}^{-1}.$$

It is very characteristic the fact that one simple differential equation, having as a unique unknown the rest mass, contains as information, and at the same time justifies, the totality of the cosmological data, as we observe and record them, from the time of Hubble up to the present. Generally, the equations of the theory of Selfvariations contain an extremely large amount of data and information.

2 The study of the selfvariations for an arbitrarily moving point particle

2.1 Introduction

In this article we present the fundamental study for the mathematical background of the theory of selfvariations. We prove a set of equations which permits us the following: We can represent in the surrounding spacetime of a material particle any kinematic characteristic which concerns the material particle. At every point of spacetime, the velocity, the acceleration, the tangent vector, the curvature and the torsion of the trajectory of the material particle can be mapped in a one-to-one correspondence. This mapping allows us to take the next step: we exactly determine the contribution of the material particle to the energy content of the surrounding spacetime. What emerges is a continuous interaction of every material particle with the surrounding spacetime. The equations are proven for a material point particle in arbitrary motion. We

present a more general statement of the equations in the paragraph 8.

2.2 Arbitrarily moving material point particle

The theory of selfvariations is based upon two hypotheses which are taken as axioms.

a) The rest mass and the electric charge of the material particles increase slightly with the passage of time. We shall call this increase "selfvariations".

b) The consequences of the selfvariations propagate within the four-dimensional spacetime with a vanishing four-dimensional arc length:

$$dS^2 = 0.$$

In an inertial frame of reference, according to the second postulate, the velocity of propagation of the selfvariations remains constant as a vector

$$\boldsymbol{v} = \begin{bmatrix} v_x \\ v_y \\ v_z \end{bmatrix} = \text{constant.} \tag{1}$$

This vector has magnitude

$$\|\boldsymbol{v}\| = \sqrt{v_x^2 + v_y^2 + v_z^2} = c. \tag{2}$$

The selfvariations cause energy changes to every material particle and, as a consequence, energy, linear momentum and angular momentum propagate into the surrounding spacetime.

We shall later call the carrier of this energy, "generalized photon". Initially, we will refer to the generalized photon as a signal emitted by the material particle, moving with velocity $\boldsymbol{v}$, and, as our study advances, its properties as a real physical object will be revealed.

We consider an inertial frame of reference $S(0, x, y, z, t)$ and a material point particle moving with velocity $\mathbf{u}$ as depicted in figure 4.

At moment t, when the particle is located at point

$$P(x_p(t), y_p(t), z_p(t), t),$$

the rest mass m_0 and the electric charge q of the particle act at point $A(x, y, z, t)$ with the value they had at time $\Delta t = \frac{\|\mathbf{r}\|}{c} = \frac{r}{c}$, when the material particle was located at $E(x_p(t - \frac{r}{c}),$ $y_p(t - \frac{r}{c}), z_p(t - \frac{r}{c}), t - \frac{r}{c})$. During the time interval $\Delta t = \frac{r}{c}$ the material particle moved from point E to point P, while the generalized photon moved from point E to point A. We now denote

$$w = t - \frac{r}{c}. \tag{3}$$

Hence, the coordinates of E are

$$E(x_p(w), y_p(w), z_p(w), w). \tag{4}$$
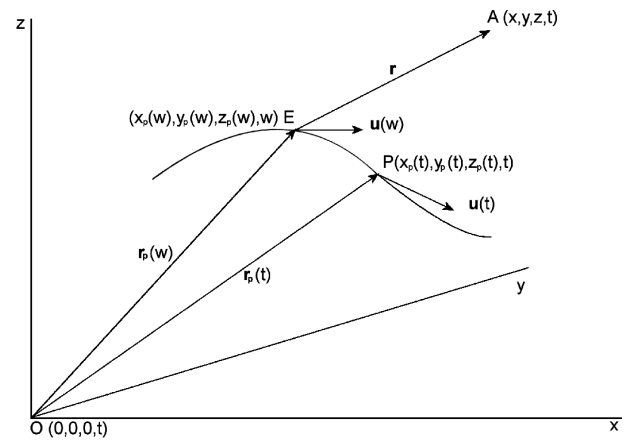
Fig. 4: Material point particle in arbitrary motion. As the material particle moves from point $E(x_p(w), y_p(w), z_p(w), w)$ to point $P(x_p(t), y_p(t), z_p(t), t)$, a generalized photon moves from point $E(x_p(w), y_p(w), z_p(w), w)$ to point $A(x, y, z, t)$.

The vector $\mathbf{r} = \overrightarrow{EA}$ of figure 4 is given by

$$\mathbf{r} = \overrightarrow{EA} = \begin{bmatrix} x - x_p(w) \\ y - y_p(w) \\ z - z_p(w) \end{bmatrix}. \tag{5}$$

The velocity of propagation of the selfvariations $\boldsymbol{v}$ is given by

$$\boldsymbol{v} = \frac{c}{r}\mathbf{r} = \frac{c}{r}\begin{bmatrix} x - x_p(w) \\ y - y_p(w) \\ z - z_p(w) \end{bmatrix}. \tag{6}$$

Here,

$$r = \|\mathbf{r}\| = \sqrt{\left(x - x_p(w)\right)^2 + \left(y - y_p(w)\right)^2 + \left(z - z_p(w)\right)^2}. \tag{7}$$

The velocity $\mathbf{u} = \mathbf{u}(w)$ of the material particle at point E, where it emitted the generalized photon, is

$$\mathbf{u} = \mathbf{u}(w) = \begin{bmatrix} \dfrac{dx_p(w)}{dw} \\ \dfrac{dy_p(w)}{dw} \\ \dfrac{dz_p(w)}{dw} \end{bmatrix}. \tag{8}$$

From equation (7) we have

$$\begin{aligned} \frac{\partial r}{\partial t} &= \frac{1}{2r}\left[2\left((x - x_p(w))\left(-\frac{dx_p(w)}{dw}\frac{\partial w}{\partial t}\right)\right)\right] \\ &+ \frac{1}{2r}\left[2\left((y - y_p(w))\left(-\frac{dy_p(w)}{dw}\frac{\partial w}{\partial t}\right)\right)\right] \\ &+ \frac{1}{2r}\left[2\left((z - z_p(w))\left(-\frac{dz_p(w)}{dw}\frac{\partial w}{\partial t}\right)\right)\right]. \end{aligned}$$

Taking into account equations (5) and (6) we have

$$\frac{\partial r}{\partial t} = -\frac{1}{r}(\mathbf{r} \cdot \mathbf{u})\frac{\partial w}{\partial t}.$$

And with equation (3) we get

$$\frac{\partial r}{\partial t} = -\frac{1}{r}(\mathbf{r} \cdot \mathbf{u})\left(1 - \frac{\partial r}{c\partial t}\right).$$

Taking into consideration that $\frac{\mathbf{r}}{r} = \frac{\upsilon}{c}$, as deduced by equation (6) we obtain

$$\frac{\partial r}{\partial t} = -\frac{\upsilon \cdot \mathbf{u}}{c}\left(1 - \frac{\partial r}{c\partial t}\right)$$

and finally

$$\frac{\partial r}{\partial t} = -\frac{\upsilon \cdot \mathbf{u}}{c\left(1 - \frac{\upsilon \cdot \mathbf{u}}{c^2}\right)} \qquad (9)$$

where $\mathbf{u} = \mathbf{u}(w)$ and $\upsilon \cdot \mathbf{u} = u_x u_x + u_y u_y + u_z u_z$.

Similarly, starting from equation (7) and differentiating with respect to x, y, z we get

$$\nabla r = \begin{bmatrix} \dfrac{\partial r}{\partial x} \\[2mm] \dfrac{\partial r}{\partial y} \\[2mm] \dfrac{\partial r}{\partial z} \end{bmatrix} = \frac{1}{1 - \dfrac{\upsilon \cdot \mathbf{u}}{c^2}}\frac{\upsilon}{c}. \qquad (10)$$

From equation (3) we obtain initially

$$\frac{\partial w}{\partial t} = \frac{1}{1 - \dfrac{\upsilon \cdot \mathbf{u}}{c^2}}. \qquad (11)$$

Similarly, from equation (3) we have

$$\nabla w = \nabla\left(t - \frac{r}{c}\right) = -\frac{1}{c}\nabla r$$

and, in combination with equation (10), we get

$$\nabla w = -\frac{1}{c^2\left(1 - \dfrac{\upsilon \cdot \mathbf{u}}{c^2}\right)}\upsilon. \qquad (12)$$

From equation (7) and after differentiating with respect to x, we get

$$\begin{aligned}\frac{\partial r}{\partial x} =& \frac{1}{2r}\left[2(x - x_p(w))\left(1 - \frac{\partial x_p(w)}{\partial x}\right)\right] - \\ &- \frac{1}{2r}\left[2(y - y_p(w))\frac{\partial y_p(w)}{\partial x}\right] - \\ &- \frac{1}{2r}\left[2(z - z_p(w))\frac{\partial z_p(w)}{\partial x}\right].\end{aligned}$$

Equivalently,

$$\begin{aligned}\frac{\partial r}{\partial x} =& \frac{1}{r}\left[(x - x_p(w))\left(1 - \frac{dx_p(w)}{dw}\frac{\partial w}{\partial x}\right)\right] - \\ &- \frac{1}{r}\left[(y - y_p(w))\left(\frac{dy_p(w)}{dw}\frac{\partial w}{\partial x}\right)\right] - \\ &- \frac{1}{r}\left[(z - z_p(w))\left(\frac{dz_p(w)}{dw}\frac{\partial w}{\partial x}\right)\right]\end{aligned}$$

and also,

$$\begin{aligned}\frac{\partial r}{\partial x} =& \frac{x - x_p(w)}{r} - \frac{1}{r}\frac{\partial w}{\partial x}\left[(x - x_p(w))\left(\frac{dx_p(w)}{dw}\right)\right] - \\ &- \frac{1}{r}\frac{\partial w}{\partial x}\left[(y - y_p(w))\left(\frac{dy_p(w)}{dw}\right) + (z - z_p(w))\left(\frac{dz_p(w)}{dw}\right)\right].\end{aligned}$$

Taking into account equations (8) and (6) we arrive at

$$\frac{\partial r}{\partial x} = \frac{\upsilon_x}{c} - \frac{\upsilon \cdot \mathbf{u}}{c}\frac{\partial w}{\partial x}$$

and substituting

$$\frac{\partial w}{\partial x} = -\frac{\upsilon_x}{c^2\left(1 - \dfrac{\upsilon \cdot \mathbf{u}}{c^2}\right)^2}$$

as inferred from equation (12), we finally obtain

$$\frac{\partial r}{\partial x} = -\frac{1}{c\left(1 - \dfrac{\upsilon \cdot \mathbf{u}}{c^2}\right)}\upsilon_x. \qquad (13)$$

Following the same procedure differentiating with respect to y and z, we finally have

$$\nabla r = \frac{1}{\left(1 - \dfrac{\upsilon \cdot \mathbf{u}}{c^2}\right)}\frac{\upsilon}{c}. \qquad (14)$$

Differentiating with respect to time t, we obtain from equation (5)

$$\frac{\partial \mathbf{r}}{\partial t} = \begin{bmatrix} -\dfrac{\partial x_p(w)}{\partial t} \\[2mm] -\dfrac{\partial y_p(w)}{\partial t} \\[2mm] -\dfrac{\partial x_p(w)}{\partial t} \end{bmatrix} = \begin{bmatrix} -\dfrac{dx_p(w)}{dw}\dfrac{\partial w}{\partial t} \\[2mm] -\dfrac{dy_p(w)}{dw}\dfrac{\partial w}{\partial t} \\[2mm] -\dfrac{dx_p(w)}{dw}\dfrac{\partial w}{\partial t} \end{bmatrix}.$$

Taking into consideration equation (8) $\frac{\partial \mathbf{r}}{\partial t} = -\frac{\partial w}{\partial t}\mathbf{u}$, and in combination with equation (11), we finally get

$$\frac{\partial \mathbf{r}}{\partial t} = -\frac{1}{\left(1 - \dfrac{\upsilon \cdot \mathbf{u}}{c^2}\right)}\mathbf{u}. \qquad (15)$$

From equation (6) we successively obtain

$$\upsilon = \frac{c}{r}\mathbf{r}$$

$$\frac{\partial \boldsymbol{v}}{\partial t} = -\frac{c}{r^2}\frac{\partial r}{\partial t}\mathbf{r} + \frac{c}{r}\frac{\partial \mathbf{r}}{\partial t}$$

$$\frac{\partial \boldsymbol{v}}{\partial t} = -\frac{1}{r}\frac{\partial r}{\partial t}\boldsymbol{v} + \frac{c}{r}\frac{\partial \mathbf{r}}{\partial t} \qquad (16)$$

taking into account that $\boldsymbol{v} = \frac{c}{r}\mathbf{r}$. Substituting into equation (16) the quantity $\frac{\partial r}{\partial t}$, from equation (9), and $\frac{\partial \mathbf{r}}{\partial t}$, from (15), we finally obtain relation

$$\frac{\partial \boldsymbol{v}}{\partial t} = \frac{c}{r\left(1 - \dfrac{\boldsymbol{v}\cdot\mathbf{u}}{c^2}\right)}\left[\frac{(\boldsymbol{v}\cdot\mathbf{u})}{c^2}\boldsymbol{v} - \mathbf{u}\right]. \qquad (17)$$

Starting from equation (6) we get

$$v_x = \frac{c}{r}(x - x_p(w))$$

and differentiating with respect to x we get

$$\frac{\partial v_x}{\partial x} = -\frac{c}{r^2}\frac{\partial r}{\partial x}(x - x_p(w)) + \frac{c}{r}\left(1 - \frac{\partial x_p(w)}{\partial x}\right)$$

$$\frac{\partial v_x}{\partial x} = -\frac{c}{r^2}\frac{\partial r}{\partial x}(x - x_p(w)) + \frac{c}{r}\left(1 - \frac{dx_p(w)}{dw}\frac{\partial w}{\partial x}\right).$$

Since $\frac{dx_p(w)}{dw} = u_x$, as arises from equation (8), we have that

$$\frac{\partial v_x}{\partial x} = -\frac{c}{r^2}\frac{\partial r}{\partial x}(x - x_p(w)) + \frac{c}{r}\left(1 - u_x\frac{\partial w}{\partial x}\right)$$

and considering that $\frac{\partial r}{\partial x} = -\frac{1}{c\left(1 - \frac{\boldsymbol{v}\cdot\mathbf{u}}{c^2}\right)}v_x$ from equation (13), and that $\frac{\partial w}{\partial x} = \frac{1}{c^2\left(1 - \frac{\boldsymbol{v}\cdot\mathbf{u}}{c^2}\right)}v_x$ from equation (12), we get

$$\frac{\partial v_x}{\partial x} = -\frac{v_x^2}{cr\left(1 - \dfrac{\boldsymbol{v}\cdot\mathbf{u}}{c^2}\right)} + \frac{c}{r}\left(1 + \frac{v_x u_x}{c^2\left(1 - \dfrac{\boldsymbol{v}\cdot\mathbf{u}}{c^2}\right)}\right)$$

and finally

$$\frac{\partial v_x}{\partial x} = \frac{c}{r} + \frac{v_x(u_x - v_x)}{cr\left(1 - \dfrac{\boldsymbol{v}\cdot\mathbf{u}}{c^2}\right)}. \qquad (18)$$

Working similarly, we finally obtain

$$\frac{\partial v_i}{\partial x_j} = \begin{cases} \dfrac{c}{r} + \dfrac{v_i(u_i - v_i)}{cr\left(1 - \dfrac{\boldsymbol{v}\cdot\mathbf{u}}{c^2}\right)}, & \text{for } i = j \\[3mm] \dfrac{v_j(u_i - v_i)}{cr\left(1 - \dfrac{\boldsymbol{v}\cdot\mathbf{u}}{c^2}\right)}, & \text{for } i \neq j \end{cases} \qquad (19)$$

where $i, j = 1, 2, 3$ and $(x_1, x_2, x_3) = (x, y, z)$.

Equations (19) can be summarized in equation [1–3]

$$\text{grad } \boldsymbol{v} = \frac{c}{r}I + \frac{1}{r\left(1 - \dfrac{\boldsymbol{v}\cdot\mathbf{u}}{c^2}\right)c} \otimes (\mathbf{u} - \boldsymbol{v}) \qquad (20)$$

where,

$$\text{grad } \boldsymbol{v} = \begin{bmatrix} \dfrac{\partial v_x}{\partial x} & \dfrac{\partial v_x}{\partial y} & \dfrac{\partial v_x}{\partial z} \\[2mm] \dfrac{\partial v_y}{\partial x} & \dfrac{\partial v_y}{\partial y} & \dfrac{\partial v_y}{\partial z} \\[2mm] \dfrac{\partial v_z}{\partial x} & \dfrac{\partial v_z}{\partial y} & \dfrac{\partial v_z}{\partial z} \end{bmatrix}$$

$$I = \begin{bmatrix} 1 & 0 & 0 \\ 0 & 1 & 0 \\ 0 & 0 & 1 \end{bmatrix}$$

$$\boldsymbol{\alpha} \otimes \boldsymbol{\beta} = \begin{bmatrix} \alpha_1\beta_1 & \alpha_2\beta_1 & \alpha_3\beta_1 \\ \alpha_1\beta_2 & \alpha_2\beta_2 & \alpha_3\beta_2 \\ \alpha_1\beta_3 & \alpha_2\beta_3 & \alpha_3\beta_3 \end{bmatrix}. \qquad (21)$$

This holds for any two arbitrary vectors

$$\boldsymbol{\alpha} = \begin{bmatrix} \alpha_1 \\ \alpha_2 \\ \alpha_3 \end{bmatrix} \quad \text{and} \quad \boldsymbol{\beta} = \begin{bmatrix} \beta_1 \\ \beta_2 \\ \beta_3 \end{bmatrix}.$$

We now have $\nabla\boldsymbol{v} = \frac{\partial v_x}{\partial x} + \frac{\partial v_y}{\partial y} + \frac{\partial v_z}{\partial z}$, and from equations (19) we get

$$\nabla\boldsymbol{v} = \frac{3c}{r} + \frac{v_x(u_x - v_x) + v_y(u_y - v_y) + v_z(u_z - v_z)}{cr\left(1 - \dfrac{\boldsymbol{v}\cdot\mathbf{u}}{c^2}\right)}$$

$$\nabla\boldsymbol{v} = \frac{3c}{r} + \frac{v_x u_x + v_y u_y + v_z u_z - \left(v_x^2 + v_y^2 + v_z^2\right)}{cr\left(1 - \dfrac{\boldsymbol{v}\cdot\mathbf{u}}{c^2}\right)}$$

and since $v_x^2 + v_y^2 + v_z^2 = c^2$ and $v_x u_x + v_y u_y + v_z u_z = \boldsymbol{v}\cdot\mathbf{u}$, we see that

$$\nabla\boldsymbol{v} = \frac{3c}{r} + \frac{\boldsymbol{v}\cdot\mathbf{u} - c^2}{cr\left(1 - \dfrac{\boldsymbol{v}\cdot\mathbf{u}}{c^2}\right)}.$$

Finally, we arrive at relation

$$\nabla\boldsymbol{v} = \frac{2c}{r}. \qquad (22)$$

Now, we consider the curl of vector $\boldsymbol{v}$

$$\nabla \times \boldsymbol{v} = \text{curl } \boldsymbol{v} = \begin{bmatrix} \dfrac{\partial v_z}{\partial x} - \dfrac{\partial v_y}{\partial z} \\[2mm] \dfrac{\partial v_x}{\partial z} - \dfrac{\partial v_z}{\partial x} \\[2mm] \dfrac{\partial v_y}{\partial x} - \dfrac{\partial v_x}{\partial y} \end{bmatrix}. \qquad (23)$$

Taking into account equations (19) we obtain

$$\nabla \times \boldsymbol{v} = \text{curl } \boldsymbol{v} = \frac{1}{cr\left(1 - \dfrac{\boldsymbol{v}\cdot\mathbf{u}}{c^2}\right)}(\boldsymbol{v} \times \mathbf{u}) \qquad (24)$$

where,

$$\boldsymbol{v} \times \mathbf{u} = \begin{bmatrix} v_y u_z - v_z u_y \\ v_z u_x - v_x u_z \\ v_x u_y - v_y u_x \end{bmatrix}.$$

We now consider the acceleration vector

$$\boldsymbol{\alpha} = \boldsymbol{\alpha}(w) = \frac{d\mathbf{u}(w)}{dw} = \begin{bmatrix} \dfrac{d\mathbf{u_x}(w)}{dw} \\[2mm] \dfrac{d\mathbf{u_y}(w)}{dw} \\[2mm] \dfrac{d\mathbf{u_z}(w)}{dw} \end{bmatrix} \qquad (25)$$

of the material particle at the moment w, located at point E of figure 4. We have that

$$\frac{\partial u_x}{\partial t} = \frac{\partial u_x(w)}{\partial t} = \frac{du_x(w)}{dw}\frac{\partial w}{\partial t} = \alpha_x \frac{\partial w}{\partial t}$$

and since, from equation (11), it is $\frac{\partial w}{\partial t} = \frac{1}{1 - \frac{v \cdot u}{c^2}}$, we get $\frac{\partial u_x}{\partial t} = \frac{\alpha_x}{1 - \frac{v \cdot u}{c^2}}$. Working similarly for the differentials $\frac{\partial u_y}{\partial t}$ and $\frac{\partial u_z}{\partial t}$, we get

$$\frac{\partial \mathbf{u}}{\partial t} = \frac{1}{1 - \dfrac{\boldsymbol{v} \cdot \mathbf{u}}{c^2}} \boldsymbol{\alpha}. \qquad (26)$$

For the differentiation of the velocity $\mathbf{u} = \mathbf{u}(w)$ with respect to x, y, z we initially get

$$\frac{\partial u_x}{\partial x} = \frac{\partial u_x(w)}{\partial x} = \frac{du_x(w)}{dw}\frac{\partial w}{\partial x} = \alpha_x \frac{\partial w}{\partial x}.$$

Similarly, from equation (12) we have that $\frac{\partial w}{\partial x} = -\frac{u_x}{c^2\left(1 - \frac{v \cdot u}{c^2}\right)}$, hence $\frac{\partial u_x}{\partial x} = -\frac{v_x \alpha_x}{c^2\left(1 - \frac{v \cdot u}{c^2}\right)}$.

Working similarly we finally obtain

$$\frac{\partial u_i}{\partial x_j} = -\frac{v_j \alpha_i}{c^2\left(1 - \dfrac{\boldsymbol{v} \cdot \mathbf{u}}{c^2}\right)} \qquad i, j = 1, 2, 3. \qquad (27)$$

Here we use the notation $(x_1, x_2, x_3) = (x, y, z)$.

From equation (27) we obtain

$$grad\,\mathbf{u} = -\frac{1}{r\left(1 - \dfrac{\boldsymbol{v} \cdot \mathbf{u}}{c^2}\right)}\frac{\boldsymbol{v}}{c} \otimes \mathbf{u}. \qquad (28)$$

We now consider the vector

$$\mathbf{b} = \mathbf{b}(w) = \frac{d\boldsymbol{\alpha}(w)}{dw}. \qquad (29)$$

Working as we did in order to prove equations (17), (26) and (27), we arrive at relations

$$\frac{\partial \boldsymbol{\alpha}}{\partial t} = \frac{1}{1 - \dfrac{\boldsymbol{v} \cdot \mathbf{u}}{c^2}}\mathbf{b} \qquad (30)$$

$$\frac{\partial \alpha_i}{\partial x_j} = -\frac{v_j b_i}{c^2\left(1 - \dfrac{\boldsymbol{v} \cdot \mathbf{u}}{c^2}\right)} \qquad i, j = 1, 2, 3 \qquad (31)$$

where $(x_1, x_2, x_3) = (x, y, z)$, and

$$grad\,\boldsymbol{\alpha} = -\frac{1}{c\left(1 - \dfrac{\boldsymbol{v} \cdot \mathbf{u}}{c^2}\right)}\frac{\boldsymbol{v}}{c} \otimes \mathbf{b}. \qquad (32)$$

The equations of this paragraph express the fact that in every inertial reference frame the velocity $\boldsymbol{v}$ of the selfvariations remains constant as a vector with magnitude $\|\boldsymbol{v}\| = c$. It can easily be proven that all the equations are consistent with the Lorentz-Einstein transformations, as we pass from one inertial reference frame to another. The equations we have proven are fundamental for the theory of selfvariations. As we advance our study, we will find that they allow us to correlate any physical quantity defined on the material particle, with any physical quantity defined on the surrounding spacetime. Using the concept of information, we can correlate any information concerning the material particle with any information concerning the surrounding spacetime. Part of this information are the potential fields, while the quantum phenomena arise spontaneously.

2.3 The trigonometric form of the velocity of selfvariations

Starting from equation (2) we get $\left\|\frac{\boldsymbol{v}}{c}\right\| = 1$ for every inertial reference frame. We express the unit vector $\frac{\boldsymbol{v}}{c}$ into the trigonometric form

$$\frac{\boldsymbol{v}}{c} = \begin{bmatrix} \dfrac{v_x}{c} \\[2mm] \dfrac{v_y}{c} \\[2mm] \dfrac{v_z}{c} \end{bmatrix} = \begin{bmatrix} \cos\delta \\ \sin\delta\cos\omega \\ \sin\delta\sin\omega \end{bmatrix} \qquad (33)$$

where $\delta = \delta(x, y, z, t)$ and $\omega = \omega(x, y, z, t)$ are functions of the coordinates x, y, z, t in an inertial frame of reference $S(0, x, y, z, t)$.

From equation (33) we see that

$$\frac{v_x}{c} = \cos\delta = \frac{\boldsymbol{v}}{c}\boldsymbol{e}_1 \qquad (34a)$$

$$\frac{v_y}{c} = \sin\delta\cos\omega = \frac{\boldsymbol{v}}{c}\boldsymbol{e}_2 \qquad (34b)$$

$$\frac{v_z}{c} = \sin\delta\sin\omega = \frac{\boldsymbol{v}}{c}\boldsymbol{e}_3 \qquad (34c)$$

where

$$\boldsymbol{e}_1 = \hat{\boldsymbol{x}} = \begin{bmatrix} 1 \\ 0 \\ 0 \end{bmatrix}, \quad \boldsymbol{e}_2 = \hat{\boldsymbol{y}} = \begin{bmatrix} 0 \\ 1 \\ 0 \end{bmatrix}, \quad \boldsymbol{e}_3 = \hat{\boldsymbol{z}} = \begin{bmatrix} 0 \\ 0 \\ 1 \end{bmatrix}.$$

We now consider the vectors

$$\boldsymbol{\beta} = \begin{bmatrix} -\sin\delta \\ \cos\delta\cos\omega \\ \cos\delta\sin\omega \end{bmatrix} \qquad (35)$$

and

$$\gamma = \begin{bmatrix} 0 \\ -\sin\omega \\ \cos\omega \end{bmatrix}. \tag{36}$$

It is easily proven that the set of vectors $\{\frac{v}{c}, \beta, \gamma\}$ form a right-handed orthonormal vector basis which is defined at every point A of figure 4. Furthermore, the following relations hold:

$$\begin{aligned} \frac{\partial}{\partial \delta}\left(\frac{v}{c}\right) &= \beta \\ \frac{\partial}{\partial \omega}\left(\frac{v}{c}\right) &= \sin\delta\,\gamma \\ \frac{\partial \beta}{\partial \delta} &= -\frac{v}{c} \\ \frac{\partial \beta}{\partial \omega} &= \cos\delta\,\gamma \\ \frac{\partial \gamma}{\partial \delta} &= 0 \\ \frac{\partial \gamma}{\partial \omega} &= -\sin\delta\frac{v}{c} - \cos\delta\,\beta \end{aligned} \tag{37}$$

Differentiating the vectors $\frac{v}{c}, \beta, \gamma$ with respect to x, y, z, t we obtain the following equations:

$$\nabla \cdot \left(\frac{v}{c}\right) = \beta \cdot \nabla\delta + \sin\delta\,\gamma \cdot \nabla\omega \tag{38a}$$

$$\frac{\partial}{\partial t}\left(\frac{v}{c}\right) = \frac{\partial\delta}{\partial t}\beta + \sin\delta\frac{\partial\omega}{\partial t}\gamma \tag{38b}$$

$$\nabla \times \frac{v}{c} = \nabla\delta \times \beta + \sin\delta\nabla\omega \otimes \gamma \tag{38c}$$

$$\text{grad}\,\frac{v}{c} = \nabla\delta \otimes \beta + \sin\delta\nabla\omega \otimes \gamma \tag{38d}$$

$$\nabla \cdot \beta = -\frac{v}{c}\nabla\delta + \cos\delta\,\gamma \cdot \nabla\omega \tag{39a}$$

$$\frac{\partial\beta}{\partial t} = -\frac{\partial\delta}{\partial t}\frac{v}{c} + \cos\delta\frac{\partial\omega}{\partial t}\gamma \tag{39b}$$

$$\nabla \times \beta = \frac{v}{c} \times \nabla\delta - \cos\delta\,\gamma \times \nabla\omega \tag{39c}$$

$$\text{grad}\,\beta = -\nabla\delta \otimes \frac{v}{c} + \cos\delta\nabla\omega \otimes \gamma \tag{39d}$$

$$\nabla \cdot \gamma = -\sin\delta\frac{v}{c}\nabla\omega - \cos\delta\,\beta \cdot \nabla\omega \tag{40a}$$

$$\frac{\partial\gamma}{\partial t} = -\sin\delta\frac{\partial\omega}{\partial t}\frac{v}{c} - \cos\delta\frac{\partial\omega}{\partial t}\beta \tag{40b}$$

$$\nabla \times \gamma = \sin\delta\frac{v}{c} \times \nabla\omega + \cos\delta\,\beta \times \nabla\omega \tag{40c}$$

$$\text{grad}\,\gamma = -\sin\delta\nabla\omega \otimes \frac{v}{c} - \cos\delta\nabla\omega \otimes \beta. \tag{40d}$$

We prove indicatively equation (38)(a). The rest of the equations are proven along similar lines. Taking into account equation (33) we get

$$\nabla \cdot \left(\frac{v}{c}\right) = \frac{\partial}{\partial x}(\cos\delta) + \frac{\partial}{\partial y}(\sin\delta\cos\omega) + \frac{\partial}{\partial z}(\sin\delta\sin\omega) =$$

$$-\sin\delta\frac{\partial\delta}{\partial x} + \cos\delta\frac{\partial\delta}{\partial y}\cos\omega + \cos\delta\frac{\partial\delta}{\partial z}\sin\omega$$

$$+ 0 - \sin\delta\sin\omega\frac{\partial\omega}{\partial y} + \sin\delta\cos\omega\frac{\partial\omega}{\partial z}$$

and considering equations (35) and (36), as well as relations

$$\nabla\delta = \begin{bmatrix} \dfrac{\partial\delta}{\partial x} \\ \dfrac{\partial\delta}{\partial y} \\ \dfrac{\partial\delta}{\partial z} \end{bmatrix}, \qquad \nabla\omega = \begin{bmatrix} \dfrac{\partial\omega}{\partial x} \\ \dfrac{\partial\omega}{\partial y} \\ \dfrac{\partial\omega}{\partial z} \end{bmatrix}$$

we finally obtain

$$\nabla \cdot \left(\frac{v}{c}\right) = \beta \cdot \nabla\delta + \sin\delta\,\gamma \cdot \omega.$$

We now expand the vector of velocity $u = u(w)$ with respect to the vector basis $\{\frac{v}{c}, \beta, \gamma\}$ as

$$u = u(w) = u_1\frac{v}{c} + u_2\beta + u_3\gamma = \left(u \cdot \frac{v}{c}\right)\frac{v}{c} + (u \cdot \beta)\beta + (u \cdot \gamma)\gamma$$

and combining with equations (17) we get

$$\frac{\partial}{\partial t}\left(\frac{v}{c}\right) = \frac{1}{r\left(1 - \dfrac{v \cdot u}{c^2}\right)}\left[\frac{(v \cdot u)}{c}\frac{v}{c} - \left(u\frac{v}{c}\right)\frac{v}{c} - (u \cdot \beta)\beta - (u \cdot \gamma)\gamma\right]$$

$$\frac{\partial}{\partial t}\left(\frac{v}{c}\right) = \frac{1}{r\left(1 - \dfrac{v \cdot u}{c^2}\right)}\left[(u \cdot \beta)\beta + (u \cdot \gamma)\gamma\right].$$

Considering equations (38)(b) we get

$$\frac{\partial\delta}{\partial t}\beta + \sin\delta\frac{\partial\omega}{\partial t}\gamma = -\frac{1}{r\left(1 - \dfrac{v \cdot u}{c^2}\right)}\left[(u \cdot \beta)\beta + (u \cdot \gamma)\gamma\right]$$

and finally

$$\frac{\partial\delta}{\partial t} = -\frac{u \cdot \beta}{r\left(1 - \dfrac{v \cdot u}{c^2}\right)} \tag{41}$$

$$\sin\delta\frac{\partial\omega}{\partial t} = -\frac{u \cdot \gamma}{r\left(1 - \dfrac{v \cdot u}{c^2}\right)} \tag{42}$$

because of the linear independence of the vectors β and γ.

We now write vectors $\nabla\delta$ and $\nabla\omega$ as a linear combination of vectors $\frac{v}{c}, \beta, \gamma$.

$$\nabla\delta = \lambda_1\frac{v}{c} + K\beta + L\gamma \tag{43}$$

$$\nabla\omega = \lambda_2 \frac{\boldsymbol{v}}{c} + M\boldsymbol{\beta} + N\boldsymbol{\gamma}. \qquad (44)$$

We combine equations (17) and (20), and get relation

$$\frac{\partial}{\partial t}\left(\frac{\boldsymbol{v}}{c}\right) + \left(grad\frac{\boldsymbol{v}}{c}\right)\boldsymbol{v} = \frac{1}{r\left(1 - \frac{\boldsymbol{v}\cdot\boldsymbol{u}}{c^2}\right)}\left[\left(\frac{\boldsymbol{v}\cdot\boldsymbol{u}}{c^2}\right)\boldsymbol{v} - \boldsymbol{u}\right] +$$

$$+ \left[\frac{1}{r}I + \frac{1}{cr\left(1 - \frac{\boldsymbol{v}\cdot\boldsymbol{u}}{c^2}\right)}\frac{\boldsymbol{v}}{c}\otimes(\boldsymbol{u}-\boldsymbol{v})\right]\boldsymbol{v} =$$

$$\frac{1}{r\left(1 - \frac{\boldsymbol{v}\cdot\boldsymbol{u}}{c^2}\right)}\left[\left(\frac{\boldsymbol{v}\cdot\boldsymbol{u}}{c^2}\right)\boldsymbol{v} - \boldsymbol{u}\right] +$$

$$+ \frac{1}{r}\boldsymbol{v} + \frac{1}{cr\left(1 - \frac{\boldsymbol{v}\cdot\boldsymbol{u}}{c^2}\right)}\left(\frac{\boldsymbol{v}}{c}\otimes(\boldsymbol{u}-\boldsymbol{v})\right)\boldsymbol{v}.$$

Using the identity

$$(\boldsymbol{\alpha}\otimes\boldsymbol{\beta})\,\boldsymbol{c} = (\boldsymbol{\alpha}\cdot\boldsymbol{c})\boldsymbol{\beta} \qquad (45)$$

which holds for every set of vectors $\boldsymbol{\alpha},\boldsymbol{\beta},\boldsymbol{c}$, we see that

$$\frac{\partial}{\partial t}\left(\frac{\boldsymbol{v}}{c}\right) + \left(grad\,\frac{\boldsymbol{v}}{c}\right)\boldsymbol{v} =$$

$$\frac{1}{r\left(1 - \frac{\boldsymbol{v}\cdot\boldsymbol{u}}{c^2}\right)}\left[\left(\frac{\boldsymbol{v}\cdot\boldsymbol{u}}{c^2}\right)\boldsymbol{v} - \boldsymbol{u}\right] + \frac{1}{r}\boldsymbol{v} + \frac{1}{r\left(1 - \frac{\boldsymbol{v}\cdot\boldsymbol{u}}{c^2}\right)}\,(\boldsymbol{v}-\boldsymbol{u}) =$$

$$\frac{1}{r\left(1 - \frac{\boldsymbol{v}\cdot\boldsymbol{u}}{c^2}\right)}\left(\frac{\boldsymbol{v}\cdot\boldsymbol{u}}{c^2}\right)\boldsymbol{v} + \frac{1}{r}\boldsymbol{v} - \frac{1}{r\left(1 - \frac{\boldsymbol{v}\cdot\boldsymbol{u}}{c^2}\right)}\boldsymbol{v} =$$

$$\frac{1}{r\left(1 - \frac{\boldsymbol{v}\cdot\boldsymbol{u}}{c^2}\right)}\left[\left(\frac{\boldsymbol{v}\cdot\boldsymbol{u}}{c^2}\right) + \left(1 - \frac{\boldsymbol{v}\cdot\boldsymbol{u}}{c^2}\right) - 1\right]\boldsymbol{v} = \boldsymbol{0}.$$

That is,

$$\frac{\partial}{\partial t}\left(\frac{\boldsymbol{v}}{c}\right) + \left(grad\,\frac{\boldsymbol{v}}{c}\right)\boldsymbol{v} = \boldsymbol{0}. \qquad (46)$$

Into equation (45) we replace $\frac{\partial}{\partial t}\left(\frac{\boldsymbol{v}}{c}\right)$ from equation (38)(b), and grad $\frac{\boldsymbol{v}}{c}$ from equation (38)(d), and obtain

$$\frac{\partial\delta}{\partial t}\boldsymbol{\beta} + \sin\delta\frac{\partial\omega}{\partial t}\boldsymbol{\gamma} + (\nabla\delta\otimes\boldsymbol{\beta} + \sin\delta\nabla\omega\otimes\boldsymbol{\gamma})\,\boldsymbol{v} = \boldsymbol{0}.$$

Using the identity (45) we get

$$\frac{\partial\delta}{\partial t}\boldsymbol{\beta} + \sin\delta\frac{\partial\omega}{\partial t}\boldsymbol{\gamma} + (\boldsymbol{u}\cdot\nabla\delta)\boldsymbol{\beta} + \sin\delta\,(\boldsymbol{v}\cdot\nabla\omega)\boldsymbol{\gamma} = 0$$

and due to the linear independence of the vectors $\boldsymbol{\beta}$ and $\boldsymbol{\gamma}$ we see that

$$\frac{\partial\delta}{\partial t} + \boldsymbol{v}\cdot\nabla\delta = 0 \qquad (47)$$

$$\frac{\partial\omega}{\partial t} + \boldsymbol{v}\cdot\nabla\omega = 0. \qquad (48)$$

Combining equations (47) and (43) we obtain

$$\frac{\partial\delta}{\partial t} + \lambda_1 = 0$$

$$\lambda_1 = -\frac{\partial\delta}{\partial t}.$$

Through equation (41) we have that

$$\lambda_1 = \frac{\boldsymbol{u}\cdot\boldsymbol{\beta}}{r\left(1 - \frac{\boldsymbol{v}\cdot\boldsymbol{u}}{c^2}\right)}$$

and replacing into equation (43) we get

$$\nabla\delta = \frac{\boldsymbol{u}\cdot\boldsymbol{\beta}}{r\left(1 - \frac{\boldsymbol{v}\cdot\boldsymbol{u}}{c^2}\right)}\frac{\boldsymbol{v}}{c^2} + K\boldsymbol{\beta} + L\boldsymbol{\gamma}. \qquad (49)$$

Performing the corresponding combinations, we arrive at equation

$$\nabla\omega = \frac{\boldsymbol{u}\cdot\boldsymbol{\gamma}}{\sin\delta\,r\left(1 - \frac{\boldsymbol{v}\cdot\boldsymbol{u}}{c^2}\right)}\frac{\boldsymbol{v}}{c} + M\boldsymbol{\beta} + N\boldsymbol{\gamma}. \qquad (50)$$

We shall now prove that $K = \frac{1}{r}$, $L = 0$, $M = 0$, $N = \frac{1}{r\sin\delta}$, hence equations (49) and (50) obtain their final form

$$\nabla\delta = \frac{\boldsymbol{u}\cdot\boldsymbol{\beta}}{r\left(1 - \frac{\boldsymbol{v}\cdot\boldsymbol{u}}{c^2}\right)}\frac{\boldsymbol{v}}{c^2} + \frac{1}{r}\boldsymbol{\beta} \qquad (51)$$

$$\nabla\omega = \frac{\boldsymbol{u}\cdot\boldsymbol{\gamma}}{\sin\delta\,r\left(1 - \frac{\boldsymbol{v}\cdot\boldsymbol{u}}{c^2}\right)}\frac{\boldsymbol{v}}{c^2} + \frac{1}{r\sin\delta}\boldsymbol{\gamma}. \qquad (52)$$

We will prove that $K = \frac{1}{r}$, $L = 0$. In a similar manner we can also calculate the factors M, N. From equation (34)(a) we successively obtain

$$\cos\delta = \frac{v_x}{c}$$

$$-\sin\delta\nabla\delta = \nabla\left(\frac{v_x}{c}\right).$$

We calculate $\nabla\left(\frac{v_x}{c}\right)$ from equations (19), hence we have

$$-\sin\delta\nabla\delta = \frac{1}{r}\boldsymbol{e}_1 - \frac{v_x - u_x}{r\left(1 - \frac{\boldsymbol{v}\cdot\boldsymbol{u}}{c^2}\right)}\frac{\boldsymbol{v}}{c} \qquad (53)$$

where $\boldsymbol{e}_1 = \begin{bmatrix} 1 \\ 0 \\ 0 \end{bmatrix}$.

We take the inner product of equation (53) with vector $\boldsymbol{\beta}$ and obtain

$$-\sin\delta\boldsymbol{\beta}\cdot\nabla\delta = \frac{1}{r}\boldsymbol{e}_1\cdot\boldsymbol{\beta}.$$

From equation (49) we have $\boldsymbol{\beta} \cdot \nabla \delta = K$, hence we have

$$-\sin \delta K = \frac{1}{r} \boldsymbol{e}_1 \cdot \boldsymbol{\beta}.$$

From equation (35) we obtain

$$\boldsymbol{e}_1 \cdot \boldsymbol{\beta} = -\sin \delta.$$

Therefore,

$$-\sin \delta K = \frac{1}{r}(-\sin \delta).$$

Finally, we obtain

$$K = \frac{1}{r}.$$

We take the inner product of equation (53) with vector $\boldsymbol{\gamma}$ and obtain

$$-\sin \delta \boldsymbol{\gamma} \cdot \nabla \delta = \frac{1}{r} \boldsymbol{e}_1 \cdot \boldsymbol{\gamma}.$$

From equation (49) it holds that $\boldsymbol{\gamma} \cdot \nabla \delta = L$, hence

$$-\sin \delta L = \frac{1}{r} \boldsymbol{e}_1 \cdot \boldsymbol{\gamma}.$$

From equation (36) we see that $\boldsymbol{e}_1 \cdot \boldsymbol{\gamma} = 0$, therefore $-\sin \delta L = 0$, and finally $L = 0$.

The equations of this paragraph promote the theory of selfvariations considerably, and their fundamental character will become obvious as our study continues. One first fundamental conclusion emerges from equations (47) and (48). The functions $\delta = \delta(x, y, z, t)$ and $\omega = \omega(x, y, z, t)$ remain invariable on the trajectory of the generalized photon. Through equations (33), (35) and (36) we conclude that the vector basis $\{\frac{\boldsymbol{v}}{c}, \boldsymbol{\beta}, \boldsymbol{\gamma}\}$ accompanies without change, that is remaining constant, the motion of the generalized photon. We can, of course, straightforwardly prove that

$$\frac{\partial}{\partial t}\left(\frac{\boldsymbol{v}}{c}\right) + \left(\text{grad } \frac{\boldsymbol{v}}{c}\right)\boldsymbol{v} = 0$$
$$\frac{\partial \boldsymbol{\beta}}{\partial t} + (\text{grad } \boldsymbol{\beta})\boldsymbol{v} = 0 \qquad (54)$$
$$\frac{\partial \boldsymbol{\gamma}}{\partial t} + (\text{grad } \boldsymbol{\gamma})\boldsymbol{v} = 0$$

by combining equations (38), (39) and (40) with equations (51) and (52).

2.4 The generalized photon as a geometric object. Representation of the trajectory of a material point particle

In the present paragraph we shall look for points A_i in the neighborhood of point $A(x, y, z, t)$ of figure 4, for which the velocity of the generalized photon is the same with the velocity at point $A(x, y, z, t)$ at the same moment t. We use the notation

$$\overrightarrow{AA_i} = d\boldsymbol{R} \qquad (55)$$

and we search for points A_i, i.e. vector $d\boldsymbol{R}$, such that

$$\boldsymbol{v}(\boldsymbol{R}+d\boldsymbol{R}, t) = \boldsymbol{v}(\boldsymbol{R}, t). \qquad (56)$$

According to equations (33), equation (56) is equivalent to the relations

$$\delta(\boldsymbol{R}+d\boldsymbol{R}, t) = \delta(\boldsymbol{R}, t) \qquad (57)$$

and

$$\omega(\boldsymbol{R}+d\boldsymbol{R}, t) = \omega(\boldsymbol{R}, t). \qquad (58)$$

After expanding the functions $\delta(\boldsymbol{R}, t)$ and $\omega(\boldsymbol{R}, t)$ in Taylor series up to the first order terms, we obtain

$$\delta(\boldsymbol{R}+d\boldsymbol{R}, t) = \delta(\boldsymbol{R}, t) + d\boldsymbol{R} \cdot \nabla \delta$$
$$\omega(\boldsymbol{R}+d\boldsymbol{R}, t) = \omega(\boldsymbol{R}, t) + d\boldsymbol{R} \cdot \nabla \omega.$$

Through equations (57) and (58) we have that

$$d\boldsymbol{R} \cdot \nabla \delta = 0 \qquad (59)$$

$$d\boldsymbol{R} \cdot \nabla \omega = 0. \qquad (60)$$

Combining equations (51) and (52) we obtain

$$\boldsymbol{t} = \nabla \delta \times \sin \delta \nabla \omega =$$
$$\frac{\boldsymbol{u} \cdot \boldsymbol{\beta}}{r^2\left(1 - \frac{\boldsymbol{v} \cdot \boldsymbol{u}}{c^2}\right)}\frac{\boldsymbol{v}}{c} \times \boldsymbol{\gamma} + \frac{\boldsymbol{u} \cdot \boldsymbol{\gamma}}{r^2\left(1 - \frac{\boldsymbol{v} \cdot \boldsymbol{u}}{c^2}\right)}\boldsymbol{\beta} \times \frac{\boldsymbol{v}}{c} + \frac{1}{r^2}\boldsymbol{\beta} \times \boldsymbol{\gamma} =$$
$$-\frac{\boldsymbol{u} \cdot \boldsymbol{\beta}}{r^2\left(1 - \frac{\boldsymbol{v} \cdot \boldsymbol{u}}{c^2}\right)}\boldsymbol{\beta} - \frac{\boldsymbol{u} \cdot \boldsymbol{\gamma}}{r^2\left(1 - \frac{\boldsymbol{v} \cdot \boldsymbol{u}}{c^2}\right)}\boldsymbol{\gamma} + \frac{1}{r^2}\frac{\boldsymbol{v}}{c}$$

taking into account that the set of the vectors $\{\frac{\boldsymbol{v}}{c}, \boldsymbol{\beta}, \boldsymbol{\gamma}\}$ form a right-handed orthonormal vector basis. We now have

$$\boldsymbol{t} = \frac{1}{r^2\left(1 - \frac{\boldsymbol{v} \cdot \boldsymbol{u}}{c^2}\right)}\left[\left(1 - \frac{\boldsymbol{v} \cdot \boldsymbol{u}}{c^2}\right)\frac{\boldsymbol{v}}{c} - \left(\frac{\boldsymbol{u}}{c} \cdot \boldsymbol{\beta}\right)\boldsymbol{\beta} - \left(\frac{\boldsymbol{u}}{c} \cdot \boldsymbol{\gamma}\right)\boldsymbol{\gamma}\right]$$

$$\boldsymbol{t} = \frac{1}{r^2\left(1 - \frac{\boldsymbol{v} \cdot \boldsymbol{u}}{c^2}\right)}\left[\frac{\boldsymbol{v}}{c} - \left(\frac{\boldsymbol{v} \cdot \boldsymbol{u}}{c^2}\right)\frac{\boldsymbol{v}}{c} - \left(\frac{\boldsymbol{u}}{c} \cdot \boldsymbol{\beta}\right)\boldsymbol{\beta} - \left(\frac{\boldsymbol{u}}{c} \cdot \boldsymbol{\gamma}\right)\boldsymbol{\gamma}\right]$$

and from equation (41) we get

$$\boldsymbol{t} = \frac{1}{r^2\left(1 - \frac{\boldsymbol{v} \cdot \boldsymbol{u}}{c}\right)}\left(\frac{\boldsymbol{v}}{c} - \frac{\boldsymbol{u}}{c}\right) \neq \boldsymbol{0}. \qquad (61)$$

According to equations (59) and (60) the vector $d\boldsymbol{R}$ is parallel to the vector $\boldsymbol{t} \neq \boldsymbol{0}$, hence we finally arrive at relation

$$d\boldsymbol{R} \parallel \left(\frac{\boldsymbol{v}}{c} - \frac{\boldsymbol{u}}{c}\right) \qquad (62)$$

Thus, we conclude that points A and A_i, at which the generalized photon moves with the same velocity $\boldsymbol{v}$, are arranged parallel to the vector $\frac{\boldsymbol{v}}{c} - \frac{\boldsymbol{u}}{c}$. This conclusion is the result of a more general theorem, which we present in the paragraph
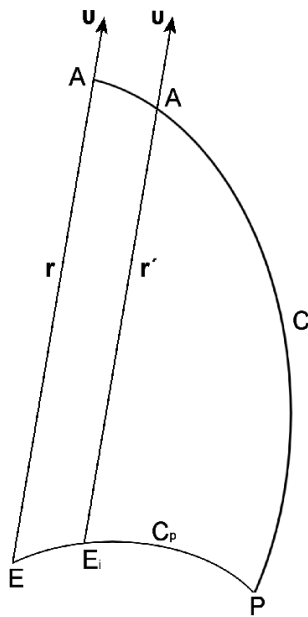
Fig. 5: A material point particle moves from point E to point P on the curved trajectory C_p in the time interval from $w = t - \frac{r}{c}$ to t. The generalized photons emitted by the material particle with the same velocity v, in the time interval $\Delta t = t - w = \frac{r}{c}$, are on curve C at moment t.

8. For the case of a material point particle the theorem gives relation (62).

In figure 4 and for the time interval from $t - \frac{r}{c}$ to t, i.e. for $t - \frac{r}{c} \leq w \leq t$, the generalized photons emitted by the material point particle reside within a sphere with center

$$E\left(x_p\left(t - \frac{r}{c}\right), y_p\left(t - \frac{r}{c}\right), z_p\left(t - \frac{r}{c}\right), t - \frac{r}{c}\right)$$

and radius $r = \|r\|$. During the same time interval the material particle moved from point E to point $P\left(x_p(t), y_p(t), z_p(t), t\right)$.

We now consider a point E_i in the neighborhood of point E and on the trajectory C_p of the material particle as it moves from point E to point P, from which point E_i was emitted the generalized photon which at moment t is located at point A_i, as depicted in figure 5.

Point E_i has coordinates

$$E_i\left(x_p\left(t - \frac{r'}{c}\right), y_p\left(t - \frac{r'}{c}\right), z_p\left(t - \frac{r'}{c}\right), t - \frac{r'}{c}\right),$$

where $v = \frac{c}{r}r = \frac{c}{r'}r'$.

The points E, P, A appear in figure 4 as well as in figure 5, while the points E_i and A_i are shown in figure 5.

For the vector $\overrightarrow{AA_i} = dr$ we have, according to figure 5

$$dr = -r + \overrightarrow{EE_i} + r'$$

$$dr = -r + u\left(\frac{r}{c} - \frac{r'}{c}\right) + r'$$

$$dr = -\frac{v}{c}(r - r') + u\left(\frac{r}{c} - \frac{r'}{c}\right)$$

$$dr = -(r - r')\left(\frac{v}{c} - \frac{u}{c}\right). \tag{63}$$

For the time interval dw, during which the material particle moved from point E to point E_i, it is

$$dw = \left(t - \frac{r'}{c}\right) - \left(t - \frac{r}{c}\right) = \frac{r}{c} - \frac{r'}{c},$$

therefore from equation (63) we obtain

$$\overrightarrow{AA_i} = dr = -c\,dw\left(\frac{v}{c} - \frac{u}{c}\right). \tag{64}$$

In figure 5 we consider curve C which includes all the generalized photons emitted by the material particle during the time interval from $w = t - \frac{r}{c}$ to t towards a particular direction $\frac{v}{c}$, that is, with the same velocity v.

We now consider the tangent vector t [4] of the curve C at point A

$$t = \frac{dr}{\|dr\|} = \frac{\frac{u}{c} - \frac{v}{c}}{\left\|\frac{u}{c} - \frac{v}{c}\right\|} = \frac{u - v}{\|u - v\|} \tag{65}$$

as follows from equation (64). For the three-dimensional arc length dS of curve C at point A we obtain from equation (64)

$$dS = \|dr\| = dw\,\|u - v\|. \tag{66}$$

Now, we calculate the curvature k and the torsion τ of curve C at point A. First, we calculate the curvature vector k

$$k = \frac{dt}{ds} = \frac{dt}{dw\,\|u - v\|} = \frac{1}{\|u - v\|}\frac{d}{dw}\left(\frac{u - v}{\|u - v\|}\right). \tag{67}$$

Taking into account that $\frac{dv}{dw} = 0$, $\frac{du}{dw} = \alpha$ and $\|u - v\| = \sqrt{c^2 + u^2 - 2(v \cdot u)}$, we calculate the vector

$$n = \frac{k}{\|k\|} = \frac{(u - v) \times [\alpha \times (u - v)]}{\|u - v\|\,\|(u - v) \times \alpha\|}. \tag{68}$$

Combining equations (65) and (68), we calculate vector $b = t \times n$ appearing in the Frenet formulas:

$$b = \frac{(u - v) \times \alpha}{\|(u - v) \times \alpha\|}. \tag{69}$$

We remind that the Frenet equations

$$\frac{d\boldsymbol{t}}{ds} = k\boldsymbol{n}$$

$$\frac{d\boldsymbol{n}}{ds} = -k\boldsymbol{t} + \tau\boldsymbol{b} \qquad (70)$$

$$\frac{d\boldsymbol{b}}{ds} = -\tau\boldsymbol{n}$$

uniquely determine the curve C. Having calculated vectors $\boldsymbol{t}, \boldsymbol{n}, \boldsymbol{b}$ we now determine the curvature k and the torsion τ of curve C from equations (70). After the necessary calculations, we obtain

$$k = \frac{\sqrt{\|\boldsymbol{u} - \boldsymbol{v}\|^2 \|\boldsymbol{\alpha}\|^2 - [\boldsymbol{\alpha} \cdot (\boldsymbol{u} - \boldsymbol{v})]^2}}{\|\boldsymbol{u} - \boldsymbol{v}\|^3} \qquad (71)$$

$$\tau = \frac{\boldsymbol{\alpha}\left[(\boldsymbol{u} - \boldsymbol{v}) \times \dfrac{d\boldsymbol{\alpha}}{dw}\right]}{\|\boldsymbol{\alpha}\|^2 \|\boldsymbol{u} - \boldsymbol{v}\|^2 - [(\boldsymbol{u} - \boldsymbol{v}) \cdot \boldsymbol{\alpha}]^2} \|\boldsymbol{u} - \boldsymbol{v}\|^2 . \qquad (72)$$

We repeat the same procedure deriving vectors $\boldsymbol{t}_p, \boldsymbol{k}_p$ and $\boldsymbol{b}_p$ at point E of the curve C_p of the material particle. For $\|\boldsymbol{u}\| \neq 0$ it is

$$\boldsymbol{t}_p = \frac{\boldsymbol{u}}{\|\boldsymbol{u}\|} \qquad (73)$$

while the three-dimensional arc length is

$$dS_p = \|\boldsymbol{u}\| \, dw. \qquad (74)$$

The curvature vector $\boldsymbol{k}_p$ is given by

$$\boldsymbol{k}_p = \frac{d\boldsymbol{t}_p}{dS_p} = \frac{1}{\|\boldsymbol{u}\|} \frac{d}{dw}\left(\frac{\boldsymbol{u}}{\|\boldsymbol{u}\|}\right) = \frac{\boldsymbol{\alpha}}{\|\boldsymbol{u}\|^2} - \frac{(\boldsymbol{u} \cdot \boldsymbol{\alpha})}{\|\boldsymbol{u}\|^4}\boldsymbol{u}$$

and finally,

$$\boldsymbol{k}_p = \frac{\boldsymbol{u} \times (\boldsymbol{\alpha} \times \boldsymbol{u})}{\|\boldsymbol{u}\|^4}. \qquad (75)$$

From equation (75) we get for vector $\boldsymbol{n}_p$

$$\boldsymbol{n}_p = \frac{\boldsymbol{k}_p}{\|\boldsymbol{k}_p\|} = \frac{\boldsymbol{u} \times (\boldsymbol{\alpha} \times \boldsymbol{u})}{\|\boldsymbol{u}\| \|\boldsymbol{\alpha} \times \boldsymbol{u}\|}. \qquad (76)$$

From equations (73) and (76) we get vector

$$\boldsymbol{b}_p = \boldsymbol{t}_p \times \boldsymbol{n}_p$$

$$\boldsymbol{b}_p = \frac{\boldsymbol{u} \times \boldsymbol{\alpha}}{\|\boldsymbol{u} \times \boldsymbol{\alpha}\|}. \qquad (77)$$

From the Frenet formulas (70) for curve C_p, we get for the curvature k_p and the torsion τ_p:

$$k_p = \frac{\sqrt{\|\boldsymbol{u}\|^2 \|\boldsymbol{\alpha}\|^2 - (\boldsymbol{u} \cdot \boldsymbol{\alpha})^2}}{\|\boldsymbol{u}\|^3} \qquad (78)$$

$$\tau_p = \frac{\boldsymbol{\alpha} \cdot \left(\boldsymbol{u} \times \dfrac{d\boldsymbol{\alpha}}{dw}\right)}{\|\boldsymbol{\alpha}\|^2 \|\boldsymbol{u}\|^2 - (\boldsymbol{u} \cdot \boldsymbol{\alpha})^2} \|\boldsymbol{u}\|^2 . \qquad (79)$$

Comparing equations (65), (68), (69), (71) and (72) for curve C, with equations (73), (76), (77), (78) and (79) for curve C_p we arrive at the following theorem:

Theorem 1. *Trajectory representation theorem.*
For every direction $\frac{v}{c}$ the following hold:

1. *The map $f : \boldsymbol{u} \to \boldsymbol{u} - \boldsymbol{v}$ maps the trajectory C_p of the material particle to the curve C of the generalized photons moving with velocity $\boldsymbol{v}$*

$$f : \left(\boldsymbol{t}_p, \boldsymbol{n}_p, \boldsymbol{b}_p, k_p, \tau_p\right) \to (\boldsymbol{t}, \boldsymbol{n}, \boldsymbol{b}, k, \tau).$$

2. *The map $f^{-1} : \boldsymbol{u} - \boldsymbol{v} \to \boldsymbol{u}$ maps the curve C of the generalized photons moving with velocity $\boldsymbol{v}$ to the curve C_p of the material particle:*

$$f^{-1} : (\boldsymbol{t}, \boldsymbol{n}, \boldsymbol{b}, k, \tau) \to \left(\boldsymbol{t}_p, \boldsymbol{n}_p, \boldsymbol{b}_p, k_p, \tau_p\right).$$

According to the theorem (1), if we know the position $P(x, y, z, t)$ of the material particle at moment t and the trajectory C_p at some past time, we can determine the distribution of the generalized photons the material particle has emitted in this specific past time. We know exactly how each kinematic characteristic of the material particle maps to its surrounding spacetime.

2.5 The fundamental mathematical theorem

The interaction of the material point particle with the surrounding spacetime depends on the following four parameters:

- The moment $w = t - \frac{r}{c}$ of emission of the generalized photon by the material particle. All the physical quantities, such as the rest mass, the electric charge, the velocity $\boldsymbol{u} = \boldsymbol{u}(w)$ and the acceleration $\boldsymbol{\alpha} = \alpha(w)$ of the material particle depend upon the moment w of the emission of the generalized photon.

- The distance $r = \|\boldsymbol{r}\|$ of the arbitrary point $A(x, y, z, t)$, as depicted in figure 4, from the point of emission

$$E\left(x_p(w), y_p(w), z_p(w), w\right)$$

of the generalized photon.

- The direction in space, i.e. the functions $\delta = \delta(x, y, z, t)$ and $\omega = \omega(x, y, z, t)$.

In this paragraph we will prove the fundamental equations concerning these four parameters.

Initially we prove that the vectors ∇w, $\nabla \delta$ and $\nabla \omega$ are linearly independent. Let us suppose that

$$\lambda_1 \nabla w + \lambda_2 \nabla \delta + \lambda_3 \nabla \omega = 0, \lambda_1, \lambda_2, \lambda_2 \in \mathbb{R}.$$

Taking into account equations (12), (51) and (52), we obtain

$$-\lambda_1 \frac{1}{c\left(1 - \frac{\boldsymbol{v}\cdot\boldsymbol{u}}{c^2}\right)}\frac{\boldsymbol{v}}{c} + \lambda_2\left(\frac{\boldsymbol{u}\cdot\boldsymbol{\beta}}{r\left(1-\frac{\boldsymbol{v}\cdot\boldsymbol{u}}{c^2}\right)}\frac{\boldsymbol{v}}{c} + \frac{1}{r}\boldsymbol{\beta}\right) +$$

$$+ \lambda_3\left(\frac{\boldsymbol{u}\cdot\boldsymbol{\gamma}}{\sin\delta\, r\left(1-\frac{\boldsymbol{v}\cdot\boldsymbol{u}}{c^2}\right)}\frac{\boldsymbol{v}}{c} + \frac{1}{r\sin\delta}\boldsymbol{\gamma}\right) = 0.$$

From the linear independence of the vectors $\frac{\boldsymbol{v}}{c}, \boldsymbol{\beta}, \boldsymbol{\gamma}$ we see that

$$\frac{-\lambda_1}{c} + \lambda_2\frac{\boldsymbol{u}\cdot\boldsymbol{\beta}}{r} + \lambda_3\frac{\boldsymbol{u}\cdot\boldsymbol{\gamma}}{r\sin\delta} = 0$$

$$\frac{\lambda_2}{r} = 0$$

$$\frac{\lambda_3}{r\sin\delta} = 0.$$

Finally, we have $\lambda_1 = \lambda_2 = \lambda_3 = 0$. Therefore the vectors $\nabla w, \nabla\delta, \nabla\omega$ are linearly independent.

We now focus our attention on the variation of the quantities w, δ, ω and r on the trajectory of the material particle and on the trajectory of the generalized photon. The following two theorems hold:

Theorem 2.

$$\frac{\partial w}{\partial t} + \boldsymbol{u}\cdot\nabla w = 1 \tag{80a}$$

$$\frac{\partial \delta}{\partial t} + \boldsymbol{u}\cdot\nabla\delta = 0 \tag{80b}$$

$$\frac{\partial \omega}{\partial t} + \boldsymbol{u}\cdot\nabla\omega = 0 \tag{80c}$$

$$\frac{\partial r}{\partial t} + \boldsymbol{u}\nabla r = 0. \tag{80d}$$

Theorem 3.

$$\frac{\partial w}{\partial t} + \boldsymbol{v}\cdot\nabla w = 0 \tag{81a}$$

$$\frac{\partial \delta}{\partial t} + \boldsymbol{v}\cdot\nabla\delta = 0 \tag{81b}$$

$$\frac{\partial \omega}{\partial t} + \boldsymbol{v}\cdot\nabla\omega = 0 \tag{81c}$$

$$\frac{\partial r}{c\partial t} + \frac{\boldsymbol{v}}{c}\cdot\nabla r = 1. \tag{81d}$$

From equations (11) and (12) we have

$$\frac{\partial w}{\partial t} + \boldsymbol{u}\cdot\nabla w = \frac{1}{1-\frac{\boldsymbol{v}\cdot\boldsymbol{u}}{c^2}} - \frac{\boldsymbol{v}\cdot\boldsymbol{u}}{c^2\left(1-\frac{\boldsymbol{v}\cdot\boldsymbol{u}}{c^2}\right)} = \frac{1-\frac{\boldsymbol{v}\cdot\boldsymbol{u}}{c^2}}{1-\frac{\boldsymbol{v}\cdot\boldsymbol{u}}{c^2}} = 1$$

$$\frac{\partial w}{\partial t} + \boldsymbol{v}\cdot\nabla w = \frac{1}{1-\frac{\boldsymbol{v}\cdot\boldsymbol{u}}{c^2}} - \frac{\|\boldsymbol{v}\|^2}{c^2\left(1-\frac{\boldsymbol{v}\cdot\boldsymbol{u}}{c^2}\right)} = 0.$$

From equations (41) and (51) we have

$$\frac{\partial \delta}{\partial t} + \boldsymbol{u}\nabla\delta = -\frac{\boldsymbol{u}\cdot\boldsymbol{\beta}}{r\left(1-\frac{\boldsymbol{v}\cdot\boldsymbol{u}}{c^2}\right)} + \boldsymbol{u}\left(\frac{(\boldsymbol{u}\cdot\boldsymbol{\beta})}{r\left(1-\frac{\boldsymbol{v}\cdot\boldsymbol{u}}{c^2}\right)}\frac{\boldsymbol{v}}{c^2} + \frac{1}{r}\boldsymbol{\beta}\right)$$

$$= -\frac{\boldsymbol{u}\cdot\boldsymbol{\beta}}{r\left(1-\frac{\boldsymbol{v}\cdot\boldsymbol{u}}{c^2}\right)} + \frac{(\boldsymbol{u}\cdot\boldsymbol{\beta})\left(\boldsymbol{u}\frac{\boldsymbol{v}}{c^2}\right)}{r\left(1-\frac{\boldsymbol{v}\cdot\boldsymbol{u}}{c^2}\right)} + \frac{\boldsymbol{u}\cdot\boldsymbol{\beta}}{r} =$$

$$= \frac{\boldsymbol{u}\cdot\boldsymbol{\beta}}{r\left(1-\frac{\boldsymbol{v}\cdot\boldsymbol{u}}{c^2}\right)}\left[-1 + \frac{\boldsymbol{v}\cdot\boldsymbol{u}}{c^2} + 1 - \frac{\boldsymbol{v}\cdot\boldsymbol{u}}{c^2}\right] = 0.$$

$$\frac{\partial \delta}{\partial t} + \boldsymbol{v}\cdot\nabla\delta = -\frac{\boldsymbol{u}\cdot\boldsymbol{\beta}}{r\left(1-\frac{\boldsymbol{v}\cdot\boldsymbol{u}}{c^2}\right)} + \boldsymbol{v}\left(\frac{(\boldsymbol{u}\cdot\boldsymbol{\beta})}{r\left(1-\frac{\boldsymbol{v}\cdot\boldsymbol{u}}{c^2}\right)}\frac{\boldsymbol{v}}{c^2} + \frac{1}{r}\boldsymbol{\beta}\right)$$

$$= -\frac{\boldsymbol{u}\cdot\boldsymbol{\beta}}{r\left(1-\frac{\boldsymbol{v}\cdot\boldsymbol{u}}{c^2}\right)} + \frac{(\boldsymbol{u}\cdot\boldsymbol{\beta})}{r\left(1-\frac{\boldsymbol{v}\cdot\boldsymbol{u}}{c^2}\right)}\frac{\|\boldsymbol{v}\|^2}{c^2} + \frac{\boldsymbol{v}\cdot\boldsymbol{\beta}}{r} = 0$$

since $\|\boldsymbol{v}\|^2 = c^2$ and $\boldsymbol{v}\cdot\boldsymbol{\beta} = 0$.

Similarly, starting from equations (42) and (52) we arrive at equations (80)(c) and (81)(c).

From equations (9) and (10) we get

$$\frac{\partial r}{c\partial t} + \frac{\boldsymbol{u}}{c}\nabla r = -\frac{\boldsymbol{v}\cdot\boldsymbol{u}}{c^2\left(1-\frac{\boldsymbol{v}\cdot\boldsymbol{u}}{c^2}\right)} + \frac{\boldsymbol{u}}{c}\left(\frac{1}{1-\frac{\boldsymbol{v}\cdot\boldsymbol{u}}{c^2}}\frac{\boldsymbol{v}}{c}\right) = 0$$

$$\frac{\partial r}{c\partial t} + \frac{\boldsymbol{v}}{c}\nabla r = -\frac{\boldsymbol{v}\cdot\boldsymbol{u}}{c^2\left(1-\frac{\boldsymbol{v}\cdot\boldsymbol{u}}{c^2}\right)} + \frac{\boldsymbol{v}}{c}\left(\frac{1}{1-\frac{\boldsymbol{v}\cdot\boldsymbol{u}}{c^2}}\frac{\boldsymbol{v}}{c}\right) =$$

$$= -\frac{\boldsymbol{v}\cdot\boldsymbol{u}}{c^2\left(1-\frac{\boldsymbol{v}\cdot\boldsymbol{u}}{c^2}\right)} + \frac{1}{1-\frac{\boldsymbol{v}\cdot\boldsymbol{u}}{c^2}} =$$

$$= \frac{1}{1-\frac{\boldsymbol{v}\cdot\boldsymbol{u}}{c^2}}\left(1-\frac{\boldsymbol{v}\cdot\boldsymbol{u}}{c^2}\right) = 1.$$

With the aid of the above theorems we can prove the following fundamental theorem:

Theorem 4. *The Fundamental Mathematical Theorem. For every function $f = f(w, \delta, \omega, r)$ the following hold:*

A)

$$\frac{\partial f}{\partial t} + \boldsymbol{u}\cdot\nabla f = \frac{\partial f}{\partial w} \tag{82}$$

$$\frac{\partial}{\partial t}\left(f\frac{\boldsymbol{v}}{c}\right) + \left(\text{grad}\left(f\frac{\boldsymbol{v}}{c}\right)\right)\boldsymbol{u} = \frac{\boldsymbol{v}}{c}\frac{\partial f}{\partial w} \tag{83}$$

$$\frac{\partial}{\partial t}(f\boldsymbol{\beta}) + (\text{grad}(f\boldsymbol{\beta}))\boldsymbol{u} = \boldsymbol{\beta}\frac{\partial f}{\partial w} \tag{84}$$

$$\frac{\partial}{\partial t}(f\boldsymbol{\gamma}) + (\mathrm{grad}\,(f\boldsymbol{\gamma}))\,\boldsymbol{u} = \boldsymbol{\gamma}\frac{\partial f}{\partial w}. \tag{85}$$

B)

$$\frac{\partial f}{\partial t} + \boldsymbol{v}\cdot\nabla f = c\frac{\partial f}{\partial r} \tag{86}$$

$$\frac{\partial}{\partial t}\left(f\frac{\boldsymbol{v}}{c}\right) + \left(\mathrm{grad}\left(f\frac{\boldsymbol{v}}{c}\right)\right)\boldsymbol{v} = \boldsymbol{v}\frac{\partial f}{\partial r} \tag{87}$$

$$\frac{\partial}{\partial t}(f\boldsymbol{\beta}) + (\mathrm{grad}\,(f\boldsymbol{\beta}))\,\boldsymbol{v} = \boldsymbol{\beta}\frac{\partial f}{\partial r} \tag{88}$$

$$\frac{\partial}{\partial t}(f\boldsymbol{\gamma}) + (\mathrm{grad}\,(f\boldsymbol{\gamma}))\,\boldsymbol{v} = \boldsymbol{\gamma}\frac{\partial f}{\partial r}. \tag{89}$$

We prove equations (82), (83) and (86). The rest of the equations of the fundamental mathematical theorem are proven similarly. For the proof of equation (82) we have

$$\frac{\partial f}{\partial t} + \boldsymbol{u}\cdot\nabla f = \frac{\partial f}{\partial w}\frac{\partial w}{\partial t} + \frac{\partial f}{\partial \delta}\frac{\partial \delta}{\partial t} + \frac{\partial f}{\partial \omega}\frac{\partial \omega}{\partial t} + \frac{\partial f}{\partial r}\frac{\partial r}{\partial t}$$

$$+\boldsymbol{u}\cdot\left(\frac{\partial f}{\partial w}\nabla w + \frac{\partial f}{\partial \delta}\nabla\delta + \frac{\partial f}{\partial \omega}\nabla\omega + \frac{\partial f}{\partial r}\nabla r\right)$$

$$=\frac{\partial f}{\partial w}\left(\frac{\partial w}{\partial t} + \boldsymbol{u}\nabla w\right) + \frac{\partial f}{\partial \delta}\left(\frac{\partial \delta}{\partial t} + \boldsymbol{u}\cdot\nabla\delta\right)$$

$$+\frac{\partial f}{\partial \omega}\left(\frac{\partial \omega}{\partial t} + \boldsymbol{u}\cdot\nabla\omega\right) + \frac{\partial f}{\partial r}\left(\frac{\partial r}{\partial t} + \boldsymbol{u}\cdot\nabla r\right)$$

and taking into account equations (80) we obtain

$$\frac{\partial f}{\partial t} + \boldsymbol{u}\cdot\nabla f = \frac{\partial f}{\partial w},$$

which is equation (82).

In order to prove equation (83) we use the identity

$$\mathrm{grad}\,(f\boldsymbol{\alpha}) = \nabla f\otimes\boldsymbol{\alpha} + f\,\mathrm{grad}\,\boldsymbol{\alpha} \tag{90}$$

which holds for every vector $\boldsymbol{\alpha}$ and scalar function f. We can now prove equation (83) as:

$$\frac{\partial}{\partial t}\left(f\frac{\boldsymbol{v}}{c}\right) + \left(\mathrm{grad}\left(f\frac{\boldsymbol{v}}{c}\right)\right)\boldsymbol{u} =$$

$$\frac{\partial f}{\partial t}\frac{\boldsymbol{v}}{c} + f\frac{\partial}{\partial t}\left(\frac{\boldsymbol{v}}{c}\right) + \left(f\,\mathrm{grad}\frac{\boldsymbol{v}}{c} + \nabla f\otimes\frac{\boldsymbol{v}}{c}\right)\boldsymbol{u}.$$

Using identity (45) $(\boldsymbol{\alpha}\otimes\boldsymbol{b})\,\boldsymbol{c} = (\boldsymbol{\alpha}\cdot\boldsymbol{c})\,\boldsymbol{b}$ we obtain

$$\frac{\partial f}{\partial t}\frac{\boldsymbol{v}}{c} + f\frac{\partial}{\partial t}\left(\frac{\boldsymbol{v}}{c}\right) + \left(f\,\mathrm{grad}\frac{\boldsymbol{v}}{c}\right)\boldsymbol{u} + (\boldsymbol{u}\cdot\nabla f)\frac{\boldsymbol{v}}{c} =$$

$$\left(\frac{\partial f}{\partial t} + \boldsymbol{u}\cdot\nabla f\right)\frac{\boldsymbol{v}}{c} + f\left(\frac{\partial}{\partial t}\left(\frac{\boldsymbol{v}}{c}\right) + \left(\mathrm{grad}\frac{\boldsymbol{v}}{c}\right)\boldsymbol{u}\right) =$$

$$\frac{\partial f}{\partial w}\frac{\boldsymbol{v}}{c}$$

since $\frac{\partial f}{\partial t} + \boldsymbol{u}\cdot\nabla f = \frac{\partial f}{\partial w}$, according to equation (82) and furthermore

$$\frac{\partial}{\partial t}\left(\frac{\boldsymbol{v}}{c}\right) + \left(\mathrm{grad}\frac{\boldsymbol{v}}{c}\right)\boldsymbol{u} =$$

$$\frac{\partial \delta}{\partial t}\boldsymbol{\beta} + \sin\delta\frac{\partial \omega}{\partial t}\boldsymbol{\gamma} + (\nabla\delta\otimes\boldsymbol{\beta} + \sin\delta\nabla\omega\otimes\boldsymbol{\gamma})\,\boldsymbol{u}$$

according to equations (38)(b),(d). Hence we obtain

$$\frac{\partial}{\partial t}\left(\frac{\boldsymbol{v}}{c}\right) + \left(\mathrm{grad}\frac{\boldsymbol{v}}{c}\right)\boldsymbol{u} =$$

$$\frac{\partial \delta}{\partial t}\boldsymbol{\beta} + \sin\delta\frac{\partial \omega}{\partial t}\boldsymbol{\gamma} + (\boldsymbol{u}\cdot\nabla\delta)\boldsymbol{\beta} + \sin\delta\,(\boldsymbol{u}\cdot\nabla\omega)\boldsymbol{\gamma} =$$

$$\left(\frac{\partial \delta}{\partial t} + \boldsymbol{u}\cdot\nabla\delta\right)\boldsymbol{\beta} + \sin\delta\left(\frac{\partial \omega}{\partial t} + \boldsymbol{u}\cdot\nabla\omega\right)\boldsymbol{\gamma} = 0$$

according to equations (80)(b),(c).

The proof of equation (86) goes as follows:

$$\frac{\partial f}{\partial t} + \boldsymbol{v}\cdot\nabla f = \frac{\partial f}{\partial w}\frac{\partial w}{\partial t} + \frac{\partial f}{\partial \delta}\frac{\partial \delta}{\partial t} + \frac{\partial f}{\partial \omega}\frac{\partial \omega}{\partial t} + \frac{\partial f}{\partial r}\frac{\partial r}{\partial t}$$

$$+\boldsymbol{v}\cdot\left(\frac{\partial f}{\partial w}\nabla w + \frac{\partial f}{\partial \delta}\nabla\delta + \frac{\partial f}{\partial \omega}\nabla\omega + \frac{\partial f}{\partial r}\nabla r\right)$$

$$=\frac{\partial f}{\partial w}\left(\frac{\partial w}{\partial t} + \boldsymbol{v}\cdot\nabla w\right) + \frac{\partial f}{\partial \delta}\left(\frac{\partial \delta}{\partial t} + \boldsymbol{v}\cdot\nabla\delta\right)$$

$$+\frac{\partial f}{\partial \omega}\left(\frac{\partial \omega}{\partial t} + \boldsymbol{v}\cdot\nabla\omega\right) + \frac{\partial f}{\partial r}\left(\frac{\partial r}{\partial t} + \boldsymbol{v}\cdot\nabla r\right).$$

Taking into consideration equations (81) we get

$$\frac{\partial f}{\partial t} + \boldsymbol{v}\cdot\nabla f = c\frac{\partial f}{\partial r},$$

which is equation (86).

An immediate consequence of the theorem (4) is the following lemma:

For every vector function $\boldsymbol{F} = \boldsymbol{F}\,(w, \delta, \omega, r)$ the following relations hold:

$$\frac{\partial \boldsymbol{F}}{\partial t} + (\mathrm{grad}\,\boldsymbol{F})\cdot\boldsymbol{u} = \frac{\partial \boldsymbol{F}}{\partial w} \tag{91}$$

$$\frac{\partial \boldsymbol{F}}{\partial t} + (\mathrm{grad}\,\boldsymbol{F})\,\boldsymbol{v} = c\frac{\partial \boldsymbol{F}}{\partial r}. \tag{92}$$

The proof is done by writing the vector function $\boldsymbol{F}$ in the form

$$\boldsymbol{F} = F_1\,(w, \delta, \omega, r)\frac{\boldsymbol{v}}{c} + F_2\,(w, \delta, \omega, r)\boldsymbol{\beta} + F_3\,(w, \delta, \omega, r)\boldsymbol{\gamma}$$

and applying the theorem.

The fundamental mathematical theorem determines the variation of any scalar, vectorial and tensorial physical quantity, both as defined on the material particle, as well as on the surrounding spacetime. Of special interest are the applications of this theorem for the variations of the rest mass, the

electric charge, the energy, the linear momentum, the angular momentum, and any other conserved physical quantity, for the system "material particle-generalized photon". The fundamental theorem allows us to correlate the variations that take place on the material particle with the corresponding variations that take place in the surrounding spacetime.

2.6 The properties of the vector basis $\frac{v}{c}, \beta, \gamma$

The properties of the right-handed orthonormal vector basis $\{\frac{v}{c}, \beta, \gamma\}$ are given by equations (38), (39) and (40). In these equations we already know their second parts from the study conducted in the preceding paragraphs. Thus, we can express them in a simpler form.

The first of equations (38), (39) and (40) can be written as:

$$\nabla \cdot \left(\frac{v}{c}\right) = \frac{2}{r} \tag{93}$$

$$\nabla \cdot \beta = -\frac{u \cdot \beta}{cr\left(1 - \frac{v \cdot u}{c^2}\right)} + \frac{\cos \delta}{r \sin \delta} \tag{94}$$

$$\nabla \cdot \gamma = -\frac{u \cdot \gamma}{cr\left(1 - \frac{v \cdot u}{c^2}\right)}. \tag{95}$$

Equation (93) results directly from equation (22). But we can also prove it in a different way, starting from the first of equations (38)

$$\nabla \cdot \left(\frac{v}{c}\right) = \beta \cdot \nabla \delta + \sin \delta \gamma \cdot \nabla \omega.$$

With the help of equations (51) and (52) we obtain

$$\nabla \cdot \left(\frac{v}{c}\right) = \frac{1}{r} + \frac{1}{r} = \frac{2}{r}$$

taking into account that the set of the vectors $\{\frac{v}{c}, \beta, \gamma\}$ form a right-handed, orthonormal vector basis.

From the first of equations (39) we obtain

$$\nabla \cdot \beta = -\frac{v}{c} \nabla \delta + \cos \delta \gamma \cdot \nabla \omega.$$

Through equations (51) and (52) we get

$$\nabla \cdot \beta = -\frac{u \cdot \beta}{cr\left(1 - \frac{v \cdot u}{c^2}\right)} + \frac{\cos \delta}{r \sin \delta}.$$

From the first of equations (40) we have that

$$\nabla \cdot \gamma = -\sin \delta \frac{v}{c} \nabla \omega - \cos \delta \beta \cdot \nabla \omega.$$

Using equation (52) we see that

$$\nabla \cdot \gamma = -\frac{u \cdot \gamma}{cr\left(1 - \frac{v \cdot u}{c^2}\right)}.$$

Accordingly we can write in a simpler form the rest of the equations (38), (39) and (40), whenever it is demanded by the mathematical calculations performed.

2.7 List of auxiliary equations

We prove the following auxiliary equations:

$$\frac{\partial (v \cdot u)}{\partial t} = \frac{v \cdot \alpha}{1 - \frac{v \cdot u}{c^2}} + \frac{(v \cdot u)^2 - c^2 u^2}{c^3 r \left(1 - \frac{v \cdot u}{c^2}\right)} \tag{96}$$

$$\nabla (v \cdot u) = -\frac{v \cdot \alpha}{c^2 \left(1 - \frac{v \cdot u}{c^2}\right)} v + \frac{c}{r} u + \frac{u^2 - (v \cdot u)}{cr \left(1 - \frac{v \cdot u}{c^2}\right)} \frac{v}{c} \tag{97}$$

$$\frac{\partial (v \cdot \alpha)}{\partial t} = \frac{v \cdot b}{1 - \frac{v \cdot u}{c^2}} + \frac{(v \cdot u)(v \cdot \alpha) - c^2 (v \cdot \alpha)}{cr \left(1 - \frac{v \cdot u}{c^2}\right)} \tag{98}$$

$$\nabla (v \cdot \alpha) = -\frac{v \cdot b}{c^2 \left(1 - \frac{v \cdot u}{c^2}\right)} v + \frac{c}{r} \alpha + \frac{u \cdot \alpha - v \cdot \alpha}{cr \left(1 - \frac{v \cdot u}{c^2}\right)} v \tag{99}$$

where $\alpha = \alpha(w) = \frac{du(w)}{dw}$ and $b = b(w) = \frac{d\alpha(w)}{dw}$ and $u^2 = \|u\|^2$.

Indeed, it holds that

$$\frac{\partial (v \cdot u)}{\partial t} = u \frac{\partial v}{\partial t} + v \frac{\partial u}{\partial t}$$

$$\frac{\partial (v \cdot u)}{\partial t} = u \frac{\partial v}{\partial t} + v \frac{\partial u}{\partial w} \cdot \frac{\partial w}{\partial t}.$$

Through equations (25) and (11) we obtain

$$\frac{\partial (v \cdot u)}{\partial t} = u \frac{\partial v}{\partial t} + \frac{v \cdot \alpha}{1 - \frac{v \cdot u}{c^2}}.$$

With the help of equation (17) we get

$$\frac{\partial (v \cdot u)}{\partial t} = \frac{c}{r \left(1 - \frac{v \cdot u}{c^2}\right)} \left[\frac{(v \cdot u)^2}{c^2} - u^2\right] + \frac{v \cdot \alpha}{1 - \frac{v \cdot u}{c^2}}$$

and performing the necessary algebraic transformations we obtain equation (96).

In order to prove equation (97) we start from the identity

$$\nabla (v \cdot u) = \left(\text{grad}^{\mathsf{T}} v\right) u + \left(\text{grad}^{\mathsf{T}} u\right) v$$

where $\text{grad}^{\mathsf{T}} v$ and $\text{grad}^{\mathsf{T}} u$ are the transpose matrices of grad v and grad u.

From equations (20) and (28) we obtain

$$\nabla (v \cdot u) = \left[\frac{c}{r} I + \frac{1}{r \left(1 - \frac{v \cdot u}{c^2}\right)} \frac{v}{c} \otimes (u - v)\right]^{T} u - $$
$$- \frac{1}{c \left(1 - \frac{v \cdot u}{c^2}\right)} \left(\frac{v}{c} \otimes \alpha\right)^{T} v$$

$$\nabla \left(\boldsymbol{v} \cdot \boldsymbol{u} \right) = \left[\frac{c}{r} I + \frac{1}{r \left(1 - \dfrac{\boldsymbol{v} \cdot \boldsymbol{u}}{c^2} \right)} \left(\boldsymbol{u} - \boldsymbol{v} \right) \otimes \frac{\boldsymbol{v}}{c} \right]^{T} \boldsymbol{u} -$$

$$- \frac{1}{c \left(1 - \dfrac{\boldsymbol{v} \cdot \boldsymbol{u}}{c^2} \right)} \left(\boldsymbol{\alpha} \otimes \frac{\boldsymbol{v}}{c} \right) \boldsymbol{v}.$$

Using identity (45) we get

$$\nabla \left(\boldsymbol{v} \cdot \boldsymbol{u} \right) = \frac{c}{r} \boldsymbol{u} + \frac{\boldsymbol{u} \cdot \left(\boldsymbol{u} - \boldsymbol{v} \right)}{r \left(1 - \dfrac{\boldsymbol{v} \cdot \boldsymbol{u}}{c^2} \right)} \cdot \frac{\boldsymbol{v}}{c} - \frac{\boldsymbol{v} \cdot \boldsymbol{\alpha}}{c \left(1 - \dfrac{\boldsymbol{v} \cdot \boldsymbol{u}}{c^2} \right)} \frac{\boldsymbol{v}}{c}$$

which is equation (97). We can similarly prove equations (98) and (99). In order to prove the last equation we use equation (32), in exactly the same manner we used equation (28). In the same way, we can prove corresponding equations for all of the inner products such as $\boldsymbol{v} \cdot \boldsymbol{b}$, $\boldsymbol{u} \cdot \boldsymbol{\alpha}$ etc., that appear in the equations of the theory of selfvariations.

3 The study of the selfvariations for a material point particle moving with constant speed

3.1 Introduction

In this paragraph we present the study of the selfvariations for a material point particle moving with constant speed. This study was regarded as necessary for two reasons. The first is that constant-speed motion is the simplest possible and, therefore, we are studying the consequences of the selfvariations in their simplest version. The second reason is that arbitrary motion can be considered as a multitude of successive constant-speed motions.

By studying the constant-speed motion of a material particle we can derive the Lorentz-Einstein transformations for the physical quantities w, δ, ω, r that appear in the equations of the theory of selfvariations. Of special interest is the transformation of the volume of the generalized photon, which differs from the volume transformation of material particles as we know it within the framework of Special Relativity. After having studied both the arbitrary motion, as well as the constant-speed motion of the material particle, we have the knowledge necessary for advancing our study in the forthcoming paragraphs.

3.2 The case of a material point particle moving with constant speed

We consider a material point particle with rest mass m_0 and electric charge q, which moves with velocity $\boldsymbol{u} = \begin{bmatrix} u \\ 0 \\ 0 \end{bmatrix}$ in the inertial frame of reference $S \left(0, x, y, z, t \right)$, as depicted in figure 6.

At moment t when the material particle is at point $P(ut, 0, 0, t)$, the rest mass m_0 and the electric charge q of the material particle act at point $A \left(x, y, z, t \right)$ through the generalized
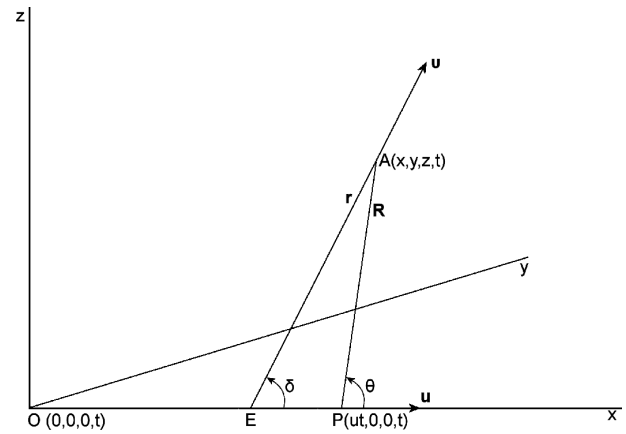
Fig. 6: Material point particle moving with constant speed along the x axis of the inertial reference frame $S \left(0, x, y, z, t \right)$. As the material particle moves from point E to point P, during the time interval $\Delta t = \frac{r}{c}$, a generalized photon moves from point E to point A.

photon that was emitted from point E and arrived at point A moving with velocity c. Therefore, the coordinates of point E are

$$E \left(ut - \frac{u}{c} r, 0, 0, t - \frac{r}{c} \right) \tag{100}$$

where $r = \| \boldsymbol{r} \| = \left\| \overrightarrow{EA} \right\|$. Due to the selfvariations, the rest mass m_0 and the electric charge q of the material particle act at point $A \left(x, y, z, t \right)$ with the value they had at time

$$w = t - \frac{r}{c} \tag{101}$$

at point $E \left(ut - \frac{u}{c} r, 0, 0, t - \frac{r}{c} \right)$, and not with the value they have at point $P \left(ut, 0, 0, t \right)$ at time t. For the vector $\boldsymbol{r}$ we have

$$\boldsymbol{r} = \overrightarrow{EA} = \begin{bmatrix} x - ut + \frac{u}{c} r \\ y \\ z \end{bmatrix}. \tag{102}$$

The magnitude of $\| \boldsymbol{r} \| = r$ can be derived from equations (102) as

$$\| \boldsymbol{r} \| = r = \gamma^2 \frac{u}{c} \left(x - ut \right) + \gamma \sqrt{\gamma^2 \left(x - ut \right)^2 + y^2 + z^2} \tag{103}$$

where $\gamma = \frac{1}{\sqrt{1 - \frac{u^2}{c^2}}}$.

Combining equations (102) and (103) we obtain

$$\boldsymbol{r} = \begin{bmatrix} \gamma^2 \left(x - ut \right) + \frac{u}{c} \gamma \sqrt{\gamma^2 \left(x - ut \right)^2 + y^2 + z^2} \\ y \\ z \end{bmatrix}. \tag{104}$$

The velocity $\boldsymbol{v}$ of the selfvariations has magnitude $\| \boldsymbol{v} \| = c$, and is parallel to the vector $\boldsymbol{r}$, thus we have

$$\boldsymbol{v} = \frac{c}{r} \boldsymbol{r} = \frac{c}{r} \begin{bmatrix} \gamma^2 \left(x - ut \right) + \frac{u}{c} \gamma \sqrt{\gamma^2 \left(x - ut \right)^2 + y^2 + z^2} \\ y \\ z \end{bmatrix}. \tag{105}$$

The position vector $\boldsymbol{R}$ of point $A\,(x, y, z, t)$ with respect to point $P\,(ut, 0, 0, t)$, where the material particle is located, is

$$\boldsymbol{R} = \overrightarrow{PA} = \left[\begin{array}{c} x - ut \\ y \\ z \end{array} \right]. \qquad (106)$$

From equation (106) we obtain

$$\|\boldsymbol{R}\| = R = \sqrt{(x - ut)^2 + y^2 + z^2}. \qquad (107)$$

From figure 6 we see that

$$\boldsymbol{r} = \overrightarrow{EA} + \boldsymbol{R}$$

$$\boldsymbol{r} = \frac{r}{c}\boldsymbol{u} + \boldsymbol{R}.$$

Finally, we obtain

$$\boldsymbol{v} = \boldsymbol{u} + \frac{c}{r}\boldsymbol{R} \qquad (108)$$

$$\boldsymbol{R} = r\left(\frac{\boldsymbol{v}}{c} - \frac{\boldsymbol{u}}{c}\right). \qquad (109)$$

Combining equations (100) and (101) we have for the coordinates of point E

$$E\,(uw, 0, 0, w). \qquad (110)$$

The relations between the scalar, vectorial and tensorial quantities of this paragraph can be derived by the corresponding relations proven in the second paragraph, considering that the acceleration of the material body vanishes, that is $\boldsymbol{\alpha} = \boldsymbol{\alpha}\,(w) = 0$, and that the velocity of the material particle is

$$\boldsymbol{u} = \boldsymbol{u}\,(w) = \left[\begin{array}{c} u\,(w) \\ 0 \\ 0 \end{array} \right] = \left[\begin{array}{c} u \\ 0 \\ 0 \end{array} \right].$$

3.3 The case of a material point particle at rest

We consider an inertial reference frame $S'\,(0', x', y', z', t')$ moving with velocity $\boldsymbol{u} = \left[\begin{array}{c} u \\ 0 \\ 0 \end{array} \right]$ with respect to the inertial reference frame $S\,(0, x, y, z, t)$ of the previous paragraph. We also suppose that for $t = t' = 0$ the origins of the axes of coordinates 0 and $0'$ of these two frames coincide. In the way we have chosen these two inertial frames, the material particle is at rest in frame S' or, equivalently, frame S' accompanies the material particle during its motion. Figure 7 is the one corresponding to figure 6 for reference frame S'.

At moment t', when the material particle is located at point $P\,(0, 0, 0, t')$, the mass m_o and the electric charge q of the material particle act at point $A\,(x', y', z', t')$ through the generalized photon that was emitted from point $E\left(0, 0, 0, t' - \frac{r'}{c}\right)$
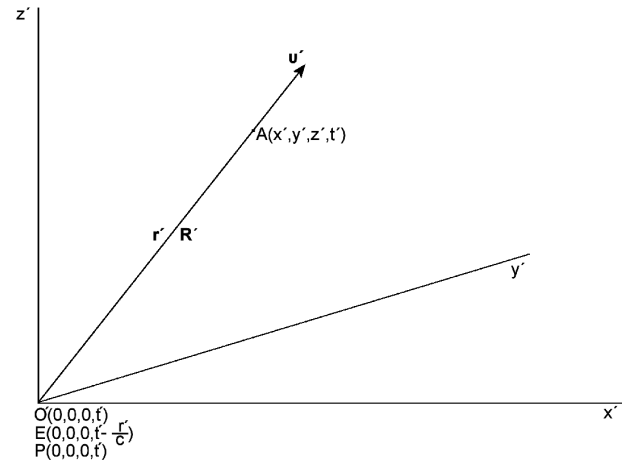
Fig. 7: A material point particle remains at rest at the origin $O'\,(0, 0, 0, 0, t')$ of the inertial reference frame $S\,(0', x', y', z', t')$. A generalized photon moves from point $E\left(0, 0, 0, 0, t' - \frac{r'}{c}\right)$ and arrives at point $A\,(x', y', z', t')$, during the time interval $\Delta t' = \frac{r'}{c}$.

and arrived at point $A\,(x', y', z', t')$ moving with velocity c. Therefore, the coordinates of point E are

$$E\left(0, 0, 0, t' - \frac{r'}{c}\right) \qquad (111)$$

where $r' = \|\boldsymbol{r}'\| = \left\|\overrightarrow{EA}\right\|$. Due to the selfvariations, the rest mass m_o and the electric charge q of the material particle act at point $A\,(x', y', z', t')$ with the value they had at time

$$w' = t' - \frac{r'}{c} \qquad (112)$$

and not with the value they have at $P\,(0, 0, 0, t')$.

For the vector $\boldsymbol{r}'$ it holds that

$$\boldsymbol{r}' = \overrightarrow{EA} = \left[\begin{array}{c} x' \\ y' \\ z' \end{array} \right] \qquad (113)$$

while its magnitude $\|\boldsymbol{r}'\| = r'$ is given by

$$\|\boldsymbol{r}'\| = r' = \sqrt{x'^2 + y'^2 + z'^2}. \qquad (114)$$

The velocity of the selfvariations $\boldsymbol{v}'$ has magnitude $\|\boldsymbol{v}'\| = c$, and is parallel to the vector $\boldsymbol{r}'$, therefore it is

$$\boldsymbol{v}' = \frac{c}{r'}\boldsymbol{r}' = \frac{c}{r'}\left[\begin{array}{c} x' \\ y' \\ z' \end{array} \right]. \qquad (115)$$

The position vector $\boldsymbol{R}'$ of point $A\,(x', y', z', t')$ with respect to $P\,(0, 0, 0, t')$, where the material particle is located, is given by

$$\boldsymbol{R}' = \overrightarrow{PA} = \left[\begin{array}{c} x' \\ y' \\ z' \end{array} \right] = \boldsymbol{r}'. \qquad (116)$$

From equation (116) we get

$$\|\boldsymbol{R}'\| = R' = \|\boldsymbol{r}'\| = r' = \sqrt{x'^2 + y'^2 + z'^2}. \qquad (117)$$

Combining equations (111) and (112) we obtain for the coordinates of point E

$$E(0, 0, 0, w'). \qquad (118)$$

The relations between the scalar, vectorial and tensorial quantities of this paragraph can be derived from the corresponding relations we proved in the second paragraph, considering that the acceleration and the velocity of the material particle vanish, that is $\boldsymbol{\alpha} = \boldsymbol{\alpha}(w) = \boldsymbol{0}$ and $\boldsymbol{u} = \boldsymbol{u}(w) = \boldsymbol{0}$.

3.4 Lorentz-Einstein transformations of the quantities w, δ, ω, r

In this paragraph we shall study the way in which the fundamental physical quantities appearing in the equations of the theory of selfvariations transform under the action of the Lorentz-Einstein transformations [5–11].

In the way we have chosen the inertial reference frames S and S', the transformations of the coordinates in the four-dimensional spacetime are given by the set of equations

$$\begin{aligned}
x &= \gamma(x' + ut') \\
y &= y' \\
z &= z' \\
t &= \gamma\left(t' + \frac{u}{c^2}x'\right) \\
x' &= \gamma(x - ut) \\
y' &= y \\
z' &= z \\
t' &= \gamma\left(t - \frac{u}{c^2}x\right)
\end{aligned} \qquad (119)$$

where $\gamma = \frac{1}{\sqrt{1 - \frac{u^2}{c^2}}}$.

The coordinates of point E are given by relation (110), and are $E(uw, 0, 0, w)$ for inertial frame S, and by relation (118), and are $E(0, 0, 0, w')$ for inertial frame S'. Applying transformations (119) we obtain

$$w = \gamma w'. \qquad (120)$$

Indeed, based on the fourth equation of the first column of transformations (119) for the coordinates of point E, we get

$$w = \gamma(w' + u \cdot 0) \\
w = \gamma w'.$$

We now consider the trigonometric form of the velocity $\boldsymbol{v}$, as defined in paragraph 2.2. From equations (34) we get for reference frames S and S' respectively

$$\begin{aligned}
\cos\delta &= \frac{v_x}{c} \\
\sin\delta\cos\omega &= \frac{v_y}{c} \\
\sin\delta\sin\omega &= \frac{v_z}{c}
\end{aligned} \qquad (121)$$

$$\begin{aligned}
\cos\delta' &= \frac{v'_x}{c} \\
\sin\delta'\cos\omega' &= \frac{v'_y}{c} \\
\sin\delta'\sin\omega' &= \frac{v'_z}{c}.
\end{aligned} \qquad (122)$$

From the Lorentz-Einstein transformations for the velocity we have

$$\begin{aligned}
v_x &= \frac{v'_x + u}{1 + \frac{uv'_x}{c^2}} & v'_x &= \frac{v_x - u}{1 - \frac{uv_x}{c^2}} \\
v_y &= \frac{v'_y}{\gamma\left(1 + \frac{uv'_x}{c^2}\right)} & v'_y &= \frac{v_y}{\gamma\left(1 - \frac{uv_x}{c^2}\right)} \\
v_z &= \frac{v'_z}{\gamma\left(1 + \frac{uv'_x}{c^2}\right)} & v'_z &= \frac{v_z}{\gamma\left(1 - \frac{uv'_x}{c^2}\right)}.
\end{aligned} \qquad (123)$$

From transformation (123) and from equations (121) and (122) the following transformations are derived for the functions $\delta = \delta(x, y, z, t)$ and $\omega = \omega(x, y, z, t)$:

$$\begin{aligned}
\cos\delta' &= \frac{\cos\delta - \frac{u}{c}}{1 - \frac{u}{c}\cos\delta} & \cos\delta &= \frac{\cos\delta' + \frac{u}{c}}{1 + \frac{u}{c}\cos\delta'} \\
\sin\delta' &= \frac{\sin\delta}{\gamma\left(1 - \frac{u}{c}\cos\delta\right)} & \sin\delta &= \frac{\sin\delta'}{\gamma\left(1 + \frac{u}{c}\cos\delta'\right)} \\
\omega' &= \omega & \omega &= \omega'.
\end{aligned} \qquad (124)$$

We shall prove the first equation. The rest are proven similarly.

From the first equation of the second column of transformations (123) we obtain

$$v'_x = \frac{v_x - u}{1 - \frac{uv_x}{c^2}}$$

$$\frac{v'_x}{c} = \frac{\frac{v_x}{c} - \frac{u}{c}}{1 - \frac{u}{c}\frac{v_x}{c}}.$$

Through equations (122) and (121) we get

$$\cos\delta' = \frac{\cos\delta - \frac{u}{c}}{1 - \frac{u}{c}\cos\delta}.$$

From equation (117) and transformations (119) we see that

$$r' = \sqrt{\gamma^2(x - ut)^2 + y^2 + z^2}. \qquad (125)$$

Combining equations (103) and (125) we get

$$r = \gamma^2 \frac{u}{c}(x - ut) + \gamma r'$$

and since

$$\gamma(x - ut) = x'$$

from transformations (119) we obtain

$$r = \gamma \frac{u}{c} x' + \gamma r'. \tag{126}$$

From equation (115) we see that

$$\upsilon'_x = \frac{c}{r'} x'$$

$$x' = r' \frac{\upsilon'_x}{c}.$$

Substituting into equation (126) we get

$$r = \gamma \frac{u\upsilon'_x}{c^2} r' + \gamma r'$$

$$r = \gamma r' \left(1 + \frac{u\upsilon'_x}{c^2}\right).$$

From equation (122) we obtain

$$r = \gamma r' \left(1 + \frac{u}{c} \cos \delta'\right)$$

and with the help of transformations (124) we get

$$r = \gamma r' \left(1 + \frac{u}{c} \frac{\cos \delta - \frac{u}{c}}{1 - \frac{u}{c} \cos \delta}\right)$$

$$r = \gamma r' \frac{1 - \frac{u^2}{c^2}}{1 - \frac{u}{c} \cos \delta}$$

$$r = \frac{r'}{\gamma \left(1 - \frac{u}{c} \cos \delta\right)}$$

$$r' = \gamma r \left(1 - \frac{u}{c} \cos \delta\right) = \gamma r \left(1 - \frac{\boldsymbol{\upsilon} \cdot \boldsymbol{u}}{c^2}\right). \tag{127}$$

From transformations (124) we obtain

$$\sin \delta' = \frac{\sin \delta}{\gamma \left(1 - \frac{u}{c} \cos \delta\right)}$$

$$\cos \delta' \frac{d\delta'}{d\delta} = \frac{\cos \delta \left(1 - \frac{u}{c} \cos \delta\right) - \sin \delta \frac{u}{c} \sin \delta}{\gamma \left(1 - \frac{u}{c} \cos \delta\right)^2}$$

$$\cos \delta' \frac{d\delta'}{d\delta} = \frac{\cos \delta - \frac{u}{c}}{\gamma \left(1 - \frac{u}{c} \cos \delta\right)^2}$$

$$\frac{\cos \delta - \frac{u}{c}}{1 - \frac{u}{c} \cos \delta} \frac{d\delta'}{d\delta} = \frac{\cos \delta - \frac{u}{c}}{\gamma \left(1 - \frac{u}{c} \cos \delta\right)^2}$$

$$\frac{d\delta'}{d\delta} = \frac{1}{\gamma \left(1 - \frac{u}{c} \cos \delta\right)}$$

$$d\delta' = \frac{1}{\gamma \left(1 - \frac{u}{c} \cos \delta\right)} d\delta. \tag{128}$$

Repeating the same procedure we also arrive at relation

$$\frac{\partial}{\partial \delta'} = \gamma \left(1 - \frac{u}{c} \cos \delta\right) \frac{\partial}{\partial \delta} \tag{129}$$

among the operators $\frac{\partial}{\partial \delta'}$ and $\frac{\partial}{\partial \delta}$.

From equation (109) we get

$$R = r \sqrt{1 + \frac{u^2}{c^2} - 2 \frac{\boldsymbol{\upsilon} \cdot \boldsymbol{u}}{c^2}}$$

$$R = r \sqrt{1 + \frac{u^2}{c^2} - 2 \frac{u}{c} \cos \delta}. \tag{130}$$

From equation (130) we are able, whenever it is necessary, to derive the Lorentz-Einstein transformation of the quantity R through the use of transformations (124) and (127).

We consider now the angle θ between the vectors $\boldsymbol{R}$ and $\boldsymbol{u}$, as depicted in figure 6. From the law of sines for the triangle EAP we have that

$$\frac{\sin \vartheta}{r} = \frac{\sin \delta}{R}$$

$$\sin \vartheta = \frac{r}{R} \sin \delta.$$

Using equation (130) we obtain

$$\sin \vartheta = \frac{\sin \delta}{\sqrt{1 + \frac{u^2}{c^2} - 2 \frac{u}{c} \cos \delta}}. \tag{131}$$
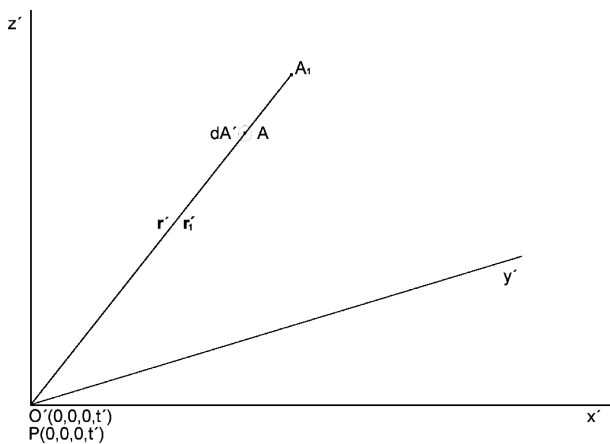
Fig. 8: The infinitesimal volume of the generalized photon in the vicinity of point A of the inertial reference frame S $(0', x', y', z', t')$. The material point particle is at position $P(0, 0, 0, t')$. The infinitesimal surface of area dA' is vertical to the vectors $r' = \overrightarrow{PA}$ and $r'_1 = \overrightarrow{PA_1}$. The points P, A and A_1 are collinear.

From the familiar identity $\sin^2 \vartheta + \cos^2 \vartheta = 1$ we have that

$$\cos \vartheta = \frac{\cos \delta - \dfrac{u}{c}}{\sqrt{1 + \dfrac{u^2}{c^2} - 2\dfrac{u}{c} \cos \delta}}. \qquad (132)$$

From transformations (124) we can, after applying equations (131) and (132), derive the Lorentz-Einstein transformations for the quantities $\sin \vartheta$ and $\cos \vartheta$. Furthermore, in the inertial reference frame S' it is $\theta' = \delta'$, as can be seen from figure 7.

3.5 The Lorentz-Einstein transformation of the volume of the generalized photon

The generalized photon moves with velocity $\boldsymbol{v}$ of magnitude $\|\boldsymbol{v}\| = c$ in any inertial reference frame. This has as a consequence that the following transformation does not hold:

$$dV' = \gamma dV.$$

This transformation holds for the volume dV of a material particle that is at rest in the inertial reference frame S'. We shall prove that the volume of the generalized photon transforms according to relation

$$dV' = \frac{dV}{\gamma \left(1 - \dfrac{u}{c} \cos \delta \right)} = \frac{dV}{\gamma \left(1 - \dfrac{\boldsymbol{v} \cdot \boldsymbol{u}}{c^2}\right)} \qquad (133)$$

for our chosen inertial reference frames S and S'.

In the region of point $A(x', y', z', t')$ of figure 7 we consider the elementary area

$$dA' = r'^2 \sin \delta' d\delta' d\omega'$$
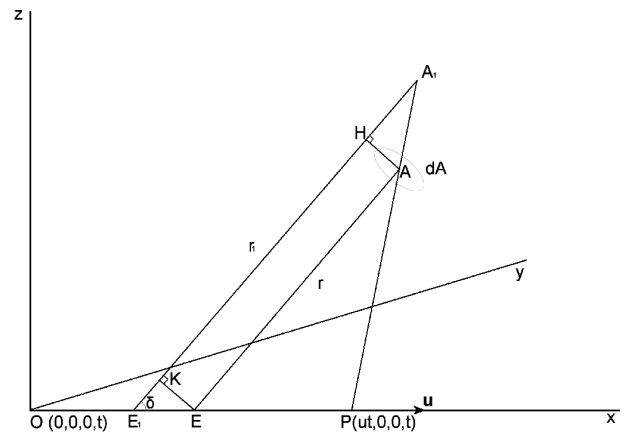
Fig. 9: Figure 8 as modulated in the inertial reference frame S $(0, x, y, z, t)$, in which the material particle moves with constant speed. The points P, A and A_1 remain collinear, as results from the Lorentz-Einstein transformations.

of a sphere with center O' and radius r'. Furthermore, we consider a point A_1 close to point A on line OA, as depicted in figure 8.

The elementary volume of the generalized photon in the inertial reference frame S' is

$$dV' = dA' \left\| \overrightarrow{AA_1} \right\| = r'^2 \sin \delta' d\delta' d\omega' \left\| \overrightarrow{AA_1} \right\| \qquad (134)$$

assuming that $A_1 \to A$.

In figure 9 we present the volume dV occupied by the generalized photon in the inertial frame of reference S.

The elementary area dA in S is

$$dA = r^2 \sin \delta d\delta d\omega$$

while the elementary volume dV is

$$dV = dA \left\| \overrightarrow{HA_1} \right\| = r^2 \sin \delta d\delta d\omega \left\| \overrightarrow{HA_1} \right\| \qquad (135)$$

since $A_1 \to A$.

From the Lorentz-Einstein transformations it directly follows that points P, A, A_1, which are collinear in reference frame S' are also collinear in reference frame S. The conclusions of paragraph 2.4 about the representation of the trajectory of the material particle in the surrounding spacetime, also lead to figure 9. Here, the trajectory of the material particle is on the x axis. We now use the following notation, as depicted in figure 9.

$$r = \left\| \overrightarrow{EA} \right\| \qquad (136)$$

$$r_1 = \left\| \overrightarrow{E_1 A_1} \right\| \qquad (137)$$

according to the notation we have established. Similarly, in figure 8 we use the notation

$$r' = \left\| \overrightarrow{O'A} \right\| \qquad (138)$$

$$r_1' = \left\| \overrightarrow{O'A_1} \right\|. \qquad (139)$$

From figure 9 we have that

$$\left\| \overrightarrow{E_1A_1} \right\| = \left\| \overrightarrow{E_1K} \right\| + \left\| \overrightarrow{KH} \right\| + \left\| \overrightarrow{HA_1} \right\|$$

and with equations (136) and (137) we get

$$r_1 = \left\| \overrightarrow{E_1K} \right\| + r + \left\| \overrightarrow{HA_1} \right\|$$

$$\left\| \overrightarrow{HA_1} \right\| = r_1 - r - \left\| \overrightarrow{E_1K} \right\|. \qquad (140)$$

From the triangle E_1KE of figure 9 we see that

$$\cos \delta = \frac{\left\| \overrightarrow{E_1K} \right\|}{\left\| \overrightarrow{E_1E} \right\|}$$

$$\left\| \overrightarrow{E_1K} \right\| = \left\| \overrightarrow{E_1E} \right\| \cos \delta. \qquad (141)$$

Similarly, we have that

$$\left\| \overrightarrow{E_1E} \right\| = u \frac{r_1 - r}{c} = u \, dw \qquad (142)$$

since in the time interval $\Delta t = \frac{r_1 - r}{c} dw$ the point particle moved from point E_1 to point E. Combining equations (141) and (142) we obtain

$$\left\| \overrightarrow{E_1K} \right\| = u \, dw \cos \delta. \qquad (143)$$

Combining equations (140) and (143) we also get

$$\left\| \overrightarrow{HA_1} \right\| = c \, dw \left(1 - \frac{u}{c} \cos \delta \right) \qquad (144)$$

since $r_1 - r = cdw$.

Combining equations (135) and (144) we get

$$dV = r^2 \sin \delta d\delta d\omega c dw \left(1 - \frac{u}{c} \cos \delta \right). \qquad (145)$$

From figure 8 we have that

$$\left\| \overrightarrow{AA_1} \right\| = \left\| \overrightarrow{O'A_1} \right\| - \left\| \overrightarrow{O'A} \right\|$$

and with equations (138) and (139) we get

$$\left\| \overrightarrow{AA_1} \right\| = r_1' - r' = cdw'. \qquad (146)$$

Combining equations (135) and (146) we also get

$$dV' = r'^2 \sin \delta' d\delta' d\omega' c dw'. \qquad (147)$$

Combining equations (145) and (147) we get

$$\frac{dV'}{dV} = \frac{r'^2 \sin \delta' d\delta' d\omega' c dw'}{r^2 \sin \delta d\delta d\omega c dw \left(1 - \frac{u}{c} \cos \delta \right)}$$

and with transformations (127), (124), (128) and (121) we get

$$\frac{dV'}{dV} = \gamma^2 \left(1 - \frac{u}{c} \cos \delta \right)^2 \frac{1}{\gamma^2 \left(1 - \frac{u}{c} \cos \delta \right)^2} \frac{1}{\gamma} \frac{1}{1 - \frac{u}{c} \cos \delta}$$

$$\frac{dV'}{dV} = \frac{1}{\gamma \left(1 - \frac{u}{c} \cos \delta \right)}$$

$$dV' = \frac{dV}{\gamma \left(1 - \frac{u}{c} \cos \delta \right)}. \qquad (148)$$

This is equation (133). Given that $\boldsymbol{u} = \begin{bmatrix} u \\ 0 \\ 0 \end{bmatrix}$ we arrive at relation

$$\frac{\boldsymbol{v} \cdot \boldsymbol{u}}{c^2} = \frac{u}{c} \frac{v_x}{c} = \frac{u}{c} \cos \delta \qquad (149)$$

since, according to equation (121), $\cos \delta = \frac{v_x}{c}$.

Combining equations (148) and (149) we have

$$dV' = \frac{dV}{\gamma \left(1 - \frac{u}{c} \cos \delta \right)} = \frac{dV}{\gamma \left(1 - \frac{\boldsymbol{v} \cdot \boldsymbol{u}}{c^2} \right)}.$$

This is the final form of equation (133).

In the form

$$dV' = \frac{dV}{\gamma \left(1 - \frac{\boldsymbol{v} \cdot \boldsymbol{u}}{c^2} \right)} \qquad (150)$$

transformation (133) also holds in the case of a material particle in arbitrary motion. In figure 5 the length of the three-dimensional arc EE_i equals $\left\| \overrightarrow{EE_i} \right\|$ at first approximation, that is, for an infinitesimal displacement of the material particle from point E to point E_i. Thus, we have exactly the situation we describe in figure 9. On the other hand, for a finite, but not infinitesimal, displacement $\overrightarrow{EE_i}$ of the material particle, the curvature $k_p(w)$ and the torsion $\tau_p(w)$ of curve C_p of figure 5 enter the transformation of the volume.

4 The study of selfvariations at macroscopic scales

4.1 Introduction

In the present paragraph we study the consequences of the selfvariations at macroscopic scales. The main conclusion we derive is the existence of energy, momentum, electric charge and electric current in the surrounding spacetime of the material particle as a direct consequence of the selfvariations. We calculate the density of energy, momentum, electric charge

and electric current in the surrounding spacetime of an arbitrarily moving material point particle.

We present the four-dimensional electromagnetic potential which is compatible with the selfvariations. An important element that emerges is the splitting of the electromagnetic potential into two individual potentials, where the first one gives the electromagnetic field that accompanies the material particle in its motion, while the second one gives the electromagnetic radiation.

We prove that the selfvariations are compatible with the principles of conservation of electric charge, energy, and momentum. This is accomplished through either direct calculation, based on the continuity equation, and also through the energy-momentum tensor of the generalized photon. These different approaches help the reader comprehend the physical reality that prevails in the surrounding spacetime of material particles.

In the preceding paragraphs we studied the generalized photon as a geometric object. In this paragraph we shall see for the first time that the generalized photon is a carrier of energy, momentum, and electric charge. The density of electric charge and electric current in the surrounding spacetime of the material particle is correlated with the electromagnetic field that accompanies the material particle in its motion. The electromagnetic radiation does not contribute to the density of electric charge and electric current.

We calculate the energy-momentum tensor for the electromagnetic field and for the generalized photon. The energy-momentum tensor describes the energy content of spacetime, but only in macroscopic scales. In microscopic scales, the energy-momentum tensor, as defined by the theory of Special Relativity, cannot describe the energy content of spacetime.

4.2 The density of electric charge and electric current in the surrounding spacetime of an electrically charged point particle

In figure 6 the electric charge q acts at point $A(x, y, z, t)$ with the value it had at point E. Thus, we have $q = q(w)$. Hence, it follows that

$$\frac{\partial q}{\partial t} = \frac{\partial q}{\partial w} \frac{\partial w}{\partial t}$$

$$\nabla q = \frac{\partial q}{\partial w} \nabla w$$

and with equations (11) and (12) we have that

$$\frac{\partial q}{\partial t} = \frac{\partial q}{\partial w} \frac{1}{1 - \frac{\boldsymbol{v} \cdot \boldsymbol{u}}{c^2}} \tag{151}$$

$$\nabla q = -\frac{\partial q}{c \partial w} \frac{1}{1 - \frac{\boldsymbol{v} \cdot \boldsymbol{u}}{c^2}} \frac{\boldsymbol{v}}{c}. \tag{152}$$

According to Special Relativity and the symbols we use

in figure 6, the intensity $\boldsymbol{\varepsilon}$ of the electric field at point A is

$$\boldsymbol{\varepsilon} = \frac{\gamma q}{4\pi\varepsilon_0 r'^3} \boldsymbol{R} \tag{153}$$

where $\boldsymbol{R}$ is given by equation (106), r' by equation (117), and $\gamma = \frac{1}{\sqrt{1 - \frac{u^2}{c^2}}}$. From Gauss's law [12–18] we obtain for the electric charge density ρ at point A:

$$\rho = \varepsilon_0 \nabla \cdot \boldsymbol{\varepsilon}$$

$$\rho = \varepsilon_0 \nabla \cdot \left(\frac{\gamma q}{4\pi\varepsilon_0 r'^3} \boldsymbol{R} \right)$$

$$\rho = \frac{q\gamma}{4\pi} \nabla \cdot \left(\frac{\boldsymbol{R}}{r'^3} \right) + \frac{\gamma}{4\pi R'^3} \boldsymbol{R} \cdot \nabla q. \tag{154}$$

We can easily prove that

$$\nabla \cdot \left(\frac{\boldsymbol{R}}{r'^3} \right) = 0. \tag{155}$$

We can avoid the calculation, if we take into account that, ignoring the selfvariations, for constant electric charge q, classical Electromagnetism predicts that $\rho = 0$ at point A. This is equivalent with equation (155).

Combining equations (154) and (155) we get

$$\rho = \frac{\gamma}{4\pi r'^3} \boldsymbol{R} \cdot \nabla q.$$

Using equation (152) we get

$$\rho = -\frac{\partial q}{c \partial w} \frac{\gamma}{4\pi r'^3 \left(1 - \frac{\boldsymbol{v} \cdot \boldsymbol{u}}{c^2} \right)} \frac{\boldsymbol{v}}{c} \cdot \boldsymbol{R}.$$

After applying equation (109) we have that

$$\rho = -\frac{\partial q}{c \partial w} \frac{\gamma r}{4\pi r'^3 \left(1 - \frac{\boldsymbol{v} \cdot \boldsymbol{u}}{c^2} \right)} \frac{\boldsymbol{v}}{c} \left(\frac{\boldsymbol{v}}{c} - \frac{\boldsymbol{u}}{c} \right)$$

$$\rho = -\frac{\partial q}{c \partial w} \frac{\gamma r}{4\pi r'^3} \frac{1}{\left(1 - \frac{\boldsymbol{v} \cdot \boldsymbol{u}}{c^2} \right)} \left(1 - \frac{\boldsymbol{v} \cdot \boldsymbol{u}}{c^2} \right)$$

$$\rho = -\frac{\partial q}{c \partial w} \frac{\gamma r}{4\pi r'^3}.$$

Using transformation (127) we get

$$\rho = -\frac{\partial q}{c \partial w} \frac{1}{4\pi\gamma^2 r^2 \left(1 - \frac{\boldsymbol{v} \cdot \boldsymbol{u}}{c^2} \right)^3}. \tag{156}$$

We can derive the same equation in a different way. We will develop the second method in the next paragraph for the calculation of the density of energy D due to the selfvariations of the rest mass of the material particle, where we will not be able to use Gauss's law. The reader can easily apply the

method of the next paragraph to the electric charge, and still come up with equation (156).

The generalized photon moves with velocity $\boldsymbol{v}$, therefore the current density $\boldsymbol{j}$ is given by equation

$$\boldsymbol{j} = \rho \boldsymbol{v} \qquad (157)$$

where the charge density ρ is given by equation (156). Equation (157) can also be easily inferred from Ampere's law

$$\nabla \times \boldsymbol{B} = \mu_0 \boldsymbol{j} + \frac{\partial \boldsymbol{\varepsilon}}{c^2 \partial t}. \qquad (158)$$

The intensity of the magnetic field $\boldsymbol{B}$ at point A of figure 6 is given initially by the Biot-Savart law:

$$\boldsymbol{B} = \frac{\boldsymbol{u}}{c^2} \times \boldsymbol{\varepsilon}. \qquad (159)$$

Combining equations (153) and (109) we get

$$\boldsymbol{\varepsilon} = \frac{\gamma q}{4\pi \varepsilon_0 r'^3} r \left(\frac{\boldsymbol{v}}{c} - \frac{\boldsymbol{u}}{c} \right)$$

and from equation (127) we have

$$\boldsymbol{\varepsilon} = \frac{q}{4\pi \varepsilon_0 \gamma^2 r^2 \left(1 - \frac{\boldsymbol{v} \cdot \boldsymbol{u}}{c^2} \right)^3} \left(\frac{\boldsymbol{v}}{c} - \frac{\boldsymbol{u}}{c} \right). \qquad (160)$$

From equation (160) we get

$$\frac{\boldsymbol{u}}{c^2} \times \boldsymbol{\varepsilon} = \frac{\boldsymbol{v}}{c} \times \boldsymbol{\varepsilon}$$

and from equation (159) we get

$$\boldsymbol{B} = \frac{\boldsymbol{v}}{c^2} \times \boldsymbol{\varepsilon}. \qquad (161)$$

In equation (161) the velocity $\boldsymbol{v}$ of the generalized photon refers to point A of figure 6. This has as a consequence that all physical quantities $\boldsymbol{B}$, $\boldsymbol{v}$, $\boldsymbol{\varepsilon}$ appearing in equation (161) refer to the same point in spacetime. On the contrary, in equation (159) the velocity $\boldsymbol{u}$ of the material particle does not refer to point A, where the electromagnetic field is manifested. Equation (161) also holds for the case where the material particle is in arbitrary motion, as we shall see in a later paragraph.

4.3 The density of energy and momentum in the surrounding spacetime of a material point particle

In the case of the rest mass we cannot apply Gauss's law in order to calculate the energy density D in the surrounding spacetime of the material particle. Because of this we will develop a completely different proving procedure. We initially calculate the energy density D' in the inertial reference frame S' in which the material particle is at rest. At point A of figure 7 the energy density D' due to the selfvariations is

$$D' = c^2 \frac{m_0 \left(t' - \frac{r'}{c} \right) - m_0 \left(t' - \frac{r' + dr'}{c} \right)}{4\pi r'^2 dr'}. \qquad (162)$$

From equation (112) and for a specific time t' we have that

$$dw' = -\frac{dr'}{c}$$

and equation (162) becomes

$$D' = c^2 \frac{\dfrac{dm_0}{dr'}}{4\pi r'^2} = -c \frac{\dfrac{dm_0}{dw'}}{4\pi r'^2}. \qquad (163)$$

We now consider the Lorentz-Einstein transformations for the energy E and the momentum $\boldsymbol{P}$ of the generalized photon:

$$
\begin{aligned}
E &= \gamma \left(E' + uP'_x \right) & E' &= \gamma \left(E - uP_x \right) \\
P_x &= \gamma \left(P'_x + \frac{u}{c^2} E' \right) & P'_x &= \gamma \left(P_x - \frac{u}{c^2} E \right) \\
P_y &= P'_y & P'_y &= P_y \\
P_z &= P'_z & P'_z &= P_z.
\end{aligned}
\qquad (164)
$$

Defining as dV the infinitesimal volume occupied by the generalized photon at point A of figure 6 we have

$$D = \frac{dE}{dV}.$$

Applying the transformations (164) and (150) we get

$$D = \frac{\gamma \left(dE' + u dP'_x \right)}{\gamma \left(1 - \frac{\boldsymbol{v} \cdot \boldsymbol{u}}{c^2} \right) dV'}$$

$$D = \frac{dE' + u \frac{v'_x}{c^2} dE'}{\left(1 - \frac{\boldsymbol{v} \cdot \boldsymbol{u}}{c^2} \right) dV'}$$

$$D = \frac{1 + \frac{u v'_x}{c^2}}{1 - \frac{\boldsymbol{v} \cdot \boldsymbol{u}}{c^2}} \frac{dE'}{dV'}$$

$$D = \frac{1 + \frac{u v'_x}{c^2}}{1 - \frac{\boldsymbol{v} \cdot \boldsymbol{u}}{c^2}} D'. \qquad (165)$$

From transformations (123) for the velocity we get

$$1 + \frac{u v'_x}{c^2} = 1 + \frac{u}{c^2} \frac{v_x - u}{1 - \frac{u v_x}{c^2}} =$$

$$\frac{1 - \frac{u^2}{c^2}}{1 - \frac{u v_x}{c^2}} = \frac{1}{\gamma^2 \left(1 - \frac{u v_x}{c^2} \right)}$$

and since $\frac{\boldsymbol{v} \cdot \boldsymbol{u}}{c^2} = \frac{u}{c} \cos \delta$, we get

$$1 + \frac{u v'_x}{c^2} = \frac{1}{\gamma^2 \left(1 - \frac{\boldsymbol{v} \cdot \boldsymbol{u}}{c^2} \right)}. \qquad (166)$$

Combining equations (165) and (166) we have

$$D = \frac{1}{\gamma^2 \left(1 - \frac{\boldsymbol{v} \cdot \boldsymbol{u}}{c^2}\right)^2} D'$$

and with (163) we get

$$D = -c \frac{1}{\gamma^2 \left(1 - \frac{\boldsymbol{v} \cdot \boldsymbol{u}}{c^2}\right)^2} \frac{\frac{dm_0}{dw'}}{4\pi r'^2}.$$

Applying transformations (120) and (127) we obtain

$$D = -c \frac{\partial m_0}{\partial w} \frac{1}{4\pi \gamma^3 r^2 \left(1 - \frac{\boldsymbol{v} \cdot \boldsymbol{u}}{c^2}\right)^4}. \qquad (167)$$

The generalized photon moves with velocity $\boldsymbol{v}$, so we have

$$\boldsymbol{J} = \boldsymbol{D} \frac{\boldsymbol{v}}{c^2} \qquad (168)$$

for the momentum density $\boldsymbol{J}$ at point A of figure 6.

Factor $\frac{\partial m_0}{\partial w}$, which appears in the equations of this paragraph, corresponds to factor $\frac{\partial q}{\partial w}$ in the equations of the previous paragraph. In figure 6, the rest mass m_0 of the point particle acts on point $A(x, y, x, t)$ with the value it had at point E, namely $m_0 = m_0(w)$. Therefore, we have

$$\frac{\partial m_0}{\partial t} = \frac{\partial m_0}{\partial w} \frac{\partial w}{\partial t}$$

$$\nabla m_0 = \frac{\partial m_0}{\partial w} \nabla w$$

and with equations (11) and (12), we get

$$\frac{\partial m_0}{\partial t} = \frac{\partial m_0}{\partial w} \frac{1}{1 - \frac{\boldsymbol{v} \cdot \boldsymbol{u}}{c^2}}$$

$$\nabla m_0 = -\frac{\partial m_0}{c \partial w} \frac{1}{1 - \frac{\boldsymbol{v} \cdot \boldsymbol{u}}{c^2}} \frac{\boldsymbol{v}}{c}. \qquad (169)$$

These equations are analogous to equations (151) and (152) for the electric charge.

4.4 The selfvariations are in accordance with the principle of conservation of the electric charge

In figure 6 and for the time interval from $w = t - \frac{r}{c}$ to t, the generalized photons emitted by the material particle are contained within a sphere with centre E and radius r. In order for the conservation of the electric charge to hold, we have to prove the validity of equation:

$$q\left(t - \frac{r}{c}\right) = q(t) + \int_V \rho dV = q(t) + q_i \qquad (170)$$

where V is the volume of the sphere with centre E and radius r, and

$$q_i = \int_V \rho dV \qquad (171)$$

is the electric charge, due to the selfvariations, contained within the sphere. From equation (145), we get for the infinitesimal volume dV

$$dV = b^2 \left(1 - \frac{u}{c} \cos \delta\right) \sin \delta d\delta d\omega c dw$$
$$0 \le \delta \le \pi$$
$$0 \le \omega < 2\pi \qquad (172)$$
$$0 \le b \le r$$
$$t - \frac{r}{c} \le w \le t.$$

Combining equations (156) and (129) we get

$$\rho = -\frac{\partial q}{c \partial w} \frac{1}{4\pi \gamma^2 r^2 \left(1 - \frac{u}{c} \cos \delta\right)^3}. \qquad (173)$$

Combining equations (171) and (173) we also get

$$q_i = \int_V \rho dV$$
$$q_i = -\int_0^\pi \int_0^{2\pi} \int_{t-\frac{r}{c}}^t \frac{\partial q}{c \partial w} \frac{1}{4\pi \gamma^2 b^2 \left(1 - \frac{u}{c} \cos \delta\right)^3}$$
$$b^2 \left(1 - \frac{u}{c} \cos \delta\right) \sin \delta d\delta d\omega c dw$$

$$q_i = -\int_0^\pi \int_0^{2\pi} \int_{t-\frac{r}{c}}^t \frac{\partial q}{\partial w} \frac{\sin \delta}{4\pi \gamma^2 \left(1 - \frac{u}{c} \cos \delta\right)^2} d\delta d\omega dw$$

$$q_i = -\frac{1}{2\gamma^2} \int_0^\pi \int_{t-\frac{r}{c}}^t \frac{\partial q}{\partial w} \frac{\sin \delta}{\left(1 - \frac{u}{c} \cos \delta\right)^2} d\delta dw. \qquad (174)$$

We now denote

$$\lambda = 1 - \frac{u}{c} \cos \delta. \qquad (175)$$

Thus, we have

$$\frac{c}{u} d\lambda = \sin \delta d\delta \qquad (176)$$

$$1 - \frac{u}{c} \le \lambda \le 1 + \frac{u}{c}. \qquad (177)$$

So we have

$$\int_0^\pi \frac{\sin \delta}{\left(1 - \frac{u}{c} \cos \delta\right)^2} d\delta = \int_{1-\frac{u}{c}}^{1+\frac{u}{c}} \frac{\frac{c}{u} d\lambda}{\lambda^2} = -\frac{c}{u} \left[\frac{1}{\lambda}\right]_{1-\frac{u}{c}}^{1+\frac{u}{c}} =$$

$$-\frac{c}{u} \left(\frac{1}{1 + \frac{u}{c}} - \frac{1}{1 - \frac{u}{c}}\right) = -\frac{c}{u} \frac{-2\frac{u}{c}}{1 - \frac{u^2}{c^2}} = \frac{2}{1 - \frac{u^2}{c^2}} = 2\gamma^2$$

and equation (174) becomes

$$q_i = -\int_{t-\frac{r}{c}}^{t} \frac{\partial q}{\partial w} dw$$

$$q_i = -\left[q\left(w\right)\right]_{t-\frac{r}{c}}^{t}$$

$$q_i = q\left(t - \frac{r}{c}\right) - q\left(t\right)$$

$$q\left(t\right) + q_i = q\left(t - \frac{r}{c}\right)$$

which is equation (170).

We can also prove the conservation of the electric charge through the equation of continuity

$$\frac{\partial \rho}{\partial t} + \nabla \cdot \boldsymbol{j} = 0. \tag{178}$$

Indeed, taking into account equation (157) we have

$$\frac{\partial \rho}{\partial t} + \nabla \cdot \boldsymbol{j} = \frac{\partial \rho}{\partial t} + \nabla \cdot (\rho \boldsymbol{v})$$

$$\frac{\partial \rho}{\partial t} + \nabla \cdot \boldsymbol{j} = \frac{\partial \rho}{\partial t} + \boldsymbol{v} \cdot \nabla \rho + \rho \nabla \cdot \boldsymbol{v}$$

and with equation (22) we get

$$\frac{\partial \rho}{\partial t} + \nabla \cdot \boldsymbol{j} = \frac{\partial \rho}{\partial t} + \boldsymbol{v} \cdot \nabla \rho + \frac{2c}{r} \rho.$$

Applying equation (86) of the fundamental mathematical theorem, for $f = \rho$, we get

$$\frac{\partial \rho}{\partial t} + \nabla \cdot \boldsymbol{j} = c \frac{\partial \rho}{\partial r} + \frac{2c}{r} \rho. \tag{179}$$

From equation (173) we have

$$\frac{\partial \rho}{\partial r} = -\frac{2\rho}{r}. \tag{180}$$

Combining equations (179) and (180) we finally get

$$\frac{\partial \rho}{\partial t} + \nabla \cdot \boldsymbol{j} = 0.$$

4.5 The selfvariations are in accordance with the conservation principles of energy and momentum

In figure 6, for the time interval from $w = t - \frac{r}{c}$ to t, the generalized photons emitted by the material particle due to the selfvariation of the rest mass are contained within the sphere with centre E and radius r. In order for the conservation of energy to hold, it is enough to prove the validity of the following equation:

$$c^2 \gamma m_0 \left(t - \frac{r}{c}\right) = c^2 \gamma m_0 \left(t\right) + \int_V D dV = c^2 m_0 \left(t\right) + E_i \tag{181}$$

where V is the volume of the sphere with centre E and radius r, and

$$E_i = \int_V D dV \tag{182}$$

is the energy due to the selfvariation of the rest mass, which is contained within the sphere. Combining equations (167) and (129) we get

$$D = -c \frac{\partial m_0}{\partial w} \frac{1}{4\pi\gamma^3 r^2 \left(1 - \frac{u}{c}\cos\delta\right)^4}. \tag{183}$$

Combining equations (182) and (183), and following the notation of equation (172), we get

$$E_i = -c \int_0^\pi \int_0^{2\pi} \int_{t-\frac{r}{c}}^{t} \frac{\partial m_0}{\partial w} \frac{1}{4\pi\gamma^3 b^2 \left(1 - \frac{u}{c}\cos\delta\right)^4}$$
$$b^2 \left(1 - \frac{u}{c}\cos\delta\right) \sin\delta d\delta d\omega c dw$$

$$E_i = -\frac{c^2}{4\pi\gamma^3} \int_0^\pi \int_0^{2\pi} \int_{t-\frac{r}{c}}^{t} \frac{\partial m_0}{\partial w} \frac{\sin\delta}{\left(1 - \frac{u}{c}\cos\delta\right)^3} d\delta d\omega dw$$

$$E_i = -\frac{c^2}{2\gamma^3} \int_0^\pi \int_{t-\frac{r}{c}}^{t} \frac{\partial m_0}{\partial w} \frac{\sin\delta}{\left(1 - \frac{u}{c}\cos\delta\right)^3} d\delta dw. \tag{184}$$

Using the notation of equations (175), (176), and (177) we have

$$\int_0^\pi \frac{\sin\delta}{\left(1 - \frac{u}{c}\cos\delta\right)^3} d\delta = \int_{1-\frac{u}{c}}^{1+\frac{u}{c}} \frac{u}{\lambda^3} d\lambda =$$

$$-\frac{c}{2u} \left[\frac{1}{\lambda^2}\right]_{1-\frac{u}{c}}^{1+\frac{u}{c}} = -\frac{c}{2u} \left(\frac{1}{\left(1+\frac{u}{c}\right)^2} - \frac{1}{\left(1-\frac{u}{c}\right)^2}\right) =$$

$$-\frac{c}{2u} \frac{-4\frac{u}{c}}{\left(1-\frac{u^2}{c^2}\right)^2} = \frac{2}{\left(1-\frac{u^2}{c^2}\right)^2} = 2\gamma^4.$$

Now (184) becomes

$$E_i = -c^2 \gamma \int_{t-\frac{r}{c}}^{t} \frac{\partial m_0}{\partial w} dw$$

$$E_i = -c^2 \gamma \left[m_0\right]_{t-\frac{r}{c}}^{t}$$

$$E_i = -c^2 \gamma m_0 \left(t\right) + c^2 \gamma m_0 \left(t - \frac{r}{c}\right)$$

$$c^2 \gamma m_0 \left(t - \frac{r}{c}\right) = c^2 \gamma m_0 \left(t\right) + E_i$$

which is equation (181).

The conservation of energy can also be proven using the continuity equation

$$\frac{\partial D}{c^2 \partial t} + \nabla \cdot \boldsymbol{j} = 0. \tag{185}$$

Indeed, if we take into account equation (168) we obtain

$$\frac{\partial D}{c^2 \partial t} + \nabla \cdot \boldsymbol{j} = \frac{\partial D}{c^2 \partial t} + \nabla \cdot \left(D \frac{\boldsymbol{v}}{c^2} \right)$$

$$\frac{\partial D}{c^2 \partial t} + \nabla \cdot \boldsymbol{j} = \frac{\partial D}{c^2 \partial t} + \frac{\boldsymbol{v}}{c^2} \nabla D + \frac{D}{c^2} \nabla \cdot \boldsymbol{v}$$

and with equation (22) we have

$$\frac{\partial D}{c^2 \partial t} + \nabla \cdot \boldsymbol{j} = \frac{\partial D}{c^2 \partial t} + \frac{\boldsymbol{v}}{c^2} \nabla D + \frac{D}{c^2} \nabla \frac{2c}{r}.$$

Using equation (86) of the fundamental mathematical theorem for $f = D$, we get

$$\frac{\partial D}{c^2 \partial t} + \nabla \cdot \boldsymbol{j} = c \frac{\partial D}{c^2 \partial r} + \frac{D}{c^2} \frac{2c}{r}. \tag{186}$$

From equation (183) we have

$$\frac{\partial D}{\partial r} = -\frac{2D}{r}. \tag{187}$$

Combining equations (186) and (187) we get

$$\frac{\partial D}{c^2 \partial t} + \nabla \cdot \boldsymbol{j} = 0.$$

In order to prove the conservation of momentum, it suffices to prove the corresponding of equation (181), that is, it is enough to prove equation

$$\gamma m_0 \left(t - \frac{r}{c} \right) \boldsymbol{u} = \gamma m_0 (t) \boldsymbol{u} + \int_V \boldsymbol{J} dV = \gamma m_0 (t) \boldsymbol{u} + \boldsymbol{P}_i \tag{188}$$

where

$$\boldsymbol{P}_i = \int_V \boldsymbol{J} dV \tag{189}$$

is the momentum due to the selfvariation of the rest mass, contained within the sphere of centre E and radius r. Combining equations (189) and (168) we obtain

$$\boldsymbol{P}_i = \int_V D \frac{\boldsymbol{v}}{c^2} dV. \tag{190}$$

We first work on the x-axis:

$$P_{ix} = \int_V D \frac{v_x}{c^2} dV.$$

Using equation (121) we get

$$P_{ix} = \int_V D \frac{\cos \delta}{c} dV$$

and with equations (183) and (172) we get

$$P_{ix} = - \int_0^\pi \int_0^{2\pi} \int_{t-\frac{r}{c}}^t \frac{\partial m_0}{\partial w} \frac{\cos \delta}{4\pi \gamma^3 b^2 \left(1 - \frac{u}{c} \cos \delta \right)^4}$$
$$b^2 \left(1 - \frac{u}{c} \cos \delta \right) \sin \delta d\delta d\omega c dw$$

$$P_{ix} = - \int_0^\pi \int_0^{2\pi} \int_{t-\frac{r}{c}}^t \frac{\partial m_0}{\partial w} \frac{\cos \delta \sin \delta}{4\pi \gamma^3 b^2 \left(1 - \frac{u}{c} \cos \delta \right)^3} d\delta d\omega c dw$$

$$P_{ix} = - \frac{c}{4\pi \gamma^3} \int_0^\pi \int_0^{2\pi} \int_{t-\frac{r}{c}}^t \frac{\partial m_0}{\partial w} \frac{\cos \delta \sin \delta}{\left(1 - \frac{u}{c} \cos \delta \right)^3} d\delta d\omega dw$$

$$P_{ix} = - \frac{c}{2\gamma^3} \int_0^\pi \int_{t-\frac{r}{c}}^t \frac{\partial m_0}{\partial w} \frac{\cos \delta \sin \delta}{\left(1 - \frac{u}{c} \cos \delta \right)^3} d\delta dw. \tag{191}$$

Using the notation appearing in equations (175), (176), and (177) we have

$$\int_0^\pi \frac{\cos \delta \sin \delta}{\left(1 - \frac{u}{c} \cos \delta \right)^3} d\delta = \int_{1-\frac{u}{c}}^{1+\frac{u}{c}} \frac{c^2}{u^2} \frac{1 - \lambda}{\lambda^3} d\lambda =$$

$$\frac{c^2}{u^2} \int_{1-\frac{u}{c}}^{1+\frac{u}{c}} \left(\frac{1}{\lambda^3} - \frac{1}{\lambda^2} \right) d\lambda = \frac{c^2}{u^2} \left(-\frac{1}{2} \left[\frac{1}{\lambda^2} \right]_{1-\frac{u}{c}}^{1+\frac{u}{c}} + \left[\frac{1}{\lambda} \right]_{1-\frac{u}{c}}^{1+\frac{u}{c}} \right) =$$

$$\frac{c^2}{u^2} \left(-\frac{1}{2} \frac{\left(1 + \frac{u}{c} \right)^2 - \left(1 - \frac{u}{c} \right)^2}{\left(1 - \frac{u^2}{c^2} \right)^2} + \frac{-2 \frac{u}{c}}{1 - \frac{u^2}{c^2}} \right) =$$

$$\frac{c^2}{u^2} \left(-\frac{1}{2} \frac{-4 \frac{u}{c}}{\left(1 - \frac{u^2}{c^2} \right)^2} - \frac{2 \frac{u}{c}}{1 - \frac{u^2}{c^2}} \right) =$$

$$\frac{2c}{u} \left(\frac{1}{\left(1 - \frac{u^2}{c^2} \right)^2} - \frac{1}{1 - \frac{u^2}{c^2}} \right) =$$

$$\frac{\frac{2c}{u}}{\left(1 - \frac{u^2}{c^2} \right)^2} \left(1 - 1 + \frac{u^2}{c^2} \right) = \frac{\frac{2u}{c}}{\left(1 - \frac{u^2}{c^2} \right)^2} = 2\gamma^4 \frac{u}{c}$$

and equation (181) becomes

$$P_{ix} = -u\gamma \int_{t-\frac{r}{c}}^t \frac{\partial m_0}{\partial w} dw = -u\gamma \left[m_0 \right]_{t-\frac{r}{c}}^t$$

$$P_{ix} = u\gamma m_0 \left(t - \frac{r}{c} \right) - u\gamma m_0 (t). \tag{192}$$

Similarly for the y-axis we get

$$P_{iy} = - \int_0^\pi \int_0^{2\pi} \int_{t-\frac{r}{c}}^t \frac{\partial m_0}{\partial w} \frac{\sin \delta}{\left(1 - \frac{u}{c} \cos \delta \right)^3} v_y d\delta d\omega dw$$

and with equation (121)

$$\frac{v_y}{c} = \sin\delta\cos\omega$$

we get

$$P_{iy} = -\int_0^\pi \int_0^{2\pi} \int_{t-\frac{r}{c}}^{t} \frac{\partial m_0}{\partial w} \frac{c\sin^2\delta\cos\omega}{\left(1 - \frac{u}{c}\cos\delta\right)^3} d\delta d\omega dw. \quad (193)$$

The presence of factor $\cos\omega$ causes integral (193) to vanish, and we have

$$P_{iy} = 0. \quad (194)$$

We can similarly prove that

$$P_{iz} = 0. \quad (195)$$

Given that

$$\boldsymbol{u} = \begin{bmatrix} u \\ 0 \\ 0 \end{bmatrix}$$

equations (192), (194) and (195) can be written as

$$\boldsymbol{P}_i = \boldsymbol{u}\gamma m_0\left(t - \frac{r}{c}\right) - \boldsymbol{u}\gamma m_0(t)$$

which is equation (188).

From equation (181) we get

$$E_i = \int_V D dV = c^2\gamma\left(m_0\left(t - \frac{r}{c}\right) - m_0(t)\right). \quad (196)$$

From equation (188) we also have

$$\boldsymbol{P}_i = \int_V \boldsymbol{J} dV = \boldsymbol{u}\gamma\left(m_0\left(t - \frac{r}{c}\right) - m_0(t)\right). \quad (197)$$

Combining equations (196) and (197) we get

$$\boldsymbol{P}_i = E_i \frac{\boldsymbol{u}}{c^2} \quad (198)$$

and

$$\int_V \boldsymbol{J} dV = \frac{\boldsymbol{u}}{c^2} \int_V D dV. \quad (199)$$

Equations (198) and (199) hold for every volume V, i.e. for every radius r of the sphere with centre E and radius r of figure 6. Therefore, they also hold for $r = 0$, that is, on the material particle at time w. Hence, the total energy E_s and the total momentum $\boldsymbol{P}_s$ emitted by the material particle at time w in all directions, are connected through the relation

$$\boldsymbol{P}_s = E_s \frac{\boldsymbol{u}}{c^2} \quad (200)$$

where $\boldsymbol{u} = \boldsymbol{u}(w)$. This equation has fundamental consequences for the material particle, and we shall encounter them as our study continues.

4.6 The electromagnetic field in the macrocosm. The electromagnetic potential of the selfvariations

Using the symbols at point $A(x, y, z, t)$ of figure 4, the scalar potential V and the vector potential A of the selfvariations are given by the following equations:

$$V = \frac{q\left(1 - \frac{u^2}{c^2}\right)}{4\pi\varepsilon_0 r\left(1 - \frac{\boldsymbol{v}\cdot\boldsymbol{u}}{c^2}\right)^2} + \frac{q(\boldsymbol{v}\cdot\boldsymbol{\alpha})}{4\pi\varepsilon_0 c^3\left(1 - \frac{\boldsymbol{v}\cdot\boldsymbol{u}}{c^2}\right)^2} \quad (201)$$

$$\boldsymbol{A} = V\frac{\boldsymbol{v}}{c^2}. \quad (202)$$

The intensity $\boldsymbol{\varepsilon}$ of the electric field, and the intensity $\boldsymbol{B}$ of the magnetic field arising from these two potentials, are given by

$$\boldsymbol{\varepsilon} = \frac{q\left(1 - \frac{u^2}{c^2}\right)}{4\pi\varepsilon_0 r^2\left(1 - \frac{\boldsymbol{v}\cdot\boldsymbol{u}}{c^2}\right)^3}\left(\frac{\boldsymbol{v}}{c} - \frac{\boldsymbol{u}}{c}\right) +$$
$$+ \frac{q}{4\pi\varepsilon_0 r\left(1 - \frac{\boldsymbol{v}\cdot\boldsymbol{u}}{c^2}\right)^2}\left[\frac{\left(\frac{\boldsymbol{v}}{c}\boldsymbol{\alpha}\right)}{1 - \frac{\boldsymbol{v}\cdot\boldsymbol{u}}{c^2}}\left(\frac{\boldsymbol{v}}{c} - \frac{\boldsymbol{u}}{c}\right) - \boldsymbol{\alpha}\right] \quad (203)$$

$$\boldsymbol{B} = \frac{q\left(1 - \frac{u^2}{c^2}\right)}{4\pi\varepsilon_0 r^2\left(1 - \frac{\boldsymbol{v}\cdot\boldsymbol{u}}{c^2}\right)^3}\frac{\boldsymbol{u}}{c}\times\frac{\boldsymbol{v}}{c} +$$
$$+ \frac{q}{4\pi\varepsilon_0 r\left(1 - \frac{\boldsymbol{v}\cdot\boldsymbol{u}}{c^2}\right)}\left[\frac{\left(\frac{\boldsymbol{v}}{c}\boldsymbol{\alpha}\right)}{1 - \frac{\boldsymbol{v}\cdot\boldsymbol{u}}{c^2}}\left(\frac{\boldsymbol{u}}{c}\times\frac{\boldsymbol{v}}{c}\right) - \frac{\boldsymbol{v}}{c}\times\boldsymbol{\alpha}\right] \quad (204)$$

where $\boldsymbol{u} = \boldsymbol{u}(w)$ is the velocity, and $\boldsymbol{\alpha} = \boldsymbol{\alpha}(w)$ is the acceleration of the material particle. Furthermore, the density of electric charge at point A is

$$\rho = -\frac{\partial q}{\partial w}\frac{1}{4\pi\gamma^2 r^2\left(1 - \frac{\boldsymbol{v}\cdot\boldsymbol{u}}{c^2}\right)^3} \quad (205)$$

exactly as given by equation (156).

In equations (203) and (204) we recognize the electromagnetic field as we know it experimentally, but also as predicted by the Lienard-Wiechert potentials. However, the electromagnetic potentials of the selfvariations have a fundamental characteristic that is not shared by the Lienard-Wiechert potentials. Namely, they split into two individual couples of potentials

$$V_u = \frac{q\left(1 - \frac{u^2}{c^2}\right)}{4\pi\varepsilon_0 r\left(1 - \frac{\boldsymbol{v}\cdot\boldsymbol{u}}{c^2}\right)^2} \quad (206)$$

$$\boldsymbol{A}_u = V_u\frac{\boldsymbol{v}}{c^2}$$

and

$$V_\alpha = \frac{q\,(\boldsymbol{v}\cdot\boldsymbol{\alpha})}{4\pi\varepsilon_0 c^3 \left(1 - \frac{\boldsymbol{v}\cdot\boldsymbol{u}}{c^2}\right)^2} \tag{207}$$

$$\boldsymbol{A}_\alpha = V_\alpha \frac{\boldsymbol{v}}{c^2}.$$

The (206) potentials express the electromagnetic field

$$\boldsymbol{\varepsilon}_u = \frac{q\left(1 - \frac{u^2}{c^2}\right)}{4\pi\varepsilon_0 r^2 \left(1 - \frac{\boldsymbol{v}\cdot\boldsymbol{u}}{c^2}\right)^3}\left(\frac{\boldsymbol{v}}{c} - \frac{\boldsymbol{u}}{c}\right)$$

$$B_u = \frac{q\left(1 - \frac{u^2}{c^2}\right)}{4\pi\varepsilon_0 r^2 \left(1 - \frac{\boldsymbol{v}\cdot\boldsymbol{u}}{c^2}\right)^3}\frac{\boldsymbol{u}}{c}\times\frac{\boldsymbol{v}}{c}. \tag{208}$$

that accompanies the material particle in its motion. The (207) potentials express the electromagnetic radiation

$$\boldsymbol{\varepsilon}_\alpha = \frac{q}{4\pi\varepsilon_0 c^2 r\left(1 - \frac{\boldsymbol{v}\cdot\boldsymbol{u}}{c^2}\right)^2}\left[\frac{\left(\frac{\boldsymbol{v}}{c}\boldsymbol{\alpha}\right)}{1 - \frac{\boldsymbol{v}\cdot\boldsymbol{u}}{c^2}}\left(\frac{\boldsymbol{v}}{c}-\frac{\boldsymbol{u}}{c}\right)-\boldsymbol{\alpha}\right]$$

$$B_\alpha = \frac{q}{4\pi\varepsilon_0 r\left(1 - \frac{\boldsymbol{v}\cdot\boldsymbol{u}}{c^2}\right)}\left[\frac{\left(\frac{\boldsymbol{v}}{c}\boldsymbol{\alpha}\right)}{1 - \frac{\boldsymbol{v}\cdot\boldsymbol{u}}{c^2}}\left(\frac{\boldsymbol{u}}{c}\times\frac{\boldsymbol{v}}{c}\right)-\frac{\boldsymbol{v}}{c}\times\boldsymbol{\alpha}\right]. \tag{209}$$

The (207) potential of the electromagnetic radiation does not depend on the distance r, while it vanishes for $\boldsymbol{v}\cdot\boldsymbol{\alpha} = 0$. Furthermore, for each couple of the electromagnetic field we can easily prove that equation (161) holds

$$B_u = \frac{\boldsymbol{v}}{c^2}\times\boldsymbol{\varepsilon}_u \tag{210}$$

$$B_\alpha = \frac{\boldsymbol{v}}{c^2}\times\boldsymbol{\varepsilon}_\alpha. \tag{211}$$

We remind the reader that the electromagnetic field can be calculated from the electromagnetic potentials via equations

$$\boldsymbol{\varepsilon} = -\nabla V - \frac{\partial\boldsymbol{A}}{\partial t} \tag{212}$$

$$B = \nabla\times\boldsymbol{A} \tag{213}$$

where $\nabla V = \begin{bmatrix}\frac{\partial V}{\partial x}\\\frac{\partial V}{\partial y}\\\frac{\partial V}{\partial z}\end{bmatrix}$, and $\nabla\times\boldsymbol{A} = \text{curl }\boldsymbol{A}$.

We shall now prove equation

$$\boldsymbol{\varepsilon}_\alpha = -\nabla V_\alpha - \frac{\partial\boldsymbol{A}_\alpha}{\partial t} \tag{214}$$

and the general equations (203) and (204) can be proven similarly. We shall make use of the equations of paragraph 2.7. From the (207) potentials we obtain

$$\boldsymbol{\varepsilon}_\alpha = -\left[\frac{q\,(\boldsymbol{v}\cdot\boldsymbol{\alpha})}{4\pi\varepsilon_0 c^3\left(1 - \frac{\boldsymbol{v}\cdot\boldsymbol{u}}{c^2}\right)^2}\right]-\frac{\partial}{\partial t}\left[\frac{q\,(\boldsymbol{v}\cdot\boldsymbol{\alpha})}{4\pi\varepsilon_0 c^5\left(1 - \frac{\boldsymbol{v}\cdot\boldsymbol{u}}{c^2}\right)^2}\boldsymbol{v}\right]$$

$$\boldsymbol{\varepsilon}_\alpha = -\nabla\left[\frac{q\,(\boldsymbol{v}\cdot\boldsymbol{\alpha})}{4\pi\varepsilon_0 c^3\left(1 - \frac{\boldsymbol{v}\cdot\boldsymbol{u}}{c^2}\right)^2}\right]-\boldsymbol{v}\frac{\partial}{\partial t}\left[\frac{q\,(\boldsymbol{v}\cdot\boldsymbol{\alpha})}{4\pi\varepsilon_0 c^5\left(1 - \frac{\boldsymbol{v}\cdot\boldsymbol{u}}{c^2}\right)^2}\right]$$

$$-\frac{q\,(\boldsymbol{v}\cdot\boldsymbol{\alpha})}{4\pi\varepsilon_0 c^5\left(1 - \frac{\boldsymbol{v}\cdot\boldsymbol{u}}{c^2}\right)^2}\frac{\partial\boldsymbol{v}}{\partial t}$$

$$\boldsymbol{\varepsilon}_\alpha = -\frac{(\boldsymbol{v}\cdot\boldsymbol{\alpha})}{4\pi\varepsilon_0\left(1 - \frac{\boldsymbol{v}\cdot\boldsymbol{u}}{c^2}\right)^2}\left(\nabla q + \frac{\partial q}{c^2\partial t}\boldsymbol{v}\right)-$$

$$-\frac{q}{4\pi\varepsilon_0\left(1 - \frac{\boldsymbol{v}\cdot\boldsymbol{u}}{c^2}\right)^2}\left[\nabla\,(\boldsymbol{v}\cdot\boldsymbol{\alpha}) + \frac{\partial\,(\boldsymbol{v}\cdot\boldsymbol{\alpha})}{c^2\partial t}\boldsymbol{v}\right]-$$

$$-\frac{2q\,(\boldsymbol{v}\cdot\boldsymbol{\alpha})}{4\pi\varepsilon_0 c^3\left(1 - \frac{\boldsymbol{v}\cdot\boldsymbol{u}}{c^2}\right)^3}\left[\nabla\left(\frac{\boldsymbol{v}\cdot\boldsymbol{u}}{c^2}\right) + \frac{\partial\,(\boldsymbol{v}\cdot\boldsymbol{u})}{c^4\partial t}\boldsymbol{v}\right]- \tag{215}$$

$$-\frac{q\,(\boldsymbol{v}\cdot\boldsymbol{\alpha})}{4\pi\varepsilon_0 c^5\left(1 - \frac{\boldsymbol{v}\cdot\boldsymbol{u}}{c^2}\right)^2}\frac{\partial\boldsymbol{v}}{\partial t}.$$

Combining equations (151) and (152) we get

$$\nabla q + \frac{\partial q}{c^2\partial t}\boldsymbol{v} = 0. \tag{216}$$

Combining equations (98) and (99) we get

$$\nabla\,(\boldsymbol{v}\cdot\boldsymbol{\alpha}) + \frac{\partial\,(\boldsymbol{v}\cdot\boldsymbol{\alpha})}{c^2\partial t}\boldsymbol{v} = \frac{c}{r}\boldsymbol{\alpha} - \frac{(\boldsymbol{v}\cdot\boldsymbol{\alpha})}{cr}\boldsymbol{v}. \tag{217}$$

Combining equations (96) and (99) we get

$$\nabla\,(\boldsymbol{v}\cdot\boldsymbol{u}) + \frac{\partial\,(\boldsymbol{v}\cdot\boldsymbol{u})}{c^2\partial t}\boldsymbol{v} = -\frac{c}{r}\left(\frac{(\boldsymbol{v}\cdot\boldsymbol{u})}{c^2}\boldsymbol{v} - \boldsymbol{u}\right). \tag{218}$$

We substitute equations (216), (217) and (218) into equation (215) and we obtain

$$\boldsymbol{\varepsilon}_\alpha = -\frac{q}{4\pi\varepsilon_0 c^3 \left(1 - \frac{\boldsymbol{v}\cdot\boldsymbol{u}}{c^2}\right)^2}\left[\frac{c}{r}\boldsymbol{\alpha} - \frac{(\boldsymbol{v}\cdot\boldsymbol{\alpha})}{cr}\boldsymbol{v}\right] +$$

$$+ \frac{2q(\boldsymbol{v}\cdot\boldsymbol{\alpha})}{4\pi\varepsilon_0 c^5 \left(1 - \frac{\boldsymbol{v}\cdot\boldsymbol{u}}{c^2}\right)^3}\frac{c}{r}\left[\frac{(\boldsymbol{v}\cdot\boldsymbol{u})}{c^2}\boldsymbol{v} - \boldsymbol{u}\right] -$$

$$- \frac{q(\boldsymbol{v}\cdot\boldsymbol{\alpha})}{4\pi\varepsilon_0 c^4 \left(1 - \frac{\boldsymbol{v}\cdot\boldsymbol{u}}{c^2}\right)^3}\left[\frac{(\boldsymbol{v}\cdot\boldsymbol{u})}{c^2}\boldsymbol{v} - \boldsymbol{u}\right]$$

$$\boldsymbol{\varepsilon}_\alpha = -\frac{q}{4\pi\varepsilon_0 c^3 \left(1 - \frac{\boldsymbol{v}\cdot\boldsymbol{u}}{c^2}\right)^2}\left[\frac{c}{r}\boldsymbol{\alpha} - \frac{(\boldsymbol{v}\cdot\boldsymbol{\alpha})}{cr}\boldsymbol{v}\right] +$$

$$+ \frac{q(\boldsymbol{v}\cdot\boldsymbol{\alpha})}{4\pi\varepsilon_0 c^4 r \left(1 - \frac{\boldsymbol{v}\cdot\boldsymbol{u}}{c^2}\right)^3}\left[\frac{(\boldsymbol{v}\cdot\boldsymbol{u})}{c^2}\boldsymbol{v} - \boldsymbol{u}\right]$$

$$\boldsymbol{\varepsilon}_\alpha = \frac{q}{4\pi\varepsilon_0 c^2 r \left(1 - \frac{\boldsymbol{v}\cdot\boldsymbol{u}}{c^2}\right)^2} \cdot$$

$$\left[-\boldsymbol{\alpha} + \frac{(\boldsymbol{v}\cdot\boldsymbol{\alpha})}{c^2}\boldsymbol{v} + \frac{(\boldsymbol{v}\cdot\boldsymbol{u})(\boldsymbol{v}\cdot\boldsymbol{\alpha})}{c^4\left(1 - \frac{\boldsymbol{v}\cdot\boldsymbol{u}}{c^2}\right)}\boldsymbol{v} - \frac{(\boldsymbol{v}\cdot\boldsymbol{\alpha})}{c^2\left(1 - \frac{\boldsymbol{v}\cdot\boldsymbol{u}}{c^2}\right)}\boldsymbol{u}\right]$$

$$\boldsymbol{\varepsilon}_\alpha = \frac{q}{4\pi\varepsilon_0 c^2 r \left(1 - \frac{\boldsymbol{v}\cdot\boldsymbol{u}}{c^2}\right)^2} \cdot$$

$$\left[-\boldsymbol{\alpha} + \frac{(\boldsymbol{v}\cdot\boldsymbol{\alpha})}{c^2\left(1 - \frac{\boldsymbol{v}\cdot\boldsymbol{u}}{c^2}\right)}\left(\left(1 - \frac{\boldsymbol{v}\cdot\boldsymbol{u}}{c^2}\right)\boldsymbol{v} + \frac{(\boldsymbol{v}\cdot\boldsymbol{u})}{c^2}\boldsymbol{v} - \boldsymbol{u}\right)\right]$$

$$\boldsymbol{\varepsilon}_\alpha = \frac{q}{4\pi\varepsilon_0 c^2 r \left(1 - \frac{\boldsymbol{v}\cdot\boldsymbol{u}}{c^2}\right)^2}\left[-\boldsymbol{\alpha} + \frac{(\boldsymbol{v}\cdot\boldsymbol{\alpha})}{c^2\left(1 - \frac{\boldsymbol{v}\cdot\boldsymbol{u}}{c^2}\right)}(\boldsymbol{v} - u)\right]$$

which is equation (209) for the electric field $\boldsymbol{\varepsilon}_\alpha$.

In order to prove equations (208) we also need equations

$$\nabla\left(u^2\right) + \frac{\partial\left(u^2\right)}{c^2\partial t}\boldsymbol{v} = 0 \tag{219}$$

$$\nabla r + \frac{\partial r}{c^2\partial t}\boldsymbol{v} = \frac{\boldsymbol{v}}{c}. \tag{220}$$

We can prove equation (219) as follows

$$\nabla\left(u^2\right) + \frac{\partial\left(u^2\right)}{c^2\partial t}\boldsymbol{v} = \frac{\partial u^2}{\partial w}\nabla w + \frac{\partial u^2}{c^2\partial w}\frac{\partial w}{\partial t}\boldsymbol{v}$$

$$= \frac{\partial u^2}{\partial w}\left(\nabla w + \frac{\partial w}{c^2\partial t}\cdot\boldsymbol{v}\right) = 0.$$

This results immediately from the combination of equations (11) and (12). Equation (220) results from the combination of equations (9) and (14).

In order to prove equation (205), we denote

$$\boldsymbol{f} = \frac{1 - \frac{u^2}{c^2}}{4\pi\varepsilon_0 r^2 \left(1 - \frac{\boldsymbol{v}\cdot\boldsymbol{u}}{c^2}\right)^3}\left(\frac{\boldsymbol{v}}{c} - \frac{\boldsymbol{u}}{c}\right) +$$

$$+ \frac{1}{4\pi\varepsilon_0 r \left(1 - \frac{\boldsymbol{v}\cdot\boldsymbol{u}}{c^2}\right)^2}\left[\frac{\left(\frac{\boldsymbol{v}}{c}\boldsymbol{\alpha}\right)}{1 - \frac{\boldsymbol{v}\cdot\boldsymbol{u}}{c^2}}\left(\frac{\boldsymbol{v}}{c} - \frac{\boldsymbol{u}}{c}\right) - \boldsymbol{\alpha}\right] \tag{221}$$

and

$$\boldsymbol{g} = \frac{1 - \frac{u^2}{c^2}}{4\pi\varepsilon_0 r \left(1 - \frac{\boldsymbol{v}\cdot\boldsymbol{u}}{c^2}\right)^3}\left(\frac{\boldsymbol{u}}{c} \times \frac{\boldsymbol{v}}{c}\right) +$$

$$+ \frac{1}{4\pi\varepsilon_0 r \left(1 - \frac{\boldsymbol{v}\cdot\boldsymbol{u}}{c^2}\right)^2}\left[\frac{\frac{\boldsymbol{v}}{c}\boldsymbol{\alpha}}{1 - \frac{\boldsymbol{v}\cdot\boldsymbol{u}}{c^2}}\left(\frac{\boldsymbol{u}}{c} \times \frac{\boldsymbol{v}}{c}\right) - \frac{\boldsymbol{v}}{c} \times \boldsymbol{\alpha}\right]. \tag{222}$$

Using the notation of equations (221) and (222), and from equations (208) and (209) we obtain

$$\boldsymbol{\varepsilon} = \boldsymbol{\varepsilon}_u + \boldsymbol{\varepsilon}_\alpha = q\boldsymbol{f} \tag{223}$$

$$\boldsymbol{B} = \boldsymbol{B}_u + \boldsymbol{B}_\alpha = q\boldsymbol{g}. \tag{224}$$

From Gauss's law we have

$$\rho = \varepsilon_0 \nabla \cdot \boldsymbol{\varepsilon}$$

and using equation (223) we have

$$\rho = \varepsilon_0 \nabla \cdot (q\boldsymbol{f})$$

$$\rho = \varepsilon_0 q \nabla \cdot \boldsymbol{f} + \varepsilon_0 \boldsymbol{f} \cdot \nabla q. \tag{225}$$

From classical electromagnetism we know that

$$\nabla \cdot \boldsymbol{f} = 0.$$

Hence, equation (225) becomes

$$\rho = \varepsilon_0 \boldsymbol{f} \cdot \nabla q.$$

Using equation (216) we obtain

$$\rho = -\varepsilon_0 \frac{\partial q}{c^2 \partial t}\boldsymbol{v} \cdot \boldsymbol{f}. \tag{226}$$

From equation (221) we see that

$$\boldsymbol{v} \cdot \boldsymbol{f} = \frac{1 - \frac{u^2}{c^2}}{r^2 \left(1 - \frac{\boldsymbol{v}\cdot\boldsymbol{u}}{c^2}\right)^3}\left(\frac{c^2}{c} - \frac{\boldsymbol{v}\cdot\boldsymbol{u}}{c}\right) +$$

$$+ \frac{1}{4\pi\varepsilon_0 r \left(1 - \frac{\boldsymbol{v}\cdot\boldsymbol{u}}{c^2}\right)^2}\left[\frac{\left(\frac{\boldsymbol{v}}{c}\boldsymbol{u}\right)}{1 - \frac{\boldsymbol{v}\cdot\boldsymbol{u}}{c^2}}\left(\frac{c^2}{c} - \frac{\boldsymbol{v}\cdot\boldsymbol{u}}{c}\right) - \boldsymbol{v}\cdot\boldsymbol{\alpha}\right]$$

$$\boldsymbol{v} \cdot \boldsymbol{f} = \frac{c\left(1 - \dfrac{u^2}{c^2}\right)}{4\pi\varepsilon_0 r\left(1 - \dfrac{\boldsymbol{v} \cdot \boldsymbol{u}}{c^2}\right)^2} +$$

$$+ \frac{1}{r\left(1 - \dfrac{\boldsymbol{v} \cdot \boldsymbol{u}}{c^2}\right)}\left[\frac{(\boldsymbol{v} \cdot \boldsymbol{\alpha})}{1 - \dfrac{\boldsymbol{v} \cdot \boldsymbol{u}}{c^2}}\left(1 - \frac{\boldsymbol{v} \cdot \boldsymbol{u}}{c^2}\right) - \boldsymbol{v} \cdot \boldsymbol{\alpha}\right]$$

$$\boldsymbol{v} \cdot \boldsymbol{f} = \frac{c\left(1 - \dfrac{u^2}{c^2}\right)}{r^2\left(1 - \dfrac{\boldsymbol{v} \cdot \boldsymbol{u}}{c^2}\right)^2} + 0. \tag{227}$$

Combining equations (226) and (227) we get

$$\rho = -\varepsilon_0 \frac{1 - \dfrac{u^2}{c^2}}{4\pi\varepsilon_0\left(1 - \dfrac{\boldsymbol{v} \cdot \boldsymbol{u}}{c^2}\right)^2}\frac{\partial q}{\partial t}$$

and with equation (151) we finally obtain

$$\rho = -\frac{\partial q}{\partial w}\frac{1 - \dfrac{u^2}{c^2}}{4\pi r^2\left(1 - \dfrac{\boldsymbol{v} \cdot \boldsymbol{u}}{c^2}\right)^3}$$

which is equation (205), since

$$\frac{1}{\gamma^2} = 1 - \frac{u^2}{c^2}.$$

Similarly we can prove equation

$$\nabla \cdot \boldsymbol{B} = 0. \tag{228}$$

From equation (224) we have that

$$\nabla \cdot \boldsymbol{B} = \nabla \cdot (q\boldsymbol{g})$$

$$\nabla \cdot \boldsymbol{B} = q\nabla \cdot \boldsymbol{g} + \boldsymbol{g} \cdot \nabla q. \tag{229}$$

From classical electromagnetism we know that

$$\nabla \cdot \boldsymbol{g} = 0.$$

Thus, equation (229) becomes

$$\nabla \cdot \boldsymbol{B} = \boldsymbol{g} \cdot \nabla q$$

and with equation (216) we obtain

$$\nabla \cdot \boldsymbol{B} = -\frac{\partial q}{c^2 \partial t}\boldsymbol{v} \cdot \boldsymbol{g}. \tag{230}$$

From equation (222) it immediately can be seen that

$$\boldsymbol{v} \cdot \boldsymbol{g} = 0$$

and from equation (230) we also obtain

$$\nabla \cdot \boldsymbol{B} = 0.$$

Combining equations (230) and (224) we have that

$$\nabla \cdot \boldsymbol{B} = -\frac{\partial q}{c^2 q \partial t}\boldsymbol{v} \cdot \boldsymbol{B}. \tag{231}$$

From equation (231) it follows that

$$\nabla \cdot \boldsymbol{B} = 0$$

if and only if

$$\boldsymbol{v} \cdot \boldsymbol{B} = 0.$$

From equations (210) and (211) we get

$$\boldsymbol{B} = \frac{\boldsymbol{v}}{c^2} \times \boldsymbol{\varepsilon}. \tag{232}$$

Therefore, it holds that

$$\boldsymbol{v} \cdot \boldsymbol{B} = 0$$

or equivalently

$$\nabla \cdot \boldsymbol{B} = 0.$$

Combining equations (226) and (223) we get

$$\rho = -\varepsilon_0 \frac{\partial q}{c^2 q \partial t}\boldsymbol{v} \cdot \boldsymbol{\varepsilon}. \tag{233}$$

From equation (233) it follows that

$$\rho = 0$$

if and only if

$$\boldsymbol{v} \cdot \boldsymbol{\varepsilon} = 0.$$

From equation (209) for the electric field $\boldsymbol{\varepsilon}_\alpha$, we can immediately deduce that

$$\boldsymbol{v} \cdot \boldsymbol{\varepsilon}_\alpha = 0. \tag{234}$$

Therefore, the electromagnetic radiation does not contribute to the charge density ρ. On the contrary, for the electric field $\boldsymbol{\varepsilon}_u$ that accompanies the material particle, it holds that

$$\boldsymbol{v} \cdot \boldsymbol{\varepsilon}_u \neq 0$$

as follows from equation (208).

From equation (232) we obtain

$$\boldsymbol{B} = \frac{\boldsymbol{v}}{c^2} \times \boldsymbol{\varepsilon}$$

$$\boldsymbol{B}^2 = \left(\frac{\boldsymbol{v}}{c^2} \times \boldsymbol{\varepsilon}\right)^2$$

$$\boldsymbol{B}^2 = \left(\frac{\boldsymbol{v}}{c^2} \times \boldsymbol{\varepsilon}\right) \cdot \left(\frac{\boldsymbol{v}}{c^2} \times \boldsymbol{\varepsilon}\right).$$

After performing the necessary calculations we finally get

$$\boldsymbol{\varepsilon}^2 = c^2 \boldsymbol{B}^2 + \left(\frac{\boldsymbol{v} \cdot \boldsymbol{\varepsilon}}{c} \right)^2 . \qquad (235)$$

We end this paragraph with an interesting observation. Comparing equations (208) for the electric field $\boldsymbol{\varepsilon}_u$ with equation (65), we conclude that the vectors $\boldsymbol{t}$ and $\boldsymbol{\varepsilon}_u$ are parallel. Then, the "trajectory representation theorem" informs us that the direction of the electric field $\boldsymbol{\varepsilon}_u$ represents the tangential vector $\boldsymbol{t}_p$ of the trajectory C_p of the material particle.

4.7 The energy-momentum tensor of the electro-magnetic field at macroscopic scales

The equations of this paragraph as well as of the remaining paragraphs of this paragraph, could be stated differently, so that they also hold for non-inertial reference frames. However, such a formulation does not serve the purposes of the present edition. Therefore, we will formulate the equations for an inertial reference frame, while simultaneously suggesting the way in which the same equations can also be formulated for a non-inertial reference frame.

From the axiomatic foundation of the theory of selfvariations, as stated in paragraph 2.2, we have that

$$dS^2 = 0$$

or, equivalently,

$$g_{ik} dx^i dx^k = 0 \qquad i, k = 0, 1, 2, 3 \qquad (236)$$

where

$$\left(x^0, x^1, x^2, x^3 \right) = (ct, x, y, z) \qquad (237)$$

and g_{ik} are the components of the metric tensor. In equation (236) we use the Einstein summation convention for the indices i and k.

We denote

$$v^i = \frac{dx^i}{dt} \qquad i = 0, 1, 2, 3 \qquad (238)$$

that is,

$$\left(v^0, v^1, v^2, v^3 \right) = \left(c, v_x, v_y, v_z \right). \qquad (239)$$

From equation (236) we obtain

$$g_{ik} = \frac{dx^1}{dt} \frac{dx^k}{dt} = 0$$

and with equation (238) we get

$$g_{ik} v^i v^k = 0 \qquad i, k = 0, 1, 2, 3. \qquad (240)$$

Using this notation, all the equations we will formulate also hold for non-inertial reference frames if we replace differentiation with respect to x^k with covariant differentiation with respect to x^k, k=0,1,2,3.

We now denote the four-vector of velocity as

$$\boldsymbol{v} = \begin{bmatrix} v^0 \\ v^1 \\ v^2 \\ v^3 \end{bmatrix} = \begin{bmatrix} c \\ v_x \\ v_y \\ v_z \end{bmatrix} \qquad (241)$$

and the four-vector of current density as

$$\boldsymbol{j} = \begin{bmatrix} j^0 \\ j^1 \\ j^2 \\ j^3 \end{bmatrix} = \begin{bmatrix} \rho v^0 \\ \rho v^1 \\ \rho v^2 \\ \rho v^3 \end{bmatrix} = \begin{bmatrix} \rho c \\ \rho v_x \\ \rho v_y \\ \rho v_z \end{bmatrix} \qquad (242)$$

as results from equations (156) and (157). Also, according to equations (201) and (202), the four-vector of the electromagnetic potential is

$$\boldsymbol{A} = \begin{bmatrix} A^0 \\ A^1 \\ A^2 \\ A^3 \end{bmatrix} = \begin{bmatrix} \dfrac{V}{c} v^0 \\ \dfrac{V}{c} v^1 \\ \dfrac{V}{c} v^2 \\ \dfrac{V}{c} v^3 \end{bmatrix} = \begin{bmatrix} V \\ \dfrac{V}{c} v_x \\ \dfrac{V}{c} v_y \\ \dfrac{V}{c} v_z \end{bmatrix} . \qquad (243)$$

Subsequently we will symbolize the differentiation with respect to $\frac{\partial}{\partial x^k}$ with $(, k)$, k=0,1,2,3.

We now consider the tensor of the electromagnetic field

$$T^{\mu\nu} = \frac{I}{4\pi} \left(F^{\mu\alpha} F^{\nu}_{\alpha} - \frac{1}{4} g^{\mu\nu} F_{\alpha\beta} F^{\alpha\beta} \right) \qquad (244)$$

where $g^{\mu\nu}$ is the inverse of the matrix $g_{\mu\nu}$, $g_{\mu k} g^{k\nu} = \delta_{\mu\nu}$

$$\delta_{\mu\nu} = \begin{cases} 1 & for \quad \mu = \nu \\ 0 & for \quad \mu \neq \nu \end{cases} \qquad (245)$$

and $F^{\mu\nu}$ is the Maxwell stress tensor

$$F^{\mu\nu} = A^{\nu}_{,\mu} - A^{\mu}_{,\nu}. \qquad (246)$$

Using this notation and taking into account that in the surrounding spacetime of the material particle there is an electric current $\boldsymbol{j}$, as given by equation (242), the energy-momentum tensor [19–21] of the electromagnetic field is given by the tensor

$$\Phi^{\mu\nu} = T^{\mu\nu} - j^{\mu} A^{\nu}. \qquad (247)$$

We now write the tensor $T^{\mu\nu}$ in the form

$$T^{ij} = \begin{bmatrix} W & cS_x & cS_y & cS_z \\ cS_x & & & \\ cS_y & & \sigma_{\alpha\beta} & \\ cS_z & & & \end{bmatrix} \qquad (248)$$

$$S = \varepsilon_0 \varepsilon \times B \qquad (249)$$

where S is the Poynting vector, and ε and B are the intensities of the electric and magnetic field, respectively. Taking into account equations (210) and (211), as summarized in equation

$$B = \frac{\upsilon}{c^2} \times \varepsilon \qquad (250)$$

equation (249) becomes

$$S = \varepsilon_0 \left(\frac{\varepsilon^2}{c^2} \right) \upsilon - \varepsilon_0 \left(\frac{\upsilon \cdot \varepsilon}{c^2} \right) \varepsilon. \qquad (251)$$

The Maxwell stress tensor $\sigma_{\alpha\beta}$ is given by relation

$$\sigma_{\alpha\beta} = \varepsilon_0 \left(-\varepsilon_\alpha \varepsilon_\beta - c^2 B_\alpha B_\beta + W\delta_{\alpha\beta} \right) \qquad (252)$$

where $\delta_{\alpha\beta}$ is given by relation (245), and

$$W = \frac{1}{2}\varepsilon_0 \left(\varepsilon^2 + c^2 B^2 \right) \qquad (253)$$

$$\varepsilon = \begin{bmatrix} \varepsilon_x \\ \varepsilon_y \\ \varepsilon_z \end{bmatrix} = \begin{bmatrix} \varepsilon_1 \\ \varepsilon_2 \\ \varepsilon_3 \end{bmatrix}$$

$$B = \begin{bmatrix} B_x \\ B_y \\ B_z \end{bmatrix} = \begin{bmatrix} B_1 \\ B_2 \\ B_3 \end{bmatrix}.$$

Combining equations (247) and (248), we arrive at the energy-momentum tensor

$$\Phi^{ij} = \begin{bmatrix} W & cS_x & cS_y & cS_z \\ cS_x & \sigma_{11} & \sigma_{12} & \sigma_{13} \\ cS_y & \sigma_{21} & \sigma_{22} & \sigma_{23} \\ cS_z & \sigma_{31} & \sigma_{32} & \sigma_{33} \end{bmatrix} -$$
$$- \frac{\rho V}{c^2} \begin{bmatrix} c^2 & c\upsilon_x & c\upsilon_y & c\upsilon_z \\ \upsilon_x c & \upsilon_x^2 & \upsilon_x \upsilon_y & \upsilon_x \upsilon_z \\ \upsilon_y c & \upsilon_y \upsilon_x & \upsilon_y^2 & \upsilon_y \upsilon_z \\ \upsilon_z c & \upsilon_z \upsilon_x & \upsilon_z \upsilon_y & \upsilon_z^2 \end{bmatrix}. \qquad (254)$$

We shall now prove that the scalar potential, as given by equation (201), satisfies the relation

$$\frac{\partial V}{\partial t} + \upsilon \cdot \nabla V = -\upsilon \cdot \varepsilon. \qquad (255)$$

From equation (212) we have that

$$-\upsilon \cdot \varepsilon = -\upsilon \left[-\nabla V - \frac{\partial A}{\partial t} \right]$$
$$-\upsilon \cdot \varepsilon = \upsilon \left(\nabla V + \frac{\partial A}{\partial t} \right).$$

Using equation (202) we have

$$-\upsilon \cdot \varepsilon = \upsilon \left(\nabla V + \frac{\partial V}{c\partial t}\frac{\upsilon}{c} + \frac{V}{c}\frac{\partial}{\partial t}\left(\frac{\upsilon}{c} \right) \right)$$
$$-\upsilon \cdot \varepsilon = \upsilon \cdot \nabla V + \frac{\partial V}{\partial t} + \frac{V}{c}\upsilon \cdot \frac{\partial}{\partial t}\left(\frac{\upsilon}{c} \right)$$
$$-\upsilon \cdot \varepsilon = \upsilon \cdot \nabla V + \frac{\partial V}{\partial t} + \frac{V}{2c}\frac{\partial}{\partial t}\left(\frac{\upsilon^2}{c} \right)$$
$$-\upsilon \cdot \varepsilon = \upsilon \cdot \nabla V + \frac{\partial V}{\partial t}$$

since $\upsilon^2 = c^2$.

We will now prove the conservation of energy and momentum, as expressed by equation

$$\Phi^{ij}_{.j} = \frac{\partial \Phi^{ij}}{\partial x^j} = 0. \qquad (256)$$

We begin with an observation which allows us to avoid complex calculations. Equation (256) holds in classical electromagnetic theory, i.e. if we ignore the consequences of the selfvariations and consider the electric charge q constant, both in the electromagnetic potential, as well as in the intensity of the electromagnetic field. Furthermore, $\rho = 0$ in equation (254). Therefore, it is enough to prove that in equation (256) the factors resulting from the selfvariation of the electric charge q, also vanish. Certainly, in equation (254) it holds that $\rho \neq 0$, where the charge density ρ is given by equation (205).

The energy density W of the electromagnetic field as given by equation (253), as well as the Poynting vector S, given by equation (251), are proportional to q^2. Therefore, in our calculations we will have to take into consideration the rate of change of the factor q^2. From equations (151) and (152) we have

$$\frac{\partial q^2}{\partial t} = 2q\frac{\partial q}{\partial t} = \frac{2q}{1 - \dfrac{\upsilon \cdot u}{c^2}}\frac{\partial q}{\partial w}$$
$$\nabla q^2 = 2q\nabla q = -\frac{2q}{1 - \dfrac{\upsilon \cdot u}{c^2}}\frac{\partial q}{\partial w}\frac{\upsilon}{c^2}.$$

Thus, we arrive at equations

$$\frac{\partial q^2}{\partial t} = \frac{2}{1 - \dfrac{\upsilon \cdot u}{c^2}}\frac{\partial q}{q\partial w}q^2 = -2\lambda q^2$$
$$\frac{\partial q^2}{\partial x} = 2\lambda\frac{\upsilon_x}{c^2}q^2 \qquad \frac{\partial q^2}{\partial y} = 2\lambda\frac{\upsilon_y}{c^2}q^2$$
$$\frac{\partial q^2}{\partial z} = 2\lambda\frac{\upsilon_z}{c^2}q^2 \qquad\qquad (257)$$
$$\lambda = -\frac{1}{1 - \dfrac{\upsilon \cdot u}{c^2}}\frac{\partial q}{q\partial w}.$$

From equation (255), and for $i = 0$, we have that

$$\frac{\partial \Phi^{0j}}{\partial x^j} = \frac{\partial \Phi^{00}}{\partial x^0} + \frac{\partial \Phi^{01}}{\partial x^1} + \frac{\partial \Phi^{02}}{\partial x^2} + \frac{\partial \Phi^{03}}{\partial x^3} =$$

$$\frac{\partial}{c\partial t}(W) \frac{\partial}{\partial x}(cS_x) + \frac{\partial}{\partial y}(cS_y) + \frac{\partial}{\partial z}(cS_z)$$

$$-\frac{1}{c^2}\left[\frac{\partial}{c\partial t}\left(\rho Vc^2\right) + \frac{\partial}{\partial x}\left(\rho Vcv_x\right) + \frac{\partial}{\partial y}\left(\rho Vcv_y\right) + \frac{\partial}{\partial z}\left(\rho Vcv_z\right)\right]$$

and using relations (257), which we apply on the quantities W, S_x, S_y, S_z, which are proportional to q^2, we get

$$\frac{\partial \Phi^{0j}}{\partial x^j} = -2\lambda W + 2\lambda v_x S_x + 2\lambda v_y S_y + 2\lambda v_z S_z$$

$$-\frac{V}{c}\left[\frac{\partial \rho}{\partial t} + \frac{\partial}{\partial x}\left(\rho v_x\right) + \frac{\partial}{\partial y}\left(\rho v_y\right) + \frac{\partial}{\partial z}\left(\rho v_z\right)\right]$$

$$-\frac{\rho}{c}\left(\frac{\partial V}{\partial t} + v_x \frac{\partial V}{\partial x} + v_y \frac{\partial V}{\partial y} + v_z \frac{\partial V}{\partial z}\right)$$

$$\frac{\partial \Phi^{0j}}{\partial x^j} = 2\lambda\left(-W + v_x S_x + v_y S_y + v_z S_z\right)$$

$$-\frac{V}{c}\left[\frac{\partial \rho}{\partial t} + \nabla \cdot (\rho \boldsymbol{v})\right] - \frac{\rho}{c}\left(\frac{\partial V}{\partial t} + \boldsymbol{v} \cdot \nabla V\right)$$

and from the equation of continuity, as well as equation (254), we get

$$\frac{\partial \Phi^{0j}}{\partial x^j} = 2\lambda\left(-W + v_x S_x + v_y S_y + v_z S_z\right) + \frac{\rho}{c}(\boldsymbol{v} \cdot \boldsymbol{\varepsilon})$$

and with equations (251) and (252) we get

$$\frac{\partial \Phi^{0j}}{\partial x^j} = 2\lambda \varepsilon_0 \left[-\frac{1}{2}\boldsymbol{\varepsilon}^2 - \frac{1}{2}\boldsymbol{B}^2 + \frac{v_x^2}{c^2}\boldsymbol{\varepsilon}^2 - v_x \varepsilon_x \left(\frac{\boldsymbol{v} \cdot \boldsymbol{\varepsilon}}{c^2}\right) + \frac{v_y^2}{c^2}\boldsymbol{\varepsilon}^2\right.$$

$$\left.-v_y \varepsilon_y \left(\frac{\boldsymbol{v} \cdot \boldsymbol{\varepsilon}}{c^2}\right) + \frac{v_z^2}{c^2}\boldsymbol{\varepsilon}^2 - v_z \varepsilon_z \left(\frac{\boldsymbol{v} \cdot \boldsymbol{\varepsilon}}{c^2}\right)\right] + \rho\left(\frac{\boldsymbol{v} \cdot \boldsymbol{\varepsilon}}{c}\right)$$

$$\frac{\partial \Phi^{0j}}{\partial x^j} = -2\lambda \varepsilon_0 \left[-\frac{1}{2}\boldsymbol{\varepsilon}^2 - \frac{1}{2}c^2 \boldsymbol{B}^2 + \frac{v_x^2 + v_y^2 + v_z^2}{c^2}\boldsymbol{\varepsilon}^2\right] -$$

$$-2\lambda \varepsilon_0 \left[-(\boldsymbol{v} \cdot \boldsymbol{\varepsilon})\left(v_x \varepsilon_x + v_y \varepsilon_y + v_z \varepsilon_z\right)\right] + \rho\left(\frac{\boldsymbol{v} \cdot \boldsymbol{\varepsilon}}{c}\right)$$

and since it is $v_x^2 + v_y^2 + v_z^2 = c^2$ and also

$$v_x \varepsilon_x + v_y \varepsilon_y + v_z \varepsilon_z = \boldsymbol{v} \cdot \boldsymbol{\varepsilon},$$

we see that

$$\frac{\partial \Phi^{0j}}{\partial x^j} = -2\lambda \varepsilon_0 \left[-\frac{1}{2}\boldsymbol{\varepsilon}^2 - \frac{1}{2}c^2 \boldsymbol{B}^2 - \left(\frac{\boldsymbol{v} \cdot \boldsymbol{\varepsilon}}{c}\right)^2\right] + \rho\left(\frac{\boldsymbol{v} \cdot \boldsymbol{\varepsilon}}{c}\right).$$

From equation (235) we obtain

$$\frac{\partial \Phi^{0j}}{\partial x^j} = -2\lambda \varepsilon_0 \frac{1}{2}\left(\frac{\boldsymbol{v} \cdot \boldsymbol{\varepsilon}}{c}\right)^2 + \rho\left(\frac{\boldsymbol{v} \cdot \boldsymbol{\varepsilon}}{c}\right)$$

$$\frac{\partial \Phi^{0j}}{\partial x^j} = \left(\frac{\boldsymbol{v} \cdot \boldsymbol{\varepsilon}}{c}\right)\left[\rho - \lambda \varepsilon_0 \frac{\boldsymbol{v} \cdot \boldsymbol{\varepsilon}}{c}\right] = 0$$

since

$$\rho - \lambda \varepsilon_0 \frac{\boldsymbol{v} \cdot \boldsymbol{\varepsilon}}{c} = 0. \tag{258}$$

Indeed, substituting the factor λ from equations (257), we have

$$\lambda \varepsilon_0 \frac{\boldsymbol{v} \cdot \boldsymbol{\varepsilon}}{c} = -\frac{1}{1 - \frac{\boldsymbol{v} \cdot \boldsymbol{u}}{c^2}}\frac{\partial q}{q \partial w}\varepsilon_0 \frac{\boldsymbol{v} \cdot \boldsymbol{\varepsilon}}{c}$$

$$\lambda \varepsilon_0 \frac{\boldsymbol{v} \cdot \boldsymbol{\varepsilon}}{c} = -\frac{1}{1 - \frac{\boldsymbol{v} \cdot \boldsymbol{u}}{c^2}}\frac{\partial q}{q \partial w}\varepsilon_0 \frac{\boldsymbol{v}}{c}(\boldsymbol{\varepsilon}_u + \boldsymbol{\varepsilon}_\alpha).$$

From equation (234) we have

$$\boldsymbol{v} \cdot \boldsymbol{\varepsilon}_\alpha = 0.$$

Hence, we see that

$$\lambda \varepsilon_0 \frac{\boldsymbol{v} \cdot \boldsymbol{\varepsilon}}{c} = -\frac{\varepsilon_0}{1 - \frac{\boldsymbol{v} \cdot \boldsymbol{u}}{c^2}}\frac{\partial q}{q \partial w}\frac{\boldsymbol{v}}{c}\boldsymbol{\varepsilon}_u$$

and with equation (208) for the electric field $\boldsymbol{\varepsilon}_u$ we get

$$\lambda \varepsilon_0 \frac{\boldsymbol{v} \cdot \boldsymbol{\varepsilon}}{c} = -\frac{\varepsilon_0}{1 - \frac{\boldsymbol{v} \cdot \boldsymbol{u}}{c^2}}\frac{\partial q}{q \partial w}\frac{q\left(1 - \frac{u^2}{c^2}\right)}{4\pi \varepsilon_0 r^2 \left(1 - \frac{\boldsymbol{v} \cdot \boldsymbol{u}}{c^2}\right)^3}\frac{\boldsymbol{v}}{c}\left(\frac{\boldsymbol{v}}{c} - \frac{\boldsymbol{u}}{c}\right)$$

$$\lambda \varepsilon_0 \frac{\boldsymbol{v} \cdot \boldsymbol{\varepsilon}}{c} = -\frac{\partial q}{\partial w}\frac{1 - \frac{u^2}{c^2}}{4\pi r^2 \left(1 - \frac{\boldsymbol{v} \cdot \boldsymbol{u}}{c^2}\right)^4}\left(1 - \frac{\boldsymbol{v} \cdot \boldsymbol{u}}{c}\right)$$

$$\lambda \varepsilon_0 \frac{\boldsymbol{v} \cdot \boldsymbol{\varepsilon}}{c} = -\frac{\partial q}{\partial w}\frac{1 - \frac{u^2}{c^2}}{4\pi r^2 \left(1 - \frac{\boldsymbol{v} \cdot \boldsymbol{u}}{c^2}\right)^3}.$$

Applying equation (205) we get

$$\lambda \varepsilon_0 \frac{\boldsymbol{v} \cdot \boldsymbol{\varepsilon}}{c} = \rho$$

$$\rho - \lambda \varepsilon_0 \frac{\boldsymbol{v} \cdot \boldsymbol{\varepsilon}}{c} = 0.$$

The validity of equation (256) for $i = 1, 2, 3$ is proven similarly.

In paragraph 4.5 we proved that the selfvariations are in agreement with the conservation of energy and momentum. The proof was done in two different ways: by direct calculation, and by applying the continuity equation. While it is of interest that the two different proofs, both lead to the conclusion that the selfvariations are compatible with the conservation principles of Physics, the calculation for the energy-momentum tensor was done for a completely different, and very substantial, reason. At macrocosmic scales, that is at large distances from the material particle, where equations

(151) and (152) hold, the energy-momentum tensor Φ^{ij}, as given by equation (254), indeed contains all the information about the energy content of spacetime. At microcosmic scales the equations of the theory of selfvariations highlight additional parameters about the energy content of spacetime. These parameters bring the quantum phenomena to the forefront.

4.8 The energy-momentum tensor of the generalized photon at macrocosmic scales

In this paragraph we shall study the energy-momentum tensor for the generalized photon that balances the selfvariation of the rest mass of the material particle. Using our notation the energy-momentum tensor is given by

$$\Phi^{ij} = \frac{D}{c^2} \begin{bmatrix} c^2 & cv_x & cv_y & cv_z \\ v_x c & v_x^2 & v_x v_y & v_x v_z \\ v_y c & v_y v_x & v_y^2 & v_y v_z \\ v_z c & v_z v_x & v_z v_y & v_z^2 \end{bmatrix} \quad (259)$$

with the energy density D given by equation (167).

We shall prove the conservation of energy and momentum as given by equation

$$\Phi^{ij}_{,j} = \frac{\partial \Phi^{ij}}{\partial x^j} = 0. \quad (260)$$

For $i = 0$ we have

$$\frac{\partial \Phi^{0j}}{\partial x^j} = \frac{\partial \Phi^{00}}{\partial x^0} + \frac{\partial \Phi^{01}}{\partial x^1} + \frac{\partial \Phi^{02}}{\partial x^2} + \frac{\partial \Phi^{03}}{\partial x^3}$$

$$\frac{\partial \Phi^{0j}}{\partial x^j} = \frac{\partial}{c \partial t}\left(\frac{Dc^2}{c^2}\right) + \frac{\partial}{\partial x}\left(\frac{D}{c^2} cv_x\right) + \frac{\partial}{\partial y}\left(\frac{D}{c^2} cv_y\right) + \frac{\partial}{\partial z}\left(\frac{D}{c^2} cv_z\right)$$

$$\frac{\partial \Phi^{0j}}{\partial x^j} = \frac{1}{c}\left[\frac{\partial D}{\partial t} + \nabla \cdot (D\boldsymbol{v})\right]$$

and with equation (168) we get

$$\frac{\partial \Phi^{0j}}{\partial x^j} = 0.$$

For $i = 1$ we have

$$\frac{\partial \Phi^{ij}}{\partial x^j} = \frac{\partial \Phi^{10}}{\partial x^0} + \frac{\partial \Phi^{11}}{\partial x^1} + \frac{\partial \Phi^{12}}{\partial x^2} + \frac{\partial \Phi^{13}}{\partial x^3}$$

$$\frac{\partial \Phi^{ij}}{\partial x^j} = \frac{1}{c^2}\left[\frac{\partial}{\partial t}(Dv_x) + \frac{\partial}{\partial x}(Dv_x v_x) + \frac{\partial}{\partial y}(Dv_x v_y)\right] +$$
$$+ \frac{1}{c^2}\left[\frac{\partial}{\partial z}(Dv_x v_z)\right]$$

$$\frac{\partial \Phi^{ij}}{\partial x^j} = \frac{1}{c^2}\left[v_x\left(\frac{\partial D}{\partial t} + \nabla \cdot (D\boldsymbol{v})\right) + D\left(\frac{\partial v_x}{\partial t} + \boldsymbol{v} \cdot \nabla v_x\right)\right]$$

and with equation (168) we get

$$\frac{\partial \Phi^{ij}}{\partial x^j} = v_x\left(\frac{\partial D}{\partial t} + \nabla \cdot \boldsymbol{j}\right) + \frac{1}{c^2}D\left(\frac{\partial v_x}{\partial t} + \boldsymbol{v} \cdot \nabla v_x\right)$$

and with (185) we arrive at

$$\frac{\partial \Phi^{ij}}{\partial x^j} = \frac{D}{c^2}\left(\frac{\partial v_x}{\partial t} + \boldsymbol{v} \cdot \nabla v_x\right). \quad (261)$$

From equation (33) we have

$$\frac{\partial v_x}{\partial t} + \boldsymbol{v} \cdot \nabla v_x = \frac{\partial}{\partial t}(c\cos\delta) + \boldsymbol{v} \cdot \nabla(c\cos\delta)$$

$$\frac{\partial v_x}{\partial t} + \boldsymbol{v} \cdot \nabla v_x = -c\sin\delta\left(\frac{\partial \delta}{\partial t} + \boldsymbol{v} \cdot \nabla\delta\right)$$

and with equation (81)(b) we get

$$\frac{\partial v_x}{\partial t} + \boldsymbol{v} \cdot \nabla v_x = 0. \quad (262)$$

Combining equations (261) and (262), we see that

$$\frac{\partial \Phi^{ij}}{\partial x^j} = 0.$$

We can similarly prove the validity of equation (259) for $i = 2, 3$.

By comparing the results of the last two paragraphs we find substantial differences between the generalized photon that counterbalances the selfvariation of the electric charge and the generalized photon that counterbalances the selfvariation of the rest mass of the material particle. Within the energy-momentum tensor of the first, there appears the electromagnetic field, as expressed by the first matrix of the second part of equation (254). On the contrary, in the expression of the energy-momentum tensor of equation (259), no corresponding matrix appears. Therefore, the generalized photon counterbalancing the rest mass does not correspond to a kind of field with the structure and content of the electromagnetic field. Furthermore, by comparing the second matrix of equation (254) with the matrix of equation (259), we observe that in place of the potential V in the first, the factor c^2 appears in the second. These observations hold even if we formulate the equations for a non-inertial reference frame (we have already suggested a way for formulating the equations in non-inertial reference frames). By careful observation of the equations appearing in paragraphs 4.2, 4.3 and 4.4, we realize that the difference in the "behavior" of the couples $(\rho, \boldsymbol{j})$ and $(D, \boldsymbol{J})$ is the result of the different way the electric charge and the energy transform according to Lorentz-Einstein. It is exactly this difference that is captured on tensors (254) and (259). The generalized photon gives us the exact mechanism of transport of energy and momentum from one material particle to the other. At the same time, it highlights the similarities and differences between the electromagnetic and the gravitational interaction.

We could call the generalized photon that counterbalances the selfvariation of the rest mass by a different name. In any case it is obvious when we refer to the electric charge and when we refer to the rest mass. We shall, therefore, keep the name "generalized photon" for both cases.

The observation we made at the end of the previous paragraph regarding the tensor given by equation (254), also holds for tensor (259). It is valid at macrocosmic scales. At microcosmic scales, further parameters emerge from the theory of selfvariations, which cannot be given by the energy-momentum tensor.

4.9 The internality of the universe to the measurement procedure

The selfvariations hypothesis brings to the foreground the "internality of the Universe to the measurement procedure". Usually, in order to measure a physical quantity, we define as unit an arbitrary quantity with which we compare other physical quantities of the same kind. If the defined unit of measurement depends on the rest mass or the electric charge, then it is itself subject to the selfvariations. This fact must be taken into account every time we perform a measurement.

The photon does not have rest mass or electric charge and is, therefore, not affected by the selfvariations. The evidence we have suggests that the selfvariations take place at extremely slow rates. Therefore, the first consequence of the selfvariations we expect to observe is the following: photons with great lifetimes will be measured to have less energy than expected.

The extremely slow rate of evolution of the selfvariations, combined with the "internality of the Universe to the measurement procedure", do not allow their immediate observation in the laboratory. In the laboratory we only observe the consequences of the selfvariations. These consequences are the potential fields and the quantum phenomena.

5 The quantitative determination of the selfvariations

5.1 Introduction

In the present paragraph we develop the main axis of the structure of the theory of selfvariations. We determine quantitatively the rate of evolution of the selfvariations, and formulate the *law of selfvariations*.

The law of selfvariations dominates from the microcosmic scales up to the observations we conduct billions of light years away. It reveals the causes of quantum phenomena, while it contains as physical information the totality of the cosmological observational data. At the same time, it sets the path for understanding the interactions between material particles.

The equations resulting from the law of selfvariations are of fundamental nature for the science of Physics and the related Physical Sciences. They contain a large amount of physical information, which permits the full understanding of physical reality.

5.2 The law of selfvariations

The conclusions derived in the previous paragraphs refer to the surrounding spacetime of the material particle. These conclusions are grounded on the second proposition-axiom of the theory of selfvariations, which states that

$$dS^2 = 0. \tag{263}$$

This proposition is equivalent to the relation $\|v\| = c$ which holds in every inertial system of reference.

In figure 4 the rest mass m_0 and the electric charge q of the material particle act at point $A(x, y, z, t)$ with the value they acquired at the moment $w = t - \frac{r}{c}$. Thus, we have that $m_0 = m_0(w)$ and $q = q(w)$. For the relevant calculations and proofs we have taken into consideration the axioms of the theory of selfvariations, but we have not yet defined the rate of evolution of their manifestation. In order to study the consequences of the selfvariations we have to determine quantitatively the first proposition-axiom of the theory of selfvariations.

Equation (263), combined with the first proposition-axiom of the selfvariations, leads directly to the concept of the *"generalized photon"*. The material particle emits generalized photons, and each generalized photon carries energy E and momentum P, in order to counterbalance the change in energy and momentum that results from the selfvariations of the rest mass of the material particle. If the material particle also carries electric charge, then the generalized photon carries electric charge as well, in order to counterbalance the variation of the electric charge of the material particle due to the selfvariations.

The rate of evolution of the selfvariations is determined axiomatically with the help of the total energy E_s and the total momentum P_s, which is emitted simultaneously and in all directions by the material particle, according to the following proposition-axiom: "The rest mass m_0 and the electric charge q of every material particle vary according to the action of the operators

$$\frac{\partial}{\partial t} \to -\frac{i}{\hbar} E_s \qquad \nabla \to \frac{i}{\hbar} P_s \tag{264}$$

where E_s and P_s denote the total energy and total momentum of the generalized photons emitted simultaneously by the material particle in all directions, and $\hbar = \frac{h}{2\pi}$, where h is Planck's constant".

Stated in the form of equations, relations (264) can be written as

$$\frac{\partial m_0}{\partial t} = -\frac{i}{\hbar} E_s m_0$$

$$\nabla m_0 = \frac{i}{\hbar} P_s m_0 \tag{265}$$

and

$$\frac{\partial q}{\partial t} = -\frac{i}{\hbar} E_s q$$

$$\nabla q = \frac{i}{\hbar} \boldsymbol{P}_s q. \tag{266}$$

In equations (265) and (266) we use the same symbol for the energy E_s and the momentum $\boldsymbol{P}_s$. But these are not the same physical quantities. In equations (265) the energy E_s and the momentum $\boldsymbol{P}_s$ counterbalance the consequences of the selfvariations of the rest mass. In equations (266) they counterbalance the consequences of the selfvariations of the electric charge. Later, we shall modify equation (266) in order to make this difference transparent.

The emission of generalized photons by the material particle comes about, initially, as a consequence of the principles of conservation of energy, momentum and electric charge. The operators given in relations (264) determine the relation between the material particle and the generalized photons, independently from the principles of conservation. Equations (265) and (266) express in a quantitative manner the *law of selfvariations.*

According to the law of selfvariations the rest mass m_0 and the electric charge q are functions of time t, as well as of the position of the material particle

$$m_0 = m_0(X_p, Y_p, Z_p, t)$$

$$q = q(X_p, Y_p, Z_p, t). \tag{267}$$

The dependence of the rest mass and the electric charge, not only on time, but also on the spatial position, is to be expected. Even if in some inertial frame of reference they only depend on time, in another inertial frame of reference they will also depend on the position, according to the Lorentz-Einstein transformations.

From equation (200), and for $\boldsymbol{u} = 0$, we take that $\boldsymbol{P}_s = 0$, so that the second equation of the couple of equations (265) gives $\nabla m_0 = \boldsymbol{0}$, whereas the first equation can be written as

$$\frac{dm_0}{dt} = -\frac{i}{\hbar} E_0 m_0$$

$$\dot{m} = -\frac{i}{\hbar} E_0 m_0$$

$$E_0 = i\hbar \frac{\dot{m}_0}{m_0}. \tag{268}$$

Here, we denote the differentiation with respect to time by ($\bullet$), and we set $E_s = E_0$ (the necessity of denoting $E_s = E_0$ will become apparent later on).

Furthermore, from the principle of conservation of energy at the instant of emission of the generalized photons, we obtain that

$$(m_0 c^2 + E_0)^\bullet = 0. \tag{269}$$

Combining equations (268) and (269) we arrive at equation

$$\left(m_0 c^2 + i\hbar \frac{\dot{m}_0}{m_0}\right)^\bullet = 0. \tag{270}$$

Equation (270) both contains as physical information, and justifies, the whole corpus of the current cosmological observational data, as described in paragraph 7.

5.3 The "percentage function" Φ

The law of selfvariations expresses the total interaction of the generalized photons, which are emitted simultaneously by the material particle, with its rest mass and electric charge. However, in a particular direction $\frac{v}{c}$, the material particle emits generalized photons of energy E and momentum $\boldsymbol{P}$. Therefore, we have to derive quantitatively the partial contribution of a single generalized photon of energy E and momentum $\boldsymbol{P}$ to the law of selfvariations.

We have to answer the following question:

"Which mathematical equation correlates the energy E and the momentum $\boldsymbol{P}$ of a single generalized photon emitted towards a particular direction $\frac{v}{c}$, to the selfvariations of the rest mass m_0 and the electric charge q of the material particle?"

Thus, we are seeking the form of equations (265) and (266) that correspond to a single generalized photon.

Based on the law of selfvariations, the answer to this physical problem can only be given by the following statement:

"The partial contribution of a single generalized photon to the selfvariations of the rest mass m_0 and the electric charge q of the material particle is given by any mathematical expression which agrees with the operators defined in equations (264). If we sum the contributions of the single generalized photons towards all directions, during their simultaneous emission by the material particle, we have to end up with the equations given in (265) and (266)".

Considering this physical problem from its mathematical aspect, we can choose arbitrarily any mathematical expression giving the partial contribution of a single generalized photon according to the law of selfvariations, which satisfies the operators (264). Then, we can compare the results obtained by our particular choice with physical reality. On the other hand, we can choose the mathematical expression taking into account some specific *physical* criteria beforehand.

A fundamental case for the partial contribution of a generalized photon according to the law of selfvariations arises from the following observation: A single generalized photon counterbalances only a percentage of the total energy, momentum and electric charge that result from the selfvariations. Therefore, we must examine whether the contribution of a single generalized photon to the law of selfvariations is correlated with a *percentage* Φ of the rest mass m_0 and electric charge q. In this case, the partial contribution to the law

of selfvariations for a single generalized photon of energy E and momentum $\mathbf{P}$ will be given by the set of equations

$$\frac{\partial(\Phi m_0)}{\partial t} = -\frac{i}{\hbar}Em_0$$
$$\nabla(\Phi m_0) = \frac{i}{\hbar}\mathbf{P}m_0 \qquad (271)$$

$$\frac{\partial(\Phi q)}{\partial t} = -\frac{i}{\hbar}Eq$$
$$\nabla(\Phi q) = \frac{i}{\hbar}\mathbf{P}q. \qquad (272)$$

Summing in all directions of emission of generalized photons in the first equation of the set of equations (271), we obtain relations

$$\sum \frac{\partial(\Phi m_0)}{\partial t} = -\frac{i}{\hbar}\sum Em_0$$
$$\frac{\partial}{\partial t}\left(\sum \Phi m_0\right) = -\frac{i}{\hbar}m_0\sum E$$
$$\frac{\partial}{\partial t}\left(m_0\sum \Phi\right) = -\frac{i}{\hbar}m_0\sum E.$$

Since it holds that $\sum E = E_s$ and the total percentage of the contributions is 1, that is $\sum \Phi = 1$, we get

$$\frac{\partial m_0}{\partial t} = -\frac{i}{\hbar}m_0 E_s.$$

This is the first equation of the set of equations (265).

Also, from the second equation of the set of equations (271) we obtain relations

$$\sum \nabla(\Phi m_0) = \frac{i}{\hbar}\sum \mathbf{P}m_0$$
$$\nabla\left(\sum(\Phi m_0)\right) = \frac{i}{\hbar}m_0\sum \mathbf{P}$$
$$\nabla\left(m_0\sum \Phi\right) = \frac{i}{\hbar}m_0\sum \mathbf{P}.$$

Since $\sum \Phi = 1$ and $\sum \mathbf{P} = \mathbf{P}_s$, we see that

$$\nabla m_0 = \frac{i}{\hbar}m_0 \mathbf{P}_s.$$

This is the second of the equations given in (265).

We can perform the same procedure for equations (272) as well. Therefore, a single generalized photon can contribute to the selfvariation with a percentage Φ of the rest mass or the electric charge, and then this contribution is expressed by equations (271) and (272).

From equations (271) we obtain

$$\Phi\frac{\partial m_0}{\partial t} + m_0\frac{\partial \Phi}{\partial t} = -\frac{i}{\hbar}Em_0$$
$$\Phi\nabla m_0 + m_0\nabla\Phi = \frac{i}{\hbar}\mathbf{P}m_0.$$

From equations (169) we also obtain

$$\Phi\frac{1}{1-\dfrac{\mathbf{v}\cdot\mathbf{u}}{c^2}}\frac{\partial m_0}{\partial w} + m_0\frac{\partial \Phi}{\partial t} = -\frac{i}{\hbar}Em_0$$
$$-\Phi\frac{1}{1-\dfrac{\mathbf{v}\cdot\mathbf{u}}{c^2}}\frac{\partial m_0}{c\partial w}\frac{\mathbf{v}}{c} + m_0\nabla\Phi = \frac{i}{\hbar}\mathbf{P}m_0.$$

Eliminating from the equations the quantity m_0, we obtain

$$\frac{1}{1-\dfrac{\mathbf{v}\cdot\mathbf{u}}{c^2}}\frac{\partial m_0}{m_0\partial w} + \frac{\partial \Phi}{\partial t} = -\frac{i}{\hbar}E$$
$$-\frac{1}{1-\dfrac{\mathbf{v}\cdot\mathbf{u}}{c^2}}\frac{\partial m_0}{m_0 c\partial w}\frac{\mathbf{v}}{c} + \nabla\Phi = \frac{i}{\hbar}\mathbf{P}.$$

Finally, we arrive at the set of equations

$$E = \Phi\frac{i\hbar}{1-\dfrac{\mathbf{v}\mathbf{u}}{c^2}}\frac{\partial m_0}{m_0\partial w} + i\hbar\frac{\partial \Phi}{\partial t}$$
$$\mathbf{P} = \Phi\frac{i\hbar}{1-\dfrac{\mathbf{v}\mathbf{u}}{c^2}}\frac{\partial m_0}{m_0 c\partial w}\frac{\mathbf{v}}{c} - i\hbar\nabla\Phi. \qquad (273)$$

The function Φ can be any mathematical function, defined on the material particle and obeying relation

$$\sum \Phi = 1 \qquad (274)$$

However, it has to be considered a function depending on the direction in space, since this is implied by the summation given in equation (274).

According to the operators defined in (264), the continuous evolution of the selfvariations with the passage of time is assured by the condition

$$E_s \neq 0. \qquad (275)$$

This condition is a straightforward consequence of the first proposition-axiom of the theory of selfvariations.

We are seeking now to derive the relation between the total momentum $\mathbf{P}_s$ and the total energy E_s. According to equation (200) this relation can be written as

$$\mathbf{P}_s = E_s\frac{\mathbf{u}}{c^2}. \qquad (276)$$

Here, $\mathbf{u}$ denotes the velocity of the material particle at the moment of the emission of the generalized photons.

This relation has to be reconsidered for the following reason: During the proof of this relation in paragraph 4.3, we have taken into consideration equation (168), that is equation

$$\mathbf{J} = D\frac{\mathbf{v}}{c^2}.$$

This equation presupposes the validity of the condition

$$\boldsymbol{P} = E\frac{\boldsymbol{v}}{c^2} \qquad (277)$$

for every single generalized photon emitted towards any direction defined by $\frac{v}{c}$, as depicted in figure 6. However, equations (273) reveal a more complex, and certainly different relation, between the momentum $\boldsymbol{P}$ and the energy E of a single generalized photon. Therefore, we have to reconsider the validity of equation (276), since we cannot base its proof on equation (277). As we shall see immediately, equation (276) is of general validity, and is compatible with the set of equations (273).

We consider a material point particle at rest, as depicted in figure 7. In order for this particle to remain at rest, the total momentum emitted simultaneously and towards all directions has to vanish, that is

$$\boldsymbol{P}'_s = \boldsymbol{0}. \qquad (278)$$

If the case were different, the material particle would undergo an arbitrary motion, as a consequence of the principle of conservation of momentum. From equation (278), and from the set of transformations (164) for the total energy E_s and the total momentum $\boldsymbol{P}_s$, we arrive at equation (276). Thus, we have

$$E_s = \gamma\left(\mathrm{E}'_s + uP'_{sx}\right)$$
$$P_{sx} = \gamma\left(P'_{sx} + \frac{u}{c^2}\mathrm{E}'_s\right)$$
$$P_{sy} = P'_{sy}$$
$$P_{sz} = P'_{sz}.$$

Since, according to equation (278) it holds that

$$\left(P'_{sx}, P'_{sy}, P'_{sz}\right) = (0, 0, 0),$$

we obtain the following relations

$$E_s = \gamma\mathrm{E}'_s$$
$$P_{sx} = \gamma\mathrm{E}'_s\frac{u}{c^2}$$
$$P_{sy} = 0$$
$$P_{sz} = 0.$$

We also have that $\boldsymbol{u} = \begin{bmatrix} u \\ 0 \\ 0 \end{bmatrix}$, thus we obtain

$$E_s = \gamma\mathrm{E}'_s$$
$$\boldsymbol{P}_s = \gamma\mathrm{E}'_s\frac{\boldsymbol{u}}{c^2}.$$

Finally, we have

$$E_s = \gamma\mathrm{E}'_s$$
$$\boldsymbol{P}_s = E_s\frac{\boldsymbol{u}}{c^2}.$$

This is equation (276). Furthermore, we also obtain equation

$$E_s = \gamma\mathrm{E}'_s = \gamma E_0 = \frac{E_0}{\sqrt{1 - \dfrac{u^2}{c^2}}}. \qquad (279)$$

Here, we denote

$$\mathrm{E}'_s = E_0. \qquad (280)$$

A material particle at rest can emit generalized photons of different energies for different directions. If the generalized photons emitted in opposite directions have opposite momenta, the material particle will remain at rest. But the momentum of a generalized photon can also be balanced by two other generalized photons emitted towards appropriate directions and with appropriate energies. In reality, there is an infinite number of combinations of emmision of generalized photons, with infinite combinations of energies and directions of emission. In each of these cases where equation (278) holds, the particle remains at rest. The case of emission of identical generalized photons in all directions by a material particle at rest is only one among the infinite number of cases satisfying equation (278).

Therefore, by rotating the unit vector $\frac{v'}{c}$ around the point particle at rest, as depicted in figure 7, we expect a change in the energy of the generalized photons. Exactly this is shown by equations (273), while at the same time they highlight the factors defining the energy and momentum of each single generalized photon.

5.4 The accompanying particle

In the previous paragraph we proved equations (276) and (279):

$$\boldsymbol{P}_s = E_s\frac{\boldsymbol{u}}{c^2}$$
$$E_s = \frac{E_0}{\sqrt{1 - \dfrac{u^2}{c^2}}}. \qquad (281)$$

Equations (281) show that the total energy and momentum emitted simultaneously and in all directions by the material particle behaves as a particle moving with velocity $\boldsymbol{u}$, and accompanying the material particle. There is a definite correspondence between equations (281) and equations

$$\boldsymbol{P} = m\boldsymbol{u}$$
$$m = \frac{m_0}{\sqrt{1 - \dfrac{u^2}{c^2}}}$$

which give the momentum $\boldsymbol{P}$ and the mass m of the material particle.

According to equations (281), the accompanying particle has rest energy E_0. This is the rest energy E_s' from equation (280). Therefore, the accompanying particle has a rest mass given by $\frac{E_0}{c^2}$.

According to the first proposition-axiom of the theory of selfvariations, the rest mass $\frac{E_0}{c^2}$ of the accompanying particle changes with the passage of time. Hence, we seek the counterparts of equations (265), which define the rate of change of the rest mass $\frac{E_0}{c^2}$, or equivalently the rest energy E_0. As such, we obtain the corresponding form of equations (265)

$$
\begin{aligned}
\frac{\partial E_0}{\partial t} &= \frac{i}{\hbar} mc^2 E_0 = \frac{i}{\hbar} \gamma m_0 c^2 E_0 = \frac{i}{\hbar} \frac{m_0 c^2}{\sqrt{1-\frac{u^2}{c^2}}} E_0 \\
\nabla E_0 &= -\frac{i}{\hbar} m\boldsymbol{u} E_0 = -\frac{i}{\hbar} \gamma m_0 \boldsymbol{u} E_0 = -\frac{i}{\hbar} \frac{m_0}{\sqrt{1-\frac{u^2}{c^2}}} \boldsymbol{u} E_0.
\end{aligned}
\tag{282}
$$

Equations (265) describe the effect of the generalized photons on the rest mass of the material particle. In nature, though, effects are always mutual. Hence, just as the generalized photons affect the material particle, the material particle in turn affects the generalized photons, and these mutual interactions must occur in the framework of the same physical law. Therefore, from the outset the issue arises of the existence of a rest mass concealed within the operators (264), and of a corresponding equation symmetrical to (265). The quest for the partial contribution of a single generalized photon to the law of selfvariations revealed the existence of the rest mass $\frac{E_0}{c^2}$ and equations (282). The existence of the rest mass $\frac{E_0}{c^2}$ is predicted by the initial equations we formulated for the macrocosmic scales, through equation (200).

A large part of the predictions of the theory of selfvariations can be made without the aid of equations (282). For example, the justification of the observational cosmological data can be obtained from (270), which is proven independently without resorting to equations (282). The same holds for equations (273). However, the accompanying particle is a direct consequence of the selfvariations. Indeed, if we combine the second of equations (281) with relation (275) we see immediately that

$$
E_0 \neq 0. \tag{283}
$$

The rest mass $\frac{E_0}{c^2}$ of the accompanying particle cannot vanish. Therefore, in order to study the consequences of the selfvariations in their totality, we have to take into account the existence and the properties of the accompanying particle. In nature there is always the system "material particle-accompanying particle".

Let M_0 be the rest mass of the system "material particle-

accompanying particle", given by

$$
M_0 = m_0 + \frac{E_0}{c^2}. \tag{284}
$$

We have that

$$
\begin{aligned}
\frac{\partial M_0}{\partial t} &= \frac{\partial}{\partial t}\left(m_0 + \frac{E_0}{c^2}\right) \\
\frac{\partial M_0}{\partial t} &= \frac{\partial m_0}{\partial t} + \frac{\partial E_0}{c^2 \partial t}.
\end{aligned}
$$

Using the first equations of the sets of equations given in (265) and (266), we obtain relation

$$
\frac{\partial M_0}{\partial t} = -\frac{i}{\hbar} E_s m_0 + \frac{i}{\hbar} \gamma m_0 E_0.
$$

And using equation (279) we get

$$
\begin{aligned}
\frac{\partial M_0}{\partial t} &= -\frac{i}{\hbar} \gamma E_0 m_0 + \frac{i}{\hbar} \gamma m_0 E_0 \\
\frac{\partial M_0}{\partial t} &= 0.
\end{aligned}
\tag{285}
$$

Similarly, using the second equations of the sets of equations (265) and (282) we have that

$$
\nabla M_0 = \boldsymbol{0}. \tag{286}
$$

From equations (285) and (286) we conclude that the rest mass M_0 of the system "material particle-accompanying particle" is a physical quantity not affected by the process of the selfvariations. Therefore, we can use the rest mass M_0 and the rest energy $M_0 c^2$ as a unit of measurement of mass and energy, respectively. By this approach we circumvent the methodological problems stemming from the principle of the *"internality of the universe with respect to the measurement procedure"*, as stated in paragraph 4.9.

The quantitative mathematical description of physical reality depends on our ability to include in our equations the consequences of the internality of the universe to the measurement procedure. In the macrocosmic scales there is a very simple way to accomplish this, as described in paragraph 7. In the microcosmic scale we use as units of measurement of mass and energy the quantities M_0 and $M_0 c^2$, respectively.

We rewrite now equations (265) in the form

$$
\begin{aligned}
\frac{\partial}{\partial t}\left(\frac{m_0}{M_0}\right) &= -\frac{i}{\hbar} E_s \left(\frac{m_0}{M_0}\right) \\
\nabla\left(\frac{m_0}{M_0}\right) &= \frac{i}{\hbar} \boldsymbol{P}_s \left(\frac{m_0}{M_0}\right).
\end{aligned}
\tag{287}
$$

These equations have the exact same physical content as equations (265). They give the rate of change of the rest mass m_0, since the rest mass M_0 is not affected by the selfvariations, according to equations (285) and (286). At the same

time, these equations highlight the action of the operators (264) on the complex number $\frac{m_0}{M_0} \in \mathbb{C}$, since the complex unit i appears within the expressions of the operators. The same procedure can be repeated for the case of equations (282) as well, by introducing the number $\frac{E_0}{M_0 c^2} \in \mathbb{C}$, and for the whole list of equations we have stated.

The accompanying particle has rest mass of magnitude $\frac{E_0}{c^2}$, which comes from the sum of the contributions of the generalized photons emitted simultaneously by the material particle. This is the physical content of equations (281). Therefore, the mechanism through which the selfvariations occur plays a fundamental role for the determination of the physical properties of the accompanying particle, and eventually for the physical properties of the actual system "material particle-accompanying particle".

5.5 The symmetrical law for the electric charge

From the study already conducted in paragraph 4.2 it follows that the generalized photons counterbalancing the selfvariation of the electric charge q carry electric charge. Therefore, the physical object resulting from their aggregation carries electric charge q_i.

The law of the selfvariations for the electric charge q is given by equations (266)

$$\frac{\partial q}{\partial t} = -\frac{i}{\hbar} E_s q$$
$$\nabla q = \frac{i}{\hbar} \boldsymbol{P}_s q. \tag{288}$$

In these equations we denote with E_s and $\boldsymbol{P}_s$ the total energy and momentum emitted by the material particle simultaneously in all directions, and which counterbalances the variations in energy resulting from the selfvariation of the electric charge. Although we have kept the same notation, these quantites are not the same as the ones appearing in equations (265).

In order to repeat the study conducted for the rest mass for the case of the electric charge, we have to define the equations symmetrical to (266). That is, we have to formulate the counterparts of equations (266) for the electric charge q_i.

The law of selfvariations for the electric charge (288) has to be modified so that it will define the interaction of the electric charges q and q_i, exactly as the law stated in equation (265) determines the interaction of the rest masses m_0 and $\frac{E_0}{c^2}$. Therefore, the second part of equation (288) has to be expressed such that the electric charge q_i appears. This can only be accomplished by the introduction of an electric potential V through equation

$$E_s = V q_i. \tag{289}$$

With this notation, and taking into account equation

(276), equations (288) can be written as

$$\frac{\partial q}{\partial t} = -\frac{i}{\hbar} V q_i q$$
$$\nabla q = \frac{i}{\hbar} V q_i \frac{\boldsymbol{u}}{c^2} q. \tag{290}$$

Equations (290) and (288) have the same physical content, if and only if the electric potential V is independent of the selfvariations.

Starting from equation (290), we can also deduce all equations inferred in the previous paragraphs for the rest mass, except now for the electric charge. The proof follows similar paths, and we shall note repeat it here in full.

Firstly, it can be deduced that the potential V can be written in the form

$$V = \gamma V_0 = \frac{V_0}{\sqrt{1 - \frac{u^2}{c^2}}}. \tag{291}$$

The potential V_0 stays invariant under the action of the Lorentz-Einstein transformations, and is independent of the selfvariations. The corresponding expressions of equations (268) and (270) are

$$q_i V_0 = i\hbar \frac{\dot{q}}{q}$$
$$\left(q + \frac{i\hbar}{V_0} \frac{\dot{q}}{q} \right)^{\bullet} = 0. \tag{292}$$

The corresponding equations to the ones given in (273) for the generalized photon, can be formulated as

$$E = \Phi \frac{i\hbar}{1 - \frac{\boldsymbol{v} \cdot \boldsymbol{u}}{c^2}} \frac{\partial q}{q \partial w} + i\hbar \frac{\partial \Phi}{\partial t}$$
$$\boldsymbol{P} = \Phi \frac{i\hbar}{1 - \frac{\boldsymbol{v} \cdot \boldsymbol{u}}{c^2}} \frac{\partial q}{qc \partial w} \frac{\boldsymbol{v}}{c} - i\hbar \nabla \Phi. \tag{293}$$

The corresponding equations to the equations (282), that is, the corresponding form of the law expressed in (290), are

$$\frac{\partial q_i}{\partial t} = \frac{i}{\hbar} \gamma V_0 q q_i$$
$$\nabla q_i = -\frac{i}{\hbar} \gamma V_0 q \frac{\boldsymbol{u}}{c^2} q_i. \tag{294}$$

The corresponding relation to relation (283) is

$$q_i \neq 0. \tag{295}$$

The corresponding expression of equation (284), that is, the electric charge Q of the system "material particle-accompanying particle" is

$$Q = q + q_i. \tag{296}$$

The corresponding equations to equations (285) and (286) take the form

$$\frac{\partial Q}{\partial t} = 0$$

$$\nabla Q = \mathbf{0}. \tag{297}$$

The electric charge Q is not affected by the selfvariations.

5.6 Fundamental study of the generalized photon

In paragraph 4 we studied the consequences of the selfvariations in the surrounding spacetime of the material particle. In that study we considered the validity of equation (168)

$$\mathbf{J} = D\frac{\mathbf{v}}{c^2}$$

which presupposes the validity of equation

$$\mathbf{P} = E\frac{\mathbf{v}}{c^2} \tag{298}$$

for the generalized photon.

We know by now that the energy E and the momentum $\mathbf{P}$ of the generalized photon are not correlated through the simple relation (298). For the generalized photon that results from the selfvariation of the rest mass, equations (273) hold

$$E = \Phi\frac{i\hbar}{1 - \dfrac{\mathbf{v} \cdot \mathbf{u}}{c^2}}\frac{\partial m_0}{m_0\partial w} + i\hbar\frac{\partial \Phi}{\partial t}$$

$$\mathbf{P} = \Phi\frac{i\hbar}{1 - \dfrac{\mathbf{v} \cdot \mathbf{u}}{c^2}}\frac{\partial m_0}{m_0 c\partial w}\frac{\mathbf{v}}{c} - i\hbar\nabla\Phi. \tag{299}$$

For the generalized photon that results from the selfvariation of the electric charge, equations (293) hold

$$E = \Phi\frac{i\hbar}{1 - \dfrac{\mathbf{v} \cdot \mathbf{u}}{c^2}}\frac{\partial q}{q\partial w} + i\hbar\frac{\partial \Phi}{\partial t}$$

$$\mathbf{P} = \Phi\frac{i\hbar}{1 - \dfrac{\mathbf{v} \cdot \mathbf{u}}{c^2}}\frac{\partial q}{qc\partial w}\frac{\mathbf{v}}{c} - i\hbar\nabla\Phi. \tag{300}$$

Equations (299) and (300) lead to a completely different relation from (298), between the energy E and the momentum $\mathbf{P}$ of a generalized photon.

We will study the generalized photon, as given in equations (299). The study of equations (300) is exactly the same.

The percentage-function Φ depends on the direction $\frac{\mathbf{v}}{c}$ and can, therefore, be written as $\Phi = \Phi(\delta, \omega)$, and can also depend on the moment, $w = t - \frac{r}{c}$, of emission of the generalized photon, so that

$$\Phi = \Phi(w, \delta, \omega). \tag{301}$$

From the first of equations (299) we have

$$E = \Phi\frac{i\hbar}{1 - \dfrac{\mathbf{v} \cdot \mathbf{u}}{c^2}}\frac{\partial m_0}{m_0\partial w} + i\hbar\frac{\partial \Phi}{\partial t}$$

and with equation (301), we get

$$E = \Phi\frac{i\hbar}{1 - \dfrac{\mathbf{v} \cdot \mathbf{u}}{c^2}}\frac{\partial m_0}{m_0\partial w} + i\hbar\left(\frac{\partial \Phi}{\partial w}\frac{\partial w}{\partial t} + \frac{\partial \Phi}{\partial \delta}\frac{\partial \delta}{\partial t} + \frac{\partial \Phi}{\partial \omega}\frac{\partial \omega}{\partial t}\right)$$

and with equations (11), (41) and (42) we get

$$E = \Phi\frac{i\hbar}{1 - \dfrac{\mathbf{v} \cdot \mathbf{u}}{c^2}}\frac{\partial m_0}{m_0\partial w} +$$

$$+ \frac{i\hbar}{1 - \dfrac{\mathbf{v} \cdot \mathbf{u}}{c^2}}\left(\frac{\partial \Phi}{\partial w} - \frac{\mathbf{u} \cdot \boldsymbol{\beta}}{r}\frac{\partial \Phi}{\partial \delta} - \frac{\mathbf{u} \cdot \boldsymbol{\gamma}}{r\sin\delta}\frac{\partial \Phi}{\partial \omega}\right). \tag{302}$$

From the second of equations (299), we have

$$\mathbf{P} = \Phi\frac{i\hbar}{1 - \dfrac{\mathbf{v} \cdot \mathbf{u}}{c^2}}\frac{\partial m_0}{m_0 c\partial w}\frac{\mathbf{v}}{c} - i\hbar\nabla\Phi$$

and with equation (301) we get

$$\mathbf{P} = \Phi\frac{i\hbar}{1 - \dfrac{\mathbf{v} \cdot \mathbf{u}}{c^2}}\frac{\partial m_0}{m_0 c\partial w}\frac{\mathbf{v}}{c} - i\hbar\left(\frac{\partial \Phi}{\partial w}\nabla w + \frac{\partial \Phi}{\partial \delta}\nabla \delta + \frac{\partial \Phi}{\partial \omega}\nabla \omega\right)$$

and with equations (12), (51) and (52), we get

$$\mathbf{P} = \Phi\frac{i\hbar}{1 - \dfrac{\mathbf{v} \cdot \mathbf{u}}{c^2}}\frac{\partial m_0}{m_0 c\partial w}\frac{\mathbf{v}}{c} +$$

$$+ \frac{i\hbar}{1 - \dfrac{\mathbf{v} \cdot \mathbf{u}}{c^2}}\frac{\partial \Phi}{\partial w}\frac{\mathbf{v}}{c^2} - \frac{i\hbar}{r}\frac{\partial \Phi}{\partial \delta}\left(\frac{\mathbf{u} \cdot \boldsymbol{\beta}}{1 - \dfrac{\mathbf{v} \cdot \mathbf{u}}{c^2}}\frac{\mathbf{v}}{c^2} + \boldsymbol{\beta}\right) - \tag{303}$$

$$- \frac{i\hbar}{r\sin\delta}\frac{\partial \Phi}{\partial \omega}\left(\frac{\mathbf{u} \cdot \boldsymbol{\gamma}}{1 - \dfrac{\mathbf{v} \cdot \mathbf{u}}{c^2}}\frac{\mathbf{v}}{c^2} + \boldsymbol{\gamma}\right).$$

We now denote

$$E_i = \Phi\frac{i\hbar}{1 - \dfrac{\mathbf{v} \cdot \mathbf{u}}{c^2}}\frac{\partial m_0}{m_0\partial w}$$

$$P_i = \Phi\frac{i\hbar}{1 - \dfrac{\mathbf{v} \cdot \mathbf{u}}{c^2}}\frac{\partial m_0}{m_0 c\partial w}\frac{\mathbf{v}}{c} \tag{304}$$

$$E_\Phi = i\hbar \frac{\partial \Phi}{\partial t} = \frac{i\hbar}{1 - \dfrac{\boldsymbol{v} \cdot \boldsymbol{u}}{c^2}} \frac{\partial \Phi}{\partial w} - \frac{i\hbar \boldsymbol{u} \cdot \boldsymbol{\beta}}{r\left(1 - \dfrac{\boldsymbol{v} \cdot \boldsymbol{u}}{c^2}\right)} \frac{\partial \Phi}{\partial \delta} -$$

$$- \frac{i\hbar \boldsymbol{u} \cdot \boldsymbol{\gamma}}{r\left(1 - \dfrac{\boldsymbol{v} \cdot \boldsymbol{u}}{c^2}\right)\sin\delta} \frac{\partial \Phi}{\partial \omega}$$

$$\boldsymbol{P}_\Phi = -i\hbar \nabla\Phi = \frac{i\hbar}{1 - \dfrac{\boldsymbol{v} \cdot \boldsymbol{u}}{c^2}} \frac{\partial \Phi}{\partial w} \frac{\boldsymbol{v}}{c^2} -$$

$$- \frac{i\hbar}{r} \frac{\partial \Phi}{\partial \delta} \left(\frac{\boldsymbol{u} \cdot \boldsymbol{\beta}}{1 - \dfrac{\boldsymbol{v} \cdot \boldsymbol{u}}{c^2}} \frac{\boldsymbol{v}}{c^2} + \boldsymbol{\beta} \right) - \qquad (305)$$

$$- \frac{i\hbar}{r\sin\delta} \frac{\partial \Phi}{\partial \omega} \left(\frac{\boldsymbol{u} \cdot \boldsymbol{\gamma}}{1 - \dfrac{\boldsymbol{v} \cdot \boldsymbol{u}}{c^2}} \frac{\boldsymbol{v}}{c^2} + \boldsymbol{\gamma} \right).$$

With this notation, equations (302) and (303) can be written as

$$\begin{aligned} E &= E_i + E_\Phi \\ \boldsymbol{P} &= \boldsymbol{P}_i + \boldsymbol{P}_\Phi. \end{aligned} \qquad (306)$$

Combining equations (302) and (303), we obtain relation

$$\boldsymbol{P} = E\frac{\boldsymbol{v}}{c^2} - \frac{i\hbar}{r} \frac{\partial \Phi}{\partial \delta} \boldsymbol{\beta} - \frac{i\hbar}{r\sin\delta} \frac{\partial \Phi}{\partial \omega} \boldsymbol{\gamma} \qquad (307)$$

relating the energy E and momentum P of the generalized photon.

The energy-momentum pair $(E_\Phi, \boldsymbol{P}_\Phi)$ can be decomposed into three partial pairs

$$\begin{aligned} E_w &= \frac{i\hbar}{1 - \dfrac{\boldsymbol{v} \cdot \boldsymbol{u}}{c^2}} \frac{\partial \Phi}{\partial w} \\ \boldsymbol{P}_w &= \frac{i\hbar}{1 - \dfrac{\boldsymbol{v} \cdot \boldsymbol{u}}{c^2}} \frac{\partial \Phi}{\partial w} \frac{\boldsymbol{v}}{c^2} \end{aligned} \qquad (308)$$

$$\begin{aligned} E_\delta &= -\frac{i\hbar \boldsymbol{u} \cdot \boldsymbol{\beta}}{r\left(1 - \dfrac{\boldsymbol{v} \cdot \boldsymbol{u}}{c^2}\right)} \frac{\partial \Phi}{\partial \delta} \\ \boldsymbol{P}_\delta &= -\frac{i\hbar}{r} \frac{\partial \Phi}{\partial \delta} \left(\frac{\boldsymbol{u} \cdot \boldsymbol{\beta}}{1 - \dfrac{\boldsymbol{v} \cdot \boldsymbol{u}}{c^2}} \frac{\boldsymbol{v}}{c^2} + \boldsymbol{\beta} \right) \end{aligned} \qquad (309)$$

$$\begin{aligned} E_\omega &= -\frac{i\hbar \boldsymbol{u} \cdot \boldsymbol{\gamma}}{r\left(1 - \dfrac{\boldsymbol{v} \cdot \boldsymbol{u}}{c^2}\right)\sin\delta} \frac{\partial \Phi}{\partial \omega} \\ \boldsymbol{P}_\omega &= -\frac{i\hbar}{r\sin\delta} \frac{\partial \Phi}{\partial \omega} \left(\frac{\boldsymbol{u} \cdot \boldsymbol{\gamma}}{1 - \dfrac{\boldsymbol{v} \cdot \boldsymbol{u}}{c^2}} \frac{\boldsymbol{v}}{c^2} + \boldsymbol{\gamma} \right) \end{aligned} \qquad (310)$$

$$\begin{aligned} E_\Phi &= E_w + E_\delta + E_\omega \\ \boldsymbol{P}_\Phi &= \boldsymbol{P}_w + \boldsymbol{P}_\delta + \boldsymbol{P}_\omega. \end{aligned} \qquad (311)$$

It is easy to prove that, in the case of constant-speed motion with velocity $\boldsymbol{u} = \begin{bmatrix} u \\ 0 \\ 0 \end{bmatrix}$, each of the energy-momentum pairs $(E_i, \boldsymbol{P}_i)$, $(E_w, \boldsymbol{P}_w)$, $(E_\delta, \boldsymbol{P}_\delta)$, $(E_\omega, \boldsymbol{P}_\omega)$ transforms autonomously, independently of the rest, according to the Lorentz-Einstein transformations. Furthermore, an invariant amount of energy corresponds to each pair.

We shall calculate the four invariant amounts of energy. In the same way, we can prove the independent Lorentz-Einstein transformations of the four energy-momentum pairs.

From equation (305) we have

$$E_i^2 - c^2 \boldsymbol{P}_i^2 = E_i^2 - c^2 E_i^2 \left(\frac{\boldsymbol{v}}{c^2}\right)^2$$

and since $\boldsymbol{v}^2 = c^2$, we get

$$E_i^2 - c^2 \boldsymbol{P}_i^2 = 0. \qquad (312)$$

From equation (308) we have

$$E_w^2 - c^2 \boldsymbol{P}_w^2 = E_w^2 - c^2 E_w^2 \left(\frac{\boldsymbol{v}}{c^2}\right)^2$$

and from $\boldsymbol{v}^2 = c^2$, we get

$$E_w^2 - c^2 \boldsymbol{P}_w^2 = 0. \qquad (313)$$

From equation (309) we have

$$E_\delta^2 - c^2 \boldsymbol{P}_\delta^2 = -\frac{\hbar^2 (\boldsymbol{u} \cdot \boldsymbol{\beta})^2}{r^2 \left(1 - \dfrac{\boldsymbol{v} \cdot \boldsymbol{u}}{c^2}\right)^2} \left(\frac{\partial \Phi}{\partial \delta}\right)^2 +$$

$$+ \frac{c^2 \hbar^2}{r^2} \left(\frac{\partial \Phi}{\partial \delta}\right)^2 \left[\frac{\boldsymbol{u} \cdot \boldsymbol{\beta}}{1 - \dfrac{\boldsymbol{v} \cdot \boldsymbol{u}}{c^2}} \frac{\boldsymbol{v}}{c^2} + \boldsymbol{\beta} \right]^2$$

and since it is $\boldsymbol{u} \cdot \boldsymbol{\beta} = 0$, $\boldsymbol{v}^2 = c^2$, $\boldsymbol{\beta}^2 = 1$, we get

$$E_\delta^2 - c^2 \boldsymbol{P}_\delta^2 = -\frac{\hbar^2 (\boldsymbol{u} \cdot \boldsymbol{\beta})^2}{r^2 \left(1 - \dfrac{\boldsymbol{v} \cdot \boldsymbol{u}}{c^2}\right)^2} \left(\frac{\partial \Phi}{\partial \delta}\right)^2 +$$

$$+ \frac{\hbar^2 (\boldsymbol{u} \cdot \boldsymbol{\beta})^2}{r^2 \left(1 - \dfrac{\boldsymbol{v} \cdot \boldsymbol{u}}{c^2}\right)^2} \left(\frac{\partial \Phi}{\partial \delta}\right)^2 + \left(\frac{c\hbar}{r} \frac{\partial \Phi}{\partial \delta}\right)^2$$

$$E_\delta^2 - c^2 \boldsymbol{P}_\delta^2 = \left(\frac{c\hbar}{r} \frac{\partial \Phi}{\partial \delta}\right)^2. \qquad (314)$$

Similarly, from equations (310) we get

$$E_\omega^2 - c^2 \boldsymbol{P}_\omega^2 = \left(\frac{c\hbar}{r\sin\delta} \frac{\partial \Phi}{\partial \omega}\right)^2. \qquad (315)$$

From the transformations (127) we get

$$\frac{c\hbar}{r'}\frac{\partial \Phi}{\partial \delta'} = \frac{c\hbar}{\gamma r\left(1 - \frac{u}{c}\cos\delta\right)}\frac{\partial \Phi}{\partial \delta}\gamma\left(1 - \frac{u}{c}\cos\delta\right)$$

$$\frac{c\hbar}{r'}\frac{\partial \Phi}{\partial \delta'} = \frac{c\hbar}{\gamma r}\frac{\partial \Phi}{\partial \delta}. \tag{316}$$

Therefore, the second part of equation (314) remains invariant according to the Lorentz-Einstein transformations.

From transformations (124) and (127) we have

$$\frac{c\hbar}{r'\sin\delta'}\frac{\partial \Phi}{\partial \omega'} = \frac{c\hbar}{\gamma r\left(1 - \frac{u}{c}\cos\delta\right)\dfrac{\sin\delta}{\gamma\left(1 - \frac{u}{c}\cos\delta\right)}}\frac{\partial \Phi}{\partial \omega}$$

$$\frac{c\hbar}{r'\sin\delta'}\frac{\partial \Phi}{\partial \omega'} = \frac{c\hbar}{r\sin\delta}\frac{\partial \Phi}{\partial \omega}. \tag{317}$$

Therefore, the second part of equation (315) remains invariant under the Lorentz-Einstein transformations.

From equation (307) we can calculate the total invariant energy of the generalized photon

$$E^2 - c^2\boldsymbol{P}^2 = E^2 - c^2\left(E\frac{\boldsymbol{v}}{c^2} - \frac{i\hbar}{r}\frac{\partial \Phi}{\partial \delta}\boldsymbol{\beta} - \frac{i\hbar}{r\sin\delta}\frac{\partial \Phi}{\partial \omega}\boldsymbol{\gamma}\right)^2$$

and taking into consideration that the set of vectors $\frac{v}{c}, \boldsymbol{\beta}, \boldsymbol{\gamma}$ constitute an orthonormal basis, we get

$$E^2 - c^2\boldsymbol{P}^2 = E^2 - E^2 + \left(\frac{c\hbar}{r}\frac{\partial \Phi}{\partial \delta}\right)^2 + \left(\frac{c\hbar}{r\sin\delta}\frac{\partial \Phi}{\partial \omega}\right)^2$$

$$E^2 - c^2\boldsymbol{P}^2 = \left(\frac{c\hbar}{r}\frac{\partial \Phi}{\partial \delta}\right)^2 + \left(\frac{c\hbar}{r\sin\delta}\frac{\partial \Phi}{\partial \omega}\right)^2. \tag{318}$$

According to equations (316) and (317), the second part of equation (318) remains invariant under the Lorentz-Einstein transformations.

We will now prove that:

"In the case of constant-speed motion with velocity

$$\boldsymbol{u} = \begin{bmatrix} u \\ 0 \\ 0 \end{bmatrix},$$

pairs $(E_i, \boldsymbol{P}_i)$, $(E_w, \boldsymbol{P}_w)$ correspond to a flow of energy and momentum into the surrounding spacetime. On the contrary, pairs $(E_\delta, \boldsymbol{P}_\delta)$ and $(E_\omega, \boldsymbol{P}_\omega)$ correspond to a redistribution of energy and momentum in the surrounding spacetime".

From equation (109) together with the second of equations (308), we get

$$\boldsymbol{P}_i \cdot \boldsymbol{R} = \frac{i\hbar}{1 - \dfrac{\boldsymbol{v}\cdot\boldsymbol{u}}{c^2}}\frac{\partial m_0}{m_0\partial w}\frac{\boldsymbol{v}}{c^2}r\left(\frac{\boldsymbol{v}}{c} - \frac{\boldsymbol{u}}{c}\right)$$

$$\boldsymbol{P}_i \cdot \boldsymbol{R} = \frac{i\hbar}{1 - \dfrac{\boldsymbol{v}\cdot\boldsymbol{u}}{c^2}}\frac{\partial m_0}{m_0 c\partial w}r\left(1 - \frac{\boldsymbol{v}\cdot\boldsymbol{u}}{c^2}\right)$$

$$\boldsymbol{P}_i \cdot \boldsymbol{R} = i\hbar r\frac{\partial m_0}{m_0 c\partial w}$$

$$\boldsymbol{P}_i \cdot \frac{\boldsymbol{R}}{r} = i\hbar\frac{\partial m_0}{m_0 c\partial w}. \tag{319}$$

Similarly, from equation (109) together with the second of equations (308) we get

$$\boldsymbol{P}_w \cdot \frac{\boldsymbol{R}}{r} = i\hbar\frac{\partial \Phi}{c\partial w}. \tag{320}$$

We conclude that both the momentum $\boldsymbol{P}_i$, as well as the momentum $\boldsymbol{P}_w$, have a component along the direction of vector $\boldsymbol{R}$, as depicted in Figure 6.

Combining equation (109) with the second of equations (309), we get

$$\boldsymbol{P}_\delta \cdot \boldsymbol{R} = -\frac{i\hbar}{r}\frac{\partial \Phi}{\partial \delta}\left(\frac{\boldsymbol{u}\cdot\boldsymbol{\beta}}{1 - \dfrac{\boldsymbol{v}\cdot\boldsymbol{u}}{c^2}}\frac{\boldsymbol{v}}{c^2} + \boldsymbol{\beta}\right)r\left(\frac{\boldsymbol{v}}{c} - \frac{\boldsymbol{u}}{c}\right)$$

and since $\boldsymbol{v}^2 = c^2$ and $\boldsymbol{v}\cdot\boldsymbol{\beta} = 0$, we obtain

$$\boldsymbol{P}_\delta \cdot \boldsymbol{R} = -i\hbar\frac{\partial \Phi}{\partial \delta}\left(\frac{\boldsymbol{u}\cdot\boldsymbol{\beta}}{1 - \dfrac{\boldsymbol{v}\cdot\boldsymbol{u}}{c^2}}\frac{\boldsymbol{v}}{c^2}\left(\frac{\boldsymbol{v}}{c} - \frac{\boldsymbol{u}}{c}\right) - \frac{\boldsymbol{u}\cdot\boldsymbol{\beta}}{c}\right)$$

$$\boldsymbol{P}_\delta \cdot \boldsymbol{R} = -i\hbar\frac{\partial \Phi}{\partial \delta}\left(\frac{\dfrac{\boldsymbol{u}}{c}\boldsymbol{\beta}}{1 - \dfrac{\boldsymbol{v}\cdot\boldsymbol{u}}{c^2}}\left(1 - \frac{\boldsymbol{v}\cdot\boldsymbol{u}}{c^2}\right) - \frac{\boldsymbol{u}\cdot\boldsymbol{\beta}}{c}\right)$$

$$\boldsymbol{P}_\delta \cdot \boldsymbol{R} = 0. \tag{321}$$

Similarly, from equation (109) and the second of equations (310) we get

$$\boldsymbol{P}_\omega \cdot \boldsymbol{R} = 0. \tag{322}$$

Both the momentum $\boldsymbol{P}_\delta$, and the momentum $\boldsymbol{P}_\omega$, are vertical to the vector $\boldsymbol{R}$ of Figure 6.

We will now prove that:

"The generalized photon carries intrinsic angular momentum $\boldsymbol{S}$, independent of the distance r. The component $\boldsymbol{S}_u$ of the intrinsic angular momentum $\boldsymbol{S}$ along the direction of the motion of the material particle does not depend upon the velocity $\boldsymbol{u}$ of the motion".

In Figure 4, the angular momentum S of the generalized photon with respect to the (constant) point of emission $E\left(x_p\left(w\right),y_p\left(w\right),z_p\left(w\right),w\right)$ is

$$S = r \times P$$

and with equation (6) written in the form

$$r = \frac{r}{c}\boldsymbol{v}$$

we get

$$S = \frac{r}{c}\boldsymbol{v} \times P = \frac{r}{c}\boldsymbol{v} \times \left(P_i + P_w + P_\delta + P_\omega\right). \qquad (323)$$

Denoting

$$\begin{aligned} S_i &= \frac{r}{c}\boldsymbol{v} \times P_i \\ S_w &= \frac{r}{c}\boldsymbol{v} \times P_w \\ S_\delta &= \frac{r}{c}\boldsymbol{v} \times P_\delta \\ S_\omega &= \frac{r}{c}\boldsymbol{v} \times P_\omega \end{aligned} \qquad (324)$$

equation (323) can be written as

$$S = S_i + S_w + S_\delta + S_\omega. \qquad (325)$$

From the first of equations (324) we have

$$S_i = \frac{r}{c}\boldsymbol{v} \times P_i$$

and with the second of equations (304) we get

$$S_i = 0. \qquad (326)$$

From the second of equations (324) we have

$$S_w = \frac{r}{c}\boldsymbol{v} \times P_w$$

and with the second of equations (308) we get

$$S_w = \boldsymbol{0}. \qquad (327)$$

From the third of equations (324) we have

$$S_\delta = \frac{r}{c}\boldsymbol{v} \times P_\delta$$

and with the second of equations (309) we have

$$S_\delta = -i\hbar\frac{\partial\Phi}{\partial\delta}\frac{\boldsymbol{v}}{c} \times \left(\frac{\boldsymbol{u}\cdot\boldsymbol{\beta}}{1-\frac{\boldsymbol{v}\cdot\boldsymbol{u}}{c^2}}\frac{\boldsymbol{v}}{c^2}+\boldsymbol{\beta}\right)$$

$$S_\delta = -i\hbar\frac{\partial\Phi}{\partial\delta}\frac{\boldsymbol{v}}{c} \times \boldsymbol{\beta}$$

and since it is $\frac{\boldsymbol{v}}{c} \times \boldsymbol{\beta} = \boldsymbol{\gamma}$, we get

$$S_\delta = -i\hbar\frac{\partial\Phi}{\partial\delta}\boldsymbol{\gamma}. \qquad (328)$$

From the fourth of equations (324) we have

$$S_\omega = \frac{r}{c}\boldsymbol{v} \times P_\omega$$

and with the second of equations (310) we get

$$S_\omega = -\frac{i\hbar}{\sin\delta}\frac{\partial\Phi}{\partial\omega}\frac{\boldsymbol{v}}{c} \times \left(\frac{\boldsymbol{u}\cdot\boldsymbol{\gamma}}{1-\frac{\boldsymbol{v}\cdot\boldsymbol{u}}{c^2}}\frac{\boldsymbol{v}}{c^2}+\boldsymbol{\gamma}\right)$$

and since $\frac{\boldsymbol{v}}{c} \times \boldsymbol{\gamma} = -\boldsymbol{\beta}$, we get

$$S_\omega = \frac{i\hbar}{\sin\delta}\frac{\partial\Phi}{\partial\omega}\boldsymbol{\beta}. \qquad (329)$$

Equation (325) can now be written as

$$S = \frac{i\hbar}{\sin\delta}\frac{\partial\Phi}{\partial\omega}\boldsymbol{\beta} - i\hbar\frac{\partial\Phi}{\partial\delta}\boldsymbol{\gamma}. \qquad (330)$$

We now calculate the component S_u of the angular momentum S along the direction of motion of the material particle.

For $\boldsymbol{u} \neq 0$ we have

$$S_u = \frac{\boldsymbol{u}}{\|\boldsymbol{u}\|}S$$

and with equation (330) we get

$$S_u = \frac{\boldsymbol{u}}{\|\boldsymbol{u}\|}\left(\frac{i\hbar}{\sin\delta}\frac{\partial\Phi}{\partial\omega}\boldsymbol{\beta} - i\hbar\frac{\partial\Phi}{\partial\delta}\boldsymbol{\gamma}\right). \qquad (331)$$

For constant-speed motion with velocity $\boldsymbol{u} = \begin{bmatrix} u \\ 0 \\ 0 \end{bmatrix}$, and taking into consideration equations (35) and (36), we obtain from equation (331)

$$S_u = \frac{i\hbar}{\sin\delta}\frac{\partial\Phi}{\partial\omega}\left(-\sin\delta\right)$$

$$S_u = -i\hbar\frac{\partial\Phi}{\partial\omega}. \qquad (332)$$

In the case of constant-speed motion with velocity $\boldsymbol{u} = \begin{bmatrix} u \\ 0 \\ 0 \end{bmatrix}$, from the transformations of equations (124) $\omega' = \omega$, we conclude that the angular momentum S_u does not depend on the inertial reference frame. Furthermore, it does not depend on the angle δ, i.e. the angle formed between the direction of emission $\frac{\boldsymbol{v}}{c}$ of the generalized photon and the velocity $\boldsymbol{u}$ of the material particle in Figure 6.

We will now study the changes in energy and momentum that take place during the motion of the generalized photon with velocity $\boldsymbol{v}$, after its emission by the material particle.

From the fundamental mathematical theorem, specifically from equation (86) for $f = E_i$, $f = E_w$, $f = E_\delta$ and $f = E_\omega$, we have

$$\frac{\partial E_i}{\partial t} + \boldsymbol{v} \cdot \nabla E_i = c\frac{\partial E_i}{\partial r}$$

$$\frac{\partial E_w}{\partial t} + \boldsymbol{v} \cdot \nabla E_w = c\frac{\partial E_w}{\partial r}$$

$$\frac{\partial E_\delta}{\partial t} + \boldsymbol{v} \cdot \nabla E_\delta = c\frac{\partial E_\delta}{\partial r}$$

$$\frac{\partial E_\omega}{\partial t} + \boldsymbol{v} \cdot \nabla E_\omega = c\frac{\partial E_\omega}{\partial r}$$

and with the first of equations (304), (308), (309) and (310), we get

$$\frac{\partial E_i}{\partial t} + \boldsymbol{v} \cdot \nabla E_i = 0$$

$$\frac{\partial E_w}{\partial t} + \boldsymbol{v} \cdot \nabla E_w = 0$$

$$\frac{\partial E_\delta}{\partial t} + \boldsymbol{v} \cdot \nabla E_\delta = -\frac{c}{r}E_\delta \qquad (333)$$

$$\frac{\partial E_\omega}{\partial t} + \boldsymbol{v} \cdot \nabla E_\omega = -\frac{c}{r}E_\omega.$$

Similarly, after combining equations (87), (88), (89) with the second parts of equations (304), (308), (309) and (310), we get

$$\frac{\partial \boldsymbol{P}_i}{\partial t} + (\text{grad } \boldsymbol{P}_i)\, \boldsymbol{v} = \boldsymbol{0}$$

$$\frac{\partial \boldsymbol{P}_w}{\partial t} + (\text{grad } \boldsymbol{P}_w)\, \boldsymbol{v} = \boldsymbol{0}$$

$$\frac{\partial \boldsymbol{P}_\delta}{\partial t} + (\text{grad } \boldsymbol{P}_\delta)\, \boldsymbol{v} = -\frac{c}{r}\boldsymbol{P}_\delta \qquad (334)$$

$$\frac{\partial \boldsymbol{P}_\omega}{\partial t} + (\text{grad } \boldsymbol{P}_\omega)\, \boldsymbol{v} = -\frac{c}{r}\boldsymbol{P}_\omega.$$

From the equations of this paragraph we conclude that there are physical quantities that do not depend on the distance r. Such physical quantities are the energy-momentum pairs $(E_i, \boldsymbol{P}_i)$ and $(E_w, \boldsymbol{P}_w)$, as well as the angular momenta S and S_u. These quantities are defined for $r = 0$, that is, on the material particle. On the contrary, the energy-momentum pairs $(E_\delta, \boldsymbol{P}_\delta)$ and $(E_\omega, \boldsymbol{P}_\omega)$, as well as the rest energies $\frac{c\hbar}{r}\frac{\partial \Phi}{\partial \delta}$ and $\frac{c\hbar}{r\sin\delta}\frac{\partial \Phi}{\partial \omega}$, are defined only in the surrounding spacetime of the material particle, due to the appearance of the factor $\frac{1}{r}$. Furthermore, they vanish for $r \to +\infty$, while they attain large values for small values of r, i.e. close to the material particle.

5.7 The simplest case of a generalized photon

The simplest generalized photon arises in the case where the percentage Φ is constant:

$$\frac{\partial \Phi}{\partial t} = 0 \qquad (335)$$
$$\nabla \Phi = 0.$$

In this case, equations (299) and (300) are rewritten, respectively

$$E = \Phi\frac{i\hbar}{1 - \dfrac{\boldsymbol{v} \cdot \boldsymbol{u}}{c^2}}\frac{\partial m_0}{m_0 \partial w}$$

$$\boldsymbol{P} = \Phi\frac{i\hbar}{1 - \dfrac{\boldsymbol{v} \cdot \boldsymbol{u}}{c^2}}\frac{\partial m_0}{m_0 c\partial w}\frac{\boldsymbol{v}}{c} \qquad (336)$$

$$E = \Phi\frac{i\hbar}{1 - \dfrac{\boldsymbol{v} \cdot \boldsymbol{u}}{c^2}}\frac{\partial q}{q\partial w}$$

$$\boldsymbol{P} = \Phi\frac{i\hbar}{1 - \dfrac{\boldsymbol{v} \cdot \boldsymbol{u}}{c^2}}\frac{\partial q}{qc\partial w}\frac{\boldsymbol{v}}{c}. \qquad (337)$$

From the second of equations (335) we obtain

$$\nabla \Phi = 0$$

and from equation (301) we get

$$\frac{\partial \Phi}{\partial w}\nabla w + \frac{\partial \Phi}{\partial \delta}\nabla \delta + \frac{\partial \Phi}{\partial \omega}\nabla \omega = 0$$

and from the linear independence of the vectors $\nabla w, \nabla \delta, \nabla \omega$ (paragraph 2.5) we get

$$\frac{\partial \Phi}{\partial w} = 0$$

$$\frac{\partial \Phi}{\partial \delta} = 0 \qquad (338)$$

$$\frac{\partial \Phi}{\partial \omega} = 0.$$

Replacing equations (338) into the equations of the last paragraph causes the energy-momentum pairs

$$(E_w, \boldsymbol{P}_w)\,,(E_\delta, \boldsymbol{P}_\delta)\,,(E_\omega, \boldsymbol{P}_\omega)$$

to become zero, the angular momentum S becomes zero, and so do the rest energies $\frac{c\hbar}{r}\frac{\partial \Phi}{\partial \delta}$ and $\frac{c\hbar}{r\sin\delta}\frac{\partial \Phi}{\partial \omega}$. The energy-momentum pair $(E_i, \boldsymbol{P}_i)$, as given by equations (336), does not become zero. Therefore, the generalized photon is defined for $r = 0$, i.e. on the material particle.

We shall now prove that the interaction of the material particle with every generalized photon is instantaneous during the moment w of the emission of the generalized photon. More specifically, we shall prove that the generalized photon keeps its energy E and moment $\boldsymbol{P}$ constant, after its emission by the material particle.

From equation (86) of the fundamental mathematical theorem, and for $f = E$, we have

$$\frac{\partial E}{\partial t} + \upsilon \cdot \nabla E = c\frac{\partial E}{\partial r}. \qquad (339)$$

From the first of equations (336), and since it holds that $m_0 = m_0(w)$, we get

$$\frac{\partial E}{\partial r} = 0 \qquad (340)$$

and from equation (339) we see that

$$\frac{\partial E}{\partial t} + \boldsymbol{v} \cdot \nabla E = 0. \qquad (341)$$

From equation (341) we conclude that the energy E of the generalized photon remains constant during its motion with velocity v, after its emission by the material particle.

Combining equations (336) we obtain relation

$$\boldsymbol{P} = E \frac{\boldsymbol{v}}{c^2} \qquad (342)$$

between the momentum $\boldsymbol{P}$ and energy E of the generalized photon.

From equation (87) for $f = \frac{E}{c}$, we obtain

$$\frac{\partial}{\partial t}\left(E \frac{\boldsymbol{v}}{c^2}\right) + \left(\mathrm{grad}\left(\mathrm{E}\frac{\boldsymbol{v}}{c^2}\right)\right)\boldsymbol{v} = \frac{\boldsymbol{v}}{c}\frac{\partial E}{\partial r}$$

and with equations (340) and (342) we get

$$\frac{\partial \boldsymbol{P}}{\partial t} + (\mathrm{grad}\ \boldsymbol{P})\,\boldsymbol{v} = \boldsymbol{0}. \qquad (343)$$

From equation (343) we conclude that the momentum $\boldsymbol{P}$ of the generalized photon remains constant during its motion with velocity v, after its emission by the material particle.

According to equations (341) and (343), the generalized photon does not exchange energy and momentum with the material particle after its emission. The interaction between the material particle and every generalized photon takes place instantaneously at the moment of emission of the generalized photon. Furthermore, according to equation (342), there is a continuous flow of generalized photons moving with velocity v, from the material particle into the surrounding spacetime, on the condition, of course, that the percentage Φ remains constant.

We can undertake a similar study for the generalized photon resulting from the selfvariation of the electric charge. It suffices to replace equations (336) with equations (337) in the above study.

5.8 The cosmological data "condensed" into a single equation

In the inertial frame of reference S', where the material particle is at rest, the first of equations (350) can be written as

$$E' = \Phi i\hbar \frac{\partial m_0}{m_0 \partial w'} + i\hbar \frac{\partial \Phi}{\partial t'}. \qquad (344)$$

Summing in all directions of emission of generalized photons, and taking into consideration that $\sum E' = E_0$ and $\sum \Phi = 1$, from equation (344) we obtain

$$E_0 = i\hbar \frac{\partial m_0}{m_0 \partial w'}. \qquad (345)$$

During the emission of the generalized photons by the material particle it is $r' = 0$, and equation (3) can be written as $w' = t'$, therefore we get $\frac{\partial m_0}{\partial w'} = \frac{dm_0}{dw'} = \frac{dm_0}{dt'} = \dot{m}_0$, and equation (345) can be written as

$$E_0 = i\hbar \frac{\dot{m}_0}{m_0} \qquad (346)$$

which is equation (268).

In the inertial reference frame S', where the material particle is at rest, and for $r' = 0$, hence for $w' = t'$, the first of equations (282) can be written as

$$\dot{E}_0 = \frac{i}{\hbar} m_0 c^2 E_0. \qquad (347)$$

Eliminating the rest energy E_0, we get

$$\left(i\hbar \frac{\dot{m}_0}{m_0}\right)^{\bullet} = \frac{i}{\hbar} m_0 c^2 i\hbar \frac{\dot{m}_0}{m_0}$$

$$\left(i\hbar \frac{\dot{m}_0}{m_0}\right)^{\bullet} = -\dot{m}_0 c^2$$

$$\left(i\hbar \frac{\dot{m}_0}{m_0} + m_0 c^2\right)^{\bullet} = 0 \qquad (348)$$

which is equation (270).

In paragraph 5.2 we derived equation (270) by combining equation (346) with the principle of conservation of energy. In the derivation we conducted in this paragraph we combined equation (346) with the symmetric law (282). Furthermore, from the derivation procedure we have followed, it becomes obvious that the percentage-function Φ does not play any role in equation (348), i.e. in equation (270).

If we borrow equation (394), $E_0 = i\hbar H$, from paragraph 7, and combine it with equation (346), we obtain $\frac{\dot{m}_0}{m_0} = H \sim 2 \times 10^{-18} s^{-1}$. In the cosmological data we observe the consequences of the real increase of the rest masses of the material particles, which takes place at an extremely slow rate.

In paragraph 7 the differential equation (348) is solved. As we shall see, this equation contains as information the totality of the cosmological data. The cosmological data are "condensed" within a single equation.

5.9 The generalized particle

From the previous study it becomes evident that the selfvariations correlate every material particle with the surrounding spacetime. Fundamental physical characteristics of the material particle, like the rest mass and the electric charge, are correlated with spacetime. Furthermore, each material particle contributes to the energy content of spacetime in a strictly defined manner.

The relation between the material particle and the surrounding spacetime is determined by two fundamental physical objects predicted by the theory of selfvariations: the generalized photon and the accompanying particle. These two

physical objects are related to each other since the accompanying particle results from the aggregation of the generalized photons. All the equations we have stated in the preceding paragraphs and preceding paragraphs, concern the relation of the material particle either with the generalized photon, or with the accompanying particle.

In the surrounding spacetime of the material particle, and for each generalized photon, we know exactly what is expressed by equation (263), $dS^2 = 0$: the generalized photon moves with velocity $\boldsymbol{v}$ of magnitude $\|\boldsymbol{v}\| = c$ in every inertial frame of reference. According to the second statement-axiom we have posed, equation $dS^2 = 0$ also holds for the accompanying particle, which, as an aggregation of generalized photons, is related with the propagation of the selfvariations in the four-dimensional spacetime. The question then arises, as to how equation $dS^2 = 0$ is expressed in the part of spacetime where the generalized photons aggregate.

The accompanying particle has rest energy E_0 and, therefore, rest mass $\frac{E_0}{c^2} \neq 0$. The combination $dS^2 = 0$ and $\frac{E_0}{c^2} \neq 0$ renders the accompanying particle an intermediate state between "matter" and the "photon". It is a completely new physical object predicted by the theory of selfvariations, which introduces us into an unknown territory of physical reality. The first question we have to answer is how do the relations $dS^2 = 0$ and $\frac{E_0}{c^2} \neq 0$ become compatible with each other.

About the intermediate state of matter we can give the following interpretation:

The aggregation of the generalized photons implies the co-incidence of different points ($dS^2 = 0$) in the part of spacetime where the aggregation takes place. This interpretation is in agreement with the strict application of the axioms of the theory of selfvariations.

At this point we are required to make two observations about the relation of the theory of selfvariations with the theory of relativity. These observations have to do with the relation between the energy content and the properties of spacetime.

For the derivation of the Lorentz-Einstein transformations we consider two observers who exchange signals moving with velocity c. If we consider the exchange of signals moving with a different velocity, for example acoustic signals, we end up with different transformations. Judging by the result, both on theoretical, and on experimental grounds, we know that the transformations derived by the first method are correct, whereas the transformations derived by the second method are wrong.

The theory of selfvariations predicts the generalized photon in the surrounding spacetime of the material particles. There is a continuous exchange of generalized photons between the material particles, in other words, a continuous exchange of signals moving with velocity c. The exchange of signals with velocity c is not simply a hypothesis we can make for the derivation of the Lorentz-Einstein transformations, but a continuous physical reality. Therefore, the theory of selfvariations strengthens the theoretical background of the special theory of relativity.

The general theory of relativity correlates the properties of spacetime with its energy content. The theory of selfvariations gives us the detailed contribution of each material particle to the energy content of spacetime. In the part of spacetime where the aggregation of generalized photons takes place, the material particle interacts with the accompanying particle. This interaction concerns a strictly distinct subset of the total energy content of spacetime. While we assume a unified spacetime, whose properties are defined by its total energy content, each particle interacts and is correlated with only a subset of the energy content of spacetime. In reality, every material particle occupies its "own" spacetime. For every material particle the properties of its "own" spacetime are determined by the generalized photons with which it interacts. Therefore, the co-incidence of different points of spacetime concerns the accompanying particle for every material particle, and does not constitute a general property of spacetime.

The law of selfvariations has been stated based on the accompanying particle. Relation (264), in combination with the symmetric laws (282) and (290), expresses the continuous interaction of the rest mass m_0 and the electric charge q of the material particle with the energy E_0 of the accompanying particle. Therefore, we cannot refer just to the material particle, or just to the accompanying particle. What exists in nature is the system of the two particles, which behaves as a "generalized particle" that occupies a part of spacetime.

The co-incidence of different points in the part of spacetime occupied by the generalized particle alters the trajectories and velocities of the generalized photons compared to the strictly defined trajectories and velocities we studied in the preceding paragraphs. In the case of co-incidence of all points belonging to this part of spacetime, the concepts of trajectory and velocity of the generalized photons loose their meaning. The trajectory and velocity of the material particle will suffer the same consequences, if the material particle belongs to the part of spacetime where the aggregation of the generalized photons takes place.

In Figures 4 and 6 imagine that, for the material particle, the points of spacetime within the interior of a sphere of centre E and radius r coincide. The physical object in the interior of the sphere constitutes a generalized particle with a specific rest mass. In every point of the spherical surface, the generalized photon moves with velocity v of magnitude $\|v\| = c$. None of the axioms of special relativity and of the theory of selfvariations are violated. Furthermore, the co-incidence of different points of spacetime within the interior of the sphere, concerns the material particle, and does not constitute a general property of spacetime.

The investigation of the internal structure and physical

properties of the generalized particle is the central issue for the theory of selfvariations. We have to answer specific questions regarding the generalized particle, and develop specific methods for the study of its physical properties.

A fundamental question concerns the distribution of the total rest mass M_0 of the generalized particle, between the material particle (m_0) and the accompanying particle $\left(\frac{E_0}{c^2}\right)$. Of equal importance is the size of the portion of spacetime occupied by the generalized particle.

A basic method for the study of the generalized particle is the elimination of the velocity, which also represents the trajectory, from the equations of the theory of selfvariations. It is not the only method, though. In the following paragraph we present the basic study for the generalized particle.

6 The quantum phenomena as a consequence of the selfvariations

6.1 Introduction

The intermediate state between "matter" and "photon" predicted by the theory of selfvariations, is responsible for the quantum phenomena. The study of the generalized photon leads to the Schrödinger and the Klein-Gordon equations, as well as to the wave equation of Maxwell's theory of electromagnetism.

The elimination of the kinematic characteristics of the material particle from the equations of the selfvariations, emerges as the fundamental method for the study of the generalized particle and, eventually, of quantum phenomena. This is what is actually done by all the theories developed during the last century in order to interpret quantum phenomena.

The basic method for the study of the generalized particle is complemented by the percentage-function Φ. The Φ function has to do with the generalized photon and, by extension, with the generalized particle. Furthermore, it is related with the interactions of the material particles. Function Φ inextricably links the quantum phenomena with the interactions of the material particles. The investigation of its properties furthers the theory of selfvariations beyond the bounds of the present edition.

6.2 The distribution functions of the rest mass

According to equation (284)

$$M_0 = m_0 + \frac{E_0}{c^2} \tag{349}$$

the rest mass M_0 of the generalized particle is equal to the sum of the rest masses of the material particle (m_0) and the accompanying particle $\left(\frac{E_0}{c^2}\right)$. One way of studying the inner structure of the generalized particle is to study how the rest mass M_0 is distributed to each of the two particles. Knowing the sum of the rest masses m_0 and $\frac{E_0}{c^2}$, it suffices to calculate

one of the "distribution functions", that is, one of the complex numbers $X = \frac{m_0}{M_0}$, $\Psi = \frac{E_0}{M_0 c^2}$, $Z = \frac{m_0 c^2}{E_0}$.

But it is

$$X + \Psi = \frac{m_0 c^2}{M_0 c^2} + \frac{E_0}{M_0 c^2} = \frac{m_0 c^2 + E_0}{M_0 c^2}$$

and with equation (349) we get $X + \Psi = 1$. Therefore, it suffices to study either function Ψ

$$\Psi = \frac{E_0}{M_0 c^2} \tag{350}$$

or function Z

$$Z = \frac{m_0 c^2}{E_0} \tag{351}$$

in order to determine the distribution of the rest mass M_0 into m_0 and $\frac{E_0}{c^2}$.

Initially, we will study the effects of the selfvariations on the function Z. From equation (351) we have

$$\frac{\partial Z}{\partial t} = \frac{1}{E_0} \frac{\partial m_0 c^2}{\partial t} - \frac{m_0 c^2}{E_0^2} \frac{\partial E_0}{\partial t}$$

and with the firsts of equations (265) and (282) we get

$$\frac{\partial Z}{\partial t} = -\frac{1}{E_0} \frac{i}{\hbar} E_s m_0 c^2 - \frac{m_0 c^2}{E_0^2} \frac{i}{\hbar} \gamma m_0 c^2 E_0$$

and with equation (279) we get

$$\frac{\partial Z}{\partial t} = -\frac{1}{E_0} \frac{i}{\hbar} \gamma E_0 m_0 c^2 - \frac{m_0 c^2}{E_0^2} \frac{i}{\hbar} \gamma m_0 c^2 E_0$$

$$\frac{\partial Z}{\partial t} = -\frac{i}{\hbar} \frac{m_0 c^2}{E_0} \gamma \left(m_0 c^2 + E_0 \right)$$

and with equation (349) we get

$$\frac{\partial Z}{\partial t} = -\frac{i}{\hbar} \frac{m_0 c^2}{E_0} \gamma M_0 c^2$$

and with equation (351)

$$\frac{\partial Z}{\partial t} = -\frac{i}{\hbar} \gamma M_0 c^2 Z. \tag{352}$$

From equation (351) we obtain

$$\nabla Z = \frac{1}{E_0} \nabla m_0 c^2 - \frac{m_0 c^2}{E_0^2} \nabla E_0$$

and with the second of equations (265) and also (266) we get

$$\nabla Z = \frac{1}{E_0} \frac{i}{\hbar} \boldsymbol{P}_s m_0 c^2 + \frac{m_0 c^2}{E_0^2} \frac{i}{\hbar} \gamma m_0 \boldsymbol{u} E_0$$

and with equation (276) we have

$$\nabla Z = \frac{1}{E_0} \frac{i}{\hbar} E_s \frac{\boldsymbol{u}}{c^2} m_0 c^2 + \frac{m_0 c^2}{E_0^2} \frac{i}{\hbar} \gamma m_0 \boldsymbol{u} E_0.$$

Using equation (279) we get

$$\nabla Z = \frac{1}{E_0}\frac{i}{\hbar}\gamma E_0 \frac{\boldsymbol{u}}{c^2}m_0 c^2 + \frac{m_0 c^2}{E_0^2}\frac{i}{\hbar}\gamma m_0 \boldsymbol{u} E_0$$

$$\nabla Z = \frac{i}{\hbar}\frac{m_0 c^2}{E_0^2}\gamma\left(\frac{E_0}{c^2}+m_0\right)\boldsymbol{u}.$$

Through equation (349) we get

$$\nabla Z = \frac{i}{\hbar}\frac{m_0 c^2}{E_0^2}\gamma M_0 \boldsymbol{u}$$

and with equation (351) we get

$$\nabla Z = \frac{i}{\hbar}\gamma M_0 \boldsymbol{u} Z. \tag{353}$$

The differential equations (352) and (353) offer the advantage that the rest mass M_0 that appears on their second part, does not depend on the selfvariations. On the other hand, they also have a disadvantage. We do not know the additional conditions we have to introduce for the rest mass M_0 in order to solve the system of differential equations (352) and (353). These additional conditions are related to a more general investigation of the equations of the theory of selfvariations, which is not included in the present edition.

We shall now study how the selfvariations affect function Ψ. From equation (350) we have

$$\frac{\partial \Psi}{\partial t} = \frac{\partial}{\partial t}\left(\frac{E_0}{M_0 c^2}\right)$$

and with equation (285) we obtain

$$\frac{\partial \Psi}{\partial t} = \frac{1}{M_0 c^2}\frac{\partial E_0}{\partial t}$$

and with the first of equations (282) we get

$$\frac{\partial \Psi}{\partial t} = \frac{1}{M_0 c^2}\frac{i}{\hbar}\gamma m_0 c^2 E_0$$

and from equation (350) we get

$$\frac{\partial \Psi}{\partial t} = \frac{i}{\hbar}\gamma m_0 c^2 \Psi. \tag{354}$$

From equation (350) we have

$$\nabla \Psi = \nabla\left(\frac{E_0}{M_0 c^2}\right)$$

and with equation (286) we obtain

$$\nabla \Psi = \frac{1}{M_0 c^2}\nabla(E_0)$$

and using the second of equations (282) we get

$$\nabla \Psi = \frac{1}{M_0 c^2}\left(-\frac{i}{\hbar}\gamma m_0 \boldsymbol{u} E_0\right)$$

and with equation (350) we arrive at

$$\nabla \Psi = -\frac{i}{\hbar}\gamma m_0 \boldsymbol{u}\Psi. \tag{355}$$

The differential equations (354) and (355) have the advantage that the rest mass m_0 of the material particle appears in their second part. This fact allows us to introduce additional conditions in order to solve the system of differential equations (354) and (355). We present this study in the following two paragraphs.

The distribution functions determine the distribution of the rest mass of the generalized particle between the material particle and the accompanying particle. For every point $A(x, y, z, t)$ in the part of spacetime where the generalized particle can reside, these distribution functions acquire specific values. These values, in turn, define the values of the rest masses m_0 and $\frac{E_0}{c^2}$.

The behavior of the generalized particle can be influenced by any cause that interacts with the generalized particle in the part of spacetime it occupies. An external cause can redistribute the rest mass of the generalized particle, directing it either to the material particle, or to the accompanying particle. In the first case, the generalized particle will behave as a material particle with a well-defined trajectory, energy, etc. In the second case, the generalized particle will spread out in spacetime, while the consequences resulting from the aggregation of the generalized photons will be strengthened and intensified. We observe such a case in the double-slit experiment for the electron and for material particles in general (we assume that the reader is familiar with the double-slit experiment).

The study of the distribution functions is a fundamental goal in order to understand the behavior of the generalized particle.

6.3 The Schrödinger equation

From equation (354) we have

$$\frac{\partial^2 \Psi}{\partial t^2} = \frac{i}{\hbar}\gamma m_0 c^2 \frac{\partial \Psi}{\partial t} + \frac{i}{\hbar}\gamma c^2 \Psi \frac{\partial m_0}{\partial t}$$

and with equation (354) and the first of equations (265), we get

$$\frac{\partial^2 \Psi}{\partial t^2} = -\frac{\gamma^2 m_0^2 c^4}{\hbar^2}\Psi + \frac{i}{\hbar}\gamma c^2 \Psi\left(-\frac{i}{\hbar}E_s m_0\right)$$

and with equation (279) we get

$$\frac{\partial^2 \Psi}{\partial t^2} = -\frac{\gamma^2 m_0^2 c^4}{\hbar^2}\Psi + \frac{i}{\hbar}\gamma c^2 \Psi\left(-\frac{i}{\hbar}\gamma E_0 m_0\right)$$

$$\frac{\partial^2 \Psi}{\partial t^2} = -\frac{\gamma^2 m_0^2 c^4}{\hbar^2}\Psi + \frac{\gamma^2 m_0 c^2 E_0}{\hbar^2}\Psi$$

$$\frac{\partial^2 \Psi}{\partial t^2} = -\frac{\gamma^2 m_0 c^4}{\hbar^2}\left(m_0 - \frac{E_0}{c^2}\right)\Psi. \tag{356}$$

From equation (355) we have

$$\nabla^2 \Psi = -\frac{i}{\hbar}\gamma m_0 \boldsymbol{u} \nabla \Psi - \frac{i}{\hbar}\gamma \Psi \boldsymbol{u} \nabla m_0$$

and with equation (355) together with the second of equations (265), we get

$$\nabla^2 \Psi = -\frac{\gamma^2 m_0^2 u^2}{\hbar^2}\Psi - \frac{i}{\hbar}\gamma \Psi \boldsymbol{u}\left(\frac{i}{\hbar}E_s \frac{\boldsymbol{u}}{c^2}m_0\right)$$

and with equation (279) we get

$$\nabla^2 \Psi = -\frac{\gamma^2 m_0^2 u^2}{\hbar^2}\Psi - \frac{i}{\hbar}\gamma \Psi \boldsymbol{u}\left(\frac{i}{\hbar}\gamma E_0 \frac{\boldsymbol{u}}{c^2}m_0\right)$$

$$\nabla^2 \Psi = -\frac{\gamma^2 m_0^2 u^2}{\hbar^2}\Psi + \frac{\gamma^2 m_0 E_0 u^2}{c^2 \hbar^2}\Psi$$

$$\nabla^2 \Psi = -\frac{\gamma^2 m_0 u^2}{\hbar^2}\left(m_0 - \frac{E_0}{c^2}\right)\Psi. \tag{357}$$

We now consider the case where the rest mass M_0 is mainly distributed to the material particle. This happens when

$$\left\|\frac{E_0}{m_0 c^2}\right\| << 1$$

or when

$$E_0 \to 0.$$

Under these conditions equation (357) can be written as

$$\nabla^2 \Psi = -\frac{\gamma^2 m_0^2 u^2}{\hbar^2}\Psi. \tag{358}$$

We will now eliminate the velocity u from equation (358), within the framework of the analysis we performed in paragraph 5.9 for the generalized particle. For small velocities u, it is $\gamma \sim 1$, and equation (358) can be written as

$$\nabla^2 \Psi = -\frac{m_0^2 u^2}{\hbar^2}\Psi. \tag{359}$$

Furthermore, denoting by ε the constant sum of the kinetic energy $\frac{1}{2}m_0 u^2$ and the potential energy $U = U(x, y, z)$ of the material particle, we have

$$\frac{1}{2}m_0 u^2 + U = \varepsilon$$

$$u^2 = \frac{2(\varepsilon - U)}{m_0}.$$

Replacing factor u^2 into equation (359) we obtain

$$\nabla^2 \Psi = -\frac{2m_0(\varepsilon - U)}{\hbar^2}\Psi \tag{360}$$

which is the time-independent Schrödinger wave-function.

From the initial conditions, $\left\|\frac{E_0}{m_0 c^2}\right\| << 1$ or $E_0 \to 0$, we set, and from equation (349) we obtain $m_0 \to M_0$, therefore equation (360) can be written in the form

$$\nabla^2 \Psi = -\frac{2M_0(\varepsilon - U)}{\hbar^2}\Psi. \tag{361}$$

From the derivation process we have followed it becomes obvious that the Schrödinger equation only approximately describes the internal structure of the generalized particle.

6.4 The Klein-Gordon equation

The way in which we chose to eliminate the velocity from equation (358) had as a consequence the appearance of the potential energy U in Schrödinger's equation (360). We will now eliminate the velocity u from function Ψ in a different manner. Combining equations (356) and (357), we obtain

$$\frac{\partial^2 \Psi}{\partial t^2} - c^2 \nabla^2 \Psi =$$
$$-\frac{\gamma^2 m_0 c^4}{\hbar^2}\left(m_0 - \frac{E_0}{c^2}\right)\Psi + \frac{\gamma^2 m_0 c^2 u^2}{\hbar^2}\left(m_0 - \frac{E_0}{c^2}\right)\Psi$$

$$\frac{\partial^2 \Psi}{\partial t^2} - c^2 \nabla^2 \Psi = -\frac{\gamma^2 m_0 c^4}{\hbar^2}\left(1 - \frac{u^2}{c^2}\right)\left(m_0 - \frac{E_0}{c^2}\right)\Psi$$

and since $\gamma = \frac{1}{\sqrt{1-\frac{u^2}{c^2}}}$, we get

$$\frac{\partial^2 \Psi}{\partial t^2} - c^2 \nabla^2 \Psi = -\frac{m_0 c^4}{\hbar^2}\left(m_0 - \frac{E_0}{c^2}\right)\Psi$$

$$\frac{\partial^2 \Psi}{\partial t^2} - c^2 \nabla^2 \Psi + \frac{m_0 c^4}{\hbar^2}\left(m_0 - \frac{E_0}{c^2}\right)\Psi = 0. \tag{362}$$

In the case where $\left\|\frac{E_0}{m_0 c^2}\right\| << 1$ or $E_0 \to 0$, equation (362) can be written as

$$\frac{\partial^2 \Psi}{\partial t^2} - c^2 \nabla^2 \Psi + \frac{m_0 c^4}{\hbar^2}\Psi = 0 \tag{363}$$

which is the Klein-Gordon equation. With the conditions we posed, it follows that $m_0 \to M_0$ in equation (363).

Of particular interest is the case $m_0 = 0$, where from equation (362) we obtain

$$\frac{\partial^2 \Psi}{\partial t^2} - c^2 \nabla^2 \Psi = 0$$

$$\nabla^2 \Psi - \frac{\partial^2 \Psi}{c^2 \partial t^2} = 0. \tag{364}$$

From equation (349) for $m_0 = 0$ we get $E_0 = M_0 c^2$. Therefore, all of the rest energy of the generalized particle has shifted to the accompanying particle. Furthermore, we get $\|\Psi\| = \left\|\frac{E_0}{M_0 c^2}\right\| = 1$. In every case we solve the differential equation (364), we should modify the final solution such that the wave-like behavior of a scalar quantity Ψ appears, for which we demand that $\|\Psi\| = 1$.

6.5 The central role of the percentage function Φ in the internal structure and the physical properties of the generalized particle

According to equations (302) and (303) the energy E and the momentum $\boldsymbol{P}$ of a single generalized photon depends on the percentage function Φ. Furthermore, according to equation (330), the intrinsic angular momentum $\boldsymbol{S}$ of a single generalized particle depends exclusively on the percentage function Φ. The generalized particle emerges in the part of spacetime where the aggregation of the generalized photons takes place. Therefore, the percentage function Φ plays a fundamental role, both for the internal structure, as well as for the physical properties of the generalized particle.

Function Φ allows the comprehension of the extent of the portion of spacetime occupied by the generalized particle. In paragraph 5.6 we determined the physical quantities that can only be defined in the surrounding spacetime of the material particle. These physical quantities are inversely proportional to the distance r. Therefore, the space occupied by the generalized photon can extend to infinity, with the consequences, of course, predicted by the corresponding equations for its energy, momentum, and angular momentum. Since each generalized photon can extend to infinity, the same also holds for the part of space where the aggregation of the generalized photons takes place. Therefore, the generalized particle can extend to infinity.

In the case of the simplest generalized photon, as we studied it in paragraph 5.7, there results an instantaneous interaction of the material particle with the accompanying particle. This interaction takes place at the instant of emission of the generalized photon, exactly at the point where the material point particle resides. Therefore, in this case the generalized particle is a point particle.

In conclusion, we can say that the generalized particle can extend from a point of spacetime up to an infinite distance from the material particle. Furthermore, in each case, the extent of the part of spacetime in which the generalized particle extends, is determined by the percentage function Φ.

For the derivation of the Schrödinger and the Klein-Gordon equations, we based our investigation on equation (349), $M_0 = m_0 + \frac{E_0}{c^2}$. A fundamental piece of information, related with the function Φ, is missing from this equation. The generalized photon carries rest energy, according to equations (314) and (315), which depends on the function Φ and the distance r. In other words, right from the start, the generalized photon, and therefore the generalized particle, are correlated with a rest energy in the surrounding spacetime of the material particle. The rest mass corresponding to this rest energy does not appear in equation (349). For the same reason, the angular momentum does not appear in the Schrödinger and the Klein-Gordon equations, since the internal angular momentum of the generalized photon depends exclusively on function Φ, according to equation (330).

Function Φ expresses the potential of a material particle to emit generalized photons of different energies for different directions. Theoretically, we cannot predict exactly how function Φ depends on the internal structure of the material particle. Quite likely we can do this by performing some measurements. But we can predict theoretically an important factor on which function Φ depends, that results from the continuous exchange of generalized photons between material particles. This exchange of generalized photons is equivalent to a variation of function Φ. According to equations (302), (303) and (330), the energy, momentum and intrinsic angular momentum of the generalized photon are exactly correlated with the variation of function Φ. We, therefore, come to the conclusion that the quantum phenomena are interrelated with the interactions of the material particles, the connecting link being function Φ. Function Φ is related with the interactions between material particles, but also with the energy of the generalized photons and, by extension, with the generalized particle.

In paragraph 5.9 we referred to the fundamental method for studying the generalized particle. We analyzed the reasons for which we have to expunge the velocity from the equations of the theory of selfvariations in order to study the internal structure and the physical properties of the generalized particle. Of equal importance is the inclusion of function Φ in the study of the generalized particle.

Observing the Schrödinger operators [22–26], as used in quantum mechanics, we realize that the first consequence of their use is the elimination of the kinematic characteristics of the material particle from the resulting differential equations. Function Φ does not appear in the final equations, since it does not exist as a concept within the physical theories of the last century. It is represented, though, by the physical quantities related with the interactions in which the material particle participates, by the potential energy or the generalized momentum of the material particle. Analogous is the procedure followed by Dirac [27] for the derivation of his eponymous equation.

One of the questions about the generalized particle, to which we deliberately did not refer in paragraph 5.9, is the probability of finding the material particle at a specific moment, in a specific position in the part of spacetime occupied by the generalized particle. There are many physical quantities related with the Schrödinger operators. Judging by the success of quantum mechanics, one way to study the generalized particle is through statistical interpretation. We must not forget, though, that a single cause suffices in order to shift the rest energy of the generalized particle, either towards the material particle, or towards the accompanying particle. One and only cause is sufficient for the corpuscular or wave-like behavior of the generalized particle to emerge.

By investigating the properties of function Φ or by making concrete hypotheses regarding function Φ, we can extend our study of quantum phenomena and the interactions of par-

ticles. On the contrary, in paragraph 5.8 we showed that equation (348) does not depend on function Φ. This allows us to solve it and investigate it completely. We present that study in the next paragraph.

7 The cosmological data as a consequence of the selfvariations

7.1 Introduction

The origin of matter is already recorded in the cosmological observational data. We just lacked a fundamental piece of information in order to decode it: the law of selfvariations.

The redshift of distant astronomical objects, the cosmic microwave background radiation and the information obtained by the analysis of this radiation, the increased luminosity distances of supernovae, the large-scale, as well as small-scale, structure of matter in the universe, the large-scale isotropy and flatness of the universe, the slight variation of the fine structure constant, and the arrow of time, all share the law of selfvariations as a common cause.

The law of selfvariations contains as information the entire corpus of the cosmological observational data, as we observe and record them since the time of Hubble. Behind the barrage of interventions made in order to bring the Standard Cosmological Model in agreement with the cosmological observational data, lies our ignorance about the fundamental law of selfvariations. The physical theories of the past century do not possess the necessary completeness in order to explain the cosmological observational data.

The improved scientific observation instruments we possess record persistently, and with ever increasing detail, the consequences of the law of selfvariations.

7.2 The fundamental equations

The cosmological data concern the observation of the Universe at long distances, that is, in the past. At a distant astronomical object, located at a distance r from Earth, the rest mass $m_0(r)$ of a material particle in the past is smaller, compared to the laboratory rest mass m_0 of the same material particle we measure "now" on Earth. The electric charge $q(r)$ also differs from the laboratory value q of the electric charge as measured "now" on Earth. We calculate the quantity $m_0(r)$ as a function of m_0, and $q(r)$ as a function of q. In this manner, we incorporate into our equations the consequences resulting from the internality of the Universe to the process of measurement.

In the following, and using the known physical laws, we determine the consequences of the selfvariations for distant astronomical objects. Furthermore, we can determine the consequences of the selfvariations in the electromagnetic spectra of the astronomical objects we receive "now" on Earth. We shall prove that equation (348)

$$\left(m_0 c^2 + i\hbar \frac{\dot{m}_0}{m_0}\right)^{\bullet} = 0 \tag{365}$$

which holds for every material particle contains as information the entirety of the cosmological data.

We will solve equation (365) for a material particle in the case of a flat and static universe. This equation contains as information the redshift of distant astronomical objects. Furthermore, it predicts that the gravitational interaction cannot play the role attributed to it by the Standard Cosmological Model. It informs us that the gravitational interaction cannot lead the Universe either to collapse or to expansion. Consequently, there is no point of solving equation (365) within an expanding Universe.

Equation (365) contains as information the fact that the total energy of the Universe is zero. Therefore, after solving the equation, it can be verified a posteriori that the Universe is flat.

From equation (365) we have that

$$\left(m_0 c^2 + i\hbar \frac{\dot{m}_0}{m_0}\right)^{\bullet} = 0$$

$$\left(\frac{i}{\hbar} m_0 c^2 - \frac{\dot{m}_0}{m_0}\right)^{\bullet} = 0$$

$$\frac{i}{\hbar} m_0 c^2 - \frac{\dot{m}_0}{m_0} = k. \tag{366}$$

Here, k is the constant of integration. From equation (366) we see that

$$m_0 = -\frac{ik\hbar}{c^2} \frac{1}{1 - \exp(kt + \mu)}. \tag{367}$$

Here, μ is the constant of integration.

Let us suppose that we observe "now" on Earth, the electromagnetic spectrum of an astronomical object located at a distance r away from Earth. The emission of the electromagnetic spectrum from the astronomical object took place before a time interval $\Delta t = \frac{r}{c}$. According to equation (367) the rest mass $m_0(r)$ of the material particle at the moment of the emission of the corresponding electromagnetic spectrum was

$$m_0 = -\frac{ik\hbar}{c^2} \frac{1}{1 - \exp\left(k\left(t - \frac{r}{c}\right) + \mu\right)}. \tag{368}$$

Combining equations (367) and (368) we have that

$$m_0(r) = m_0 \frac{1 - \exp(kt + \mu)}{1 - \exp\left(k\left(t - \frac{r}{c}\right) + \mu\right)}.$$

Setting

$$A = \exp(kt + \mu) \tag{369}$$

we obtain

$$m_0(r) = m_0 \frac{1 - A}{1 - A\exp\left(-\frac{kr}{c}\right)}. \tag{370}$$

Equation (370) expresses the rest mass $m_0(r)$ of the material particle in the distant astronomical object and before a

time interval $\Delta t = \frac{r}{c}$, compared with the laboratory value of the rest mass m_0 of the same material particle. In this way we include in the equations we state the consequences of the internality of the Universe with respect to the measurement process, as set forth in paragraph 4.9.

If we remove the imaginary unit i from equation (365), or replace it by any arbitrary constant $b \neq 0$, we will again end up with equations (369) and (370). The problems caused by the internality of the Universe with respect to the measurement procedure can only be evaded through equation (370). Only after comparing the rest masses $m_0(r)$ and m_0 can we measure the consequences of the selfvariations.

From equation (369) we obtain for the parameter A

$$\frac{dA}{dt} = \dot{A} = kA. \tag{371}$$

From equation (367) we also obtain

$$\dot{m}_0 = m_0 \frac{k \exp(kt + \mu)}{1 - \exp(kt + \mu)}.$$

Through equation (369) we see that

$$\dot{m}_0 = m_0 \frac{kA}{1 - A}. \tag{372}$$

Combining equations (268) and (372) we obtain

$$E_0 = i\hbar \frac{kA}{1 - A}. \tag{373}$$

In the case of the electric charge the corresponding equation to equation (365) is the second of equations (292)

$$\left(q + \frac{i\hbar}{V_0} \frac{\dot{q}}{q} \right)^{\bullet} = 0. \tag{374}$$

This gives us the corresponding solution

$$q(r) = q \frac{1 - B}{1 - B \exp\left(-\frac{k_1 r}{c}\right)} \tag{375}$$

$$B = \exp(k_1 t + \mu_1) \tag{376}$$

$$\frac{dB}{dt} = \dot{B} = k_1 B. \tag{377}$$

Here, k_1 and μ_1 are the constants of integration.

The corresponding equation to equation (372) is equation

$$\dot{q} = q \frac{k_1 B}{1 - B}. \tag{378}$$

Combining the first of equations (292) with equation (378) we obtain

$$q_i V_0 = i\hbar \frac{k_1 B}{1 - B}. \tag{379}$$

This equation is the corresponding equation to equation (373).

If we remove from equation (374) the imaginary unit i, or if we replace it by any arbitrary constant $b \neq 0$, we will still arrive at equations (375) and (376). The problems caused by the internality of the Universe with respect to the measurement procedure can only be evaded through equation (375). We can only measure the consequences of the selfvariations by comparing the electric charges $q(r)$ and q.

7.3 The redshift of the far distant astronomical objects

The wavelength λ of the linear spectrum of an atom is inversely proportional to the factor $m_0 q^4$, where m_0 is the rest mass and q the electric charge of the electron. We denote by λ the wavelength of the linear spectrum we observe "now" on Earth, and which originates from the atoms of an astronomical object located at distance r. With λ_0 we denote the wavelength of the same kind of atom as measured in the laboratory "now" on Earth.

We have that

$$\frac{\lambda}{\lambda_0} = \frac{m_0 q^4}{m_0(r) q^4(r)}.$$

Using equations (370) and (375) we obtain

$$\frac{\lambda}{\lambda_0} = \frac{1 - A \exp\left(-\frac{kr}{c}\right)}{1 - A} \left(\frac{1 - B \exp\left(-\frac{k_1 r}{c}\right)}{1 - B} \right)^4. \tag{380}$$

For the redshift z of the astronomical object we obtain

$$z = \frac{\lambda - \lambda_0}{\lambda_0}$$

$$z = \frac{\lambda}{\lambda_0} - 1.$$

Using equation (380) we see that

$$z = \frac{1 - A \exp\left(-\frac{kr}{c}\right)}{1 - A} \left(\frac{1 - B \exp\left(-\frac{k_1 r}{c}\right)}{1 - B} \right)^4 - 1. \tag{381}$$

This equation constitutes the full mathematical expression for the redshift z of the linear spectrum of distant astronomical objects.

We shall now perform an approximation. From the cosmological data we know that the fine structure constant

$$\alpha = \frac{e^2}{4\pi\varepsilon_0 c\hbar}$$

remains constant for observations we make at very large distances from Earth. Therefore, the value of the electric charge

$q(r)$ differs minimally from the laboratory value q in the region of the Universe we observe. Therefore, we can write equation (381) in a simpler form, that is

$$z = \frac{1 - A \exp\left(-\dfrac{kr}{c}\right)}{1 - A} - 1.$$

(382)

Here, we used the approximation $q(r) = q$.

Equation (382) holds for the regions of the Universe that can be surveyed by the scientific observation instruments we currently have at our disposal. We shall return to the issue of the fine structure constant in another paragraph.

From equation (369) we see that

$$A > 0.$$

(383)

According to equation (382), and since the value of the redshift z increases with the distance r, it holds that

$$k > 0.$$

(384)

From equation (382), and for $r \rightarrow +\infty$, we obtain

$$z_{\max} = \frac{1}{1 - A} - 1$$

$$z_{\max} = \frac{A}{1 - A}.$$

(385)

We have that $z_{\max} > 0, A > 0$, as given in relation (383), thus we get

$$1 - A > 0$$

$$A < 1.$$

(386)

Now, it holds that

$$z < z_{\max}.$$

Using equation (385) we obtain

$$z < \frac{A}{1 - A}.$$

Due to relation (386) we obtain

$$z(1 - A) < A$$
$$z - zA < A$$
$$z < (1 + z)A$$
$$\frac{z}{1 + z} < A.$$

Through relation (386) we finally arrive at

$$\frac{z}{1 + z} < A < 1.$$

(387)

This inequality holds for every redshift z, and allows us to estimate the range of values the parameter A acquires.

From equation (382), and for $r = 0$, we obtain $z = 0$, thus

$$z' = \frac{dz}{dr} = \frac{1 - A \exp\left(-\dfrac{kr}{c}\right)}{1 - A} \frac{kA \exp\left(-\dfrac{kr}{c}\right)}{c(1 - A)}.$$

For $r = 0$ we get

$$z'(0) = \left.\frac{dz}{dr}\right|_{r=0} = \frac{kA}{c(1 - A)}.$$

We expand equation (382) giving $z = z(r)$ into a Taylor series, and only to first order terms

$$z(r) = z(0) + z'(0)$$

$$z(r) = 0 + \frac{kA}{c(1 - A)}r$$

$$cz = \frac{kA}{1 - A}r.$$

Comparing with Hubble's law $cz = Hr$, we obtain

$$\frac{kA}{1 - A} = H.$$

(388)

where H is the Hubble parameter.

From equation (388) we obtain $k = H\frac{1-A}{A}$. The range of values of parameter A, as determined from inequality (387), allows us to estimate the extremely small value of the constant k. Now, according to equation (371), the parameter A increases at an extremely slow rate, and remains practically constant in the measurements we conduct.

For the energy E, which results during nuclear fission, nuclear fusion, and more generally, every case where the conversion of rest mass into energy takes place, we obtain

$$\frac{E(r)}{E} = \frac{m_0(r)c^2}{m_0 c^2}.$$

Using equation (370) we see that

$$\frac{E(r)}{E} = \frac{1 - A}{1 - A \exp\left(-\dfrac{kr}{c}\right)}$$

$$E(r) = E\frac{1 - A}{1 - A \exp\left(-\dfrac{kr}{c}\right)}.$$

(389)

For the photons which result from the conversion of mass into energy we have

$$\frac{\lambda_\gamma}{\lambda_{0\gamma}} = \frac{\dfrac{ch}{E(r)}}{\dfrac{ch}{E}} = \frac{E}{E(r)}.$$

Using equation (389) we obtain

$$\frac{\lambda_\gamma}{\lambda_{0\gamma}} = \frac{1 - A \exp\left(-\dfrac{kr}{c}\right)}{1 - A}$$

$$\frac{\lambda_\gamma - \lambda_{0\gamma}}{\lambda_{0\gamma}} = \frac{1 - A \exp\left(-\dfrac{kr}{c}\right)}{1 - A} - 1$$

$$z_\gamma = \frac{1 - A \exp\left(-\dfrac{kr}{c}\right)}{1 - A} - 1. \qquad (390)$$

Equations (390) and (382) are identical. However, beyond the limits reached by our current observations, the redshift z of the linear spectrum is given in general by equation (381).

From equation (382) we obtain

$$1 + z = \frac{1 - A \exp\left(-\dfrac{kr}{c}\right)}{1 - A}. \qquad (391)$$

Combining equations (370) and (391) we have that

$$m_0(z) = \frac{m_0}{1 + z}. \qquad (392)$$

Combining equations (389) and (391) we see that

$$E(z) = \frac{E}{1 + z}. \qquad (393)$$

Combining equations (373) and (388) we obtain

$$E_0 = i\hbar H \qquad (394)$$

for the laboratory value of the energy E_0.

7.4 The graphs of the functions r = r(z) and R = R(z)

From equation (382) we have that

$$z = \frac{1 - A \exp\left(-\dfrac{kr}{c}\right)}{1 - A} - 1$$

$$z = \frac{A}{1 - A} \exp\left(-\dfrac{kr}{c}\right).$$

Solving for r we obtain

$$r = \frac{c}{k} \ln\left(\frac{A}{A - z(1 - A)}\right). \qquad (395)$$

This equation gives the distance r of the astronomical object as a function of the redshift z.

From equation (388) we obtain $k = H\frac{1-A}{A}$, and after replacing the constant k into equation (395), we get

$$r = \frac{c}{H} \frac{A}{1 - A} \ln\left(\frac{A}{A - z(1 - A)}\right). \qquad (396)$$
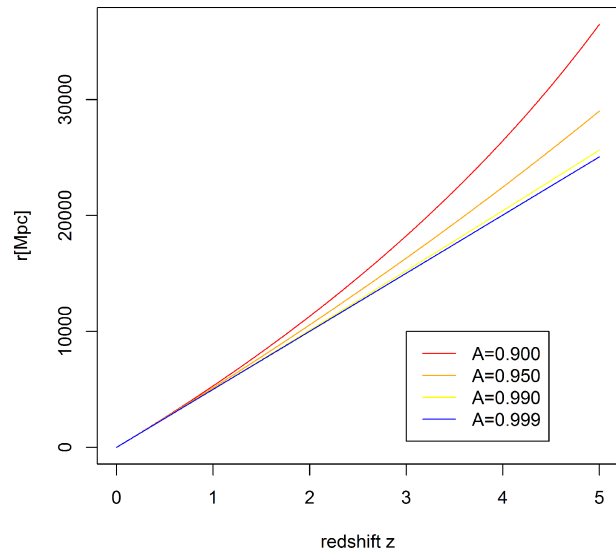
Fig. 10: The graph of distance r of a distant astronomical object as a function of the redshift z. As we increase the value of the parameter A from 0.900 to 0.999, the curve $r = r(z)$ approaches a straight line. The graph has been made with $H = 60\frac{\text{km}}{\text{sMpc}}$ as the value of Hubble's constant.

This equation is more convenient than equation (395), since we know the value of the Hubble parameter H, as well as the range of values of the parameter A from inequality (387), that is

$$\frac{z}{1 + z} < A < 1.$$

In Figure 10 we present the graph of the curve $r = r(z)$ for $H = 60\frac{\text{km}}{\text{sMpc}}$, and for the values of $A = 0.900$, $A = 0.950$, $A = 0.990$, $A = 0.999$ up to $z = 5$. We observe that as the value of the parameter A increases, the curve tends to be a straight line.

We shall now prove that for $A \to 1^-$ the equivalent equations (382) and (396) tend to Hubble's law

$$cz = Hr \qquad (397)$$

From equation (388) we have $k = \frac{1-A}{A}H$, and after substituting into equation (382), we obtain

$$z = \frac{1 - A \exp\left(-\dfrac{1 - A}{A}\dfrac{H}{c}r\right)}{1 - A} - 1.$$

We denote by $x = \frac{1-A}{A}$, therefore $x \to 0^+$ for $A \to 1^-$, and

$A = \frac{1}{x+1}$, so we have

$$z = \frac{1 - \frac{1}{x+1}\exp\left(-x\frac{Hr}{c}\right)}{1 - \frac{1}{x+1}} - 1 = \frac{x + 1 - \exp\left(-x\frac{Hr}{c}\right)}{x} - 1$$

$$\lim_{A \to 1^-}(z) = \lim_{x \to 0^+}(z) = \lim_{x \to 0^+}\left(\frac{x + 1 - \exp\left(-x\frac{Hr}{c}\right)}{x} - 1\right) \overset{0}{\underset{0}{=}}$$

$$\lim_{x \to 0^+}\left(1 + \frac{Hr}{c}\exp\left(-x\frac{Hr}{c}\right) - 1\right) = \frac{Hr}{c}.$$

Equation (396) gives the distance r of the astronomical object, when we know the value of its redshift z. On the other hand, if we measure the distance based on the luminosity of the astronomical object, we shall always find it to be larger than the one given by equation (396). The reason is simple: The energy feeding the radiation of the astronomical objects originates from nuclear fusion, and more generally, from the conversion of rest mass into energy. According to equation (389), this energy $E(r)$ is less than the expected energy E. Therefore, the luminosity of the astronomical object is itself lower than the standard luminosity we use.

The luminosity distance R of an astronomical object is defined by equation

$$J = \frac{1}{4\pi R^2}\frac{dE}{dt}. \tag{398}$$

In this equation, J denotes the power per unit surface we receive from the astronomical object, whereas the power $\frac{dE}{dt}$ refers to the "standard candle" we are using.

If the real distance of the astronomical object is r, then we obtain for the power per unit surface J

$$J = \frac{1}{4\pi r^2}\frac{dE(r)}{dt}. \tag{399}$$

From equations (398) and (399) we get

$$\frac{1}{R^2}\frac{dE}{dt} = \frac{1}{r^2}\frac{dE(r)}{dt}.$$

Using equation (393) we have that

$$\frac{1}{R^2}\frac{dE}{dt} = \frac{1}{r^2}\frac{1}{1+z}\frac{dE}{dt}$$

$$R^2 = r^2(1+z)$$

$$R = r\sqrt{1+z}. \tag{400}$$

Combining equations (400) and (396) we see that

$$R = \frac{c}{H}\frac{A}{1-A}\sqrt{1+z}\ln\left(\frac{A}{A - z(1-A)}\right). \tag{401}$$
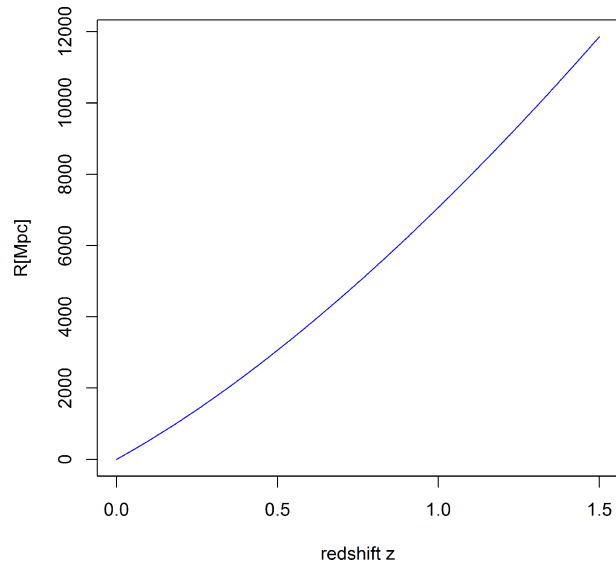
Fig. 11: The graph of the luminosity distance R of astronomical objects as a function of the redshift z. The measurement of the luminosity distances of type Ia supernova confirms the theoretical prediction of the law of selfvariations.

The measurements conducted for the determination of Hubble's constant H, have not taken into account the consequences of equation (400). Even for the case of small values of the redshift z it holds that $R > r$. The measurement of Hubble's parameter H with the use of the luminosity distances of astronomical objects is correct only for very small values of z, where it holds that $R \sim r$. Such measurements result in a value of $H = 60\frac{km}{sMpc}$. Measurements performed have included astronomical objects with large values of the redshift z, thus increasing the value of the parameter H to values ranging between 72 and $74\frac{km}{sMpc}$.

Today, we perform measurements with high accuracy. Taking into consideration the consequences of equation (400) we expect the parameter H to be measured close to $60\frac{km}{sMpc}$, independently of the redshift z of the astronomical object. We, of course, refer to measurements of the parameter H, on the basis of the luminosity distances of astronomical objects.

Equally well to equation (401) we can also use the equation which results after combining equations (400) and (397), that is

$$R = \frac{c}{H}z\sqrt{1+z}. \tag{402}$$

For $H = 60\frac{km}{sMpc}$ and $c = 3 \times 10^5\frac{km}{s}$ this can be written as

$$R = 5000\,z\sqrt{1+z}. \tag{403}$$

The luminosity distance R is given in Mpc. In the graph of figure 11 we present the graph of the function $R = R(z)$, as given in equation (403) and up to values of the redshift $z = 1.5$.

Type *Ia* supernova are cosmological objects for which we can measure their luminosity distance R. Furthermore, this measurement can be conducted at large distances, where the consequences of equation (393) are measurable.

At the end of the last century this kind of measurements were conducted by independent scientific groups. The graph thet results from these measurements exactly matches graph 7.4.2 which is predicted theoretically by the theory of self-variations. In order to explain the inconsistency of the Standard Cosmological Model with graph 7.4.2, the existence of dark energy was invented and introduced [28–30].

7.5 Gravity cannot play the role attributed to it by the Standard Cosmological Model

From equation (388) we obtain $k = \frac{1-A}{A}H$, and

$$\frac{k}{c} = \frac{1-A}{A}\frac{H}{c}. \tag{404}$$

For $H = 60 \frac{\text{km}}{\text{sMpc}}$, $A = 0.999$, $c = 3 \times 10^5 \frac{\text{km}}{\text{s}}$ we have that

$$\frac{k}{c} = 2 \times 10^{-7} \frac{1}{\text{Mpc}}. \tag{405}$$

We replace this value of $\frac{k}{c}$ into equation (370) and obtain

$$m_0(r) = m_0 \frac{0.001}{1 - 0.999 \, \exp(-2 \times 10^{-7}r)}. \tag{406}$$

Here, the distance r is measured in Mpc.

For values of r of the order of magnitude of kpc, equation (406) gives that $m_0(r) = m_0$. Therefore, the strength of the gravitational interaction is not affected in the scale of galactic distances. For example, for distance $r = 100$ kpc, equation (406) gives $m_0(r) = 0.99999 \, m_0$. Therefore, the selfvariations do not affect the stability of the solar system, galaxies, and galaxy clusters.

On the contrary, for distances of order of magnitude of Mpc, equation (406) predicts a clearly smaller value of $m_0(r)$, compared to m_0. For example, for $r = 100$ Mpc equation (406) gives $m_0(r) = 0.98 \, m_0$. The strength of the gravitational interaction exerted on our galaxy by a galaxy from a distance of 100 Mpc is 98% of the expected. For $r = 2 \times 10^3$ Mpc equation (406) gives $m_0(r) = 0.7145 \, m_0$. The strength of the gravitational interaction exerted by a galaxy, which is located at a distance of 2000 Mpc, on our galaxy is only 71.45% of the expected.

Therefore, we conclude that due to the selfvariations the gravitational interaction is weakened at cosmological distances and cannot play the role attributed to it by the Standard Cosmological Model. The gravitational interaction dominates and rules at a local level, at scales of a few hundreds or thousands of kpc.

We note that if we chose a different value for the parameter A, from the values permitted by inequality (387), all the arithmetic values appearing in equation (406) shall be altered. However, the same conclusions will be drawn about the relation between rest masses $m_0(r)$ and m_0.

The rest mass is given as a function of the redshift z from equation (392)

$$m_0(z) = \frac{m_0}{1+z}.$$

For $z = 0.1$ we get $m_0(z) = 0.9091 \, m_0$, for $z = 1$ we have $m_0(z) = 0.5 \, m_0$, and for $z = 9$ we see that $m_0(z) = 0.1 \, m_0$. The strength of the gravitational interaction exerted by an astronomical object with redshift $z = 9$ on our galaxy is only 10% of the expected.

For even greater distances the gravitational interaction practically vanishes.

7.6 The very early Universe

All the equations we have stated in this paragraph are compatible with the condition $r \to \infty$. The equations are stated in such a way that the condition $r \to \infty$ offers us information about the very early Universe.

For $r \to \infty$ equation (370) gives

$$m_0(r \to \infty) \to m_0(1 - A). \tag{407}$$

The inequality (387)

$$\frac{z}{1+z} < A < 1$$

holds for every value of the redshift z, hence $A \to 1$. Therefore, from relation (407) we conclude that the initial form of the Universe only slightly differs from the vacuum.

Similarly, from equation (375) we have that

$$q(r \to \infty) \to q(1 - B). \tag{408}$$

This relation does not lead to the same consequences as relation (407). We know that the electric charge exists in opposite physical quantities in the Universe. Because of this, the total electric charge of the Universe is zero. Relation (407) informs as that the energy content of the very early Universe also tends to zero. The very early Universe only slightly differs from the vacuum. It possesses, though, a very important property which determines its evolution. It is temporally variable due to the selfvariations.

The increase of the rest masses and the electric charges destroys the initial homogeneity and state of rest, induces the first minute motions of the particles, and shifts the system to a temperature slightly above 0 K (temperature reflects the kinetic state of the particles in the system). The evolution of the selfvariations with the passage of time leads the Universe to the form in which we observe it today.

In general, this is the prediction for the begining and evolution of the Universe from the equations we have stated. This prediction is also verified from the calculations presented in the following paragraphs.

7.7 The Universe is flat

From the principle of conservation of energy we conclude that the total energy content of the Universe is constant, and remains the same at every moment. Relation (407) informs us that the energy content of the very early Universe tends to zero. Therefore, the same holds today as we observe the Universe. Because of this, the Universe is flat.

The difference between the current state of the Universe and its initial state is the following: The rest masses of particles have increased, but this increase is counterbalanced by the generalized photons that flood spacetime, and by the strengthening of all kinds of negative potential energies that result as a consequence.

The observations conducted by the COBE and WMAP satellites confirm that the Universe is flat. Other observational data lead us to the same conclusion.

7.8 The origin of the cosmic microwave background radiation

The laboratory value for the Thomson scattering coefficient [31, 32] is

$$\sigma_\tau = \frac{8\pi}{3} \frac{q^4}{m_0^2 c^2}.$$ (409)

Here, q and m_0 are the electric charge and the rest mass of the electron, respectively. At a distant astronomical object the Thomson coefficient is

$$\sigma_\tau(r) = \frac{8\pi}{3} \frac{q^4(r)}{m_0^2(r) c^2}.$$ (410)

Combining these equations we get that

$$\frac{\sigma_\tau(r)}{\sigma_\tau} = \left(\frac{m_0}{m_0(r)}\right)^2 \left(\frac{q(r)}{q}\right)^4.$$ (411)

From the observations we have made on the variation of the fine structure constant we know that, for large distances r, it holds that $q(r) = q$. Therefore, at a very good approximation, equation (411) can be written as

$$\frac{\sigma_\tau(r)}{\sigma_\tau} = \left(\frac{m_0}{m_0(r)}\right)^2.$$

Using equation (370) we obtain that

$$\frac{\sigma_\tau(r)}{\sigma_\tau} = \left(\frac{1 - A \exp\left(-\frac{kr}{c}\right)}{1 - A}\right)^2.$$ (412)

For very large distances ($r \to \infty$) very close to the initial state of the Universe, and at a temperature of about 0 K, equation (412) gives

$$\frac{\sigma_\tau(r \to \infty)}{\sigma_\tau} = \left(\frac{1}{1 - A}\right)^2.$$ (413)

But according to inequality (387), $A \to 1$. Therefore, in the very distant past, and for a temperature of the Universe just slightly above 0 K, the Thomson scattering coefficient acquires enormous values, rendering the Universe opaque. The cosmic microwave background radiation we observe today, originates in this phase of the evolution of the Universe. The conditions we described refer to the whole expanse of the Universe. That is why the cosmic microwave background radiation seems to originate "from everywhere".

Equation (412) gives the value of the scattering coefficient at distant astronomical objects. Combining this equation with equation (382) gives

$$\frac{\sigma_\tau(z)}{\sigma_\tau} = (1 + z)^2$$

$$\sigma_\tau(z) = \sigma_\tau (1 + z)^2.$$ (414)

This equation is easier to use, since it expresses the Thomson scattering coefficient as a function of the redshift z of the distant astronomical object. We can also write equation (414) in the form

$$\sigma_\tau(z) = \frac{8\pi}{3} \frac{e^4}{m_e^2 c^2} (1 + z)^2$$ (415)

where e and m_e denote the electric charge and the mass of the electron, respectively.

The Thomson coefficient concerns the scattering of photons of low energy E. For high energy photons it is replaced by the Klein-Nishina coefficient, given in the laboratory by

$$\sigma = \frac{3}{8}\sigma_\tau \frac{m_0 c^2}{E} \left[\ln\left(\frac{2E}{m_0 c^2}\right) + \frac{1}{2}\right]$$ (416)

and by relation

$$\sigma(z) = \frac{3}{8}\sigma_\tau(z) \frac{m_0(z) c^2}{E(z)} \left[\ln\left(\frac{2E(z)}{m_0(z) c^2}\right) + \frac{1}{2}\right]$$ (417)

for the distant astronomical object.

From equations (392) and (393) we obtain

$$\frac{m_0(z) c^2}{E(z)} = \frac{m_0 c^2}{E}.$$

Therefore, equation (417) can be written as

$$\sigma(z) = \frac{3}{8}\sigma_\tau(z) \frac{m_0 c^2}{E} \left[\ln\left(\frac{2E}{m_0 c^2}\right) + \frac{1}{2}\right].$$

Using equation (416) we have

$$\frac{\sigma}{\sigma(z)} = \frac{\sigma_\tau}{\sigma_\tau(z)}.$$

Using equation (414) we take that

$$\sigma(z) = \sigma (1 + z)^2.$$ (418)

The two scattering coefficients depend in the same way upon the redshift z, and the distance r.

7.9 The decrease of the atomic ionization energies at distant astronomical objects

The ionization and excitation energy X_n of the atoms is proportional to the factor $m_0 q^4$, where m_0 is the rest mass of the electron and q is its electric charge. Thus, we have

$$\frac{X_n(r)}{X_n} = \frac{m_0(r)}{m_0}\left(\frac{q(r)}{q}\right)^4.$$

After applying the familiar approximation $q(r) = q$ we obtain

$$\frac{X_n(r)}{X_n} = \frac{m_0(r)}{m_0}.$$

Using equation (370) we have

$$\frac{X_n(r)}{X_n} = \frac{1-A}{1 - A\exp\left(-\dfrac{kr}{c}\right)}. \tag{419}$$

Through equation (382) we see that

$$X_n(z) = \frac{X_n}{1+z}. \tag{420}$$

According to this equation the redshift z affects the rate of ionization of the atoms in distant astronomical objects. Boltzmann's equation

$$\frac{N_n}{N_1} = \frac{g_n}{g_1}\exp\left(-\frac{X_n}{KT}\right) \tag{421}$$

expresses the number of the ionized atoms N_n occupying the energy level n in a stellar surface which is at thermodynamic equilibrium. With X_n we denote the excitation energy from the energy level 1 to the level n, T stands for the temperature of the stellar surface in *Kelvin*, $K = 1.38 \times 10^{-23}$ J/K is Boltzmann's constant, and g_n is the degree of degeneracy multiplicity of level n, that is, the number of energy levels into which level n splits in the presence of a magnetic field.

Combining equations (420) and (421), we obtain for the distant astronomical object relation

$$\frac{N_n}{N_1} = \frac{g_n}{g_1}\exp\left(-\frac{X_n}{KT(1+z)}\right). \tag{422}$$

In the case of the hydrogen atom, for $n = 2$, $X_2 = 10.15$ eV $= 16.24 \times 10^{-19}$ J, $g_1 = 2$, $g_2 = 8$ and for a solar surface temperature $T \sim 6000$ K, equation (421) shows that only one atom out of 10^8 occupies the $n = 2$ state. At the same temperature, equation (422) gives that for a redshift value of $z = 1$ we have $\frac{N_2}{N_1} = 2.2 \times 10^{-4}$, for $z = 2$ we have $\frac{N_2}{N_1} = 5.8 \times 10^{-3}$, and for $z = 5$ we have $\frac{N_2}{N_1} = 0.15$.

The conclusions drawn from the current and the previous paragraph demand a reexamination of the conclusions we have drawn from the observation of the electromagnetic spectrum of distant astronomical objects.

For very large distances, that is, in the very distant past, equation (419) gives

$$X_n(r \to \infty) = X_n(1-A). \tag{423}$$

This equation informs us that the very early Universe was ionized at some stage [33]. The ionization energies of the atoms had very small values. We can reach the same conclusion if we substitute into equation (420) very large values of the variable z, or if in equation (421) we replace the energy X_n with $X_n(1-A)$.

7.10 On the fine structure constant

In the preceding paragraphs we saw that due to the manifestation of the selfvariations, energy, momentum, angular momentum and electric charge flow from the material particles to the surrounding spacetime. The first consequence of the selfvariations is the potential to transfer energy, momentum, angular momentum and electric charge from one material particle to another, i.e. the interaction between the material particles. The gravitational and electromagnetic interactions determine the starting point for the quantitative determination of the selfvariations. Because of this, we supposed that the rest masses and the electric charges, and not any other physical quantity, vary with the passage of time. We offer this remark since, at cosmological scales, equation (365) justifies all of the cosmological observational data we possess, and it could be supposed that the electric charge remains constant. Such an assumption cannot hold within the framework of the theory of selfvariations, where the selfvariations of the electric charge are responsible for the electromagnetic field.

By analyzing the electromagnetic spectra reaching Earth from distant quasars from distances up to $6 \times 10^9 ly$ [34–36], the value of the fine structure constant α remains constant. More precisely, there are indications of a very slight variation of the parameter α.

The parameter α depends on the electron charge q, as given in

$$\alpha = \frac{q^2}{4\pi\varepsilon_0 c\hbar}. \tag{424}$$

Therefore, this parameter is not constant. We have

$$\frac{\alpha(r)}{\alpha} = \left(\frac{q(r)}{q}\right)^2.$$

Using equation (375) we also have

$$\frac{\alpha(r)}{\alpha} = \left(\frac{q(r)}{q}\right)^2 = \left(\frac{1-B}{1 - B\exp\left(-\dfrac{k_1 r}{c}\right)}\right)^2. \tag{425}$$

From this equation it can be inferred that the parameter $\alpha(r)$ (essentially the electric charge $q(r)$), remains constant

for large distances r when the constant k_1 or the parameter B acquire extremely small values. According to relation (408) we have that

$$q(r \to \infty) \to q(1 - B).$$

This relation can be written as

$$\alpha(r \to \infty) \to \alpha(1 - B)^2.$$

Therefore, the value of the electric charge and of the parameter α in the very early Universe are only determined by the value of the parameter B. Hence, the parameter B has a very small value, independently of the value of constant k_1.

For very small values of the parameter B we see that

$$q(r \to \infty) \to q(1 - B) \to q.$$

This prediction does not cause any problems at the initial state of the Universe, since the electric charge exists in couples of opposite physical quantities. Such a relation cannot hold for the case of the rest mass, and indeed we know that

$$\frac{z}{1 + z} < A < 1$$
$$m_0(r \to \infty) \to m_0(1 - A) \to 0.$$

From equation (376) we obtain $B > 0$. Thus, we arrive at the conclusion that the parameter B acquires extremely small positive values.

The extremely small value of the parameter B assures the stability of the value of the parameter α for large distances r. Hence, we turn our attention not to the arithmetic value (which is likely to be extremely small, as is the case for the constant $k = \frac{1-A}{A}H$), but to the sign of the constant k_1.

For $k_1 > 0$ we obtain successively that

$$k_1 > 0$$

$$-\frac{k_1 r}{c} < 0$$

$$\exp\left(-\frac{k_1 r}{c}\right) < 1, \qquad (B > 0)$$

$$B\exp\left(-\frac{k_1 r}{c}\right) < B$$

$$-B\exp\left(-\frac{k_1 r}{c}\right) > -B$$

$$1 - B\exp\left(-\frac{k_1 r}{c}\right) > 1 - B, \qquad \left(1 - B\exp\left(-\frac{k_1 r}{c}\right) > 0\right)$$

$$\frac{1 - B}{1 - B\exp\left(-\frac{k_1 r}{c}\right)} < 1.$$

From equation (425) we have that

$$\frac{\alpha(r)}{\alpha} = \left(\frac{q(r)}{q}\right)^2 < 1 \qquad k_1 > 0.$$

Therefore, for $k_1 > 0$ we will measure a slight decrease of the parameter α at large distances. Similarly, it turns out that for $k_1 < 0$ we will measure a slight increase of the parameter α at large distances [37]

$$\frac{\alpha(r)}{\alpha} = \left(\frac{q(r)}{q}\right)^2 > 1, \qquad k_1 < 0.$$

Based on the observational data we currently have, measurements of the variation of the parameter α have to be conducted for distances greater than 6×10^9 ly. The extremely small value of the (positive) parameter B renders these measurements difficult, in both cases.

7.11 The large structures in the Universe

The increase of the rest masses with the passage of time strengthens the gravitational interaction and accumulates matter towards various directions. The consequences of the accumulation of matter depend upon the quantity of the accumulated matter, as well as on the volume it occupies. In all cases, the total initial energy of the accumulated matter is zero, according to relation (407).

At large scales, at distances of order of magnitude 10^9 ly, the distribution of matter must have been determined by a large-scale destruction of the absolute homogeneity of the vacuum in the very early Universe. This explains the colossal webs of matter through vast expances of empty space that we observe with the modern observational instruments.

At smaller scales, within the dimensions of a galaxy, the accumulation of matter increases the temperature, as a result of the conversion of the gravitational potential energy into heat. A percentage of the particles of matter accumulates in a first central core of high temperature, while the remaining percentage remains distributed in the surrounding space during the period of accumulation. The slow rate at which the selfvariations occur, strengthens, also at a slow rate, the magnitude of the gravitational interaction, and allows a considerable percentage of the particles to remain in the surrounding space.

A further accumulation of the first core will lead to the formation of a second, more centralized core, until the temperature reaches the point where nuclear fusion starts. The initiation of nuclear fusion prevents the further accumulation of matter.

We separated the process of the accumulation into two phases, and we mentioned two cores for the following reason: The initial percentage of matter which remained outside the initial central core concerns the initial phase of the accumulation and is at a low temperature, slightly above $0K$ [38]. However, the percentage of matter which stays outside the second, and real central core, already has a high temperature. If we take into account the very high value of the Reynolds coefficient in this region, turbulent vortices will be generated. Therefore, the formation of stars should occur in this region.

In the final central core, the density of matter should be larger than in the rest of the galaxy. Clusters of galaxies are formed through similar processes.

Rough calculations give an equation correlating the mass and the volume of a galaxy [39–42]. This relation is consistent with the data we possess about galaxies (and galaxy clusters). But in reality, the process of accumulation is not separated into phases, but evolves in a continuous manner, from its beginning up to the formation of a galaxy. Therefore, we can only reach safe conclusions on the issue through computer simulations.

7.12 The origin of matter and the arrow of time

The equations of the theory of selfvariations predict at the limit, in the very distant past, that the beginning of the Universe was the vacuum. Therefore, we cannot consider a point to be the beginning of the universe, as proposed by the Standard Cosmological Model. All the points within the Universe are equivalent. The Universe originates "from everywhere", exactly as the cosmic microwave background radiation does (paragraph 7.8). Which physical mechanism can lead to such a result?

The theory of selfvariations predicts that the generalized particle can behave in such a way. The correlation of the vacuum with the condition $dS^2 = 0$ leads to such an interpretation, as we analyzed it in paragraph 5.9 and in paragraph 6.

What happens at the microcosm is a repetition at a local level, in a region of spacetime, of the condition that dominated throughout the spacetime occupied by the Universe during its emergence from the vacuum. That is how the slight perturbations of enormous spatial dimensions emerged within the initial homogeneity of the vacuum.

These perturbations were recorded on the cosmic microwave background radiation that followed (2.74 K) and which also originates from the whole Universe, as discussed in paragraph 7.8. Moreover, these perturbations are responsible for the large-scale distribution of matter in the Universe (paragraph 7.11).

The theory of selfvariations solves a fundamental problem of physical reality, which the physical theories of the last century are unable to solve. The equations of the theory of selfvariations include the arrow of time. The Universe originates from the vacuum and evolves towards a particular direction, which is determined by the selfvariations. The selfvariations continuously "distance" the Universe from the state of vacuum, but the Universe remains consistent with its origin:

The origin of matter from the vacuum, combined with the principles of conservation, has as a consequence that the energy content of the Universe is zero.

In the laboratory, the internality of the Universe to the process of measurement apparently "freezes" the time evolution of the selfvariations. On the contrary, the consequences of the selfvariations are directly imprinted on the observations we conduct at large distances. The Universe we observe today, and the complex processes taking place in Nature, are the results of the evolution of the selfvariations with the passage of time.

7.13 The future evolution of the Universe

The range of values parameter A takes is given by inequality (387)

$$\frac{z}{1+z} < A < 1.$$

Furthermore, equation (371) informs us that the parameter A approaches unity at an exceptionally slow rate, due to the extremely small value of the constant $k = \frac{1-A}{A}H$.

The parameter A appears in all of the equations we have stated. Because of this, the evolution of this parameter through time also determines the future evolution of the Universe, at least in the observations we will conduct in the far future.

From equation (388) we have that

$$\dot{H} = k\frac{\dot{A}(1-A) + A\dot{A}}{(1-A)^2}.$$

Using equation (371) we obtain

$$\dot{H} = k\frac{kA}{(1-A)^2}$$

$$\dot{H} = \frac{1}{A}\left(\frac{kA}{1-A}\right)^2$$

$$\dot{H} = \frac{1}{A}H^2.$$

For $A \sim 1, H = 60\frac{\text{km}}{\text{sMpc}} = 2 \times 10^{-18} \text{ s}^{-1}$

$$\dot{H} = 4 \times 10^{-36}\text{s}^{-2}.$$

The Hubble parameter varies at an extremely slow rate.

We shall now see how the redshift z varies with the passage of time. From equation (382) we get

$$z = \frac{1 - A\exp\left(-\dfrac{kr}{c}\right)}{1 - A} - 1 \tag{426}$$

$$z = \frac{A}{1-A}\left(1 - \exp\left(-\frac{kr}{c}\right)\right).$$

For the same distance r we have that

$$\dot{z} = \left(\frac{A}{1-A}\right)^{\bullet}\left(1 - \exp\left(-\frac{kr}{c}\right)\right)$$

$$\dot{z} = \frac{\dot{A}}{(1-A)^2}\left(1 - \exp\left(-\frac{kr}{c}\right)\right).$$

Using equation (371) we see that

$$\dot{z} = \frac{kA}{(1-A)^2}\left(1 - \exp\left(-\frac{kr}{c}\right)\right).$$

Considering equation (426) we obtain

$$\dot{z} = \frac{k}{1-A}z$$

$$\dot{z} = \frac{1}{A}\frac{kA}{1-A}z.$$

Through equation (388) we arrive at

$$\dot{z} = \frac{H}{A}z. \tag{427}$$

For $H = 2 \times 10^{-18}\text{s}^{-1} = 6.3 \times 10^{-11}\text{year}^{-1}$ and $A \sim 1$ we obtain

$$\dot{z} = z \cdot 6.3 \times 10^{-11}\text{year}^{-1}. \tag{428}$$

The rate of increase of the redshift z is a measure with which to evaluate the future evolution of the Universe.

8 The Topographic Theorem

For a material point particle, the velocity υ of the selfvariations is defined by equation (6)

$$\upsilon = \frac{c}{r}\boldsymbol{r}. \tag{429}$$

This equation refers solely to the material point particle. On the contrary, equation (33)

$$\frac{\boldsymbol{\upsilon}}{c} = \begin{bmatrix} \cos\delta \\ \sin\delta\cos\omega \\ \sin\delta\sin\omega \end{bmatrix} \tag{430}$$

has more general validity. The velocity in equation (430) satisfies the relation $\|\upsilon\| = c$, without necessarily having the form (429). Therefore, we have to study the properties of the velocity υ, as they follow from equation (430). The differentiation between the two equations occurs in equations (43) and (44)

$$\nabla\delta = \lambda_1\frac{\boldsymbol{\upsilon}}{c} + K\boldsymbol{\beta} + L\boldsymbol{\gamma}$$

$$\nabla\omega = \lambda_2\frac{\boldsymbol{\upsilon}}{c} + M\boldsymbol{\beta} + N\boldsymbol{\gamma}$$

which take the form

$$\nabla\delta = -\frac{\partial\delta}{c\partial t}\frac{\boldsymbol{\upsilon}}{c} + K\boldsymbol{\beta} + L\boldsymbol{\gamma}$$

$$\nabla\omega = -\frac{\partial\omega}{c\partial t}\frac{\boldsymbol{\upsilon}}{c} + M\boldsymbol{\beta} + N\boldsymbol{\gamma}. \tag{431}$$

We will mention the general properties of the velocity υ, without citing the relevant proofs.

The coefficients $\frac{\partial\delta}{c\partial t}$, K, L, $\frac{\partial\omega}{c\partial t}$, M, N are not independent from each other, but are constrained by the following compatibility equations:

$$\frac{\partial\delta}{c\partial t}(L - M\sin\delta) + (KM + LN)\cos\delta - \boldsymbol{\gamma}\cdot\nabla K +$$
$$+\boldsymbol{\beta}\cdot\nabla L = 0$$

$$\frac{\partial\omega}{c\partial t}(L - M\sin\delta) + \left(M^2 + N^2\right)\cos\delta - \boldsymbol{\gamma}\cdot\nabla M +$$
$$+\beta\cdot\nabla N = 0$$

$$\frac{\partial K}{\partial t} + \boldsymbol{\upsilon}\cdot\nabla K = -c\left(K^2 + LM\sin\delta\right)$$

$$\frac{\partial L}{\partial t} + \boldsymbol{\upsilon}\cdot\nabla L = -cL\left(K + N\sin\delta\right) \tag{432}$$

$$\frac{\partial M}{\partial t} + \boldsymbol{\upsilon}\cdot\nabla M = -cM\left(K + N\sin\delta\right)$$

$$\frac{\partial N}{\partial t} + \boldsymbol{\upsilon}\cdot\nabla N = -c\left(LM + N^2\sin\delta\right)$$

$$\frac{\partial}{\partial t}\left(\frac{\partial\delta}{c\partial t}\right) + \boldsymbol{\upsilon}\cdot\nabla\left(\frac{\partial\delta}{c\partial t}\right) = -K\frac{\partial\delta}{\partial t} - L\sin\delta\frac{\partial\omega}{\partial t}$$

$$\frac{\partial}{\partial t}\left(\frac{\partial\omega}{c\partial t}\right) + \boldsymbol{\upsilon}\cdot\nabla\left(\frac{\partial\omega}{c\partial t}\right) = -M\frac{\partial\delta}{\partial t} - N\sin\delta\frac{\partial\omega}{\partial t}.$$

These equations are valid in every inertial frame of reference.

For the inertial reference frames S and S', as we defined them in paragraph 3, the following Lorentz-Einstein transformations hold

$$\frac{\partial\delta'}{c\partial t'} = \frac{\partial\delta}{c\partial t} + \frac{u}{c}\frac{K\sin\delta}{1 - \frac{u}{c}\cos\delta}$$

$$K' = \frac{K}{\gamma\left(1 - \frac{u}{c}\cos\delta\right)} \qquad L' = \frac{L}{\gamma\left(1 - \frac{u}{c}\cos\delta\right)}$$

$$\frac{\partial\omega'}{c\partial t'}\sin\delta' = \frac{\partial\omega}{c\partial t}\sin\delta - \frac{u}{c}M\sin\delta\frac{\sin\delta}{1 - \frac{u}{c}\cos\delta} \tag{433}$$

$$M'\sin\delta' = \frac{M\sin\delta}{\gamma\left(1 - \frac{u}{c}\cos\delta\right)}$$

$$N'\sin\delta' = \frac{N\sin\delta}{\gamma\left(1 - \frac{u}{c}\cos\delta\right)}.$$

We define the vector

$$\boldsymbol{t} = \nabla\delta \times \sin\delta\nabla\omega = t_1\frac{\boldsymbol{\upsilon}}{c} + t_2\boldsymbol{\beta} + t_3\boldsymbol{\gamma} =$$

$$= (KN\sin\delta - LM\sin\delta)\frac{\boldsymbol{\upsilon}}{c} +$$

$$+\left(\frac{\partial\delta}{c\partial t}N\sin\delta - L\frac{\partial\omega}{c\partial t}\sin\delta\right)\boldsymbol{\beta} \tag{434}$$

$$+\left(K\frac{\partial\omega}{c\partial t}\sin\delta - \frac{\partial\delta}{c\partial t}M\sin\delta\right)\boldsymbol{\gamma}.$$

The topography of the generalized photon is defined by the following theorem:

Theorem 5. *The Topographic Theorem. For every inertial frame of reference and for every generalized photon, the following hold:*

1. *If it is $(t_1, t_2, t_3) \neq (0, 0, 0)$, then the generalized photon is of one spatial dimension. The material points of the generalized photon are arranged on a curve. At each point of the curve the vector t is tangent on the curve.*

2. *The generalized photon can have two spatial dimensions, with its material points arranged on a surface. Then at each point of the surface, the vector n, vertical to the surface, is given by $\boldsymbol{n} = \frac{\nabla\delta}{\|\nabla\delta\|} = \frac{\nabla\omega}{\|\nabla\omega\|}$.*

3. *If the material points of the generalized photon are arranged in the three-dimensional space, then it is $K = L = M \sin\delta = N \sin\delta = \frac{\partial\delta}{c\partial t} = \frac{\partial\omega}{c\partial t} \sin\delta = 0$.*

For the material point particle and for the velocity vector (429), we obtain from equations (51) and (34)

$$\frac{\partial\delta}{c\partial t} = -\frac{\boldsymbol{u}\cdot\boldsymbol{\beta}}{cr\left(1 - \frac{\boldsymbol{v}\cdot\boldsymbol{u}}{c^2}\right)}$$

$$K = \frac{1}{r} \qquad\qquad L = 0$$

$$\sin\delta\frac{\partial\omega}{c\partial t} = -\frac{\boldsymbol{u}\cdot\boldsymbol{\gamma}}{cr\left(1 - \frac{\boldsymbol{v}\cdot\boldsymbol{u}}{c^2}\right)}$$

$$M\sin\delta = 0 \qquad\qquad N\sin\delta = \frac{1}{r}.$$

Thus, we get

$$t_1 = KN\sin\delta - LM\sin\delta = \frac{1}{r^2} \neq 0$$

and, therefore, it is $t \neq (0,0,0)$. Consequently, in the case of equation (429) the generalized photon is of one spatial dimension. Therefore, the trajectory representation theorem emerges, as we saw in paragraph 2.4.

The topographic theorem permits the study of the self-variations for non-point material particles.

References

1. Mase C.C. Continuum Mechanics. 1970, Schaum Publ. Co.

2. Hunter S.C. Mechanics of Continuous Media. 1976, Halsted Press.

3. Wallace P.R. Mathematical Analysis of Physical Problems. 1984, New York, Dover.

4. Spivak M. A Comprehensive Introduction to Differential Geometry. 1999.

5. French A.P. Special Relativity. 1968, Nelson, London.

6. Bohm D. The special Theory of Realitivity. 1965, Benjamin, New York.

7. Couderc P. La Relativite. 1963, Presses Univeritaires de France.

8. Good R.H. Basic concepts of Relativity. 1968, Reinhold book corporation.

9. Rindler W. Relativity. Special, General and Cosmological. 2001, Oxford University Press.

10. Rindler W. Introduction to Special Relativity. 1991, Clarendon Press, Oxford.

11. Synge J.L. Relativity: The Special Theory. 1972, North-Holland Publishing Company.

12. Landau L.D., Lifshitz E.M. Fluid Mechanics, Vol. 6, 1987, Butterworth-Heinemann.

13. Wang C.C. Mathematical Principles of Mechanics and Electromagnetism. Part A: Analytical and Continuum Mechanics, 1979, Plenum Press.

14. Schwartz M. Principles of Electrodynamics. 1987, New York, Dover.

15. Shadowitz A. The Electromagnetic Field. 1988, New York, Dover.

16. Griffiths D.J. Introduction to Electrodynamics. 1989, Englewood Cliffs, NJ: Prentice Hall, p. 368.

17. Reitz J.R., Milford F.J., Christy R.W. Foundations of Electromagnetic Theory. 2000, MA: Addison-Wesley.

18. Landau L.D., Lifshitz E.M., Pitaevskii L.P. Electrodynamics of Continuous Media. 1984, Butterworth-Heinemann.

19. Flugge W. Tensor Analysis and Continuum Mechanics. 1972, Springer-Verlag.

20. Davies W.R. Classical Fields, Particles and the Theory of Relativity. 1970, Gordon and Breach.

21. Corson E.M. Introduction to Tensors, Spinors, and Relativistic Wave-Equations. 1953, Blackie and Son.

22. French A. An introduction to Quantum Mechanics. 1978, W.W. Norton.

23. Feynman R. Lectures on Physics, Vol. III, 1965, Addison-Wesley.

24. Bohm D. Quantum Theory, 1951, Prentice-Hall.

25. Dicke R.H., Wittke J.P. Introduction to Quantum Mechanics. 1960, Addison-Wesley.

26. Gasiorowitz S. Quantum Physics. 1974, Wiley International.

27. Dirac P.A.M. The Principles of Quantum Mechanics. 1967, Oxford University Press.

28. Riess A.G. et al. Observational Evidence from Supernovae for an Accelerating Universe and a Cosmological Constant, *Astronomical Journal*, 1998, v. 116, 1009–1038.

29. Perlmutter S., Turner M.S., White M. Constraining Dark Energy with Type Ia Supernovae and Large-Scale Structure. *Physical Review Letters*, 1999, v. 83, 670–673.

30. Baldi M., Pettorino V. High-z massive clusters as a test for dynamical coupled dark energy. *MNRAS*, 2011, v. 412:L.

31. Rybicki G.B., Lightman A.P. Radiative Processes in Astrophysics. 1985, John Wiley-Interscience.

32. Malcolm S.L. High Energy Astrophysics. 2011, University of Cambridge.

33. Spergel D.N. et al. Wilkinson Microwave Anisotropy Probe (WMAP) Three Year Results: Implications for Cosmology. 2007, ApJS 170, 377.

34. Clifford M.W. Theory and Experiment in Gravitational Physics. 1981, Cambridge University Press.

35. Webb J.K., Flambaum V.V., Churchill C.W., Drinkwater M.J., Barrow J.D. Search for time variation of the fine structure constant. *Physical Review Letters*, 1999, v. 82, 884–887.

36. Tzanavaris P., Webb J.K., Murphy M.T., Flambaum V.V., Curran S.J. Limits on variations in fundamental constants from 21-cm and ultraviolet Quasar absorption lines. *Physical Review Letters*, 2005, v. 95, pp. 41301-41304.

37. Webb J.K., King J. A., Murphy M. T., Flambaum V. V., Carswell R. F., Bainbridge M. B., Indications of a Spatial Variation of the Fine Structure Constant. *Physical Review Letters*, 2011, v. 107, pp. 191101-1-191101-5.

38. Knebe A., Devriendt J.E.G., Gibson B.K., Silk J. Top-down fragmentation of warm dark matter filament. *Monthly Notices of the Royal Astronomical Society*, 2003, v. 345, 1285.

39. Manousos E. The theory of self-variations. A continuous slight increase of the charges and the rest masses of the particles can explain the cosmological data. *Nuovo Cimento B*, 2007, v. 122, 359-388.

40. Gott J.R. et al. A Map of the Universe. 2005, ApJ, 624, 463.

41. Labini F.S., Vasilyev N.L., Baryshev Y.V. Persistent fluctuations in the distribution of galaxies from the Two-degree Field Galaxy Redshift Survey. *EPL*, 2009, v. 85, 29002.

42. Peacock J.A. et al. A measurement of the cosmological mass density from clustering in the 2dF Galaxy Redshift Survey. *Nature*, 2001, v. 410, 169–173.

————————————

On the Uniform Dimension System. Is There the Necessity for Coulomb?

Anatoly V. Belyakov

E-mail: belyakov.lih@gmail.com

The dimensions of electrical units (Ampere, Coulomb, etc.) are surplus. It is shown that the most appropriate is to replace the electric charge with the ultimate momentum of the electron. Then all the dimensions of electrical and magnetic values get simplified and assume physically obvious form.

Although electric and magnetic dimensions in systems CGSE and CGSM are expressed in the terms of mass, length, and time units (in SI units Ampere was added), they seem strange and bizarre. The exception is a unit of capacity in the system CGSE whose dimension (centimeters) looks convincing. Of course, the dimensions are relative; however, it causes internal resistance, misunderstanding, and difficulties in the perception of the relevant areas of physics, especially for students. Is there need of having electrical values proper, above all Ampere (or Coulomb)?

Indeed, the basic formulae (the electrical force between the charges and the magnetic force between current-carrying conductors) can be represented with a single dimensional factor of force. Only the number of electric charges z is meaningful for the force of electrical and magnetic interaction. In the Coulomb formula a unit of the charge can be expressed through the electron mass m_e and the classical electron radius r_e. Then Coulomb formula can be obtained as:

$$F_e = \frac{m_e c^2}{r_e} \left(\frac{r_e}{r} \right)^2 z_1 z_2,$$

where r, c, z_1, z_2 are, respectively, the distance between the charges, the velocity of light, and the number of the electric charges.

Here dimensional coefficient $m_e c^2 / r_e$ is the centrifugal force that occurs when an electron moves with the light velocity c of the radius r_e. This force is equivalent to the force acting between two elementary charges by the given distance and its numerical value is a very ordinary magnitude equal 29.06 N.

In what units electric charge should be measured? According to John A. Wheeler' idea, the charged microparticles are special points in the three-dimensional spatial surface of our world, connected to each other through "wormholes" — vortical tubes analogous to the lines of current working according to the "input-output" ("source-drain") principle, but in an additional dimension of space (but that does not mean that it is necessary to add a fourth spatial dimension [1]). In this model the electric charge is not a special kind of matter: the electric charge only manifests the degree of the non-equilibrium state of physical vacuum; it is proportional to the momentum of physical vacuum in its motion along the contour of the vortical current tube.

Therefore, the most appropriate is to replace the electric charge in formulae Coulomb and Ampere with the ultimate momentum of the electron $m_e c$. Then all the dimensions of electrical and magnetic values get strikingly simplified and assume sensible and physically obvious form. So, in SI units: current becomes force — [kgm/sec^2] or [N], the potential becomes velocity — [m/sec], capacity becomes mass of the electrons accumulated on the plates of the capacitor — [kg], conductivity becomes mass velocity — [kg/sec], inductance becomes the reciprocal value of mass acceleration — [sec^2/kg], the magnitude of the solenoid magnetic field becomes the number of turns per unit of solenoid length — [m^{-1}], etc.

The numerical values of the expressions for the electrical and magnetic forces, written in a "Coulombless" form with the charge replaced by the ultimate momentum of the electron, coincide with these values based on standard expressions at the following conditions:

— the value $4\pi\varepsilon_0$, which in SI units is 1.11×10^{-10} Farad/metre, is replaced by a new electric constant $\varepsilon_0 = m_e / r_e = 3.23 \times 10^{-16}$ [kg/m];

— magnetic constant μ_0, which in SI units is $4\pi \times 10^{-7}$ Henry/metre, is replaced by a new magnetic constant $\mu_0 = 1/\varepsilon_0 c^2 = 0.0344$ [N^{-1}].

Thus, the electric constant ε_0 makes sense the linear density of the vortex tube current, and the magnetic constant μ_0 makes sense the reciprocal value of the interaction force between two elementary charges.

With such mechanistic interpretation Wheeler's scheme numerical values of the electric charge and radiation constants were successfully obtained [2]. In such system value $587\, m_e c$ [kgm/sec] is the momentum of the vortical tube current the whole, it numerically corresponds to the electron charge $e_0 = 1.602 \times 10^{-19}$ Coulomb; at the same time the value $m_e c$ [kgm/sec] corresponds to the "point-like" electron charge. The value of 587 [m/sec] corresponds to one Volt in SI units, the value of $4\pi/587^2 = 3.6 \times 10^{-5}$ [kg] corresponds to one Farad in SI units etc. Thus there would be no need for the systems of CGSE units, CGSM units and the Gaussian units. Replacing the dimensions and introducing new electromagnetic constants is a purely technical problem, although it is hardly practicable today. It is more important that mechanistic interpretation of the electromagnetic parameters

reveals theirs physical meaning and gives help understanding the nature of phenomena.

For example, the electrical capacity of a sphere of radius $R = 1$ [m] is equal to 3.23×10^{-16} [kg], which corresponds to 3.5×10^{14} electrons distributed over its surface and be responsible for the movement of the charges, while the average distance between the charges is $r = \pi \sqrt{R r_e} = 1.67 \times 10^{-7}$ [m].

The capacitor charge is proportional to the potential, and it is easy to determine the satiation potential φ when the number of electric charges becomes equal with the number of electrons carrying the charges. Since the "point-like" electron cannot carries momentum over $m_e c$, for an only charge: $\varphi = m_e c / m_e = c$ [m/sec] or, in SI units, $c/587 = 511000$ Volts. If this potential is exceeded the mentioned magnitude, the charge is spontaneously flowing into the surrounding space.

In these examples (and in others) quite reasonable values have been obtained, which could not be if all above-stated would be wrong. Of course, such associations of electrical and magnetic values with mechanical ones do not yet mean reduction of electromagnetic phenomena to mechanical ones. The question immediately arises, how does the electron be able to carry momentum which exceeds many times your own one? However, this question implicitly always existed because the term "charge" is, in fact, the delicate symbol of not properly understood electricity essence. To some extent, the response has been received in this article, as well as in [2, 3].

References

1. Belyakov A.V. On the Independent Determination of the Ultimate Density of Physical Vacuum. *Progress in Physics*, 2011, v.2, 27–29.

2. Belyakov A.V. Charge of the electron, and the constants of radiation according to J. A. Wheeler's geometrodynamic model. *Progress in Physics*, 2010, v.4, 90–94.

3. Belyakov A.V. Macro-analogies and gravitation in the micro-world: further elaboration of Wheeler's model of geometrodynamics. *Progress in Physics*, 2012, v.2, 47–57.

Further Problems with Integral Spin Charged Particles

E. Comay

Charactell Ltd., PO Box 39019, Tel-Aviv, 61390, Israel. E-mail: elicomay@post.tau.ac.il

The structure of the Lagrangian density of quantum theories of electrically charged particles is analyzed. It is pointed out that a well known and self-consistent expression exists for the electromagnetic interactions of a spin-1/2 Dirac particle. On the other hand, using the Noether theorem, it is shown that no such expression exists for the spin-0 Klein-Gordon charged particle as well as for the $W^\pm$ spin-1 particle. It is also explained why effective expressions used in practical analysis of collider data cannot be a part of a self-consistent theory. The results cast doubt on the validity of the electroweak theory.

1 Introduction

Since its very beginning, quantum theory has provided expressions describing electromagnetic interactions. In particular, the Dirac equation of spin-1/2 charged particle takes a covariant form [1, see pp. 16–24]. As is well known, electromagnetic interactions of a Dirac particle have an extraordinary experimental support. Later, a quantum theory of a spin-0 Klein-Gordon (KG) charged particle was published [2, see pp. 188–205]. In the electroweak theory which was constructed several decades later, the $W^\pm$ spin-1 charged boson plays a cardinal role. The discussion presented in this work examines the Lagrangian density of quantum theories. As is well known, the electromagnetic interaction term of these theories depends on a contraction of the charged particle's 4-current and the external 4-potential $j_\mu A^\mu$. Thus, the Noether theorem is used for deriving expressions for the charged particle's 4-current. In this way the analysis proves that electromagnetic theories of spin-0 and spin-1 particles contain inherent contradictions.

Units where $\hbar = c = 1$ are used in this work. Hence, only one dimension is required and it is the length, denoted by [L]. For example, mass, energy and momentum have the dimension $[\mathrm{L}^{-1}]$, etc. Greek indices run from 0 to 3 and the diagonal metric used is $g_{\mu\nu} = (1, -1, -1, -1)$. The symbol $_{,\nu}$ denotes the partial differentiation with respect to x^ν. The summation convention is used for Greek indices. The second section presents theoretical elements that are used in the discussion. The third section contains a proof showing that electromagnetic interactions cannot be a part of a self-consistent theory of spin-0 and of spin-1 quantum particles. Concluding remarks can be found in the last section.

2 The theoretical basis of the analysis

The following discussion examines the structure of a quantum theory of an electrically charged particle and its interaction with electromagnetic fields. The need for a Lagrangian density as basis for a relativistic quantum theory has become a common practice. This issue can be derived from the fact that the phase is an argument of an exponent. Thus, the power series expansion of the argument proves that the phase must be a dimensionless Lorentz scalar. This requirement is satisfied if the action (divided by $\hbar$) is used for the phase and the Lagrangian density is a Lorentz scalar whose dimension is $[\mathrm{L}^{-4}]$. Indeed, in this case, the action

$$S = \int \mathcal{L} \, d^4x \tag{1}$$

is a dimensionless Lorentz scalar.

The form of the required Lagrangian density is

$$\mathcal{L}(\Phi^\dagger, \Phi^\dagger_{,\mu}, \Phi, \Phi_{,\mu}, A^\mu, F^{\mu\nu}), \tag{2}$$

where Φ denotes the function of the charged quantum particle and $A^\mu, F^{\mu\nu}$ denote the electromagnetic 4-potential and its fields, respectively. In the discussion presented herein the quantum function Φ represents either scalar, spinor or vector particle. In specific cases the notation ϕ represents a KG charged particle, ψ denotes a Dirac particle and W^μ denotes the $W^\pm$ particles. Evidently, (1) and (2) prove that the function Φ has dimension.

Maxwellian electrodynamics is derived from the following Lagrangian density [3, see pp. 71–81]

$$\mathcal{L} = -\frac{1}{16\pi} F_{\mu\nu} F^{\mu\nu} - j_\mu A^\mu, \tag{3}$$

where j^μ denotes the charge's 4-current and the last term of (3) represents the electromagnetic interaction.

This expression demonstrates the crucial role of the 4-current in a self-consistent theory of an electrically charged particle. As is well known, the charge 4-current must satisfy the continuity equation

$$j^\mu_{,\mu} = 0. \tag{4}$$

The standard method used for constructing such a 4-current relies on Noether's theorem [4, see p. 20]. Thus, in the present case, the expression for the 4-current boils down to the following form

$$j^\mu = i \frac{\partial \mathcal{L}}{\partial \Phi^\dagger_{,\mu}} \Phi^\dagger - i \frac{\partial \mathcal{L}}{\partial \Phi_{,\mu}} \Phi. \tag{5}$$

(Note that due to the opposite phase sign of $\Phi^\dagger$ and Φ, corresponding terms derived from these functions have opposite

sign.) Thus, in the case of a charged particle, the Noether 4-current (5) is multiplied by the electric charge e. Relying on (5), one concludes that the 4-current is derived from terms of the Lagrangian density that contain a derivative of the field function with respect to the coordinates x^μ. The 0-component of (5) represents the particle's density. Hence, the dimension of j^μ is $[L^{-3}]$.

A standard method used for the introduction of electromagnetic interaction is to substitute the following transformation in the free Lagrangian density of the particle (see e.g. [1, p. 10])

$$-i\frac{\partial}{\partial x^\mu} \rightarrow -i\frac{\partial}{\partial x^\mu} - eA_\mu(x^\nu). \tag{6}$$

Later, this substitution is called the standard form of electromagnetic interaction. This form as well as other forms of electromagnetic interactions are discussed in the next section.

3 Quantum charged particles

The Dirac Lagrangian density of a free spin-1/2 particle is [4, see p. 54]

$$\mathcal{L} = \bar{\psi}\left[\gamma^\mu i\partial_\mu - m\right]\psi. \tag{7}$$

This expression is linear in the mass. Hence, the dimension $[L^{-4}]$ of the Lagrangian density means that the dimension of the Dirac function ψ is $[L^{-3/2}]$. An application of the Noether relation (5) for a construction of the 4-current yields the well known Dirac expression [1, see pp. 23–24] which is written below in the standard notation

$$j^\mu = e\bar{\psi}\gamma^\mu\psi. \tag{8}$$

The dimension $[L^{-3/2}]$ of the Dirac function ψ shows that (8) has the required dimension.

The case of the KG and of the W Lagrangian density is different. Here the mass term takes the form (see [4, p. 26] and [5, p. 309], respectively)

$$-m^2\Phi^\dagger\Phi. \tag{9}$$

Different numerical factors of (9) are not mentioned and the same is true for the contraction of the 4 components of the W function. Relationship (9) means that the dimension of the KG and of the W functions is $[L^{-1}]$. Thus, in order to satisfy the $[L^{-4}]$ dimension of the Lagrangian density of these particle, it must contain terms that are *bilinear* in derivatives with respect to the space-time coordinates x^μ. Applying the Noether relation for the 4-current (5), one finds that *the 4-current of the KG and of the W particles contains a derivative with respect to x^μ.* This property means that utilizing of the standard form of the introduction of electromagnetic interactions (6), one finds that *the 4-current of the KG and of the W particles depends linearly on the 4-potential of the electromagnetic fields.* (This is certainly inconsistent with gauge invariance, because here a gauge transformation alters charge density and the associated field values as well. However, this matter is not discussed in the present work.) The dependence of the charged KG 4-current on the external electromagnetic 4-potential has already been shown a long time ago [2, see p. 199].

Let us turn to the electromagnetic fields. The interaction term of the Maxwellian Lagrangian density (3) is $j_\mu A^\mu$. Now, if the 4-current j^μ of the KG and of the W particles depends linearly on the 4-potential of electromagnetic fields then *there is a quadratic term of the 4-potential in the expression for the interaction term in the Maxwellian Lagrangian density (3).* This is a contradiction because in Maxwellian electrodynamics the interaction term must be linear in the 4-potential [3, see pp. 78–79].

The foregoing discussion proves that there is no theoretically valid expression for the electromagnetic interaction of a KG particle and of the W boson as well. Thus, in the case of the W boson people resort to a phenomenological expression that goes by the name *effective Lagrangian density* [6, 7]. Using standard notation for the W field, one of the nonvanishing electromagnetic interaction terms of the effective Lagrangian density is

$$\mathcal{L}_{int} = -ie\,(W_{\mu\nu}^\dagger W^\mu A^\nu - W_\mu^\dagger W^{\mu\nu} A_\nu). \tag{10}$$

The articles [6,7] have been cited many times and (10) is still used in a collider data analysis [8, see eq. (1)] [9, see eq. (3)].

The following argument proves that (10) is indeed an effective expression which cannot be justified theoretically. Let us assume that (10) is a term in a theoretically justifiable Lagrangian density. In this case the following expression

$$j^\nu = -ie\,(W_\mu^{\dagger\nu} W^\mu - W_\mu^\dagger W^{\mu\nu}) \tag{11}$$

represents the electric 4-current of the W boson. But (11) contains the factors $W^{\dagger\mu\nu}$ and $W^{\mu\nu}$, and by the definition $W_{\mu\nu} = \partial_\mu W_\nu - \partial_\nu W_\mu$, each of which is a derivative with respect to x^μ. Therefore, due to the Noether theorem (5), the interaction term (10) alters the 4-current of the W boson and adds to it a troublesome term that is proportional the the external electromagnetic 4-potential A^μ. Hence, *contrary to the assumption examined herein, (11) does not represent the 4-current of the W boson.* This contradiction substantiates the proof.

A second electromagnetic term which is introduced into the effective Lagrangian density of the W is [6–9]

$$\mathcal{L}_{int} = ie\,W_\mu^\dagger W_\nu F^{\mu\nu}. \tag{12}$$

This term is certainly inconsistent with electromagnetic interactions because these interactions are proportional to the 4-current of the charged particle and the dimension of the 4-current is $[L^{-3}]$. On the other hand, it is proved above that the dimension of the W function is $[L^{-1}]$ and that of $W_\mu^\dagger W_\nu$ is $[L^{-2}]$. Therefore, (12) cannot represent a consistent electromagnetic interaction.

4 Conclusions

The solid mathematical structure of the spin-1/2 Dirac equation and its successful experimental status are pointed out above. Here a self-consistent relativistically covariant electromagnetic interaction exists. Thus, nobody finds the need to resort to "effective Lagrangian density".

A different situation holds for the cases of spin-0 and spin-1 elementary particles. It is proved in this work that for these particles the standard methods used for constructing electromagnetic interactions fail. Furthermore, it is proved above that the authors of [6, 7] are right in their description of the W boson electromagnetic interaction (10) as an effective expression. However, a proof presented in the previous section shows that (10) cannot be a part of a theoretically self-consistent Lagrangian density. This outcome means that *the W boson cannot carry an electric charge.* Now, the W boson takes a vital part in the unification of electrodynamics with weak interaction which is called electroweak theory. Therefore, the results cast doubt on the validity of the electroweak theory.

Another result of the discussion presented above is that the experimentally detected W boson cannot be an elementary particle described by a field function that takes the form $W^{\pm\mu}(x^\nu)$. Indeed, a dependence on a single set of space-time coordinates x^μ is a property of a structureless pointlike elementary particle like the electron etc. Thus, the actual $W^\pm$ particles must be composite particles and it looks plausible to regard them as a combination of mesons of the top quark and either of the d, s, b antiquarks or vice versa. It turns out that the conclusions of this work provide an independent support to similar conclusions that have been published earlier [10]. It should also be noted that the results of this work are consistent with Dirac's lifelong objection to the KG equation [11].

References

1. Bjorken J. D. and Drell S. D. Relativistic Quantum Mechanics. McGraw-Hill, New York, 1964.

2. Pauli W. and Weisskopf V. The quantization of the scalar relativistic wave equation. *Helvetica Physica Acta*, 1934, v. 7, 709–731. English translation in Miller A. I. Early Quantum Electrodynamics. University Press, Cambridge, 1994. (In the text, page references apply to the English translation.)

3. Landau L. D. and Lifshitz E. M. The Classical Theory of Fields. Elsevier, Amsterdam, 2005.

4. Bjorken J. D. and Drell S. D. Relativistic Quantum Mechanics. McGraw-Hill, New York, 1965.

5. Weinberg S. The Quantum Theory of Fields, Vol II. Cambridge University Press, Cambridge, 1996.

6. Hagiwara K., Peccei R. D., Zeppenfeld D. and Hikaso K. *Nuclear Physics*, 1987, v. B282, 253.

7. Hagiwara K., Woodside J., Zeppenfeld D. *Physical Review*, 1990, v. D41, 2113.

8. Abazov V. M. et al (D0 collaboration). *Physics Letters*, 2012, v. B718, 451.

9. Aad G. et al (ATLAS collaboration). *Physics Letters*, 2012, v. B712, 289.

10. Comay E. Quantum Constraints on a Charged Particle Structure. *Progress in Physics*, 2012, v. 4, 9–13.

11. Dirac P. A. M. Mathematical Foundations of Quantum Theory. In Marlow A. R. (ed.) Mathematical Foundations of Quantum Theory. Academic, New York, 1978.

Studies of Pulsed Signals in High-precision Experiments (Antarctica)

Sergey N. Shapovalov*, Oleg A. Troshichev†, Vacheslav I. Povazhny‡ and Igor V. Moskvin**

SSC Arctic and Antarctic Research Institute. 38 Beringa st., 199397 St-Petersburg, Russia
*E-mail: shapovalov@aari.ru; †E-mail: olegtro@aari.ru; ‡E-mail: povazviach@gmail.com; **E-mail: im_geo@aari.ru

The paper presents the results of studies on pulsed signals in photocurrent (PCC-2 instrument), in the 565-nm LED spectrum, and in the atmospheric zenith spectrum (342.5 nm). According to the results of statistical analysis of data measurements for the period from 24.04.04 till 01.02.06 a correlation between the temporal distribution of pulsed signals in photocurrent PCC-2 and CA F10.7 cm (2800 MHz) index and the total solar radiation (TSI) was established. In the course of the parallel measurements of photocurrent in PCC-2 and fluctuations in the spectra frequencies of the LED and the atmosphere zenith, based on the average daily values of the standard deviation, the identical trend in the photocurrent pulse signals (PCC-2) and the fluctuations at 520-nm LED spectrum and 342.5-nm atmosphere zenith spectrum was detected (AvaSpec–2048 spectrometer).

1 Introduction

The way towards recognition of the role of unknown cosmophysical effects on the Earth processes presents certain difficulties. At the first stage of research, the existence of non-electromagnetic radiation affecting the physical and biological systems was hypothesized. Among these, the conclusion about the advanced (4–6 days lead time) increase of corynebacteria sensitivity to the emergence of active formations on the surface of the Sun made by A. L. Chizhevsky and S. T. Velkhover [1] should be mentioned. It may be only assumeday be tions ioned that these formations are linked to perturbations in the deep spheres of the Sun and are accompanied by the topography changes in its gravitational field. At least, this is supported by the existence of lead time phenomenon undetected by other methods.

The applied research of the cosmophysical radiation and its impact on physical systems started with the works of N. A. Kozyrev [2], who had registered with a telescopic system the effect of unknown factor of high penetrating power. Due to the fact that the optical entrance of the telescope was overlaid with a metal screen, a non-electromagnetic origin of the registered radiation may be suggested. The results received by N. A. Kozyrev were confirmed later, in the experiments of the workgroup headed by M. M. Lavrentiev, Fellow Russian Academy [3]. Valuable results were obtained at the recent stage of research [4–8].

2 Studies of pulsed signals in photocurrent measurements with PCC-2

Technical characteristics of PCC-2 instrument: Photoelectric concentration colorimeter (PCC-2) is designed for measuring coefficients of transmission and optical density of solutions in the range of 315–980 nm (a set of optical light filters), as well as to determine the concentration of substances in solution by constructing calibration curves. Radiation detectors: F-26 photocell for operating in 315–540 nm range and FD-7K photodiode for operating in 590–980 nm range (Fig. 1).

Fig. 1: Photoelectric concentration colorimeter (PCC-2).

Recording device of the instrument is M 907-10 microammeter with digitized scale for coefficients of transmission and optical density. Power supply 220 ± 22 V, $50/60 \pm 0.5$ Hz. The source of radiation – KGM 6.3 – 15 small-size halogen lamp. The range of readings that characterizes random errors does not exceed 0.3%.

The normal running conditions for PCC-2 are: temperature $(20 \pm 5)°$C, relative humidity 45–80%, mains voltage 220 ± 4.4V, 50 Hz.

In the course of the Antarctic expedition to Mirny station, 1996–1997, during measurements of the dynamics rate of biochemical reactions [9], sharp microammeter deflections on PCC-2 panel were recorded, which corresponded to the increased optical density of the reaction under study. Since the bursts are uncharacteristic of the instrument properties and admissible estimates under the experimental procedure, it was

suggested that the reason for the observed bursts might be associated with non-trivial fluctuations (pulsed signals) [10, 11]. The general characteristics of pulsed signals is as follows:

— The polarity of pulsed signals corresponded to the decrease of photocurrent magnitude;

— Pulsed signals were observed at any time of the day, including around midnight;

— The duration of bursts was less than one second;

— Bursts were registered under various shielded conditions in the laboratory building coated with duralumin sheets (Antarctica); in ship-board space, multiple-shielded by steel deck grillage (RSV "Akademik Fedorov"); and in a cast-concrete building (AARI, St.Petersburg). The intensity of pulsed signals in Antarctica was considerably higher than in St.Petersburg;

— Pulsed signals have no geographic restrictions, they were recorded both in the Southern and Northern hemispheres, from 70°S (Antarctica, 2000) to 86°N (Arctic, 2000).

Since the receiving unit in the instrument is represented by a photocell, where the photocurrent is recorded with a micro-ammeter, variation recording on the instrument panel was transformed through the recording of photocurrent values in the absence of working substance. Testing of photocurrent measurements was performed in a cast-concrete building (AARI, St. Petersburg) in automatic mode via the COM-port of a PC, using DM3600 digital multimeter. The experiment was supplemented by PCC-2 thermal stabilization 20°C (±1). Uninterrupted power supply to the entire system was ensured by UPS-525 bt. In the course of measurements, abrupt changes of photocurrent in the form of a pulsed signal, in the direction of its decrease, was recorded. Sample registration of pulsed signals in photocurrent is shown in Fig. 2.

The practice of geophysical observation involves methods of testing the effects of artificial electromagnetic interference on the recording systems. Testing may be valid if the experiment is placed away from the metropolis, to minimize the impact of anthropogenic factors. Following these requirements, photocurrent measurements with PCC-2 were conducted at Novolazarevskaya station (Antarctica) in 2004.

3 Checking the integrity of the experiment

At the primary stage of automated measurements, PCC-2 sensitivity to the effects of artificial electromagnetic field (AEMF) was tested. The following instruments were used in the experiment:

1. Coil–to generate an electromagnetic field:

— Radius of turn: 0.055 m;
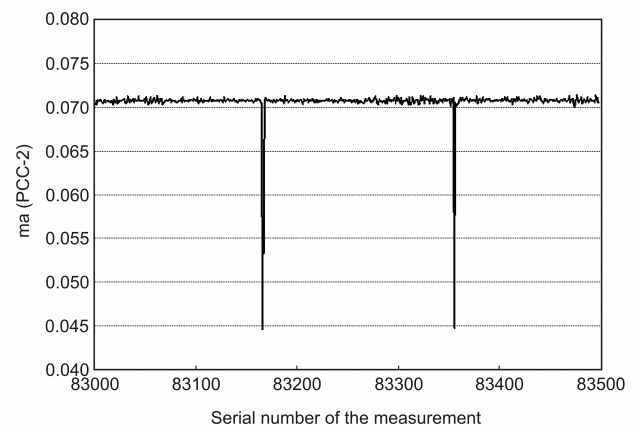
Fig. 2: Sample registration of pulsed signals in photocurrent (PCC-2)

— Coil dimensions: width of turn–0.07 m, diameter–0.11 m;

— Number of turns: 17;

2. Self-contained DC power source: storage battery 24 V, 75 A×hour;

3. Dropping resistor R_D = 2 Ohms;

4. "Mastech" M-832 digital multimeter;

5. Stationary recording magnetometer at Novolazarevskaya station;

6. PCC-2 photocurrent recording system:

— PCC-2 microphotocolorimeter;

— M3850D digital multimeter (with RS-232 cable outlet);

— Power supply unit for multimeter.

The magnetic field was excited by a pulsed current without a dropping resistor. The protocol of PCC-2 testing effects is provided in Table 1.

3.1 Measurements of the magnetic field generated by the coil

Measurements of the magnetic field induced by coil were conducted with stationary recording magnetometer (SRM) at Novolazarevskaya station. The magnetic field was excited by a pulsed current without a dropping resistor, and by a constant current with a dropping resistor (R = 2 Ohms). Generation of DC magnetic field for longer than 1 second without limiting resistance was not possible, because the strength of current could be as high as 100A against the resistance of coil ∼ 0.2 Ohms. For this case, the magnetic field of coil was measured additionally with dropping resistor included in the circuit.

3.2 Measurement results

Since the three-component magnetic variometer can not be considered as a point-source instrument at a distance of 1 me-

Time (GMT)	The distance to the PCC-2	The position of the coil	The mode of influence	Vector magnitude of induction of a magnetic field (nT)
16:16:30	1.5 m	vertical	a single pulse pulse duration ~ 0.2 c	450 – 900
16:17:00	1.5 m	vertical	a single pulse pulse duration ~ 0.2 c	450 – 900
16:17:35	1.5 m	vertical	a single pulse pulse duration ~ 0.2 c	450 – 900
16:18:20	1.5 m	horizontal E-W	a single pulse pulse duration ~ 0.2 c	450 – 900
16:18:30	1.5 m	horizontal E-W	a single pulse pulse duration ~ 0.2 c	450 – 900
16:18:40	1.5 m	horizontal E-W	a single pulse pulse duration ~ 0.2 c	450 – 900
16:19:30	1.5 m	horizontal N-S	a single pulse pulse duration ~ 0.2 c	450 – 900
16:19:45	1.5 m	horizontal N-S	a single pulse pulse duration ~ 0.2 c	450 – 900
16:20:00	1.5 m	horizontal N-S	a single pulse pulse duration ~ 0.2 c	450 – 900
16:20:15	1.5 m	horizontal N-S	a single pulse pulse duration ~ 0.2 c	450 – 900
16:21:30	1.9 m	vertical	a single pulse pulse duration ~ 0.2 c	250 – 500
16:21:40	1.9 m	vertical	a single pulse pulse duration ~ 0.2 c	250 – 500
16:21:45	1.9 m	vertical	a single pulse pulse duration ~ 0.2 c	250 – 500
16:22:00	1.9 m	horizontal E-W	a single pulse pulse duration ~ 0.2 c	250 – 500
16:22:10	1.9 m	horizontal E-W	a single pulse pulse duration ~ 0.2 c	250 – 500
16:22:15	1.9 m	horizontal E-W	a single pulse pulse duration ~ 0.2 c	250 – 500
16:23:00	1.9 m	horizontal N-S	a single pulse pulse duration ~ 0.2 c	250 – 500
16:23:10	1.9 m	horizontal N-S	a single pulse pulse duration ~ 0.2 c	250 – 500
16:23:15	1.9 m	horizontal N-S	a single pulse pulse duration ~ 0.2 c	250 – 500

Table 1: Results of AEMF testing effects on PCC-2.

ter (three sensors located along a straight line, at a distance of 16 cm), the numeric value (module of vector) of magnetic induction in the coil with current could be calculated only approximately, based on the data from three variometers. Variations in 3 components of the magnetic field were registered – D (WE), H (SN), and Z (vertical). Module of the vector T was calculated by the equation:

$$T = \sqrt{\Delta D^2 + \Delta H^2 + \Delta Z^2}. \qquad (1)$$

The results of calculations are presented in Table 2.

Given that the value of coil resistance R_{cat} equaled 0.2 Ohms and in dropping resistor 2 Ohms, it could be expected that the magnetic field in the coil carrying current would be ∼10 times higher with the switched dropping resistance than without it. However, we did not account for the internal resistance of the battery, which depends both on the current frequency (essential in case of a current pulse) and its strength. Table 2 demonstrates that other conditions being equal, a coil powered by the same battery creates a magnetic field, which is 4–5 times greater under dropping resistor, as compared to the field generated without it. This ratio is probably even more, due to the low frequency of ADC sampling used in measurements of pulsed fields.

As is known, the maximum and minimum values of magnetic induction vector differ two-fold exactly, if measured equidistant from the center of the magnetic dipole. The coil size being ∼ 0.1 m, the field of the coil can be regarded with good accuracy as a dipole field, at a distance above 1 m from its center. Thus, when the coil is powered by a battery in a pulsed mode, magnetic induction measured at 1 m off the coil center ranges from 1500 nT (in the plane perpendicular to the coil axis) to 3000 nT (on its axis). The findings of the experiment showed that the photocurrent readings in PCC-2 are not affected by pulsed electromagnetic field with the magnetic component value > 6000 nT, which is greater by 2–3 orders of magnitude than the maximum amplitude of geomagnetic pulsations at 0.1–0.001 Hz frequencies, and several times higher than the intensity of the strongest magnetic storms. The second experiment on the effects on PCC-2 was conducted with high-frequency transmitter (1782 MHz), ACS-1 radiosonde aerological service at Novolazarevskaya station. Characteristics of the transmitter: — Operating frequency 1782±20 MHz — Pulse recurrence frequency 457.5±0.2 Hz — Pulse duration 1 mcs — Transmitter power 2 W / 300 W The distance between the PCC-2 location "geophysicists' premises") and the aerological service was measured with a GPS receiver and made 145±15) m along a straight line. Effects of ACS-1 were estimated through sessions, of 18 minutes total duration, in 2 W and 300 W modes.

Emission series under transmitter power 2W: a) from 22^h 34^m till 22^h at 37 m, at 0° vertical deviation b) from 22^h 37^m till 22^h 39^m, at +1° vertical deviation c) from 22^h 39^m till 22^h 43^m, at +3° vertical deviation, aimed to receive the signal reflected from the adjacent rocks (∼ 50 m) and the ice cap

(∼ 500 m). The signal reflected from the ice cap was fixed on the radar screen. The signal reflected from the rocks was within the measurement error, due to time delay arising from the proximity to the transmitter. Emission series under transmitter power 300W: a) from 22^h 51^m till 22^h 56^m, at 0° vertical deviation b) from 22^h 56^m till 22^h 59^m, at +1° vertical deviation c) from 22^h 59^m till 23^h 02^m, at 1° vertical deviation.

The experimental result proved that photocurrent readings are unaffected by PCC-2 exposure to the high-frequency electromagnetic field.

4 Data analysis and search of driving factor

Data processing and analysis of photocurrent measurements were carried out with "Statistica" software using the following statistical methods:

— Calculation of the parameters of the distribution (standard error, standard deviation, variance);

$$S = \sqrt{\frac{1}{n-1} \sum_{i=1}^{n} (x_i - \bar{x})^2}. \qquad (2)$$

— Spectral (Fourier) analysis (periodograms, estimate of the spectral density), cross-analysis, the value of coherence;

— Identification of the time series model (trend analysis), and analysis of the inadequacy of the model (analysis of residuals), $e_i = (y_i - y_i - hat)$;

— Parabolic polynomial interpolation of the best approximation $y = b_0 + b_1 x + b_2 x^2 + b_3 x^3 + ... + b_n x^n$;

— Selection of the filtering method, use of the moving average (from 3 to 23 points);

— Cross-correlation, correlation factor (r).

During the period of photocurrent measurements with PCC-2 at Novolazarevskaya station, from 24.04.2004 till 01.02.2006, over 20,000 events of pulsed signals were registered. The average daily number of signals comprised ≈300 events, with a minimum of about 80 and a maximum of 580 events. All registered signals are characterized by the polarity in the direction of decreasing photocurrent, 30–50%, on average. The long-period variations of about one year duration may be distinguished in the general distribution pattern of pulsed signals (Fig. 3). The figure also reveals that broad maxima correspond to the end periods of the polar night (July–August). Hence, the number of signals (intensity) does not depend on the influx of solar radiation. In search for the connection of these variations with cosmophysical factors, attention was given to the annual Earth motion along the orbit (the ecliptic). As is known, the equation of time [12] is the sum of two following components. These are the *eccentricity equation* and the *ecliptic inclination equation* (the declination

Time (GMT)	The distance to the SRM	The position of the coil	The mode of influence	Vector magnitude of induction of a magnetic field (nT)
15.07.2006 14:03:10–14:03:16	2 m	horizontal E-W	a single pulse pulse duration ~ 0.2 c	~ 200 nT
15.07.2006 14:06:33–14:06:34	1.5 m	horizontal E-W	a single pulse pulse duration ~ 0.2 c	~ 700 nT
15.07.2006 14:09:42–14:09:51	1 m	vertical	a single pulse pulse duration ~ 0.2 c	~ 2500 nT
20.07.2006 10:43:30–10:44:00	1 m	vertical	constant field	~ 600 nT
20.07.2006 10:51:00–10:51:35	1 m	vertical	constant field	~ 650 nT
20.07.2006 10:53:45–10:54:15	1 m	vertical	constant field	~ 550 nT
20.07.2006 10:56:45–10:57:15	1 m	horizontal E-W	constant field	~ 360 nT

Table 2: Results of AEMF testing effects on SRM.

of the Sun). While the bonding of the connection of the signals and the *ecliptic inclination equation*, we obtained a correlation whose coefficient is close to $r \sim 0.7$. Fig. 3 (a, b) gives the comparision of the numerical values of the daily impulse signals in the photocurrent (KFK-2) and the numerical values of the Sun's declination during 24.04.2004–01.02.2006.

In general distribution of the signals, variations of different duration are traced. Their behavior was identified by comparing the total signal distribution with the indices of solar activity and the total solar radiation (TSI), as well as with fluxes of solar cosmic rays and geomagnetic activity indices. These comparisons revealed that the changes of the daily values of signals best correspond to the SA F10.7 cm index changes and the average daily standard deviation of energy TSI (SD). Standard deviation (SD) shows the variance of the random variable values, with respect to its statistical expectation, i.e., the rate of within-group variability of a given indicator. Comparisons of the series are shown in Figs. 4–5 (a, b). The less pronounced relationship is viewed in case of K-index (Fig. 6) and the SCR fluxes (Fig. 7). Figure 7 demonstrates good matching in the value's trends starting from 425 days (late June 2005).

5 The parallel measurements of the photocurrent (KFK-2) and the fluctuations at the 520 nm wavelength, in the light-emitting diode 565 nm (AvaSpec-2048).

Assuming that the effects in PCC-2 photocurrent were caused by heliophysical impact, similar effects should be expected in the readings of other instruments.

AvaSpec-2048 (www.avantes.com) is a multifunctional fiber optic spectrometer intended for a wide range of studies (Fig. 8). The spectrometer is designed on AvaBench-75 platform with symmetric optical bench (Czerny-Turner). The elemental profile of spectral distribution is read by the operated

electronic board and is further transferred from the detector matrix to PC via USB/RS-232.

The task of the second experiment was to conduct "PCC-2 –AvaSPec–2048" parallel measurements referenced to GPS universal time. The measurements were performed from 16.05.05 till 01.11.05, with spatial separation of the instruments up to 5 m distance, in a continuous automatic mode. When processing fluctuations in different LED (565nm) spectral lines, the 520 nm line was selected, where the observed pulsed signals had the same specifics as in PCC-2. Fig. 9 shows an example of the registration. The first estimates of fluctuations comparing the two methods were obtained for the period from 31.05.04 till 08.09.04. Figure 10 shows the temporal comparisons for daily values of bursts in photocurrent FD-7K and energy fluctuations the wavelength 520 nm converted into the average daily standard deviation (SD).

6 Parallel measurements of photocurrent (PCC-2) and fluctuations within the 339.5–346 nm range of the atmosphere zenith (AvaSpec–2048)

Measurements of fluctuations within the 339.5–346 nm range of the atmosphere zenith were conducted with fiber optic spectrometer AvaSpec–2048. The data acquisition chart on spectral zenith observations of solar UV–radiation is presented in Fig. 11.

The measurements were performed during the polar summer, in accordance with the methodology of zenith observations on the ozone content, at the Sun angle $> 5°$. Data were recorded in the files in automatic mode, with a sampling interval of 2–3 seconds. Observations were accompanied by time corrections from GPS. The initial phase of observations aimed at the search of non-instrumental fluctuations at the full range of frequencies, within 297–780 nm range. At 0.3 nm resolution of diffraction grating, more than 1,300 spectrum lines were analyzed. To conduct parallel measurements with

Fig. 4: Comparison of temporal changes in solar activity index F10.7 cm (2800 MHz) with distribution of the daily values of pulsed signals in PCC-2, for the period 24.04.2004–01.02.2006 (Novolazarevskaya station).

where, h = Planck's constant $6.62606876 \times 10^{-34}$; c = velocity of light, 2.998×10^8 m/s; λ = wavelength in meters.

The average estimates of pulsed signals of energy within the 339.5–346 nm range were as follows:

$$E_{min} (346nm) = 3.583 \text{ (eV/photons)},$$

$$E_{mean} (342.5nm) = 3.619 \text{ (eV/photons)},$$

$$E_{max} (339.5nm) = 3.652 \text{ (eV/photons)}.$$

Comparison of fluctuations within the tested ranges with pulsed signals in PCC-2 showed an ambiguous correlation. The most consistent changes in PCC-2 pulsed signals were observed within a 339.5–346 nm range. Comparison of the series for the period from 25.09.07 till 17.12.07 illustrates this example in Fig. 13.

7 Prognostic functionalities of the observed effects

In addition to the obtained results, the general distribution pattern was detected in the daily values of pulsed signals measured with PCC-2, which corresponded to $\approx$ 300-day cycle. This period was revealed through the comparison of the annual intervals of the general series, with a difference of about two months. The second interval was compared to the first against the difference minus $\approx$ 60 days from the start of the first interval. For example, the top graph in Figure 14 (a, b) shows the intervals comparison for 24.04.2004–23.04.2005 and 21.02.2005–01.02.2006. On the bottom figure, the cross-correlation function of two series by logs, with corresponding correlation factors, is shown. It can be seen that the maximum correlation value reaches $r \sim 0.7$. Assuming all the above relationships between pulsed signals and variations of the SA index and TSI, a 300-day cycle was also detected in the F10.7 cm index and TSI. A comparison of F10.7 cm and TSI distribution patterns within the annual intervals is provided in

Fig. 3: the comparison of the distributions of the daily numerical values of the impulse signals of KFK-2 and the general number polynomial b) and the ecliptic inclination (the declination of the Sun) during 24.04.2004–01.02.2006 (Novolazarevskaya station).

the spectrometer and PCC-2, four ranges of the atmosphere zenith spectrum were selected (303–305 nm, 331–332.5 nm, 329.5–334 nm, 339.5–346 nm), for which the standard deviation of energy (SD_E) exceeded the instrumental fluctuations by an order, or above [13, 14]. Figure 12 shows a sample recording of fluctuations in the range of 339.5–346 nm. The profile demonstrates bipolar fluctuations reaching 339.5 nm and 346 nm levels, measured in the center of 342.5-nm frequency range.

The energy estimates (eV/photon) of pulsed signals were defined. For example, according to the formula:

$$\text{photon energy} \quad E(\lambda) = \frac{h c}{\lambda_e}, \quad (3)$$

Fig. 5: Comparison of temporal changes in energy TSI, and b) — Comparison of the daily average standard deviation TSI (SD) with distribution of the daily values of pulsed signals in PCC-2, for the period from 24.04.2004 till 01.02.2006 (Novolazarevskaya station).
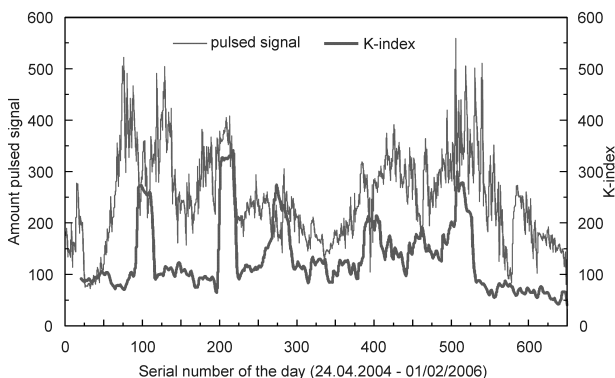

Fig. 6: Comparison of temporal changes in K-index variations with distribution of the daily values of pulsed signals in PCC-2, for the period from 24.04.2004 till 01.02.2006 (Novolazarevskaya station).

Fig. 15 (a, b): 24.04.2004–24.04.2005 and 24.02.2005–01.02.2006. Figure 15 (a) indicates the matching of F10.7 cm index variation in phase opposition of variations.
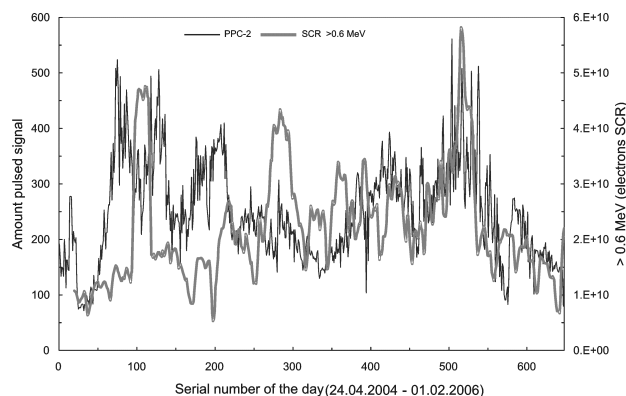
Fig. 7: Comparison of the temporal changes in SCR electron variations (> 0.6 MeV) with distribution of the daily values of pulsed signals in PCC-2, for the period from 24.04.2004 till 01.02.2006 (Novolazarevskaya station).
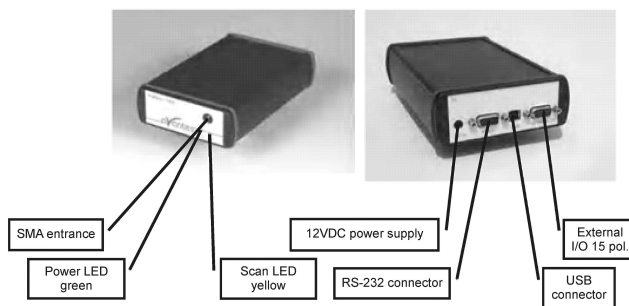
Fig. 8: Spectrometer AvaSpec-2048 (www.avantes.com).
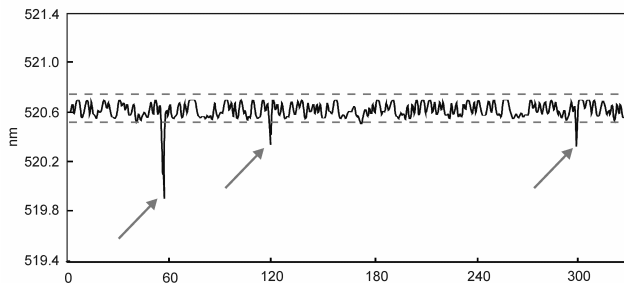
Fig. 9: Sample recording of pulsed signals at 520-nm frequency in 565-nm LED spectrum (AvaSpec–2048) (Novolazarevskaya station).

Comparison is presented upon the unfiltered values (without leveling). Unlike F10.7 cm, the daily average standard deviation of the energy TSI reveal matching of variations in the same phase character but if applying the moving average filter to 21 pts. The maximum amplitude in SD (TSI) is associated with a solar flare.

As regards the contribution of geomagnetic factors to the 300-day period, its manifestation was traced in the interplanetary magnetic field component (By). Figure 16 shows the comparison of By values for the intervals 01.01.2003–
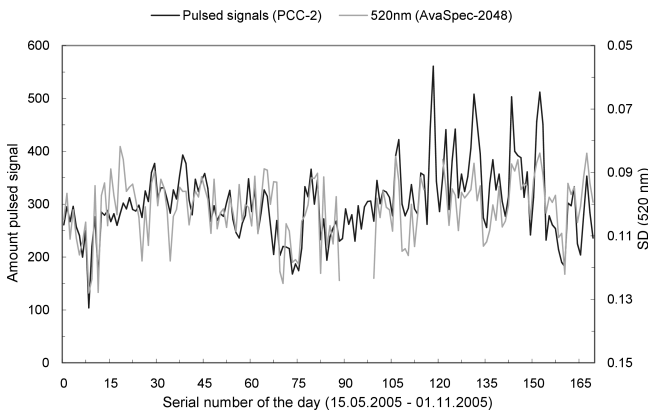
Fig. 10: Comparison of daily values of bursts in photocurrent with the average daily standard deviation (SD) of fluctuations at the 520 nm wavelength (AvaSpec–2048), for the period from 15.05.05 to 01.11.05 (Novolazarevskaya station).
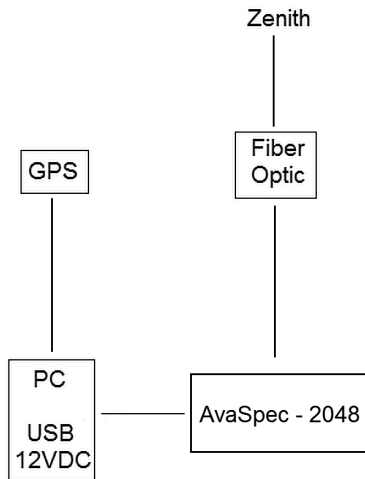

Fig. 11: Data acquisition chart on spectral zenith observations of solar UV–radiation in the atmosphere zenith (Novolazarevskaya station).
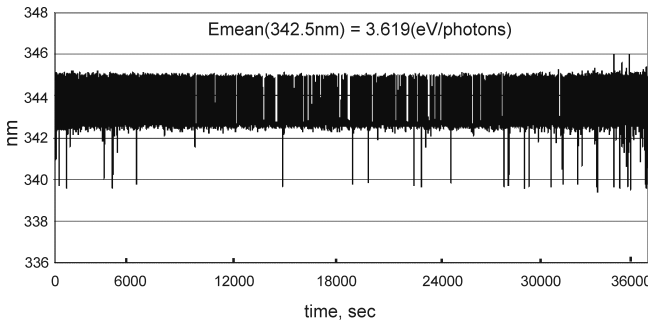

Fig. 12: Sample registration of fluctuations in 339.5–346 nm range (AvaSpec–2048), at clear atmosphere zenith, from 07^h 00^m till 17^h 00^m (09.03.2005, Novolazarevskaya station).

01.01.2004 and 27.10.2003–27.10.2004. The identity in variations and the phase convergence of the series, as demon-
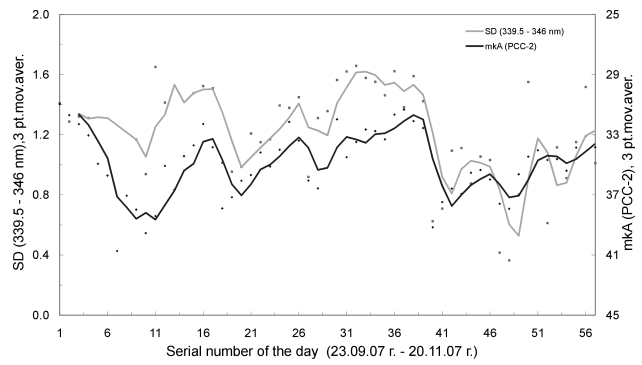

Fig. 13: Comparison of the daily average standard deviation of fluctuations in energy (SD_E) within the 339.5-346 nm range (AvaSpec-2048) in the atmosphere zenith and PCC-2 pulsed signals, for the period from 23.09.07 to 20.11.07 (Novolazarevskaya station).
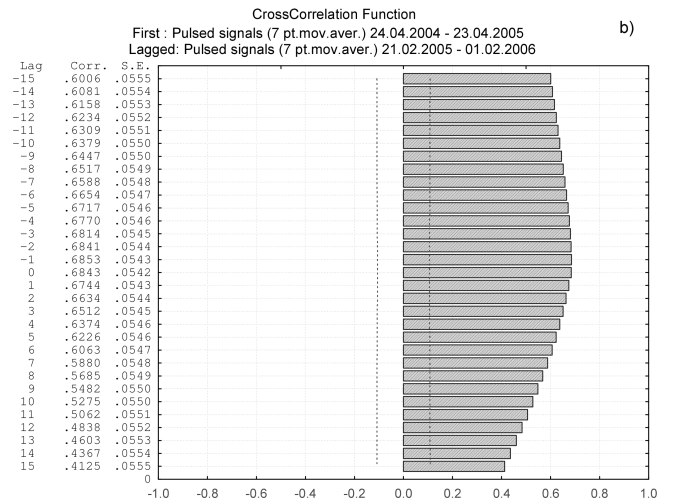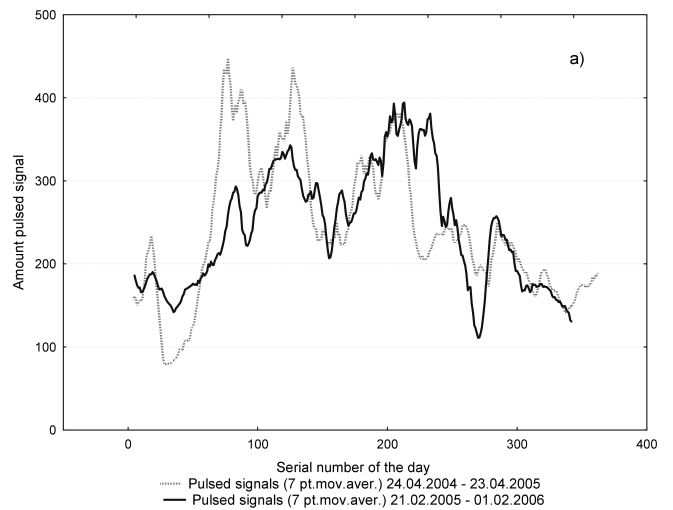

Fig. 14: Comparison of PCC-2 daily values of pulsed signals within the intervals 24.04.2004–24.04.2005 (a) and 21.02.2005–01.02.2006 (b) (Novolazarevskaya station).

strated in Figure 16, is the most indicative of the existence of the 300-day cycle. As in the case with F10.7 cm, unfil-
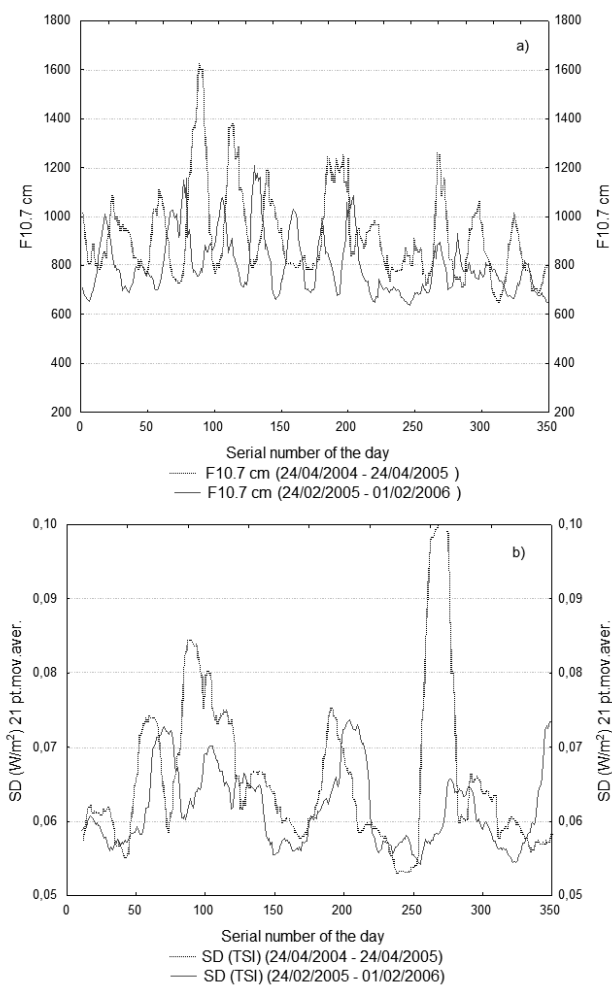
Fig. 15: Comparison of F10.7 cm and TSI distribution patterns within the intervals 24.04.2004–24.04.2005 (a) and 24.02.2005–01.02.2006 (b).

tered series were compared. This convincing fact is not yet explained through the known mechanisms of solar-terrestrial relationships.

Thus, pulsed signals bear prognostic characteristics associated, in our opinion, with the unknown heliophysical factor.

Similar results were obtained under extensive laboratory experiments conducted by Sergey Korotaev at Geoelectromagnetic Research Institute RAS (Troitsk, Moscow Region, Russia) [6].

His publication considers the phenomenon of non-locality and correlation of isolated dissipative processes, as well as description of the experiment and the results of investigations. Using two types of detectors based on the link between the entropy and the potential barrier height U, reliable correlations were established between: lead variations of dark current and temporal events in the atmospheric pressure (69, 73 days), variations of geomagnetic activity (Dst-index) (33 days) and variations of the F10.7 cm index (42 days). Based
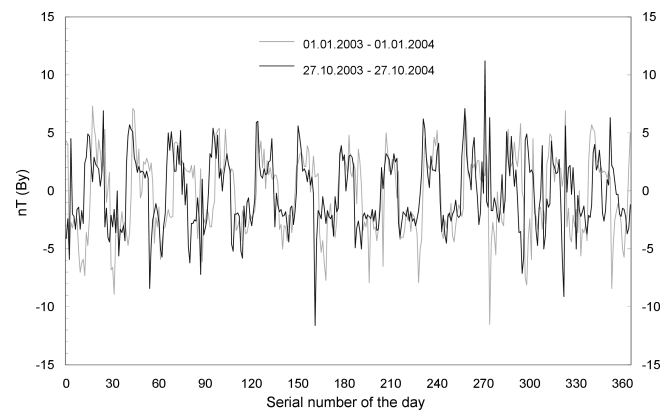

Fig. 16: Comparison of variations of the interplanetary magnetic field component By, by intervals: 01.01.2003–01.01.2004 and 27.10.2003–27.10.2004.

on the established correlations between the detectors and SA, the author established a temporal range of the lead coupling, from 42 to 280 days.

8 Conclusion

In our assumptions on the source of pulsed signals, the impact of cosmic particles fluxes and their secondary radiation (protons and products of their interaction with atmospheric nuclei — *positrons, muons, pi-mesons, K-mesons, electron pairs, gamma ray quanta, atmospheric neutrinos,* etc.) should be first considered. In determining the relation of the observed pulsed effects to the secondary cosmic rays, a comparison of distribution of pulse signals with variations of atmospheric cosmic rays of geomagnetic, solar and galactic origin would be quite sufficient. Assuming that similar pattern in temporal variations of the compared series would persist for a long time interval (within months), the penetrating component should be identified, since pulses are observed in shielded conditions. The penetrating component of cosmic rays can be defined by the type of interaction of cosmic rays with the substance.

For instance, among those well-known are: the nuclear-active component, soft component of secondary cosmic rays, electron-photon showers and the penetrating component of the secondary radiation — muons and neutrinos. Of the above mentioned, muons are the most likely source, as the muon flux represents a penetrating component and, against a relatively moderate energy power (~ 10 GeV), can easily enter the atmosphere and penetrate the shielding conditions of PCC-2. However, this version contradicts with the significant differences between the diurnal statistics of muons and neutrinos and pulsed signals. E.g., according to the observations in NT-200 neutrino telescope located at a depth of 1100–1200 m in the Baikal Lake, the daily number of atmospheric muons reaches $\approx 1,000,000$ and for atmospheric neutrinos – one oc-

currence in two days, on average.*

The hypothetical factor of heliophysical origin that causes simultaneous effects in photocurrent, the LED spectrum, and the zenith spectrum of the atmosphere, remains unknown. On the one hand, a good coincidence between the number of signals and variations in F10.7cm and TSI is observed, which may be regarded as conclusive indication of their solar origin. On the other hand, signals are registered, regardless of the shielding conditions, which is indicative of a high penetration capacity of the heliophysical factor. Further, no reliable evidence of a link between pulsed signals, cosmic ray fluxes and geomagnetic activity is revealed. It is as well obvious that the known mechanisms of the solar-terrestrial relationships do not represent direct implications of the effects observed in the experiment. An especially characteristic indicator of the signal intensity is the statistical correlation with the declination of the Sun, i.e., the position of the Earth on the orbit (the ecliptic). We do not exclude the assumption about the directed impact of this "hypothetical" factor in the ecliptic plane.

According to the results demonstrated in figures 14–16, it is evident that the studied pulsed signals in photocurrent have 60–65 days lead time, on average, compared to the solar events. If such pattern is scaled against the 11-year cycle of the solar activity (SA), we should expect that solar variations, recurrent in 300 days, would return to the starting point in 5.5 years (in our case, the measurement starting point was 24.04.2004), which makes approximately a half of the 11-year SA cycle. This presents a point of interest. The solar cycles are known to have a progression: 11-year, 22-year, 44-year, 88-year, etc. According to our results, we can not exclude the possibility of declining values of the SA cycles, down to 5.5 years, or less. Possibly, the 300-day cycle refers to the initial cycles in this progression. Its physical component may be determined by the processes occurring in the central zone of the Sun.

References

1. Chizhevsky A.L. Cosmic pulse of life. Mysl', Moscow, 1995.

2. Kozyrev N.A. Selected Papers. Leningrad Univ. Publ., Leningrad, 1991.

3. Lavrent'ev M.M., and others. On the registration of the true position of the Sun. *Doklady AN USSR*, 1990, v.315, no.2, 368–370.

4. Shnol' S.E., and others. Regular variation of the fine structure of statistical distributions as a consequence of cosmophysical agents. *Physics-Uspekhi*, 2000, v.170, no.2, 214–218.

5. Parkhomov A.G., Maklyaev E.F. Research on rhythms and fluctuations through long-term measurement of radioactivity, crystal frequency, semiconductor noise, temperature and atmosphere pressure. *Fizicheskaya Mysl' Rossii* (*Russian Physics Reports*), 2005, no.1, 1–12.

6. Korotayev S.M. Heliogeophysical nonlocality effects — shadows of future in the present. *Quantum Magic*, 2004, v.1, issue 2, 2219–2240.

7. Kondratyev K.Y., Nikol'skiy G.A. Impact of solar activity on structure components of the Earth. *Issledovanie Zemli iz Kosmosa*, 2005, no.3, 1–10.

8. Sizov A.D. Current fluctuations in the Wheatstone bridge. Possible cosmophysical correlations. *Biofizika* (*Biophysics*), 1998, v.43, issue 4, 726–729.

9. Gorshkov E.S., Shapovalov S.N., Sokolovskiy V.V., Troshichev O.A. On the reaction rate of the unitiol oxidation by nitrite ion. *Biofizika* (*Biophysics*), 2000, v.45, issue 4, 631–635.

10. Shapovalov S.N., Gorshkov E.S., Troshichev O.A. Cosmophysical effects observed in impulses of the microphotocolorimeter current. *Biofizika* (*Biophysics*), 2004, v.49, Suppl. 1, 119–121.

11. Shapovalov S.N., Troshichev O.A., Povazhny V.I. Study of short time pulses in the photoelectric effect under conditions of Antarctica (station Novolazarevskaya). *T2-8 Heliosphere Impact on Geospace IPY Oslo Science Conference*, 08–12 June 2010.

12. The Astronomical Calendar (permanent part). Nauka, Moscow, 1981.

13. Troshichev O.A., Shapovalov S.N., Lozovskiy V.T. Study of pulsed signals in UV spectra lines of free atmosphere above Novolazarevskaya station (Antarctica): effect of the solar irradiance? *37th COSPAR Scientific Assembly*, 13–20 July 2008, Montreal, Canada, p.322.

14. Shapovalov S.N., Troshichev O.A. Study of pulsed energy fluctuations and solar UV variations by data of spectral measurements in zenith of free atmosphere at Novolazarevskaya station (Antarctica). *39th COSPAR Scientic Assembly*, 14–22 July 2012, Mysore, India (C2.3-0009-12).

---

*http://nuclphys.sinp.msu.ru/neutrino/newtrino_s/baik.htm

Is Space-Time Curved?

Benjamin Prather

E-mail: benjamin.prather@gmail.com

This paper considers the possibility of a teleparallel approximation of general relativity where the underlying space-time of a compact massive source is related to the isotropic coordinate chart rather than the geometric chart. This results in a 20 percent reduction of the expected shadow radius of compact objects. The observation of the shadow radius of Sagittarius A* should be possible in the near future using VLBI. The theoretical reduction is within the uncertainty of the expected shadow radius, however any observation less than a critical radius would indicate that gravity is not the result of space-time curvature alone. If space-time curvature does not act alone it is simpler to adopt the teleparallel view, with the tetrad field representing the index of refraction of the required material field in a flat space-time.

Introduction

General relativity is highly successful in explaining the first order corrective terms to Newtonian gravity observed in the classical solar system test known at the time of its proposal. Further, it has predicted higher order effects not originally anticipated such as the orbital decay of binary pulsars. Any competing theory of gravity must agree with general relativity in these predictions. The bounds on these measurements have significantly improved since the introduction of general relativity [1].

The central tenant of general relativity is that gravity is a pseudo-force due to the curvature of space-time. This produces a theory lacking an absolute sense of parallelism. General relativity has been expressed as a teleparallel theory, thus restoring absolute parallelism [2].

The teleparallel equivalent of general relativity allows the curvature of a metric to be rephrased as contorsion in a flat space-time due to a tetrad field [2]. The geodesic equation becomes non-inertial forces as a result of the variation in the local index of refraction and motion the tetrad field represents.

This paper considers the implications of a teleparallel theory of gravity where the underlying space-time corresponds to a flattened version of the isotropic solutions rather than the usual geometric coordinates. This non-inertial flattening process produces pseudo-forces, which are taken to be actual forces due to the presence of a material field.

Globally, space-time is likely to be closer to a DeSitter space-time than the Minkowski space-time used in the limiting behaviour here. In this sense, space-time is demonstrably curved. The issue here is the local nature of space-time in the presence of strong gravitational fields.

1 Is space-time curved?

Despite its broad empirical success, and lack of any viable alternatives, general relativity continues to generate detractors who raise philosophical objections to its core propositions. These detractors, near or beyond the fringe of science, often lack the mathematical knowledge needed to properly discuss general relativity in a rigorous setting. Indeed, many of these objections stem from a rejection of the abstract mathematics required for general relativity or perceived errors in general relativity arising from subtle misunderstandings of these advanced notions.

The descendants of neo-Kantianism assert that space-time curvature caused by matter and energy is impossible, since matter and energy already require the concepts of space and time. A Galilean space-time is also claimed by these critics to be necessary to form an understanding of the world [3].

As Lie groups, however, the Poincaré group is equally descriptive as the Galilean group. These differences in symmetries can be empirically measured, strongly favouring a Minkowskian space-time over a Galilean space-time. In both geometries it is almost always helpful to select a convenient fixed frame to work within. General relativity, in its usual presentation, breaks this Lie symmetry globally.

General relativity can also be expressed as a teleparallel theory, restoring absolute parallelism by replacing the curvature of space with an embedded tetrad field. Tetrad fields can be viewed as representing the flow and refractive properties of a Lorentzian aether.

In classical fluid mechanical one can use a Lagrangian reference frame co-moving with a fluid or an inertial Eulerian reference frame. In a relativistic aether, using the Levi-Civita connection produces the Lagrangian description while using the Weitzenböck connection produces the Eulerian description.

The geodesic equation then becomes changing speed due to an index of refraction, bending due to Huygens' principle and frame dragging due to advection. In the teleparallel equivalent of general relativity this tetrad field exists as an independent structure. This can be viewed as a flowing index of refraction emerging in the absence of a refractive medium.

This theory can be bashed into a flat model using a non-inertial transformation. The use of a non-inertial reference

frame introduces pseudo-forces to the equations of motion. Interpreting these forces as originating from a material field creates a flat theory of gravity while simultaneously providing a material medium responsible for the tetrad field.

It is in this sense that the question is raised, is space-time curved?

2 Flat teleparallel approximation

In general relativity, the gravity of a compact, spherically symmetric, uncharged, acceleration-free and isolated mass generates can be described by the well known Schwarzschild metric in spherical coordinates.

$$r_s = \frac{2GM}{c^2}, \tag{1}$$

$$\mathbf{g}_{ij} = \text{diag}\left(\left(1 - \frac{r_s}{r}\right)c^2, \left(1 - \frac{r_s}{r}\right)^{-1}, r^2, r^2 \sin^2\theta\right). \tag{2}$$

This solution implies that the speed of light depends on the angle of inclination of the trajectory relative to the coordinate chart. It is possible to transform the radial component to a new chart where the speed of light is isotropic [4].

$$r = r'\left(1 + \frac{r_s}{4r'}\right), \qquad r' = r\left(\frac{1}{2} - \frac{r_s}{4r} + \sqrt{\frac{1}{4}\left(1 - \frac{r_s}{r}\right)}\right), \tag{3}$$

$$\mathbf{g}_{ij} = \left(1 + \frac{r_s}{4r'}\right)^4 \text{diag}\left(\frac{(4r' - r_s)^2}{(4r' + r_s)^6}c^2, 1, r^2, r^2 \sin^2\theta\right). \tag{4}$$

A flat teleparallel approximation of general relativity can be made by eliminating the $\left(1 + \frac{r_s}{4r'}\right)^4$ coefficient. This results in a flat space-time with an index of refraction.

$$\mathbf{g}_{ij} = \text{diag}\left(\frac{(4r' - r_s)^2}{(4r' + r_s)^6}c^2, 1, r^2, r^2 \sin^2\theta\right). \tag{5}$$

Determining the pseudo-forces caused by this non-inertial transformation, much less the fields needed to generate them, is beyond the scope of this paper. All that is of interest here is that a model should exist with this geometry in the limit of the Schwarzschild metric, and has an event horizon a quarter the size of general relativity.

Bashing the Schwarzschild metric into a flat teleparallel theory may be a convenient way to get a model that agrees with observation, but is a very ad hoc way to approach the problem. A far better approach would be to build a teleparallel theory from the ground up based on first principles. Once the numerous obstacles are overcome, any resulting theory will agree with general relativity in the weak field limit.

This would require differences in the strong field limit to distinguish between theories. Given the significant change in event horizon radius, the optical shadow radius of a compact object should provide a useful parameter to compare potential theories in the strong field limit.

3 Optical shadow, General Relativity

An image showing the neighbourhood of the singularity, including the event horizon, photon sphere and optical shadow is given in Figure 1.
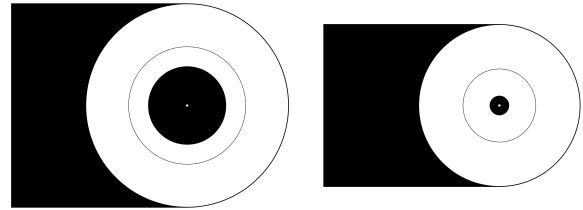

Fig. 1: Singularity Neighbourhood. The neighbourhood of a compact gravitational source is shown, with the Schwarzschild solution to the left and the flattened version to the right. The central black circle represents the event horizon, with a white circle showing the location of the singularity. This is surrounded by a thin circle representing the photon sphere. The outermost circle represents the optical shadow of the black hole, which is shown extending to the left using a tangent line approximation.

The depicted shadow region is a right circular cylinder with the singularity on its axis. The optical radius can be defined as the largest radius such that no unbound trajectory can have both an infinite length within the depicted shadow region and avoid the event horizon. In general relativity, the optical radius is $r_{crit} = \frac{3}{2}\sqrt{3}\, r_s$ [5].

4 Optical shadow, flat teleparallel approximation

In the flat teleparallel approximation, the dynamics are expected to be identical except for a rescaling of the radius near the singularity.

Almost all of the shadowing effect occurs near the singularity. An estimate of the asymptotic trajectory can be made using a tangent line to a circle about the singularity with a radius of r_{crit}. The radius of this circle is transformed by (3).

$$r'_{crit} = r_{crit}\left(\frac{1}{2} - \frac{1}{6\sqrt{3}} + \sqrt{\frac{1}{4}\left(1 - \frac{2}{3\sqrt{3}}\right)}\right) \approx 0.8\, r_{crit}. \tag{6}$$

This reduction in radius is accomplished by the forces generated by a material component of the gravitational field.

5 VLBI measurements

Expected advances in submillimetre very long baseline interferometry are expected to be able to soon resolve the optical shadow of the compact radio source Sagittarius A*, based on the size expected by general relativity [5]. The factor of 0.8 is close enough to unity that the flat teleparallel approximation should produce a visible shadow under similar assumptions.

Observing the optical shadow is confounded by several known issues, much less measuring the radius. The optical

properties of the medium surrounding Sagittarius A*, the 20 percent uncertainty in the mass of and distance to Sagittarius A* and the 10 percent uncertainty introduced by the dependency on the optical shadow on the rotation of Sagittarius A* are three significant issues [5].

A successful imaging of the shadow could help to determine some of these uncertainties, allowing a determination to be made between general relativity and any potential teleparallel theory including a material gravitational field.

While other effects can account for an optical shadow larger than r_{crit} within general relativity, an optical shadow less than $r_{crit} = 30 \pm 7\mu_{as}$ cannot be reconciled with general relativity [5].

6 Conclusion

Given that the event horizon in the flat teleparallel approximation is a quarter of that predicted by general relativity, the reduction in optical shadow of 20 percent is a disappointingly small change. This is less than the expected uncertainty in the optical shadow of Sagittarius A* due to its uncertain mass and possible rotation.

This also means that the same assumptions for observing the shadow expected for general relativity using VLBI can be applied to the flat teleparallel approximation. Such measurements can be expected on the order of years, not centuries.

This reduction would vary for different models of the material gravitational field, possibly resulting in a smaller optical radius. This would confound the ability to observe the optical shadow but simplify the ability to distinguish the predictions of general relativity and the model in question.

While other effects can account for an optical shadow larger than r_{crit} within general relativity, an optical shadow less than r_{crit} would indicate that gravity is not determined by space-time curvature alone.

The teleparallel equivalent of general relativity phrases the effects of gravity as due to an index of refraction in a flat space-time. If this is not acting alone, it is simpler to view this index of refraction as a property of the material field required to explain the super compact optical shadow.

If a super compact optical shadow is demonstrated, space-time curvature should then be abandoned in favour of a material, refractive gravitational field in a flat or DeSitter space-time.

References

1. Will C. M. 2006 Confrontation between GR and experiment. *Living Rev. Relativity*, 2006, v.9(3), (cited on 6/5/2013: http://relativity.livingreviews.org/Articles/lrr-2006-3/)

2. Aldrovandi R., Pereira J.G. An Introduction to Teleparallel Gravity. Springer, New York, 2013

3. D.H. et al. 2013 Criticism of the theory of relativity. *Wikipedia* (cited on 6/5/2013, oldid=551162068)

4. Buchdahl H. A. Isotropic coordinates and Schwarzschild metric. *Int. J. Theor. Phys.*, 1985, v.24, 731–739.

5. Falcke H., Melia F., Agol E., Viewing the Shadow of the Black Hole at the Galactic Center. *Astrophys. J.*, 2000, v.528, L13–L16.

LETTERS TO
PROGRESS IN PHYSICS

LETTERS TO PROGRESS IN PHYSICS

Comment on N. A. Kozyrev's "Possibility of Experimental Study of the Properties of Time"

Joseph C. Hafele

Retired Physicist; Home Office: 618 S. 24th St., Laramie, WY, USA
E-mail: cahafele@bresnan.net

More than 60 years ago, N. A. Kozyrev predicted the need for a second universal velocity, one that is associated with rotational motion, in addition to the well-known first universal velocity, the velocity of light, which is associated with linear motion. Kozyrev predicted that there should be additional forces which act along the axis of rotation and are on the order of 10^{-4} or 10^{-5} of the applied forces. For the neoclassical causal theory (Hafele J. C. *Zelm. Journ.*, 2012, v. 5, 134), the values for the ratios for the Moon are in order of magnitude consistent with Kozyrev's predicted ratios.

The neoclassical causal version for Newtonian gravitational theory requires a hypothetical induction field F_λ and a corresponding induction speed v_k [1]. The purpose of this letter is to indicate that, more than 60 years ago, N. A. Kozyrev developed a similar concept for rotational motion in classical Newtonian theory [2].

The experimental verification of Kozyrev's theoretical concepts started in the winter of 1951–1952. Kozyrev stipulates: 1) the velocity of light is a universal velocity that is to be associated with linear motion, and 2) there should be a second universal velocity that is associated with rotational motion. In his notation, c_1 is the known speed of light, and c_2 is an unknown rotational universal speed.

The following is a direct quote from page 199 of Kozyrev's article [2]:

> "Now, utilizing the Plank constant in any scalar universal constant, it is necessary to obtain a value having the dimensionality of velocity. It is easy to establish that the expression
>
> $$c_2 = \frac{\alpha e^2}{h} = \alpha \times 350 \text{ km/sec} \qquad (7)$$
>
> comprises a unique combination of this type. Here e equals the charge of an elementary particle and α equals a certain dimensionless factor. Then, based on (6), at $u = 100$ m/s, the additional forces will be of the order of 10^{-4} or 10^{-5} (at a considerable α-value) from the applied forces."

Kozyrev defines u to be the linear velocity of the rotating object. He finds that the value for $\alpha \cong 2$, and the value for $c_2 \cong 7 \times 10^5$ m/s $\cong 2.3 \times 10^{-3} c_1$ [2, p. 203]. He predicts that a small additional force is proportional to $u/c_2 \cong 100/7 \times 10^5 \cong \cong 1.4 \times 10^{-4}$ [2, p.198], which is the basis for his "of the order of 10^{-4} or 10^{-5}". (The numerical value for e^2/h, 350 km/s, is calculated according to CGS system of units.)

For the neoclassical causal theory, the ratio of the transverse to the radial field for the NEAR flyby at perigee,

$g_{\mathrm{trt}}/g_\mathrm{r} \cong 4 \times 10^{-6}$ [1, p.169]. A better comparison with Kozyrev's theory is obtained by using the case for the Moon, where the orbital motion is nearly circular [1, p.172]. Let v_{co} be the orbital speed for an equivalent circular orbit. Then

$$v_{\mathrm{co}} \cong 1 \times 10^3 \text{ m/s}, \qquad \frac{v_{\mathrm{co}}}{c_2} \cong 1.4 \times 10^{-3},$$

which is within one order of magnitude of Kozyrev's u/c_2. Let $\langle g_{\mathrm{trt}} \rangle$ be the RMS average value for the time-retarded transverse field for the Moon, and let $\langle F_\lambda \rangle$ be the RMS average value for the induction field. Then

$$\langle g_{\mathrm{trt}} \rangle \cong 1 \times 10^{-11} \text{ m/s}, \quad \langle F_\lambda \rangle \cong 1.4 \times 10^{-14} \text{ m/s},$$

$$\frac{\langle F_\lambda \rangle}{\langle g_{\mathrm{trt}} \rangle} \cong 1.4 \times 10^{-3}.$$

These results show that the relative ratios for the secondary fields are close to the same order of magnitude as they are for Kozyrev's theory.

More than 60 years ago, N. A. Kozyrev could not have known about recently discovered flyby anomalies and a lunar orbit anomaly, but he did have an uncanny insight that has now been brought to fruition. If more attention had been paid to Kozyrev's theory, it may have preempted the neoclassical causal theory. It may also be helpful in designing a ground-based instrument for detecting the Earth's time-retarded transverse gravitational field.

References

1. Hafele J. C. Earth flyby anomalies explained by a time-retarded causal version of Newtonian gravitational theory. *The Abraham Zelmanov Journal*, 2012, v. 5, 134–187.

2. Kozyrev N. A. Possibility of experimental study of the properties of time. *The Abraham Zelmanov Journal*, 2012, v. 5, 188–220.

LETTERS TO PROGRESS IN PHYSICS

Commentary Relative to the Emission Spectrum of the Solar Atmosphere: Further Evidence for a Distinct Solar Surface

Pierre-Marie Robitaille

Department of Radiology, The Ohio State University, 395 W. 12th Ave, Columbus, Ohio 43210, USA.
robitaille.1@osu.edu

The chromosphere and corona of the Sun represent tenuous regions which are characterized by numerous optically thin emission lines in the ultraviolet and X-ray bands. When observed from the center of the solar disk outward, these emission lines experience modest brightening as the limb is approached. The intensity of many ultraviolet and X-ray emission lines nearly doubles when observation is extended just beyond the edge of the disk. These findings indicate that the solar body is opaque in this frequency range and that an approximately two fold greater region of the solar atmosphere is being sampled outside the limb. These observations provide strong support for the presence of a distinct solar surface. Therefore, the behavior of the emission lines in this frequency range constitutes the twenty fifth line of evidence that the Sun is comprised of condensed matter.

> *Every body has a surface.*
> St. Thomas Aquinas [1]

Observationally, the chromosphere of the Sun represents a rarefied region located immediately above the solar surface [2–5]. In 1877, Father Angelo Secchi described the chromosphere in detail including, most notably, a description of its spicules [6, p. 31-36]. For just a few seconds prior to and following the onset of totality during solar eclipses, the "flash" emission spectrum of the chromosphere can be detected. Typically, such studies focus on the visible and ultraviolet regions of the electromagnetic spectrum.

The existence of the visible "flash" spectrum has been known since the early days of spectral analysis. In fact, the famous D3 line, first observed in a prominence during an eclipse, would lead to the discovery of helium on the Sun by Pierre Jules César Janssen and Joseph Norman Lockyer [7, 8]. Since then, great attention has been given to identifying the lines which are contained within the flash spectrum of the chromosphere, particularly through the efforts of astronomers like John Evershed [9, 10] and Donald Menzel [11, 12]. In 1909, George Ellery Hale and Walter Adams photographed the flash spectrum outside of eclipse conditions, opening up new avenues for the study of the chromosphere [13, 14]. Today, spectroscopic emission lines in the visible spectrum of the chromosphere and corona continue to be relevant and spectacular images of the solar atmosphere have now been obtained using spectroscopic lines from highly ionized iron (e.g. FeX–FeXIV) [15–18].

Photographing the chromosphere is slightly more complex in the ultraviolet range, since UV light is absorbed by the Earth's atmosphere. As a result, that spectral region of the flash spectrum could not be sampled until the launch of scientific rockets after World War II [3, p. 180]. In 1946, while at the U.S. Naval Research Laboratory, Baum, Johnson, Oberly, Rockwood, Strain and Tousey [19] obtained the first measurements of the Sun's ultraviolet spectrum using a V2 rocket. A flurry of activity in this area soon followed [20–25] and the ultraviolet spectrum of the Sun has now become a field of great scientific interest [26–28].
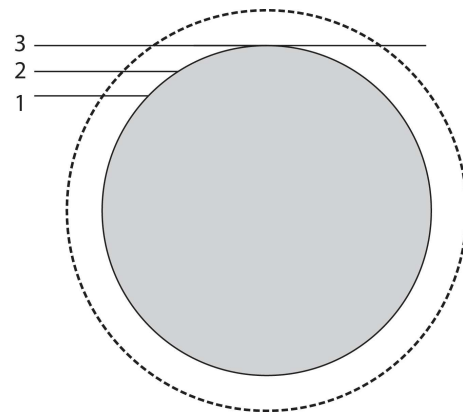

Fig. 1: Schematic representation of path lengths present when the outer atmosphere (area outlined by dashes) of the Sun (body in gray) is viewed from the Earth. Paths 1 and 2 terminate on the solar surface. Just beyond the limb, path 3 samples the front and back side of the solar atmosphere, resulting in a two fold increase in line intensity. This figure is an adaptation based on Fig. 2.4 in [28].

An elementary observation constitutes the focus of this work: the intensity of ultraviolet and X-ray emission lines increases dramatically, as observations are moved from the center of the solar disk to the limb of the Sun. The problem is illustrated in Figure 1. Harold Zirin describes the associated findings as follows: *"The case in the UV is different, because the spectrum lines are optically thin. Therefore one*

would expect limb brightening even in the absence of temperature increase, simply due to the secant increase of path length. Although the intensity doubles at the limb, where we see the back side, the limb brightening inside the limb is minimal . . . Similarly, X-ray images show limb brightening simply due to increased path length." [29]. This situation is observed both in the ultraviolet and in the X-ray spectrum of the Sun which sample processes in the chromosphere and the corona [28, p. 38-39]. An exquisite image of this effect has been published [28, p. 38].

Though this simple observation appears almost trivial as a source of scientific comment, it nonetheless demands attention; for it provides strong evidence that the body of the Sun is not gaseous in nature. If the Sun is gaseous, then these effects should not be visible as sampling extends beyond the solar limb. As such, this observation constitutes the twenty fifth line of evidence that the Sun is comprised of condensed matter (see [30–32] and references therein for the others).

Dedication

This work is dedicated to Amir Abduljalil in recognition of his many years of faithful scientific collaboration throughout my career in magnetic resonance imaging, and for his undying service to The Ohio State University relative to the design, assembly, and operation of the world's first ultra high field magnetic resonance imaging system [33].

References

1. Aquinas T. Summa Theologica — V. 1, Part 1, Question 7 — *On the Infinity of God*, Cosimo Inc., New York, 2007, Art. 3, p. 32.

2. Thomas R.N. and Athay R.G. Physics of the Solar Chromosphere: Monographs and Texts in Physics and Astronomy - Vol. VI. Interscience Publishers, Inc., New York, N.Y., 1961.

3. Bray R.J. and Loughhead R.E. The Solar Chromosphere. Chapman and Hall Ltd., London, U.K., 1974.

4. Heinzel P. Understanding the solar chromosphere. In: *"Exploring the Solar System and the Universe"*, (V. Mioc, C. Dumitrache, N.A. Popescu, Eds.), American Institute of Physics, 2008, 238–244.

5. Athay R.G. The solar chromosphere and corona: Quiet Sun. D. Reidel Publishing Company, Dordrecht, Holland, 1976.

6. Secchi A. Le Soleil (2nd Edition, Part II). Guathier-Villars, Paris, 1877.

7. Janssen J. Indications de quelques-uns des résultats obténus à Guntoor, pendant l'éclipse du mois d'aôut dernier. *Compte Rendus*, 1868, v. 67, 838–39.

8. Lockyer J.N. Notice of an observation of the spectrum of a solar prominence. *Proc. Roy. Soc. London*, 1868, v. 17, 91–92.

9. Evershed J. Wave-length determinations and general results obtained from a detailed examination of spectra photographed at the solar eclipse of January 22, 1898. *Phil. Trans. Roy. Soc. London*, 1901, v. 197, 381–413.

10. Evershed J. Preliminary report of the expedition to the south limit of totality to obtain photographs of the flash spectrum in high solar latitudes. *Proc. Roy. Soc. London*, 1900, v. 67, 370–385.

11. Menzel D.H. A Study of the Solar Chromosphere. *Publications of the Lick Observatory*, University of California Press, Berkeley, CA, v. 17, 1931.

12. Menzel D.H. and Cillié G.G. Hydrogen emission in the chromosphere. *Astrophys. J.*, 1937, v. 85, 88–106.

13. Hale G.E. and Adams W.S. Photography of the "flash" spectrum without an eclipse. *Astrophys. J.*, 1909, v. 30, 222–230.

14. Adams W.S. and Burwell C.G. The flash spectrum without an eclipse region $\lambda 4800$–$\lambda 6600$. *Astrophys. J.*, 1915, v. 41, 116–146.

15. Wood B.E., Karovska M., Cook J.W., Brueckner G.E., Howard R.A., Korendyke C.M. and Socker D.G. Search for brightness variations in FeXIV coronagraph observations of the quiescent solar corona. *Astrophys. J.*, 1998, v. 505, 432–442.

16. Habbal S.R., Druckmüller M., Morgan H., Daw A., Johnson J., Ding A., Arndt M., Esser R., Rušin V. and Scholl I. Mapping the distribution of electron temperature and Fe charge states in the corona with total solar eclipse observations. *Astrophys. J.*, 2010, v. 708, 1650–1662.

17. Habbal S.R., Druckmüller M., Morgan H., Scholl I., Rušin V., Daw A., Johnson J. and Arndt M. Total solar eclipse observations of hot prominence shrouds. *Astrophys. J.*, 2010, v. 719, 1362–1369.

18. Habbal S.R., Morgan H. and Druckmüller M. A new view of coronal structures: Implications for the source and acceleration of the solar wind – First Asia-Pacific Solar Physics Meeting. *ASI Conf. Ser.*, 2011, v. 2, 259–269.

19. Baum W.A, Johnson F.S., Oberly J.J., Rockwood C.C., Strain C.V. and Tousey R. Solar ultraviolet spectrum to 88 km. *Phys. Rev.*, 1946, v. 70, 781–782.

20. Tousey R. The extreme ultraviolet spectrum of the Sun. *Space Sci. Reviews*, 1963, v. 2, 3-69.

21. Zirin H. and Dietz R.D. The structure of the solar chromosphere I. A picture based on extreme ultraviolet, millimeter, and λ 10830 data. *Astrophys. J.*, 1963, v. 138, 664–679.

22. Pottasch S.R. On the interpretation of the solar ultraviolet emission line spectrum. *Space Sci. Reviews*, 1964, v. 3, 816–855.

23. Pottasch S.R. On the iron lines observed in the solar ultraviolet spectrum. *Bull. Astr. Inst. Netherlands*, 1966, v. 18, 237-246.

24. Goldberg L. Ultraviolet and X-Rays from the Sun. *Ann. Reviews Astron. Astrophys.*, 1967, v. 5, 279–324.

25. Doscheck G.A., Meekins J.F., Kreplin R.W., Chubb T.A., and Friedman H. Iron-line emission during solar flares. *Astrophys. J.*, 1971, v. 170, 573–586.

26. Dwivedi B.N. EUV spectroscopy as a plasma diagnostic. *Space Sci. Reviews*, 1994, v. 65, 289–316.

27. Feldman U. and Widing K.G. Elemental abundances in the solar upper atmosphere derived from spectroscopic means. *Space Sci. Reviews*, 2003, v. 107, 665-720.

28. Phillips K.J.H., Feldman U. and Landi E. Ultraviolet and X-Ray Spectroscopy of the Solar Atmosphere: Cambridge Astrophysics Series - Vol. 44, Cambridge University Press, Cambridge, U.K., 2008.

29. Zirin H. The mystery of the chromosphere. *Solar Phys.*, 1996, v. 169, 313–326.

30. Robitaille P.M. Liquid Metallic Hydrogen: A Building Block for the Liquid Sun. *Progr. Phys.*, 2011, v. 3, 60–74.

31. Robitaille J.C. and Robitaille P.M. Liquid Metallic Hydrogen III. Intercalation and Lattice Exclusion Versus Gravitational Settling and Their Consequences Relative to Internal Structure, Surface Activity, and Solar Winds in the Sun. *Progr. Phys.*, 2013, v. 2, 87-97.

32. Robitaille P.M. Commentary on the liquid metallic hydrogen model of the Sun. Insight relative to coronal rain and splashdown events. *Progr. Phys.*, 2013, v. 2, L10–L11.

33. Robitaille P.M., Abduljalil A.M., Kangarlu A., Zhang X., Yu Y., Burgess R., Bair S., Noa P., Yang L., Zhu H., Palmer B., Jiang Z., Chakeres D.M. and Spigos D. Human magnetic resonance imaging at 8 T. *NMR Biomed.*, 1998, v. 11, no. 6, 263–265.

LETTERS TO PROGRESS IN PHYSICS

The Liquid Metallic Hydrogen Model of the Sun and the Solar Atmosphere I. Continuous Emission and Condensed Matter Within the Chromosphere

Pierre-Marie Robitaille

Department of Radiology, The Ohio State University, 395 W. 12th Ave, Columbus, Ohio 43210, USA.
robitaille.1@osu.edu

The continuous spectrum of the solar photosphere stands as the paramount observation with regard to the condensed nature of the solar body. Studies relative to Kirchhoff's law of thermal emission (e.g. Robitaille P.-M. Kirchhoff's law of thermal emission: 150 years. *Progr. Phys.*, 2009, v. 4, 3–13.) and a detailed analysis of the stellar opacity problem (Robitaille P.M. Stellar opacity: The Achilles' heel of the gaseous Sun. *Progr. Phys.*, 2011, v. 3, 93–99) have revealed that gaseous models remain unable to properly account for the generation of this spectrum. Therefore, it can be stated with certainty that the photosphere is comprised of condensed matter. Beyond the solar surface, the chromospheric layer of the Sun also generates a weak continuous spectrum in the visible region. This emission exposes the presence of material in the condensed state. As a result, above the level of the photosphere, matter exists in both gaseous and condensed forms, much like within the atmosphere of the Earth. The continuous visible spectrum associated with the chromosphere provides the twenty-sixth line of evidence that the Sun is condensed matter.

In order to explain the occurrence of the dark lines in the solar spectrum, we must assume that the solar atmosphere incloses a luminous nucleus, producing a continuous spectrum, the brightness of which exceeds a certain limit. The most probable supposition which can be made respecting the Sun's constitution is, that it consists of a solid or liquid nucleus, heated to a temperature of the brightest whiteness, surrounded by an atmosphere of somewhat lower temperature.

Gustav Robert Kirchhoff, 1862 [1]

When Gustav Kirchhoff was contemplating the origin of the solar spectrum [1], he was probably unaware that structures beyond the photosphere also had the ability to emit continuous spectra. Still, he understood that continuous thermal emission was a property of the condensed state [1]. Gases emit in bands [2] and even compressed gases cannot produce the required thermal spectrum, outside the confines of an enclosure and in the absence of a perfect absorber [3, 4].

Despite these physical realities, over the course of the past 150 years, scientists have moved away from Kirchhoff's realization that the solar surface must be comprised of condensed matter. Instead, gaseous solar models were adopted (e.g. [5, 6]). Sadly, Kirchhoff himself enabled this misstep through his erroneous formulation of the law of thermal emission (see [3, 4] and references therein). Discounting problems with the law of emission [3, 4], it can be said that the gaseous models have been based on a false premise: that the thermal spectrum of the Sun could be generated using a vast combination of non-thermal processes [7]. The solar opacity problem [7] reflects the fact that the gaseous models can never

properly account for the thermal spectrum. The generation of a continuous solar spectrum has become an insurmountable hurdle for these models [7]. Though gaseous opacity calculations have been used in an attempt to account for the Sun's emission, such calculations are of no value in mirroring the simple graphitic spectrum on Earth, which the solar spectrum strongly emulates. Therefore, gaseous opacity calculations cannot have any lasting merit in generating the continuous spectrum of the Sun [7]. The emission of a thermal spectrum requires an underlying thermal mechanism, not a large sum of non-thermal processes [7]. Condensed matter is required, as illustrated by earthly black bodies (see [3,4] and references therein). In fact, the continuous spectrum of the Sun acts as the most important line of evidence that the Sun is condensed matter (see [8–14] and references therein). This was recognized long ago by Gustav Kirchhoff: gases cannot properly account for the solar spectrum [1].

The presence of continuous thermal emission by the photosphere is complemented in the outer atmosphere of the Sun. The chromosphere also supports weak continuous emission. Hence, an additional line of evidence that the Sun is comprised of condensed matter can be harvested by extending Kirchhoff's insight to the solar atmosphere, above the photospheric surface.

The weak continuous spectrum of the chromosphere [15–18] has drawn the attention of solar observers for over 100 years [19–22]. The great astronomer, Donald Howard Menzel [23], commented as follows on its nature: *"...we assumed that the distribution in the continuous chromospheric spectrum is the same as that of a black body at 5700°, and*

that the continuous spectrum from the extreme edge is that of a black body at 4700°. There is evidence in favor of a lower temperature at the extreme limb in the observations by Abbot, Fowle, and Aldrich of the darkening towards the limb of the Sun" [22]. From early days, the continuous chromospheric spectrum was known to vary in temperature with height [24–27]. Consequently, solar observers rapidly introduced temperature variations with increasing height into their atmospheric models (e.g. [17, p. 187-213]; [18, p. 271–352]; [24–31]).

At the same time, problems remained surrounding the formation of the weak continuous chromospheric spectrum. This layer of the Sun, in the context of the modern gaseous models, had an average density of only $\sim 10^{-12}$ g/cm^3 [32, p. 32]. In fact, as one proceeds out from the photosphere to the top of the chromosphere, the density was hypothesized to be changing from $\sim 10^{-7}$ g/cm^3 to $\sim 10^{-15}$ g/cm^3, respectively [33]. It was known that in the chromosphere *"...the intensity of the emitted radiation is several tens of thousand times less than that of the photosphere"* [32, p. 32]. As a result, since the gas models were reducing photospheric densities to the levels of laboratory vacuums, the chromospheric densities had to be even lower.

In order to explain the continuous chromospheric spectrum, theoretical approaches (e.g. [16, 25–27]) exactly paralleled the methods applied for treating the emission from the photosphere (see [7] for a complete discussion). In early contributions, attention focused on neutral H, H$^-$, Rayleigh scattering, and electron scattering (see [17, p. 151–157] and [26, 27]). This was precisely because, devoid of condensed matter, no other mechanism could be invoked. A continuous spectrum, from which Menzel had extracted black body temperatures [22], was being explained using processes unrelated to any experimental production of a thermal spectrum on Earth [7]. Such approaches remain in use, but have already been dismissed relative to explaining the occurrence of continuous spectra [7].

Conversely, the position is now adopted that the presence of a continuous spectrum in the visible range within the chromosphere [15–18] represents a direct manifestation of condensed matter in this region of the solar atmosphere. The proper means of explaining continuous emission in the visible region of the electromagnetic spectrum, especially when it can be hypothesized to hold a thermal lineshape [22], will always remain linked to the presence of condensed matter [7].

The chromosphere corresponds to a region of the Sun where hydrogen atoms are re-entering the condensed state, prior to their recombination with photospheric material.

However, unlike the liquid metallic hydrogen advanced to be present in the solar body [8–14], chromospheric condensed matter appears to lack metallic properties. Chromospheric material, though in the condensed state, might therefore be substantially different than photospheric material. Nonetheless, though the continuous spectrum of the chromosphere remains weak, it demonstrates the presence of condensed matter within a gaseous matrix, much like drops of water can exist within the gaseous atmosphere of the Earth. In this regard, the intensity of the chromospheric emission spectrum can provide some sense of material densities in this layer. The presence of a continuous visible thermal spectrum in the chromosphere thereby constitutes the twenty-sixth line of evidence (and the sixth Planckian proof [34]) that the Sun is comprised of condensed matter (see [8–14] and references therein for the others).

Dedication

This work is dedicated to Marge Marrone, for her friendship and example in leading a joyous life.

References

1. Kirchhoff G. The physical constitution of the Sun. In: *Researches on the Solar Spectrum and the Spectra of the Chemical Elements*. Translated by H.E. Roscoe, Macmillan and Co., Cambridge, 1862, p. 23.

2. Robitaille P.M. The little heat engine: Heat transfer in solids, liquids, and gases. *Progr. Phys.*, 2007, v. 4, 25–33.

3. Robitaille P.M. Blackbody radiation and the carbon particle. *Progr. Phys.*, 2008, v. 3, 36–55.

4. Robitaille P.M. Kirchhoff's law of thermal emission: 150 years. *Progr. Phys.*, 2009, v. 4, 3–13.

5. Bahcall J.N. and Pinsonneault M.H. Standard solar models, with and without helium diffusion, and the solar neutrino problem. *Rev. Mod. Phys.*, 1992, v. 64, no.4, 885–926.

6. Bachall J.N., Pinsonneault M.H. and Wasserburg G.J. Solar models with helium and heavy-element diffusion. *Rev. Mod. Phys.*, 1995, v. 67, no. 4, 781–808.

7. Robitaille P.M. Stellar opacity: The Achilles heel of the gaseous Sun. *Progr. Phys.*, 2011, v. 3, 93–99.

8. Robitaille P.M. A high temperature liquid plasma model of the Sun. *Progr. Phys.*, 2007, v. 1, 70–81 (also in arXiv: astro-ph/0410075).

9. Robitaille P.M. Liquid metallic hydrogen: A building block for the liquid Sun. *Progr. Phys.*, 2011, v. 3, 60–74.

10. Robitaille P.M. Liquid metallic hydrogen II: A critical assessment of current and primordial helium levels in Sun. *Progr. Phys.*, 2013, v. 2, 35–47.

11. Robitaille J.C. and Robitaille P.M. Liquid metallic hydrogen III. Intercalation and lattice exclusion versus gravitational settling and their consequences relative to internal structure, surface activity, and solar winds in the Sun. *Progr. Phys.*, 2013, v. 2, 87–97.

12. Robitaille P.M. Commentary on the liquid metallic hydrogen model of the Sun: Insight relative to coronal holes, sunspots, and solar activity. *Progr. Phys.*, 2013, v. 2, L7–L9.

13. Robitaille P.M. Commentary on the liquid metallic hydrogen model of the Sun II. Insight relative to coronal rain and splashdown events. *Progr. Phys.*, 2013, v. 2, L10–L11.

14. Robitaille P.M. Commentary on the liquid metallic hydrogen model of the Sun III. Insight into solar lithium abundances. *Progr. Phys.*, 2013, v. 2, L12–L13.

15. Menzel D.H. A Study of the Solar Chromosphere. *Publications of the Lick Observatory*, University of California Press, Berkeley, CA, v. 17, 1931.

16. Thomas R.N. and Athay R.G. Physics of the Solar Chromosphere. Interscience Publishers, New York, N.Y., 1961.

17. Bray R.J. and Loughhead R.E. The Solar Chromosphere, Chapman and Hall, London, U.K., 1974.

18. Athay R.G. The Solar Chromosphere and Corona: Quiet Sun – Astrophysics and Space Science Library – v. 53. D. Reidel Publishing Company, Dordrecht, Holland, 1976.

19. Evershed J. Wave-length determinations and general results obtained from a detailed examination of spectra photographed at the solar eclipse of January 22, 1898. *Phil. Trans. Roy. Soc. London*, 1901, v. 197, 381–413.

20. Evershed J. Preliminary report of the expedition to the south limit of totality to obtain photographs of the flash spectrum in high solar latitudes. *Proc. Roy. Soc. London*, 1900, v. 67, 370–385.

21. Grotian W. Über die intensitätsverteilung des kontinuierlichen spektrums der inneren korona. *Zeitschrift fur Astrophysik*, 1931, v. 3, 199–226.

22. Menzel D.H. and Cillié G.G. Hydrogen emission in the chromosphere. *Astrophys. J.*, 1937, v. 85, 88–106.

23. Goldberg L. and Aller L.H. Donald Howard Menzel 1901–1976. In: *Biographical Memoires*, The National Academy of Sciences USA, 1991 (accessed online on 2/11/2013).

24. Athay R.G., Billings D.E., Evans J.W. and Roberts W.O. Emission in hydrogen Balmer lines and continuum in flash spectrum of 1952 total solar eclipse at Karthoum, Sudan. *Astrophys. J.*, 1954, v. 120, 94–111.

25. Athay R.G., Menzel D.H., Pecker J.C., and Thomas R.N. The thermodynamic state of the outer solar atmosphere V. A model of the chromosphere from the continuous emission. *Astrophys. J. Suppl. Ser.*, 1955, v. 1, 505–519.

26. Hiei E. Continuous spectrum in the chromosphere. *Publ. Astron. Soc. Japan*, 1963, v. 15, 277–300.

27. Weart S.R. and Faller J.E. Photoelectric eclipse observation of the continuum at the extreme solar limb. *Astrophys. J.*, 1969, v. 157, 887–901.

28. Gingerich O. and de Jager C. The Bilderberg model of the photosphere and low chromosphere. *Solar Phys.*, 1968, v. 3, 5–25.

29. Gingerich O., Noyes R.W., Kalkofen W. and Cuny Y. The Harvard-Smithsonian reference atmosphere. *Solar Phys.*, 1971, v. 18, 347–365.

30. Athay R.G. Boundary conditions on model solar chromospheres. *Solar Phys.*, 1969, v. 9, 51-55.

31. Fontenla J.M., Balasubramaniam K.S. and Harder J. Semiemperical models of the solar atmosphere II. The quiet-Sun low chromosphere at moderate resolution. *Astrophys. J.*, 2007, v. 667, 1243–1257.

32. Bhatnagar A. Instrumentation and observational techniques in solar astronomy. In: *Lectures on Solar Physics* (H.M. Antia, A. Bhatnagar and R. Ulmschneider, Eds.), Springer, Berlin, 2003, p. 27–79.

33. Ulmschneider P. The physics of the chromospheres and coronae. In: *Lectures on Solar Physics* (H.M. Antia, A. Bhatnagar and R. Ulmschneider, Eds.), Springer, Berlin, 2003, p. 232–280.

34. Robitaille P. Magnetic fields and directional spectral emissivity in sunspots and faculae: Complimentary evidence of metallic behavior on the surface of the Sun. *Progr. Phys.*, 2013, v. 1, 19–24.

LETTERS TO PROGRESS IN PHYSICS

The Liquid Metallic Hydrogen Model of the Sun and the Solar Atmosphere II. Continuous Emission and Condensed Matter Within the Corona

Pierre-Marie Robitaille

Department of Radiology, The Ohio State University, 395 W. 12th Ave, Columbus, Ohio 43210, USA.
robitaille.1@osu.edu

The K-corona, a significant portion of the solar atmosphere, displays a continuous spectrum which closely parallels photospheric emission, though without the presence of overlying Fraunhofer lines. The E-corona exists in the same region and is characterized by weak emission lines from highly ionized atoms. For instance, the famous green emission line from coronium (FeXIV) is part of the E-corona. The F-corona exists beyond the K/E-corona and, like the photospheric spectrum, is characterized by Fraunhofer lines. The F-corona represents photospheric light scattered by dust particles in the interplanetary medium. Within the gaseous models of the Sun, the K-corona is viewed as photospheric radiation which has been scattered by relativistic electrons. This scattering is thought to broaden the Fraunhofer lines of the solar spectrum such that they can no longer be detected in the K-corona. Thus, the gaseous models of the Sun account for the appearance of the K-corona by distorting photospheric light, since they are unable to have recourse to condensed matter to directly produce such radiation. Conversely, it is now advanced that the continuous emission of the K-corona and associated emission lines from the E-corona must be interpreted as manifestations of the same phenomenon: condensed matter exists in the corona. It is well-known that the Sun expels large amounts of material from its surface in the form of flares and coronal mass ejections. Given a liquid metallic hydrogen model of the Sun, it is logical to assume that such matter, which exists in the condensed state on the solar surface, continues to manifest its nature once expelled into the corona. Therefore, the continuous spectrum of the K-corona provides the twenty-seventh line of evidence that the Sun is composed of condensed matter.

In order to explain the occurrence of the dark lines in the solar spectrum, we must assume that the solar atmosphere incloses a luminous nucleus, producing a continuous spectrum, the brightness of which exceeds a certain limit. The most probable supposition which can be made respecting the Sun's constitution is, that it consists of a solid or liquid nucleus, heated to a temperature of the brightest whiteness, surrounded by an atmosphere of somewhat lower temperature.

Gustav Robert Kirchhoff, 1862 [1]

Providence has made of the pastoral State of Iowa one of the most important locations in the history of solar physics. From primitive observatories in Des Moines and Burlington respectively, William Harkness and Charles Young monitored the total eclipse of August 7, 1869 [2, 3], an event which still has the power to redefine our understanding of the corona.

From the heart of Iowa, William Harkness _"obtained a coronal spectrum that was continuous except for a single bright green line, later known as the coronal line K1474"_ on the Kirchhoff scale [3, p. 199]. Harkness concluded that the corona was _"a highly rarefied self-luminous atmosphere surrounding the Sun, and, perhaps, principally composed of_ _the incandescent vapor of iron"_ [3, p. 199]. Eventually, John Evershed provided additional photographic evidence that the corona displayed a continuous spectrum without Fraunhofer lines and he established the wavelength of Harkness' K1474 coronal line at 5303.3 Å [4]. In addition, Evershed would document the presence of two other coronal spectral lines [2–4]. Today, the gaseous models of the Sun do not support the idea that the corona of the Sun is self-luminous. Rather, it is currently believed that the continuous coronal spectrum arises from the scattering of photospheric light by relativistic electrons in the outer solar atmosphere. In this work, Harkness' conclusion will be re-evaluated, with the intent of demonstrating that the K-corona is indeed self-luminous, as first postulated in 1869 [3, p. 196–205].

To begin understanding the corona, it is important to properly classify the spectra which it produces. It was the spectrum of the inner corona, or K-corona, which was measured long ago by Harkness, Young, and Evershed [2–4] and which has been the subject of several classic reports [5–10]. For nearly one hundred years, the inner coronal spectrum was known to be polarized [6, 10]. According to Bernard Lyot, this polarization did not extend beyond $\sim 6'$ from the limb, increased rapidly as observations were made towards the Sun,

and remained constant within ∼ 3′ of the solar surface [6].*
Textbooks now state that the polarized K-corona can extend
to distances approaching 10 solar radii (∼ 160′) [12, p. 187].

As Gustav Kirchhoff understood [1], Fraunhofer lines are
produced when light is absorbed by gaseous atoms located
above the level of the solar surface where the continuous pho-
tospheric spectrum is emitted. The absorption of light by
these atoms superimposes dark lines onto the thermal spec-
trum of the Sun. As a result, the photospheric spectrum is al-
ways characterized by the presence of Fraunhofer lines. Con-
versely, these dark lines are absent in the continuous spec-
trum of the inner corona [13–15]. This was certainly the find-
ing which convinced William Harkness that the corona was
self-luminous [3]. For if the inner corona was simply scatter-
ing light produced by the photosphere, the Fraunhofer lines
should be visible. This is the case in the outer corona, or F-
corona, where photospheric light is being scattered by dust
particles contained in the interplanetary medium [13, p. 33].

Within the gaseous models of the Sun, the absence of
Fraunhofer lines in the K-corona is explained by scattering
photospheric light with high energy electrons (see e.g. [13,
p. 33] and [16]. The corona in these models has no means
of directly generating a continuous spectrum. As a result,
gaseous models must assume that the continuous component
of coronal emission originates at the level of the photosphere.
Coronal electrons must then be used to broaden the Fraun-
hofer lines, making them disappear from the spectrum moni-
tored in the K-corona [13–16].

Oddly, while the gaseous models invoke electron based
scattering of Fraunhofer lines, causing them to disappear in
the K-corona, scattering by dust particles preserves the lines
of the F-corona. The situation is further complicated because
the K-corona is in the same physical space as the E-corona,
which is producing emission lines, including the coronal line
at 5303.3 Å [13–16]. The Fraunhofer lines are being broad-
ened by electrons in the K-corona, but emission lines from
the same region of the solar atmosphere, namely in the E-
corona, remain visible and sharp. Presumably, this occurs be-
cause only a small fraction of the photospheric light is being
scattered. By analogy, only a small fraction of the E-corona
should be scattered. Hence, it would not be expected that the
emission lines from the E-corona would be affected in a no-
ticeable manner.

The corona is so tenuous, its emission is ∼1–100 mil-
lion times less intense than that of the photosphere [13, 15].
Still, the continuous nature of its emission, and the absence
of Fraunhofer lines in the inner corona has been well docu-
mented [2–10].

Speaking of the continuous coronal spectrum, Athay et
al. would comment that *"It is well known (Grotrian 1931;
Allen 1946) that the coronal continuum is essentially a repro-*

*When visualized from the Earth, the solar diameter corresponds to
∼ 32′ or ∼ 1920″ [11]. One arc-second, (″), corresponds to ∼700 km on
the Sun [12, p. 123].

*duction of the photospheric continuum and does not change
color with height"* [9]. Yet, Grotrian's [5] and Ludendorff's
discovery (see [9]) that *"the color of the corona is the same as
that of the Sun"* was not completely supported by Allen [8].
In fact, Athay [9] was misquoting Allen [8]. The latter actu-
ally found that *"microphotograms for solar distances varying
from R=1.2s to R=2.6s show that the coronal radiation red-
dens slightly as the distance from the Sun is increased"* [8].
Allen's measurements had extended farther above the pho-
tosphere than those of Crotrian and Ludendorff, helping to
explain why his predecessors had not reported reddening [8,
p. 140].

Reddening of the continuous spectrum implied that the
corona was cooling when one moved away from the solar sur-
face, as would be expected. The presence of emission lines
from highly ionized atoms in the E-corona appeared to be
making the opposite point, the corona seemed to be much
warmer than the photosphere. This issue will be addressed in
detail in a separate treatment [17]. For the time being, suf-
fice it to emphasize that the K-corona possesses a continuous
spectrum which appears to be blackbody in nature and which
reddens slightly with distance from the solar surface.

In the end, the simplest means of accounting for the con-
tinuous emission observed in the K-corona, the absence of
overlying Fraunhofer lines, and the presence of sharp emis-
sion lines in this same region of the solar atmosphere, is to
invoke a condensed matter model of the Sun [18–20]. In
1869, William Harkness had concluded that the corona was
self-luminous, precisely as expected should this layer possess
condensed matter.

In this regard, when the Sun is active, it is known to expel
enormous amounts of material into its corona in the form of
flares and coronal mass ejections. Within the liquid metal-
lic hydrogen model of the Sun [18–20], the presence of con-
densed matter within the corona and the existence of an asso-
ciated continuous spectrum presents little difficulty, as metal-
lic hydrogen has already been hypothesized to be metastable
(see [17] for a detailed discussion). As a result, once con-
densed metallic hydrogen has been produced in the solar in-
terior, it is expected that it could retain its condensed state
under the lower pressures in the corona.

The presence of condensed matter in the K-corona imme-
diately accounts for the existence of a continuous spectrum
from this region of the solar atmosphere.

At the same time, the Fraunhofer lines are not visible be-
cause insufficient levels of gaseous atoms are present in the
K-corona to significantly absorb coronal radiation. There-
fore, scattering by relativistic electrons does not need to be
invoked to account for the presence of a continuous spectrum
in the K-corona devoid of Fraunhofer lines. Conversely, the
F-corona is indeed produced by the scattering of photospheric
light by dust particles in interplanetary space.

As such, the continuous spectrum of the K-corona can
be said to represent the twenty-seventh line of evidence that

the Sun is condensed matter and the seventh Planckian proof (see [21, 22] and references therein for the others).

Dedication

Dedicated to Thomas Kerner Helgeson and Barbarra Anne Helgeson who have shown the author, and provided him with, the very best from Iowa.

References

1. Kirchhoff G. The physical constitution of the Sun. In: *Researches on the Solar Spectrum and the Spectra of the Chemical Elements*. Translated by H.E. Roscoe, Macmillan and Co., Cambridge, 1862, p. 23.

2. Hufbauer K. Exploring the Sun: Solar Science since Galileo. The Johns Hopkins University Press, Baltimore, 1991, p. 112–114.

3. Dick S. Sky and Ocean Joined: The U.S. Naval Observatory 1830–2000. Cambridge University Press, Cambridge, 2003, p. 196-205.

4. Evershed J. Wave-length determinations and general results obtained from a detailed examination of spectra photographed at the solar eclipse of January 22, 1898. *Phil. Trans. Roy. Soc. London*, 1901, v. 197, 381–413.

5. Grotian W. Über die intensitätsverteilung des kontinuierlichen spektrums der inneren korona. *Zeitschrift für Astrophysik*, 1931, v. 3, 199–226.

6. Lyot B. La couronne solaire étudiée en dehors des éclipses. *Comptes Rendus*, 1930, v. 191, 834–837.

7. Lyot B. A study of the solar corona and prominences without eclipses – George Darwin Lecture. *Mon. Not. Roy. Astron. Soc.*, 1939, 580-=594 (22 pages with plates).

8. Allen C.W. The spectrum of the corona at the eclipse of 1940 October 1. *Mon. Not. Roy. Astron. Soc.*, 1946, v. 106, 137–150.

9. Athay R.G., Billings D.E., Evans J.W. and Roberts W.O. Emission in hydrogen Balmer lines and continuum in flash spectrum of 1952 total solar eclipse at Karthoum, Sudan. *Astrophys. J.*, 1954, v. 120, 94–111.

10. Minnaert M. On the continuous spectrum of the corona and its polarisation. *Zeitschrift für Astrophysik*, 1930, v. 1, 209–236.

11. Robitaille P.M. Commentary on the radius of the Sun. Optical illusion or manifestation of a real surface? *Progr. Phys.*, 2013, v. 2, L5-L6.

12. Zirin H. The Solar Atmosphere. Blaisdell Publishing Company, Waltham, MA, 1966.

13. Bhatnagar A. Instrumentation and observational techniques in solar astronomy. In: *Lectures on Solar Physics* (H.M. Antia, A. Bhatnagar and R. Ulmschneider, Eds.), Springer, Berlin, 2003, p. 27–79.

14. Ulmmschneider P. The physics of the chromosphere and corona. In: *Lectures on Solar Physics* (H.M. Antia, A. Bhatnagar and R. Ulmschneider, Eds.), Springer, Berlin, 2003, p. 232–280.

15. Dwivedi B.N. The solar corona. In: *Lectures on Solar Physics* (H.M. Antia, A. Bhatnagar and R. Ulmschneider, Eds.), Springer, Berlin, 2003, p. 281–298.

16. van de Hulst H.C. The electron density of the corona. *Bull. Astronom. Inst. Netherlands*, 1950, v. 11, no. 410., 135–149.

17. Robitaille P.M. The liquid metallic hydrogen model of the Sun and the solar atmosphere V. On the nature of the corona. *Progr. Phys.*, 2013, v. 3, L21–L24.

18. Robitaille P.M. Liquid metallic hydrogen: A building block for the liquid Sun. *Progr. Phys.*, 2011, v. 3, 60–74.

19. Robitaille P.M. Liquid metallic hydrogen II: A critical assessment of current and primordial helium levels in Sun. *Progr. Phys.*, 2013, v. 2, 35–47.

20. Robitaille J.C. and Robitaille P.M. Liquid metallic hydrogen III. Intercalation and lattice exclusion versus gravitational settling and their consequences relative to internal structure, surface activity, and solar winds in the Sun. *Progr. Phys.*, 2013, v. 2, 87–97.

21. Robitaille P.M. Magnetic fields and directional spectral emissivity in sunspots and faculae: Complimentary evidence of metallic behavior on the surface of the Sun. *Progr. Phys.*, 2013, v. 1, 19–24.

22. Robitaille P.M. The liquid metallic hydrogen model of the Sun and the solar atmosphere I. Continuous emission and condensed matter within the chromosphere. *Progr. Phys.*, 2013, v. 3, L5–L7.

The Liquid Metallic Hydrogen Model of the Sun and the Solar Atmosphere III. Importance of Continuous Emission Spectra from Flares, Coronal Mass Ejections, Prominences, and Other Coronal Structures

Pierre-Marie Robitaille

Department of Radiology, The Ohio State University, 395 W. 12th Ave, Columbus, Ohio 43210, USA.
robitaille.1@osu.edu

The solar corona and chromosphere are often marked by eruptive features, such as flares, prominences, loops, and coronal mass ejections, which rise above the photospheric surface. Coronal streamers and plumes can also characterize the outer atmosphere of the Sun. All of these structures, fascinating in their extent and formation, frequently emit continuous spectra and can usually be observed using white-light coronagraphs. This implies, at least in part, that they are comprised of condensed matter. The continuous spectra associated with chromospheric and coronal structures can be viewed as representing the twenty-eighth line of evidence, and the eighth Planckian proof, that the Sun is condensed matter. The existence of such objects also suggests that the density of the solar atmosphere rises to levels well in excess of current estimates put forth by the gaseous models of the Sun. In this work, the densities of planetary atmospheres are examined in order to gain insight relative to the likely densities of the solar chromosphere. Elevated densities in the solar atmosphere are also supported by coronal seismology studies, which can be viewed as constituting the twenty-ninth line of evidence that the Sun is composed of condensed matter.

In order to explain the occurrence of the dark lines in the solar spectrum, we must assume that the solar atmosphere incloses a luminous nucleus, producing a continuous spectrum, the brightness of which exceeds a certain limit. The most probable supposition which can be made respecting the Sun's constitution is, that it consists of a solid or liquid nucleus, heated to a temperature of the brightest whiteness, surrounded by an atmosphere of somewhat lower temperature.

Gustav Robert Kirchhoff, 1862 [1]

Observation of a white-light flare was initially reported by Richard Carrington in 1859 [2]. Though once considered rare events [3,4], the production of such emission has now become associated with many, if not all, flares [5]. It has been well-established that hard X-ray class flares ($\geq$ M5) emit white-light [3]. However, the mechanism for producing this light has remained elusive [6, 7], despite the prevalence of these objects [3–5]. Devoid of condensed matter, a gaseous model has little means to account for the generation of white-light flares. In 2010, Watanabe et al. [8] proposed that the emission generated by white-light flares was associated with electrons accelerated to half of the speed of light [9]. More than 150 years after Carrington's discovery, astrophysicists advanced a scenario through which white-light could be produced within the theoretical constraints imposed by accepting the idea of a gaseous Sun [10–14].

Beyond solar flares, many coronal structures are associated with the emission of white-light. These include prominences and coronal mass ejections [15–23], streamers [24–26], plumes [27], and loops [28–30]. Indeed, coronal structures have long been observed with white-light coronagraphs [25, 26], an instrument invented by Bernard Lyot [31, 32].

The existence of white-light in coronal structures presents a significant problem for the gaseous models of the Sun [10–14]. In these models, white-light at the photosphere is produced by a vast sum of processes (bound-bound, bound-free, free-free, and scattering) taking place within the Sun itself (see [33] for a complete review of this topic). In order to generate the thermal spectrum at the surface, this light must leave the hypothetically gaseous solar body through a photospheric layer regarded as an 'optical illusion' created by a dramatic change in solar opacity [34]. The current solution is so convoluted that it has been described by the author as the Achilles' Heel of gaseous solar models [33]. In no other instance is a simple spectroscopic line, such as the thermal spectrum of the Sun, produced by the extensive summation of vastly unrelated spectroscopic processes [33]. Furthermore, the mechanisms associated with the generation of the solar spectrum are of no value in explaining the thermal emission from graphite on Earth, material from which Planckian radiation was initially studied [33]. As a result, these approaches are not relevant in accounting for the thermal signature of the Sun [33].

The observation of white-light in coronal structures only

acts to accentuate this problem for the gaseous models. These objects are fleeting and devoid of the long time-lines (millions of years) currently required by the gaseous models to produce white-light from the center of the Sun. Moreover, these structures lack the large complement of processes summed within the gaseous models of the Sun to generate the white-light of the photosphere [33]. As a result, though some of the same mechanisms are invoked [3, 4], scientists who adhere to the gaseous models must now have recourse to additional effects: the scattering of photospheric light [16] or the acceleration of electrons to sub-relativistic velocities [8].

In the end, the simplest means of accounting for the presence of white-light, both on the photosphere and within coronal structures, is to recognize that the Sun is comprised of condensed matter [35–37]. The material found on the photosphere is being ejected into the solar atmosphere. Hence, it can be found within the corona. In fact, since photospheric metallic hydrogen has been hypothesized to be metastable (see [35] and references therein), it is reasonable that material ejected into the corona remains partially metallic in nature. In time, sparse filaments of condensed metallic hydrogen might come to constitute the framework for coronal streamers for instance, helping to explain why these objects also emit white-light. As a result, it is now advanced that the white-light emission of coronal structures constitutes the twenty-eighth line of evidence (see [35–39] and references therein for the others), and the eighth Planckian proof, that the Sun is comprised of condensed matter.[*]

Unlike the gaseous models of the Sun [10–14], the metallic hydrogen model [35–37] advances that the solar body has a nearly uniform density throughout which approaches ~1 g/cm^3 at the level of the photosphere. Thus, the presence of condensed matter, expelled from the photosphere into the chromosphere and corona, strongly suggests that the densities in these regions are not negligible. In sharp contrast, within the context of a gaseous Sun and calculated electron densities, the coronal solar atmosphere is said to possess *"densities which are many trillions times smaller than that of the gas composing the Earth's atmosphere; in fact, coronal densities are low enough to be considered an almost perfect vacuum in laboratories"* [40, p. 284]. These statements are directly linked to the use of the gaseous equations of state [10, p. 130ff] and the belief that the solar body retains most of its mass in its core [10–12]. As a result, the question must naturally arise as to whether or not trillion fold decreases in densities, relative to the Earthly atmosphere, are reasonable for the solar corona. This is especially concerning relative to the realization that the Sun is expelling condensed matter [35–39] into its outer atmosphere.

To get some sense of reasonable densities for the corona, one can have recourse to the characteristic features of planetary atmospheres, with several important cautionary notes. First, the temperatures around the Sun and the inner planets are not at all comparable. Second, the molecular weight of material around the Sun might be either much smaller, or in the case of condensed hydrogen, *much larger*, than found in planetary atmospheres. Thirdly, the solar atmosphere might have substantial local density fluctuations well beyond anything observed in planetary atmospheres. This is especially relevant since condensed matter is being expelled into a partially gaseous solar atmosphere. These factors will impact the comparisons that can be extracted.

Consider the known densities of the Earth's atmosphere at sea level (1.229 kg/m^3 or 0.0012 g/cm^3 [41]) while taking into account that the Sun/Earth ratio of acceleration due to gravity is a factor of 28 [42]. The simple product of these values (ignoring temperature effects and assuming that the Sun's atmosphere is composed of particles of the same mean molecular weight as in the Earth's atmosphere (28.97 g/mole [43])), results in a density of 0.0336 g/cm^3 near the solar surface. This is well above current estimates for the solar atmosphere. In fact, the gaseous models of the Sun predict that, as one proceeds out from the photosphere to the top of the chromosphere, the density drops from ~10^{-7} g/cm^3 to ~10^{-15} g/cm^3, respectively [44, p. 32].

In reality, the aforementioned assumption that the average molecular weight in the lower solar atmosphere is similar to the Earth's cannot be correct. At the same time, temperature effects should substantially raise the amount of material found in the Sun's atmosphere. The Sun is known to expel matter into the corona and, if this is condensed matter, may have local densities well beyond that found in the atmosphere of the Earth at sea level. But even this simple calculation, based on the characteristics of the Earth's atmosphere, points to significant problems with current estimates of chromospheric densities, inferred from gaseous solar model [44] which it exceeds by a factor on the order of 10^5–10^{10}. Similar conclusions can be reached by considering Venus [45] or Mars [46].

Though some may dislike such comparisons, as too many variables could alter the final result, the author is not attempting to set a final density for the lower atmosphere of the Sun. The discussion rests simply in highlighting that the currently accepted solar values are well outside the bounds of reason, especially when considering that the Sun is much hotter than the inner planets and constantly expelling matter into its corona. This implies that a much higher average molecular weight for the solar atmosphere can be expected than one based on the atomic weight of hydrogen. Unlike the Sun, the inner planets do not eject much material into their atmospheres. As a result, the atmosphere of the Sun is likely to possess great local variability in its densities. This may also be true when comparing the atmosphere of the quiet Sun near the solar poles with that above the equator, as a result of coro-

---

[*]The Planckian proofs are all related to thermal emission in condensed matter. They do not imply that the objects which are the subject of these proof necessarily display a perfect thermal spectrum. The proofs are invoked when the spectrum is continuous and when an object's emissivity is most simply accounted for by invoking condensed matter.

nal holes above the former.

Finally, it remains highly significant that, when a comet approaches the Sun, it can result in intense shock wave propagation throughout the corona (e.g. [47]). Such behavior calls for highly elevated atmospheric densities. It is not reasonable to expect that shock waves and seismic activity could propagate within a corona whose density remains inferior to earthly vacuums. As such, seismological findings and shock wave propagation are highly supportive of the realization that the solar chromosphere and corona are much denser than currently surmised from the gaseous models of the Sun. Along these lines, it is concerning that the Sun can be studied using coronal helioseismology [48–51] which suggests a twenty-ninth line of evidence that it is comprised of condensed matter. It is not possible to conduct coronal seismological studies in an atmosphere sparser than the best laboratory vacuums. Seismology is a science which can be applied exclusively to the condensed states of matter.

Dedication

Dedicated to Gregory Gribbon, my longtime Canadian childhood friend, in thanksgiving for his faithfulness and support.

References

1. Kirchhoff G. The physical constitution of the Sun. In: *Researches on the Solar Spectrum and the Spectra of the Chemical Elements*. Translated by H.E. Roscoe, Macmillan and Co., Cambridge, 1862, p. 23.

2. Carrington R.C. Description of a singular appearance seen in the Sun on September 1, 1859. *Mon. Not. Roy. Astron. Soc.*, 1859, v. 20, 13–15.

3. Machado M.E., Emslie A.G., Avrett E.H. Radiative backwarming in white-light flares. *Solar Phys.*, 1989, v. 124, 303–317.

4. Hiei E. A continuous spectrum of a white-light flare. *Solar Phys.*, 1982, v. 80, 113–127.

5. Wang H. Study of white-light flares observed by Hinode. *Res. Astron. Astrophys.*, 2009, v. 9, no. 2, 127–132.

6. Priest E.R. Solar flare theory and the status of flare understanding. *High Energy Solar Physics: Anticipating HESSI (R. Ramaty and N. Mandzhavidze, Eds.), ASP Conf. Ser.*, 2000, v. 206, 13–26.

7. Kahler S.W. Solar flares and coronal mass ejections. *Annu. Rev. Astron. Astrophys.*, 1992, v. 30, 113–141.

8. Watanabe K., Krucker S., Hudson H., Shimizu T., Masuda S., and Ichimoto K. G-band and hard X-ray emissions of the 2006 December 14 flares observed by HINODE/SOT and RHESSI. *Astrophys. J.*, 2010, v. 715, 651–655.

9. Anderson J.L. Hinode discovers origin of white-light flares. NASA–Marshall Space Flight Center. Accessed online on 4/17/2013: http://www.nasa.gov/centers/marshall/news/news/releases/2010/10-052.html

10. Kippenhahn R. and Weigert A. Stellar structure and evolution. Springer-Verlag, Berlin, 1990.

11. Bahcall J.N. and Pinsonneault M.H. Standard solar models, with and without helium diffusion, and the solar neutrino problem. *Rev. Mod. Phys.*, 1992, v. 64, no. 4, 885–926.

12. Bachall J.N., Pinsonneault M.H. and Wasserburg G.J. Solar models with helium and heavy-element diffusion. *Rev. Mod. Phys.*, 1995, v. 67, no. 4, 781–808.

13. Robitaille P.M. A thermodynamic history of the solar constitution – I: The journey to a gaseous Sun. *Progr. Phys.*, 2011, v. 3, 3–25.

14. Robitaille P.M. A thermodynamic history of the solar constitution – II: The theory of a gaseous Sun and Jeans' failed liquid alternative. *Progr. Phys.*, 2011, v. 3, 41–59.

15. Tandberg-Hanssen E. Solar prominences — An intriguing phenomenon. *Solar Phys.*, 2011, v. 269, 237–251.

16. Tandberg-Hanssen E. A spectroscopic study of quiescent prominences. *Astrophysica Novegica*, 1964, v. 9, no. 3, 13–32.

17. Yakovkin N.A. and Zeldina M.Yu. The prominence radiation theory. *Solar Phys.*, 1975, v. 45, 319–338.

18. Gopalswamy N. and Hanaoka Y. Coronal dimming associated with a giant prominence eruption. *Astrophys. J.*, 1998, v. 498, L179–L182.

19. Gopalswamy N., Shimojo M., Lu W., Yashiro S., Shibasaki K. and Howard R.A. Prominence eruptions and coronal mass ejections: A statistical study using microwave observations. *Astrophys. J.*, 2003, v. 586, 562–578.

20. Sheeley N.R., Walters J.H., Wang Y.M. and Howard R.A. Continuous tracking of coronal outflows: Two kinds of coronal mass ejections. *J. Geophys. Res.*, 1999, v. 104, no. A11, 24739–24767.

21. St. Cyr O.C., Howard R.A., Sheeley N.R., Plunkett S.P., Michels D.J., Paswaters S.E., Koomen M.J., Simnett G.M., Thompson B.J., Gurman J.B., Schwenn R., Webb D.F., Hildner E. and Lamy P.L. Properties of coronal mass ejections: SOHO LASCO observations from January 1996 to June 1998. *J. Geophys. Res.*, 2000, v. 105, no. A8, 18169–18185.

22. Hudson H.S. and Cliver E.W. Observing coronal mass ejections without coronagraphs. *J. Geophys. Res.*, 2001, v. 106, no. A11, 25199–25213.

23. Yashiro S., Gopalswamy N. Michaelek G, St. Cyr O.C., Plunkett S.P., Rich N.B. and Howard R.A. A catalog of white-light coronal mass ejections observed by the SOHO spacecraft. *J. Geophys. Res.*, 2004, v. 109, A07105(11 pages).

24. Wang Y.M. Nonradial coronal streamers. *Astrophys. J.*, 1996, v. 456, L119–L121.

25. Wang Y.M., Sheeley N.R., Walters J.H., Brueckner G.E., Howard R.A., Michels D.J., Lamy P.L., Schwenn R. and Simnett G.M. Origin of streamer material in the outer corona. *Astrophys. J.*, 1998, v. 498, L165–L168.

26. Vourlidas A. A review of white-light streamers at the end of cycle 23. *Proc. IAU: Solar Activity and its Magnetic Origin*, 2006, v. 233, 197–204.

27. Del Zanna G., Bromage B.J.I. and Mason H.E. Spectroscopic characteristics of polar plumes. *Astron. Astrophys.*, 2003, v. 398, 743–763.

28. Mouschovias T.Ch. and Poland A.I. Expansion and broadening of coronal loop transients: A theoretical explanation. *Astrophys. J.*, 1978, v. 220, 675–682.

29. Kjeldseth-Moe O. and Brekke P. Time variability of active region loops observed with the coronal diagnostic spectrometer (CDS) on SOHO. *Solar Phys.*, 1998, v. 182, 73–95.

30. Landi E., Miralles M.P., Curdt W. and Hara H. Physical properties of cooling plasma in quiescent active region loops. *Astrophys. J.*, 2009, v. 695, 221-237.

31. Lyot B. La couronne solaire étudiée en dehors des éclipses. *Comptes Rendus*, 1930, v. 191, 834–837.

32. Lyot B. A study of the solar corona and prominences without eclipses – George Darwin Lecture. *Mon. Not. Roy. Astron. Soc.*, 1939, 580-=594 (22 pages with plates).

33. Robitaille P.M. Stellar opacity: The Achilles' heel of the gaseous Sun. *Progr. Phys.*, 2011, v. 3, 93–99.

34. Robitaille P.M. On the Presence of a Distinct Solar Surface: A Reply to Hervé Faye. *Progr. Phys.*, 2011, v. 3, 75–78.

35. Robitaille P.M. Liquid Metallic Hydrogen: A Building Block for the Liquid Sun. *Progr. Phys.*, 2011, v. 3, 60–74.

36. Robitaille P.M. Liquid Metallic Hydrogen II: A Critical Assessment of Current and Primordial Helium Levels in Sun. *Progr. Phys.*, 2013, v. 2, 35–47.

37. Robitaille J.C. and Robitaille P.M. Liquid Metallic Hydrogen III. Intercalation and Lattice Exclusion Versus Gravitational Settling and Their Consequences Relative to Internal Structure, Surface Activity, and Solar Winds in the Sun. *Progr. Phys.*, 2013, v. 2, 87–97.

38. Robitaille P.M. Commentary on the liquid metallic hydrogen model of the Sun II: Insight relative to coronal rain and splashdown events. *Progr. Phys.*, 2013, v. 2, L10–L11.

39. Robitaille P.M. The Liquid Metallic Hydrogen Model of the Sun and the Solar Atmosphere II. Continuous Emission and Condensed Matter Within the Corona. *Progr. Phys.*, 2013, v. 3, L8–L10.

40. Dwivedi B.N. The solar corona. In: *Lectures on Solar Physics* (H.M. Antia, A. Bhatnagar and R. Ulmschneider, Eds.), Springer, Berlin, 2003, p. 281–298.

41. NASA. Air properties definitions. (accessed online on 2/13/2013) www.grc.nasa.gov/WWW/k-12/airplane/airprop.html

42. NASA. Sun/Earth Comparison. (accessed online on 2/13/2013) nssdc.gsfc.nasa.gov/planetary/factsheet/sunfact.html

43. NASA. Earth Fact Sheet. (accessed online on 2/13/2013) nssdc.gsfc.nasa.gov/planetary/factsheet/earthfact.html

44. Bhatnagar A. Instrumentation and observational techniques in solar astronomy. In: *Lectures on Solar Physics* (H.M. Antia, A. Bhatnagar and R. Ulmschneider, Eds.), Springer, Berlin, 2003, p. 27–79.

45. NASA. Venus/Earth Comparison. (accessed online on 2/13/2013) nssdc.gsfc.nasa.gov/planetary/factsheet/venusfact.html

46. NASA. Mars/Earth Comparison. (accessed online on 2/13/2013) nssdc.gsfc.nasa.gov/planetary/factsheet/marsfact.html

47. SOHO NASA/ESA [2011/05/10 20:00:00 to 2011/05/11 08:00:00 UTC]. These events have been captured in video format and displayed online: e.g. youtube.com/watch?v=igeBrSGk5FA; *Russia Today* youtube.com/watch?NR=1&v=Mat4dWpszoQ&feature=fvwp. (Accessed online on January 29, 2013: Examine beginning at 2011/05/10 2:48:00 to 2011/05/10 4:00:00).

48. Nakariakov V.M. and Verwichte E. Coronal waves and oscillations. *Living Rev. Solar Phys.*, 2005, v. 2, 3–65.

49. Roberts B. Progress in coronal seismology. *Proc. IAU: Waves and Oscillations in Solar Atmosphere*, 2007, v. 247, 3–19.

50. Zaqarashvili T.V. and Erdélyi R. Oscillations and waves in solar spicules. *Space Sci. Rev.*, 2009, v. 149, 355–388.

51. De Moortel I. An overview of coronal seismology. *Phil. Trans. R. Soc. A*, 2005, v. 363, 2743–2760.

The Liquid Metallic Hydrogen Model of the Sun and the Solar Atmosphere IV. On the Nature of the Chromosphere

Pierre-Marie Robitaille

Department of Radiology, The Ohio State University, 395 W. 12th Ave, Columbus, Ohio 43210, USA.
robitaille.1@osu.edu

The chromosphere is the site of weak emission lines characterizing the flash spectrum observed for a few seconds during a total eclipse. This layer of the solar atmosphere is known to possess an opaque Hα emission and a great number of spicules, which can extend well above the photosphere. A stunning variety of hydrogen emission lines have been observed in this region. The production of these lines has provided the seventeenth line of evidence that the Sun is comprised of condensed matter (Robitaille P.M. Liquid Metallic Hydrogen II: A critical assessment of current and primordial helium levels in Sun. *Progr. Phys.*, 2013, v. 2, 35–47). Contrary to the gaseous solar models, the simplest mechanism for the production of emission lines is the evaporation of excited atoms from condensed surfaces existing within the chromosphere, as found in spicules. This is reminiscent of the chemiluminescence which occurs during the condensation of silver clusters (Konig L., Rabin I., Schultze W., and Ertl G. Chemiluminescence in the Agglomeration of Metal Clusters. *Science*, v. 274, no. 5291, 1353–1355). The process associated with spicule formation is an exothermic one, requiring the transport of energy away from the site of condensation. As atoms leave localized surfaces, their electrons can occupy any energy level and, hence, a wide variety of emission lines are produced. In this regard, it is hypothesized that the presence of hydrides on the Sun can also facilitate hydrogen condensation in the chromosphere. The associated line emission from main group and transition elements constitutes the thirtieth line of evidence that the Sun is condensed matter. Condensation processes also help to explain why spicules manifest an apparently constant temperature over their entire length. Since the corona supports magnetic field lines, the random orientations associated with spicule formation suggests that the hydrogen condensates in the chromosphere are not metallic in nature. Spicules provide a means, not to heat the corona, but rather, for condensed hydrogen to rejoin the photospheric layer of the Sun. Spicular velocities of formation are known to be essentially independent of gravitational effects and highly supportive of the hypothesis that true condensation processes are being observed. The presence of spicules brings into question established chromospheric densities and provides additional support for condensation processes in the chromosphere, the seventh line of evidence that the Sun is comprised of condensed matter.

> *In order to explain the occurrence of the dark lines in the solar spectrum, we must assume that the solar atmosphere incloses a luminous nucleus, producing a continuous spectrum, the brightness of which exceeds a certain limit. The most probable supposition which can be made respecting the Sun's constitution is, that it consists of a solid or liquid nucleus, heated to a temperature of the brightest whiteness, surrounded by an atmosphere of somewhat lower temperature.*

Gustav Robert Kirchhoff, 1862 [1]

Nearly 150 years have now passed since Kirchhoff wrote about the Sun [1] and Father Angelo Secchi illustrated chromospheric spicules for the first time [2, p. 32]. Secchi viewed the chromospheric region as clearly defined on one side, like the surface of a liquid layer [2, p. 33]. Though he had con-

cluded that the body of the Sun was gaseous, he believed that condensed matter was "suspended" within the photosphere [3]. Secchi would comment on the appearance of spicules and the outer portion of the chromosphere: *"In general, the chromosphere is poorly terminated and its external surface is garnished with fringes . . . It is almost always covered with little nets terminated in a point and entirely similar to hair".* Secchi mentioned the tremendous variability in spicule orientation, their enormous size, and how these structures reminded him of flames present in a field wherein one burns grasses after the harvest . . . *"It often happens, especially in the region of sunspots, that the chromosphere presents an aspect of a very active network whose surface, unequal and rough, seems composed of brilliant clouds analogous to our cumulus; the*

---

*All translations from French were accomplished by the author.

disposition of which resembles the beads of our rosary; a few of which dilate in order to form little diffuse elevations on the sides" [2, p. 31–36]. He would emphasize that "*there is thus no illusion to worry about, the phenomena that we have just exposed to the reader are not simple optical findings, but objects which really exist, faithfully represented to our eyes using instruments employed to observe them*" [2, p. 35–36].

The chromosphere is a region of intense magnetic activity, but its nature, and in particular that of its mottles and spicules [4–15], remains a mystery [16]. The low chromosphere is dominated by emission lines from neutral atoms and rare earths, but near its upper boundary strong lines from CaII and H are present [16]. Harold Zirin highlights that "*The chromosphere is the least-well understood layer of the Sun's atmosphere... Part of the problem is that it is so dynamic and transient. At this height an ill-defined magnetic field dominates the gas and determines the structure. Since we do not know the physical mechanisms, it is impossible to produce a realistic model. Since most of the models ignored much of the data, they generally contradict the observational data. Typical models ignore other constraints and just match only the XUV data; this is not enough for a unique solution. It reminds one of the discovery of the sunspot cycle. While most of the great 18th century astronomers agreed that the sunspot occurrence was random, only Schwabe, an amateur, took the trouble to track the number of sunspots, thereby discovering the 11-year cycle*" [16].

The struggle to understand the chromosphere is, in large measure, a direct result of the adherence to gaseous models of the Sun and a rejection of condensed matter [17–21]. The chromosphere is hypothesized to be only 2–3,000 km thick [7, p. 232]. Yet, chromospheric emission lines from hydrogen, calcium, and helium can extend up to 10,000 km above the solar surface [6, p. 8]. Zirin comments on the chromosphere as follows: "*Years ago the journals were filled with discussions of 'the height of the chromosphere'. It was clear that the apparent scale height of 1000 km far exceeded that in hydrostatic equilibrium. In modern times, a convenient solution has been found – denial. Although anyone can measure its height with a ruler and find it extending to 5000 km, most publications state that it becomes the corona at 2000 km above the surface. We cannot explain the great height or the erroneous models... While models say 2000 km, the data say 5000*" [16].

Though the chromosphere contains bright floculi in the K line of Ca II, which coincide in position with Hα rosettes [6, p. 85–86], and though it is laced with bright/dark mottles and spicules, gaseous solar models [22–24] have no direct means of accounting for such structures [25].

It remains fascinating that spicule formation velocities appear to be largely independent of gravitational forces [9–15], though some efforts have been made to establish such a relationship [26]. In general, while most velocities of spicules formation seem to move at nearly uniform speeds [4, p. 61],

some actually increase with elevation, rise in jerks, or stop suddenly upon reaching their maximum height [6, p. 45–60]. Spicules have been said to "*expand laterally or slit into two or more strands after being ejected*" [26]. Such behavior is strongly suggestive of a condensation process.

Spicules are often associated with magnetic phenomena in the chromosphere [4–15]. They can be represented as lying above photospheric intergranular lanes. In so doing, they seem to be experiencing lateral magnetic pressure from the material trapped within the field lines that originate in the solar surface, as displayed in Fig. 1.
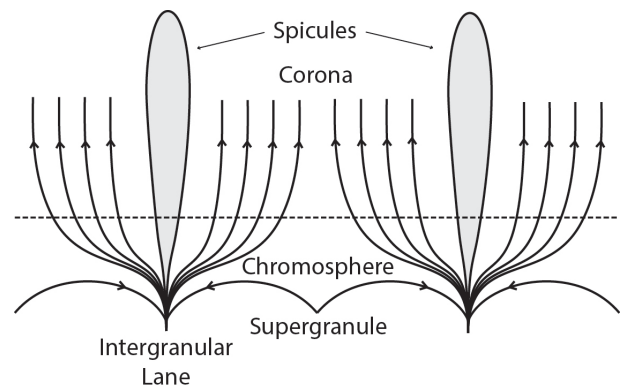

Fig. 1: Schematic representation of spicules overlying the intergranular lane on the outer boundary of a supergranule and surrounded by magnetic field lines emanating from the solar surface. This figure is an adaptation based on Fig. IV–13 in [4, p. 162].

Numerous magnetic field lines escape from the solar interior through the photospheric surface. These fields must traverse the chromospheric material. As a result, most solar observers believe that chromospheric structures are inherently magnetic [4–15]. Spicules are though to be propelling matter upwards into the corona [27] and not gathering matter, through condensation, for rejoining the photosphere.

However, given the appearance of chromospheric structures, such as rosettes and mottles, and the somewhat random orientations of spicules [4–15], it seems unlikely that these objects can be of magnetic origin. What is more probable is that, while non-metallic, chromospheric structures are being confined by charged plasmas, or metallic hydrogen [17–21], flowing in conjunction with the solar magnetic fields lines, much as illustrated in Fig. 1.

Since the gaseous models [22–24] depend on excessive temperatures in order to explain emission lines, spicules have been advanced as partly responsible for heating the corona [27]. Two forms of spicules were postulated from observations. Type I spicules can be viewed as classic spicules with lifetimes on the order of 3–7 minutes [27]. Type II spicules were believed to form rapidly, be short lived (10–150 s) and thin (<200 km), and capable of projecting material into the upper chromosphere at great velocities [27]. Type I spicules

were said to move up and down, while Type II spicules faded [27]. Type II spicules were claimed to be potentially important in heating the outer atmosphere [27]. But recently, their existence and role appears to have been soundly refuted [28].

Though chromospheric observers remain intrigued with structure [4–15, 26], they adhere to the gaseous solar models [22–24], even though gases cannot exhibit true condensation. As a result, all chromospheric and coronal structures must be viewed as gasoues plasmas of exceedingly low densities [7]. Since they are not condensed matter in the context of the gaseous models [22–24], the strange properties of spicule formation and the structures of rosettes and mottles, remain an anomaly, rather than indicators of the nature of the chromosphere.

In contrast, this work now advances that chromospheric structures represent solar material in the condensed state [17–21]. Matter in this region fluctuates between gaseous and condensed, as spicules and mottles form and dissipate [9–15, 26]. This is reminiscent of phenomena such as critical opalescence [25]. The chromosphere appears to be a site of hydrogen condensation. The mystery lies only in how this can be achieved.

In order to better understand the chromosphere, one can revisit the classic work of Donald H. Menzel published 1931, *"A Study of the Solar Chromosphere"* [29]. Within this volume, three revelations continue to make their mark. First, there is an amazing prevalence of emission lines from a wide variety of atoms within this layer of the Sun (see Table I [29, p. 18–113]). Second, the chromosphere contains an extensive group of emission lines from hydrogen (see Table 3 [29, p. 128]). Menzel lists more than twenty-three hydrogen emission lines in his Table 3 [29]. Along with Cillié, Menzel soon observed Balmer series emission up to H31, with higher states limited only by resolution [30]. Third, he outlines a hydrogen abundance in the chromosphere which is 100 times more elevated than in the Sun (see Table 20 [29, p. 281]). Menzel's chromospheric hydrogen abundance was nearly 1,000 times more elevated [29, p. 275–281] than that which had been reported by Henry Norris Russell from the Fraunhofer spectrum of the Sun itself just a few years before [31].

While eighty years have passed since *"A Study of the Solar Chromosphere"* was published [29], much remains to be understood relative to this region of the Sun. P. Heinzel writes that *"Moreover, the energy supply into these layers is largely unknown, we only know that the radiation is not the dominant source of heating. The solar chromosphere is probably the least understood part of the Sun, even compared to the solar interior on which helioseismology has focused during last decades"* [8]. Much like other physical processes in the Sun, local heating is being tentatively attributed to magnetic mechanisms. Yet, if the chromosphere remains a mystery, the cause rests on the insistence that the Sun must exist in the gaseous state. Donald Menzel reminds us, *"The province of the scientist is the untangling of mysteries, the rendering of*

complex things into simple ones" [29, p. 1].

A condensed solar model provides elegant solutions to the most perplexing questions relative to the chromosphere. This is especially true relative to apparent heating, as best understood through the careful consideration of how chromospheric emission lines are produced.

Within gaseous models, line emission requires either photon absorption, or electron collision, to excite the emitting atom [4, p. 228]. This represents an attempt to explain spectra using random processes. In the condensed model [17–21] spectra are tied to the formation of chromospheric structures. Line emission becomes inherently linked to understanding the very nature of the chromosphere.

The quest for answers begins with the consideration of condensation processes in clusters, the smallest precursors to condensed matter [32–37]. Clusters can be super-stable and act as superatoms [38]. In addition, their most favorable configurations can be linked to highest electron affinity and not to the energy of the ground state [39]. Condensation processes in clusters have been known to be associated with light emission [40, 41] and are exothermic. Thus, the apparent heating of the chromosphere might best be understood by considering these reactions.

In 1996, chemiluminescence was first reported to occur during the agglomeration of silver clusters [40]. By necessity, the reactions involved took place at low temperature (~30K), but the lessons learned directly translate to other conditions. Gerhart Ertl (Nobel Prize, Chemistry, 2007) and his team highlight: *"Exothermic chemical reactions may be accompanied by chemiluminescence. In these reactions, the released energy is not adiabatically damped into the heat bath of the surrounding medium but rather is stored in an excited state of the product; decay from this excited state to the ground state is associated with light emission"* [40].

The reactions presented by Ertl [40], which are of interest relative to the chromosphere, are illustrated by the condensation of two silver fragments, resulting in an activated cluster species: $M_n + M_m \rightarrow M^*_{m+n}$. The activated cluster returns to the ground state by ejecting an excited atom: $M^*_{m+n} \rightarrow M_{m+n-1} + M^*$. Finally, the excited silver atom is able to relax to the ground state by emitting light: $M^* \rightarrow M + h\nu$. Consequently, since condensation processes are exothermic, they are capable of producing excited atoms which result in emission. To extend these concepts to the solar chromosphere, it is useful to consider the types of condensation reactions which might be present in this region of the Sun.

In the chromosphere, it is possible to observe spectroscopic emission lines from atomic hydrogen corresponding to the Lyman ($n_2 > 1 \rightarrow n_1 = 1$ [42]), Balmer ($n_2 > 2 \rightarrow n_1 = 2$ [30]), and Paschen series ($n_2 > 3 \rightarrow n_1 = 3$ [43]).[*] Lyman emission lines involve relaxation back to the ground state and

---

[*]Up to eleven separate Lyman emission lines have been recorded (n_2=7 through n_2=17 [42, p. 47]), Balmer lines at least up to n_2=31 [30], and at least nine Paschen lines (n_2=8 through n_2=16) [43]

can directly be deduced to arise from the condensation of hydrogen fragments, $H_n + H_m \rightarrow H^*_{m+n}$, relaxation of the resultant condensation product through the ejection of an excited hydrogen atom, $H^*_{m+n} \rightarrow H_{m+n-1} + H^*$, and finally the return to the ground state of the excited hydrogen atom with light emission, $H^* \rightarrow H + h\nu$.

In reality, it is reasonable to postulate that reactions in the chromosphere primarily involves the combination of molecular hydrogen with much larger condensed hydrogen structures or seeds, CHS, since this region of the Sun displays tangible signs of condensed matter in the form of spicules and mottles [9–15, 26].

In this case, molecular hydrogen, H_2, initially combines with these larger structures, $CHS + H_2 \rightarrow CHS-H^*_2$, resulting in mass increase, CHS–H, and the subsequent line emission from the ejected hydrogen atom, $H^* \rightarrow H + h\nu$. Given the extensive quantities of hydrogen in the Sun, it would be expected that numerous such reactions could take place simultaneously on any given CHS and result in the rapid appearance of spicules and mottles in the solar atmosphere [9–15, 26]. Since these reactions are *"not adiabatically dumped into the heat bath of the surrounding medium"* [40], condensation processes could result in the emission of Balmer [30] and Paschen lines [43]. In fact, the first line of the Balmer series ($n_2 = 3 \rightarrow n_1 = 2$), known as the H_α line, is responsible for the reddish hue of the chromosphere [7, p. 232].

The aforementioned reactions depend on the presence of molecular hydrogen in the chromosphere. Unfortunately, the concentrations of molecular hydrogen are extremely difficult to estimate in astrophysics, even if this species is widely considered to the most abundant molecule in the universe. The difficulty in establishing molecular hydrogen concentrations stems from the fact that all rotational-vibrational transitions from the ground electronic state of this diatom are forbidden [44]. As a result, astronomers typically use indirect methods to compute molecular hydrogen fractions in the galaxies [44–47] and sunspot umbra where the molecule is thought to be abundant [48].

Nonetheless, molecular hydrogen has been directly observed in sunspots in the extreme ultra-violet, a region of the electromagnetic spectrum were the emission lines are relatively strong [49, 50]. Furthermore, Jordan et al. [49] report a significant enhancement of the molecular hydrogen signal when chromospheric material lies over the sunspot of interest. While these signals are generally weak on the quiet Sun and in the limb [51], the emission from flares [50] and chromospheric plages [52] can be rather strong. Given the difficulty in observing molecular hydrogen in the ground state, these findings are significant and highlight that this species should be available to support condensation reactions in the chromosphere.

Therefore, it is likely that the hydrogen emission lines at the chromospheric level are related to the growth of CHS and the recapture of hydrogen from the outer solar atmosphere.

Przybilla and Buttler have already simulated the linewidth of hydrogen emission lines in the chromosphere and reached the conclusion that some of the lines *"couple tightly to the continuum"* [53]. But within the context of the gaseous solar models, it is impossible to *"couple tightly to the continuum"*, as the latter merely represents an opacity change, not a physical structure [54]. It is for this reason that the emission lines of hydrogen have already been ascribed to the seventeenth line of evidence that the Sun is comprised of condensed matter [19]. Line emission can be linked to condensation, as Ertl has already elegantly demonstrated [40, 41]. Moreover, within the condensed models of the Sun, it would be natural that hydrogen emission associated with condensation would *"couple tightly to the continuum"*.

Before closing the discussion of hydrogen, it is important to digress slightly from addressing emission in order to discuss the hydrogen Fraunhofer absorption lines of the Balmer series. These lines are known to be broad and, as first reported by Unsöld [55], their relative intensities do not decrease in the manner predicted from quantum mechanical considerations. This has already been discussed by the author [19]. Therefore, Fraunhofer lines are not directly related to condensation processes. Isolated atoms, unlike diatoms, lack the ability to add protons to condensed structures, while at the same time removing heat. It is unlikely that isolated atoms can condense onto larger structures. It is more probable that they combine with one another to make a molecular species which, in turn, can condense. Hence, the broadening associated with the Balmer Fraunhofer lines can be linked to collisional processes whereby atoms are strongly interacting with the condensed matter which surrounds them, but not condensing. This represents, as previously mentioned, the sixteenth line of evidence that the Sun is comprised of condensed matter [19].

Returning to line emission, in addition to molecular hydrogen, the chromosphere may well possess other species which can facilitate the condensation of hydrogen atoms. Indeed, many hydrides have been identified either on the solar disk itself or within sunspots [56, 57], including CaH, MgH, CH, OH, H_2O, NH, SH, SiH, AlH, CoH, CuH, and NiH. The presence of CaH and MgH in the Sun have been known since the beginning of the 20th century [58]. In the laboratory hydrides from the main group elements (Li, Na, K, Rb, Cs, Be, Mg, Ca, St, Ba, B, Al, Ga, In, Tl, C, Si, Ge, Sn, N, P, As, Sb, Bi, O, S, Se, Te, F, Cl, Br, and I) and many of the transition metals (including amongst others V, Fe, Co, Ni, Cu, Ag, Zn, and Cd) are readily synthesized [59]. Hydrogen appears to have a great disposition to form hydrides of all kinds and this is an important realization relative to understanding the lower solar atmosphere.

Interestingly, the emission lines from CaII and MgII are particularly important in the chromosphere (e.g. [4, p. 361–369]). The second ionization state is singly charged (Ca^+ and Mg^+). But, the inert gas structure of these ions would demand

a doubly charged species, i.e. Ca^{+2} and Mg^{+2}. As such, why is it that the most important ions of calcium and magnesium on the Sun are singly charged? The answer is likely to rest with their role in making hydrogen available for condensation.

Consider the reactions for calcium. It should be possible for CaH and a condensed hydrogen structure to create an activated complex, CHS + CaH → CHS–HCa*. This would then be followed by an exothermic step involving the expulsion of an activated CaII ion, CHS–HCa → CHS–H + Ca^{+*}, followed by the line emission from CaII*, Ca^{+*} → Ca^{+} + hv.

An identical scenario could be advanced for all the monohydrides, resulting in the observed line emission from their associated cations. Indeed, chromospheric emission lines, involving cations in modest oxidation states, are likely to be generated following a very similar mechanism. Some atoms, like oxygen or iron, may well exist as dihydride or higher complexes of hydrogen. They should participate similarly in condensation reactions, bringing in the process one or more hydrogen atoms to the site of condensation. The metal hydrides thereby would constitute important building blocks in the resynthesis of condensed forms of hydrogen.

When molecular hydrogen delivers a single proton to the condensation reactions, it is also delivering a single electron, if a neutral hydrogen atom subsequently emits. The same can be said for all hydrides wherein neutral atoms are ejected from the condensate to then produce emission lines. Atoms like oxygen have higher ionization potentials that the alkali, alkaline, or transition metals and may well prefer to hold on to their electrons. Emission lines from neutral oxygen are well know to be present during spicule formation [60].

Conversely, a species like CaH is delivering two electrons when generating CaII, as the negative hydrogen ion is being released. This suggests that condensed hydrogen structures, CHS, in the chromosphere might have reasonable electron affinities, though perhaps slightly less than that of oxygen in the lower chromosphere.

Importantly, the delivery of hydrogen to condensed hydrogen structures will involve potentially strong interactions between the carrier atoms (H, Ca, Mg, etc.) and the condensate surface. This would be expected to result in substantial line broadening of the ejected excited species. In support of such an idea, CaII and MgII spicule lines are known to be broad, and the H_α emission lines also display increased linewidths (see e.g. [60–62]). Such findings suggest tight coupling of these atoms to the condensate prior to ejection. Conversely, spicule emission linewidths from the H_β, H_γ, H_ϵ emission line, the D3 line from He, and the line from neutral oxygen are all sharp [60] in spicules, suggesting weaker coupling in those cases.

Contrary to gaseous models of the Sun which have ascribed no reasonable function to the chromosphere, the liquid metallic hydrogen framework [17–21] appears to provide a sound purpose for this layer. A condensed Sun does not per-

mit hydrogen to simply escape, without recovery, into extra-solar space. Rather, molecular hydrogen and hydrides are likely to be participating in the continued recondensation of hydrogen within the chromosphere generating the observed emission lines. The resulting material appears to be non-metallic since spicules can display orientations which are not coupled to the magnetic field lines of the Sun [9–15]. This material may then rejoin the photosphere and travel into the solar interior, perhaps using intergranular lanes [63]. Once in the interior of the Sun, pressure would facilitate the re-synthesis of metallic hydrogen.

In summary, for the first time, it is advanced that complex condensation reactions take place in the chromosphere. These result in line-emission and provides a novel way to explain both spectra and structures on the Sun. The chromosphere appears to be rich in atomic and molecular hydrogen. Furthermore, a wide array of hydride based reactions seem to occur within the chromosphere and these provide a powerful incentive to further the understanding of condensation and hydride chemistry on Earth. In this respect, the presence of metal hydrides [56–58] and the line emission of main group and transition elements in the chromosphere constitutes the thirtieth line of evidence that the Sun is comprised of condensed matter.

Dedication

Dedicated to the poor, who sleep, nearly forgotten, under the light of the Southern Cross.

References

1. Kirchhoff G. The physical constitution of the Sun. In: *Researches on the Solar Spectrum and the Spectra of the Chemical Elements*. Translated by H.E. Roscoe, Macmillan and Co., Cambridge, 1862, p. 23.

2. Secchi A. Le Soleil (2nd Edition, Part II). Guathier-Villars, Paris, 1877.

3. Robitaille P.M. A thermodynamic history of the solar constitution – I: The journey to a gaseous Sun. *Progr. Phys.*, 2011, v. 3, 3–25.

4. Athay R.G. The Solar Chromosphere and Corona: Quiet Sun. D. Reidel Publishing Co., Boston, M.A., 1976.

5. Thomas R.N. and Athay R.G. Physics of the Solar Chromosphere. Interscience Publishers, New York, N.Y., 1961.

6. Bray R.J. and Loughhead R.E. The Solar Chromosphere. Chapman and Hall Ltd., London, U.K., 1974.

7. Ulmschneider P. The physics of the chromosphere and corona. In: *Lectures on Solar Physics* (H.M. Antia, A. Bhatnagar and R. Ulmschneider, Eds.), Springer, Berlin, 2003, p. 232–280.

8. Heinzel P. Understanding the solar chromosphere. In: *"Exploring the Solar System and the Universe"*, (V. Mioc, C. Dumitrache, N.A. Popescu, Eds.), American Institute of Physics, 2008, 238–244.

9. Woltjer L. A photometric investigation of the spicules and the structure of the chromosphere. *Bull. Astron. Inst. Netherlands*, 1954, v. 12, no. 454, 165–176.

10. Rush J.H. and Roberts W.O. Recent studies of chromospheric spicules. *Australian J. Phys.*, 1954, v. 7, 230–243.

11. Beckers J.M. Solar spicules. *Ann. Rev. Astron. Astrophys.*, 1972, v. 10, 73–100.

12. Lorrain P. and Koutchmy S. Two dynamical models for solar spicules. *Solar Phys.*, 1996, v. 165, 115–137.

13. Sterling A. Solar spicules: A review of recent models and targets for future observations. *Solar Phys.*, 2000, v. 196, 79–111.

14. Zaqarashvili T.V. and Erdélyi R. Oscillations and waves in solar spicules. *Space Sci. Rev.*, 2009, v. 149, 355–388.

15. Pasachoff J.M., Jacobson W.A. and Sterling A.C. Limb spicules from ground and from space. *Solar Phys.*, 2009, v. 260, 59–82.

16. Zirin H. The mystery of the chromosphere. *Solar Phys.*, 1996, v. 169, 313–326.

17. Robitaille P.M. A high temperature liquid plasma model of the Sun. *Progr. Phys.*, 2007, v. 1, 70–81 (also in arXiv: astro-ph/0410075).

18. Robitaille P.M. Liquid Metallic Hydrogen: A Building Block for the Liquid Sun. *Progr. Phys.*, 2011, v. 3, 60–74.

19. Robitaille P.M. Liquid Metallic Hydrogen II: A Critical Assessment of Current and Primordial Helium Levels in Sun. *Progr. Phys.*, 2013, v. 2, 35–47.

20. Robitaille J.C. and Robitaille P.M. Liquid Metallic Hydrogen III. Intercalation and Lattice Exclusion Versus Gravitational Settling and Their Consequences Relative to Internal Structure, Surface Activity, and Solar Winds in the Sun. *Progr. Phys.*, 2013, v. 2, 87–97.

21. Robitaille P.M. Commentary on the liquid metallic hydrogen model of the Sun. Insight relative to coronal holes, sunspots, and solar activity. *Progr. Phys.*, 2013, v. 2, L7–L9.

22. Kippenhahn R. and Weigert A. Stellar structure and evolution. Springer-Verlag, Berlin, 1990.

23. Bahcall J.N. and Pinsonneault M.H. Standard solar models, with and without helium diffusion, and the solar neutrino problem. *Rev. Mod. Phys.*, 1992, v. 64, no.4, 885–926.

24. Bachall J.N., Pinsonneault M.H. and Wasserburg G.J. Solar models with helium and heavy-element diffusion. *Rev. Mod. Phys.*, 1995, v. 67, no. 4, 781–808.

25. Robitaille P.M. The solar photosphere: Evidence for condensed matter. *Progr. Phys.*, 2006, v. 2, 17–21.

26. Tsiropoula G., Tziotsious K., Kontogiannis I., Madjarska M.S., Doyle J.G. and Suematsu Y. Solar fine-scale structures I. Spicules and other small-scale, jet-like events at the chromospheric level: Observations and physical parameters. *Space Sci. Rev.*, 2012, v. 169, 181–244.

27. De Pontieu B., McIntosh S.W., Hansteen V.H., Carlsson M., Schrijver C.J., Tarbell T.D., Title A.M., Shine R.A., Suematsu Y., Tsuneta S., Katsukawa Y., Ichimoto K., Shimizu T. and Nagata S. A tale of two spicules: The impact of spicules on the magnetic chromosphere. *Publ. Astron. Soc. Japan*, 2007, v. 59, 655–660.

28. Zhang Y.Z., Shirata K, Wang J.X., Mao X.J., Matsumoto T., Liu Y. and Su T.T. Revision of spicule classification. *Astrophys. J.*, 2012, v. 750, 16 (9 pages).

29. Menzel D.H. A Study of the Solar Chromosphere. *Publications of the Lick Observatory*, University of California Press, Berkeley, CA, v. 17, 1931.

30. Menzel D.H. and Cillié G.G. Hydrogen emission in the chromosphere. *Astrophys. J.*, 1937, v. 85, 88–106.

31. Russell H.N. On the composition of the Sun's atmosphere. *Astrophys. J.*, 1929, v. 70, 11–82.

32. Khanna S.N. and Jena P. Atomic clusters: Building blocks for a class of solids. *Phys. Rev. B*, 1995, v. 51, no. 19, 13705–13716.

33. Bačić Z. and Miller R.E. Molecular clusters: Structure and dynamics of weakly bound systems. *J. Phys. Chem.*, 1996, v. 100, 12945–12959.

34. Alivisatos A.P., Barbara P.F., Castleman A.W., Chang J., Dixon D.A., Klein M.L, McLendon G.L., Miller J.S., Ratner M.A., Rossky P.J., Stupp S.I., Thompson M.E. From molecules to materials: Current trends and future directions. *Adv. Materials*, 1998, v. 10, no. 16, 1297–1336.

35. Claridge S.A., Castleman A.W., Khanna S.N., Murray C.B., Sen A. and Weiss P.S. Cluster-assembled materials. *ACS Nano*, 2009, v. 3, no. 2, 244–255.

36. Castleman A.W. and Bowen K.H. Clusters: Structure, energetics, and dynamics of intermediate states of matter. *J. Chem. Phys.*, 1996, v. 100, no. 31, 12911–12944.

37. Castlemann A.W. and Khanna S.N. Clusters, superatoms, and building blocks of new materials. *J. Phys. Chem. C*, 2009, v. 113, 2664–2675.

38. Bergeron D.E., Castleman A.W., Morisato T. and Khanna S.N. Formation of $Al_{13}I^-$: Evidence for the superhalogen character of Al_{13}. *Science*, 2004, v. 304, no. 5667, 84–87.

39. Kronik L., Fromherz R., Ko E., Ganterför G. and Chelikowsky J.R. Highest electron affinity as a predictor of cluster anion structures. *Nature Materials*, 2002, v. 1, no. 1, 49–53.

40. Konig L., Rabin I, Schultze W. and Ertl G. Chemiluminescence in the agglomeration of metal clusters. *Science*, 1996, v. 274, no. 5291, 1353–1355.

41. Ievlev D., Rabin I., Schulze W. and Ertl G. Light emission in the agglomeration of silver clusters. *Chem. Phys. Let.*, 2000, v. 328, 142–146.

42. Phillips K.J.H., Feldman U. and Landi E. Ultraviolet and X-ray Spectroscopy of the Solar Atmosphere. Cambridge University Press, Cambridge, U.K., 2008.

43. Babcock H.W. The Paschen series of hydrogen line in the spectrum of the solar chromosphere. *Pub. Astron. Soc. Pacific*, 1932, v. 44, no. 261, 323–324.

44. Becker R. Molecular hydrogen emission from star-forming regions in the Large Magellanic Cloud. *The Messanger*, 1989, v. 56, 57–59.

45. Arimoto N., Sofue Y. and Tsujimoto T. CO-to-H_2 conversion factor in galaxies. *Publ. Astron. Soc. Japan*, 1996, v. 48, 275–284.

46. Bolatto A.D., Wolfire M. and Leroy A.K. The CO-to-H_2 conversion factor. arXiv:1301.3498v2 [astro-phGA] (March 8, 2013).

47. Spinrad H. Observation of stellar molecular hydrogen. *Astrophys. J.*, 1966, v. 145, 195–205.

48. Jaeggli S.A., Lin H. and Uitenbroek H. On molecular hydrogen formation and the magnetohydrostatic equilibrium of sunspots. *Astrophys. J.*, 2012, v. 745, 133 (16pages).

49. Jordan C., Bueckner G.E., Bartoe J.D.F., Sandlin G.D. and Vanhoosier M.E. Emission lines of H_2 in the extreme-ultraviolet solar spectrum. *Astrophys. J.*, 1978, v. 226, 687–697.

50. Bartoe J.D.F., Brueckner G.E., Nicolas K.R., Sandlin G.D., Vanhoosier M.E. and Jordan C. H_2 emission in the solar atmosphere. *Mon. Not. Roy. Astron. Soc.*, 1979, v. 187, 463–471.

51. Sandlin G.D., Bartoe J.D.F., Brueckner G.E., Tousey R. and Vanhoosier M.E. The high-resolution solar spectrum, 1175–1770Å. *Astrophys. J. Suppl. Ser.*, 1986, v. 61, 801–898.

52. Innes D.E. SUMER-Hinode observations of microflares: excitation of molecular hydrogen. *Astron. Astrophys.*, 2008, v. 481, no. 1, L41–L44.

53. Przybilla N. and Butler K. The solar hydrogen spectrum in non-local thermodynamic equilibrium. *Astrophys. J.*, 2004, v. 610, L61–L64.

54. Robitaille P.M. Stellar opacity: The Achilles' heel of the gaseous Sun. *Progr. Phys.*, 2011, v. 3, 93–99.

55. Unsöld A. Über die Struktur der Fraunhofersehen Linien und die quantitative Spektralanalyse der Sonnenatmosphäre. *Zeitschrift für Physik*, 1928, v. 46, no. 11–12, 765–781.

56. Wöhl H. On molecules in sunspots. *Solar Phys.*, 1971, v. 16, 362–372.

57. Sinha K. Molecules in the Sun. *Proc. Astron. Soc. Australia*, 1991, v. 9, 32–36.

58. Olmsted C.M. Sun-spot bands which appear in the spectrum of a calcium arc burning in the presence of hydrogen. *Astrophys. J.*, 1908, v. 27, 66–69.

59. Shaw B.L. Inorganic Hydrides. Pergamon Press, Oxford, 1967.

60. Athay R.G. Line broadening in chromospheric spicules. *Astrophys. J.*, 1961, v. 134, 756–765.

61. Zirker J.B. The solar H and K lines of ionized calcium. *Solar Phys.*, 1968, v. 3, 164–180.

62. Gulyaev R.A. and Livshits M.A. Width of Ca^+H line in spicules. *Soviet Astron.*, 1966, v. 9, no. 4, 661–663.

63. Robitaille P.M. On solar granulations, limb darkening, and sunspots: Brief insights in remembrance of Father Angelo Secchi. *Progr. Phys.*, 2011, v. 3, 79–88.

LETTERS TO PROGRESS IN PHYSICS

The Liquid Metallic Hydrogen Model of the Sun and the Solar Atmosphere V. On the Nature of the Corona

Pierre-Marie Robitaille

Department of Radiology, The Ohio State University, 395 W. 12th Ave, Columbus, Ohio 43210, USA.
robitaille.1@osu.edu

The E-corona is the site of numerous emission lines associated with high ionization states (i.e. FeXIV-FeXXV). Modern gaseous models of the Sun require that these states are produced by atomic irradiation, requiring the sequential removal of electrons to infinity, without an associated electron acceptor. This can lead to computed temperatures in the corona which are unrealistic (i.e. ~30–100 MK contrasted to solar core values of ~16 MK). In order to understand the emission lines of the E-corona, it is vital to recognize that they are superimposed upon the K-corona, which produces a continuous spectrum, devoid of Fraunhofer lines, arising from this same region of the Sun. It has been advanced that the K-corona harbors self-luminous condensed matter (Robitaille P.M. The Liquid Metallic Hydrogen Model of the Sun and the Solar Atmosphere II. Continuous Emission and Condensed Matter Within the Corona. *Progr. Phys.*, 2013, v. 3, L8–L10; Robitaille P.M. The Liquid Metallic Hydrogen Model of the Sun and the Solar Atmosphere III. Importance of Continuous Emission Spectra from Flares, Coronal Mass Ejections, Prominences, and Other Coronal Structures. *Progr. Phys.*, 2013, v. 3, L11–L14). Condensed matter can possess elevated electron affinities which may strip nearby atoms of their electrons. Such a scenario accounts for the high ionization states observed in the corona: condensed matter acts to harness electrons, ensuring the electrical neutrality of the Sun, despite the flow of electrons and ions in the solar winds. Elevated ionization states reflect the presence of materials with high electron affinities in the corona, which is likely to be a form of metallic hydrogen, and does not translate into elevated temperatures in this region of the solar atmosphere. As a result, the many mechanisms advanced to account for coronal heating in the gaseous models of the Sun are superfluous, given that electron affinity, not temperature, governs the resulting spectra. In this regard, the presence of highly ionized species in the corona constitutes the thirty-first line of evidence that the Sun is composed of condensed matter.

> *In order to explain the occurrence of the dark lines in the solar spectrum, we must assume that the solar atmosphere incloses a luminous nucleus, producing a continuous spectrum, the brightness of which exceeds a certain limit. The most probable supposition which can be made respecting the Sun's constitution is, that it consists of a solid or liquid nucleus, heated to a temperature of the brightest whiteness, surrounded by an atmosphere of somewhat lower temperature.*
>
> Gustav Robert Kirchhoff, 1862 [1]

Superimposed on the continuous spectrum of the inner K-corona are emission lines, including one at 5303.3 Å, the famous line from coronium, first discovered by Harkness and Young [2, 3], photographed by Evershed [4], and eventually identified as FeXIV by Bengt Edlén [5–7]. Walter Grotian suggested that this line originated from highly ionized atoms, supported by early reports of similar findings from Bengt Edlén in such atoms [5–8]. The wonderful story of coronium [5, 6], along with the roles played by Walter Grotian and Bengt Edlén has been presented by Edward A. Milne [7].

Milne's account provides a key fact relative to coronium: the formation of FeXIV requires energy in the soft X-ray range of the electromagnetic spectrum [7], but the Sun emits very few of these rays. As such, how does one produce ions with such elevated ionization states in the corona?

Today, X-ray spectroscopy reveals that the Sun can produce emission lines from ions with ionization states as high as FeXXV [9]. Within the context of the gaseous models [10–12], the formation of such species calls for the removal of electrons from electronic shells to infinity, requiring energies associated with temperatures of ~30 MK [9, p. 26]. It has also been postulated that superhot thermal components ($>10^8$ K) can be generated above the limb in association with some flares [13] and radio studies initially called for temperatures of 10^8–10^{10} K in the corona [14, p. 128].

In 2000, the Bastille Day flare produced FeXII lines, but with a spine emmiting FeXXIV lines [9, p. 19]. If such findings are to be explained within the context of a gaseous solar model [10–12], it is not surprising that extreme temperatures must be invoked. A gaseous Sun has no other means of pro-

ducing highly ionized species.

At the same time, the extreme temperatures currently associated with the corona must be viewed with caution, given that the core of the Sun has been postulated to harbor temperatures of only ~16 MK [10, p. 9]. In addition, it is claimed that the energy source driving such extremes in temperature *"must be magnetic since all the other possible sources are completely inadequate"* [13]. Such statements, and the computed temperatures from which they stem, directly reflect the shortcomings of the gaseous solar models [10–12]. The need to explain the synthesis of highly ionized ions in the corona within a gaseous context is so acute that numerous schemes have been advanced to heat the chromosphere and corona [15, 16]. Ulmschneider states that *"The chromosphere and corona are thus characterized as layers which require large amounts of mechanical heating"* [15, p. 235] and further *"To clarify the zoo of coronal heating processes much further work remains to be done"* [15, p. 278].

Since the corona must be excessively hot to produce such ions in a gaseous context, the continuous spectrum of the K-corona has been dismissed as a strange artifact, produced by electronic scattering of photospheric light [17]. Otherwise, the coronal continuous spectrum would be indicating that *apparent coronal temperatures are no warmer than those of the photosphere.* It would be impossible for the gaseous models [10–12] to account for the presence of highly ionized species within the outer solar atmosphere. Consequently, sufficient electron densities are inferred to exist in the corona to support the idea that the spectrum of the K-corona is being produced by the scattering of photospheric light: *"The reason we see the corona in white, or integrated, light is that the photospheric light is scattered by coronal electrons: we see the light that does not get through but is scattered towards us. This scattered light is about 10^{-6} as intense as the photospheric light, which means it has been scattered by 10^{19} electrons; these are distributed along a path about equal to the diameter of the sun, or 1.4×10^{11} cm, so the average coronal density close to the surface must be 10^8 electrons/cm^3"* [14, p. 75]. Much like the solar surface [18], the relevance of a thermal spectrum in the K-corona has been rejected as little more than an optical illusion [17].

In the end, all extreme temperatures obtained from line emission should be dismissed as erroneous. Discovery of FeXXV within X-ray flares suggests that we do not properly understand the formation of emission lines with high ionization levels in the corona. Current temperature estimates are flirting with violations of both the first and second laws of thermodynamics: it is difficult to conceive that localized temperatures within flares and the corona could greatly *exceed* the temperature of the solar core.

Instead, line emission spectra from highly ionized ions might best be viewed as direct evidence that materials with elevated electron affinities exist within the corona. Such a solution can be readily associated with the condensed nature of the Sun [19–23].

In this regard, the continuous spectrum of the K-corona must be regarded as genuine [17]. The slight reddening of the K-corona, reported long ago by Allen [24], indicates that *apparent* coronal temperatures are gently decreasing with increasing distance above the solar surface. The corona seems to contain condensed matter of the same nature as found on the photosphere, since the spectrum of the K-corona, though devoid of Fraunhofer lines, is essentially identical to that produced by the solar surface [18]. This proposal is compelling, given that the Sun is expelling material into its corona which is also known to emit continuous visible spectra [25].

By extension, *apparent* coronal temperatures, which are likely to represent vibrational lattice phenomena [26–29], can be no greater than those found on the surface of the Sun. Therefore, contrary to popular scientific belief [15, 16], the corona of the Sun is *not* being heated. Rather, free atoms in the corona are being stripped of their electrons, as they interact with condensed matter which possesses much higher electron affinity. Neutral atoms have limited electron affinities, but molecules can have higher values.* However, condensed matter can develop enormous attractive forces for electrons.

This lesson is well manifested on Earth, as lightning attempts to equalize charge imbalance between separate regions of condensed matter [31–33]. Typically, lightning forms in clouds containing solid or liquid water particles. But it can also occur *"above volcanoes, in sandstorms, and in nuclear explosions"* [33, p. 67]. Usually, lightning forms between different cloud regions, or between clouds and the Earth's surface [31–33]. Lightning represents the longest standing example of the power of electron affinity in condensed matter. In this respect, while temperatures in the tens of thousands of degrees could be inferred from Hα line analysis during lightning activity,† scientists do not claim that the atmosphere of the Earth exists at these temperatures.

Thunderhead clouds can generate substantial steady electric fields on the order of 100 kVm^{-1} [33, p. 494]. Such fields have have been associated with runaway electrons capable of generating X-rays with energies of 100 KeV or more [33, p. 493-495]. Nonetheless, these energies are not translated into associated temperatures, as values in excess of 10^9 K would be derived. Still, for the purpose of this discussion, it is important to note that the presence of condensed matter in the atmosphere of the Earth can lead to amazing phenomena, when electric potentials are eliminated through charge transfer.

The author has advanced that the corona of the Sun is filled with sparse remnants of liquid metallic hydrogen [18] which have been expelled from the body of the Sun [25]. Such material is expected to have a highly conductive nature

---

*Of the elements, chlorine has the highest electron affinity at ~3.6 eV, calcium has the lowest value at ~0.02 eV; molecular RuF$_6$ has a value of ~7.5 eV [30]

†Peak temperatures of ~35,000 K have been reported [33, p. 163]

and could be used to harvest electrons from the corona, helping to ensure the continued neutrality of the solar body and solar winds. The presence of metallic hydrogen in the corona may then promote, through its elevated electron affinity, the creation of highly ionized species.

For instance, when iron comes in contact with metallic hydrogen, MH, it could initially form an activated complex, MH–Fe*, MH + Fe → MH–Fe*. This excited complex then relaxes by capturing n electrons from the iron atom. This could be accomplished with the simultaneous ejection of an activated iron species, Fe^{+n*}, leading to the following reaction: MH–Fe* → MH–$n\bar{e}$ + Fe^{+n*}. The resulting excited iron could then relax back to the ground state through line emission, Fe^{+n*} → Fe^{+n} + hv. Depending on the local electron affinity of metallic hydrogen, n could range from single digits to ∼25 [9] in the case of iron. A similar process could be invoked to create the other highly ionized species of the corona. In this regard, it is interesting to note that most of the ions observed in the solar *"XUV spectrum are principally those with one or two valence electrons"* remaining [14, 173].

In this scenario, the electron affinity of metallic hydrogen in the outer atmosphere responds to charge imbalances, either in the corona itself or on the surface of the Sun, by capturing electrons locally. Metallic hydrogen in the corona thereby acts as a conductive medium surrounding the solar body, constantly ensuring overall charge neutrality for the Sun. The arrangement of coronal steamers is highly suggestive of such a role from these objects, though all coronal structures might be involved in the recapture of electrons from the outer solar atmosphere.

Outstanding images of the corona have been obtained using spectroscopic lines from highly ionized iron (e.g. FeX–FeXIV) [34–37]. The presence of FeX–FeXIV throughout the solar atmosphere strengthens the concept that interactions between atoms and metallic hydrogen in the corona act to maintain neutrality on the Sun by producing highly ionized atoms throughout this region.

Moreover, flare studies indicate that coronal structures can display highly organized local electron affinities. As mentioned earlier, the TRACE team has produced a flare image where central spine structures produce line emission from FeXXIV and CaXVII, while the exterior of the flare emits in FeXII [9, p. 19]. Such images would be nearly impossible to explain in the context of a gaseous model of the Sun. Instead, organized structures within the corona and its components are strongly supportive of the idea that the Sun is comprised of condensed matter.

In closing, the liquid metallic hydrogen model of the Sun [19–23] provides an elegant solution for the production of highly ionized species in the corona. The wide variety of oxidation states can be simply obtained by invoking regions of varying electron affinity within the condensed structures that comprise the corona. The complete, or significant, removal of electrons from atoms can be explained using a single interaction, namely the temporary contact between atoms and metallic hydrogen.

The production of such ions in the gaseous models [10–12] requires the repeated ejection of electrons from their orbitals in a multistage process, whereby up to two dozen events must logically follow one another. Studies indicate the existence of species such as C^{+6}, Fe^{+14} and Fe^{+16} in the solar wind [38, p. 114]. Such ions require multiple steps for production in a gaseous context [10–12] and would be the result of random processes.

Conversely, the synthesis of highly ionized atoms requires but a single step in the liquid metallic hydrogen model [19–23]. The generation of such ions is no longer a random act, but rather a direct manifestation of the function of the corona, *facilitation of electron capture in the outer atmosphere of the Sun in order to preserve solar neutrality*. The production of highly ionized species throughout the corona therefore constitutes the thirty-first line of evidence that the Sun is composed of condensed matter.

Dedication

Dedicated to the poor, who sleep, nearly forgotten, under the light of the Southern Cross.

References

1. Kirchhoff G. The physical constitution of the Sun. In: *Researches on the Solar Spectrum and the Spectra of the Chemical Elements*. Translated by H.E. Roscoe, Macmillan and Co., Cambridge, 1862, p. 23.

2. Hufbauer K. Exploring the Sun: Solar Science since Galileo. The Johns Hopkins University Press, Baltimore, 1991, p. 112–114.

3. Dick S. Sky and Ocean Joined: The U.S. Naval Observatory 1830–2000. Cambridge University Press, Cambridge, 2003, p. 196-205.

4. Evershed J. Wave-length determinations and general results obtained from a detailed examination of spectra photographed at the solar eclipse of January 22, 1898. *Phil. Trans. Roy. Soc. London*, 1901, v. 197, 381–413.

5. Claridge G.C. Coronium. *J. Roy. Astron. Soc. Canada*, 1937, v. 31, no. 8, 337–346.

6. Unsigned. Origin of the coronium lines. *Nature*, 1942, v. 150, no. 3817, 756–759.

7. Milne A.E. Presidential Address – Award of the Gold Medal to Professor Bengt Edlén. *Mon. Not. Roy. Astron. Soc.*, 1945, v. 105, 138–145.

8. Grotian W. über die intensitätsverteilung des kontinuierlichen spektrums der inneren korona. *Zeitschrift fur Astrophysik*, 1931, v. 3, 199–226.

9. Phillips K.J.H., Feldman U. and Landi E. Ultraviolet and X-ray Spectroscopy of the Solar Atmosphere. Cambridge University Press, Cambridge, 2008.

10. Kippenhahn R. and Weigert A. Stellar structure and evolution. Springer-Verlag, Berlin, 1990.

11. Bachall J.N., Pinsonneault M.H. and Wasserburg G.J. Solar models with helium and heavy-element diffusion. *Rev. Mod. Phys.*, 1995, v. 67, no. 4, 781–808.

12. Robitaille P.M. The solar photosphere: Evidence for condensed matter. *Progr. Phys.*, 2006, v. 2, 17–21.

13. Priest E.R. Solar flare theory and the status of flare understanding. *High Energy Solar Physics: Anticipating HESSI (R. Ramaty and N. Mandzhavidze, Eds.), ASP Conf. Ser.*, 2000, v. 206, 13–26.

14. Zirin H. The Solar Atmosphere. Blaisdell Publishing Company, Waltham, M.A., 1966.

15. Ulmschneider P. The physics of the chromosphere and corona. In: *Lectures on Solar Physics* (H.M. Antia, A. Bhatnagar and R. Ulmschneider, Eds.), Springer, Berlin, 2003, p. 232–280.

16. Dwivedi B.N. The solar corona. In: *Lectures on Solar Physics* (H.M. Antia, A. Bhatnagar and R. Ulmschneider, Eds.), Springer, Berlin, 2003, p. 281–298.

17. Robitaille P.M. The Liquid Metallic Hydrogen Model of the Sun and the Solar Atmosphere II. Continuous Emission and Condensed Matter Within the Corona. *Progr. Phys.*, 2013, v. 3, L8–L10.

18. Robitaille P.M. On the Presence of a Distinct Solar Surface: A Reply to Hervé Faye. *Progr. Phys.*, 2011, v. 3, 75–78.

19. Robitaille P.M. A high temperature liquid plasma model of the Sun. *Progr. Phys.*, 2007, v. 1, 70–81 (also in arXiv: astro-ph/0410075).

20. Robitaille P.M. Liquid Metallic Hydrogen: A Building Block for the Liquid Sun. *Progr. Phys.*, 2011, v. 3, 60–74.

21. Robitaille P.M. Liquid Metallic Hydrogen II: A Critical Assessment of Current and Primordial Helium Levels in Sun. *Progr. Phys.*, 2013, v. 2, 35–47.

22. Robitaille J.C. and Robitaille P.M. Liquid Metallic Hydrogen III. Intercalation and Lattice Exclusion Versus Gravitational Settling and Their Consequences Relative to Internal Structure, Surface Activity, and Solar Winds in the Sun. *Progr. Phys.*, 2013, v. 2, 87-97.

23. Robitaille P.M. Commentary on the liquid metallic hydrogen model of the Sun. Insight relative to coronal holes, sunspots, and solar activity. *Progr. Phys.*, 2013, v. 2, L7–L9.

24. Allen C.W. The spectrum of the corona at the eclipse of 1940 October 1. *Mon. Not. Roy. Astron. Soc.*, 1946, v. 106, 137–150.

25. Robitaille P.M. The Liquid Metallic Hydrogen Model of the Sun and the Solar Atmosphere III. Importance of Continuous Emission Spectra from Flares, Coronal Mass Ejections, Prominences, and Other Coronal Structures. *Progr. Phys.*, 2013, v. 3, L11–L14.

26. Robitaille P.M. On the validity of Kirchhoff's law of thermal emission. *IEEE Trans. Plasma Sci.*, 2003, v. 31, no. 6, 1263–1267.

27. Robitaille P.M. A critical analysis of universality and Kirchhoff's law: A return to Stewart's law of thermal emission. *Prog. Phys.*, 2008, v. 3, 30–35.; arXiv:0805.1625.

28. Robitaille P.M. Blackbody radiation and the carbon particle. *Progr. Phys.*, 2008, v. 3, 36–55.

29. Robitaille P.M. Kirchhoff's Law of Thermal Emission: 150 years. *Progr. Phys.*, 2009, v. 4, 3–13.

30. Hayes W.M (Editor-in-Chief), CRC Handbook of Chemistry and Physics, 93rd Edition, Internet version 2013, 10:147–10:162.

31. Uman M.A. Lightning. Dover Publicatons. New York, N.Y., 1984.

32. Uman M.A. The Lightning Discharge (International Geophysics Series – Vol. 39), Academic Press, Inc., New York, N.Y., 1987.

33. Rakov V.A. and Uman M.A. Lightning: Physics and Effects. Cambridge University Press, Cambridge, U.K., 2003.

34. Wood B.E., Karovska M., Cook J.W., Brueckner G.E., Howard R.A., Korendyke C.M. and Socker D.G. Search for brightness variations in FeXIV coronagraph observations of the quiescent solar corona. *Astrophys. J.*, 1998, v. 505, 432–442.

35. Habbal S.R., Druckmüller M., Morgan H., Daw A., Johnson J., Ding A., Arndt M., Esser R., Rušin V. and Scholl I. Mapping the distribution of electron temperature and Fe charge states in the corona with total solar eclipse observations. *Astrophys. J.*, 2010, v. 708, 1650–1662.

36. Habbal S.R., Druckmüller M., Morgan H., Scholl I., Rušin V., Daw A., Johnson J. and Arndt M. Total solar eclipse observations of hot prominence shrouds. *Astrophys. J.*, 2010, v. 719, 1362–1369.

37. Habbal S.R., Morgan H. and Druckmüller M. A new view of coronal structures: Implications for the source and acceleration of the solar wind – First Asia-Pacific Solar Physics Meeting. *ASI Conf. Ser.*, 2011, v. 2, 259–269.

38. Gosling J.T. The solar wind in *Encyclopedia of the Solar System, 2nd Edition*, (L.A. McFadden, P.R. Weissman and T.V. Johnson, Eds.), Academic Press, San Diego, C.A., 2007, 99–116.

The Liquid Metallic Hydrogen Model of the Sun and the Solar Atmosphere VI. Helium in the Chromosphere

Pierre-Marie Robitaille

Department of Radiology, The Ohio State University, 395 W. 12th Ave, Columbus, Ohio 43210, USA.
robitaille.1@osu.edu

Molecular hydrogen and hydrides have recently been advanced as vital agents in the generation of emission spectra in the chromosphere. This is a result of the role they play in the formation of condensed hydrogen structures (CHS) within the chromosphere (P.M. Robitaille. The Liquid Metallic Hydrogen Model of the Sun and the Solar Atmosphere IV. On the Nature of the Chromosphere. *Progr. Phys.*, 2013, v. 3, 15–21). Next to hydrogen, helium is perhaps the most intriguing component in this region of the Sun. Much like other elements, which combine with hydrogen to produce hydrides, helium can form the well-known helium hydride molecular ion, HeH^+, and the excited neutral helium hydride molecule, HeH^*. While HeH^+ is hypothesized to be a key cosmological molecule, its possible presence in the Sun, and that of its excited neutral counterpart, has not been considered. Still, these hydrides are likely to play a role in the synthesis of CHS, as the He I and He II emission lines strongly suggest. In this regard, the study of helium emission spectra can provide insight into the condensed nature of the Sun, especially when considering the 10830 Å line associated with the $2^3P \rightarrow 2^3S$ triplet state transition. This line is strong in solar prominences and can be seen clearly on the disk. The excessive population of helium triplet states cannot be adequately explained using the gaseous models, since these states should be depopulated by collisional processes. Conversely, when He-based molecules are used to build CHS in a liquid metallic hydrogen model, an ever increasing population of the 2^3S and 2^3P states might be expected. The overpopulation of these triplet states leads to the conclusion that these emission lines are unlikely to be produced through random collisional or photon excitation, as required by the gaseous models. This provides a significant hurdle for these models. Thus, the strong $2^3P \rightarrow 2^3S$ lines and the overpopulation of the helium triplet states provides the thirty-second line of evidence that the Sun is comprised of condensed matter.

In order to explain the occurrence of the dark lines in the solar spectrum, we must assume that the solar atmosphere incloses a luminous nucleus, producing a continuous spectrum, the brightness of which exceeds a certain limit. The most probable supposition which can be made respecting the Sun's constitution is, that it consists of a solid or liquid nucleus, heated to a temperature of the brightest whiteness, surrounded by an atmosphere of somewhat lower temperature.

Gustav Robert Kirchhoff, 1862 [1]

Estimates of solar helium abundances have varied widely over the years. For instance, *"different methods and different data sets give values ranging from 20% to 40% of the Sun's mass"* [2, p. 381]. 'Primordial' helium levels strongly guide all solar helium abundance determinations, as the amount of helium in the stars is said to be closely correlated with the synthesis of this element soon after the Big Bang [3–6]. Helium abundances currently act as one of the "Great Pillars" of cosmology (see [7] for detailed discussion). As such, any attempt to alter accepted helium levels within the Sun has great implications throughout astrophysics.

Recently, the author has reviewed the determination of solar helium abundances and reached the conclusion that these levels are likely to have been overstated [7]. The most prudent outlook remains that the Sun, like the visible universe, is composed primarily of hydrogen, as first outlined by Cecilia Payne [8]. In this regard, Robitaille and Robitaille have highlighted that the solar body is apt to be excluding helium from its interior [9]. It is well-known that this element can be expelled from the Sun during periods of elevated solar activity with widely varying quantities observed in the associated solar wind [10–14]. As a result, it is unlikely that the Sun is harboring much helium [7, 9]. Significant levels of helium above the photosphere merely represent eons of helium synthesis in a hydrogen based Sun. It can be hypothesized that since helium cannot re-enter the Sun once expelled, it slowly accumulates as a gas within the chromospheric region.

In his classic textbook, *"Astrophysics of the Sun"*, Harold Zirin emphasized that the helium D3 line can be enhanced

more than 20 fold, as viewing moves from the center of the solar disk to just beyond the limb, displaying *"a sharp spike"* [15, p. 199–200]. He outlined that this emission *"comes from a low thin layer"* [15, p. 198]. Similarly, Zirin states that the triplet He I transition at 10830 Å is barely visible on the disk, but almost as strong as Hα at the limb [15, p. 199–200]. Moreover, he adds that the λ1640 line is known to increase in intensity at least fifteen times near the limb, while lines from neutral helium are enhanced 50 fold [15, p. 199–200]. Since helium emission peaks at ~1200 km above the photosphere, these findings strongly suggest that the element is floating in a cloud lying several hundred kilometers above the surface, although He remains sparse over coronal holes [15, p. 198].

At the same time, though relatively faint, helium lines are present in the spicules [16]. Since chromospheric structures, like spicules, have been hypothesized to be the site of hydrogen condensation in the solar atmosphere, it is important to understand why helium emission lines are associated with such objects.

Based on the chemiluminescence observed when silver clusters condense [17], the author has recently stated that all emission lines originating in the flash spectrum are a direct consequence of condensation in this region of the Sun [18]. By necessity, these exothermic condensation reactions involve the ejection of an excited atomic species from the condensate which can then relax back to a lower energy level through the emission of a photon. For instance, the Ca II emission, which is so typical of the chromospheric spectrum, has been hypothesized to involve the reaction of CaH and a condensed hydrogen structure, CHS [18], to create an excited complex, CHS + CaH $\rightarrow$ CHS–HCa*. This step is then followed by the exothermic expulsion of an excited Ca II ion, CHS–HCa $\rightarrow$ CHS–H + Ca^{+*}, and later by line emission from Ca II*, Ca^{+*} $\rightarrow$ Ca^{+} + $h\nu$. Similar reactions have been invoked for all the hydrides present on the Sun [18]. The most significant of these take place using molecular hydrogen, and this explains the prevalence of strong emission lines from this element in the chromosphere. In order to account for the He I and He II emission lines associated with the flash spectrum, a directly analogous scenario must be invoked, which this time requires a helium hydride molecular species.

Many charged molecular ions of helium have been studied. The most famous, helium hydride, HeH^{+}, *is ubiquitous in discharges containing hydrogen and helium.*" [19]. This molecular cation was first discovered experimentally in 1925 by Hogness and Lunn [20]. It has been the focus of extensive spectroscopic studies [21, 22] and also postulated to play a key role in chemical astrophysics [23–25]. Wolfgang Ketterle (Nobel Prize, Physics, 2001) was the first to obtain its spectroscopic lines [26, 27]. The molecule has a bond distance of 0.77Å and a dissociation energy of ~44.6 kcal mol^{-1} [19]. Although it exists only in the gas phase, its Brønsted acidity should be extremely powerful. As a result, the hydrogen hydride cation should have a strong tendency to donate a proton,
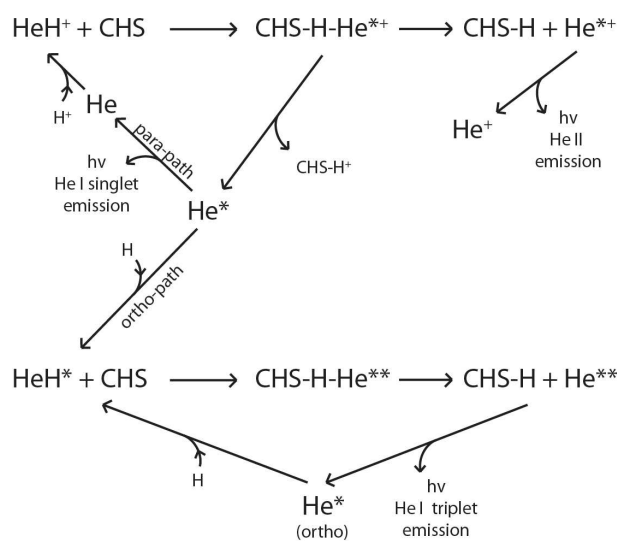

Fig. 1: Schematic representation of possible pathways involved when the helium hydride ion, HeH^{+}, or the excited helium hydride molecule, HeH*, react with condensed hydrogen structures, CHS, in the chromosphere of the Sun. The pathways presented can account for all emission lines observed from He I and He II. Note in this scheme that excited helium, He*, is being produced initially through the interaction of HeH^{+} with CHS. This excited helium, He*, if it assumes the triplet state (orthohelium — electrons in the same orientation: spin up/up or down/down), will then become trapped in the excited state. This triplet helium can then be used repeatedly, in cyclic fashion, to condense hydrogen atoms onto chromospheric structures, CHS (as shown in the lower half of the figure). Alternatively, if excited helium He* is initially produced in the singlet state (parahelium — electrons in different orientation: spin up/down), emission can immediately occur generating the singlet lines from He I. This scheme accounts for the strong triplet He I transition at 10830 Å observed in the flash spectrum of the chromosphere. Unlike the situation in the gas models, random collisional or photon excitations are not invoked to excite the helium atoms. As a result, de-excitation processes would also be absent, helping to ensure the buildup of triplet state orthohelium in this model.

without the concerted transfer of an electron.

In the chromosphere, the interaction between the helium hydride ion, HeH^{+}, and condensed hydrogen structures, CHS [18], could lead to an array of reactions as outlined in Fig. 1.

The simple combination of HeH^{+} and CHS could form an activated complex: CHS + HeH^{+} $\rightarrow$ CHS–H–He^{+*}. Exothermic expulsion of an excited helium ion, He^{+*}, could follow with full transfer of a proton and an electron to the condensed hydrogen structure: CHS–HHe^{+*} $\rightarrow$ CHS–H + He^{+*}. The resulting He^{+*} would be able to relax back to a lower energy state through emission, He^{+*} $\rightarrow$ He^{+} + $h\nu$, leading to the well known He II lines in the chromosphere (see Fig. 1).

Alternatively, when HeH^{+} reacts with CHS, it could lead initially to the same condensation adduct, CHS–H–He^{+*}, but this time, exothermic expulsion of an excited helium atom

could follow (see Fig. 1). Since HeH$^+$ should be a strong Brønsted acid, the transfer of a proton to the CHS could occur without electron transfer: CHS–HHe^{+*} → CHS–H$^+$ + He*. This leads to several phenomena.

First, the relaxation of an excited helium atom, does not involve the same processes which occur in the helium ion. This is because the He^{+*} possesses only a single electron. As such, the electron in He^{+*} can simply relax back down to any lower energy level, including the ground state, giving the well-known He II lines on the Sun.

Conversely, because an excited helium atom contains two electrons, the possible fate of this species is more complicated. Since one of the electrons has not been excited, it remains in the lowest energy state, with a given spin, either up or down. The excited electron is only allowed by selection rules to return to the ground state, if and only if, its spin is opposed to that of the ground state electron.

If the ground state electron is 'spin down', then the excited electron can make the transition back to the ground state if it is 'spin up'. Helium in this case is known as *parahelium* (or singlet helium), emphasizing that its two electrons have spins with opposite orientation. The singlet He* would simply relax back to the ground state, given rise to the emission lines from the neutral atom, He I, He* → He + $h\nu$. Likewise, if the ground state electron is 'spin up', the excited electron must be 'spin down' to enable the transition, He* → He + $h\nu$, again producing the identical He I lines from singlet state parahelium.

However, if the two electrons of He* have the same spin (both up or both down), then the excited electron cannot relax back to the ground state. It remains *trapped* in the excited state. Helium in this case is known as *orthohelium* (or triplet state helium), emphasizing that its two electrons have spins with the same orientation. It is the reactions of orthohelium which are of particular interest in this work, as their existence is elegantly accounted for through the condensation of hydrogen [18], as described below.

Since orthohelium is trapped in the excited triplet state, it has an opportunity to once again react with hydrogen, as displayed in the lower portion of Fig. 1. Wolfgang Ketterle has demonstrated that excited helium hydride also exists [28, 29]. Therefore, given a lack of relaxation, triplet He* could capture a hydrogen atom, forming neutral excited helium hydride: He* + H → HeH*. This species could once again react with CHS [18], but this time forming a doubly activated complex: CHS + HeH* → CHS–H–He**. The net transfer of a hydrogen atom in this case leads to release from the CHS of doubly excited helium.* When this occurs, the He** atom is now able to relax, as the excited electron which is now in the 2p or 3s orbital, undergoes a transition down to the 2s orbital. The

2^{3}P→2^{3}S transition is associated with the strong triplet He I line at 10830 Å observed in the prominences and on the disk of the Sun [30, p. 95]. Alternatively, a 3^{3}P→2^{3}S transition produces the triplet He I line at 3890 Å [30, p. 95].

As illustrated in Fig. 1, once the doubly excited helium atom has partially relaxed to regenerate orthohelium, it can react once again with atomic hydrogen, leading to the renewed synthesis of excited helium hydride, HeH*. A cyclic pathway has been created, wherein triplet hydrogen is preserved and continuously working to assist in the resynthesis of condensed hydrogen structures, as the Sun recaptures any atomic hydrogen lost to its atmosphere.

Importantly, the entire process is being 'primed' through the use of a single HeH$^+$ molecular ion and the intial transfer of a single proton to the CHS. This feature is noteworthy, since true condensation requires the transfer of electrons and protons to the chromospheric structures. In this regard, the generation of Ca II emission lines from analogous condensations of calcium hydride, involves the transfer of two electrons per hydrogen atom [18]. Such parallel reactions could help to ensure that overall charge balance in the building of condensed hydrogen structures can be maintained.

In the end, this approach holds many advantages over the random processes invoked by the gaseous models of the Sun in order to account for line emission in the chromosphere. All line emission in the chromosphere become directly associated with ordered reactions, whose product, CHS, are vital to preserving the solar mass. The Sun does not simply eject hydrogen into its atmosphere, without any hope of regaining these atoms. Rather, in the chromosphere, hydrogen atoms are constantly being recaptured through hydride based reactions. The triplet state of orthohelium, so strongly manifested within prominences and in the chromospheric emission spectrum, becomes not an incidental artifact, but rather, a necessary and direct manifestation that organized chemical reactions are taking place within the chromosphere. As such, the existence of this abundant orthohelium and the strong emission lines which it produces can be said to constitute the thirty-second line of evidence that the Sun is comprised of condensed matter.

Acknowledgment

Dedication

Dedicated to the poor, who sleep, nearly forgotten, under the light of the Southern Cross.

References

1. Kirchhoff G. The physical constitution of the Sun. In: *Researches on the Solar Spectrum and the Spectra of the Chemical Elements*. Translated by H.E. Roscoe, Macmillan and Co., Cambridge, 1862, p. 23.

---

*We can assume that the ground state electron remains stationary, but that the initially excited electron has now been transferred to an even higher atomic orbital. Alternatively, both electrons could be excited, but this case will not be considered.

2. Bhatnagar A. and Livingston W. Fundamentals of Solar Astronomy (World Scientific Series in Astronomy and Astrophysics – Vol. 6), World Scientific, New Jersey, 2005.

3. Peebles P.J.E. Primordial helium abundance and the primordial fireball. II. *Astrophys. J.*, 1966, v. 146, 542–552.

4. Danzinger I.J. The cosmic abundance of helium. *Ann. Rev. Astron. Astrophys.*, 1970, v. 8, 161–178.

5. Izotov Y.I. and Thuan T.X. The primordial abundance of 4He revisited. *Astrophys. J.*, 1998, v. 500, 188–216.

6. Olive K.A., Steigman G. and Walter T.P. Primordial nucleosynthesis: Theory and observations. *Phys. Rep.*, 2000, v. 333-334, 389–407.

7. Robitaille P.M. Liquid Metallic Hydrogen II: A critical assessment of current and primordial helium levels in Sun. *Progr. Phys.*, 2013, v. 2, 35–47.

8. Payne C.H. The relative abundances of the elements. Stellar Atmospheres. Harvard Observatory Monograph no. 1 (Harlow Shapley, Editor), Harvard University Press, Cambridge, MA, 1925 (reprinted in part in Lang K.R. and Gingerich O. A source book in astronomy and astrophysics, 1900–1975, Harvard University Press, Cambridge, MA, 1979, p. 245–248).

9. Robitaille J.C. and Robitaille P.M. Liquid metallic hydrogen III. Intercalation and lattice exclusion versus gravitational settling and their consequences relative to internal structure, surface activity, and solar winds in the Sun. *Progr. Phys.*, 2013, v. 2, 87–97.

10. Robbins D.E., Hundhausen A.J. and Bame S.J. Helium in the solar wind. *J. Geophys. Res.*, 1970, v. 75, no. 7, 1178-1187.

11. Bame S.J., Asbridge J.R., Feldman W.C. and Gosling J.T. Evidence for a structure-free state at high solar wind speeds. *J. Geophys. Res.*, 1977, v. 82, no. 10, 1487–1492.

12. Borrini G., Gosling J.T., Bame S.J. and Feldman W.C. Helium abundance enhancements in the solar wind. *J. Geophys. Res*, 1982, v. 87, no. A9, 7370–7378.

13. Aellig M.R., Lazarus A.J. and Steinberg J.T. The solar wind helium abundance: Variations with wind speed and solar cycle. *Geophys. Res. Let.*, 2001, v. 28, no. 14, 2767–2770.

14. Kasper J.C., Stevens M.L., Lazarus A.J. and Ogilvie K.W. Solar wind and helium abundance as a function of speed and heliographic latitude: Variation through a solar cycle. *Astrophys. J.*, 2007, v. 660, 901–910.

15. Zirin H. Astrophysics of the Sun. Cambridge University Press, Cambridge, U.K., 1988.

16. Zirin H. The mystery of the chromosphere. *Solar Phys.*, 1996, v. 169, 313–326.

17. Konig L., Rabin I, Schultze W. and Ertl G. Chemiluminescence in the agglomeration of metal clusters. *Science*, 1996, v. 274, no. 5291, 1353–1355.

18. Robitaille P.M. The Liquid Metallic Hydrogen Model of the Sun and the Solar Atmosphere IV. On the Nature of the Chromosphere. *Progr. Phys.*, 2013, v. 3, L15–L21.

19. Grandinetti F. Helium chemistry: A survey of the role of the ionic species. *Inter. J. Mass Spectrom.*, 2004, v. 237, 243–267.

20. Hogness T.R. and Lunn E.G. The ionization of hydrogen by electron impact as interpreted by positive ray analysis. *Phys. Rev.*, 1925, v. 26, 44–55.

21. Tolliver D.E., Kyrala G.A and Wing W. H. Observation of the infrared spectrum of helium-hydride molecular ion ^{4}HeH$^+$. *Phys. Rev. Let.*, 1979, v. 43, no. 23, 1719–1722.

22. Crofton M.W., Altman R.S., Haese N.N. and Oka T. Infrared spectra of ^{4}HeH$^+$, ^{4}HeD$^+$, ^{3}HeH$^+$, and ^{3}HeD$^+$. *J. Chem. Phys.*, 1989, v. 91, 5882–5886.

23. Roberge W. and Dalgarno A. The formation and destruction of HeH$^+$ in astrophysical plasmas. *Astrophys. J.*, 1982, v. 255, 489–496.

24. Engel E.A., Doss N., Harris G.J. and Tennyson J. Calculated spectra for HeH$^+$ and its effect on the opacity of cool metal-poor stars. *Mon. Not. Roy. Astron. Soc.*, 2005, v. 357, 471–477.

25. Galli D. and Palla F. The chemistry of the early universe. *Astron. Astrophys.*, 1998, v. 335, 403–420.

26. Ketterle W., Figger H. and Walther H. Emission spectra of bound helium hydride. *Phys. Rev. Lett.*, 1985, v. 55, no. 27, 2941–2944.

27. www.nobelprize.org/nobel_prizes/physics/laureates/2001/ketterle.html

28. Ketterle W., Figger H. and Walther H. Emission spectra of bound helium hydride. *Phys. Rev. Lett*, 1985, v. 55, 2941–2944.

29. Ketterle W., Dodhy A. and Walther H. Bound-free emission of the helium hydride molecule. *Chem. Phys. Let.*, 1986, v. 129, no. 1, 76–78.

30. Zirin H. The Solar Atmosphere. Blaisdell Publishing Company, Waltham, MA, 1966.

The Liquid Metallic Hydrogen Model of the Sun and the Solar Atmosphere VII. Further Insights into the Chromosphere and Corona

Pierre-Marie Robitaille

Department of Radiology, The Ohio State University, 395 W. 12th Ave, Columbus, Ohio 43210, USA.
robitaille.1@osu.edu

In the liquid metallic hydrogen model of the Sun, the chromosphere is responsible for the capture of atomic hydrogen in the solar atmosphere and its eventual re-entry onto the photospheric surface (P.M. Robitaille. The Liquid Metallic Hydrogen Model of the Sun and the Solar Atmosphere IV. On the Nature of the Chromosphere. *Prog. Phys.*, 2013, v. 3, L15–L21). As for the corona, it represents a diffuse region containing both gaseous plasma and condensed matter with elevated electron affinity (P.M. Robitaille. The Liquid Metallic Hydrogen Model of the Sun and the Solar Atmosphere V. On the Nature of the Corona. *Prog. Phys.*, 2013, v. 3, L22–L25). Metallic hydrogen in the corona is thought to enable the continual harvest of electrons from the outer reaches of the Sun, thereby preserving the neutrality of the solar body. The rigid rotation of the corona is offered as the thirty-third line of evidence that the Sun is comprised of condensed matter. Within the context of the gaseous models of the Sun, a 100 km thick transition zone has been hypothesized to exist wherein temperatures increase dramatically from 10^4–10^6 K. Such extreme transitional temperatures are not reasonable given the trivial physical scale of the proposed transition zone, a region adopted to account for the ultra-violet emission lines of ions such as C IV, O IV, and Si IV. In this work, it will be argued that the transition zone does not exist. Rather, the intermediate ionization states observed in the solar atmosphere should be viewed as the result of the simultaneous transfer of protons and electrons onto condensed hydrogen structures, CHS. Line emissions from ions such as C IV, O IV, and Si IV are likely to be the result of condensation reactions, manifesting the involvement of species such as CH_4, SiH_4, H_3O^+ in the synthesis of CHS in the chromosphere. In addition, given the presence of a true solar surface at the level of the photosphere in the liquid metallic hydrogen model, it follows that the great physical extent of the chromosphere is supported by gas pressure, much like the atmosphere of the Earth. This constitutes the thirty-fourth line of evidence that the Sun is comprised of condensed matter.

> *In order to explain the occurrence of the dark lines in the solar spectrum, we must assume that the solar atmosphere incloses a luminous nucleus, producing a continuous spectrum, the brightness of which exceeds a certain limit. The most probable supposition which can be made respecting the Sun's constitution is, that it consists of a solid or liquid nucleus, heated to a temperature of the brightest whiteness, surrounded by an atmosphere of somewhat lower temperature.*
>
> Gustav Robert Kirchhoff, 1862 [1]

1 Introduction

If our current understanding of the solar atmosphere appears strained, it is because the gaseous models of the Sun offer no means, other than elevated temperatures, to account for the presence of highly ionized ions in the corona [2]. As a consequence, temperature values ranging from 10^7–10^{11} K have been inferred to exist in the solar atmosphere [3, p. 172].

Such extreme temperatures should have suggested long ago that the methods utilized to infer coronal temperatures could not be valid, given that the core of the Sun is believed to sustain temperatures of only $\sim 1.6 \times 10^7$ K [4, p. 9]. The claim that temperatures in localized regions of the corona can be 1 000 times higher than within the solar core, challenges reason.

Furthermore, by accepting elevated coronal temperatures, proponents of the gaseous models must discount the continuous emission of the K-corona as illusionary and produced by the photosphere (see [2] for a completed discussion). The continuous spectrum of the K-corona, devoid of Fraunhofer lines, does closely replicate the emission of the photosphere itself, but the spectrum reddens with elevation [2]. If this spectrum was considered as generated by the corona, then the apparent temperature of the outer solar atmosphere would be no higher than that observed on the surface of the Sun.*

---

*Note that the apparent temperature of the photosphere ($\sim$6 000 K), does not manifest the true energy content of this region. Rather, the author has claimed that it reflects that amount of energy which is contained within the

Should it be true that coronal apparent temperatures are no greater than photospheric values, then it is impossible, within the context of a gaseous Sun, to account for the presence of highly ionized ions (e.g. CaXVII and FeXXIV [6, p. 19]) in the corona. Devoid of condensed matter, the only possible means of generating such ions must rest on temperature. As a result, despite the realization that the spectrum of the K-corona implies that the corona is self-luminous and displays an apparent temperature no higher than that of the photosphere [2], advocates of the gaseous models of the Sun have no choice but to postulate that coronal apparent temperatures far exceed those of the solar surface.

Two problems come to the forefront relative to using elevated temperatures to explain the presence of highly ionized species within the corona. First, extreme temperatures (10^7–10^{11} K [3, p. 172]) must be assumed. Second, the continuous spectrum of the K-corona must be discounted as a byproduct of photospheric light which has been scattered in the solar atmosphere by relativistic electrons (see [2] for a complete discussion).

Moreover, in order to account for the emission lines from ions such as C IV, O IV, and Si IV, gaseous models must incorporate an extremely thin transition zone, whereby apparent temperatures rapidly rise from chromospheric to coronal values over the span of 100 km or less, as illustrated in Fig. 1.
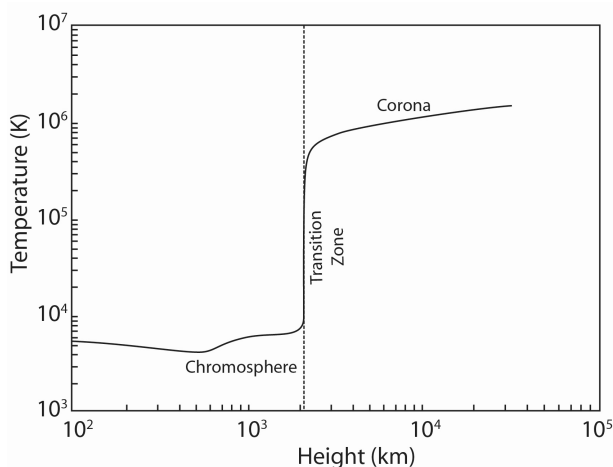

Fig. 1: Schematic representation of the temperature stratification in the solar atmosphere displaying the pronounced increase in the transition zone located at an elevation of ~2 000 km (dashed line). This figure is based on a discussion presented by Phillips, Feldman, and Landi [6] and is an adaptation of their Fig. 1.1.

2 Temperature Stratification

In his chapter on the chromosphere and corona, P. Ulmschneider states, *"While the corona extends to many solar radii the*

vibrational degrees of freedom found in the photospheric lattice [5].

chromosphere is a layer of only 2 or 3 thousand km thickness which becomes visible near the start and end of a total eclipse. The chromosphere got its name from the prominent red emission of the Hα line of neutral hydrogen at 6563Å. The chromosphere is a layer where the temperature rises from photospheric values of between 4 000 and 6 000 K to about 20 000 K and where neutral hydrogen is still present. In the region of a few 100 km thickness between the chromosphere and corona, called transition layer, hydrogen becomes ionized and the temperature increases from 20 000 to millions of K" [7, p. 232–233].

A. Bhatnagar outlines that *"Between the upper layer of the chromosphere and corona (although the demarcation is not sharp) lies the 'transition layer', where the temperature rises very steeply, from about 25 000 to 500 000 K in height difference of just 1 000 km"* expanding the extent of the transition region by a factor of 10 [8, p. 32]. Conversely, Phillips, Felman, and Landi emphasize *"Model calculations indeed suggest that the transition zone is extremely thin, less than 100 km"* [6, p. 220].

Such dimensions on the Sun are essentially beyond the limit of reliable detection with current instrumentation. Thus, it is interesting to highlight that *"A growing corpus of observations, particularly those starting with the Skylab mission, showed that the transition zone has a much larger extent than was indicated in the earlier models, leading to a revision of our ideas of its nature..."* [6, p. 210].

Harold Zirin, in candid fashion, reminds his readers that anyone with a ruler can establish that the chromosphere can attain elevations of at least 5 000 km from Hα emissions [9]. He reports that, when viewed in Hα, macrospicules can be seen to extend to 20 000 km [9]. How can neutral hydrogen be found at these heights, if the corona already reaches temperatures of 10^6 K just after the transition zone? If the corona was at millions of degrees, neutral hydrogen should not be found at 20 000 km, a region well within the coronal domain.

The situation is aggravated by the realization that H_{Lym} lines have been known to exist in the corona beyond $1.5 R_\odot$ for more than forty years [10]. This region extends beyond the entire vertical range displayed in Fig. 1. Furthermore, Dermendjiev et al. report, from direct photographic visualization in Hα, that faint lines from neutral hydrogen can be observed far into the corona, causing the authors to postulate how the corona could be 'cooled' to allow for the presence of such a line [11]. Yet, models of the solar atmosphere predict that neutral hydrogen should be absent at elevations beyond 2 000 km, where temperatures approaching 10 000 K already result in the complete ionization of this element (see e.g. Table 4.6 in [12, p. 146–147]).

At the same time, highly ionized Fe lines (FeX–FeXIV) have been used to image the solar corona in great detail and indicate that these species can be found at elevations well inferior to the known locations of neutral hydrogen emission lines [13–16]. Clearly, it is not possible for emission lines

which, according to the gaseous models of the Sun, require millions of degrees for formation (FeX–FeXIV) to be juxtaposed with Hα lines which are unable to withstand such temperatures. The only solution rests in recognizing that the formation of highly ionized emission lines in the corona stems not from extreme temperatures, but from electron affinity [2]. It should not be inferred that the outer atmosphere of the Sun maintains a temperature stratification which *increases* with increased distance away from the solar body.

3 On The Validity of Temperature Measurements

In order to support the gaseous models, coronal temperatures have been estimated using four key methods [17, p. 178–185]: 1) doppler broadening of emission lines, 2) density gradients in the corona, 3) radio brightness, and 4) ionization equilibrium. All of these methods provide slightly differing answers [3, p. 165–166], but they share a common overarching result: coronal temperatures are thought to be extremely high. In the end, careful analysis reveals that each of these methods is problematic.

3.1 Doppler Broadening of Emission Lines

Doppler broadening of emission lines (e.g. [6, p. 41–43], [17, p. 178–180], [18, p. 90–94]) has been used extensively to set coronal temperatures. The broadening of an emission line, in this case, is assumed to be thermal in nature. The problems of assigning temperatures with such methods are numerous. Zirin [17, p. 178-180] outlines how separate elements can easily produce differing line widths and associated temperatures. Nonetheless, he concludes that valid coronal temperatures can be derived from such methods.

More than fifty years ago, Jefferies and Orrall addressed the problem of obtaining prominence temperatures by employing spectral line widths stating, *"If the broadening is supposed due to thermal motions of the emitting atoms, then, to the extent that the profiles are Gaussian, the hydrogen line widths imply temperatures of over a hundred thousand degrees and the metals of over five million degrees"* [19]. However, it is not possible to have neutral hydrogen present at a temperature of over a hundred thousand degrees, given that the element has been modeled as fully ionized at ∼10 000 K (see e.g. Table 4.6 in [12, p. 146–147]).

Jefferies and Orrall continue, *"To avoid the necessity of considering such unacceptably high and discordant temperatures, the hypothesis is frequently made that the line broadening is due both to thermal motions of atoms and to mass motions of small prominence elements having a Maxwellian distribution of velocities. One may, on this basis, compare the widths of lines from two ions of very different atomic weights to find a hypothetical "temperature," T_H and "mean velocity," ξ_H. If the hypothesis is wrong, T_H and ξ_H will, in general, bear no obvious relationship to the kinetic temperature or mean random-velocity fields which they are intended to describe.* While the truth of the hypothesis has come more and more to be taken for granted, it seems to us that the evidence in its favor is rather slight and certainly insufficient to allow its uncritical acceptance. We have already ... suggested that the hypothesis may be invalid for analyzing widths of hydrogen and helium lines in quiescent prominences; in this paper we present evidence for its possible failure in active flare-type events"* [19].

Though the discussion by Jefferies and Orrall cannot be cited in its entirety, the authors go on to make the point that the use of line width analysis could, in fact, lead to *negative* temperatures. Furthermore, they clearly discount the existence of temperatures in the 500 000–1 000 000 K range [19].

Despite Jefferies and Orrall [19], today it is commonplace to infer temperatures from line widths and ascribe any *excessive line shape distortion* to velocity. That is, if the line shape is distorted, either in the low (red) or high (blue) frequency range, net velocities will be added (e.g. see Eq. 2.30 in [6]) which can help account for the distortion. Examples can be found throughout the astrophysical literature (e.g. [20]).

The situation is complicated by the realization that, in addition to thermal effects, the line widths of atoms can be altered by pressure, Stark, and electron broadening mechanisms [21, p. 202-233]. However, the derivation of temperatures from line widths in the solar atmosphere is much more precarious than these considerations or the discussions from Jefferies and Orrall [19] might suggest.

Collisional line broadening with condensed matter could greatly impact the line widths under observation. Such line broadening will be affected by the abundances of condensed material and gaseous atoms in the corona and, most importantly, by the extent of the interaction between any given element and such objects. Furthermore, tight coupling between gaseous atoms and condensed matter could dramatically alter line shapes outside the effects of velocity. In light of the evidence for the presence of condensed matter in the corona [2], all temperature measurements from line widths should be reconsidered.

3.2 Density Gradients

Density gradient approaches rely on the use of the white-light continuous spectrum observed in the corona [17, p. 178–180] or chromosphere [22, p. 170–228]. Modern theory assumes that this spectrum has been produced by scattering photospheric light through the action of relativistic electrons, thereby enabling a temperature for the corona to be inferred [17, p. 111–121]. The difficulty with such an approach lies in the assumption that the corona is not self-luminous and that its spectrum arises from photospheric light which must be scattered. However, if the corona is indeed self-luminous and cool [2], as implied by the presence of neutral hydrogen even up to 1.5R$_\odot$ [10], then this entire line of reasoning must be re-evaluated.

3.3 Radio Measurements

Of the four methods for determining coronal temperatures, the final two are perhaps the weakest [17, p. 178–180]. In the end, radio measurements [18, p. 242–247] should be considered with great caution, even though Professor Zirin has stated that they are *"the most dependable data we have"* [9]. Radio data are highly dependent on the input variables (i.e. electron and ion density) which must be modeled in order to obtain brightness temperatures (e.g. see Table I in [9], [12, p. 133–141], and [23]). All determinations of solar brightness temperatures are inherently linked to *a priori* knowledge of electron densities [22, p. 265] which can only be estimated using modeling, *". . . it is evident that the quantities $N_e(h)$ and $T_e(h)$ are too inextricably mixed to be seperately derivable from radio observations alone"* [12, p. 137]. Since radio models cannot disentangle electron density from brightness temperatures, they are often guided by results obtained using optical density gradient methods [22, p. 266]. Direct measurements of electron density remain unavailable and theoretical values may not be accurate.

Radio measurements of brightness temperatures are also highly dependent on wavelength and scattering processes (see e.g. [12, p. 133–141], [22, p. 261–271], and [23]). Widely conflicting data can be obtained (e.g. temperatures of only $300\,000$ at $1.6R_\odot$ [23]). In fact, radio observations appear to be the source of the most extreme temperature values 10^8–10^{10} K [17, p. 128], while scientists remain confronted with addressing values as low as 10^4 K obtained with such methods (see e.g. [12, p. 133–141] and [23]). As a result, it would be imprudent to place an emphasis on coronal or chromospheric temperatures obtained from radio measurements.

3.4 Ionization Equilibrium

It has already been established that ionization calculations result in models of the solar atmosphere which greatly underestimates the presence of neutral hydrogen in the corona. Consequently, it is evident that temperatures derived from ionization equilibrium must be regarded with caution.

As a rule, coronal temperatures derived from ionization equilibrium tend to be too low to accomodate the gaseous models of the Sun [17, p. 181]: *"We must admit, however, that the ionization theory not only gives the wrong temperature, but fails to account for the many stages of ionization observed in the corona. It is possible that temperature variations explain that fact; we can only wait for better observations of the line profiles of intermediate ions to confirm the existence of temperature differences. It is more likely that there is something erroneous in our basic concept of how ionization takes place; but so far, we do not know what this is"* [17, p. 183]. Immediately after writing these lines, Professor Zirin offers what he believes to be the answer: recombination, a process whereby a single electron is captured by an ion leaving it in double excited state, could be much more

important in the corona, resulting in a calculated temperature near 2 MK [17, p.184].

In 1966, Zirin had hoped that more UV data would soon be available to lift the cloud of mystery which surrounded ionization equilibrium calculations [17, p. 181–185]. In fact, the new data only added further confusion. Thirty years later, he would write, *"One would think that observations of the solar ultraviolet would solve many of the problems. However, the intensity of these lines was very much lower than expected and to this day images with adequate resolution have not been obtained. While the UV mimics the radio images, brightening in the network, it is impossible to tell if it comes from the spicules or the magnetic regions at their base. The lines show a deep minimum in intermediate ionization stages of C, N, and O . . . and the brightness temperature in the extreme ultraviolet scarcely exceeds 4 000 degrees. This gives a remarkable contradiction. Lines are observed of high ionization stages such as carbon 4, neon 5, oxygen 5, which are only formed at temperatures of 100 000 degrees or more but with brightness temperatures 20 times less"* [9]. Nearly forty years after Professor Zirin produced his classic text [17], coronal temperatures from ionization equilibrium are still viewed as too low [3, p. 165–166].

The proper discussion of ionization equilibrium is best reserved for a full treatment. However, suffice to state that methods which depend on the ionization equations are complex (see [24] for a partial review), involving knowledge of whether or not the region of interest can be considered to be in local thermal equilibrium (LTE). E.A. Milne highlighted that the exterior regions of the Sun cannot be considered to adhere to LTE conditions [25, p. 81–83]. Even chromospheric ionization processes depend on non-equilibrium treatments [18, p. 194–198], even if LTE methods continue to be used (see [26] for a brief discussion). Unfortunately, the fluxes associated with such processes remain largely unknown and numerous assumptions will be involved in extracting temperatures with such methods.

In the end, none of the methods utilized to extract coronal temperatures are reliable. Rather, any perceived agreement between approaches is likely to be the result of the desire to *set a reasonable temperature for the corona.* Each method contains enough latitude to permit conformity by altering the value of those input parameters which can only be obtained from theory.

4 The Corona Revisited

Professor Harold Zirin had suspected that *". . . there is something erroneous in our basic concept of how ionization takes place"* [17, p. 183]. However, given the belief that the Sun was a gas, no other plausible mechanism of formation could be advanced. Today, the situation has changed dramatically, as a great deal of evidence is building that the Sun is condensed matter (see [2, 24, 27–30] and references therein).

For instance, it is now understood that the corona possesses *"...a radially rigid rotation of 27.5 days synodic period from 2.5 $R_\odot$ to >15$R_\odot$"* [3, p. 116]. This finding by Lewis et al. [31] provides the thirty-third line of evidence that the Sun is comprised of condensed matter. The rigid rotation of the corona is highly suggestive that it possesses condensed matter whose associated magnetic field lines are anchored at the level of the photosphere. Such a structure, if endowed with a elevated electron affinity [2], would provide an elegant network for channeling electrons from the outer reaches of the solar atmosphere onto the photospheric surface. Thus, the corona should be viewed as being in direct contact with the photosphere.

In order to understand ionization states it is important to recognize that condensed matter controls the behavior of the Sun. As previously stated [2], within the solar atmosphere, atoms and ions are being stripped of their electrons by metallic hydrogen present in the corona. Such a process can help ensure that the solar body remains electrically neutral, as electrons are continually conducted back onto the solar surface from the far reaches of the corona. It is known that the electrical conductivity of the corona is extremely high [3, p. 174]. This is in accord with a condensed solar state, which extends into the corona, even if gases are also present in this region.

5   The Chromosphere Revisited

The author has already addressed the chromosphere in detail, as a region of hydrogen re-condensation, superimposed on the corona in the lower portion of the solar atmosphere [28, 29]. He has suggested, that unlike the corona, the chromosphere is not composed of hydrogen in the metallic state. Rather, in the chromosphere, atomic and ionic hydrogen is interacting with other atoms to form hydrides [28, 29] which can be used to build condensed hydrogen structures (CHS). CHS can then bring the harvested hydrogen back onto the solar surface, perhaps using intergrannular lanes [28]. As such, the chromosphere overlaps with the corona. The two regions contain different types of material: metallic in the corona [2] and non-metallic in the chromosphere [28, 29]. Chromospheric material will regain metallic properties once it enters the solar interior, where increased pressures can be used to re-synthesize metallic hydrogen [30].

The tremendous height, 5 000 to 10 000 km, of the chromosphere has posed a longstanding problem for the gaseous models of the Sun [3, p, 140-142]. Early chromospheric models inferred a density scale height of only 150 km [3, p. 140-142]. McCrea [32] attempted to build additional scale height by suggesting that turbulent motions might provide additional support for the chromosphere [3, p. 140-142]. Modern models have extended the theoretical treatment of the scale height problem (see [26] for a brief discussion). But, still today, it remains difficult for the gaseous models of the Sun to account for the presence and extent of the chromosphere. Zirin highlights, *"It was clear that the apparent scale height of 1 000 km far exceeded that in hydrostatic equilibrium. In modern times a convenient solution has been found – denial ... We cannot explain the great height or the erroneous models ... While models place this at 2 000 km, the data say 5 000"* [9]. If it is impossible for the gaseous models to properly account for the great height of the chromosphere, the cause is simple to understand. It is not possible for a gas to support itself. But relative to structural support, gas pressure has been utilized in modern solar theory to explain why a gaseous Sun does not collapse on itself. However, such arguments have been discounted, precisely because a gaseous object cannot possess true surfaces [33]. Without a support mechanism, a gaseous Sun cannot exist [33].

Conversely, within the context of a condensed solar body [33], the Sun does not collapse upon itself because liquids and solids are essentially incompressible. Furthermore, unlike the case with the gaseous Sun, the chromosphere can now be easily supported using gas pressure. This same mechanism is responsible for the support of the Earth's atmosphere (see [33] for a larger discussion). When a gaseous atom encounters a real surface, it reverses its course creating a net upward force. Such a mechanism provides a genuine means of supporting the chromosphere and thereby constitutes the thirty-fourth line of evidence that the Sun is condensed matter (see [2, 24, 27–30, 33] and references therein for the others).

6   The Transition Zone Revisited

Within the gaseous models of the Sun, a transition zone has been conceived in order to account for the existence of ions with *intermediate* levels of ionization. Species such as C IV, O IV, and Si IV come to mind in this regard. Since the intensity of all transition zone lines are low, modern models simply create an extremely narrow region of the solar atmosphere to account for this lack of signal, as illustrated in Fig. 1. Nonetheless, C IV, O IV, and Si IV remain interesting, as they could be created by stripping hydrides such as CH_4, H_3O^+, and SiH_4 of their hydrogen [28]. The vibrational signatures of these molecules (the C-H, O-H, and Si-H stretches) have been observed on the Sun [34]. The author has already suggested that the chromosphere is a region of hydrogen re-condensation where hydrides play an important role [28, 29]. It remains reasonable to conclude that the transition zone does not exist. Rather, the ions which are currently associated with this region of the solar atmosphere are simply involved in the transfer of multiple protons and electrons onto the condensed hydrogen structures, CHS, which constitute the chromosphere. This region of the solar atmosphere therefore plays a vital role in preserving the mass of the Sun and ensuring that metallic hydrogen can eventually be re-synthesized within its interior.

7 Conclusion

Through a recent series of publications (most notably [2, 28, 29]), the author has endeavored to alter our understanding of the solar atmosphere. Rather than a chaotic assembly of gaseous plasma, the chromosphere and corona become the site of both structure and function in the Sun. Such structure is dismissed by the gaseous models, whose advocates prefer to speak of visualizing *"force balance"* [26], rather than real objects. At the same time, the history observational solar physics is replete with scientists, like Father Angelo Secchi, who believed that they were seeing real structures on the Sun [35, 36]. In a parallel line of reasoning, the gaseous models provide no true function, either for the chromosphere or the corona. Conversely, in the liquid metallic model, the corona harnesses electrons [2], the chromosphere condenses hydrogen atoms [28, 29]. In the corona, highly ionized ions are produced when their parent atoms, or ions, come into contact with metallic hydrogen which possesses an elevated electron affinity. They are thereby stripped of their electrons [2]. The metallic hydrogen which is present in the corona has been projected into the solar atmosphere from its site of formation below the surface of the Sun [2]. Since condensed matter appears likely to exist in the corona, it is not tremendously hot, but maintains an apparent temperature which decreases with elevation from the solar body. In the chromosphere, where non-metallic condensed hydrogen structures are formed, the ionization states revealed from emission lines are linked to key hydride based chemical processes [28, 29]. The transition zone does not exist. It serves a purpose only in the context of the gaseous solar models. Much has been advanced recently relative to the condensed nature of the Sun [2, 24, 27–30, 33] and much remains to be considered. In the end, given the ever mounting evidence for condensed matter (see [2, 24, 27–30, 33] and references therein), eventually the elegance and simplicity of these models will surely come to be recognized.

Acknowledgment

Luc Robitaille is acknowledged for figure preparation.

Dedication

This work is dedicated to the memory of Captain Corona [37], Professor Harold Zirin, whose books [17,18] and articles (e.g. [9]) were both illuminating in their discourse and refreshing in their candor.

References

1. Kirchhoff G. The physical constitution of the Sun. In: *Researches on the Solar Spectrum and the Spectra of the Chemical Elements*. Translated by H.E. Roscoe, Macmillan and Co., Cambridge, 1862, p. 23.

2. Robitaille P.M. The Liquid Metallic Hydrogen Model of the Sun and the Solar Atmosphere V. On the nature of the corona. *Progr. Phys.*, 2013, v. 3, L22-L25.

3. Bhatnagar A. and Livingston W. Fundamentals of Solar Astronomy (World Scientific Series in Astronomy and Astrophysics - Vol. 6), World Scientific, New Jersey, 2005.

4. Kippenhahn R. and Weigert A. Stellar structure and evolution. Springer-Verlag, Berlin, 1990.

5. Robitaille P.M. On the temperature of the photosphere: Energy partition in the Sun. *Progr. Phys.*, 2011, v. 3, 89–92.

6. Phillips K.J.H., Feldman U. and Landi E. Ultraviolet and X-ray Spectroscopy of the Solar Atmosphere. Cambridge University Press, Cambridge, 2008.

7. Ulmschneider P. The physics of the chromospheres and coronae. In: *Lectures on Solar Physics* (H.M. Antia, A. Bhatnagar and R. Ulmschneider, Eds.), Springer, Berlin, 2003, p. 232–280.

8. Bhatnagar A. Instrumentation and observational techniques in solar astronomy. In: *Lectures on Solar Physics* (H.M. Antia, A. Bhatnagar and R. Ulmschneider, Eds.), Springer, Berlin, 2003, p. 27–79.

9. Zirin H. The mystery of the chromosphere. *Solar Phys.*, 1996, v. 169, 313–326.

10. Gabriel A.H., Garton W.R.S., Goldberg L., Jones T.J.L., Jordan C., Morgan F.J., Nicholls R.W., Parkinson W.J., Paxton H.J.B., Reeves E.M., Shenton C.B., Speer R.J. and Wilson R. Rocket observations of the ultraviolet solar spectrum during the total eclipse of 1970 March 7. *Astrophys. J.*, 1971, v. 169, 595–614.

11. Dermendjiev V.N, Mouradian Z., Duchlev P. and Leroy J.L. Faint H alpha emission in the solar corona: Morphological, situational and hydromagnetic analysis. *Solar Phys.*, 1994, v. 149, no. 2, 267–277.

12. Bray R.J. and Loughhead R.E. The Solar Chromosphere (The International Astrophysics Series), Chapman and Hall, London, U.K., 1974.

13. Wood B.E., Karovska M., Cook J.W., Brueckner G.E., Howard R.A., Korendyke C.M. and Socker D.G. Search for brightness variations in FeXIV coronagraph observations of the quiescent solar corona. *Astrophys. J.*, 1998, v. 505, 432–442.

14. Habbal S.R., Druckmüller M., Morgan H., Daw A., Johnson J., Ding A., Arndt M., Esser R., Rušin V. and Scholl I. Mapping the distribution of electron temperature and Fe charge states in the corona with total solar eclipse observations. *Astrophys. J.*, 2010, v. 708, 1650–1662.

15. Habbal S.R., Druckmüller M., Morgan H., Scholl I., Rušin V., Daw A., Johnson J. and Arndt M. Total solar eclipse observations of hot prominence shrouds. *Astrophys. J.*, 2010, v. 719, 1362–1369.

16. Habbal S.R., Morgan H. and Druckmüller M. A new view of coronal structures: Implications for the source and acceleration of the solar wind – First Asia-Pacific Solar Physics Meeting. *ASI Conf. Ser.*, 2011, v. 2, 259–269.

17. Zirin H. The Solar Atmosphere. Blaisdell Publishing Company, Waltham, M.A., 1966.

18. Zirin H. Astrophysics of the Sun. Cambridge University Press, Cambridge, U.K., 1988.

19. Jefferies J.T and Orrall F.Q. On the interpretation of prominence spectra. II. The line and continuous spectrum of the spray-type limb event of March 7, 1959. *Astrophys. J.*, 1961, v. 133, 946–962.

20. Fleck B., Brekke P., Haugan S., Sanchez Duarter L., Domingo V., Gurman J.B. and Poland A.I. Four years of SOHO discoveries – Some highlights. *ESA Bulletin 102*, May 2000. (Available online sohowww.nascom.nasa.gov/publications/ESA_Bull102.pdf).

21. Gray D.F. The observation and analysis of stellar photospheres (Cambridge Astrophysics Series), 2nd Edition, Cambridge University Press, Cambridge, U.K., 1995.

22. Thomas R.N. and Athay R.G. Physics of the Solar Chromosphere. Interscience Publishers, New York, N.Y., 1961.

23. Thejappa G. and MacDowall R.J. Effects of scattering on radio emission from the quiet Sun at low frequencies. *Astrophys. J*, 2008, v. 676, no. 2, 1338–1345.

24. Robitaille P.M. Liquid metallic hydrogen II. A critical assessment of current and primordial helium levels in the Sun. *Progr. Phys.*, 2013, v. 2, 35–47.

25. Milne E.A. Thermodynamics of the stars. *Handbuch der Astrophysik*, 1930, v. 3, Part 1, 65–255 (also in Menzel D.H. Selected Papers on the Transfer of Radiation: 6 papers by Arthur Schuster, K. Schwarzschild, A.S. Eddington, S. Rosseland, E.A. Milne. Dover Publications, Inc., New York, 1966, 77–269).

26. Judge P. Observations of the solar chromosphere (Solar MHD Theory and Observations: A High Spatial Resolution Perspective). *ASP Conf. Series*, 2006, v. 354, 259–275.

27. Robitaille P.M. The liquid metallic hydrogen model of the Sun and the solar atmosphere III. Importance of continuous emission spectra in flares, coronal mass ejections, prominences, and other coronal structures. *Progr. Phys.*, 2013, v. 3, L11–L14.

28. Robitaille P.M. The liquid metallic hydrogen model of the Sun and the solar atmosphere IV. On the nature of the chromosphere. *Progr. Phys.*, 2013, v. 3, L15–L21.

29. Robitaille P.M. The liquid metallic hydrogen model of the Sun and the solar atmosphere VI. Helium in the chromosphere. *Progr. Phys.*, 2013, v. 3, L26–L28.

30. Robitaille P.M. Liquid metallic hydrogen: A building block for a liquid Sun. *Progr. Phys.*, 2011, v. 3, 60–74.

31. Lewis D.J., Simnett G.M., Brueckner G.E., Howard R.A., Lamy P.L. and Schwenn R. LASCO observations of the coronal rotation. *Solar Phys.*, 1999, v. 184, no. 2, 297–315.

32. McCrea W.H. The hydrogen chromosphere. *Mon. Not. Roy. Astron. Soc.*, 1929, v. 29, 483–497.

33. Robitaille J.C. and Robitaille P.M. Liquid Metallic Hydrogen III. Intercalation and Lattice Exclusion Versus Gravitational Settling and Their Consequences Relative to Internal Structure, Surface Activity, and Solar Winds in the Sun. *Progr. Phys.*, 2013, v. 2, 87-97.

34. Sinha K. Molecules in the Sun. *Proc. Astron. Soc. Australia*, 1991, v. 9, 32–36.

35. Robitaille P.M. A thermodynamic history of the solar constitution – I: The journey to a gaseous Sun. *Progr. Phys.*, 2011, v. 3, 3–25.

36. Robitaille P.M. A thermodynamic history of the solar constitution - II: The theory of a gaseous Sun and Jeans' failed liquid alternative. *Progr. Phys.*, 2011, v. 3, 41–59.

37. Caltech News 1/12/2012, Harold Zirin, 82 (http://www.caltech.edu/article/295 Accessed online on 5/23/2013).